

FINAL REPORT

STUDY OF AEROTHERMODYNAMIC PHENOMENA  
ASSOCIATED WITH REENTRY OF MANNED SPACECRAFT

by

L. F. Hearne

J. H. Chin

L. W. Woodruff

Y-78-66-1

May 1966

Work Carried Out Under Contract NAS 9-3531

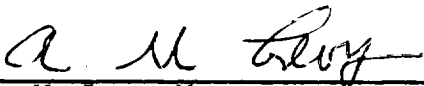
LOCKHEED MISSILES & SPACE COMPANY

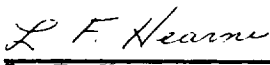


FOREWORD

This document comprises the Final Report on a study performed by Lockheed Missiles & Space Co. for the National Aeronautics and Space Administration under Contract NAS 9-3531. The work was conducted during the period from November 1964 to May 1966 under the direction of the Manned Spacecraft Center, Houston, Texas. Dr. John Bertin was the NASA technical monitor.

Approved by:

  
A. M. Levy, Manager  
Launch & Entry Thermodynamics

  
L. F. Hearne, Project Leader  
Launch & Entry Thermodynamics



## SUMMARY

This study was conducted to provide a comprehensive description of the phenomena affecting aerothermal heating of manned vehicles traveling in the atmosphere at superorbital velocity. It has culminated with the development of techniques for prediction of heating and for interpretation of heat sensor measurements. This report presents a review of the phenomenological studies and a discussion of analysis methods. Application of the prediction techniques is also illustrated. The results have direct application to the Apollo Command Module.

The problem of describing the aerothermal environment is a formidable one, involving consideration of many complex, interacting processes. The phenomena governing the inviscid flow, radiative heat transfer, and convective heat transfer have been investigated. Consideration is given to the effects of non-equilibrium chemistry, radiative energy transport, mass injection and flow asymmetry in analysis of the shock-layer conditions. The influence on radiative heat transfer of energy loss, spectral absorption, and flow contamination by ablation products is examined. The dependence of convective heating on chemical-reaction kinetics, shock generated vorticity, mass transpiration, heterogeneous surface reactions, boundary-layer transition, and flow separation is assessed. The most important of these phenomena are identified and prediction techniques accounting for their effects are formulated after review of the existing theory and experimental results. A series of computer programs which may be used for detailed calculations of the aerothermal environment or for routine heating history computations are presented.

The results obtained for Apollo reflect the importance of energy loss and self-absorption on radiative heating. The influence of ablation

product injection on radiative energy transport appears to be small, but the effect on convective heating is major. Flow asymmetry and boundary-layer transition also exert large influence on the convective heating.

Verification of predictions by in-flight measurement of the actual heat transfer is highly desirable. Ideally, this may be accomplished by mounting calorimeters on the heat shield. In practice, sensor design and data interpretation problems arise. Installation of a sensor in an ablating heat shield disturbs the homogeneity of the surface conditions and thus the heating sensed by the calorimeter differs from that to the surrounding heat shield. Furthermore, sensor output is perturbed by internal heat exchange.

The factors affecting heat transfer measurements are delineated in this report. Procedures are presented for a first order estimate of the effects on sensor heating due to the streamwise variations in surface temperature and the discontinuities in surface mass injection and wall chemical reactivity. The thermal performance characteristics of both capacitance and asymptotic type calorimeters are analyzed and theoretical models for characterizing their response under transient, non-uniform heating conditions are presented. Automated procedures for reduction of data to be obtained in Apollo flight tests are given.

## ACKNOWLEDGEMENTS

The authors wish to express their sincere appreciation for the many contributions made by their associates in conduct of this study and in preparation of the final report. Particular thanks are due to J. M. Lefferdo for his aid in investigations of the inviscid flow field and convective heat transfer; to W. D. Coleman for his work on theoretical modeling of heat shield performance and heat sensor-environment interactions; and to L. Gallagher for his effort in formulating and coding numerical schemes for digital computer solution of the equations governing the aerothermal environment. We are also grateful to P. J. Schneider for his support and technical review of heat sensor performance analyses; to J. D. Weisner and H. E. Goldstein for their respective work on absorption coefficients and thermochemical properties; to W. E. Nicolet and A. C. Buckingham for their work on non-equilibrium radiation; and to H. Hoshizaki for his many helpful suggestions. Acknowledgement is given to C. J. Lambert and D. W. Gillette for their support in performing the computations and preparing illustrations.





## CONTENTS

Section		Page
	FOREWORD	iii
	SUMMARY	v
	ACKNOWLEDGEMENTS	vii
	ILLUSTRATIONS	xiii
	TABLES	xxi
1	INTRODUCTION	1-1
	1.1 Study Objectives	1-2
	1.2 Study Scope	1-2
	1.3 Technical Approach	1-3
	1.4 Plan of Report	1-4
2	AEROTHERMAL ENVIRONMENT PREDICTION	2-1
	2.1 Inviscid Flow	2-2
	2.1.1 Phenomenological Review	2-2
	2.1.2 Prediction Techniques	2-8
	2.1.3 Flow Field Results	2-33
	2.2 Radiation Heat Transfer	2-41
	2.2.1 Phenomenological Review	2-42
	2.2.2 Prediction Techniques	2-46
	2.2.3 Radiation Heating Results	2-72
	2.3 Convective Heat Transfer	2-78
	2.3.1 Phenomenological Review	2-79
	2.3.2 Prediction Techniques	2-96
	2.3.3 Convective Heating Results	2-124
	2.4 Afterbody Environment	2-128
	2.4.1 Phenomenological Review	2-128
	2.4.2 Prediction Techniques	2-132

2.5	Environmental Histories	2-138
2.5.1	Unified Calculation Procedure	2-139
2.5.2	Entry Heating	2-140
2.6	Summary	2-144
2.6.1	Conclusions	2-145
2.6.2	Recommendations	2-148
	References	2-151
	Notation	2-172
Appendices		
2A	Spreading Coordinate	2A-1
2B	Thermodynamics and Transport Properties	2B-1
2C	Non-Equilibrium Effects	2C-1
2D	Convective Heating with Three-Dimensional Flow	2D-1
2E	Convective Heating with External Vorticity	2E-1
2F	Empirical Criterion for Boundary Layer Transition	2F-1
2G	Performance Model for Heat Shield Material	2G-1
2H	Mass Transpiration Effects on Convective Heat Transfer	2H-1
2I	Protuberance Effects on Convective Heat Transfer	2I-1
3	AERODYNAMIC HEATING MEASUREMENT	3-1
3.1	Calorimeter Environment	3-2
3.1.1	Phenomenological Review	3-2
3.1.2	Prediction Techniques	3-8
3.2	Calorimeter Performance	3-29
3.2.1	Slug Calorimeter	3-41
3.2.2	Asymptotic Calorimeter	3-55
3.3	Data Interpretation Techniques	3-64
3.3.1	Prediction of Calorimeter Response	3-65
3.3.2	Prediction of Environment	3-69
3.3.3	Influence of Uncertainties	3-70

3.4	Summary	3-72
3.4.1	Conclusions	3-72
3.4.2	Recommendations	3-75
	References	3-76
	Notation	3-79



## ILLUSTRATIONS

Figure		Page
1-1	General Configuration of Apollo Command Module	1-8
1-2	Apollo Trajectory I	1-9
1-3	Apollo Trajectory II	1-10
1-4	Apollo Trajectory III	1-11
2-1	Apollo Flow Field Characteristics	2-179
2-2	Influence of Non-Equilibrium on Thermodynamics State, Trajectory III, Stagnation Point	2-180
2-3	Influence of Shock Density Ratio on Shock Layer Thickness	2-181
2-4	Chemical History for Non-Equilibrium Flow, Altitude 200,000 Ft., Velocity 30,000 Ft./Sec.	2-182
2-5	Variation of Non-Equilibrium Zone Thickness with Altitude	2-183
2-6	Boundary-Layer Displacement Thickness, Trajectory III, Geometric Center	2-184
2-7	Ablation History of Heat Shield, Trajectory III, Geometric Center	2-185
2-8	Mass-Injection-Parameter History, Trajectory III, Geometric Center	2-186
2-9	Geometry for Spreading Coordinate Calculation	2-187
2-10	Comparison of Surface Pressure Distribution Predictions for a Hemisphere	2-188
2-11	Shock Layer Thickness and Surface Pressure Distribution for Apollo, Ideal Gas Flow	2-189
2-12	Shock Layer Characteristics for a Spherically-Blunted Body at 20 Deg. Angle-of-Attack	2-190

2-13	Predicted Shock Layer Conditions for Apollo, Velocity 35,000 Ft./Sec., Altitude 200,000 Ft.	2-191
2-14	Shock Configuration in Plane of Symmetry	2-192
2-15	Influence of Flight Condition on Shock Layer Flow Profiles, Geometric Center of Apollo	2-193
2-16	Spreading Coordinate for Apollo, 25 Deg. Angle-of-Attack	2-194
2-17	Influence of Energy Losses on Shock Layer Conditions Apollo, 25 Deg. Angle-of-Attack	2-195
2-18	Influence of Uncertainty in Stagnation Point Location	2-196
2-19	Influence of Spreading Coordinate	2-197
2-20	Radiation Regimes	2-198
2-21	Influence of Radiative Energy Loss on Shock Layer Radiation	2-199
2-22	Absorption Coefficient of Heated Air	2-200
2-23	Equilibrium Composition of Boundary Layer	2-201
2-24	Apollo Boundary Layer Profile with Injection of Ablation Products	2-202
2-25	Absorption Coefficient for the Contaminated Boundary Layer	2-203
2-26	Stagnation Point Heat Flux	2-204
2-27	Spectral Stagnation Heat Fluxes	2-205
2-28	Stagnation Region Shock Layer Thicknesses	2-206
2-29	Stagnation Region Flow Profiles	2-207
2-30	Spectral Stagnation Heat Fluxes, Six-Band Model	2-208
2-31	Apollo Stagnation Point Radiation	2-209
2-32	Apollo Shock Layer Optical Thicknesses, Two Bands, Stagnation Region	2-210
2-33	Apollo Radiation Loss Parameter	2-211
2-34	Apollo Radiation Loss Parameter	2-212
2-35	Apollo Stagnation Point Radiation	2-213
2-36	Apollo Configuration and Surface Pressure Distribution	2-214
2-37	Optical Thickness Distribution for Apollo, Two Bands	2-215
2-38	Total Heat Flux Distribution for Apollo, Two Bands	2-216

2-39	High Frequency Heat Flux Distributions for Apollo, Two Band Model	2-217
2-40	Low Frequency Heat Flux Distributions for Apollo, Two Band Model	2-218
2-41	Temperature Profiles for Apollo, $S/R_{\max} = 0.25$	2-219
2-42	Temperature Profiles for Apollo, $S/R_{\max} = 1.61$	2-220
2-43	Effect of Altitude on Total Heat Flux for Apollo, Two Band Model	2-221
2-44	Comparison of Two-Band and Six-Band Heat Fluxes, Apollo	2-222
2-45	Optical Thicknesses Distribution, Apollo, Six-Band Model	2-223
2-46	Effect of Pressure Distribution and Absorption Coefficients on Apollo Heat Flux	2-224
2-47	Outer-Edge Conditions for Apollo Boundary Layer	2-225
2-48	Inner-Edge Conditions for Apollo Boundary Layer	2-226
2-49	Influence of Flow Geometry on Apollo Convective Heating Distribution	2-227
2-50	Characteristics of Protuberance - Boundary Layer Interaction	2-228
2-51	Comparison of Vorticity Interaction Solutions	2-229
2-52	Influence of Shock-Generated Vorticity on Apollo Heating	2-230
2-53	Limiting Effects of Wall Catalycity on Apollo Heating with Chemically Frozen Boundary Layer	2-231
2-54	Damkohler Numbers for Apollo Boundary Layer	2-232
2-55	Extent of Departure from Chemical Equilibrium	2-233
2-56	Influence of Non-Equilibrium on Apollo Heating with a Highly Catalytic Wall	2-234
2-57	Ablation Product Injection History, Geometric Center, Trajectory III	2-235
2-58	Influence of Mass Injection on Apollo Heating	2-236
2-59	Influence of Radiative Energy Loss on Convective Heating, Neglecting Absorption Effects	2-237
2-60	Comparison of the Effects of Mass Injection and Radiative Energy Loss in Apollo Heating	2-238

2-61	Influence of Non-Similar Wall Conditions on Apollo Heating	2-239
2-62	Comparison of Laminar and Turbulent Transfer Rates for Apollo	2-240
2-63	Turbulence Pattern for Several Assumed Transition Reynolds Number	2-241
2-64	Influence of Transition Criterion on Total Heat Transfer	2-242
2-65	Variation of Transition Reynolds Number with Local Mach Number	2-243
2-66	Transpiration Uncertainty	2-244
2-67	Correlating Functions for Foreign Gas Injection	2-245
2-68	Predicted Laminar Heating Distribution for Apollo at Wind Tunnel Conditions	2-246
2-69	Influence of Flight Condition on Laminar Heat Transfer Distribution	2-247
2-70	Influence of Shock-Generated Vorticity on the Heat Transfer Distribution	2-248
2-71	Predicted Turbulent Heat Transfer Distribution for Apollo at Wind Tunnel Conditions	2-249
2-72	Influence of Flight Conditions on Turbulent Heat Transfer Distribution	2-250
2-73	Momentum Thickness Reynolds Number Distribution Factor for Apollo	2-251
2-74	Transition Sensitivity to Altitude	2-252
2-75	Empirical Pressure Distribution for Afterbody, Windward Side	2-253
2-76	Predicted Laminar Heat Transfer Distribution over Apollo Afterbody	2-254
2-77	Influence of Free Stream Conditions on Convective Heat Transfer Distribution over Apollo Afterbody	2-255
2-78	Turbulent Heat Transfer Distribution over Apollo Afterbody, Windward Side	2-256



2-79	Computer Codes for Prediction of Environment	2-257
2-80	Influence of Entry Condition on Apollo Heating	2-258
2-81	Heat Transfer and Shield Ablation, Trajectory III, Geometric Center	2-259
2-82	Heat Transfer and Shield Ablation, Trajectory III, $\bar{S}/R_M = 0.72$	2-260
2-83	Heat Transfer and Shield Ablation, Trajectory III, $\bar{S}/R_M = -0.93$	2-261
2-84	Predicted Movement of Boundary Layer Transition, Trajectory III	2-262
2-85	Heat Transfer and Shield Ablation, Trajectory III, Geometric Center, Laminar Flow	2-263
2-86	Predicted Total Heat Transfer for Apollo, Trajectory III	2-264
2-87	Predicted Afterbody Heating Histories, Trajectory I	2-265
2-88	Influence of Mass Injection on Afterbody Heating	2-266
2-89	Heat Shield Response on Apollo Afterbody	2-267
2B-1	Low-Frequency Air Absorption Coefficients	2B-12
2B-2	High-Frequency Air Absorption Coefficients, Two Band Model	2B-13
2B-3	N <sub>2</sub> Burge-Hopfield Band System Frequency-Dependent Factor	2B-14
2B-4	N Continuum Spectral Absorption Coefficients, Six-Band Model	2B-15
2C-1	Location of Overshoot Region	2C-14
2C-2	Radiation Heating Data	2C-15
2F-1	Comparison of Observed and Predicted Heat Rates, X-17 Flight R-2	2F-5
2F-2	Apparent Boundary Layer Transition Times, RTV X-17 Vehicle, Flight R-26	2F-6
2F-3	Reynolds Number at Time of Boundary Layer Transition	2F-7
2F-4	Influence of Roughness Ratio on Transition Reynolds Number	2F-8
2F-5	Boundary Layer Conditions on Apollo Vehicle at Approxi- mate Time of Peak Heating	2F-9
2G-1	Specific Heat of a Typical Heat Shield Material and Char	2G-20
2G-2	Enthalpy of a Typical Heat Shield Material and Char	2G-21

2G-3	Thermal Conductivity of a Typical Heat Shield Material	2G-22
2G-4	Enthalpy of a Typical Heat Shield Material Pyrolysis Gases	2G-23
2G-5	Specie Concentrations in a Typical Heat Shield Material Pyrolysis Gases	2G-24
2G-6	Heat of Decomposition of a Typical Heat Shield Material	2G-25
2G-7	Experimental TGA Data for a Typical Heat Shield Material	2G-26
2G-8	Arrhenius Correlation of TGA Rate Data for a Typical Heat Shield Material	2G-27
2G-9	TGA Data for a Typical Heat Shield Material	2G-28
2G-10	Comparison of Air-Arc Test Data and Predictions	2G-29
2H-1	Correlation of Foreign Gas Injection for Laminar Axi- symmetric Stagnation Point Flow	2H-18
2H-2	Comparison of Experimental and Theoretical Laminar Mass Transfer Cooling at the Axisymmetric Stagnation Point	2H-19
2H-3	Influence of Mass Injection and Its Distribution on Skin Friction	2H-20
2H-4	Influence of Pressure Gradient on Mass Transfer Cooling in the Laminar Boundary Layer	2H-21
2H-5	Correlation of Foreign Gas Injection	2H-22
2H-6	Variation of Transformed Surface Coordinate for Apollo Vehicle in Plane of Symmetry	2H-23
2H-7	Effect of Air Injection on the Turbulent Stanton Number and Recovery Factor	2H-24
2H-8	Influence of Pressure Gradient on the Mass Transfer Cool- ing in Turbulent Flow	2H-25
2H-9	Effect of Foreign Gas Injection on the Turbulent Stanton Number	2H-26
2H-10	Effect of Foreign Gas Injection on the Turbulent Heat Flux	2H-27
2I-1	Distribution of Interference Factors for a Protruding Cylinder in Flat Plate Turbulent Flow	2I-10

2I-2	Correlation of Center Line Interference Factors for a Protruding Cylinder in Flat Plate Turbulent Flow	2I-11
2I-3	Approximate Boundary Layer Characteristics on Apollo Forebody	2I-12
3-1	Calorimeter-Environment Interaction	3-83
3-2	Heat Transfer to Graphite Sensor	3-84
3-3	Decay of the Laminar Skin Friction Reduction Downstream of the Transpiration Region	3-85
3-4	Decay of the Laminar Heat Transfer Reduction Downstream of the Transpiration Region - Comparison with Exact Solution	3-86
3-5	Influence of Upstream Injection on the Downstream Heat Transfer	3-87
3-6	Influence of Upstream Injection on Non-Isothermal Effect	3-88
3-7	Qualitative Comparison of Actual and Approximate Com- bustion Rates	3-89
3-8	Influence of Reaction Rate Discontinuity on Surface Combustion	3-90
3-9	Calorimeter Characteristics	3-91
3-10	Ideal Aerothermal Heat Rate Sensors	3-92
3-11	Slug and Asymptotic Calorimeters	3-93
3-12	Temperature Measurement Disturbances	3-94
3-13	Corrected Heat-Flux History for Calorimeter Study Input	3-95
3-14	Calorimeter Geometry and Principle Temperature Calcula- tion Points	3-96
3-15	Steady-State Effectiveness of Rhodium Shields	3-97
3-16	Instantaneous Calorimeter Surface Temperature Distribution	3-98
3-17	Instantaneous Temperature Distribution at $\theta = 60$ Sec.	3-99
3-18	Sensor Data Reduction	3-100
3-19	Influence of Sensor Tabs on Temperature Response	3-101
3-20	Comparison of Approximate and Detailed Temperature Solutions	3-102

3-21	Non-Isothermal Wall Effect on Asymptotic Calorimeter Output	3-103
3-22	Non-Isothermal Wall Effect on the Heating Rate to an Asymptotic Calorimeter	3-104
3-23	Non-Isothermal Wall Effect on the Temperature of an Asymptotic Calorimeter	3-105
3-24	Heat Shield-Sensor Interactions	3-106
3-25	Calorimeter Temperature Response	3-107
3-26	Surface Erosion	3-108
3-27	Sensor Temperature Response	3-109
3-28	Asymptotic Calorimeter Response	3-110
3-29	Environment Prediction Uncertainty	3-111
3-30	Sensor Convective Heating Uncertainty	3-112
3-31	Sensor Temperature Uncertainty	3-113

## TABLES

Table		Page
1-1	Phenomena Affecting Aerothermal Environment	1-6
1-2	Phenomena Affecting Heat Transfer Measurement	1-7
2-1	Unit Conversion Factors	2-42
2-2	Radiation-Coupling Effect on Convection	2-92
2-3	Summary of Boundary Layer Investigations	2-100
2B-1	Correlation Formula Coefficients, Air	2B-10
2B-2	Spectral Ranges and Absorption Processes for "Six-Band" Model	2B-6
2C-1	Non-Equilibrium Characteristics of the Streamlines Traced	2C-7
2C-2	Oscillator Strengths and Statistical Weights	2C-10
2G-1	Materials Properties	2G-18
2G-2	Comparison of Air-Arc Data - Surface Recession with Prediction	2G-19
2H-1	Experimental Measurements of the Effects of Gas Injec- tion on the Turbulent Heat Transfer	2H-17
3-1	Assumed Calorimeter's Thermophysical Constants	3-82



## Section 1

### INTRODUCTION

The design of manned spacecraft for Earth return from lunar and planetary missions is sensitively dependent upon the heating experienced during atmospheric braking. Extreme heat loads may be experienced with resultant high heat shielding weights. In order to insure design adequacy while avoiding costly conservatism, procedures for realistic description of the aerothermal environment are required. In addition, verification of these procedures at simulated flight conditions or in actual flight tests is necessary.

The flow about a vehicle traveling at superorbital velocity may be influenced by a number of complex, interacting processes including chemical-kinetic processes, radiative energy transport, and ablation product injection. While extensive research has been performed on the various phenomena, much of it has been highly specialized and as a consequence the results cannot be easily adopted for engineering applications. On the other hand, the heat transfer prediction techniques conventionally utilized in design analysis have neglected interacting effects which may be of importance.

Experimental corroboration of heat transfer predictions cannot at present be completely achieved in ground tests because of facility limitations. Thus some reliance must be placed on flight measurements. The sensing instruments must be carefully designed to afford credible data. Furthermore, data interpretation procedures accurately accounting for any local environmental perturbations must be formulated. These tasks are difficult when the sensor is mounted in an ablative surface.

## 1.1 STUDY OBJECTIVES

Two major objectives were pursued during this study. The first objective was to conduct a detailed investigation of the aerothermal environment experienced by manned spacecraft during atmospheric entry. Phenomena not previously considered and problem areas lacking reliable analysis techniques were to be studied. Results of theoretical and experimental research were to be adapted for design analysis application. The second major objective was to formulate techniques for reduction of flight-test heat-sensor data. A comprehensive analysis of the interactions between heat-flux sensors, the surrounding heat shield material, and the aerothermal environment was to be performed.

## 1.2 STUDY SCOPE

The scope of this study and guidelines for its conduct were established by the NASA Manned Spacecraft Center. Study results were to be oriented toward the Apollo Command Module. The intent was to obtain realistic representations of the inviscid flow field, the convective heat transfer, and the radiative heat transfer for Apollo. Also, the performance characteristics of heat sensors which will be used on Apollo test vehicles were to be described.

The general configuration of the Apollo Command Module is shown in Fig. 1-1. Angle-of-attack of the vehicle during atmospheric entry was prescribed as 25 deg. Three trajectories, which are illustrated in Figs. 1-2 to 1-4, were provided for use in the study. Trajectory I is representative of early development-test flights and is characterized by relatively low entry velocity. Trajectories II and III, respectively, correspond approximately to the undershoot and overshoot extremes anticipated upon lunar return. The flight paths are qualitatively the same for the three trajectories, but the velocity-altitude conditions differ substantially. In subsequent discussions of these



trajectories, the time from initial atmospheric entry to the point of maximum altitude will be referred to as the pullout period and the remaining time period will be termed the final descent phase. Primary attention will be given to conditions existing during the pullout period since most of the heating is accomplished during that phase of flight.

Two distinct calorimeter designs were provided for analysis. One is of the slug or capacitance type and will be used on the forebody where heating is relatively high. The other is an asymptotic calorimeter intended for afterbody heating measurement. These calorimeters are subsequently described in detail.

The various effects which have been investigated in study of the aerothermal environment are summarized in Table 1.1. These include most of the known phenomena which might be of consequence at flight conditions where heating is significant. The interactions treated in evaluation of heat sensor performance and in formulation of data interpretation procedures are listed in Table 1-2.

### 1.3 TECHNICAL APPROACH

The prediction of vehicle heating at superorbital speeds is a formidable task involving many disciplines. A rigorous accounting for the effects of all active phenomena is precluded at present by deficiencies in the relevant theory and fundamental data. However, it should be possible to obtain an adequate description of the environment by considering only the more important phenomena and by introducing suitable approximations.

With this philosophy, initial effort in study of the aerothermal environment was made to delineate the important flight regimes. Then, a critical assessment of the influence of each of the phenomena was made using theoretical estimation techniques and existing experimental data.

Upon selection of the phenomena warranting attention in heating predictions, a comprehensive review of available research work was conducted to determine the utility of existing information and methods. While all important phenomena have been subjected to some theoretical or experimental study, a unified procedure for calculating the flow field and wall heating has not yet been approached. Means of accounting for the various effects were selected from the available work for direct application or adaptation where possible. Where this was not expeditious, or where this would require neglect of significant interactions, new techniques were formulated. The choice of methods was guided by the considerations of reliability and computational ease.

The adopted prediction techniques were sufficiently complex so as to require a high degree of automation in their application. To this end, all major computations were coded for digital computer solution. The resulting programs were validated by comparison of predictions with experimental data and/or specialized theoretical solutions when such information was available. Finally, the prediction techniques were exercised for representative Apollo entry trajectories to demonstrate their use.

The investigation of the heat-transfer measurement problem followed along parallel lines. First, the various interactions influencing sensor heating were delineated and procedures were developed to account for the important effects. The performance characteristics of specific sensor designs were then analyzed in detail to establish measurement error sources. Based upon these results, design modifications intended to minimize interactions and improve data quality were recommended. An uncertainty analysis was conducted to determine the approximate accuracy to which heat flux could be determined. Having tentatively established the feasibility of obtaining useful information, automated techniques for interpreting flight data were developed. Application of these methods was illustrated for representative heating conditions.

#### 1.4 PLAN OF REPORT

The major results of the study are given in two sections, one dealing with prediction of the environment and the other with measurement of heating. Each is essentially self-supporting and contains final conclusions and recommendations in the subject area as well as a discussion of analysis procedures. The computer programs which have been developed are described in a separate volume.

Table 1 - 1

PHENOMENA AFFECTING AEROTHERMAL ENVIRONMENT

	INVISCID FLOW	CONVECTIVE HEATING	RADIATIVE HEATING
ASYMMETRIC GEOMETRY	X	X	X
NON-EQUILIBRIUM	X	X	X
RADIATIVE ENERGY LOSS	X	X	X
SELF-ABSORPTION	X	X	X
ABLATION PRODUCT INJECTION	X	X	X
VORTICITY	-	X	-
TRANSITION	-	X	-
SEPARATION	X	X	X
SURFACE IRREGULARITY	-	X	-

Table 1 - 2

PHENOMENA AFFECTING HEAT TRANSFER MEASUREMENT	CAPACITANCE CALORIMETER	ASYMPTOTIC CALORIMETER
MASS INJECTION DISCONTINUITY	X	X
SURFACE TEMPERATURE VARIATION	X	X
SURFACE REACTIVITY DISCONTINUITY	X	-
NON-UNIFORM HEAT FLUX	-	X
SENSOR SURFACE EROSION	X	-
INTERNAL HEAT LOSS	X	-
IMPERFECT THERMOCOUPLE INSTALLATION	X	-
TRANSIENT EFFECTS	X	X

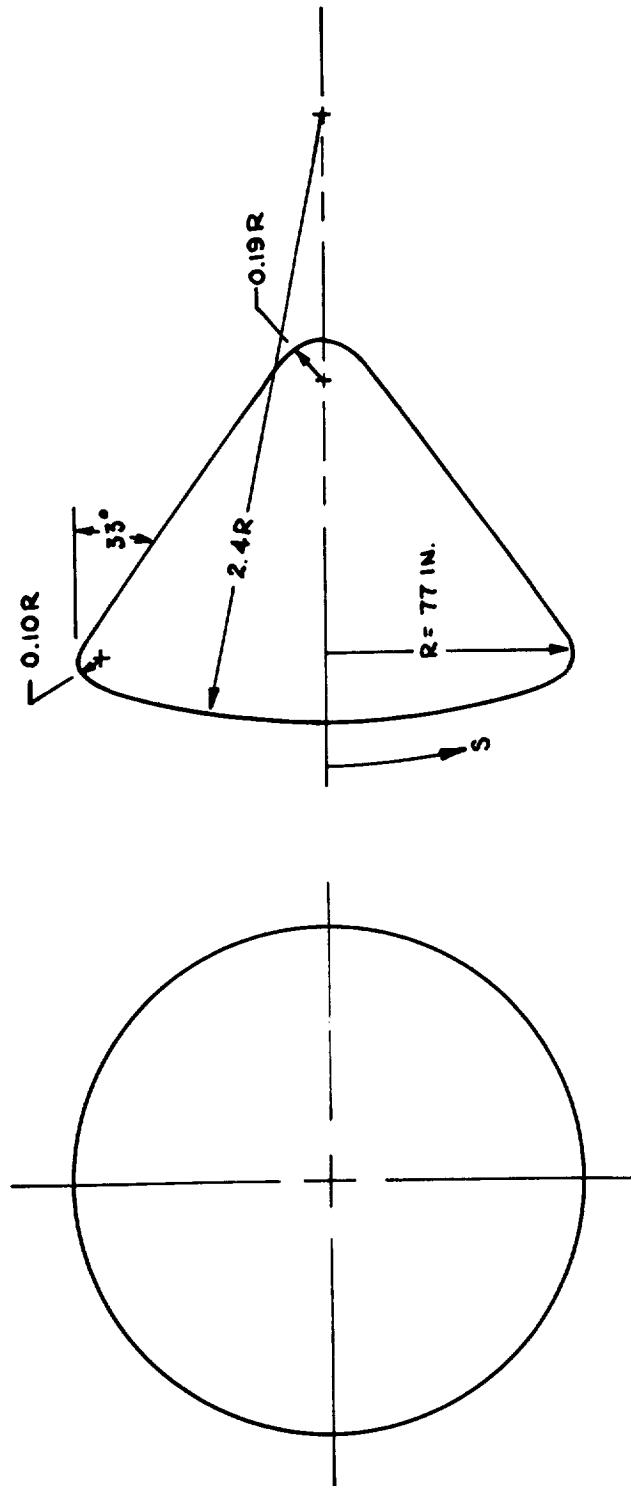


FIGURE 1-1 GENERAL CONFIGURATION OF APOLLO COMMAND MODULE

PREPARED BY \_\_\_\_\_  
DATE \_\_\_\_\_  
CHECKED BY \_\_\_\_\_

LOCKHEED MISSILES & SPACE COMPANY  
A GROUP DIVISION OF LOCKHEED AIRCRAFT CORPORATION

PAGE \_\_\_\_\_  
MODEL \_\_\_\_\_  
REPORT NO. \_\_\_\_\_

FIGURE 1-2  
APOLLO TRAJECTORY I

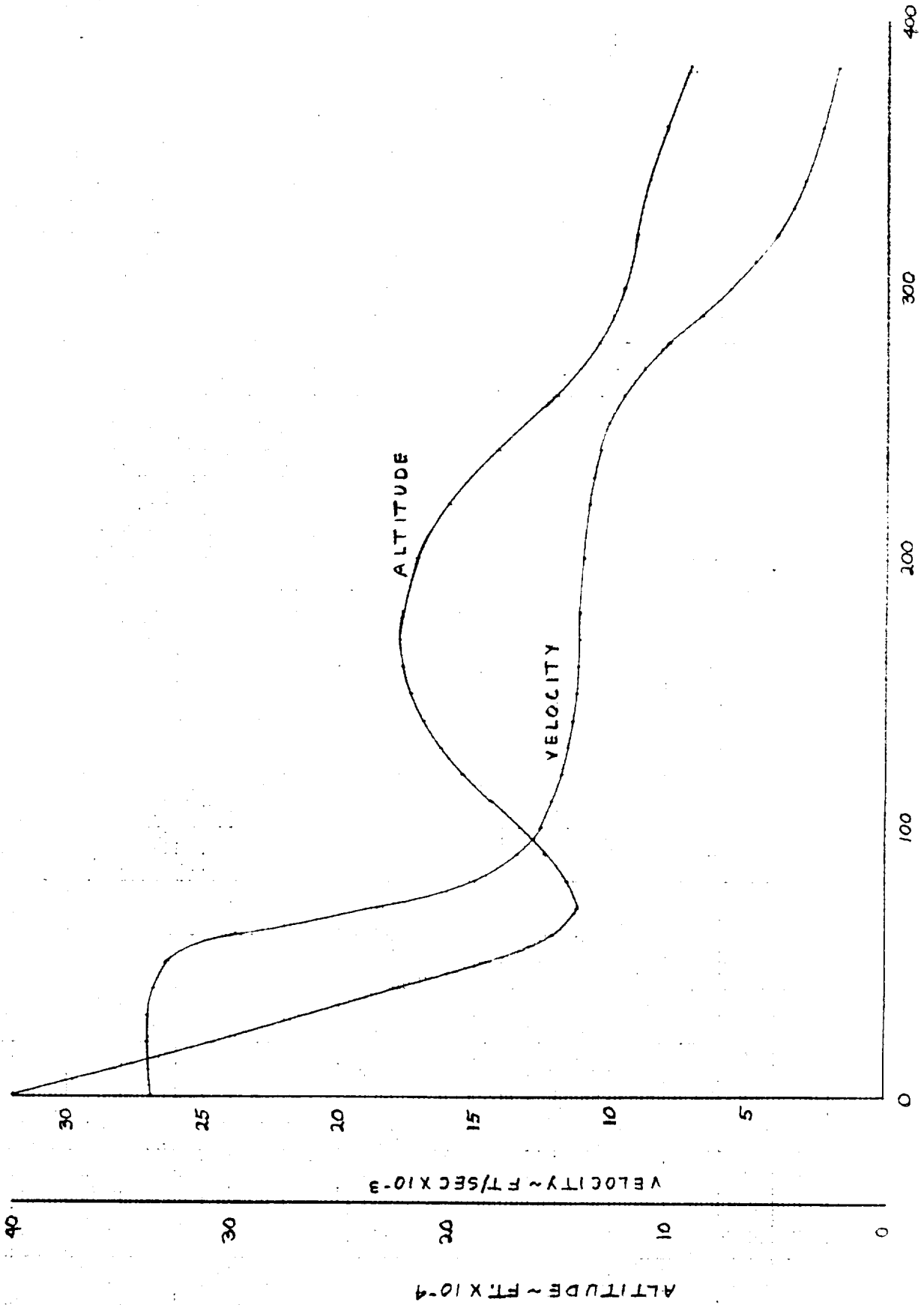


FIGURE 1-3  
APOLLO TRAJECTORY II

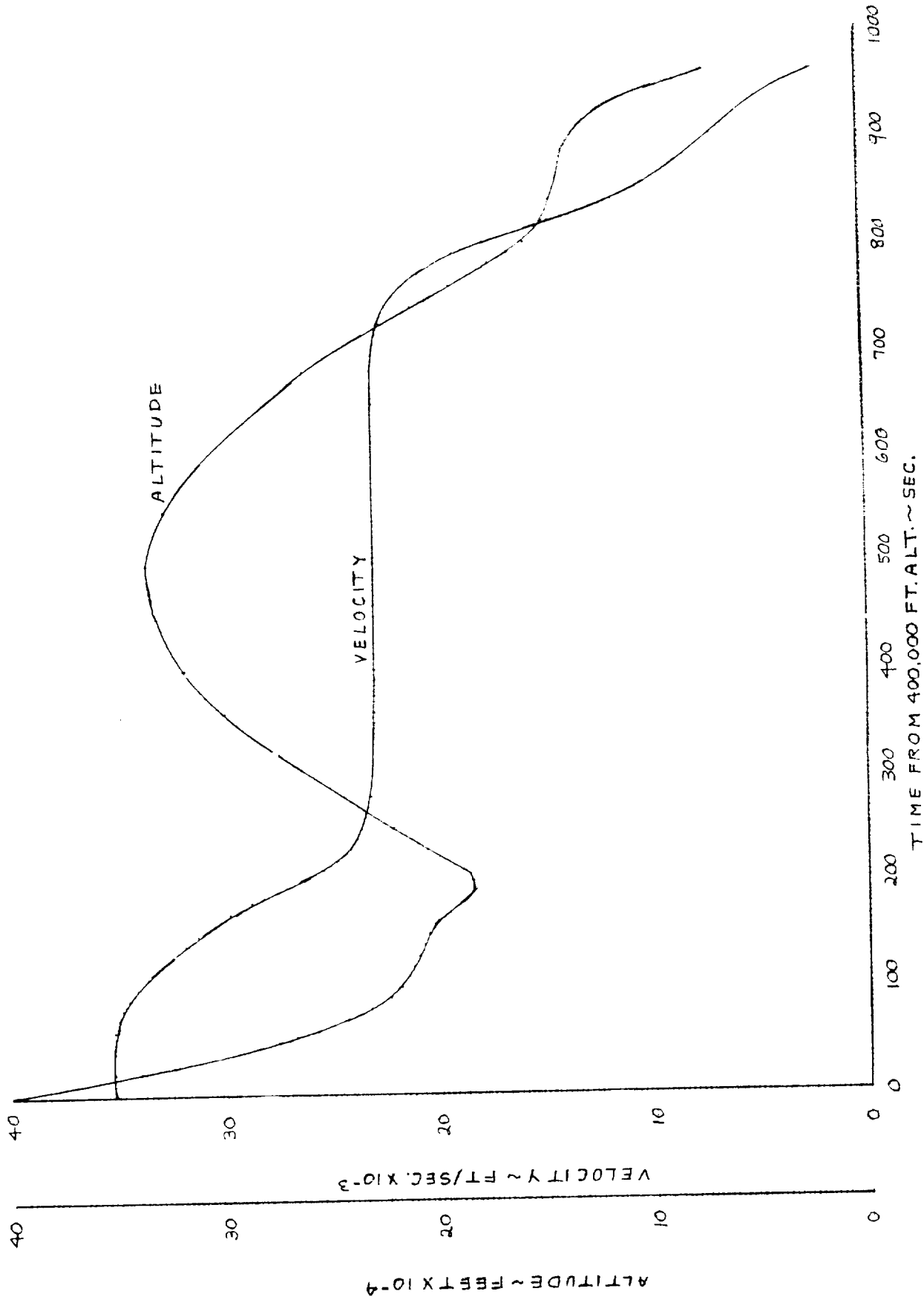
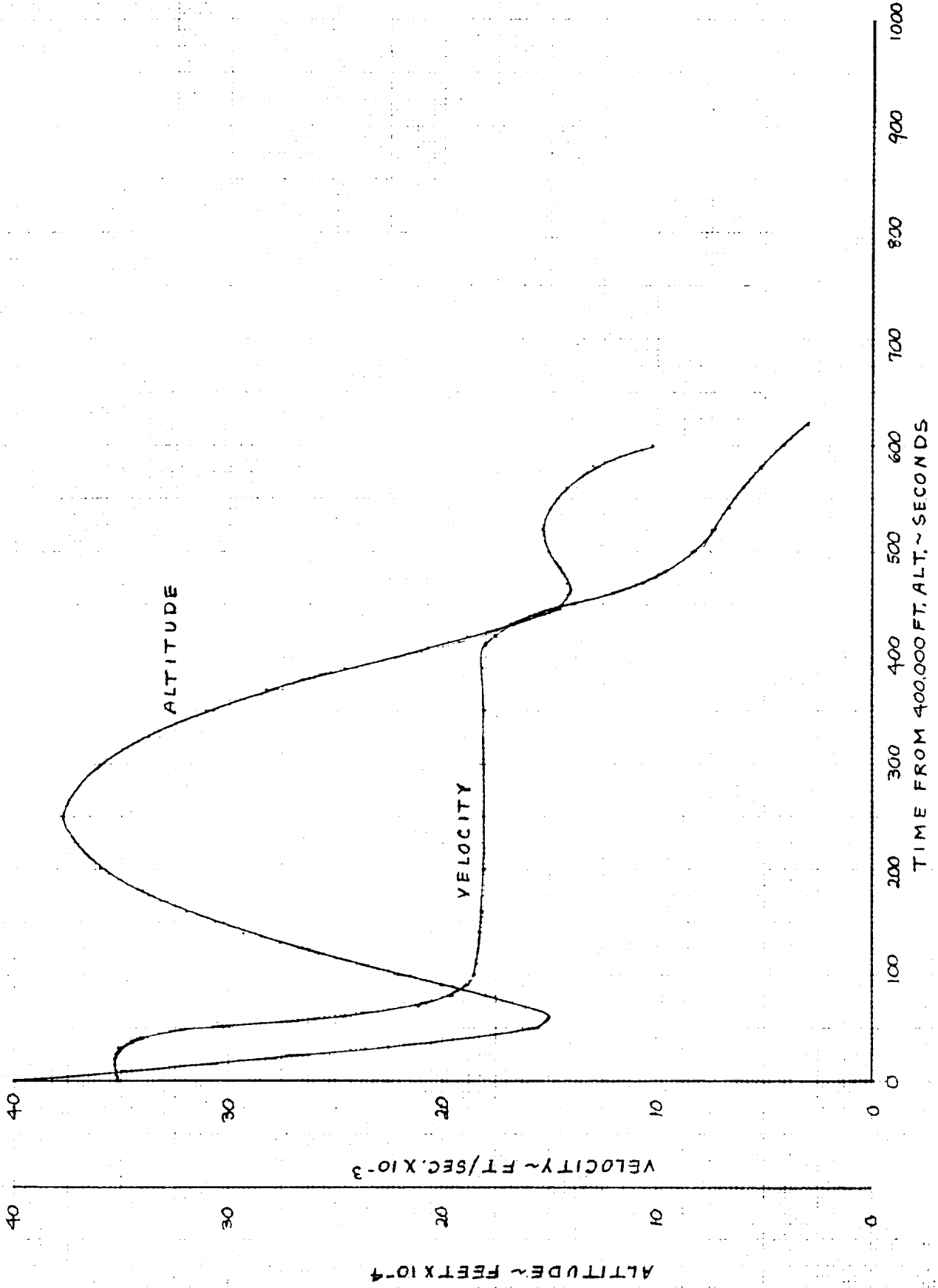




FIGURE 1-4  
APOLLO TRAJECTORY III





## Section 2

### AEROTHERMAL ENVIRONMENT PREDICTION

The problem of predicting the heating experienced by manned spacecraft during atmospheric entry at superorbital velocity is examined in this section. The phenomena influencing heat transfer are identified and their relative importance is assessed. Analysis procedures accounting for the major effects are developed and then applied for representative reentry situations to indicate the character of the aerothermal environment.

Considered first is the inviscid, shock-layer flow since its description is prerequisite to evaluation of heat transfer. Perturbations to the flow resulting from non-equilibrium flow chemistry, radiative energy transport, and mass injection are examined. An approximate, numerical procedure for solution of the flow field about a vehicle at angle-of-attack is developed and qualified by comparison of results with existing data.

Radiative heat transfer is discussed next. Various regimes are delineated according to the importance of non-equilibrium, radiative energy loss, and self-absorption effects. The effects of injection of ablation products are quantitatively assessed. Theoretical means for computation of the radiative heat transfer with non-adiabatic flow of non-grey, absorbing gases are formulated. Semi-empirical procedures for determining the non-equilibrium contribution are presented.

Consideration is then given to convective heating and its dependence on shock-induced vorticity, mass transpiration, transition, surface chemical reactions, and surface contour irregularities. Both experimental and theoretical results are reviewed in selection of suitable procedures for predicting the convective heat rate.

Afterbody heating is treated separately since the influencing phenomena are in part distinct from those of the forebody. Flow separation is considered in analysis of base region convective heating and contaminated wakes are considered for base radiation.

The environmental investigations and the results presented are directed specifically toward the Apollo Command Module application. The fundamental analysis techniques have a relatively wide range of application, but in some instances the computational procedures have been specialized for the Apollo. The results presented are sensitively dependent upon the coupled ablation behaviour of the heat shield material. A theoretical performance model and properties data for the assumed heat shield material, which is considered representative of that for Apollo, are presented in Appendix 2G.

## 2.1 INVISCID FLOW

The characteristics of the shock layer enveloping a vehicle entering the atmosphere at superorbital speed are dependent upon a complex of interacting physico-chemical processes. This section examines the relative influence of the governing phenomena and develops an approximate technique for prediction of the inviscid flow field. Results are presented which typify conditions existing during Apollo reentry. Consideration is given to flow geometry and the effects of chemical non-equilibrium, radiative energy transport, and mass injection.

### 2.1.1 Phenomenological Review

A number of environmental regimes are experienced during the course of Apollo reentry. In the initial descent, non-continuum conditions will at first prevail. When a bow shock forms, the inflowing air will attain energies sufficient to cause dissociation and ionization. The extent and rate of these reactions will vary with altitude and velocity. As the vehicle penetrates to the less tenuous regions of the atmosphere, radiative energy transport will significantly affect the flow. Mass injection

from the ablating surface of the vehicle may further perturb the flow field. For the present considerations, attention may be restricted to the continuum flow situation, but an assessment of the effects of finite rate chemistry, radiation, and mass injection must be made.

#### General Characteristics

It is of interest first to examine the general characteristics of the Apollo flow field. Because the vehicle operates at relatively large angle-of-attack in order to attain the desired lifting characteristics, the shock-layer flow field is highly asymmetric. Experimental observations of the flow show the characteristics schematically presented in Fig. 2-1. The detached shock wave, together with the body surface, bounds the region of interest. Asymmetries in the bow shock, streamline pattern, and flow separation position are particularly notable. Flow over the forebody is largely subsonic as indicated by the sonic line positions. The stagnation point is not located at the Newtonian position. On the lee side, flow separation occurs in the corner expansion whereas the flow remains attached along the top surface resulting in a complex base flow geometry. The separating streamlines enclose a recirculating flow in which both velocity and pressure are low. A free shear layer divides this recirculation region from the external inviscid flow. The wake is formed where the free shear layer coalesces.

It is necessary, in principle, to describe local gas state and flow velocity throughout the complete region in accomplishing the flow field solution. In practice, a number of approximations can generally be introduced. Here, emphasis will be given to the forebody region, and the possibility of treating the shock layer as an inviscid flow in chemical equilibrium will be examined.

#### Non-Equilibrium Effects

For high flow energies, appreciable change in air composition may occur in compression or expansion processes. If the flow times are not large

with respect to the times required for chemical reaction the gas mixture will deviate from an equilibrium composition. Examples of the effects for blunt-body flows are given in Refs. 2.1 - 2.3. Non-equilibrium may occur as a result of the sudden compression at the bow shock or as a consequence of the rapid expansion around the body shoulder. The sudden compression is of primary concern in considering flow over the Apollo forebody.

The detached shock wave may be considered for the altitudes of interest to be a surface where flow conditions change discontinuously. The Rankine-Hugoniot equations together with appropriate thermodynamic state relations enable evaluation of this change. In examining non-equilibrium effects, it may be assumed that immediately behind the shock front only molecular oxygen and nitrogen will be present. Subsequent collisions between particles will cause dissociation, ionization, and other chemical processes as the gas tends to approach an equilibrium composition. At Apollo velocities, this chemical equilibrium composition will be markedly different from the initial molecular mixture. Figure 2-2 compares two of the state conditions, density and kinetic temperature, for the molecular and chemical equilibrium compositions. These data were computed for the stagnation streamline and are presented as a function of time in Trajectory III. Temperatures for the non-equilibrium mixture of molecular oxygen and nitrogen exceed the equilibrium temperature by a factor of about 3 whereas the density is somewhat less than the equilibrium value. Clearly, the influence of non-equilibrium on local state conditions is very significant.

Non-equilibrium may also influence the streamline pattern and shock stand-off distance. The shock layer thickness depends almost linearly on the ratio of free stream density to the average shock layer density. The relation is graphically shown for a hemisphere in Fig. 2-3. Thus, if the flow remains far out of equilibrium for appreciable distances behind the shock wave, it can be expected that the shock layer will be thickened significantly. At very high altitudes, the approach to equilibrium will be slow and the flow may be considered to be frozen at its initial composition.

At lower altitudes, the collisions between particles become more frequent and the chemical equilibrium composition may be reached. Flight velocity also affects the rate of equilibration. The non-equilibrium distance will decrease with increasing velocity as discussed in Section 2.2. Figure 2-4 shows the actual variation of the composition along a streamline entering the shock-layer near the geometric center of the vehicle. The results are for an altitude of 200,000 ft and were obtained from Refs. 2.2 and 2.4. They show that equilibrium is approached in a relatively short distance, about 0.1 ft, at this altitude.\* Noting that the streamline obliquely intersects the shock wave, the local thickness of the non-equilibrium zone is determined to be about 0.03 ft. This compares with a total shock thickness of about 0.8 ft and thus the non-equilibrium zone composes a relatively small portion of the shock. This result may be used to infer conditions at other altitudes as well. The time required for equilibration is, to a first approximation, linearly dependent on the collision rate. Since this rate is proportional to the density, the non-equilibrium thickness should vary inversely with the free stream density. The variation is shown in Fig. 2-5. For altitudes below 200,000, where most of the re-entry heating is experienced, the non-equilibrium thickness will be relatively small. Flow chemistry will differ significantly from equilibrium only in a narrow region immediately behind the shock-layer.

It is concluded that for the flight regime of primary interest the effects of non-equilibrium on the gross characteristics of the shock layer may be neglected. Surface pressure distribution, shock configuration, and shock-layer velocity profiles may be determined assuming equilibrium chemistry. Then, for the remainder of the flow-field discussion, the flow will be assumed to be in chemical equilibrium. Although the shock layer flow pattern will be well represented under this assumption, it should

\* Since the equilibrium composition is approached asymptotically, a precise definition of the non-equilibrium zone is not possible. Here, the non-equilibrium zone is considered to be that region where the concentration of the major constituents (e.g., atomic nitrogen and oxygen and nitrogen ions) differs by more than a factor of two from the equilibrium value.

be noted that the results may not suffice for such purposes as evaluation of radiation or electro-magnetic signal attenuation. For example, even when the non-equilibrium zone is relatively thin, the extremely high temperatures in this zone may promote significant increases in radiation. This aspect of non-equilibrium will be examined in Section 2.2.

#### Viscous Effects and Mass Injection

The velocity and temperature field in the immediate vicinity of the body surface will be significantly perturbed by viscous effects. These perturbations will in turn cause some degree of warping, or displacement, of the external flow. If the displacement is small, shock-layer conditions outside the viscous layer may be evaluated considering the complete flow to be inviscid.

Elementary boundary layer theory indicates that the displacement thickness will be dependent on the Reynolds number, local pressure gradient, wall cooling ratio, and flow Mach number. For the relatively high Reynolds numbers, favorable pressure gradients, and strong wall cooling existing for Apollo during the period of interest, relatively thin boundary layers would be expected. This is borne out in Fig. 2-6 where the computed displacement thickness for the geometric center is shown. These results neglect any influence of mass injection, however, and Kaattari has experimentally shown in Ref. 2.5 that gaseous products of heat shield ablation can have significant effects on the shock layer.

A predicted mass injection history for the geometric center location is shown in Fig. 2-7. In this case, which corresponds to Trajectory III, the mass injection history roughly follows the radiation heat transfer history. Mass injection rates are sufficiently high so that the thermal boundary layer is "blown-off" the surface at the early times. During this period the primary means of accelerating the injected gas around the body is pressure gradient rather than viscous forces. Under these conditions, Kaattari's results indicate that the displacement thickness when



ratioed to the unperturbed shock layer thickness varies in almost linear fashion with the parameter,  $\sqrt{\frac{P_s}{P_\infty}} \frac{\sqrt{P_{10}}}{P_\infty U_\infty}$ . The magnitude and variation of this parameter during Apollo reentry is described in Fig. 2-8. In order to place the results in proper perspective, they are plotted as a function of the instantaneous heat rate rather than the time. The parameter is maximum at low heat rates (early times) when the surface strata of the heat shield begins to decompose. The shock layer thickness would be increased by as much as 100 percent at these times according to the results of Kaattari. During the important period of high heating the value of the parameter is much smaller and relatively minor effects of mass injection would be expected. While the exact magnitude of the thickness increase is uncertain, it can be concluded from the experimental correlation that the perturbation is sufficiently small to neglect.

In summary, an examination of viscous effects including mass injection indicates that the shock layer flow may be treated as inviscid for the important time period.

#### Radiation Effects

At high velocities, radiative emission may result in appreciable loss of energy from the shock-heated air flowing over the body. Temperature of the shock layer is thereby reduced with consequent alteration of the density and velocity fields. These effects have been examined by a number of investigators. It has been shown that the shock detachment distance may be significantly decreased by energy losses. Conversely, pressure distribution is little affected.

The radiative heat transfer for Apollo is discussed in detail in Section 2.2. Energy loss is determined to be appreciable and therefore an accounting for the aforementioned effects is desirable in description of the flow field.

### 2.1.2 Prediction Techniques

An adequate description of the Apollo shock layer will require a three-dimensional flow field solution. The foregoing review indicates that non-equilibrium and viscous effects may be neglected for the important altitude-velocity regime. Radiative energy loss effects should be accounted for, however.

The relations governing the flow are stated in this section. Alternative techniques of solution are examined and an approximate computation procedure is described.

#### State-of-the-Art

The conservation equations for the flow about blunt bodies at angle-of-attack are simply stated. However, their solution is a formidable task due to number of independent variables involved and to the form of the boundary conditions. Until recently, no rigorous numerical formulations of the problem were available. Semi-empirical techniques have therefore been relied upon to a great extent.

A relatively simple procedure for estimating the shock configuration and stagnation point location for spherically-blunted bodies has been devised by Kaattari (Ref. 2.6). In this technique, the normal shock density ratio and a simple angle-of-attack function are used as parameters in an empirical correlation. The method yields results in good agreement with experimental data for low velocity flows. Considering the approximations involved, the technique works very well. It apparently may be used to obtain a reasonable first approximation on shock shape and surface pressure distribution. The procedure affords little information on velocity and density fields, however.

Swigart (Ref. 2.7) has extended an inverse method for application to asymmetric flows over blunt configurations. Flow variables are expanded in power series about the shock wave axis of symmetry and about zero angle-

of-attack. Swigart's work indicates that the maximum entropy streamline will in general not wet the surface. Instead, the stagnation streamline will emanate from the oblique portion of the shock. His procedure is valid only for relatively small angles-of-attack since the shock is assumed symmetric and since only first order terms in angle-of-attack are retained. A genuine three-dimensional formulation of the indirect method has more recently been accomplished by Webb and Dresser (Ref. 2.8). The numerical procedure has been successfully applied for several distinct asymmetric flow configurations with real gas properties being used.

The method of integral relations has been applied to the blunt body at angle-of-attack by Waldman (Ref. 2.9). A single strip is used to represent the shock layer and the solution is restricted to the plane-of-symmetry. Difficulty is encountered where discontinuity in surface curvature occurs.

A numerical scheme for direct solution of the transient flow equations has been developed by Bohachevsky (Ref. 2.10). The quasi-steady flow field for a three-dimensional body is obtained in the limit as time increases. The technique provides a powerful tool for evaluation of a wide variety of flows. It has been exercised for a configuration simulating that of the Apollo, but only for low velocity conditions.

Of these various methods, the inverse technique of Webb and Dresser and the direct, time dependent solution of Bohachevsky appear superior. They both afford means for determining in detail the complete three-dimensional flow field. However, they require large computation times even with fairly coarse space grids and they are subject to truncation errors.

#### Analysis Approach

A means for efficiently obtaining realistic representations of the shock-layer - flow field was sought in this study. In particular, a technique which would rapidly yield data sufficient to describe quantitatively the dependence of convective and radiative heat transfer was desired. The

procedure must then account for angle-of-attack effects and should account for radiative energy loss effects.

Evolution of a technique for calculation of the complete, three-dimensional field was beyond the scope of this study. Consideration has therefore been given to the plane of symmetry where problem complexity is reduced. A streamtube calculational procedure was adopted since it lends itself to evaluation of radiation effects while providing detailed flow profiles. An additional consideration in this selection was the existence of a rudimentary streamtube code which could be modified to incorporate the desired capabilities.

To obtain a tractable solution for the plane of symmetry and to increase computational efficiency, approximations have been introduced in the problem formulation. These approximations are subsequently identified and the influence of the more important are examined.

The conservation equations are first written in an orthogonal, curvilinear co-ordinate system. They are then specialized for the case of negligible cross flow. At this point attention is focussed on the plane of symmetry and the streamline pattern in that vicinity is examined. Next the streamtube calculation procedure is described. Finally, approximate integral solutions for the stagnation region, which cannot be adequately treated by the streamtube method, are obtained.

#### Flow Field Equations

The differential equations expressing conservation of mass, momentum, and energy are written in an orthogonal system of curvilinear co-ordinates (s, n, y) with the surface y = 0 coincident with the body surface. The element of length,  $l$ , is related to the co-ordinates by

$$dl^2 = h_1^2 ds^2 + h_2^2 dn^2 + dy^2$$

The shock layer is assumed physically thin (thickness small with respect to local body radius of curvature) so that the length parameters  $h_1$  and

$h_2$  are functions of  $s$  and  $n$  only. The velocity components in the  $s$ ,  $n$ , and  $y$  direction, respectively, are  $u$ ,  $w$ , and  $v$ . The normal velocity  $v$  is assumed small so that the conservation equations are

$$\frac{\partial}{\partial s}(\rho h_2 u) + \frac{\partial}{\partial n}(\rho h_1 w) + \frac{\partial}{\partial y}(\rho h_1 h_2 v) = 0 \quad (2.1)$$

$$\frac{u}{h_1} \frac{\partial u}{\partial s} + \frac{w}{h_2} \frac{\partial u}{\partial n} + v \frac{\partial u}{\partial y} + \frac{1}{h_1 h_2} \frac{\partial h_1}{\partial n} u w \quad (2.2)$$

$$- \frac{1}{h_1 h_2} \frac{\partial h_2}{\partial s} w^2 = - \frac{1}{\rho h_1} \frac{\partial \rho}{\partial s}$$

$$\frac{u}{h_1} \frac{\partial w}{\partial s} + \frac{w}{h_2} \frac{\partial w}{\partial n} + v \frac{\partial w}{\partial y} + \frac{1}{h_1 h_2} \frac{\partial h_2}{\partial s} u w \quad (2.3)$$

$$- \frac{1}{h_1 h_2} \frac{\partial h_1}{\partial n} u^2 = - \frac{1}{\rho h_2} \frac{\partial \rho}{\partial n}$$

$$\frac{u}{h_1} \frac{\partial v}{\partial s} + \frac{w}{h_2} \frac{\partial v}{\partial n} + v \frac{\partial v}{\partial y} - k(u^2 + w^2) = - \frac{1}{\rho} \frac{\partial \rho}{\partial y} \quad (2.4)$$

$$\frac{u}{h_1} \frac{\partial H_T}{\partial s} + \frac{w}{h_2} \frac{\partial H_T}{\partial n} + v \frac{\partial H_T}{\partial y} = - \frac{4\pi\mu B}{\rho} \quad (2.5)$$

where the last term in the energy equation,  $-\frac{4\pi\mu B}{\rho}$ , represents the local rate of radiative emission per unit mass. For solution of these equations, a simple boundary condition,  $v = 0$ , is available at the body surface. The remaining boundary conditions are provided at the shock wave surface by the Hugoniot relations and free stream conditions. It is the unknown location of the shock surface which causes difficulty in the flow field solution. The system of equations and boundary conditions can be solved, but only with great effort for the asymmetric flow field.

The problem complexity is reduced if the assumption of negligible cross-flow is introduced. (This assumption implies that all streamlines passing directly above any body station are aligned when projected onto the local body-surface tangent plane.) With this assumption the conservation relations are simplified by choosing the  $s$  co-ordinate to correspond with the streamline direction. A particular streamline may be followed by letting the orthogonal co-ordinate,  $n$ , remain constant. For this situation the length parameter  $h_1$ , has a value of unity and the conservation equations become\* (see Ref. 2.11, for example)

$$\frac{\partial}{\partial s}(\rho h_2 u) + \frac{\partial}{\partial y}(\rho h_2 v) = 0 \quad (2.6)$$

$$\left( u \frac{\partial u}{\partial s} + v \frac{\partial u}{\partial y} \right) = -\frac{1}{\rho} \frac{\partial p}{\partial s} \quad (2.7)$$

$$u \frac{\partial v}{\partial s} + v \frac{\partial v}{\partial y} - K u^2 = -\frac{1}{\rho} \frac{\partial p}{\partial y} \quad (2.8)$$

$$u \frac{\partial H}{\partial s} + v \frac{\partial H}{\partial y} = -\frac{4\pi\mu B}{\rho} \quad (2.9)$$

\* Because of the prior assumption of small normal velocity, the term  $K uv$  conventionally appearing in the tangential momentum equation is not contained. This term is of relative order  $\epsilon$  (where  $\epsilon$  is the shock wave density ratio,  $\rho_\infty/\rho_0$ ) and thus its omission does not lead to significant error.

The equations are in exactly the form for axially symmetric flow except that the length element  $h_2$  replaces the radial co-ordinate. This length element is simply a measure of the streamline divergence (i.e., distance between streamlines). It will be termed the spreading co-ordinate in this discussion. The means for its evaluation are developed in Appendix 2A. A brief review of the pertinent relations is given here.

In order to accomplish a solution of the foregoing equations an auxiliary expression for the spreading co-ordinate must be supplied, and for this purpose the pressure gradient in the direction transverse to the streamlines must be estimated. Attention is directed to the plane of symmetry where a tractable solution may be obtained. Noting that the Apollo consists of a spherical segment as indicated in Fig. 2-9, it will be assumed that along any line formed by the intersection of the body surface and a meridional plane the pressure varies as the cosine squared of the angle between the local surface normal and the free stream velocity vector.

$$\left( \frac{p}{z=0} \right) = \frac{(\cos^2 \psi)}{(\cos^2 \psi)_{z=0}} \quad (2.10)$$

This assumption is justified by the available experimental data. The streamline path may then be determined by solution of the familiar normal pressure gradient relation

$$\frac{1}{R_S} = \frac{1}{\rho u^2} \frac{\partial p}{\partial n} \quad (2.11)$$

where  $R_S$  is the radius of curvature of the streamline in the plane of the surface and  $\frac{\partial p}{\partial n}$  is the pressure gradient in the plane of the surface normal to the streamline direction. For streamlines close to the plane of symmetry

$$-\frac{1}{R_S} = \frac{z}{R_C^2} + \frac{d^2 z}{ds^2} \quad (2.12)$$

where  $z$  is the distance from the plane of symmetry and  $R_C$  is the surface radius of curvature.

$$\frac{\partial P}{\partial \eta} = \sin \varphi \frac{\partial P}{\partial m} - \cos \varphi \frac{\partial P}{\partial S} \quad (2.13)$$

where  $\varphi$  is the angle in the plane of the surface between the streamline and the meridional plane (see Fig. 2.9). For small  $z$ , this angle is

$$\varphi = \cos^{-1} \frac{dz}{ds} \quad (2.14)$$

The pressure gradient in the meridional direction is from the assumption of Eq. (2.10)

$$\frac{\partial P}{\partial m} = -\frac{2}{R_c} \frac{z}{R_c} \cos^2 \theta_B P_t \quad (2.15)$$

where  $\theta_B$  is the local surface inclination at the plane of symmetry and  $P_t$  is the stagnation pressure. Thus, from Eqs. (2.11) through (2.15),

$$\frac{d^2 z}{ds^2} = -\frac{z}{R_c^2} + \frac{1}{\rho u^2} \left[ \rho \frac{2}{R_c} \frac{z}{R_c} \cos^2 \theta_B + \frac{dz}{ds} \frac{\partial P}{\partial S} \right] \quad (2.16)$$

The co-ordinate  $z$  is equivalent to the spreading co-ordinate for streamlines close to the plane of symmetry.

$$h_2 \sim z$$

(Equation (2.16) and the conservation equations are linear in the  $Z$  or  $h$  co-ordinate and hence the magnitude of this co-ordinate is arbitrary insofar as the flow field solution is concerned.) Therefore Eq. (2.16) is the auxiliary relation for the spreading co-ordinate required in solution of the conservation equations. It will be evaluated by integrating along the surface streamline.

It is convenient to solve the mass, tangential momentum, and energy conservation equations using a streamline co-ordinate system. The transformation to this system is accomplished by first defining a stream function,  $\psi$ ,



which satisfies the continuity equation. It may be seen from inspection of Eq. (2.6) that such a function is, in terms of its derivatives

$$\begin{aligned}\frac{\partial \psi}{\partial s} &= -\rho h_2 v \\ \frac{\partial \psi}{\partial y} &= \rho h_2 u\end{aligned}\tag{2.17}$$

Thus, the stream function at any location within the shock layer is simply

$$\psi = \int_0^y \rho h_2 u \, dy\tag{2.18}$$

and at the shock surface the function is\*

$$\psi = \int_0^{r_i} \rho_\infty u_\infty h_2 \, dr\tag{2.19}$$

where  $r_i$  is the radial distance from the stagnation point. The stream function is constant along any streamline and thus it serves to identify the particular streamline. Equating (2.18) and (2.19) then yields a relation for the  $y$  position at any surface station of the streamline entering the shock layer at radial position  $r_i$ .

$$\int_0^y \rho h_2 u \, dy = \psi = \rho_\infty u_\infty \int_0^{r_i} h_2 \, dr\tag{2.20}$$

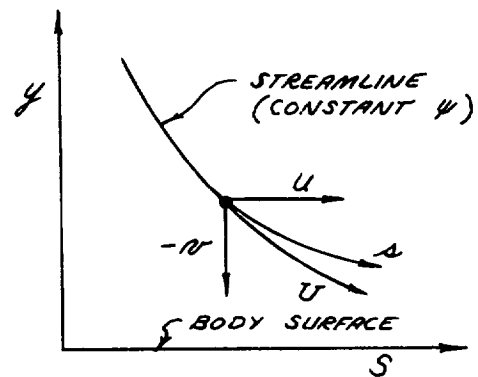
This is the continuity equation to be used in the streamtube calculation.

\* This result is obtained in integration of Eq. (2.17) by noting that for constant  $y$  immediately ahead of the shock wave,  $v \, ds = u_\infty \, dr$ .

The desired form of the tangential momentum and energy equations is obtained by introducing the substantial derivative defined below

$$\frac{D}{Dt} = v \frac{\partial}{\partial s} = u \frac{\partial}{\partial s} + v \frac{\partial}{\partial y}$$

This derivative expresses the rate of change of a flow parameter with time as the fluid moves along a streamline. Alternatively, it can be considered for the present steady flow situation as the rate of change of the flow parameter with distance along a streamline. In the substantial derivative  $v$  is the total velocity and  $s$  is the distance traversed along the streamline. The relation between the streamline and body-oriented quantities is depicted in the sketch. It may be seen that



$$\frac{u}{v} = \frac{ds}{ds}$$

and thus the substantial derivative may be alternatively expressed in the body-oriented co-ordinate system as

$$v \left. \frac{\partial}{\partial s} \right|_{\psi} = u \left. \frac{\partial}{\partial s} \right|_{\psi} = u \left. \frac{\partial}{\partial s} \right|_{y} + v \left. \frac{\partial}{\partial y} \right|_{s} \quad (2.21)$$

The subscripts are used to distinguish the direction in which change is to be measured. Thus, on the right hand side of the equation the partial with respect to  $s$  denotes rate of change with surface distance at constant  $y$ . In the center, the partial with respect to  $s$  denotes the rate of change with surface distance at constant  $\psi$  (or rate of change along a streamline per unit surface distance). The required tangential momentum and energy equations are obtained by substituting the substantial derivative of Eq. (2.21) in Eqs. (2.7) and (2.9). The results are:

$$u \left. \frac{\partial u}{\partial s} \right|_{(\psi)} = - \frac{1}{\rho} \left. \frac{\partial p}{\partial s} \right|_{(\psi)} \quad (2.22)$$

$$u \left. \frac{\partial H}{\partial s} \right|_{(\psi)} = - \frac{4\pi\mu B}{\rho} \quad (2.23)$$

The normal momentum equation is unchanged from the form of Eq. (2.8), except that the lead term is omitted to simplify integration. (No significant error is incurred by this approximation since the neglected term,  $u \frac{\partial u}{\partial s}$  is of relative order  $\epsilon$ .) The differential relation is

$$r \left. \frac{\partial r}{\partial y} \right|_{(\psi)} - \kappa u^2 = \frac{1}{\rho} \left. \frac{\partial p}{\partial y} \right|_{(\psi)} \quad (2.24)$$

Equations (2.21) through (2.24), together with Eq. (2.16) for the spreading co-ordinate, suffice for solution of the shock layer flow when they are supplemented by the following boundary conditions and an equation of state.

At the shock surface\*

$$\begin{aligned} u_i &= u_\infty \sin \theta_s \cos (\theta_B - \theta_s) + \epsilon \cos \theta_s \sin (\theta_B - \theta_s) \\ -w_i &= \epsilon u_\infty \cos \theta_s \\ p_i &= p_\infty + (1 - \epsilon) u_\infty^2 \cos^2 \theta_s \\ H_i &= h_\infty + u_\infty^2 / 2 \end{aligned}$$

Because the local shock angle is not initially defined, these boundary conditions are ill-posed and a non-iterative solution of the conservation

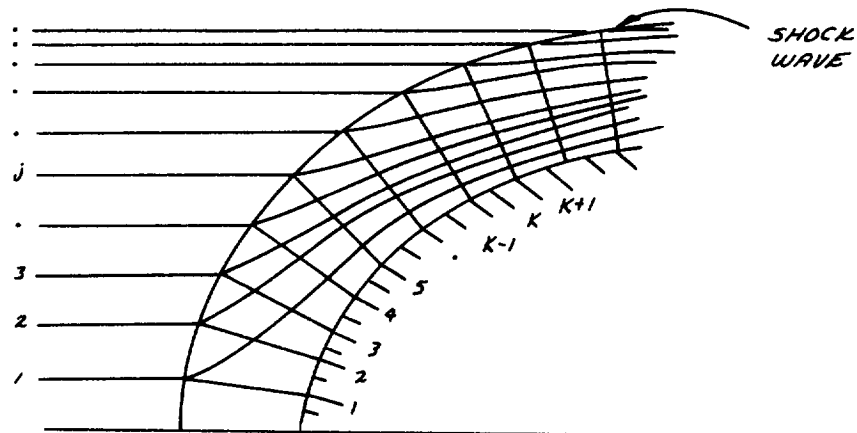
\* The thin shock layer approximation is used for the normal velocity,  $v_i$

equation becomes impossible. The following subsection develops a successive approximation technique for solution of the direct problem.

### Streamtube Flow Field Calculation

The foregoing differential conservation equations have been expressed in finite difference form and incorporated in a digital computer code for numerical calculation of the shock layer flow field. Operation of the code, which is designated as STREAMTUBE, is discussed in Volume II. Formulation of the difference equations is described here.

The shock layer is represented by a network composed of streamlines and lines normal to the body surface, as indicated in the sketch below.



The normal lines are spaced at even intervals along the body surface. A stream line enters the shock layer at each location where a normal line intersects the shock surface. The surface normals are numbered in order 1, 2, 3, . . . . K, proceeding from the stagnation region. The stream lines are also numbered in order 1, 2, 3, 4, . . . . j. The first

normal is removed a small distance from the stagnation point in order to avoid singularities in the solution. The relative coarseness of the grid in the stagnation region will introduce local inaccuracy in results. For this reason, an approximate integral solution which will subsequently be discussed is used to provide shock layer data in this region.

As indicated previously, a non-iterative solution of the conservation equations cannot be obtained since application of the boundary conditions requires knowledge of the shock configuration. This information is not initially available and hence the calculation must proceed in an iterative manner. In essence, the procedure is to calculate repeatedly the flow field, each time using improved estimates of the boundary conditions, until finally a solution of satisfactory accuracy is achieved. Each calculation provides a new shock configuration. Provided that the calculations are convergent, each new calculated shock configuration enables refinement of the boundary conditions for the next shock layer calculation.

The procedure in which the calculations are performed in the streamtube program is briefly outlined here before giving the detail of each step.

The order is:

- (1) Estimate shock angle, pressure distribution and spreading co-ordinate variation along the surface
- (2) Calculate velocity and static enthalpy variations along individual streamlines
- (3) Calculate streamline pattern
- (4) Iterate on shock angle
- (5) Iterate on pressure
- (6) Iterate on spreading co-ordinate.

After each iteration is completed, a return is made to step (2). The iteration of step (4) is not initiated until shock angle convergence has been obtained. Similarly, the iteration of step (6) begins only after convergence in steps (4) and (5) is achieved.

In the first phase of the calculation, the momentum and energy equations are solved along each streamline. From Eqs. (2.22) and (2.23)

$$\frac{u^2}{2} - \frac{u_i^2}{2} = - \int_{s_i}^s \frac{1}{\rho} \left( \frac{d\rho}{ds} \right) ds \quad (2.25)$$

$$h - h_i = - \int_{s_i}^s \left[ \frac{4k\sigma T^4}{u} - \frac{1}{\rho} \frac{d\rho}{ds} \right] ds \quad (2.26)$$

where the subscript i refers to (initial) conditions immediately behind the shock. In evaluation of the tangential velocity, u, the slight dependence of the tangential pressure gradient on distance above the surface is neglected. The surface pressure gradient is used. Equations (2.25) and (2.26) may be rewritten as\*

$$\left( \frac{u}{u_i} \right)^2 = 1 - \frac{2\rho_i}{\rho_i u_i^2} \int_{s_i/R}^{s/R} \left( \frac{\rho_i}{\rho} \right) \frac{d(\rho/\rho_i)}{d(s/R)} d(s/R) \quad (2.27)$$

$$\frac{h}{h_i} = 1 - \frac{4(k\sigma T_i^4)R}{u_i h_i} \int_{s_i/R}^{s/R} \frac{k\sigma T^4}{\rho_i \sigma T_i^4} \left( \frac{u}{u_i} \right)^{-1} d(s/R) - \frac{u_i^2}{2h_i} \left[ \left( \frac{u}{u_i} \right)^2 - 1 \right] \quad (2.28)$$

where R is a characteristic body dimension. In order to solve the above equations, the following approximate fits for thermodynamic and radiative properties are introduced:

$$\frac{\rho}{\rho_i} = \left( \frac{p}{p_i} \right)^\gamma \left( \frac{h_i}{h} \right) \quad (2.29)$$

\* The indexing convention for summations is defined in the Notation Section.

$$\frac{k \sigma T^4}{k_i \sigma T_i^4} = \left( \frac{p}{p_i} \right)^\alpha \left( \frac{h}{h_i} \right)^\beta \quad (2.30)$$

(The power law exponent,  $\gamma$ , appearing in Eq. (2.29) should not be confused with the familiar isentropic exponent.) With these substitutions, Eqs. (2.27) and (2.28) become in finite difference form

$$\left( \frac{u}{u_i} \right)_k^2 = 1 - \frac{2 p_i}{p_i u_i^2} \sum_{l=k_i+1}^{l=k} \left( \frac{p}{p_i} \right)_l^{-\gamma} \left( \frac{h}{h_i} \right)_l \left[ \left( \frac{p}{p_i} \right)_l - \left( \frac{p}{p_i} \right)_{l-1} \right] \quad (2.31)$$

$$(2.32)$$

$$\left( \frac{h}{h_i} \right)_k = 1 - \frac{4 (k_i \sigma T_i^4) R}{u_i h_i} \sum_{l=k_i+1}^{l=k} \left\{ \left( \frac{u}{u_i} \right)_l^{-1} \left( \frac{p}{p_i} \right)_l^\alpha \left( \frac{h}{h_i} \right)_l^\beta \right\} \left[ \left( \frac{s}{R} \right)_l - \left( \frac{s}{R} \right)_{l-1} \right] - \frac{u_i^2}{2 h_i} \left[ \left( \frac{u}{u_i} \right)_k^2 - 1 \right]$$

After the velocity and enthalpy are determined at every (j, k) point in the co-ordinate grid, the streamline pattern and shock layer thickness may be determined using the continuity relation of Eq. (2.21). This expression may be written as

$$y = \frac{\rho_\infty u_\infty}{h_2} \int_0^{r_i} \frac{h_2 dr}{\rho u} \quad (2.33)$$

It is placed in a finite difference form in a procedure similar to that for Eqs. (2.25) and (2.26). It is assumed that over any small interval in r, the spreading co-ordinate varies linearly with r. Further, it is assumed that between streamlines  $\rho u$  varies linearly with distance. The result is

$$\begin{aligned}
 \frac{y_{i,k}}{R} = & \frac{p_0 u_0}{(h_2/R)} \sum_{k=2}^{p-j} \left\{ \frac{p_i u_i}{\left( \frac{p}{p_i} \right)^{1/2} \left( \frac{h}{h_i} \right)^{-1} \left( \frac{u}{u_i} \right)} \right\}_p + \left\{ \frac{p_i u_i}{\left( \frac{p}{p_i} \right)^{1/2} \left( \frac{h}{h_i} \right)^{-1} \left( \frac{u}{u_i} \right)} \right\}_{p-1} \\
 & \cdot \left[ \left( \frac{h_2 + h_{2p-1}}{2R} \right) \left( \frac{\kappa_p - \kappa_{p-1}}{R} \right) \right]
 \end{aligned} \tag{2.34}$$

This relation provides the space co-ordinate of each point in the streamline grid. Furthermore, it yields the shock layer thickness since

$$y_{i,k} - y_{i,k-1} = \Delta k$$

Having established the velocity and enthalpy fields to a first order approximation, the iterative process for refinement of the boundary conditions is initiated. The shock layer thickness results enable calculation of a new shock angle,  $\theta_s$ , since

$$\theta_s = \theta_B - \frac{d\Delta}{ds} \tag{2.35}$$

The derivative is evaluated by a central difference method in the subsonic region and a forward difference method in the supersonic region. The equations are, respectively:

$$\theta'_{s_k} = \theta_B - \frac{\Delta_{k+2} - \Delta_{k-2}}{s_{k+2} - s_{k-2}} \tag{2.36}$$

$$\theta'_{s_k} = \theta_B - \frac{\Delta_k - \Delta_{k-2}}{s_k - s_{k-2}}$$

The shock angle used for the next calculation is an average of the newly computed value,  $\theta'_s$ , and the value used for the last calculation,  $\theta_s^0$ . Iteration is continued until the used and computed values differ by less than 0.25 degree at each (k) location.



When shock angle has converged, a new surface pressure distribution is computed using the finite difference form of Eq. (2.24). In particular, the local body surface pressure is related to the shock surface pressure by

$$P_y = \Delta - P_{y=0} = \int_0^{\Delta} \left( \kappa \rho u^2 - \rho \frac{\partial v^2/2}{\partial y} \right) dy$$

Employing the boundary conditions at the shock and introducing the approximation that

$$\rho \frac{\partial v^2/2}{\partial y} = \rho_i \frac{\partial v^2/2}{\partial y}$$

this becomes

$$\frac{P}{P_t} = 1 - \sin^2 \theta_s \left[ 1 + \frac{\kappa}{1 - \frac{1}{2}\epsilon} \int_0^{\Delta} \frac{\rho u^2}{\rho_\infty u_s^2} dy \right] \quad (2.37)$$

where  $P_t$  is the hypersonic approximation for the stagnation point pressure

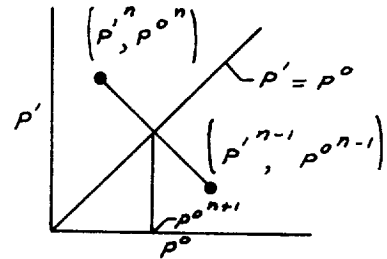
$$P_t = \left( 1 - \frac{1}{2}\epsilon \right) \rho_\infty u_\infty^2 \quad (2.38)$$

Equation (2.37) has the finite difference equivalent

$$\left( \frac{P}{P_t} \right)'_k = 1 - \sin^2 \theta_{sk}' \left\{ 1 + \frac{1}{1 - \frac{1}{2}\epsilon} \frac{R}{R_c} \sum_{j=1}^k \frac{\rho_j u_j^2}{\rho_\infty u_s^2} \left[ \left( \frac{\rho}{\rho_i} \right)'_k \left( \frac{u}{u_i} \right)'_k \frac{y_{i+1} - y_{j-1}}{2\epsilon} \right] \right\} \quad (2.39)$$

This expression enables calculation of new surface pressures which are used to select values for the next iteration. Proper selection of the values is critical to convergence of the solution and hence several different procedures are used in the numerical calculation depending on the circumstances. Generally, the values are computed by

$$\rho^{o^{n+1}} = \frac{\rho^{i^{n-1}} \rho^{o^n} - \rho^{i^n} \rho^{o^{n-1}}}{\rho^{i^{n-1}} - \rho^{i^n} - \rho^{o^{n-1}} + \rho^{o^n}}$$



where the superscripts  $o^n$  and  $i^n$  represent the used and computed values, respectively, for the  $n^{\text{th}}$  iteration.

After convergence has been obtained in the shock angle and pressure iterations, the spreading co-ordinate iteration is initiated. The finite difference analogy to Eq. (2.16) for the spreading co-ordinate is

$$\frac{h_2 k}{R} = \sum_{j=2}^k \frac{1}{2} \left[ \left( \frac{dh_2}{ds} \right)_j + \left( \frac{dh_2}{ds} \right)_{j-1} \right] \left[ \left( \frac{s}{R} \right)_j - \left( \frac{s}{R} \right)_{j-1} \right] + \frac{h_2 k=1}{R} \quad (2.40)$$

with

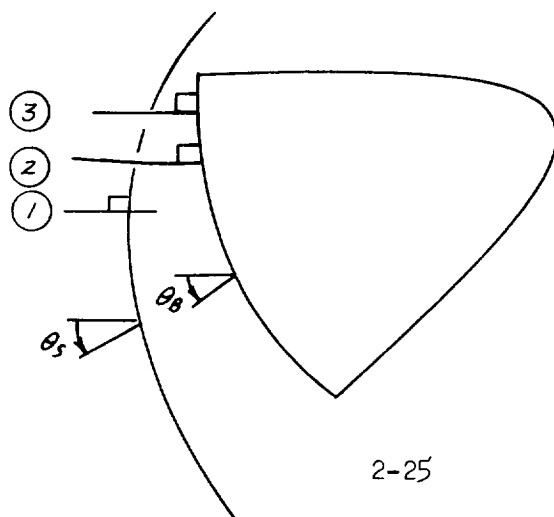
$$\left( \frac{dh_2}{ds} \right)_j = \sum_{m=1}^{j-1} \left\{ - \left( \frac{R}{R_c} \right)^2 \left( \frac{h_2}{R} \right)_m + \left[ 2 \left( \frac{R}{R_c} \right)^2 \frac{h_2}{R} \cos \theta_{Bm} + \left( \frac{dh_2}{ds} \right)_m \left( \frac{\rho_{m+1} - \rho_{m-1}}{\left( \frac{s}{R} \right)_{m+1} - \left( \frac{s}{R} \right)_{m-1}} \right) \right] \left[ \frac{1}{\rho_{i,m} u_{i,m}^2} \left( \frac{\rho}{\rho_{i,m}} \right)^{-\gamma} \left( \frac{h}{h_{i,m}} \right)_m \left( \frac{u}{u_{i,m}} \right)_m^{-2} \right] \right\} \left[ \left( \frac{s}{R} \right)_{m+1} - \left( \frac{s}{R} \right)_m \right] \quad (2.41)$$

The value computed from these equations is used directly for the next flow field computation. Upon convergence of the spreading co-ordinate iteration, the flow field solution is complete.

The finite-difference, streamtube calculation is inaccurate within the immediate neighborhood of the stagnation point for two reasons. First, the stagnation point, itself, cannot be included because of singularities and thus starting conditions for the calculation are not well defined. Second, the streamline grid is coarse in the stagnation region. These deficiencies do not appreciably affect results a small distance away (at positions removed a distance  $S/R_c$  greater than  $\approx 0.1$ ), but they do induce error in the local velocity gradient and shock layer thickness. In order to circumvent these problems, an approximate integral solution for the stagnation region is patched to the streamtube calculation. The integral solution is developed next.

#### Stagnation Region Calculation

Treatment of the stagnation region problem for the angle-of-attack situation requires consideration of some special problems. It has been demonstrated by Swigart (Ref. 2.7) and others that the maximum entropy streamline (the streamline passing through the normal point of the shock) will not wet the surface. Thus, the stagnation streamline cannot be simply identified even when the shock configuration is known. Reference is made to the sketch below in examination of this problem.



2-25

Streamline (1) is the maximum entropy streamline and streamline (3) is a hypothetical streamline which enters the shock obliquely and follows a straight trajectory intersecting the body normally. The shock entry positions of these two streamlines are respectively

$$\theta_{s(1)} = 0 \quad (2.42)$$

$$\theta_{s(3)} = \sin^{-1} \left[ -\epsilon \cos \theta_s \tan(\theta_B - \theta_s) \right] \approx -\epsilon (\theta_B - \theta_s) \quad (2.43)$$

where the latter result is obtained from the oblique shock relations and the hypothetical streamline geometry. Noting that the body surface pressure gradient at the stagnation point must be zero, it can be shown through use of Eq. (2.37) and the shock boundary conditions that the stagnation streamline will lie between streamlines (1) and (3). The stagnation streamline, identified as (2) in the sketch, will curve away from the maximum entropy streamline and intersect the surface normally. Curvature of the stagnation streamline indicates the existence of crossflow in the region.

In order to describe rigorously the stagnation region flow it is then necessary to identify the stagnation streamline and account for its curvature. Fortunately, the possible range of shock entry location as given by the two limiting angles above is small, being about 0.3 deg for representative flight conditions.\* Thus it may suffice to estimate the entry location or use one of the limiting entry positions. In order to retain the orthogonal, body-oriented co-ordinate system previously introduced, the stagnation streamline will be assumed to follow a straight trajectory

---

\* The angle,  $\theta_B - \theta_s$ , is about 5 deg and the density ratio,  $\epsilon$ , is about 0.06 at velocities and altitudes of primary interest.

normal to the surface with entry position given by Eq. (2.43) (corresponding to streamline (3) of the sketch). The integral solution will be developed for a normal shock stagnation streamline, however, and then extended for application to the oblique entry situation assumed.

The major assumption in the integral solution is that the tangential velocity varies linearly across the shock layer. This approximation is justified by the results of both theory and numerical calculations for rotationally symmetric flows. It becomes less accurate for two-dimensional flows. The density is assumed constant through the shock layer in development of the basic relations. This assumption is reasonable except when radiative energy losses become significant. A correction is therefore introduced to account for the energy loss effects. Throughout the development, advantage is taken of the relations

$$\begin{aligned} \sin \theta_B &\approx \tan \theta_B \approx \theta_B = s/R_c \approx r/R_c \\ \sin \theta_S &\approx \tan \theta_S \approx \theta_S \\ \cos \theta_S &\approx \cos \theta_B \approx 1 \end{aligned}$$

which are exact in the limit at the stagnation point.

In the immediate vicinity of the stagnation point, the tangential velocities at the body surface and immediately behind the shock, respectively, can be represented by

$$\frac{u_0}{u_\infty} = \beta_0 s/R_c \quad (2.44)$$

$$\frac{u_s}{u_\infty} = \beta_s s/R_c \quad (2.45)$$

where from the streamwise momentum equation and the shock boundary conditions

$$\beta_0 = \sqrt{2 \frac{P_x}{\rho_x}} \frac{d}{dS/R_c} \left[ 1 - \frac{P}{P_t} \right]^{1/2}$$

$$= \left[ 2\epsilon \left( 1 - \frac{1}{2}\epsilon \right) \right]^{1/2} \frac{d}{dS/R_c} \left[ 1 - \left( \frac{P}{P_t} \right) \right]^{1/2} \quad (2.46)$$

$$\beta_s = \frac{d\theta_s}{dS/R_c} \quad (2.47)$$

Thus, in accordance with the aforementioned assumption, the local velocity is

$$\frac{u}{u_\infty} = \left[ \beta_0 + \left( \beta_s - \beta_0 \right) \frac{y}{\Delta} \right] \frac{S}{R_c} \quad (2.48)$$

Substitution of this relation in Eq. (2.37) provides an expression for the local pressure

$$\frac{P}{P_t} = 1 - \sin^2 \theta_s \left[ 1 + \frac{K \Delta}{3 \left( 1 - \frac{1}{2}\epsilon \right) \left( \epsilon \right)} \left( 1 + \frac{\beta_0}{\beta_s} + \frac{\beta_0^2}{\beta_s^2} \right) \right] \quad (2.49)$$

Equation (2.49) may, upon differentiation, be combined with Eq. (2.46) to obtain the velocity gradient parameter. The result is

$$\beta_0 = \left[ a + \sqrt{a^2 + 4(a+b)} \right] \beta_s \quad (2.50)$$

where

$$a = \frac{2/3 K \Delta}{1 - 2/3 K \Delta}$$

$$b = \frac{\left( 1 - \frac{1}{2}\epsilon \right) \epsilon}{1 - 2/3 K \Delta}$$

It may be noted that this yields the modified Newtonian velocity gradient, as it should, when shock layer thickness approaches zero  $\left(\beta_{0\Delta \rightarrow 0} = \left[2\epsilon\left(1 - \frac{1}{2}\epsilon\right)\right]^{1/2}\right)$ .

The spreading co-ordinate may be calculated from Eq. (2.16). The equation is first rewritten, using the streamwise momentum equation, to obtain a more convenient form

$$\frac{d^2 h_2}{ds^2} = -\frac{h_2}{R_c^2} + \frac{1}{\rho u^2} \left[ \frac{2h_2}{R_c^2} \cos^2 \theta_B (p_t) - \frac{dh_2}{ds} \rho u \frac{du}{ds} \right] \quad (2.51)$$

By specializing for the stagnation region where density may be considered constant this can be alternatively expressed as

$$\frac{d^2 h_2}{ds^2} = -\frac{h_2}{R_c^2} + \frac{2h_2}{R_c^2} \frac{\left(1 - \frac{\epsilon}{2}\right) \epsilon}{\beta_0^2 \left(s/R\right)^2} - \frac{1}{s} \frac{dh_2}{ds} \quad (2.52)$$

Equation (2.52) has the solution for small s of

$$h_2 = \frac{\left[2\left(1 - \frac{\epsilon}{2}\right)\epsilon\right]^{1/2}}{(s/R_c)} \frac{1}{\beta_0} = \frac{\beta_z/\beta_0}{(s/R_c)} \quad (2.53)$$

where  $\beta_z$  is simply the surface velocity gradient in the direction normal to the plane of symmetry. Noting that for small s the radial and surface distances are equivalent, it may be seen that for rotationally symmetric flow  $\left(\beta_z/\beta_0 = 1\right)$  the spreading co-ordinate reduces to the radial co-ordinate as it should.

Application of Eqs. (2.48) and (2.53) enables integration of Eq. (2.21) for the shock layer thickness. The result is\*

$$\Delta = \frac{2\epsilon R_c}{\left[1 + \frac{\beta_s}{\beta_0}\right] \left[\beta_0 + \beta_s\right]} \quad (2.54)$$

It is of interest to compare the equation with more rigorous solutions. For this purpose, rotationally symmetric and two-dimensional flows can be considered. Noting that the velocity gradient parameter,  $\beta_s/R_c$ , is just equal to the reciprocal of the shock radius, Eq. (2.54) reduces for small  $\epsilon$  to

$$\left. \frac{\Delta}{R_s} \right|_{2D} = \frac{2\epsilon}{1 + \sqrt{2\epsilon} \left(1 - \frac{\epsilon}{2}\right)} \quad (2.55)$$

$$\left. \frac{\Delta}{R_s} \right|_{AXI} = \frac{\epsilon}{1 + \sqrt{2\epsilon} \left(1 - \frac{\epsilon}{2}\right)} \quad (2.56)$$

These solutions have been compared with the constant density solutions given by Hayes and Probstein (Ref. 2.12) and were found to be in good agreement for the small shock-density ratios of interest.

Equation (2.54), together with Eqs. (2.47), (2.50), and (2.53) constitute the complete set required for description of shock layer conditions within the stagnation region. Although developed for normal entry of the stagnation streamline into the shock layer, they are directly applied for

---

\* Equation (2.54) was developed neglecting the effects of energy losses. A correction for these effects is made by introducing the multiplying factor,  $1 - \sqrt{s}$ , where  $\sqrt{s}$  is the energy loss parameter discussed in Section 2.3. The factor is derived from the work of Ref. 2.13.



the oblique entry situation. While this is not mathematically correct, it is considered physically reasonable. Application of the relations requires specification of the shock curvature at the stagnation point  $\left(\frac{d\theta_s}{d(s/R_c)}\right)$ . This can be accomplished by matching the similarity solution for shock layer thickness with downstream results obtained by the stream-tube calculational procedure.

The dependence of shock layer thickness on location is assumed to be represented near the stagnation point by a third degree equation

$$\Delta = a + bs + cs^2 + ds^3 \quad (2.57)$$

where a portion of the coefficients are to be determined by satisfying necessary conditions at the stagnation point and the remainder are to be determined from the streamtube calculation results. The shock wave curvature at the stagnation point may then be determined from

$$\left(\frac{d\theta_s}{d(s/R_c)}\right)_{s=0} = \left(\frac{d\theta_B}{d(s/R_c)}\right)_{s=0} - \frac{1}{R_c} \left(\frac{d^2\Delta}{d(s/R_c)^2}\right)_{s=0}$$

or

$$\left(\frac{d\theta_s}{d(s/R_c)}\right)_{s=0} = 1 - 2R_c c \quad (2.58)$$

In selecting the coefficients, two conditions must be satisfied at the stagnation point

$$\Delta \Big|_{s=0} = a = \Delta_0 \quad (2.59)$$

$$\left(\frac{d\Delta}{ds}\right)_{s=0} = b = \theta_{B_0} - \theta_{S_0} = \epsilon \sin(\theta_{S_0} - \theta_{B_0}) + \theta_{B_0} \approx \frac{\theta_{B_0}}{1 - \epsilon} \quad (2.60)$$

The two undefined coefficients are obtained by fitting streamtube-calculation results for shock layer thickness at the  $k = 3$  and  $k = 5$  stations. The results are

$$c = \frac{\Delta_3 - \Delta_0 - \left(\frac{\theta_{\theta_0}}{1-\epsilon}\right) S_3 - \left[\Delta_5 - \Delta_0 - \left(\frac{\theta_{\theta_0}}{1-\epsilon}\right) S_5\right] \left(\frac{S_3}{S_5}\right)^3}{S_3^2 - S_5^2 \left(\frac{S_3}{S_5}\right)^3} \quad (2.61)$$

and

$$d = \left( \Delta_3 - \Delta_0 - \frac{\theta_{\theta_0}}{1-\epsilon} S_3 - c S_3^2 \right) / S_3^3 \quad (2.62)$$

Equations (2.58) and (2.61) provide the shock layer curvature. They must be solved simultaneously with Eqs. (2.47), (2.50), (2.53), and (2.54) to obtain the stagnation point shock layer conditions. In the numerical calculations of the STREAMTUBE program, the simultaneous solution is obtained by iterating on the stagnation point shock layer thickness. The solution yields the variation with location (near the stagnation point) of shock-layer thickness, surface pressure, and spreading co-ordinate. The stagnation region calculation is repeated each time a new downstream streamline pattern is computed. Thus it provides starting conditions for the next streamtube calculation in the iterative process previously described for determining the flow field.

In the present formulation of the flow field calculation procedure, the location of the stagnation point on the body must be specified to initiate the solution. The position is estimated using the approximate procedure developed by Kaattari (Ref. 2.6). It would be possible to refine the estimate through an iterative procedure. In particular, development of the shock layer along the plane of symmetry can be computed in opposite directions away from the stagnation point. There will be one unique stagnation point location where results for the stagnation point thickness, as computed for shock layer development in the two directions, agree

exactly. By iterating the assumed stagnation point location, the unique solution may be found. This feature has not been incorporated in the digital computer code since it is believed that the shock configuration can be estimated with sufficient accuracy by the method of Kaattari to locate satisfactorily the stagnation point.

### 2.1.3 Flow Field Results

The foregoing section presented an approximate procedure for solving the flow field about blunt bodies at angle-of-attack. Results obtained in application of the technique are given in this section. Validity of the technique is first examined by comparing current results with previously available data. The range of these comparisons is necessarily limited. Next, results relevant to the prediction of Apollo heat transfer are discussed. Particular consideration is given to identification of differences in the flow field for flight conditions and wind tunnel test conditions. Finally, the influence of uncertainties and approximations in the calculation procedure is quantitatively assessed. In this process all major assumptions are delineated and means for improvement of the computational technique are indicated.

#### Validating Results

The flow field calculation procedure has been developed for the specific purpose of predicting conditions within the Apollo shock-layer during reentry at lunar return speeds. Ideally, the procedure would be validated by comparing prediction with data obtained either theoretically or experimentally for these conditions. Such information is not available and therefore other comparisons must be made. For a first simple test case, a hemisphere has been considered. This case affords a check on the accuracy of the basic method. A more interesting case is the second, wherein the Apollo shape is treated for wind-tunnel-test conditions. For the final test case, a spherically blunted body at angle-of-attack is examined. In all cases, the flow is assumed to be adiabatic.

The hemisphere calculations were made for hypervelocity conditions representative of Apollo reentry. In particular, the altitude and velocity were 160,000 ft and 30,000 ft/sec, respectively. These conditions were selected to enable direct comparison with the results obtained by Inouya (Ref. 2.14) by the indirect method. Pressure distribution calculations are compared in Fig. 2-10. (Inouya's calculations do not extend appreciably beyond the sonic line and thus the comparison is discontinued at this point.) Very favorable agreement is obtained. The computed stagnation point velocity gradient is also in good agreement with Inouya's result; the two values obtained for the parameter  $\beta_0$  are respectively 1.14 and 1.12. Similarly, the computed stagnation point shock layer thickness of  $\Delta/R = .047$  compares well with the result  $\Delta/R = .049$  obtained by the indirect method. It is concluded that the streamtube calculation yields results of good accuracy, at least for axisymmetric flows.

The Apollo calculations were performed for an angle-of-attack of 25 deg. Hypersonic flow of an ideal gas with isentropic exponent of 1.4 was considered to simulate the conditions of the wind tunnel tests reported in Ref. 2.15. For these tests, air behaves almost ideally. The density ratio across the shock,  $\epsilon$ , is 0.170. Numerical calculations involving the full iteration process of the STREAMTUBE program were limited to the large-radius sector of the body since the thin-shock-layer assumptions incorporated in the program become poor on the small-radius, toroidal corner sections.\* For these latter regions, the pressure distribution was provided as an input for the STREAMTUBE calculations. The pressure over the subsonic portion of the windward corner was determined in hand calculations by using an average streamline curvature. Over the leeward corner and the supersonic portion of the windward corner, a Prandtl-Meyer expansion was assumed to approximate the surface pressure distribution. Results obtained by the STREAMTUBE program for the shock-layer thickness and surface pressure distribution are presented in Fig. 2.11. The pressure predictions

---

\* This limitation is fully discussed in a subsequent review of the computation method.

may be compared with the experimental data of Ref. 2.15. Schlieren photographs, from which shock-layer thickness may be measured, are presented in Ref. 2.16. The experimental data provide corroboration of the theoretical prediction technique. Over the spherical sector predicted shock layer thicknesses do not deviate by more than 6 percent from the experimental results. Predicted pressures are within 0.03  $p_0$  of the measured pressures. Surprisingly good agreement is maintained even on the corner section where the predictions are of a more approximate nature.

The last test case was selected to enable comparison of the streamtube calculational procedure with the time dependent technique of Bohachevsky (Ref. 2.10). Flow of an ideal gas with isentropic exponent of 1.4 over a spherical segment having an included angle of 70 deg is considered. The angle-of-attack is 20 deg and the stagnation point is located 15 deg from the axis of symmetry. Results for the leeward side of the vehicle are compared in Fig. 2-12. The agreement is good considering the truncation errors which exist in the numerical solution of the transient problem. The spherical segment geometry roughly simulates that of the Apollo and hence experimental data obtained with the Apollo configuration may be examined in further comparison of the two theoretical prediction techniques. The experimental data of Ref. 2.15 are for the most part bracketed by the two predictions. In general, they agree more closely with the STREAMTUBE results.

The comparisons which have been made indicate that the STREAMTUBE program yields realistic results. Accuracy of the technique has been demonstrated in the results obtained for a hemisphere. The ideal gas calculations made for the Apollo and spherical segment configurations substantiate its validity for asymmetric flows. It is concluded that the procedure may be reliably extended for prediction of shock layer conditions existing for Apollo at superorbital velocity.

#### Flight Conditions

Conditions existing within the shock layer of an Apollo vehicle are described here for representative flight situations. The conditions are compared

with those for conventional wind tunnel tests to delineate the significant differences. The influence of radiative energy loss is also discussed. Refined predictions are presented only for the spherical segment of the Apollo. As previously indicated, results obtained for the toroidal corners employ estimated surface pressure distributions.

Characteristics of the shock layer are primarily dependent upon the shock density ratio,  $\epsilon$ . This parameter does not vary markedly during the period of high heating and thus a single set of results may be considered as representative. Shock layer thickness and surface pressure distribution predictions are shown in Fig. 2-13 for a velocity of 35,000 ft/sec and an altitude of 200,000 ft. These data were obtained assuming adiabatic flow. The shock density ratio is 0.063. In discussion of these results, it is instructive to compare them with predictions for the wind-tunnel shock density ratio of 0.170.

Figure 2-14, which is to scale, compares shock configurations for the two density ratios. It may be seen that with decreasing density ratio, the shock wave wraps more tightly about the body as would be expected. As a consequence the stagnation point shifts out further toward the corner. (It approaches the Newtonian location as the shock density ratio decreases.) The leeward sonic line moves closer to the center. This is due both to increased shock inclination and to differences in the equation of state. The quantitative differences are better seen by comparison of Figs. 2-11 and 2-13. Shock layer thickness is reduced by a factor slightly in excess of two. Pressure ratio is somewhat lower over the lee side.

Velocity and density distributions through the shock-layer at the geometric center of the vehicle are compared for the two different shock density ratios in Fig. 2-15. The characteristics of these distributions are similar. That is, the velocity increases almost linearly with distance away from the surface. Density increases monotonically away from the surface. Vorticity of the flow is significantly greater for the hypervelocity case. Similarly, density gradients are larger. At other locations on the surface

the results are qualitatively the same. The normalized velocity distributions ( $u/u_s$ ) vary only slightly with position whereas the density gradient increases in expansion of the flow around the body.

It is of interest next to examine the spreading co-ordinate which is essentially a measure of the divergence of adjacent streamlines. Figure 2-16 shows the spreading co-ordinate as a function of distance from the stagnation point for the two cases.\* Also included in the figure for comparative purposes are the radial distances from the stagnation point and from a fictitious axis of symmetry. (If the flow were rotationally symmetric, the spreading co-ordinate would vary as the radial distance from the stagnation point.) Considering first the spreading co-ordinate behaviour on the windward side, it is seen from Fig. 2-16 that the flow tends toward two-dimensional. The streamlines (or spreading co-ordinate) curve moving away from the stagnation point and become nearly parallel to the plane of symmetry. This is due to the relatively rapid acceleration around the corner. On the leeward side, the flow tends toward rotationally symmetric away from the stagnation point. The streamlines curve and approach the paths that would be followed in a rotationally symmetric flow from the fictitious axis of symmetry. This is because the pressure distribution on the lee side is little different than for a hemisphere. Pressure gradients are therefore such as to accelerate the fluid in a direction coincident with the local ray from the effective axis of symmetry.

The velocity gradient ratios,  $\beta_z/\beta_0$ , for the wind tunnel and flight conditions are .59 and .58 respectively. The stagnation region flow thus differs substantially from rotational symmetry in both cases. The results of Fig. 2-16 suggest that for the flight case the leeward streamline pattern might be reasonably approximated by assuming the flow to be goverened

---

\* The magnitude of the spreading co-ordinate is arbitrary. It is the variation with distance of this parameter which is important. For the purpose of comparison, the computed values are multiplied by a factor.

by the rotationally symmetric equations with the radial co-ordinate measured from the effective axis of symmetry rather than from the stagnation point. Advantage of this fact is taken in radiation heat transfer calculations.

The influence of radiative energy losses on shock layer conditions is now examined by comparing adiabatic and non-adiabatic flow solutions for the aforementioned flight situation. The energy loss parameter has a value of 0.07 for this situation. This is near the maximum experienced during Apollo reentry and hence the results are indicative of the greatest effects of energy loss. Figure 2-17 compares the adiabatic and non-adiabatic solutions for surface pressure distribution and shock layer thickness. The influence of energy losses on surface pressure is seen to be negligible in agreement with the predictions of Wilson and Hoshizaki (Ref. 2.17). Shock layer thickness is reduced somewhat, particularly near the stagnation point where energy losses are maximum. Thickness in this region varies approximately as the factor  $1 - \Gamma_s$  for  $\Gamma_s \ll 1$ . The velocity and density profile perturbations arising from energy loss are quantitatively discussed in Section 2.2. Density and velocity are slightly altered near the body surface but are essentially unchanged at the shock surface since the gas just entering the shock layer has not had time to radiate. The spreading co-ordinate is not significantly affected.

#### Review of Method

At this point it is beneficial to review the prediction technique summarizing the important assumptions and identifying its deficiencies. The major assumptions which have been made are:

- the gas flowing through the shock layer is in thermochemical equilibrium
- viscous effects are unimportant
- the shock layer is physically thin as compared to the local radius of curvature of the body surface
- cross flow is small



- the stagnation point location may be estimated with satisfactory accuracy
- pressure variation in the plane transverse to the axis of symmetry is approximated by Newtonian theory
- self-absorption of radiation is unimportant

It was shown in the section on flow phenomenology that the first two assumptions are valid for the altitude-velocity conditions of primary interest in Apollo reentry.

The assumption of a thin shock layer is seen from the shock layer thickness results to be well satisfied on the spherical sector of the Apollo vehicle. The thickness-radius ratio is about 0.1 for wind tunnel conditions. The assumption is poor on the toroidal corners, however. The assumption introduces error primarily in the surface pressure calculation since the normal pressure gradient arising from centrifugal forces is sensitive to the local streamline radius of curvature which in this region may differ substantially from the surface radius. The pressure calculation is further upset by the discontinuous change in radius of curvature. It is therefore inadvisable to use the STREAMTUBE program in its present form for calculation of pressure distribution over the toroidal corners. The computational procedure could be modified to enable calculation of the flow for this region. The modification would entail computation of streamline radius of curvature for use in normal pressure gradient determination and computation of the spreading co-ordinate variation with distance from the surface for use in the continuity solution.

The last assumption concerning the influence of self-absorption appears valid insofar as the gross characteristics of the shock layer are concerned. It was seen that radiative energy losses do not significantly affect the pressure distribution and only slightly affect the shock layer thickness. Since the effect of self-absorption on radiation transport is to reduce

energy loss from the shock layer, it can be concluded that self-absorption will have but second order influence on shock configuration.

The validity of the remaining assumptions is substantiated by the comparisons which were given of ideal gas solutions with experiment and distinct theory. Nevertheless, it is of interest to examine the influence of these assumptions on the solution. For this purpose extreme errors in stagnation point placement and streamline pattern have been considered. Computations were performed for the flight situation. Figures 2-18 and 2-19 present the results obtained together with a description of the limit errors assumed. The assumed stagnation point was shifted  $0.1R_M$  from the nominal location to reflect what is considered to be a maximum possible error. Pressures are affected, but only in the vicinity of the stagnation point. Shock layer thickness is reduced by shifting the assumed stagnation point toward the geometric center, as would be expected. In consideration of the spreading co-ordinate the limit assumption of rotationally symmetric flow was treated together with the assumption of a displaced, effective axis of symmetry.\* Surface pressures are not much affected by the streamline divergence. The shock layer thickness is appreciably reduced by assumption of rotationally symmetric flow. When axi-symmetric flow with a displaced radial co-ordinate is assumed, a reasonably good representation of the shock layer thickness is obtained. It is concluded from these comparisons that rather large errors in the assumed conditions may be made without introducing serious error in the prediction of gross shock layer characteristics.

#### Summary

The characteristics of the Apollo inviscid flow field have been examined in detail. The phenomena affecting shock layer conditions have been identified and a numerical procedure for computation of the flow field has been

---

\* The uncertainty in pressure gradient transverse to the plane of symmetry is not sufficient to induce such large errors in the spreading co-ordinate, but these were convenient and interesting cases to consider.

developed. Predictions of the shock layer structure for Apollo have been presented for subsequent application in evaluation of heat transfer.

Consideration was given to the influence of non-equilibrium chemistry, viscous and mass injection effects, radiation transport, and configuration asymmetries. For the conditions during the period of peak heating, non-equilibrium and viscous effects are not important. Radiative energy losses perturb the flow field slightly. Vehicle angle-of-attack has major influence.

The numerical procedure developed for solution of the flow field uses a streamline co-ordinate system and incorporates an approximate similarity solution for the stagnation point. The technique is limited in application to the plane of symmetry. It accounts for radiative energy loss and angle-of-attack effects. The major approximations and assumptions involved in the method have been delineated and the influence of uncertainties in the assumptions has been described. The accuracy of the method has been demonstrated by comparing results with experimental data and alternate numerical solutions.

## 2.2 RADIATION HEAT TRANSFER

At the superorbital entry speeds associated with lunar return, radiation is a dominant mode of heat transfer to the vehicle surface. The radiation phenomena are reviewed first in this section. Consideration is given to the effects of non-equilibrium chemistry, self-absorption, and energy losses. The influence of ablation products is also examined. Then techniques for prediction of the radiative flux are discussed. Numerical computation techniques accounting for the coupled effects of energy loss and self-absorption are formulated. Finally, the results of radiative calculations are presented.

In general, flow field predictions are prerequisite to the calculation of radiative heating of the vehicle. The material presented in Section 2.1 is therefore complimentary to the discussion here. The surface pressure

distribution and shock configuration results of Section 2.1 are used throughout the radiation calculations. The numerical computation schemes are restricted in application to two-dimensional and rotationally-symmetric geometries. Therefore, certain artifices have been introduced in treating the blunt body at angle-of-attack. The influence of flow asymmetry on radiative heat transfer distribution about the Apollo vehicle is approximated by displacing the radial co-ordinate origin in a rotationally symmetric solution. This approximation was shown to be reasonable in Section 2.1.3. (See Fig. 2-19 and associated text.) The stagnation region flow for Apollo is simulated by using a fictitious surface radius of curvature in a rotationally symmetric calculation.

Throughout the radiative heat transfer discussion, the metric system is used in displaying magnitudes. This system is convenient since the data fundamental to the calculations are generally presented in such units. In order to relate results to the remainder of the discussion of this report, Table 2.1 is provided for useful conversion factors.

Table 2.1 UNIT CONVERSION FACTORS

Length	0.03281 ft/cm	;	$10^4$ micron/cm	;	$10^{80}$ A/cm
Velocity	3.281 (Kft/sec)/(Km/sec)				
Heat Flux	0.881 (Btu/ft <sup>2</sup> sec)/(watts/cm <sup>2</sup> )				
Enthalpy	$h_{sat} = 12,484$ Btu/lb <sub>m</sub>				
Temperature	11605.7°K/1 ev	;	1.8°R/°K		
Frequency	8067.4 cm <sup>-1</sup> /ev	;	0.8067.4 micron <sup>-1</sup> /ev		
Wavelength					

### 2.2.1 Phenomenological Review

The radiative heat transfer to the vehicle surface is dependent upon the temperature field and the distribution of molecular species within the shock layer. Once these are established, the computation of the radiative flux is straight forward in concept. Unfortunately, the temperature and particle

concentration distributions are influenced to some degree by radiative energy transport, thus complicating the situation.

Early calculations of shock layer radiation were made assuming inviscid, adiabatic flow of a transparent gas in chemical equilibrium. Under some circumstances, these simplifying assumptions may lead to appreciable error. At low altitudes the shock layer may be optically thick in some regions of the spectrum. At high altitudes where chemical change processes occur slowly, radiation levels may be markedly affected by non-equilibrium chemistry. At high velocities, radiative emission rates may be sufficient to cause appreciable cooling of the gas as it flows over the surface. The relatively cool viscous boundary layer on the body surface may substantially alter the radiative flux to the surface, particularly if the boundary layer is contaminated by ablation products.

In order to illustrate the various radiation regimes and to identify the phenomena of importance, Fig. 2-20 shows the radiative heat flux to the stagnation region of a 295 cm nose radius body (simulating the Apollo stagnation region) as a function of altitude at two flight velocities. The solid lines represent the actual heat transfer whereas the broken lines represent various limits or contributions as defined by the alphabetical symbols.

#### Energy Loss Effects

The upper set of limiting lines in Fig. 2-20 arises as a consequence of the fact that the gas cannot emit energy in excess of the free stream total energy. Since one-half of the emitted energy is directed toward the body surface and the other half is directed out to space, the limiting radiative fluxes as shown in Fig. 2-20 are equal to one-half of the ambient stream total energy flux ( $\rho_{\infty} u_{\infty}^3 / 4$ ).

The ratio of the radiative heat transfer to this limiting flux provides a measure of the influence of radiative energy losses. When this ratio,

which is termed the radiative energy loss parameter  $\Gamma$ , is very much less than unity the shock layer may be treated as adiabatic. For values of the parameter approaching 0.1, radiative cooling of the gas as it flows away from the shock wave is appreciable and consequently the radiative flux to the body surface is diminished below that for an adiabatic shock layer. Figure 2-21, which is taken from the results of Ref. 2.13, quantitatively describes the dependence of radiative flux level on the energy loss parameter.

It may be determined from the data of Fig. 2-20 that for the Apollo vehicle at altitudes of primary interest (150,000 ft and above), the radiative energy loss parameter will have values of the order of  $10^{-3}$  and  $10^{-1}$ , respectively, for flight velocities of 27,500 ft/sec and 35,000 ft/sec. Thus, at the lower velocity, the shock layer will be essentially adiabatic. However, the influence of energy losses will become significant as velocity is increased to 35,000 ft/sec. For  $\Gamma_a = 0.1$ , Fig. 2-21 shows that the actual radiation transfer is roughly 25% less than the adiabatic shock layer value.

#### Self-Absorption Effects

At low altitudes, the radiative flux to the body surface approaches the black body limit, which is shown in Fig. 2-20 as the line A-B. In this limit the monochromatic absorption coefficient is large over the complete spectrum, hence the Planck-mean emissivity of the shock layer approaches one and the shock layer radiates as a black body. Little of the radiation emitted in the central and outer portions of the shock layer reaches the vehicle surface because of the strong self-absorption.

As the altitude increases, the influence of self-absorption decreases. For the altitudes of primary interest, the radiative flux is far below the black body limit. If air were considered to be a grey gas, it would be concluded that the shock-layer is optically thin and that self-absorption could be neglected. However, the absorption coefficient of air varies markedly over the spectrum. For example, radiative property calculations indicate that oxygen and nitrogen atom deionization processes lead to emis-

sion over the relatively narrow wave length region up to about  $1300\text{\AA}$ , which can account for almost 90 percent of the total emission. Figure 2-22 shows the spectral variation of the absorption coefficient of heated air at a representative temperature-pressure condition. In the visible region, the absorption coefficient is very small being about  $10^{-4} \text{ cm}^{-1}$ , whereas it reaches values in excess of  $1 \text{ cm}^{-1}$  in the vacuum-ultraviolet region. The optical thickness of the shock layer will thus be large in this region of the spectrum and significant self-absorption can be expected. Meaningful predictions of the radiative heating must then account for absorption and its spectral dependence.

#### Non-Equilibrium Effects

Temperatures in the non-equilibrium zone immediately behind the shock wave are significantly above equilibrium values as was shown in Fig. 2-2. Thus, emission from this zone may contribute appreciably to the total radiation received by the body surface. As a result of the binary nature of the chemical and excitation processes (changes induced by two-body collisions) the thickness of the non-equilibrium zone varies inversely with the density and the emission per unit volume varies directly with the density. Thus the total radiation from the non-equilibrium zone is practically independent of altitude. Figure 2-20 shows the constant non-equilibrium contribution as line C-H. As the altitude is increased, the non-equilibrium contribution becomes increasingly important. In the vicinity of 200,000 ft altitude, the non-equilibrium emissions dominate and the total radiation reaches a plateau.

At altitude F in Fig. 2-20, the whole shock layer is essentially out of equilibrium. Further increase in altitude causes truncation of the non-equilibrium radiation profile and the radiative flux is limited by the line F-G. At these very high altitudes, the frequency of particle collisions is not sufficient to maintain the population of the excited states for radiative emission. This "collision limiting" effect further reduces the radiation, causing the drop-off indicated in Fig. 2-20 by line D-E.

### Influence of Ablation Products

At flight conditions where appreciable heating occurs, ablation of the heat shield will cause contamination of the air boundary layer. Foreign species such as carbon monoxide, hydrogen, and cyano may be found in abundance near the wall. For example, Fig. 2-23 shows predicted particle concentration distributions through the Apollo boundary layer at a representative flight condition. Certain of these foreign species have much larger absorption cross sections than do air molecular. As a consequence, the attenuation of radiation from the external inviscid shock-layer is increased by the presence of ablation products in the boundary layer. Emission from the boundary layer is also increased.

#### 2.2.2 Prediction Techniques

From the foregoing review, it is evident that the radiation phenomena are complex. For the flight conditions where radiative heating is large, both energy losses and self-absorption will significantly affect the radiative heat transfer. Non-equilibrium emission will contribute appreciably to the total radiative load. The boundary layer may assume an important role due to the presence of strongly absorbing ablation products.

Existing theories and data generally concern only one or two of the many radiation mechanisms. Large uncertainties exist in the results of different investigators. Much research has yet to be carried out to resolve these uncertainties and to generate a unified procedure for calculating the flow field and wall heating for the general flight situation.

During this study, major effort in the radiation area was placed upon development of methods accounting for the spectral nature of the emission and absorption on the radiative heat transfer to arbitrary two-dimensional and axisymmetric bodies. The detailed results have been given by Chin (Refs. 2.18 and 2.19) recently and are summarized here. First, however, radiative properties of air are briefly discussed. An examination of the influence of ablation products is also given and means for prediction of the non-



equilibrium radiation are reviewed prior to describing the radiation coupled flow field with self-absorption. The section is concluded with a discussion of the application of results.

#### Radiation Properties

For early calculations of shock-layer radiation wherein the air was assumed to be in equilibrium and transparent, Planck-mean absorption coefficients such as those given by Kivel and Bailey (Ref. 2.20) and by Meyerott, et al (Ref. 2.21), were useful. Later publications on equilibrium air radiative properties include those by Armstrong, et al (Ref. 2.22), Nardone, et al (Ref. 2.23), Churchill, et al (Ref. 2.24), Gilmore (Ref. 2.25), Armstrong, et al (Ref. 2.26), Hahne (Ref. 2.27), Allen (Ref. 2.28), and Churchill, et al (Ref. 2.29). Differences among results of the different investigators exist. These differences are due to the different models and approximations used in the calculation, to the different values of oscillator strengths or cross sections employed, and to the number of radiative processes considered. For estimate of the effects of the different radiative phenomena, a consistent set of radiative properties must be selected. In this study, the data of Gilmore (Ref. 2.25) and Hahne (Ref. 2.27) have been used for the most part. Appendix 2B describes in detail the alternate models which have been employed.

#### Non-Equilibrium Radiation

Non-equilibrium profiles in the flow field have been discussed in Section 2.1. The study of non-equilibrium phenomena in shock waves has been the subject of many published works (e.g., Refs. 2.30 and 2.31). Investigations of non-equilibrium air radiation have also been reported by a number of authors (e.g., Refs. 2.32, 2.33 and 2.34). Theoretically, the calculation of histories of species concentrations, temperature and density is required for the calculation of non-equilibrium radiation. These histories may be calculated by integrating the conservation equations with consideration of the pertinent kinetics, both chemical and excitational rate processes. However, large uncertainties in the rate constants exist; the rate constant value

can differ by several orders of magnitude depending on the source (Ref. 2.2).

Theoretical computation of the non-equilibrium radiation was attempted in this study. The procedure and results are reported in Appendix 2C. While the analysis is instructional, the results are highly uncertain. The predicted positional variation of radiation is, in fact, in conflict with the expectations from binary collision theory. Because empirical data of non-equilibrium radiation exist for the velocities of interest (to 35,000 ft/sec), these data are used in the present study in favor of the more sophisticated theoretical calculations.

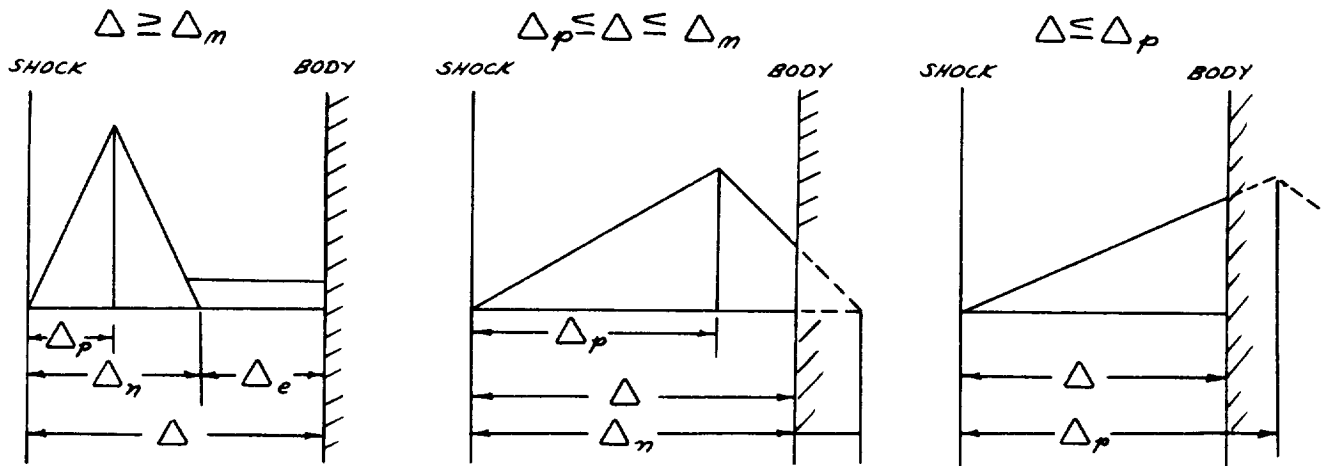
The non-equilibrium radiation data of Allen et al (Refs. 2.32 and 2.34) may be represented by the following correlation:

$$q_{rn} = 10 \frac{u_{\infty} - 19400}{8500}, \quad u_{\infty} < 38000 \text{ FT/SEC} \quad (2.63)$$

where  $u_{\infty}$  is in ft/sec and  $q_{rn}$  in watts/cm<sup>2</sup>. The extent of the non-equilibrium region, or the non-equilibrium distance  $\Delta_n$ , may be represented by

$$\Delta_n = 2.5 \times 10^{-6} \left( \frac{\rho_{SL}}{\rho_{\infty}} \right) \exp \left( \frac{13.7 \times 10^4}{u_{\infty}} \right) \quad (2.64)$$

where  $u_{\infty}$  is in ft/sec and  $\Delta_n$  in cm. Equation (2.64) is obtained by correlating the results of Allen (Ref. 2.32). When the non-equilibrium distance is greater than the shock standoff, truncation of the radiation profile occurs and  $q_{rn}$  is reduced from that given by Eq. (2.63). The effects of truncation may be estimated approximately if the following simplified radiation profile is used:



$$q_{R,t} = \left( \frac{q_{R,e}}{\Delta} \right) \Delta_e + q_{R,m} \quad ; \quad q_{R,t} = q_{R,m} \left[ 1 - \frac{(\Delta_m - \Delta)^2}{\Delta_m(\Delta_m - \Delta_p)} \right] \quad ; \quad q_{R,t} = q_{R,m} \frac{\Delta^2}{\Delta_p \Delta_m}$$

The radiation intensity is assumed to rise linearly to a peak and then decrease linearly to the equilibrium value. The distance to the radiation peak,  $\Delta_p$ , may be calculated by the following equation:

$$\Delta_p = 8.78 \times 10^{-6} \left( \frac{P_{SL}}{P_0} \right)^{-1} \exp \left( \frac{2.66 \times 10^4}{u_\infty} \right) \quad (2.65)$$

where  $u_\infty$  is in ft/sec and  $\Delta_p$  in cm. Equation (2.65) is also obtained by correlating the result of Allen (Ref. 2.32). The expressions for the total radiation,  $q_{R,t}$ , for the three different situations are given also in the above sketches.

The non-equilibrium radiation may be further reduced by collision limiting (Ref. 2.34), by energy loss effects, and by self-absorption. The latter two effects cannot be treated except in detailed theoretical calculations of the non-equilibrium phenomena. Qualitatively, collision limiting reduces the heat flux by a factor,  $F_{C.L.}$ , given by

$$F_{c.l.} = \frac{1}{1 + \left(\frac{\rho_{SL}}{\rho_{\infty}}\right) \left(\frac{\rho_{\infty}}{\rho_{SL}}\right)_c} \quad (2.66)$$

where  $(\rho_{\infty} / \rho_{SL})_c$  is a critical density ratio (Ref. 2.35) at which the time of de-excitation of excited states by radiative emission equals that by collision. A value of  $(\rho_{\infty} / \rho_{SL})_c = 10^{-5}$  was used in Fig. 2-20. As data on collision limiting are limited, this calculation must be considered preliminary.

#### Ablation Products Radiation

Ablation of the heat shield results in high concentrations of foreign species in the boundary layer, as was indicated by the results of Fig. 2-23. Because some of the ablation product species exhibit vastly different absorption characteristics than do air molecules, radiation transport through the boundary layer may be appreciably perturbed. Thus, quantitative examination of ablation products is warranted.

Rigorous description of the boundary layer conditions with ablation and radiative coupling is very complex, unfortunately. In solution of the energy equation, for example, conduction, diffusion, and radiative transport must be accounted for. Species conservation equations must be introduced and reaction kinetics must be considered. A myriad of basic properties data, including molecular transport, chemical kinetic, radiative, and thermodynamic, must be accumulated.

The intent of this analysis has been to assess the order of magnitude of the radiative heat transfer perturbation induced by the presence of ablation products. In keeping with this goal, many simplifying approximations have been introduced. The major assumptions relating to the description of the boundary layer profiles are as follows:

- 1) Thermochemical equilibrium exists.
- 2) Lewis and Prandtl numbers are one.
- 3) Density-viscosity product is constant through the boundary layer.
- 4) Pressure gradient influence on velocity profile is negligible.
- 5) Mass injection distribution is similar.
- 6) Radiation influence on enthalpy profile is negligible.

With these several assumptions, the momentum equation may be transformed to the incompressible, flat-plate form. In particular, with (cf. Lees, Ref. 2.36)

$$\rho u h_2 = \frac{\partial \psi}{\partial y} ; \quad \rho v h_2 = -\frac{\partial \psi}{\partial s} ; \quad \psi = \sqrt{2 \tilde{s}} \mu_0 f \quad (2.67)$$

then

$$f''' + ff'' = 0 \quad (2.68)$$

where the prime denotes differentiation with respect to the transformed co-ordinate  $\eta$  defined below

$$\eta = \frac{1}{\mu_0} \left( \frac{u_e h_2}{2 \tilde{s}} \right) \int_0^\eta \rho dy \quad (2.69)$$

$$\tilde{s} = \int_0^s \rho_w \mu_w u_e h_2^2 ds / \mu_0^2 \quad (2.70)$$

The solution to this equation for the conventional boundary conditions is tabulated for a range of mass injection rates ( $f_w$ ) by Emmons and Leigh (Ref. 2.37). With the foregoing assumptions, the total enthalpy and elemental mass concentration distributions are similar to the velocity distribution (cf. Lees, Ref. 2.38)

$$\frac{H - H_w}{H_e - H_w} = \frac{\tilde{K}_i - \tilde{K}_{iw}}{\tilde{K}_e - \tilde{K}_{iw}} = \frac{u}{u_e} = \frac{f'}{2} \quad (2.71)$$

In utilizing these relations, the outer boundary conditions, denoted by the subscript e, are known as is the wall enthalpy,  $H_w$ . The wall concentration of the i elements may be determined from the known mass injection conditions and ablator composition according to the relations of Ref. 2.38.

$$\tilde{K}_{iw} = \frac{\bar{K}_i B_w' + \tilde{K}_{ie}}{1 + B_w'} \quad (2.72)$$

where  $\bar{K}_i$  represents the mass fraction of element i in the gases being injected into the boundary layer and  $B_w'$  is a mass transfer parameter defined by

$$B_w' = \frac{(P_w)_{\omega}}{C_{H_0}} = \frac{f_w}{0.664} \frac{C}{C_H} \quad (2.73)$$

Thus, the tabulated results of Ref. 2.37 may be used to obtain elemental concentration and enthalpy, as well as local tangential velocity, in terms of the transformed normal co-ordinate,  $\eta$ . With this information (enthalpy and elemental mass fractions) and the local static pressure, the concentration of individual species may be computed from chemical equilibrium theory. A computer code is used to solve for the chemical equilibrium composition. It yields temperature and density together with molecular concentrations. The results are sufficient to determine from Eq. (2.69) the physical co-ordinate,  $y$ , as a function of  $\eta$ . Thus, the thermodynamic state and composition of the gas may be described as a function of distance from the wall.

This approximate procedure for determination of boundary layer conditions has been applied for one select case. Conditions existing at the geometric center of Apollo at the approximate time of peak radiative heating in

Trajectory III (40 seconds time) were selected as representative of the extreme situation with regard to boundary layer contamination. (The ablation rate is near maximum at the time of peak radiative heating in this trajectory.) These conditions are:

$$\begin{array}{ll}
 \tilde{S} = 0.31 & u_e = 5800 \text{ ft/sec} \\
 f_w = -1.05 & P_e = 0.39 \text{ atm} \\
 H_w = 4400 \text{ Btu/lb}_m & H_e = 23,400 \text{ Btu/lb} \\
 \tilde{K}_{Ow} = .29 & \tilde{K}_{Cw} = .56 \\
 \tilde{K}_{Nw} = .07 & \tilde{K}_{Hw} = .08
 \end{array}$$

The velocity, temperature, and density profiles computed for this situation are shown in Fig. 2-24. The corresponding distribution of molecular species has been shown in Fig. 2-23. Because of the high mass injection rate, the velocity gradient is small near the wall and the boundary layer is relatively thick, being somewhat in excess of 2 cm. The gas near the wall is predominantly composed of diatomic and polyatomic ablation product species. However, these ablation product species are almost completely dissociated at a distance of less than one cm from the wall and at greater distances they are largely diluted by the air atoms.

With the temperature and particle concentration distributions through the boundary layer established, the radiation transport problem may be considered. For this purpose, the spectral absorption coefficient within the boundary layer must be defined. The absorption cross section data presented by Weisner (Ref. 2.39) are used here. His results, while not exhaustive, include detailed data for the most prominent band systems of the diatomic species of interest. Figure 2-25 describes the absorption coefficient at a location 0.6 cm from the wall. The dashed line in the figure presents for comparative purposes the absorption coefficient of air at the same pressure-temperature condition. The minimum value shown for the absorption coefficients is  $10^{-4} \text{ cm}^{-1}$ . Many of the relatively well known absorption bands (e.g. CN red, CO Asundi) lie for the most part below the cut-off

value. Similarly, the air absorption coefficient lies below  $10^{-4} \text{ cm}^{-1}$  for wave lengths above about  $3000\text{\AA}$ . The location for which data are presented in Fig. 2-25 is a representative one. Nearer the wall, the absorption coefficients are somewhat greater in accordance with the increased concentration of ablation products. Further from the wall, the absorption coefficient falls off rapidly since the molecules disappear. (Atomic carbon and hydrogen have absorption coefficients similar to nitrogen and oxygen atoms. The atomic absorption coefficients are low relative to the molecular absorption coefficients in the visible region of the spectrum. See Fig. 2-22, for example.)

Figure 2-25 shows that absorption coefficients for the contaminated boundary layer are much larger than for an air boundary layer. However, the optical thicknesses of the contaminated boundary layer are still small everywhere through the visible region of the spectrum. The peak value of the optical thickness in the visible occurs at  $3850\text{\AA}$  and is about 0.08. Thus absorption of visible radiation from the inviscid, air shock layer will not be significant. In the ultraviolet region of the spectrum, the optical thicknesses are somewhat larger. The peaks of the optical thicknesses due to  $\text{H}_2$  photoionization,  $\text{H}_2$  Lyman and the  $\text{CO } 4^{\text{th}}$  positive systems are about 0.64, 0.32, and 0.36 respectively. The  $\text{H}_2$  Lyman and  $\text{CO } 4^{\text{th}}$  positive bands lie largely in a spectral region where the incident spectral flux from the air shock layer is small and thus they are not of great importance. (The dominant emission from the shock layer - that due to ion electron recombinations - occurs below  $1130\text{\AA}$ .) The  $\text{H}_2$  photoionization process lies in the important vacuum ultraviolet radiation region, but at the low wavelength end where again the incident spectral flux is not large.

Although absorption coefficients are large in portions of the ultraviolet due to the presence of  $\text{CO}$  and  $\text{H}_2$ , little emission from the boundary layer results since the Planck radiation function is very small at the low wavelengths. (At  $5000\text{K}$  less than 0.1 percent of the black body radiation is emitted at wavelengths less than  $2000\text{\AA}$ .) The  $\text{CN}$  violet and  $\text{C}_2$  Swan bands,



which lie in a region where the Planck function is larger, result in increases in radiative flux to the surface of about 6.5 and 2.5 watts/cm<sup>2</sup>, respectively. These increases are not very significant in comparison with the unperturbed radiation from the inviscid shock layer, which is approximately 150 watts/cm<sup>2</sup>.

The present assessment has not accounted for many of the radiative absorption processes due largely to a lack of absorption coefficient data. Most of the photoionization processes and all polyatomic absorption bands have been neglected. However, the results are considered indicative. The tentative conclusion is that ablation products will have second-order influence for the Apollo flight conditions. Emission from the boundary layer is small. Optical thicknesses of the boundary layer are small except in narrow regions of the ultraviolet.\* These conclusions are reinforced by the work of Ref. 2.40 wherein the coupled radiation-convection problem was treated with injection of a single contaminant, CO. The results of Ref. 2.40 indicated that presence of the CO has a very minor influence on radiative transfer to the wall.

#### Equilibrium Radiation

Previous investigators have shown that energy loss and self-absorption can lead to large reductions in the radiation from air shock layers. Yoshikawa and Chapman (Ref. 2.41) studied the problem of emission, absorption, and radiant energy loss behind a one-dimensional shock wave. Studies of non-adiabatic effects on the radiation transfer to blunt bodies have been reported in Refs. 2.13, 2.17, 2.42-2.47. A variety of restrictive assumptions and approximations appear in these works. One potentially important effect which has been commonly neglected concerns spectral effects and self-absorption. The aforementioned studies employ the grey gas approximation which is valid only when the absorption coefficient is independent of

---

\* Further and more detailed study of absorption in the ultraviolet is desirable. Inclusion of additional absorption processes may indicate significant influence of contaminants. Certainly absorption will become significant for conditions only slightly more severe than considered here. Therefore, predictions which neglect ablation products will be conservative.

wave length or when the radiating layer is optically thin for all wave lengths. These conditions generally are not satisfied as was indicated in consideration of the data of Fig. 2-22.

For isothermal layers, the effects of spectral self-absorption may be integrated to yield the total radiation intensity or wall heat flux (Refs. 2.23, 2.28). For non-isothermal layers with known distributions of thermodynamic properties, spectral integrations may be similarly performed to obtain the self-absorption effect. Since the spectral characteristics of emission and absorption are different, the results obtained by integration with practical spectral representations are subjected to large uncertainties. When the distributions of thermodynamic properties must be calculated by coupling with the radiative transport calculations, the spectral representation must be gross in order to reduce the time required for numerical calculations.

The present work has been directed toward the development of methods accounting for the spectral nature of the emission and absorption on inviscid, non-adiabatic flows around arbitrary two-dimensional and axi-symmetric bodies. Numerical techniques for solution of the radiation coupled flow field have been formulated for two separate regions - the stagnation region and the non-stagnation region. The mathematical models are incorporated in two computer programs -- I. STAGRADS (STAGnation-point, RADiation-coupled, with External Source, and II. STRADS (STreamtube, RADiation-coupled with External Source).

#### Problem Formulation

The problem is formulated for two separate regions -- the stagnation region and the non-stagnation region. Several approximations are introduced in order to make the mathematical model more tractable and to minimize the computation time. Some of the approximations apply to both body regions; they will be mentioned first. Others are employed only for a single region and they will be discussed under the appropriate body regions.

The following approximations applicable to both the stagnation and non-stagnation regions are introduced:

1. The shock layer is physically thin compared to the local body radius. This is a generally-made hypersonic assumption when the density ratio across the shock is small compared with one.
2. The shock layer gas is inviscid and in complete thermodynamic equilibrium. Precursor effects due to the outward radiation from the shock layer are not considered.
3. The shock layer is considered, for radiative transport calculations, locally as a semi-infinite plane-parallel slab with the local distribution of properties. This approximation simplifies the mathematical derivation and numerical calculation greatly. There are two sources of error in this approximation. First, the geometry simplification and neglect of streamwise radiation gradient induce error in the integration over solid angle to obtain the wall heat flux. The magnitude of this error has been examined for spherical geometries by several investigators (e.g., Refs. 2.32, 2.43, and 2.48) and has been found to be small; the radiation is overestimated by about 10 percent. For small-radius, expansion corner regions the magnitude of the error increases, however. The second source of error concerns the neglect of streamwise radiation variation in solution of the energy conservation equation. The error is small provided that the net rate of streamwise radiative energy transport is small relative to the convective rate of energy transport. This ratio can be shown to be small for the conditions of interest. Furthermore, a refinement of this model is at present premature since it does not correspond to the accuracy with which the optical properties of the shock layer gases are known.
4. The body surface is black and the shockwave reflectivity is small. The spectral properties of heat shield surfaces at high temperatures are not very well known. Neglecting reflections by surfaces bounding the shock layer simplifies the transport calculations.

5. The spectral absorption coefficients do not fluctuate rapidly with frequency. In other words, the contributions due to individual discrete lines are not considered, although it has been shown that several strong lines in an air plasma contribute significantly to the total emission (Refs. 2.28, 2.49). Weak lines may be assumed smeared and treated integrally. The results obtained have been based on a "two-band" model and a "six-band" model of the spectral absorption coefficient, which will be discussed in Appendix 2B. There is no difficulty, other than the increase of computing time, to increase the number of "bands". The problem of individual lines, however, must be left for future study.

The following approximations are applicable to the stagnation region:

1. It is assumed that the region considered is within a distance from the stagnation point of the order of the shock standoff.
2. The pressure gradient in the direction normal to the body is negligible. The justification of this approximation is discussed by Howe and Viegas (Ref. 2.44).
3. The shockwave is concentric with the body.
4. The kinetic energy may be neglected so that the total enthalpy may be approximated by the static enthalpy. This is a good approximation for hypersonic speeds in the vicinity of the stagnation point.
5. It is assumed that similarity exists.

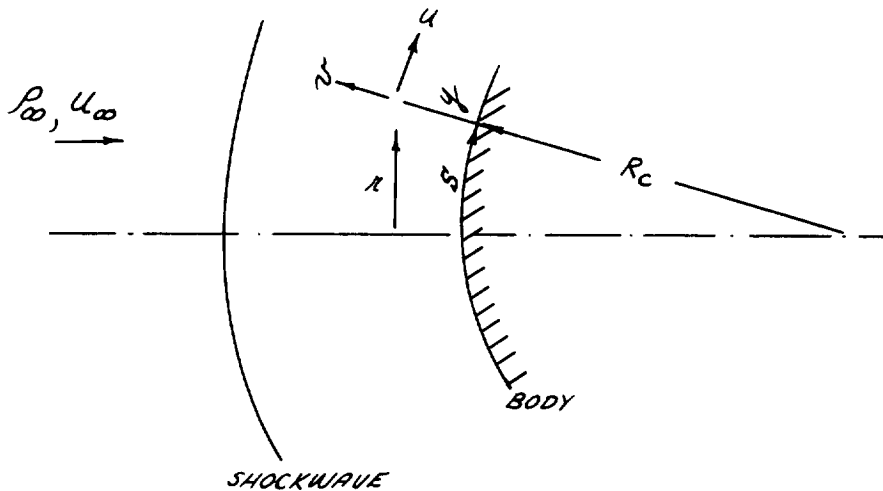
The following approximations are applicable to the non-stagnation region:

1. The normal pressure variation across the shock layer is small.
2. The surface pressure distribution is given by the adiabatic flow solution. The justification given by Bird (Ref. 2.50) may be cited.

### Governing Equations

The governing equations for the two body regions will be described separately.

#### Stagnation Region



In the above sketch, the velocity components  $u, v$  at the point  $s, y$  are parallel and normal to the body surface, respectively. The distance along the body surface from the stagnation point is  $s$ . In the region  $s/\Delta \approx 1$  and with  $\Delta/R_c \ll 1$ , the conservation equations for inviscid flow (here implying non-conducting and non-diffusing as well) may be written as follows (see Ref. 2.44 for analogous equations for a viscous shock layer):

$$\frac{\partial}{\partial s}(\rho u r^2) + \frac{\partial}{\partial y}(A \rho v r^2) = 0 \quad (2.74)$$

$$\rho u \frac{\partial u}{\partial s} + A \rho v \frac{\partial u}{\partial y} = - \frac{\partial p}{\partial s} \quad (2.75)$$

$$\rho u \frac{\partial v}{\partial s} + A \rho w \frac{\partial w}{\partial y} - \frac{\rho u^2}{R} = -A \frac{\partial p}{\partial y} \quad (2.76)$$

$$\rho u \frac{\partial H}{\partial s} + A \rho w \frac{\partial H}{\partial y} = A q \quad (2.77)$$

where

$$r(s, y) = As \quad (2.78)$$

$$A = 1 + y/R_c \quad (2.79)$$

$$H = h + (u^2 + w^2)/2 \approx h \quad (2.80)$$

$q$  = radiative power gain per unit volume, to be discussed later.

The boundary conditions are given below.

At the shock wave,  $y = \Delta$ ,

$$u = u_s = \frac{u_\infty s}{R_c} \quad (2.81)$$

$$w = w_s = -\epsilon u_\infty \left( 1 - \frac{1}{2} \frac{s^2}{R_c^2} \right) \quad (2.82)$$

$$p = p_s = \rho_\infty u_\infty^2 (1 - \epsilon) \left( 1 - \frac{s^2}{R_c^2} \right) \quad (2.83)$$

$$H = H_S = \frac{u_\infty^2}{2} + h_\infty \quad (2.84)$$

where

$$\epsilon = \rho_\infty / \rho_S, \quad \text{density ratio across shock wave.}$$

At the body surface,  $y = 0$ ,

$$v = 0 \quad (2.85)$$

For an inviscid flow, the wall conditions for  $u$  and  $H$  cannot be specified; they are part of the solution to be obtained.

With the assumption of a negligible  $y$  pressure gradient, the  $y$  momentum equation may be eliminated. The other three conservation equations may be simplified by introducing the following transformation similar to the Lees-Dorodnitsyn transformation for compressible laminar boundary layers:

$$\xi(s) = \int_0^s \left(\frac{r}{A}\right)^{2L} u_s ds \quad (2.86)$$

$$\eta(s, y) = \frac{u_s}{\sqrt{2\xi}} \left(\frac{r}{A}\right)^L \int_0^y A^L \rho dy \quad (2.87)$$

$$\frac{\partial \psi}{\partial y} = \rho u r^L, \quad \frac{\partial \psi}{\partial s} = -A \rho v r^L \quad (2.88)$$

$$f(\xi, \eta) = \frac{\psi}{\sqrt{2\xi}} \quad (2.89)$$

$$g(\xi, \eta) = \frac{H}{H_s} \quad (2.90)$$

With  $s/R_c \ll 1$  and  $\Delta/R_c \ll 1$ , A may be approximated by unity, although the gradient of A may not be neglected. From Eqs. (2.78), (2.79), (2.86), (2.87), (2.88) and (2.89)

$$\frac{u}{u_s} = \frac{\partial f}{\partial \eta} \quad , \quad \frac{\rho v}{\rho_s v_s} = \frac{f}{f_s} \quad (2.91)$$

The transformed momentum and energy equations are:

$$f \frac{\partial^2 f}{\partial \eta^2} = 2\xi \left\{ \frac{1}{u_s} \frac{\partial u_s}{\partial \xi} \left[ \left( \frac{\partial f}{\partial \eta} \right)^2 - 2 \frac{\rho_\infty}{\rho} (1 - \epsilon) \right] + \frac{\partial f}{\partial \eta} \frac{\partial^2 f}{\partial \eta \partial \xi} - \frac{\partial^2 f}{\partial \eta^2} \frac{\partial f}{\partial \xi} \right\} \quad (2.92)$$

$$f \frac{\partial g}{\partial \eta} = - \left[ \frac{2R_c}{(L+1)\rho u_\infty^3} \right] g - 2\xi \left( \frac{\partial f}{\partial \xi} \frac{\partial g}{\partial \eta} - \frac{\partial f}{\partial \eta} \frac{\partial g}{\partial \xi} \right) \quad (2.93)$$

If similarity is assumed so that all dependent variables are functions of  $\eta$  alone, Eqs. (2.92) and (2.93) reduce to



$$f \frac{d^2 f}{d\eta^2} = \frac{1}{L+1} \left[ \left( \frac{df}{d\eta} \right)^2 - 2\epsilon(1-\epsilon) \frac{\rho_s}{\rho} \right] \quad (2.94)$$

$$f \frac{dg}{d\eta} = - \left[ \frac{2R_c}{L+1} \rho u_\infty^3 \right] g \quad (2.95)$$

The transformation and simplification also yield the following relations:

$$f = -\rho u_\infty \sqrt{R_c / u_\infty (L+1)} \quad (2.96)$$

$$f_s = -\rho_s u_s \sqrt{R_c / u_\infty (L+1)} = \rho_\infty u_\infty \sqrt{R_c / u_\infty (L+1)} \quad (2.97)$$

$$\Delta = \left[ \frac{R_c}{L+1} u_\infty \right]^{1/2} \int_0^{\eta_s} \frac{d\eta}{\rho} \quad (2.98)$$

where  $\eta_s$  is the value of  $\eta$  at the shock wave.

The boundary conditions in the transformed co-ordinates are:

$$\text{at } \eta = 0, \quad f = 0 \quad (2.99)$$

$$\text{at } \eta = \eta_s, \quad f = f_s, \quad \frac{df}{d\eta} = 1.0, \quad g = 1.0$$

Since there are more known boundary conditions at the shock wave than at the body surface, it will be more convenient to have a further change in variables by letting:

$$F = -\frac{P\eta}{P_{\infty} u_{\infty}} = \frac{f}{P_{\infty} u_{\infty} \sqrt{R_c} / u_{\infty} (L+1)} \quad (2.100)$$

$$d\beta = \frac{-d\eta}{P_{\infty} u_{\infty} \sqrt{R_c} / u_{\infty} (L+1)} = (L+1) \frac{\rho}{P_{\infty}} \frac{dz}{R_c} \quad (2.101)$$

where

$$z = \Delta - y \quad , \text{ distance beyond shock wave}$$

Then, Eqs. (2.94) and (2.100) become

$$F \frac{d^2 F}{d\beta^2} = \frac{1}{(L+1)} \left[ \left( \frac{dF}{d\beta} \right)^2 - 2\epsilon(1-\epsilon) \frac{\rho_s}{\rho} \right] \quad * \quad (2.103)$$

\* For an isothermal shock layer, Eq. (2.103) may be integrated analytically. The expressions for the shock standoff may be shown to be

$$\frac{\Delta}{R_c} = \frac{\epsilon}{1+a} \quad \text{for } L=1$$

$$\frac{\Delta}{R_c} = \epsilon(1-a^2)^{-1/2} \ln \left[ \frac{1+(1-a^2)^{1/2}}{a} \right] \quad \text{for } L=0$$

where

$$a = [2\epsilon(1-\epsilon)]^{1/2}$$

$$F \frac{dq}{d\xi} = \left[ \frac{2R}{(L+1) \rho u_\infty^3} \right] q \quad (2.104)$$

Another form of Eq. (2.104) more useful for later numerical analysis is

$$F dq = \frac{2R}{\rho_\infty u_\infty^3} dz \quad (2.105)$$

The boundary condition now becomes

$$\text{at } \xi = 0 \quad , \quad F = -\frac{dF}{d\xi} = q = 1 \quad (2.106)$$

$$\text{at } \xi = \xi_w \quad , \quad F = 0 \quad (2.107)$$

where  $\xi_w$  is the value of  $\xi$  at the body surface. The value of  $\xi_w$  must be determined from the solution.

The assumption of similarity and plane layer permits the approximation that  $q$  depends only on  $\xi$ .

With appropriate state equations and optical properties for the shock layer gases, Eqs. (2.103) and (2.104) with boundary conditions given by Eqs. (2.106) and (2.107) may be integrated by any of the numerical schemes for ordinary differential equations. Because of the last term in Eq. (2.103), the momentum equation is coupled to the energy equation. An iterative procedure must be used to obtain the solution. The following enthalpy distribution (Ref. 2.13) is used for the first trial:

$$g = \left\{ 1 + 5 \Gamma_{1,2} \left[ (1 - \xi)^{-0.8} - 1 \right] \right\}^{-0.25} \quad (2.108)$$

where

$$\Gamma_{1,2} = 2\sigma \mu_{1,2} T_s^4 \epsilon R_c$$

$$\xi = \rho_s z / \rho_w R_c$$

$\mu_{1,2}$  = low frequency (visible) absorption coefficient, see Appendix 2B.

### Non Stagnation Region

The governing equations for the streamtube formulation have been given in Section 2.1 and are not repeated here.

### Radiative Terms

The radiative terms in Eq. (2.77) for the stagnation region and the corresponding ones for the non-stagnation region may be written as:

$$g = \int_{\nu=0}^{\infty} g_{\nu} d\nu \quad (2.109)$$

with

$$g_{\nu} = -4\pi \mu_{\nu} B_{\nu} + 2\pi \mu_{\nu} B_{\nu} \omega E_2 \left( \int_0^y \mu_{\nu}' dy' \right)$$

$$+ 2\pi \mu_{\nu} \sum_0^{\Delta} g_{s\nu,0} \tau_0 \left( \int_y^{\Delta} \mu_{\nu}' dy' \right)$$

$$+ 2\pi \mu_{\nu} \int_0^{\Delta} \mu_{\nu}' B_{\nu}' E_1 \left( \left| \int_y^y \mu_{\nu}'' dy'' \right| \right) dy' \quad (2.110)$$

where

$$\begin{aligned}
 \nu &= \text{radiation frequency} \\
 A_\nu &= \text{spectral absorption coefficient at} \\
 B_\nu &= \frac{2h\nu^3}{c^2} \left( e^{h\nu/kT} - 1 \right)^{-1}, \text{ Planck distribution function} \\
 E_1(\eta) &= \text{exponential integrals of first and second orders,} \\
 E_2(\eta) &= \text{respectively} \\
 q_{s,\nu,\theta} &= \text{spectral heat flux from external source as parallel} \\
 &= \text{beam at angle } \theta \text{ to body normal; subscript } \theta \text{ omitted} \\
 &= \text{for isotropic volume source} \\
 y &= \text{normal distance from body surface} \\
 F_0(\eta) &= \begin{cases} e^{-\eta/\cos\theta}, & \text{for oblique parallel beam at angle } \theta \\ E_2(\eta) & \text{for isotropic volumem source} \end{cases}
 \end{aligned}$$

The succeeding terms on the right-hand side of Eq. (2.110) can be recognized as (1) radiative loss, (2) absorption of radiation from body surface attenuated by streamlines between the body and the local streamline, (3) absorption of radiation from external sources attenuated by streamlines between the shock wave and the local streamline, and (4) absorption of radiation emitted by other streamlines. A derivation of Eq. (2.110) is given in Ref. (2.19).

The heat flux to the wall is given by

$$q_w = \int_{\nu=0}^{\infty} q_{w,\nu} d\nu \quad (2.111)$$

with

$$\begin{aligned}
 q_{w,2} = & 2\pi \int_0^{\Delta} \mu_{,2} B_{,2} E_2 \left( \int_0^y \mu'_{,2} dy' \right) dy \\
 & + 2\pi \sum_{\theta} q_{s,2,\theta} Trw_{\theta} \left( \int_0^{\Delta} \mu_{,2} dy \right)
 \end{aligned}
 \tag{2.112}$$

where

$$Trw_{\theta}(\xi) = \begin{cases} e^{-\xi/\cos\theta} \cos\theta, & \text{for oblique parallel beam at angle } \theta \\ E_3(\xi) & , \text{ for isotropic volume source} \end{cases}$$

In the stagnation region, the integration is from the shockwave to the body. The substitution of a normal distance  $z = \Delta - y$  may be made in Eqs. (2.110) and (2.112) for this case.

For the present study, external radiation sources are not present so that

$$q_{s,2,\theta} = 0 \quad \text{in Eqs. (2.110) and (2.112).}$$

#### Method of Solution

For the stagnation region, the velocity and enthalpy profiles are very approximately linear near the shockwave. A simple forward finite-difference scheme is therefore used to integrate Eqs. (2.103) and (2.105). The finite-difference form for Eq. (2.105) used is given by

$$q_{i+1} - q_i = \frac{\rho_{\infty} u_{\infty}^3}{E_i + E_{i+1}} Q_i \tag{2.113}$$

where

$$q_i = \int_{v=0}^{\infty} q_{i,v} dv = \int_{v=0}^{\infty} dv \int_{z_i}^{z_{i+1}} q_{i,v} dz \tag{2.114}$$

$$\begin{aligned}
Q_{i,v} = & 2\pi B_{\omega,v} \left[ \epsilon_3 \left( \tau_{\Delta,v} - \tau_{i+1,v} \right) - \epsilon_3 \left( \tau_{\Delta,v} - \tau_{i,v} \right) \right] \\
& + 2\pi \sum_{\theta} \rho_{s,v,\theta} \left[ \text{Tr} \omega_{\theta} \left( \tau_{i,v} \right) - \text{Tr} \omega_{\theta} \left( \tau_{i+1,v} \right) \right] \\
& + 2\pi \sum_{j=1}^n B_{j,v} \left[ \epsilon_3 \left( \left| \tau_{i,v} - \tau_{j+1,v} \right| \right) - \epsilon_3 \left( \left| \tau_{i,v} - \tau_{j,v} \right| \right) \right] \\
& + \epsilon_3 \left( \left| \tau_{i+1,v} - \tau_{j,v} \right| \right) - \epsilon_3 \left( \left| \tau_{i+1,v} - \tau_{j+1,v} \right| \right)
\end{aligned} \tag{2.115}$$

with

$$\tau_{i,v} = \sum_{j=1}^{i-1} \Delta \tau_{j,v} \quad , \quad \tau_{1,v} = 0 \tag{2.116}$$

$$\Delta \tau_{j,v} = \mu_{j,v} \Delta z_j = \mu_{j,v} \left( z_{j+1} - z_j \right) \tag{2.117}$$

$$\tau_{\Delta,v} = \tau_{n+1,v} \tag{2.118}$$

$i$  = layer index

$n$  = total number of layers

Since the velocity field is only weakly coupled to the enthalpy field, according to Eq. (2.103), the following approximation may be made:

$$\frac{P_s}{P_i} \approx \frac{h_i}{h_s} \approx g_i \quad (2.114)$$

In deriving Eq. (2.115), constant properties are assumed across the width of the individual layers, but radiation traversing through is attenuated by each of the differential widths within  $\Delta z_i$ .

Equation (2.103) is first integrated with an initial enthalpy profile given by Eq. (2.108). Then Eq. (2.113) is used to obtain  $g$ . The resulting  $g$  is used for the next integration of the momentum equations if the difference between the calculated and the assumed values of  $g$  exceeds the specified limit.

For the non-stagnation region, conservation equations (2.17), (2.22) and (2.23) (but including self-absorption effects) are first integrated across the width  $\Delta y_i = y_{i+1} - y_i$  of the streamtube. As with the stagnation region, constant properties are assumed across the width of the streamtube, but radiation traversing through is attenuated by each of the differential widths within  $\Delta y_i$ . The conservation equations with the appropriate initial conditions are integrated with a fourth-order Runge-Kutta integration scheme. The body surface pressure distribution, the spectral frequency divisions, the source description, the body station locations, the characteristic vehicle dimension (i e., nose radius) and body shape, and other environmental conditions (e.g. ambient pressure, velocity, etc.) are input to the program. The details of the numerical approaches may be found in Ref. (2.19).

The computation techniques have been formulated for arbitrary two-dimensional and rotationally-symmetric flows. Thus, they are not directly applicable to Apollo at angle-of-attack. However, by artificially modifying the problem conditions, an approximate account for the flow asymmetry effects on



radiation can be made. Flow asymmetry affects shock layer thickness and velocity profiles. The radiative heat transfer depends almost linearly on the shock-layer thickness, but is weakly dependent on velocity profile. Thus, radiative heating from a three-dimensional flow can be closely approximated if the shock layer thickness is closely matched. It was demonstrated in Section 2.1 that the Apollo shock configuration was adequately given by an axi-symmetric flow solution if the radial co-ordinate was measured from the "virtual axis of symmetry" rather than from the stagnation point. Accordingly, the radial co-ordinate origin is displaced in application of the STRADS program to Apollo. In use of the STAGRADS program, an effective body radius of curvature is introduced in place of the actual body radius of curvature. For an isothermal stagnation region flow, the conservation equations used by STAG-RADS may be integrated to obtain the following result for the shock layer thickness

$$\Delta = \frac{\epsilon}{1 + [2\epsilon(1 - \epsilon)]^{1/2}} R_{c\text{eff}} \quad (2.120)$$

The shock layer thickness for the blunt body at angle of attack is from Eq. (2.54) of Section 2.1

$$\Delta = \frac{\epsilon}{\frac{1}{2} \left[ 1 + \frac{\beta_2}{\beta_0} \right] [\beta_0 + \beta_5]} R_c \quad (2.54)$$

Thus, the effective radius of curvature for which the rotationally symmetric solution yields the three-dimensional results is

$$R_{c\text{eff}} = \frac{1 + \sqrt{2\epsilon(1 - \epsilon)}}{\frac{1}{2} \left[ 1 + \frac{\beta_2}{\beta_0} \right] [\beta_0 + \beta_5]} R_c \quad (2.121)$$

For the Apollo vehicle at 25 deg angle of attack, the streamtube program yields the following results with  $\epsilon = 0.061$

$$\beta_0 = 0.59 , \beta_s = 1.46 , \beta_z/\beta_0 = 0.59$$

These yield upon substitution into the above equation

$$R_{c\text{eff}} = 0.82 R_c$$

or

$$R_{c\text{eff}} = 385 \text{ cm}$$

The STAGRADS calculations which are subsequently discussed were made using a preliminary value of 295 cm for  $R_{c\text{eff}}$  cm. Thus they underestimate the shock layer standoff and the stagnation point radiation to some extent.

### 2.2.3 Radiation Heating Results

As discussed previously in Sections 2.2.1 and 2.2.2, many radiation phenomena are encountered by vehicles during reentry at super-satellite velocities. Depending upon the velocity-altitude-body configuration conditions, the determination of the radiation heating level requires the consideration of one or more of the following effects: spectral self-absorption, energy loss, contamination by ablation species, and non-equilibrium including truncation and collision limiting. For conditions where the radiative heating level is relatively high (say, 100 watts/cm<sup>2</sup> and higher), the shock layer is generally in equilibrium for lunar reentry velocities. Results calculated for equilibrium shock layer with spectral self-absorption and energy loss are therefore presented first. The influences of other effects are then discussed. The results for the stagnation region and the non-stagnation region are presented separately.

#### Stagnation Region

Stagnation point results as calculated by STAGRADS for the inviscid, equilibrium-air shock layer are given in Figs. 2-26 to 2-35. Figures 2-26 to 2-30 are for conditions more severe than for Apollo lunar reentry. They are included to show the effects of the parameters (such as the nose radius) and the effects of the assumptions (adiabatic, self-absorption).

Figure 2-26 shows the total stagnation heat flux versus nose radius. Most of the calculated points are based on the two-band model. The six-band results are indicated by the arrow-head tips. The curves are for a flight velocity of 15.24 Km/sec and ambient to sea-level density ratio of  $1.8 \times 10^{-4}$  (210,000 ft altitude). The top curve is calculated for an isothermal shock layer with a transparent gas assumption. The middle curve is calculated allowing absorption to attenuate the heat flux given by the top curve. If both energy loss and absorption are considered, the heat flux is further reduced, as shown by the bottom curve. It is apparent that both energy loss and absorption are important in determining the wall heat flux. The effects of varying velocity and altitude are also depicted by symbolized calculated points in Fig. 2-26. The differences between the two-band and six-band results are seen to be small.

Figure 2-27 shows the heat fluxes computed for the two spectral bands. The spectral and non-adiabatic nature is evident. It is interesting to note that for the non-adiabatic-absorbing case the low-frequency heat flux "catches up" with the high-frequency heat flux as the nose radius increases.

Figure 2-28 shows the fact that energy loss reduces the shock standoff. Figure 2-29 shows the velocity and enthalpy distributions across the shock layer. The velocity fields are perturbed by energy loss and absorption only slightly, whereas the temperature and enthalpy distributions are changed appreciably. The six-band model yields a slightly warmer layer and hence a slightly larger shock standoff than the two-band model.

Figure 2-30 shows the six-band spectral heat fluxes. With the discrete-band approximation, the intensity within each band is assumed uniform and represents an average although in reality intensity variations within each band exist.

Figure 2-31 shows the total stagnation point heat fluxes for Apollo at several velocity-altitude conditions of interest, calculated using the

two-band model. An effective nose radius of 295 cm is employed. Both the Planck-mean absorption coefficient data of Gilmore-Hahne (Refs. 2.25, 2.27; see Appendix 2A) and of Churchill (Ref. 2.29), excluding the far ultra-violet contributions, are used in the calculation. A single point calculated using the six-band model is also shown in Fig. 2-31. The two-band model with the Churchill coefficients is also used for the equilibrium results given in Fig. 2-20.

Figure 2-32 shows the two-band Apollo stagnation optical thicknesses. The far ultra-violet optical thickness is of the order of unity or larger for altitudes below 230 Kft; therefore, self-absorption effects must be considered for the far UV under most conditions. For altitudes below 100 Kft, the black body limiting flux is approached and self-absorption effects in the longer wavelength region become important. It is noted that the black-body limiting regime, the low-frequency absorption coefficients used in the two-band and six-band models become inadequate. More refined spectral resolutions or more bands must be used. On the other hand, at the high heating levels near the black-body limiting regime, the effects of ablation species contamination are expected to over-shadow the inaccuracy of the two-band model.

The effects of energy loss are determined by the value of the radiation loss parameter  $\bar{\alpha}$  according to Ref. 2.13, where  $\bar{\alpha}$  is defined as the ratio of the transparent, adiabatic shock layer emission to the limiting radiation flux. Since the far UV is generally not transparent, the use of a Planck-mean absorption coefficient over the whole spectral region will yield a  $\bar{\alpha}$  overpredicting the energy loss effects. For lunar reentry velocities, less than about two percent of the black-body radiation is in the spectral region with  $\lambda < 0.113\mu$ . The use of the low-frequency ( $\lambda > 0.113\mu$ ) absorption coefficients in defining the radiation loss parameter may be more appropriate. Figure 2.33 shows the radiation loss parameter calculated according to the above basis.

Still a better definition of a radiation loss parameter is defined as the ratio of the total wall heat flux divided by the limiting radiative flux, including the effects of self-absorption, energy loss and non-equilibrium. This effective parameter,  $\Gamma_e$ , is shown in Fig. 2-34. Unfortunately,  $\Gamma_e$  may be calculated only after a solution of the problem is obtained. When both energy loss and spectral absorption are important, a simple correlation in terms of a certain energy loss parameter alone may not be feasible.

Figure 2-35 summarizes the Apollo stagnation heat flux at various velocity-altitude conditions. The equilibrium calculation is based on a two-band model using the low-frequency absorption coefficients of Churchill. The correction for non-equilibrium effects must be considered very approximate at present.

#### Non-stagnation Region

Radiative heat transfer distributions as calculated by STRADS for an inviscid, equilibrium shock layer are given in Figs. 2-36 to 2-46. The results are for the Apollo flying at a  $25^\circ$  angle of attack. In order to simulate the actual attitude by an axisymmetric configuration, the effective axis of symmetry is put at a distance  $R_0$  from the stagnation point, as shown in Fig. 2-36. The spectral coefficients are based on the "two-band" model with the Gilmore-Hahne coefficients. The surface pressure distribution used for Figs. 2-37 to 2-45 is given by the solid curve in Fig. 2-36. (Note that this pressure distribution is subsequently corrected, as given by the broken curve in Fig. 2-36. The effect is shown in Fig. 2-46.)

The environmental conditions for Figs. 2-36 to 2-42 correspond to a flight velocity of 10.37 Km/sec and ambient to sea-level density ratio of  $2.56 \times 10^{-4}$ . Figure 2-37 shows the optical thickness for the two "bands". It is seen that the longer wavelength region is transparent ( $\tau \ll 1$ ) and the shorter wavelength region is not transparent ( $\tau \approx 1$ ). The effects of energy loss and absorption on the optical thickness are indicated.

Figure 2-38 shows the total wall heat flux as a function of surface location. It is seen that both energy loss and absorption have very significant effects. The curves for small values of  $S/R_{\max}$  are dotted to indicate that the results there are not to be accepted. The approximations used in the streamtube formulation are inaccurate near the stagnation region.

Figure 2-39 shows the wall heat flux within the ultra-violet region (400 - 1130 $\overset{\circ}{\text{A}}$ ) and Fig. 2-40 shows that for the longer wavelength region. It is of interest to note that for the non-adiabatic cases absorption increases the wall heat flux in the longer wavelength region but decreases that in the shorter wavelength region. This is because absorption maintains a higher temperature in the shock layer than for the case without absorption. Since the optical thickness in the longer wavelength region is small, the increase in wall heat flux in this spectral region is due to the increase in temperature. On the otherhand, the optical thickness in the shorter wavelength region is large; therefore, the attenuation effect of absorption decreases the wall heat flux in this spectral region.

Figures 2-41 and 2-42 show the shock layer temperature profiles at two surface locations. It is seen that both energy loss and absorption modify the temperature distribution.

Figure 2-43 shows the effects of altitude on the total wall heat fluxes. The differences between the adiabatic-non-absorbing and non-adiabatic-absorbing cases decrease as the altitude increases.

The effects of spectral absorption coefficient models on the total wall heat flux to Apollo are indicated in Fig. 2-44. The six-band model yields a slightly smaller total heat flux. The six-band optical thicknesses are given in Fig. 2-45.

After the results given in Figs. 2-37 to 2-45 were obtained, an improved Apollo pressure distribution was calculated using the STREAMTUBE Code.

This improved pressure distribution is given by the dotted curve in Fig. 2-36. Figure 2-46 shows the effects of the pressure distribution on the Apollo heat flux distribution. The effects of using a different set of absorption coefficient for  $\lambda > 0.113\mu$  are also shown in Fig. 2-46.

#### Application of Results

For a single point (fixed altitude and velocity) description of the wall heat flux, detailed computations of the flow field and radiative energy transport are desirable. However, when radiative heating histories must be determined for several trajectories, the use of more expeditious techniques is warranted.

According to the results presented in Fig. 2-43, the heat flux distributions when normalized to the maximum or to the stagnation point value are approximately similar. Thus, the distribution may be assumed frozen as an engineering approximation and the local heat flux may be calculated using the stagnation heat function and the normalized distribution. To obtain the stagnation heat flux, data such as presented in Fig. 2-31 suffice if small interpolation errors are admitted.

At the higher altitudes where non-equilibrium radiation is significant the heat flux computed in the above manner must be corrected. The local non-equilibrium flux and non-equilibrium distances are assumed dependent on the local free-stream velocity component normal to the shock wave. (This assumption is strictly valid when the thickness of the non-equilibrium zone is small compared with the shock layer thickness. It becomes approximate when the normal and tangential velocities vary appreciably through the local non-equilibrium zone.) With this assumption, the non-equilibrium flux and zone thickness may be estimated from the normal shock formulae (Eqs. 2.63 - 2.66) by replacing the free stream velocity with the normal component of velocity. Then the total radiation is given approximately by

$$q_{xt} = q_{xe} \left[ \frac{\Delta - \Delta_n}{\Delta} \right] + q_{rn} \quad \Delta > \Delta_n \quad (2.122)$$

$$q_{rx} = q_{rn} \quad \Delta \leq \Delta_n \quad (2.123)$$

where  $q_{re}$  is the radiation from a shock layer in complete equilibrium and  $q_{rn}$  is the non-equilibrium radiation computed via Eqs. (2.63 - 2.66). This method is considered satisfactory for the trajectories of interest since the high radiative heating generally occurs when equilibrium radiation predominates.

The foregoing calculation procedures are embodied in the ENVIRONMENT program, which is used to generate rapidly histories of the aerothermal environment. The program is described in Volume II.

### 2.3 CONVECTIVE HEAT TRANSFER

The problem of predicting convective heat transfer to blunt vehicles traveling at hypersonic speeds has received wide attention. The effects of dissociation and ionization, non-equilibrium, mass injection, pressure gradient, and other influencing factors have been determined by rigorous numerical solution of the boundary layer equations. While the numerous investigations have produced a good understanding of the phenomena influencing boundary layer development, the prediction of convective heating involves application of many simplifying assumptions and approximations.

Most theoretical studies have treated only one or two of the many phenomena important in an actual flight situation. The turbulent boundary layer has not been well characterized because of uncertainties in the turbulent transport mechanism. For these reasons, approximate correlation formulae and semi-empirical relations are generally used in computation of the convective heating experienced by an entering vehicle. The purpose of this work has been to select methods enabling a realistic accounting for the interactions important during superorbital entry. Development of efficient means for solution of the complete boundary layer equations was beyond the study scope. Hence, existing theoretical developments and experimental



results have been used for the most part. This section first examines the dependence of convective heating on the various influencing factors. The literature is then reviewed in selection of suitable computation techniques. Finally, results obtained in application of the adopted procedures are presented. Subsidiary analyses and data correlations are given in the appendices.

### 2.3.1 Phenomenological Review

As the reentering vehicle descends through the atmosphere, a number of convective regimes will be encountered. Hayes and Probstein (Ref. 2.12) identify seven separate classes ranging between the free molecule flow and boundary layer regimes. Because convective heating rates are very small in the rarefied gas flows, only the vorticity interaction and boundary layer regimes are examined. In this latter regime consideration must be given to both laminar and turbulent flows.

It has been shown in the previous sections that non-equilibrium and radiative energy transport influence the flow to some degree. The effects on convective heating of these phenomena, together with mass injection, surface reactions, and shock generated vorticity, are examined in the following paragraphs. Also treated is the influence of non-similar wall conditions.

#### General Flow Conditions

The magnitude and spatial variation of some of the fundamental parameters affecting boundary layer development on Apollo are presented here for future reference. Figure 2-47 depicts conditions at the outer edge of the boundary layer for the approximate flight conditions of peak convective heating. Temperature, Mach number, and pressure gradient parameter are shown as a function of normalized distance from the stagnation point. At the indicated temperature level, the air is almost completely dissociated but the degree of ionization is very slight. The pressure gradient parameter does not vary appreciably over the spherical sector, but increases abruptly on the toroidal corners, reflecting the rapid expansion. Mach

number becomes sufficiently large so as to make viscous dissipation important. Figure 2-48 shows the inner boundary conditions of wall temperature and normalized injection velocity.\* Both quantities vary significantly along the surface thus destroying similarity. The surface will be highly reactive for the temperature shown. Gas composition at the surface will be strongly influenced by ablation products at the indicated injection velocity. By comparison of the results of Figs. 2-47 and 2-48, it can be inferred that the wall enthalpy ratio,  $\frac{h_w}{H_e}$ , is much less than unity.

#### Flow Geometry

It was shown in Section 2.1 that a three-dimensional, inviscid-flow pattern is induced by vehicle angle-of-attack. As a consequence, rotational symmetry cannot be assumed in description of boundary layer development. The nature and techniques for analysis of three-dimensional boundary layers have been reviewed by Cooke and Hall (Ref. 2.11). Boundary layer thickness and temperature gradients are affected by the rate of divergence of adjacent streamlines. Cross flow within the boundary layer results from pressure gradients normal to the streamwise direction. Beckwith (Ref. 2.72) has examined the influence of cross flow and found it to be small, particularly for strong wall cooling and moderate, favorable pressure gradients such as those of interest here. With the assumption of small cross flow, the three-dimensional boundary layer equations are directly analogous to those for rotationally symmetric flow. The usual radial coordinate appearing in the axi-symmetric equations is simply replaced by the spreading coordinate,  $h_2$ , which was introduced in Section 2.1. Thus the influence of flow pattern is simply determined using solutions derived for axi-symmetric flow.

---

\* These conditions were computed assuming laminar boundary layer flow. With turbulent flow, both the wall temperature and injection rate are increased.

Figure 2-49 shows the convective heating distribution for Apollo at 25 deg angle-of-attack as computed by the methods outlined in Section 2.3.2. To illustrate the effect of flow geometry, results obtained assuming rotationally symmetric flow and two-dimensional flow are compared with those obtained using the spreading coordinate of Fig. 2-16. (All results in the figure are normalized by dividing the local convection coefficient by the convection coefficient which would exist at the zero-angle-of-attack stagnation point with a Newtonian velocity gradient.) It may be observed that the convective heating level is not well approximated by either of the two limit predictions. At the stagnation point, the heating is somewhat less than for rotationally symmetric flow. The trends away from the stagnation point reflect the streamline pattern. On the lee side, the heating tends toward the rotationally symmetric level. On the windward corner, the flow tends toward two-dimensional. It is apparent from the results of Fig. 2-49 that flow geometry should be properly accounted for in prediction of the convective heating.

#### Surface Protrusions

Irregularities in surface contour may also be of concern in establishing local heating level. The smooth Apollo surface is interrupted by launch load-bearing pads and other protruding equipment. It has been demonstrated in numerous experimental investigations that such projections can cause significant changes in magnitude of heating. As depicted in Fig. 2-50, the flow pattern in the vicinity of the protuberance may be greatly altered. Pressure increase with attendant flow separation occurs upstream of the protuberance. A dead air region, reattachment point, and wake occur downstream of the protuberance. The extent of the interference region and degree of heat transfer coefficient perturbation are dependent on local Mach number, Reynolds number, pressure gradient, wall cooling, mass injection, protuberance shape, and protuberance size. Interference factors (ratio of local heat transfer coefficient to undisturbed heat transfer coefficient) of greater than two have been measured in wind-tunnel testing of scale models of the Apollo configuration. Thus an accounting for protuberances is of first-order importance in design heating predictions.

### Shock Generated Vorticity

Curvature of the bow-shock wave enveloping a blunt body induces an entropy gradient in the flow which is manifested by velocity and density variations normal to the wall. The vortical character of the inviscid flow was described in Fig. 2-15 where it was shown that velocity increases rapidly in the direction away from the body surface. The shock-generated vorticity interacts with the boundary layer to cause an increase in heating level. The extent of the interaction is dependent on the magnitude of the inviscid flow velocity gradient relative to the viscous boundary-layer velocity gradient. Thus, it would not be expected that external vorticity would appreciably affect the development of a very thin boundary layer. In such a situation the boundary layer may be described by application of classical boundary layer theory with the boundary-layer edge conditions taken from the inviscid solution for the surface streamline. However, it is apparent that for very thick boundary layers the shock generated vorticity will significantly alter the edge conditions. In this case, the edge velocity is increased and the edge velocity gradient can no longer be considered negligible. The application of second-order boundary layer theory is required to obtain a solution for a viscous flow region which merges smoothly into the external rotational flow field.

Solutions which have the desired characteristics have been obtained by several different techniques. Results showing the influence of the vorticity interaction at a rotationally symmetric stagnation point are shown in Fig. 2-51. The different investigators have obtained widely varying results. Van Dyke (Ref. 2.73) and Maslen (Ref. 2.74) employed inner and outer expansion techniques. Ho and Probstein (Ref. 2.75), Herring (Ref. 2.76), and Cheng (Ref. 2.77) carried out viscous shock layer analyses. An approximate matching method was utilized by Ferri, Zakkay, and Ting (Ref. 2.78). The latter workers present experimental data substantiating their theoretical results. However, the solutions by Van Dyke and Maslen are the most rigorous and hence should yield the correct results. While the various results differ somewhat in level, the predicted trends are generally the same. The

vorticity effect is greatest at high altitude and flight speed. This is in agreement with expectation since inviscid flow velocity gradients are increased by increasing flight speed (or decreasing shock density ratio) as indicated by the results of Fig. 2-15 and viscous flow velocity gradients are decreased by increasing altitude (or decreasing Reynolds number).

The influence of vorticity on Apollo heating is indicated in Fig. 2-52 by comparison of predictions with and without the vorticity interaction correction. The non-blowing heat transfer history at the stagnation point shown in this figure is for Trajectory II. This trajectory was selected for the comparison since it yields the maximum vorticity interaction. The extent of the vorticity interaction was predicted by the approximate method described in Appendix 2E. This technique yields results in essential agreement with the rigorous solutions of Van Dyke and Maslen and hence the results are considered realistic. It may be seen from Fig. 2-52 that shock-generated vorticity will have small influence on Apollo convective heat transfer. During the period of peak heating, the heat rate is increased by only about 4 percent. It is concluded that an accounting for vorticity in prediction of heat transfer is desirable, but not of first-order importance.

It is noted that radiative energy loss from the shock layer will also induce vorticity in the flow. This problem is subsequently considered in discussion of radiation-convection coupling.

#### Non-Equilibrium

At lunar return velocity, a substantial fraction of the shock-heated-air energy is invested in chemical modes, i.e., dissociation and ionization. Hence energy transport through the boundary layer depends not only on molecular conduction, but also on the diffusional flux of atoms and ions. The local chemical state and therefore the concentration gradients giving rise to diffusion are dependent in part upon kinetically-controlled reaction processes. The sensitivity of convective heat transfer to finite-rate chemical kinetics is examined here. Consideration is given to the

effects of (1) the chemical state at the boundary-layer outer edge, (2) the rate of homogeneous reactions within the boundary layer, and (3) the rate of heterogeneous and wall-catalyzed reactions at the boundary-layer inner edge.

Relaxation rates in the inviscid flow govern the chemical state at the boundary-layer outer edge. In the stagnation region, dissociation and ionization may be incomplete so that molecular species concentrations and kinetic temperature are somewhat greater than at equilibrium. The air, in expanding away from the stagnation point, may tend to chemically freeze resulting in local atom and ion concentrations that are greater than for equilibrium air. For this situation, the temperature is below the equilibrium value. Thus, inviscid-flow chemical kinetics may act to perturb edge conditions in either direction away from equilibrium. In addition to the composition and temperature perturbations, there will be attendant velocity and density perturbations.

Within the boundary layer, the flow may be in equilibrium, partly out of equilibrium, or frozen. For the latter cases, concentration gradients will depend sensitively on the catalytic efficiency of the wall. For certain materials, such as metals, recombination on the surface is promoted and a near-equilibrium condition prevails at the wall. For other materials, no recombination occurs or reaction between the surface elements and air takes place.

Numerous investigations of the non-equilibrium, dissociated boundary layer have been conducted. The non-equilibrium, ionized boundary layer has also been investigated, but to a lesser extent. The results of these studies may be used to infer the importance of non-equilibrium chemistry on Apollo heating. At early times during Apollo entry the air is almost completely dissociated whereas the degree of ionization is slight. This is indicated by the inset in Fig. 2-53 where the equilibrium composition at the inviscid, stagnation point is shown as a function of time. At time of peak heating,

ion concentration is less than 0.06. Thus, ionization effects do not assume overwhelming importance.

For the non-equilibrium dissociated boundary layer, it has been demonstrated by Fay and Riddell (Ref. 2.79), Goulard (Ref. 2.80), and others that the convective heat transfer is to a good first approximation linearly dependent on the enthalpy potential across the boundary layer. With a frozen boundary-layer and non-catalytic surface, the heat transfer is reduced in proportion to the ratio of chemical enthalpy to total enthalpy. With a catalytic surface, the chemical energy released at the wall by atom recombination brings the total heat flux up very close to the value for an equilibrium boundary layer. This results because the Lewis number, which is a measure of the relative conduction and diffusion resistances, is near unity and because transport properties do not strongly depend on the composition. From this observation, the approximate limiting values of convective heat transfer to Apollo may be simply predicted. Figure 2-53 compares the lower limit on heat flux, corresponding to a frozen boundary-layer and non-catalytic surface, with the approximate upper limit, corresponding to an equilibrium boundary layer. The results neglect mass injection effects and are for Trajectory II, which will be most influenced by non-equilibrium. It may be seen that the two limits are widely different and thus the proper boundary-layer regime must be established.

First, the boundary-layer-edge conditions are considered. It was previously indicated in Section 2.1 that the non-equilibrium zone in the inviscid shock layer would be confined to a small region immediately adjacent to the shock layer for the period of peak heating. At the relatively high altitudes where heating rates are low, the inviscid flow at the boundary-layer edge may be out of equilibrium. Non-equilibrium will not alter the total energy, but only its division among the different modes. Thus, from the aforementioned dependence of heat transfer on the enthalpy potential, it would not be expected that non-equilibrium edge conditions would appreciably affect heat transfer if equilibrium is attained at the wall.

This has been borne out in several calculations for the dissociated boundary layer (e.g., Clutter and Smith, Ref. 2.81). Rose and Stankevics (Ref. 2.82) note that heat transfer from an ionized boundary layer is also essentially independent of the degree of equilibration at the boundary-layer edge. Anticipating that an equilibrium surface condition will exist for Apollo, it is concluded that inviscid-flow chemical kinetics will not be important in evaluation of convective heat transfer.

The reaction rate regime within the boundary layer may be characterized by a Damkohler number, which is the ratio of characteristic flow time to characteristic reaction time (Refs. 2.79 and 2.80).

$$D = \frac{t_{DIFF}}{t_{CHEM}}$$

For large values of the Damkohler number, the boundary layer is considered to be in equilibrium whereas for small values it is considered frozen. The characteristic flow time has conventionally been taken equal to the inverse of the stagnation point velocity gradient. For dissociated boundary layers, the rate of oxygen recombination is generally used to define the characteristic reaction time since nitrogen recombination occurs more rapidly. For the present purpose, Damkohler numbers for deionization, nitrogen recombination and oxygen recombination are defined. Following Fay and Riddell, but taking an improved estimate of recombination rate constant from Ref. 2.83, the Damkohler number for oxygen recombination is

$$D_o = \left[ 4.6 \times 10^{13} \frac{(\text{°R})^{2.5}}{(\text{ATM})^2 (\text{SEC})} \right] \frac{P_o^2}{T_o^{2.5}} \frac{1}{\frac{du_e}{ds}} \quad (2.124)$$

Similarly, using the rate constant for nitrogen from Ref. 2.83,

$$D_N = \left[ 6.1 \times 10^{15} \frac{(\text{°R})^3}{(\text{ATM})^2 (\text{SEC})} \right] \frac{P_o^2}{T_o^3} \frac{1}{\frac{du_e}{ds}} \quad (2.125)$$

For electrons, the dominant recombination process is assumed to be collisional-radiative with rate constant obtained from Ref. 2.84



$$D_e = 8.2 \times 10^5 \left[ \frac{^\circ R^{1.7}}{\text{atm sec}} \right] \left( \frac{P_o}{T_o / 10^4} \right)^{2.7} \left( \frac{du_o}{ds} \right)^{-1} \quad (2.126)$$

Figure 2-54 describes the variation of these Damkohler numbers for Trajectory II. The instantaneous values are plotted as functions of the non-blowing convective heat rate. It may be seen that nitrogen recombination and deionization will occur at relatively rapid rate, at least during the period of high heating. Thus, the boundary layer cannot be considered out of equilibrium.

Goodwin and Chung (Ref. 2.85) have shown that the heat transfer from a non-equilibrium boundary layer to a non-catalytic surface can be correlated in terms of a parameter involving the Damkohler number, the ratio of edge chemical enthalpy to total enthalpy, and the edge atom concentration. The correlation has been extended by Inger (Ref. 2.86) to include the influence of wall temperatures. Figure 2-55 presents the correlation and shows the magnitude of the correlating parameter for Apollo. It appears from these results that for the period of high heating the heat flux will be close to that for an equilibrium boundary layer. In this regard, it is noted that the correlation is based on calculations using the slower oxygen recombination rate for both oxygen and nitrogen recombination. Thus the correlation exaggerates the departure from the equilibrium heating level.

For the lower heating rate phases of flight where the results of Fig. 2-55 show the boundary layer to be far out of equilibrium, the wall catalycity will greatly affect Apollo convective heating. As was indicated in Fig. 2-53 the heat flux may vary between wide limits depending on the nature of the wall and its ability to catalyze recombination reactions. Goulard (Ref. 2.80) has quantitatively established the dependence of the convective heat flux on the catalytic recombination rate constant. He shows that pyrex walls may be considered non-catalytic, that metal surfaces can be treated as having essentially infinite catalycity, and that oxides must be considered as having finite recombination efficiency. The Apollo heat shield will

be charred very early after heating begins and thus the surface presented to the boundary layer will consist of carbon intermixed with ceramic fibers (e.g., silica). This material configuration results in a system of wall reactions distinct from those considered in previous non-equilibrium boundary analyses since the possibility of heterogeneous reactions (carbon monoxide and cyano formation) must now be admitted. (The ceramics are only mildly catalytic and their effects will be largely masked by the carbon.) The reaction behavior of carbon and atomic oxygen has been studied by Rosner and Allendorf (Ref. 2.87). They found that almost all oxygen atoms hitting a carbon surface will react to form carbon monoxide. Goldstein (Ref. 2.88) and Zinman (Ref. 2.89) examined atomic nitrogen reactions with carbon and determined that kinetics of the cyano formation reaction are very slow. Their results suggest that the competing nitrogen recombination reaction is predominant for temperatures below about 4000<sup>o</sup>F. The Apollo surface will thus act as a highly catalytic wall in depleting atom concentration near the surface, but oxygen atom depletion will be accomplished by heterogeneous surface reaction rather than by catalytic recombination. Although the reaction system is different from that treated in previous non-equilibrium analyses, the existing solutions for highly catalytic walls may be employed in prediction of Apollo convective heating. To enable this, the concept of a two-step reaction is introduced. It is assumed that the oxygen atoms first recombine on the surface, liberating the dissociation energy, and subsequently react forming carbon monoxide, yielding an additional quantity of heat. (The assumed reaction path does not affect the total heat liberated.) The non-equilibrium solution for heat transfer is thus perturbed simply by accounting for the additional heat release. The manipulation is identical to that subsequently discussed for the analogous equilibrium boundary layer reaction.

Thus far the general non-equilibrium boundary-layer phenomena have been discussed, it has been shown that the Apollo boundary layer will be partially out of equilibrium, and it has been established that the wall may be considered highly catalytic. For these conditions, the ionized-boundary-

layer solutions of Fay and Kemp (Ref. 2.90) and Fenster (Ref. 2.91) may be used to estimate the non-equilibrium influence. Figure 2-56 compares their solutions for the limit situations of equilibrium and frozen boundary-layer flows. The results of Fay and Kemp indicate the non-equilibrium effect to be very small for Apollo entry. The heat flux is increased sensibly by non-equilibrium effects only at the early times when the velocity is above 30,000 ft/sec. Fenster's more recent calculations suggest a larger effect which persists down to much lower velocity. The maximum difference between frozen and equilibrium boundary layer heating is about 75 percent. Referring to the previously discussed results of Figs. 2-54 and 2-55, it appears probable that the actual heating will lie closer to the equilibrium prediction than to the frozen prediction. It is then tentatively concluded that the non-equilibrium effects will perturb the convective heating by an amount of the order of 10 percent at most.

Consideration has not been given to the influence of foreign specie injection on the non-equilibrium boundary layer. Chemical kinetics and transport properties within the boundary layer may be markedly changed by the introduction of typical ablation products. A conclusion as to foreign specie effects must await detailed solution of the multi-component boundary layer equations for the situations of interest.

#### Mass Injection

It is well recognized that convective heating is very sensitive to mass injection. The boundary layer is thickened with consequent reduction of wall enthalpy gradient. Figure 2.7 was previously introduced to describe the mass injection history at the geometric center position for a representative lunar return trajectory. Those results are recast in Fig. 2-57 where the transformed injection velocity,  $-f_w = \frac{4}{\mu_0 \sqrt{23}}$ , is presented. The effect of the mass injection on convective heat transfer may be qualitatively determined by examining boundary layer solutions for the problem of air injection into air. The inset of Fig. 2-57 shows results obtained by Libby (Ref. 2.92) for injection at the stagnation point into an undis-

sociated boundary layer. The convection coefficient, when ratioed to the non-blowing convection coefficient, is almost a unique function of the transformed injection velocity. Similar results have been obtained for dissociated and ionized boundary layers by Pallone and Van Tassel (Ref. 2.93). The correlation obtained by Libby is applied in Fig. 2-58 to show the heat transfer reduction resulting from mass injection for the conditions depicted in Fig. 2-57. These results demonstrate that mass injection has first-order effect on the convective heating for Apollo. In fact, they indicate that at the extreme conditions mass injection may cause boundary-layer blow-off and cessation of convective heating.

It is then clear that special attention must be given to description of the mass injection effect. The available theoretical and experimental results show that pressure gradient and injectant composition may appreciably influence the convective shielding afforded by mass injection. Also, the boundary layer regime is important. Transpiration is much less effective for turbulent boundary layer flows. These factors must all be considered in selection of procedures for prediction of the convective heating.

#### Radiation Coupling

It was shown in Section 2.2 that radiative energy transport is of sufficient magnitude for some Apollo flight conditions to appreciably affect local state conditions within the inviscid flow field. Under these circumstances the structure of the viscous boundary layer is altered and convective heat transfer may be changed. The interaction of radiation on convection is two-fold. First, conditions at the outer edge of the boundary layer are changed due to radiative cooling of the inviscid flow. Second, radiation competes with conduction and diffusion as a mechanism of energy transfer within the boundary layer.

Referring to the results of Fig. 2-20, it may be recalled that both the temperature and velocity of the inviscid flow near the wall are reduced by radiative energy loss. The temperature perturbation reduces the

potential for heat transfer and the velocity reduction increases the convective resistance. Clearly then, radiative energy loss acts to reduce the convective heat flux. Due to the total enthalpy gradient, the effect will be maximum for thin boundary layers. (Thin boundary layers will entrain air which has experienced the greatest energy loss.)

Emission and absorption within the boundary layer was discussed in Section 2.2.2. Near the wall where temperature is relatively low, absorption will generally exceed emission. Thus, radiative transport tends to increase fluid temperature in the inner portion of the boundary layer (or temperature gradient at the wall) and convective heat transfer is accordingly increased. The magnitude of the effect is dependent on the opacity of the boundary layer gas. The direction of the effect is to compensate for radiative energy loss effects.

A rigorous accounting for radiation effects on convective heat flux is complex and therefore few solutions to the problem have been obtained. In the general case, radiative transport terms must be included in the viscous flow energy equation. The inviscid-flow temperature and velocity gradients must be accounted for in formulation of the outer boundary conditions. Burgraff (Ref. 2.94) has developed a second-order solution for the case of a transparent gas. He applies the method of inner and outer expansions to couple the inviscid and viscous layers. Because of the transparency assumption, his technique should yield the maximum reduction in convective heat transfer. It has been applied to determine the limit effect of radiation on Apollo stagnation point convective heating. Computations were performed for Trajectory III since the conditions prevailing in this trajectory (high Reynolds number and high values of the radiation energy loss parameter) are such as to maximize the coupling between radiation and convection. The results are shown in Fig. 2-59. The maximum reduction in convective heating occurs at the approximate time of peak radiation and is 10 percent.

A more realistic situation involving radiation absorption and injection of a single foreign species has been treated by Hoshizaki and Wilson (Ref. 2.95). They have obtained radiation-coupled solutions by means of a combined integral-finite difference scheme wherein the complete shock layer is assumed viscous. While the conditions for which they have performed numerical calculations do not duplicate those of Apollo, their results provide insight as to the magnitude of radiation effects on convective heating. The results are reproduced in Table 2.2. The first column of

Table 2.2  
RADIATION-COUPLING EFFECT ON CONVECTION

FLIGHT CONDITION				CONVECTIVE HEAT RATE	
Velocity	Altitude	Nose Radius	Carbon Monoxide Injection Rate	Uncoupled	Radiation Coupled
(ft/secx10 <sup>-3</sup> )	(ftx10 <sup>-5</sup> )	(ft)	( $\rho v_w / \rho_\infty u_\infty$ )	(Btu/ft <sup>2</sup> sec)	(Btu/ft <sup>2</sup> sec)
5.0	2.0	2.0	{ 0	2210	2000
			{ 0.05	728	750
4.1	1.8	1.0	{ 0	1390	1320
			{ 0.053	174	211
3.7	2.3	4.0	0	200	193

results presents convective heat transfer rates in the absence of radiation effects. The second column gives the heat flux accounting for energy loss and absorption. The influence of carbon monoxide injection is shown for two of the flight conditions. (Carbon monoxide was selected by Hoshizaki as representative of ablation products. This molecule is a dominant absorber as previously indicated in discussion of Fig. 2-25.) For all cases with zero mass injection the convective heat transfer is reduced slightly by radiation effects. In these cases, energy loss effects dominate over absorption effects. The reverse is true with mass injection. Thickness

and hence opacity of the low temperature portion of the boundary layer is increased by mass injection. Thus absorption assumes greater importance. For the relatively high blowing rates considered, absorption overcompensates for energy loss effects and the net effect of radiation coupling is a small increase in the convective heat flux.

The results of Table 2. indicate that the convective heat transfer is influenced to a much greater extent by mass injection than by radiation coupling. This point is emphasized in Fig. 2-60 by comparison of the blowing and limit radiative corrections to Apollo heating. Of further interest is the fact that when the radiation correction to convective heating is maximum, radiative heating dominates over convective heating.

It is concluded from the available results that radiation coupling will be of minor significance for Apollo flight predictions. For engineering prediction of the convective heating, this coupling may be neglected.

#### Surface Temperature and Mass Transfer Parameter Variations

The assumption of boundary-layer similarity is frequently invoked in prediction of convective heat transfer even though the necessary conditions are rarely satisfied. The attendant simplifications are great and excellent results are often obtained.

Streamwise variation of boundary layer edge and wall conditions, finite-rate chemical kinetics, and radiative energy transport will all tend to destroy similarity of the Apollo boundary layer. However, it has previously been shown that non-equilibrium and radiation effects on convective heating are small. Furthermore, it is well known that application of the local similarity principle enables an adequate accounting for edge condition variations. Thus, an assessment of the influence of wall conditions assumes importance.

Similarity requires that the wall temperature and transformed injection velocity,  $-f_w$ , be constant. The qualitative influence of a departure from these conditions is immediately determined from consideration of the dependence of local boundary layer profiles on the upstream wall conditions. Lower upstream wall temperatures would cause greater cooling of the fluid adjacent to the wall and hence local heat transfer would be reduced. Greater upstream mass injection would result in a thicker boundary layer with reduced temperature gradient and thus heat transfer would again be reduced.

Representative mass transfer and surface temperature distributions for Apollo were shown in Fig. 2-48. Both the wall temperature and injection parameter vary appreciably along the surface. Figure 2-61 shows the influence of these non-similar distributions by comparing the "actual" heat transfer with that obtained assuming local similarity.\* The effects of wall temperature and injection velocity variation, when evaluated separately or in combination, are small. At worst, the local heat transfer deviates 10 percent from that predicted assuming similarity. The perturbation is considered sufficiently small to neglect.

It is well recognized that convective heat transfer levels differ markedly for laminar and turbulent boundary layers. The difference, which is dependent primarily upon Reynolds number, is quantitatively described as a function of time in Fig. 2-62 for the geometric center position of the Apollo entry vehicle. The results shown are for Trajectory I. During the period of peak heating, the levels differ by a factor of almost three. In this regard, it is noted that the results represent the heating to a cold, non-ablating wall. With mass injection accounted for, the difference would become even greater. It is obvious, then, that an accurate knowledge of the transition time is vital to design of a minimum weight heat shield design.

---

\* The methods used for predicting the non-similar effects are given in Appendix 2H. The solution incorporates several approximations. Since the approximations were applied consistently for the "actual" and similar predictions, the magnitude of the non-similar effects should be accurately represented.



Various transition criteria have been proposed. Of these, the Reynolds number based on momentum thickness is often used. The boundary layer is assumed to transit when  $Re_{\theta}$  exceeds some critical value. This value is not well defined and, in fact, should depend on the particular circumstances. For example, it is known that edge Mach number, pressure gradient, surface roughness, mass injection, and wall cooling may exert significant influence. A value in the neighborhood of 200 is generally used to predict the occurrence of transition. (For the configuration of interest, the value of 200 corresponds to a Reynolds number value based on wetted surface distance of approximately 300,000.) The location of the transition position on the Apollo vehicle, assuming a critical  $Re_{\theta}$  value of 200, is shown as a function of time in Fig. 2-63. During the initial descent, the transition position moves forward to a position about 6 ft from the stagnation point. As the vehicle pulls-out and ascends to higher altitudes, the transition location moves aft. In the final descent phase of the trajectory, the transition position again moves forward. Also shown on the figure are transition-position histories predicted by perturbing the assumed  $Re_{\theta}$  value. With the more conservative criterion,  $Re_{\theta} = 100$ , a turbulent boundary layer is predicted over a greater portion of the surface and for a much longer period of time. With the optimistic criterion, laminar flow prevails over the complete surface during the period of peak heating. It is only at late times that turbulence creeps forward.

The variation in total heat transfer (cold-wall, non-blowing values) with position is described in Fig. 2-64 with the transition Reynolds number as a parameter. Although the Reynolds number range considered is not large, it is seen that total heat transfer differs markedly between the extremes. With  $Re_{\theta} = 400$ , turbulence does not contribute significantly to the total heat transfer. However, with  $Re_{\theta} = 100$ , the heat transfer over half of the surface is predominantly by the turbulent mechanism. Unfortunately the trajectory followed by the Apollo vehicle is such as to maximize the influence of transition uncertainty on total heat transfer. Thus, reduction of the uncertainty in the occurrence of transition is of particular importance in the Apollo application.

### 2.3.2 Prediction Techniques

The foregoing review has served to identify the phenomena exerting greatest influence on Apollo convective heating. It is apparent that mass injection and boundary layer transition are of major significance. Also important is the asymmetry of the flow. The influence of shock-generated vorticity is not appreciable except at high altitudes where convective heating is low. The combined effect of radiative energy loss and absorption on convective heating is small. Non-equilibrium and non-similar wall boundary conditions have only second-order effect.

Prediction techniques which account approximately for the more important effects are set forth in this section. First the general boundary layer equations are presented and available solutions are briefly reviewed. Then the relations recommended for prediction of laminar and turbulent heat transfer are given together with an empirical transition criterion. Subsidiary developments and data correlations are contained in the appendices.

#### Governing Equations

The radiating, chemically reacting boundary layer is governed by the following system of conservation equations.

Mass

$$\frac{\partial \rho u h_2}{\partial s} + \frac{\partial \rho v h_2}{\partial y} = 0 \quad (2.127)$$

Species

$$\rho u \frac{\partial k_i}{\partial s} + \rho v \frac{\partial k_i}{\partial y} = \frac{\partial}{\partial y} \left( D_i \rho \frac{\partial k_i}{\partial y} \right) + \dot{w}_i \quad (2.128)$$

Tangential Momentum

$$\rho u \frac{\partial u}{\partial s} + \rho v \frac{\partial u}{\partial y} = - \frac{\partial p}{\partial s} + \frac{\partial}{\partial y} \left( \mu \frac{\partial u}{\partial y} \right) \quad (2.129)$$

Energy

$$\rho u \frac{\partial H}{\partial s} + \rho v \frac{\partial H}{\partial y} = \frac{\partial}{\partial y} \left[ k \frac{\partial T}{\partial y} + \mu \frac{\partial u^2/2}{\partial y} \right. \\ \left. + \sum_j \rho D_j h_j \frac{\partial K_j}{\partial y} + \sum_j \rho D_j^T K_j h_j \frac{\partial T}{\partial y} \right] + q_r \quad (2.130)$$

Incorporated in these equations are several simplifying assumptions. In particular, the boundary layer is assumed thin and cross flow, normal pressure gradient, and pressure diffusion are neglected. The spreading coordinate,  $h_2$ , appearing in the continuity equation accounts for the three-dimensional flow pattern. Its application is discussed in Ref. 2.11 and means for its evaluation are presented in Section 2.1. Radiative energy transport is accounted for in the energy equation by the term,  $q_r$ , which is the net volumetric rate of radiative energy absorption. The chemical source term,  $\dot{w}_j$ , in the continuity equation for the  $j^{\text{th}}$  specie is equal to the net creation rate of the specie due to chemical reactions. Auxiliary relations must be provided for both  $q_r$  and  $\dot{w}_j$ . The net radiative energy absorption is given by Eq. (2.109). The chemical source terms are given by equations of the form

$$\dot{w}_j \equiv M_j \frac{dN_j}{d\theta} = M_j \sum_{r=1}^R \left\{ k_f \prod_{l=1}^L (N_l)^{\alpha_l} - k_r \prod_{k=1}^K (N_k)^{\beta_k} \right\} \gamma_k \quad (2.131)$$

where  $k_f$  and  $k_r$  are the forward and reverse reaction-rate constants, and  $\alpha_l$ ,  $\beta_k$ , and  $\gamma_k$  are the stoichiometric coefficients for the  $R$  reactions involving specie  $j$

$$\sum_{l=1}^L \alpha_l N_l \frac{k_f}{k_r} \beta_j N_j + \sum_{k=1}^K \gamma_k N_k \quad (2.132)$$

An equation of state and relations for the transport properties of the mixture must also be provided. The conservation equations may be applied to the turbulent boundary layer as well as the laminar boundary layer if time-mean flow properties are used and if the molecular transport properties are replaced by the analogous terms accounting for turbulent transport.\*

In the presence of an ablating surface the wall boundary conditions required for solution of the conservation equations are

$$\begin{aligned} u &= 0 \\ T &= T_w \end{aligned} \quad (2.133a)$$

$$K_{jw} \sum_j (\rho N)_{jw} + \rho D_j \left( \frac{\partial K_j}{\partial y} \right)_w = (\rho N)_{jw}$$

where the injection rates of the various molecular species,  $\rho N_{jw}$ , and the wall temperature are obtained by coupled solution for the ablative material response. At the outer edge, boundary conditions on the velocity, total enthalpy, and molecular specie concentrations may be specified from the results of the inviscid flow solution. It should be noted that for the general case with radiative energy loss and shock-generated vorticity the outer-edge boundary conditions must be posed so as to obtain a smooth merging of the viscous flow into an external flow having total enthalpy, velocity, and molecular specie gradients. The conditions to be satisfied may be expressed as

$$\left. \begin{aligned} K_j(y) &\longrightarrow K_{je}(y - \delta^*) \\ u(y) &\longrightarrow u_e(y - \delta^*) \\ H(y) &\longrightarrow H_e(y - \delta^*) \end{aligned} \right\} \quad (2.133b)$$

\* Ness and Lew (Ref. 2.96) present in detail the differential equations for the chemically-reacting turbulent boundary layer.

where  $K_{j_e}$ ,  $u_e$ , and  $H_e$  are the flow quantities obtained from an inviscid solution as a function of  $y$ , and  $\delta^*$  is the boundary-layer displacement. It should be understood from these conditions that as  $y$  becomes large both the magnitude and gradient must be matched. All of the outer-edge and wall boundary conditions may vary with streamwise distance with the exception of the tangential wall velocity which is assumed to be zero.

#### Available Solutions

The foregoing system of equations has not been solved for the general situation involving ablation product injection, finite reaction kinetics, and radiative coupling.\* However, solutions have been obtained for a variety of special cases. Some of the more important contributions are summarized in Table 2.3.

The stagnation-point boundary layer has received relatively wide attention since it may be treated with least difficulty. Symmetry permits reduction of the boundary-layer equations to a set of ordinary differential equations at this point alone. Several numerical solutions for dissociated and ionized air boundary layers have been carried out. The majority have treated the limiting conditions of either frozen or equilibrium flow. While transport property models of differing degrees of sophistication have been employed, the results are generally in good quantitative agreement. Simple correlation formulas which accurately reproduce the numerical results have been devised by the various investigators.

The effects of blowing at the stagnation point have been extensively studied. Theoretical description of the boundary layer has been obtained for injection rates ranging up to and beyond the thermal boundary-layer

---

\* The immense computational effort required in numerical integration of the differential equations has precluded general solutions until recently. With large electronic data-processing machines the computation becomes feasible. Calculation procedures which approach complete generality are currently being formulated for solution of the laminar boundary-layer problem.

Table 2.3  
SUMMARY OF BOUNDARY LAYER INVESTIGATIONS

				PHENOMENA CONSIDERED												
				Compressibility	Pressure Gradient	Viscous Dissipation	Dissociation	Ionization	Finite Reaction Rates	Mass Injection	Foreign Specie Injection	Coupled Ablation	External Vorticity	Radiative Energy Loss	Radiation Absorption	
TRANSPORT PROPERTY SOURCE																
LAMINAR INVESTIGATIONS																
Stagnation Point Solutions																
Fay & Riddell	(2.79)	Approx		x	x	-	x			x						
Hoshizaki	(2.97)	Hansen		x	x	-	x	x								
Fay & Kemp	(2.90)	Yun		x	x	-	x	x								
Fenster	(2.91)	Peng		x	x	-	x	x								
Libby	(2.92)	Approx		x	x	-					x					
De Rienzo & Pallone	(2.98)	Yos		x	x	-	x	x			x					
Scala & Gilbert	(2.99)	Scala		x	x	-	x				x	x				
Van Dyke	(2.73)	Approx		x	x	-								x		
Maslen	(2.74)	Approx		x	x	-								x		
Burggraf	(2.94)	-		x	x	-								x	x	
Howe & Sheaffer	(2.100)	Hanson		x	x	-	x	x			x			x	x	x
Local Similarity Theories																
Lees	(2.101)	-		x												
Kemp, Rose, & Detra	(2.102)	Approx		x	x	x										
Cohen	(2.103)	Hansen		x	x	x	x	x								
Non Similar Solutions																
Blottner	(2.104)	Blottner		x	x	x	x	x	x							
Pallone & Moore	(2.105)	Bade		x	x	x	x	x	x							
Hoshizaki & Wilson	(2.95)	Hansen		x	x	x	x	x			x		x	x	x	
TURBULENT THEORIES																
Eckert	(2.106)	-		x		x										
Bromberg	(2.107)	-		x		x										
Denison	(2.108)	-		x	x	x										
Burggraf	(2.109)	-		x		x										
Ness	(2.110)	-		x		x					x	x				
Denison	(2.111)	-		x		x					x	x	x			

"blow-off" condition. The recent results for dissociated and ionized boundary layers compare reasonably well with early computations for chemically inert flows, but they do show a slight dependence of the transpiration effect on velocity. Coupled ablation has been examined by Scala. He treated the multi-component diffusion problem for a chemically reacting system by imposing the constraint of chemical equilibrium everywhere including at the surface between gaseous and condensed phases. As in Denison's analysis for the turbulent boundary layer, a chemically simple ablator, carbon, was chosen for the computation.

The second-order boundary-layer theory solutions for the influence of vorticity and radiative energy loss on stagnation-point convective heating have been obtained by the method of matched inner and outer expansions. Gross approximations to the transport properties have usually been introduced to facilitate the theoretical developments and thus the results are not to be applied independently. Instead, the relations which are derived may be used to correct first-order numerical solutions for the second-order effects.

A relatively complete study of the stagnation point heating was undertaken by Howe and Sheaffer. They numerically solved a set of integro-differential equations describing the flow in the complete region between the body and shock surfaces. The trends shown by their results are the same as obtained in more specialized solutions, but the precise variations were influenced to an appreciable extent by interactions of the different phenomena.

Away from the stagnation point, the variation of flow parameters at the outer edge and wall destroys boundary-layer similarity. Rigorous solution of the boundary layer equations requires retention of the streamwise derivatives thus greatly complicating the problem. However, Lees has argued that for the usual situation of a highly cooled wall the variation of edge conditions is not important. He shows that for a flow in chemical equilibrium the wall enthalpy gradient is reasonably well represented by the

zero pressure gradient solution and thus the local heating can be simply related to the stagnation point heating by use of a transformed streamwise coordinate and local edge conditions. This procedure has been refined through the local similarity concept wherein the ordinary differential equations resulting from the similarity assumption are solved for the local conditions including variable pressure gradient and wall temperature. The local similarity solutions are conveniently applied by means of correlation equations.

The non-similar boundary-layer equations have been solved by several investigators in study of such effects as non-uniform wall temperature, discontinuous mass injection, and finite reaction kinetics. The early work was concerned primarily with non-similar wall boundary conditions and was performed for the case of uniform flow over flat plates (e.g., Refs. 2.112 - 2.115). Solution of the equations with variable edge conditions and finite reaction kinetics is more difficult and the available results are limited. A number of different techniques including multi-strip integral, implicit finite difference, and semi-similar methods have been employed in study of reaction kinetics effects on the air boundary layer.

The computations have been directed primarily to the description of ion concentration distributions through the boundary layer. Hoshizaki and Wilson have carried out what is perhaps the most comprehensive work on non-similar boundary layers. They have solved the viscous shock layer problem with mass injection and full radiation coupling by means of an approximate integral method. Their limited results show surprisingly small shift from the convective heating distribution obtained assuming boundary-layer similarity.

The turbulent boundary layer has been studied to a lesser extent than the laminar boundary layer due largely to the necessity for partial reliance on empiricism. Eckert has extended the incompressible theory by means of an empirically derived reference condition for evaluation of properties



in a compressible flow. By employing the Dorodnitsyn compressibility transformation and several reasonable assumptions in analysis of the turbulent boundary layer, Burggraf has succeeded in providing a theoretical foundation for the reference property method. Several theories have been formulated to account approximately for the influence of streamwise property variations. Of those analyses listed in Table 2.3 only Denison's has considered pressure gradient influence in detail. In view of the gross approximation which must be made in all of the theories, it does not appear that there is much to favor the more complicated treatments.

Finally, the powerful approximations of Lees (Ref. 2.38) for treating laminar and turbulent boundary layers in the presence of reacting surfaces should be mentioned. Provided the Lewis and Prandtl numbers are close to unity he has shown that the concentration of foreign elements may be simply related to the velocity distribution and, further, that the additional heat transfer due to chemical reactions can be determined without detailed knowledge of molecular species distributions through the boundary layer. In this regard, it is noteworthy that the results of Scala's multi-component boundary layer solution for heat transfer to and erosion rate of a reacting carbon surface can be closely reproduced by application of Lees' simple theory.

#### Recommended Techniques

The preceding review has included only a small portion of the large literature on convective heating of blunt bodies at high speed. However, the referenced works provide a representative sample of the considerations which have been made and the techniques which have been employed. Almost all important phenomena have been considered, but generally the various affects have been examined independently. Simple formulas accurately correlating numerical results of first-order laminar boundary-layer analyses are available. Relations enabling corrections for certain of the second-order effects have been derived for laminar flow. Turbulent boundary layer theory is not far advanced.

A complete and rigorous accounting for the various factors affecting convective heat transfer would entail very lengthy computations. Development and application of an involved finite-difference solution procedure was beyond the scope of this study. For these reasons, existing results are utilized to provide rapid, approximate means for prediction of the convective heat transfer. The following simplifying assumptions are made:

- (1) Radiative coupling has small effect
- (2) Chemical equilibrium prevails
- (3) Local similarity is assumed
- (4) Mass injection and heterogeneous surface reaction effects may be decoupled.

With the exception of the latter approximation which is subsequently discussed, these assumptions have been justified in Section 2.3.1. It was indicated that radiation predominates over convection during periods when coupling occurs and, furthermore, that the coupling effect is small when both energy loss and absorption are considered. Regarding chemistry, it was shown that recombination rates are relatively fast during the period of peak convective heating and thus the equilibrium heating level is approached. In any event, the difference in heating between the limiting conditions of equilibrium and frozen flow is no greater than the differences among the equilibrium results of various investigators. It was shown that with realistic spatial variations of the surface temperature and transformed injection velocity, the local heat transfer can be accurately predicted assuming local similarity.

With the above assumptions, the relations for prediction of convective heating reduce to a concise set which can be employed in a straightforward manner. The following paragraphs treat stagnation point heating, the laminar heat transfer distribution, and turbulent heating. Three-dimensional-flow geometry, vorticity, and surface combustion effects are accounted for. A boundary-layer transition criterion is given and approximate means for evaluation of the mass injection effect are presented. Protuberance effects are briefly discussed.

### Stagnation Point Heating

Several stagnation point solutions are available for the assumed conditions as indicated in Table 2.3. Some differences, arising largely from the use of different transport-property models, exist among the theoretical results. The scatter and uncertainty of experimental data is too large to enable identification of the most accurate predictions (see Ref. 2.82, for example). The results of Hoshizaki (Ref. 2.97) are adapted arbitrarily. They are in good agreement for the velocity range of interest with results obtained by De Rienzo and Pallone (Ref. 2.98) and by Cohen (Ref. 2.103). They lie appreciably above the results of Fenster (Ref. 2.91) and somewhat below those of Fay and Kemp (Ref. 2.90).\*

Hoshizaki found that his numerical results for heat transfer could be correlated by a simple equation. The correlation formula is, after conversion to yield the convection coefficient rather than the heat flux

$$C_{H_0} = 2.2 \rho_{\infty}^{0.5} \left( \frac{U_{\infty}}{10^4} \right)^{1.19} \beta_0^{0.5} \quad (2.134)$$

This relation reproduces the numerical results to within 7 percent for the complete velocity, pressure, and wall temperature ranges of interest.

The correlation equation (2.134) applies for an axi-symmetric stagnation point and must be generalized for the three-dimensional flow situation. Furthermore, it must be corrected for vorticity effects. The pertinent relations are developed in Appendices 2D and 2E. The effect of a departure from axial symmetry is given by

$$\frac{q_{3D}}{q_{axi}} = \left[ \frac{1}{2} \left( 1 + \frac{\beta_2}{\beta_0} \right) \right]^{0.5} \left[ \frac{1.033}{1.116 + 0.411 \left( \frac{1 + \beta_2/\beta_0}{1 + \beta_2/\beta_0} \right)^{-0.686}} \right] \quad (2.135)$$

\* The solutions of Fay and Kemp are not strictly comparable since they were obtained for pure nitrogen rather than air.

where  $\beta_0$  and  $\beta_z$  are the inviscid-surface-velocity gradients at the stagnation point along the plane of symmetry and in the transverse direction, respectively. The first bracketed term in Eq. (2.135) may be recognized as the correction obtained by Reshotko (Ref. 2.116) for the case of a very cold wall. The effect of pressure gradient parameter change, which is neglected in Reshotko's cold wall solution, is accounted for by the second bracketed term. This term is derived from the correlations of Cohen (Ref. 2.103). It is very near unity as may be seen by substitution of the value, 0.58, obtained in Section 2.1 for  $\beta_z/\beta_0$ . The influence of vorticity is given to a first approximation by

$$\frac{C_{H_0 \text{ VORT}}}{C_{H_0 \text{ NO VORT}}} = \left\{ 1 + \frac{3}{2} \left( \frac{M_0}{P_{\infty} U_{\infty} R} \right)^{0.5} \left[ \frac{1 - 2 P_{\infty}/P_0}{2^{3/4} (P_{\infty}/P_0)^{5/4}} \right] \right\}^{0.25} \quad (2.136)$$

This relation, derived from first-order boundary layer theory by introducing the concept of an effective edge velocity, is in essential agreement with the rigorous second-order boundary-layer solutions of Van Dyke (Ref. 2.73) and Maslen (Ref. 2.74). The vorticity correction is small except at high altitudes as a consequence of the inverse dependence on stagnation point Reynolds number (see Fig. 2-52).

The final equation for the non-blowing heat transfer coefficient at the stagnation point is obtained by combining Eqs. (2.134) - (2.136). The result is

$$C_{H_0} = 2.2 P_{\infty}^{0.5} \left( \frac{U_{\infty}}{10^4} \right)^{1.19} \left[ \frac{\beta_0 + \beta_z}{2} \right]^{0.5} \left[ \frac{1.033 + 0.545 \left( \frac{1 + \beta_z/\beta_0}{1 + \beta_z/\beta_0} \right)^{-0.686}}{1.116 + 0.411 \left( \frac{1 + \beta_z/\beta_0}{1 + \beta_z/\beta_0} \right)^{-0.686}} \right] \cdot \left\{ 1 + \frac{3}{2} \left( \frac{M_0}{P_{\infty} U_{\infty} R} \right)^{0.5} \left[ \frac{1 - 2 P_{\infty}/P_0}{2^{3/4} P_{\infty}^{5/4}} \right] \right\}^{0.25} \quad (2.137)$$

### Laminar Heating Distribution

Of the various local-similarity techniques which have been devised for prediction of the convective heat flux distribution, Cohen's procedure (Ref. 2.103) is considered most rigorous. In this method, the integral energy equation is satisfied. Local boundary layer profiles are determined by solution of the similarity boundary-layer equations using the appropriate local values of the pressure gradient parameter, edge static enthalpy-total enthalpy ratio, and wall enthalpy-edge total enthalpy ratio. Cohen has numerically solved the similar equations for a wide range of conditions and developed correlation relations giving the influence of each of the similarity parameters. His procedure and correlation formulae form the basis for the method adopted here.

In applying Cohen's results, the influence of wall temperature variation on the convection coefficient is neglected since the effect has previously been shown in Section 2.3.1 to be small.\* Pressure gradient and edge static enthalpy-total enthalpy ratio effects are considered. Three-dimensional effects are accounted for by replacing the radial coordinate in Cohen's equations by the spreading coordinate. (The analogy between the three-dimensional and axi-symmetric flows has been discussed in Section 2.3.1. The application of the spreading coordinate in the boundary-layer equations is shown in Appendix 2D.) Vorticity influence is approximately determined by using effective edge conditions.

The relation given by Cohen for the convective heat transfer distribution is

$$\frac{q}{q_0} = \left[ \frac{\frac{\rho_w \mu_w}{\beta H_e} \frac{d\eta_e}{ds}}{\left( \frac{\rho_w \mu_w}{\beta H_e} \right)_0 \left( \frac{d\eta_e}{ds} \right)_0} \right]^{1/2} \quad (2.138)$$

\* Neglect of the wall temperature influence does not significantly reduce the effort required to compute the convection coefficient distribution for a given set of conditions. However, it does enable the computation to be performed independently of the solution for wall temperature response. This is a great advantage.

where

$$\tilde{\beta} = \frac{2H_0 \frac{dU_e}{ds}}{\rho_w \mu_w U_e^2 H_e h_2^2 \Gamma^2} \int_0^s \rho_w \mu_w U_e h_2^2 \Gamma^2 ds \quad (2.139)$$

and, for the assumed condition of constant wall temperature, the transformed wall enthalpy gradient ratio is

$$\Gamma = \frac{q'}{q_0} = \left\{ \frac{1.116 + 0.411 \tilde{\beta}_0^{0.686}}{1 + 0.527 \tilde{\beta}_0^{0.686}} \frac{1 + 0.527 \tilde{\beta}^{0.686}}{1.116 + 0.411 \tilde{\beta}_0^{0.686}} \right\}$$

$$\left\{ 1.1 - 0.1625 \left( 1 - \frac{U_e^2}{2H_0} \right) + 0.0625 \left( 1 - \frac{U_e^2}{2H_0} \right)^2 \right\}$$

$$\left\{ \frac{1 - 0.15 \frac{U_e^2}{2H_0} - H_w/H_0}{1 - H_w/H_0} \right\} \quad (2.140)$$

The parameter  $\Gamma$  will generally vary slowly along the surface. Therefore, small error is incurred by moving  $\Gamma$  outside the integral in Eq. (2.139). With this simplification, Eqs. (2.138) and (2.139) may be combined to yield

$$\frac{q}{q_0} = \frac{\rho_w \mu_w U_e h_2 \Gamma}{\left[ \left( \frac{\rho_w \mu_w}{\tilde{\beta}_0} \right) \left( \frac{dU_e}{ds} \right)^2 \int_0^s \rho_w \mu_w U_e h_2^2 ds \right]^{1/2}} \quad (2.141)$$

For constant wall temperature

$$\frac{P_w H_w}{(P_w H_w)_0} = \frac{P_e}{P_0} \quad (2.142)$$

and with a recovery factor of 0.85

$$\frac{h}{h_0} = \frac{f}{f_0} \left\{ \frac{1 - H_w/H_0}{1 - 0.15 \frac{U_e^2}{2H_0} - H_w/H_0} \right\} \quad (2.143)$$

The convective heat transfer coefficient distribution may therefore be determined according to

$$\frac{C_H}{C_{H_0}} = \frac{\frac{P_e}{P_0} U_e h_2 G}{\left[ \frac{2}{\beta_0} \frac{dU_e}{ds} \int_0^s \left( \frac{P_e}{P_0} \right) U_e h_2^2 ds \right]^{1/2}} \quad (2.144)$$

where

$$G = \left\{ \frac{1.116 + 0.411 \beta_0^{\sim 0.686}}{1.116 + 0.411 \beta_0^{\sim 0.686}} \frac{1 + 0.527 \beta^{\sim 0.686}}{1 + 0.527 \beta^{\sim 0.686}} \right\} \\ \left\{ 1.1 - 0.1625 \left( 1 - \frac{U_e^2}{2H_0} \right) + 0.0625 \left( 1 - \frac{U_e^2}{2H_0} \right)^2 \right\} \quad (2.145)$$

The stagnation point and local values of the pressure gradient parameter are, from Eqs. (2.139) and (2.142)\*

\* The derivation of Eq. (2.146) from (2.139) is described in Appendix 2D.

$$\tilde{\beta}_0 = \frac{1}{\beta_z / \beta_0 + 1} \quad (2.146)$$

$$\tilde{\beta} = 2 \frac{H_e}{h_e} \frac{\tilde{\xi}}{u_e} \frac{du_e}{d\tilde{\xi}} \quad (2.147)$$

where

$$\tilde{\xi} = \left( \frac{\rho_w \mu_w}{\rho_0^2} \right)_0 \int_0^s \frac{P_e}{\rho_0} u_e h_1^2 ds \quad (2.148)$$

The preceding equations (2.144 to 2.148) constitute the set to be used in computation of the convective-heat-transfer distribution for laminar boundary-layer flow. In evaluation of these expressions, "effective" outer-edge conditions may be used to provide an approximate accounting for shock-generated vorticity effects. A method for selecting the effective edge conditions has been described in Ref. 2.52. The essential features of this method are reviewed in Appendix 2E and a computational scheme for applying the technique is given in Volume II in discussion of the VORTICITY computer program.

#### Turbulent Heat Transfer

The present status of turbulent heat transfer prediction techniques is not well advanced. Many of the phenomena of possible importance have not been studied. All of the existing theories are semi-empirical in nature. In view of this situation, it does not appear profitable to consider involved computational methods. The more elaborate techniques do not offer any real improvement in prediction accuracy. For this reason, the relatively simple theory developed by Bromberg, Fox, and Ackermann (Ref. 2.107) is



adopted. It provides no direct accounting for the influence of pressure gradient, but it does enable description of the effect of streamwise variation of outer-edge conditions.

Bromberg, Fox, and Ackermann initiate their development with the integral energy equation

$$\dot{q}_0 h_2 = \frac{d}{ds} \left\{ \int_0^{\delta} \rho u h_2 (H - H_e) dy \right\} \quad (2.149)$$

By introduction of the coordinate transformation  $y^* = \int_0^y \frac{\rho dy}{\rho^*}$ , this becomes\*

$$\dot{q}_0 h_2 = \frac{d}{ds} \left\{ \delta_x \rho^* u_e h_2 (H_e - H_w) \int_0^1 \frac{u}{u_e} \left[ 1 - \frac{H_e - H}{H_e - H_w} \right] dy^* \right\} \quad (2.150)$$

where

$$\delta^* = \int_0^{\delta} \frac{\rho}{\rho^*} dy \quad (2.151)$$

Reynolds analogy is invoked and one-seventh power profiles are assumed

$$\frac{u}{u_e} = \frac{H_e - H}{H_e - H_w} = \left( \frac{y^*}{\delta^*} \right)^{1/7} \quad (2.152)$$

with the result that

$$\dot{q}_0 h_2 = \frac{7}{12} \frac{d}{ds} \left\{ \delta^* \rho^* u_e h_2 (H_e - H_w) \right\} \quad (2.153)$$

or, with the  $H_w$  assumed constant

$$c_H h_2 = \frac{7}{12} \frac{d}{ds} \left\{ \delta^* \rho^* u_e h_2 \right\} \quad (2.154)$$

\* Bromberg, Fox, and Ackermann treated the density as constant through the boundary layer. The compressibility transformation is introduced here for a more orderly development. The \* subscript denotes evaluation at the Eckert reference enthalpy condition.

A second relation between the heating rate and the transformed boundary layer thickness is now obtained using an incompressible, flat-plate skin-friction law. Based upon the results of Burggrat's study of the compressibility transformation, the skin friction law is assumed invariant under transformation so that

$$\frac{c_{f*}}{2} = 0.0225 \left( \frac{\mu_*}{\rho_* u_e \delta_*} \right)^{1/4} \quad (2.155)$$

Reynolds analogy is again applied to convert Eq. (2.155) to an expression for the heat transfer coefficient

$$C_H = 0.0225 \rho_* u_e \left( \frac{\mu_*}{\rho_* u_e \delta_*} \right)^{1/4} \quad (2.156)$$

Equations (2.154) and (2.156) may be combined to obtain the following relation for the growth of the boundary layer

$$\frac{d}{ds} \left\{ \delta_* \rho_* u_e h_2 \right\} = \frac{12}{7} (0.0225) \frac{h_2^{5/4} \rho_* u_e \mu_*^{1/4}}{(\rho_* u_e h_2 \delta_*)^{1/4}} \quad (2.157)$$

which upon integration yields

$$\delta_* = \frac{\left\{ \frac{5}{4} \left( \frac{12}{7} \right) (0.0225) \int_0^s h_2^{5/4} \rho_* \mu_*^{1/4} u_e ds \right\}^{4/5}}{\rho_* u_e h_2} \quad (2.158)$$

Substitution of this result in Eq. (2.156) provides the final expression for the heat transfer coefficient

$$C_H = \frac{0.289 \rho_* \mu_*^{1/4} u_e h_2^{1/4}}{\left\{ \int_0^s \rho_* \mu_*^{1/4} u_e h_2^{5/4} ds \right\}^{1/5}} \quad (2.159)$$

The starred properties are evaluated at the Eckert reference enthalpy condition

$$\begin{aligned} \rho_* &= \rho \left( h_*, p_e \right) \\ \mu_* &= \mu \left( h_*, p_e \right) \end{aligned} \quad (2.160)$$

where

$$h_* \approx 0.5 \left( h_e + h_w \right) + 0.2 \frac{u_e^2}{2} \quad (2.161)$$

It may be noted that no accounting is made in Eq. (2.159) for the laminar boundary-layer run preceding the turbulent boundary-layer region. The local convection coefficient is obtained assuming that turbulent flow extends from the stagnation point to the local position,  $s$ . Bromberg, Fox, and Ackermann include in their development a correction for the laminar run. The correction is small except near the transition location. In view of this result and the uncertainty in the transition location, incorporation of the correction is not considered worthwhile.

It is convenient in prediction of the convective heat transfer to express Eq. (2.159) in a different form. The purpose is to separate terms depending on flight condition, surface location, and surface temperature. In this manner repeated solution of the complete equation in computation of a heating history may be avoided. The form adopted is\*

\* To obtain this form, the approximation given below is made

$$\int_0^s \rho_* \mu_*^{1/4} u_e^{1/2} ds \approx \frac{\rho_* \mu_*^{1/4}}{\rho_e \mu_e^{1/4}} \int_0^s \rho_e \mu_e^{1/4} u_e^{1/2} ds$$

Because of the one-fifth power dependence of the convection coefficient on the integral term and because of the slow variation of the quantity,  $\frac{\rho_* \mu_*^{1/4}}{\rho_e \mu_e^{1/4}}$  along the surface, the approximation has little effect.

$$C_H = \left[ \frac{0.0289}{(R_M)^{0.2}} \left( \frac{\rho}{\rho_0} \right)^{0.4} \left( \frac{h_2}{h_0} \right)^{0.2} \right] C_c F_T \quad (2.162)$$

where the compressibility term,  $C_c$ , is

$$C_c = \left( \frac{\rho^*}{\rho_e} \right)^{0.8} \left( \frac{\mu^*}{\mu_e} \right)^{0.2} \quad (2.163)$$

and the turbulent distribution function is

$$F_T = \frac{\left( \frac{\rho_e}{\rho_0} \right) \left( \frac{u_e}{a_0} \right) \left[ \left( \frac{\mu_e}{\mu_0} \right) \left( \frac{h_2}{R_M} \right) \right]^{0.25}}{\left[ \int_0^S \left( \frac{\rho_e}{\rho_0} \right) \left( \frac{u_e}{a_0} \right) \left( \frac{\mu_e}{\mu_0} \right)^{0.25} \left( \frac{h_2}{R_M} \right)^{1.25} d \left( \frac{S}{R_M} \right) \right]^{0.2}} \quad (2.164)$$

The latter function, which describes the convective heat flux distribution along the surface, exhibits a very weak dependence on flight conditions. Hence, after evaluation of the function for a single, representative flight condition, the convective heat transfer at any location may be simply determined from knowledge of the stagnation point thermodynamic conditions and the local compressibility factor.

#### Boundary Layer Transition

Numerous theoretical and experimental works on transition have been performed. However, the transition phenomenon is complex and is influenced by a large number of parameters. The basic investigations provide some understanding of the governing factors, but they do not provide well defined criteria for practical application. The following general observations can be made:

- (1) Stability of the laminar boundary layer is increased in a region of negative pressure gradients.
- (2) The boundary layer is more stable at high Mach numbers than at low.
- (3) Mass injection has a destabilizing influence on the boundary layer.
- (4) Surface roughness hastens the occurrence of transition.
- (5) The degree of wall cooling (ratio of wall enthalpy to edge total enthalpy) exhibits an appreciable influence on transition. Moderate wall cooling increases stability, but there is some indication that this effect is reversed with extreme wall cooling.

Considering the situation for Apollo, pressure gradients are favorable but the boundary-layer-edge Mach numbers are relatively low. Surface roughness and mass injection conditions are such as to adversely affect boundary layer stability. The wall is highly cooled. The prediction of boundary-layer transition under these conditions must be accomplished on an empirical basis. Ideally, transition data obtained at conditions simulating in all important aspects, the Apollo conditions should be used to form the empirical basis. Unfortunately, such information is not available. In fact, very little interpretable data is available for conditions approximating those of interest. Results obtained on ablating surfaces are especially meager. Some data is available, however, for highly-cooled, blunt bodies flying at hypersonic speeds. In particular, the RTV X-17 flights resulted in acquisition of data which is pertinent. This data has been reviewed and correlated. The results are summarized and their application to Apollo is discussed in Appendix 2F.

The Reynolds number based on momentum thickness is used as a basic parameter in the data correlation. An approximate expression for the local

value of this Reynolds number is simply obtained by applying the transformation used by Lees (Ref. 2.101) to the incompressible, flat-plate formula (Blasius result). The equation obtained is

$$Re_{\theta} = 0.664 \frac{\left[ \int_0^s \frac{\rho_e u_e \mu_e h_2^2 ds}{\mu_e h_2} \right]^{1/2}}{\mu_e h_2} \quad (2.165)$$

This relation accounts for three-dimensional flow geometry and indirectly for pressure gradient. It is based on the assumption that the velocity profile in the transformed coordinate system is identical with the Blasius profile. It gives results in good agreement with the more rigorous local-similarity formula developed by Cohen which accounts for the effects of real gas properties, pressure gradient, and Mach number on the velocity profile. Equation (2.165) is adopted in preference to Cohen's formula because of its relative simplicity. In order to expedite computations of the Reynolds number history at a number of locations, Eq. (2.165) is written in an alternate form

$$Re_{\theta} = 0.664 \left[ \frac{\rho_0 a_0 \sqrt{\gamma_0}}{\mu_0} \right]^{0.5} F_M \quad (2.166)$$

where

$$F_M = \frac{\left[ \sqrt{\gamma_0} \int_0^s \frac{\rho_e}{\rho_0} \frac{\mu_e}{\mu_0} \frac{u_e}{a_0} \left( \frac{h_2}{R} \right)^2 d \left( \frac{s}{R_M} \right) \right]^{0.5}}{\frac{\mu_e}{\mu_0} \frac{h_2}{R}} \quad (2.167)$$

In this form trajectory condition and location dependent terms are separated. The distribution function  $F_M$  is essentially independent of altitude and velocity and thus can be evaluated once and for all.

The momentum thickness Reynolds number at boundary layer transition exhibits a strong dependence on local Mach number as evidenced by the RTV X-17 results. The correlation obtained with the X-17 data is shown in Fig. 2-65. As discussed in Appendix 2F, the X-17 wall-cooling ratios did not differ significantly from those expected on Apollo. The inviscid flow Mach numbers on Apollo are within the range covered by the X-17 data. However, the surface roughness of the X-17 vehicle was relatively small as compared with Apollo and mass injection was absent.

The experimental results reported in Refs. 2.117 - 2.120 give indication of the influence of surface roughness and mass injection, but the conditions under which the data were obtained are sufficiently different so as to preclude any quantitative conclusions for the Apollo application. The reported results demonstrate that increased roughness and mass injection will promote transition. They suggest, however, that the roughness influence will be decreased by mass injection. Considered as a whole, the results of Refs. 2.117 - 2.120 together with the data of Ref. 2.121 support the use of the RTV X-17 correlation as an upper bound on the transition Reynolds number. No data suitable for defining a lower bound on the transition Reynolds number have been found.

For prediction of transition on Apollo, the lower envelope of the transition data of Fig. 2-65 may be used to define the critical value of the momentum thickness Reynolds as a function of the local Mach number. However, it must be recognized that the prediction may be optimistic in that the effects of large surface roughness and mass injection are not accounted for in the correlation.

#### Mass Injection

It was shown in Section 2.3.1 that mass injection will have first-order influence on convective heating. Thus it is very important that the mass transfer effect be accurately described. Ideally, this would be accomplished by solving the boundary-layer equations with multi-component

diffusion and chemical reaction in combination with the equations governing response of the ablative heat shield. However, such a solution is difficult and therefore an alternate and more approximate approach has been taken. Specifically, the interface conditions coupling ablator response and boundary layer phenomena are obtained using the simplified diffusion model of Lees. The reduction of the heat-transfer coefficient resulting from mass transfer is determined by applying approximate correlation formulae. With this approach the equations previously given for prediction of the non-blowing heat transfer may be applied after introducing suitable corrections. The essential features of the technique are described here. The detailed relations are developed in appendices.

The Apollo heat shield material decomposes to form both gaseous products and a residual carbonaceous char which may react with boundary layer species. The total injection rate is thus composed of two separate fluxes

$$(\rho v)_w = (\rho v)_g + \sum_j \dot{w}_j \quad (2.168)$$

The first term on right hand side is the pyrolysis gas contribution. The second term is the net rate of production of gaseous species in surface chemical reactions. Means for evaluation of each term are described in the following paragraphs.

The pyrolysis gas injection rate,  $(\rho v)_g$ , is determined from solution of the transient conduction equation, which for one-dimensional heat flow may be expressed as (Ref. 2.122)

$$\rho_s c_s \frac{\partial T}{\partial \theta} = \frac{\partial}{\partial y} \left( k \frac{\partial T}{\partial y} \right) + (\rho v)_g \frac{\partial H_g}{\partial y} + \frac{d\rho_s}{d\theta} H_D \quad (2.169a)$$

where the decomposition rate is given by a kinetics law of the form

$$\frac{d\rho_s}{d\theta} = -k_f \rho_{vm} \left( \frac{\rho_s - \rho_c}{\rho_{vm}} \right)^w \quad (2.169b)$$



and the local pyrolysis gas flux is obtained from

$$\left(\dot{m}\right)_g = - \int_y^{\delta} \frac{d\rho_s}{d\sigma} dy \quad (2.169c)$$

The injection rate is obtained when the latter integration is performed starting from the surface. The solution of Eq. (2.169) is obtained using either of two computer programs, CHIRP or TRANSIENT. A rigorous, numerical integration of the conduction equation is performed by an explicit finite-difference technique in the CHIRP program (Ref. 2.123). The TRANSIENT code utilized a more approximate technique which is described in Volume II. The properties data required in solution of the conduction equation are given in Appendix 2G for a heat-shield material formulation simulating that of Apollo.

The chemical source term of Eq. (2.168) is intimately coupled to the boundary layer conservation equations since its magnitude depends in general upon molecular species concentration gradients at the surface. In order to evaluate this term, the multi-component boundary-layer diffusion system is treated as a binary mixture with Lewis and Prandtl numbers of unity.\* Lees (Ref. 2.38) has shown that with this approximation the molecular species continuity equations can be replaced by elemental species conservation equations which are identical in form to the energy conservation equation. Thus the need for consideration of the complex chemical situation away from the wall is obviated. The diffusion rate of any element may be related to the edge and wall elemental concentrations and the convection coefficient.

\* Lees has pointed out that if a multi-component gas mixture is composed of two separate groups, each with about the same atomic or molecular weight and about the same mutual cross sections, it can be taken as effectively binary insofar as diffusion is concerned. Admittedly, this condition is not well satisfied for the chemical system of interest. However, the approximation has been applied with considerable success by Kratsch, et al (Refs. 2.122, 2.124) in describing the chemical erosion of materials with similar composition.

Following the work of Lees, the net flux of each element at the surface is

$$B'_{iW} = \tilde{K}_{iW} (1 + B'_W) - \tilde{K}_{ie} \quad (2.170)$$

where the mass transfer parameter,  $B'_W$ , is simply the ratio of the mass flux to the blowing value of the convection coefficient

$$B'_{iW} = \frac{(P_{iW})_{iW}}{C_H} \quad (2.171)$$

$$B'_W = \sum_i B'_{iW} \quad (2.172)$$

Referring to Eq. (2.168), the two components of the ablation flux are

$$B'_{qW} = \frac{(P_{qW})_q}{C_H} \quad (2.173)$$

$$B'_{EW} = \sum_j \frac{\dot{w}'_{jW}}{C_H} \quad (2.174)$$

The latter flux is assumed due solely to chemical erosion of the carbon. Then the total flux of carbon is given by

$$B'_{CW} = B'_{EW} + \tilde{c}_{cg} B'_{qW} \quad (2.175)$$

and the surface chemical erosion rate can be obtained from Eq. (2.170) after noting that the edge concentration of carbon is zero

$$B'_{EW} = \tilde{K}_{CW} (1 + B'_W) - \tilde{c}_{cg} B'_{qW} \quad (2.176)$$

The fluxes of other elements are obtained similarly. For example,

$$B'_{Ow} = \tilde{C}_{Og} B'_g = \tilde{K}_{Ow} (1 + B'_w) - \tilde{K}_{Oe} \quad (2.177)$$

In order to complete the system of equations for mass transfer, the surface reaction situation must be described. This is accomplished either by imposition of a chemical equilibrium constraint or by specification of reaction kinetics. It has been assumed that only oxygen reacts with the carbon surface. The pyrolysis gases and ceramic fibers in the residual char are considered inert. Cyanogen production and carbon sublimation have been neglected since the maximum surface temperatures achieved are not high enough to make these reactions favorable. Both the rate-limited oxidation regime and the diffusion limited regime in which combustion is complete have been treated. Relations for each situation are developed in Appendix 2G. For the reaction-limited case in which

$$B'_F = \frac{M_C}{M_{CO}} \dot{w}_{CO} = k_f (P_{O_2})_w^n = k_f \left[ K_{O_2} \left( \frac{M_w}{M_{O_2}} \right) P_e \right]^n \quad (2.178)$$

the following relation is obtained for the wall oxygen concentration after manipulation of the foregoing relations and auxiliary specie conservation statements

$$\frac{\left( \frac{K_{O_2w}}{\tilde{K}_{Oe}} \right)^n \left[ 1 + \frac{3}{4} \frac{\tilde{K}_{Oe}}{K_{Oe}} \left( \frac{K_{O_2w}}{K_{Oe}} \right) \right]}{1 - (1 + B'_g) \left( \frac{K_{O_2w}}{\tilde{K}_{Oe}} \right)} = \frac{\frac{3}{4} \tilde{K}_{Oe} \bar{C}_H}{k_f \left[ \tilde{K}_{Oe} \left( \frac{M_w}{M_{O_2}} \right) P_e \right]^n} \quad (2.179)$$

Solution of this equation and substitution of the result in Eq. (2.178) yields the char erosion rate. As the kinetics of the carbon monoxide production rate become very fast, almost all oxygen transported to the wall reacts and the diffusion-limiting condition is approached. In this

regime, the char erosion rate is given by the relatively simple formula

$$B_e' = 3/4 \tilde{K}_{oe} = 0.174 \quad (2.180)$$

For both regimes the net heat transfer to the surface excluding radiation is given, according to Lees by

$$q = \bar{c}_H \left[ H_{rec} - (1 + B_w') H_w + B_f' H_{f,w} + B_E' H_E \right] \quad (2.181)$$

It is shown in Volume II in discussion of the TRANSIENT program that this may be rewritten as

$$q = \bar{c}_H \left[ H_{rec} - H_{a,w} + B_E' Q_{co} \right] \quad (2.182)$$

where  $H_{a,w}$  is the enthalpy of undissociated air at the wall temperature and  $Q_{co}$  is the heat of combustion of carbon. Thus the effect of chemical reactions appears as a simple additive factor in the enthalpy potential.

The influence of mass transfer on the convection coefficient is examined in Appendix 2H. While the transpiration effect has been studied extensively, almost all theoretical treatments have been for the injection of air or some inert species. The experimental investigations have been similarly limited. As indicated by the foregoing discussion of ablation, it has been assumed that the effects of chemical reaction between the injected species and air can be decoupled from the "direct" effect of transpiration, i.e., thermal and velocity boundary layer thickening. The chemical reaction effects are accounted for by adjusting the enthalpy potential as shown by Eq. (2.182). The direct transpiration effect is introduced as a multiplicative factor on the convection coefficient. This factor is considered to be a function of the normalized mass injection rate, i.e.,  $\frac{PM_w}{C_H}$

$$\bar{c}_H = f \left( \frac{PM_w}{C_H} \right) C_H$$

The influence of injectant composition and pressure gradient, as well as boundary-layer regime, on the transpiration factor is reviewed in Appendix 2H. Approximate correlation functions for the laminar and turbulent boundary layer cases are selected. The adopted functions are presented in Fig. 2-66. Also shown in this figure are the estimated uncertainties in the transpiration factor as applied to Apollo. The laminar correlation is based upon the theoretical results of Libby (Ref. 2.92) for injection of air into air. The turbulent transpiration factor was empirically derived by Woodruff (Ref. 2.125). The influence of injectant composition is grossly accounted for in these correlation functions by incorporating a factor depending upon molecular weight (laminar boundary layer) or specific heat (turbulent boundary layer) of the injectant. The values of these correction factors are shown as a function of surface temperature in Fig. 2-67 for an injectant representative of the Apollo heat shield ablation products.

#### Surface Protuberances

Considerable progress has been made in analysis of the effects of two-dimensional protuberances on heating and a large body of experimental data has been accumulated. However, in the case of three-dimensional protuberances such as on Apollo, theoretical techniques for accurately predicting the interference factors are lacking. Furthermore, the complex dependence of heating distribution on flow conditions and protuberance shape precludes the development of general empirical relations. The effect of each geometry of interest must be experimentally examined at the approximate conditions of interest. In view of this situation, analysis effort in this study has been limited to a brief investigation of the application of interference factors obtained in wind tunnel tests of scale models of the Apollo configuration. Appendix 2I reviews the considerations which have been made and the conclusions derived. With a few qualifications, it appears that the experimental factors may be directly applied for prediction of flight heating.

### 2.3.3 Results

The distribution of convective heat transfer over the Apollo vehicle is described here. Predictions for wind tunnel and flight conditions are compared in order to infer the validity of directly applying empirically-determined distribution factors. Also, the adopted prediction techniques are compared with alternative methods. All of the results presented are for the plane of symmetry and an angle-of-attack of 25 deg. The actual heating levels and transition pattern are not discussed. This is deferred to Section 2.5 where representative environmental histories and associated heat shield ablation histories are described in detail.

#### Laminar Heating Distribution

Measurements of the convective heating distribution on Apollo have been obtained in a number of wind-tunnel tests of the configuration. For zero angle-of-attack attitude, any of the existing prediction techniques yield results in good agreement with the experimental data. However for the actual angle-of-attack condition, flow asymmetry induces some uncertainty in the heating prediction. It was shown in Fig. 2-49 that the limit predictions of two-dimensional and axi-symmetric flow yield widely differing results. In this study, the spreading coordinate defined in Section 2.1 has been used to account for three-dimensional flow effects on the heating distribution. In order to determine the validity of this technique, predictions were made for the approximate test conditions reported in Ref. 2.15. Results obtained with both the adopted local-similarity solution of Cohen and the simpler Lees formula are shown in Fig. 2-68 for the case of 25 deg. angle-of-attack. For ease in comparison, the predictions are presented in the form of the local heat-transfer coefficient ratioed to the stagnation point coefficient computed for zero-angle-of-attack.\* The experimental data reported in Ref. 2.15 are in good agreement with the predictions. Except for the region  $|S/R| > 1.05$ , the deviation between

\* This form is obtained by multiplying the result of Eq. (2.144) by the factor  $[(\beta_0 + \beta_\infty)_\alpha / 2(\beta_0)_{\alpha=0}]^{1/2}$

theory and experiment is generally no greater than 5 percent. The most accurate prediction technique cannot be identified. For positive values of  $\bar{S}/R$ , the Cohen prediction best correlates the data. The comparison reverses for negative  $\bar{S}/R$ . The good agreement obtained between the predicted and measured distributions is considered to substantiate the validity of the spreading coordinate.

The laminar heat transfer distribution for flight and wind tunnel conditions is depicted in Fig. 2-69. The results are again shown in the form of the local heat-transfer coefficient ratioed to the zero angle-of-attack stagnation-point coefficient. The predictions for wind-tunnel and flight situations, respectively, are based upon the pressure distributions defined in Figs. 2-11 and 2-13. For the wind-tunnel case with a free stream velocity of 5000 ft/sec, flow of an ideal gas with isentropic exponent of 1.4 was assumed. The computation for the flight case was performed using real gas properties of air, assuming flight at a velocity of 25,000 ft/sec and altitude of 150,000 ft. It may be seen from Fig. 2-69 that the influence of free-stream velocity on the laminar heating distribution is slight, except on the windward corner. This might have been anticipated since the pressure distributions for the two cases do not differ markedly. It appears from these results that relatively little error would be incurred in using low-speed wind-tunnel data to define the flight heating distribution. However, it is considered preferable to use theoretical means since the appreciable shift in the distribution on the windward corner is then accounted for.

The influence of shock-generated vorticity on the laminar-heat-transfer distribution is described in Fig. 2-70. For the conditions considered, the stagnation-point heating is increased 30 percent by vorticity. The effect decreases away from the stagnation point, but only slightly. That is, the ratio of local heating to stagnation-point heating is not significantly changed when vorticity is accounted for. The situation for which the results are presented is an extreme one. For the lower altitudes where

most of the convective heating occurs. The vorticity correction will be much smaller. (See Fig. 2-52, for example.) It is concluded that the convective heating distribution may be considered frozen. The small vorticity affect may be accounted for by adjusting the local heating level by the same amount as computed for the stagnation point.

#### Turbulent Heating Distribution

The turbulent heat-transfer distribution predicted for the wind tunnel situation is shown in Fig. 2-71. The distribution function  $F_T$  remains relatively constant at a high value over the major portion of the spherical sector of the forebody. It dips rapidly near the stagnation point because of the reduced flow velocities and again on the toroidal corner sections because of the reduced flow density. The adopted technique of Bromberg, Fox, and Ackermann, which accounts for the three-dimensional flow geometry by means of the spreading coordinate and for streamwise variation of edge conditions, yields results which do not differ greatly from the flat plate formula of Eckert. The comparison of these two methods in Fig. 2-71 shows that on the spherical sector the difference is less than 15 percent. No experimental data were found for comparison with these predictions.

Figure 2-72 shows the effect of free stream velocity on the turbulent heating distribution. Except near the windward corner the distribution factor is little influenced. The difference in that region is caused by the outward shift of the stagnation point location with increasing flight velocity.

#### Reynolds Number Distribution

The momentum thickness Reynolds number distribution, as reflected by the factor  $F_M$  defined in Eq. (2.167), is shown in Fig. 2-73 for a representative flight condition. Over the spherical sector the Reynolds number grows almost linearly with distance away from the stagnation point in a manner similar to the Mach number. (See Fig. 2-47, for comparison.) Recalling



the correlation of Fig. 2-65 for transition Reynolds number as a function of Mach number, this suggests that the transition position will not gradually creep forward over the surface, but instead will rapidly sweep forward as the vehicle descends. This behavior is illustrated in Fig. 2-74. The local Reynolds number is shown for several closely-spaced altitudes together with the assumed Reynolds number for transition. At 170,000 ft altitude, laminar flow prevails over the majority of the surface. In moving to a slightly lower altitude the transition Reynolds number is exceeded over a wide area and turbulent flow occurs.

#### Summary

The many phenomena which may affect convective heat transfer at superorbital entry speeds have been individually examined. Non-equilibrium chemistry and radiation coupling effects appear to be of second-order importance for Apollo. The influence of non-uniform wall temperature and non-similar mass injection distribution on local heat flux is not important. Shock-generated vorticity effects are minor, except at high altitude. Flow asymmetry and mass injection significantly affect heating levels. Boundary-layer transition, with attendant large increase in heat flux, is probable during the period of peak heating.

Techniques for prediction of heat transfer, which may be simply applied, have been presented. The fundamental relations were selected from existing developments after review of the available theories and numerical results. The prediction technique incorporates approximate theoretical means for establishing the influence of three-dimensional flow and vorticity effects. The mass transfer boundary condition with a chemically reacting ablator is theoretically modeled, but the transpiration effect is treated semi-empirically. An approximate correlation for the transition Reynolds number is provided.

The development of a more rigorous procedure for prediction of the heat transfer, which would account for coupling between the various phenomena

of importance, is highly desirable. In particular, diffusion and chemical reactions with injection of ablation products should be examined using realistic compositions and properties.

#### 2.4 AFTERBODY ENVIRONMENT

Heat transfer to the afterbody region of the Apollo vehicle is relatively low. This is fortunate since there are many complications which make accurate predictions of the environmental conditions very difficult. Theoretical techniques for treating the relevant phenomena are poorly developed and therefore heavy reliance on empiricism is necessary in prediction of heating levels. For this purpose, a large body of experimental data on Apollo afterbody heating has been acquired by testing scale models in hypersonic flow facilities.

In view of this situation, the scope of afterbody heating investigations in this study was purposely limited. It was not considered profitable to expend much effort in theoretical analysis. Instead, a brief review of the experimental data and its application to flight predictions was undertaken. This section provides a qualitative description of the phenomena affecting heating and a discussion of the existing semi-empirical methods for prediction of heating levels.

##### 2.4.1 Phenomenological Review

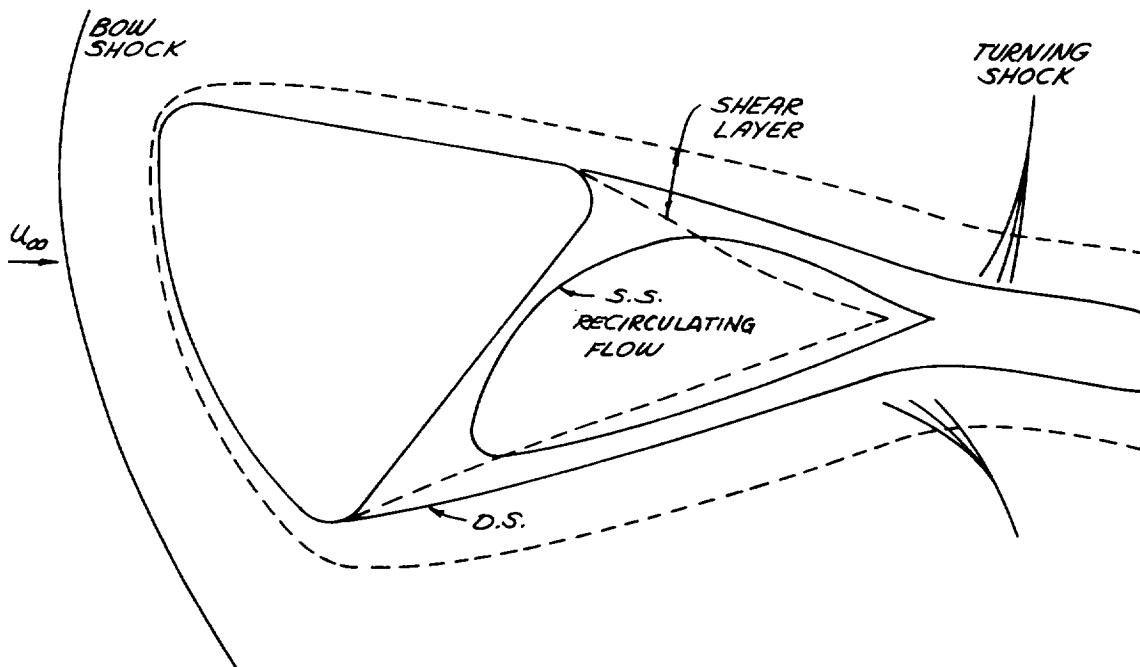
Most of the factors influencing forebody heating will also have some effect on the afterbody. Mass injection, non-equilibrium chemistry, boundary-layer transition, and other phenomena have been discussed at some length in consideration of the forebody. The important differences between the forebody and afterbody will be discussed here.

##### Flow Field

The general configuration of the flow field for Apollo was described in Fig. 2-1. It was seen that a three-dimensional flow pattern arose on the forebody as a consequence of the vehicle's attitude with respect to the

free stream. The flow asymmetry is magnified on the afterbody. For the angle-of-attack of interest, 25 deg, the flow remains attached on one side but separates on the other. A low-speed, recirculating flow of complex geometry lies between the body surface and the separating stream surface.

The inviscid flow over the afterbody is strongly influenced by viscous effects. The features of the flow are indicated in the sketch below for the general case with mass injection from the afterbody surface.



The stagnating streamline (S.S.) is the one which separates the streamlines which continue downstream from those which turn back into the recirculating region. The dividing streamline (D.S.) emanates from the boundary layer separation point and divides the flow which has passed through the bow shock from that emanating from the base. The fluid injected from the afterbody surface passes out between the stagnation and dividing streamlines. (With no mass injection, the stagnation and dividing streamlines are therefore identical.) The dashed lines indicate the extent of the viscous region. The boundary-layer thickness rapidly is expanding about the forebody corner. Upon separation, the viscous layer continues to grow

as a free shear layer and finally entrains a portion of the recirculating flow. In the neck region where the free shear layer coalesces, the pressure rises. Only that fluid which has sufficient momentum to overcome the adverse pressure gradient continues downstream. The remainder is turned back into the recirculation region. For this reason, viscous effects strongly influence the wake closure angle. The geometry must be such that shear forces acting on the injected fluid provide sufficient acceleration for the fluid to negotiate the region of increasing pressure.

For rapid closure of the wake, the turning angle at the neck is large and hence the pressure rise is greater. The length along which fluid is accelerated becomes smaller. Thus, fluid is least likely to negotiate the pressure rise for a short closure length. From this consideration, it may be inferred that mass injection from the afterbody will cause the wake closure angle to decrease and the neck to move downstream. Mass injection from the forebody will have a similar, but weaker, effect. The smaller closure angle indicates increased pressures in the base region and a tendency for earlier boundary layer separation.

Radiative energy loss was previously shown to appreciably reduce temperature and velocity of the inviscid flow over the forebody. This effect will be reflected in the afterbody flow. However, the influence on pressure levels and flow geometry should be of second-order magnitude.

It was indicated that the forebody shock layer will be in a near-chemical-equilibrium condition for the altitudes where heating is greatest. It is unlikely that this condition will persist over the afterbody. The pressures are very much less and consequently reaction kinetics are relatively slow. It is probable that the flow will chemically freeze at some point during expansion around the corners of the forebody. Thus the extent of dissociation will be greater than would be predicted assuming chemical equilibrium. With the chemical energy unavailable, temperatures will drop more rapidly than in an equilibrium expansion.

### Radiation Heat Transfer

As a result of the low pressures and temperatures of the flow over the afterbody, the local radiative emission rates will be very small. It may be seen from Fig. 2-46 that the equilibrium radiative flux falls off to an insignificant level on the forebody corner. The non-equilibrium contribution to the radiation does not decay as rapidly around the corner. However, the work of Ref. 2.1 shows that even for velocities in excess of those for lunar return the non-equilibrium flux is small along most of the afterbody surface as compared with the convection flux.

The flow temperature increases in the wake neck region as a consequence of flow compression. Pressures in this region remain low relative to those on the forebody, but the radiating volume is relatively large. Thus, the neck region may be an important source of radiation. It is contaminated by ablation products which are very strong radiators compared to pure air species.

The extent of wake radiation will depend, of course, on the temperature and particle concentration distributions. In order to determine the radiation, the ablation rate and injectant composition must be known. Further, the diffusion, momentum, chemical kinetics, and energy transfer processes in the boundary-layer, free shear layer, and neck region must be described.

### Convective Heat Transfer

Over the surface area where the boundary layer is attached, the convective heating phenomena will be essentially the same as on the forebody. However, the inviscid flow entrained by the boundary-layer will be out of equilibrium and chemical kinetics within the boundary layer will be much slower.

The convective heating mechanism is quite different in the separated zone. The energy is transported through the shear layer heating the recirculating flow which in turn heats the body surface. It might then be expected that convective flux to the wall will be relatively small in this region.

#### 2.4.2 Prediction Techniques

Available methods for calculation of the afterbody flow field and convective heating are reviewed. Because of the many uncertainties and difficulties involved in theoretical techniques, semi-empirical methods are favored.

##### Flow Field

The theories of Chapman (Ref. 2.126) and Korst (Ref. 2.127) are generally applied for calculation of laminar and turbulent flows, respectively. According to the Chapman model, the geometry of the stagnating streamline may be determined by requiring that the total pressure on the stagnating streamline at the neck be equal to the pressure in the external inviscid flow immediately behind the oblique turning shock. It is assumed in applying the model that the shear layer is thin and the recompression region at the neck is short. The pressure is assumed constant in the separated region and simple approximations to the transport properties are used to obtain a similar solution for the shear layer velocity profile. The actual separation condition and shear layer geometry are determined by iteration of the inviscid flow and shear layer solutions. In this process, a separation position is assumed and the associated inviscid flow field is calculated. Then the shear layer solution is obtained. The latter yields the stagnation streamline total pressure and the former provides the pressure immediately behind the turning shock. The process is repeated until a solution is obtained where the two pressures coincide.

Chapman did not account for a finite boundary layer thickness at the separation point. However, his model has been extended by Baum, King, and Denison (Ref. 2.128) to include the initial profile and mass injection effects as well. They show that the effects of initial profile are very important.

The Korst theory for turbulent flow follows along the same general lines as the Chapman model. A greater number of approximations are necessary, however, in dealing with the turbulent situation. The upstream boundary

layer is grossly accounted for by using an effective base radius which is the sum of the actual radius and the boundary layer momentum thickness.

Because of the complex geometry presented by the Apollo at angle-of-attack, application of these theoretical techniques for description of the separated flow field would be difficult and the results would be uncertain. Three-dimensional method-of-characteristics solutions would be required for the inviscid flow. The approximations inherent in the current techniques (e.g., zero pressure gradient solution for initial profile, negligible shear-layer displacement thickness, constant  $\rho\mu$  product and unity Prandtl number for laminar flow) are not well satisfied. These approximations could be relaxed. However, the basic methods do not yield information on the thermodynamic state of the important recirculating flow region. Further, the recompression region treatment is overly simplified.

As a result of these theoretical difficulties, an empirical approach to definition of the flow field appears desirable. For the present purposes, it is assumed sufficient to prescribe the static pressure distribution over the surface. The thermodynamic quantities are then obtained assuming the flow to be isentropic. Experimental pressure data at differing angles-of-attack are available for a wide range of Mach numbers and Reynolds numbers. The influence of these parameters appears to be small and therefore the pressure distribution has been assumed frozen. The adopted distribution in the plane of symmetry is shown for the windward side in Fig. 2-75. In the separated zone the pressure has been assumed constant at a value of  $0.012 p_0$ .

#### Radiative Heat Transfer

The radiative heating from wakes contaminated by ablation products has been experimentally studied by Stephensen (Ref. 2.129). Small, ablating models were flown in a ballistic range at speeds ranging up to about 30,000 ft/sec and measurements of the spectral luminosity of the wake were obtained. The materials tested included polycarbonate, polyethylene, teflon, delrin

and an epoxy formulation. Significant increases in emission over air wake values were observed with some of the materials. The data were correlated by Stephenson and approximate scaling relations were devised to enable flight predictions.

The differences in wake emission levels for the different material models were extreme. Under some conditions, radiation from the teflon and delrin wakes was almost three orders of magnitude less than from the polycarbonate wake. The epoxy and polyethylene radiation was somewhat less than that of polycarbonate, but their spectral emission distributions were roughly similar. The observed differences might be attributed to differences in material formulation and ablation rate. It appears unlikely that the ablation rates differed markedly. The elemental composition of the materials, with the exception of teflon, is similar. With the one exception, all are composed of carbon, hydrogen, and oxygen in varying amounts. The molecular structures are significantly different. This would be important if the initial pyrolysis products did not decompose and enter into reactions with the air during their transit of the body. It is speculated that this latter non-equilibrium effect is a prime contributor to the observed radiation differences.

Extrapolation of the experimental results to flight conditions is highly uncertain as a consequence of the unknown reaction kinetics situation. For the same reason, the material most representative of the Apollo heat shield cannot be distinguished. However, there is no alternative approach which can be considered more reliable. Therefore, the experimental data and scaling relations of Stephenson are adopted. The radiative heat flux to the afterbody surface is given by

$$q = K \sqrt{R_M} \rho_{\infty} \left( \frac{U_{\infty}}{10^4} \right)^{1.5} \cos \theta_B \quad (2.183)$$



The constant has been evaluated from the data for the epoxy material since the Apollo heat shield has an epoxy base. The cosine term is included to account approximately for the local wake view factor. The angle  $\theta$  is measured between the surface normal and the free stream wind direction.

#### Convective Heat Transfer

The relations described in Section 2.3.2 have been applied to predict the convective heating distribution over the attached flow region of the afterbody surface. Figure 2-76 presents the laminar heating distribution computed using the empirical pressure distribution of Fig. 2-75. The results were obtained assuming flow of undissociated air with isentropic exponent of 1.4 in order that the prediction might be compared with the wind tunnel results reported in Refs. (2.15) and (2.16). The general level is correctly predicted. However, the distribution is poorly correlated. The experimental data exhibit a much weaker dependence on position. The discrepancy between prediction and measurement may be a result of the assumed flow geometry. It was assumed in application of Eq. (2.144) that the spreading coordinate remained constant along the afterbody surface (i.e., that the streamlines did not diverge). In reality, the flow will be three-dimensional due to the peripheral pressure gradient. If this effect were accounted for, the predicted convection coefficient would decrease less rapidly along the surface and the degree of data correlation would probably be improved.

The attached flow heating prediction was repeated for a representative flight situation (altitude: 150,000 ft; velocity: 25,000 ft/sec) for comparison with the wind tunnel prediction. The results, which are shown in Fig. 2-77, indicate an increase in the local heating level relative to the zero angle-of-attack stagnation point heating. This effect is attributed primarily to the shift in the stagnation point location. For the flight case, the stagnation point is closer to the toroidal corner. Hence the boundary layer run is shorter and the relative heating level is increased. The effect is not large, being about 15 percent. The predicted

shift may be overshadowed by pressure distribution changes which have not been accounted for.

The turbulent heating distribution function  $F_T$ , which was defined by Eq. (2.164), is shown for the attached flow region in Fig. 2-78. The results are for the flight case. They do not differ substantially from predictions for the wind-tunnel condition. This is because the local turbulent heating is relatively insensitive to the boundary-layer run length.

Prediction of convective heat transfer to the separated flow regions of the afterbody is more difficult. Sprinks (Ref. 2.130) has reviewed the relevant theoretical and experimental work conducted prior to 1960. He concluded at that time that "in general no existing theories for separated flow heat transfer are suitable for application at hypersonic speeds". However, he indicated that Chapman's model yielded results for laminar flow which were at least qualitatively correct. Chapman's model, which has been partially described in the foregoing discussion of the separated flow field, assumes the air in the low speed reverse flow region to be at wall temperature when entrained in the shear layer. Then, assuming similarity between the enthalpy and velocity profiles in the shear layer, the heat transfer across the stagnating streamline can be computed from the shear solution. Because the stagnating streamline separates the recirculating flow from that entering the wake, all the heat transfer across the stagnating streamline must be delivered to the body surface. The Chapman model thus provides the average heat transfer to the surface exposed to separated flow. The average heat flux is predicted to be 56 percent of that for an attached boundary layer with the same external-inviscid-flow conditions. The model is substantiated by the experimental results of Larsen (Ref. 2.131) for heating in a cavity. As noted previously, the model has been refined by Baum, King, and Denison (Ref. 2.128). They include an accounting for finite boundary-layer thickness at the separation point and examine the influence of mass injection. They show that for base flow separation, the effects of the upstream boundary-layer will reduce the convective

heating below that predicted by Chapman. They also show that mass injection from either the forebody or base will appreciably reduce base heating.

Experimental data on convective heat transfer to the separated region of the Apollo afterbody have been obtained for a relatively wide range of Mach numbers and Reynolds numbers. However, most of the data has been obtained with sting mounted models at enthalpy levels much lower than in flight. Most of the measurements indicate that the convective heat transfer does not vary significantly over the forward half of the afterbody but increases somewhat near the aft tip. This result may be associated with the presence of a sting. Lee (Ref. 2.132) has correlated a great part of the data by plotting the local Stanton number as a function of Reynolds number. The results generally fall somewhat below the Chapman prediction and they exhibit a different Reynolds number dependence. The Stanton number varies approximately as the inverse fourth root of the Reynolds number rather than the inverse square root. This trend has also been observed by Murphy (Ref. 2.133) in flight test data correlations. A qualitative explanation of this dependence may be found in consideration of the effect of the recirculation flow on heat transfer (Ref. 2.128).\*

Application of the Chapman theory indicates that the local separated-flow heating relative to the zero angle-of-attack stagnation-point heating will not differ significantly between wind-tunnel and flight conditions. It therefore is reasonable to directly apply the experimentally derived heat transfer distribution. To maintain conservatism, the high Reynolds number results may be used. (According to the empirically observed Stanton number dependence on Reynolds number, the ratio of the local convection coefficient to the stagnation point convection coefficient increases approximately as the fourth root of the Reynolds number.) A value for  $C_{H}/C_{H0_{\alpha=0}}$  of

---

\* In the Chapman model, the recirculating flow does not impede the transfer of heat from the dividing streamline to the body surface by virtue of the assumption that the reverse flow is at the temperature of the wall. Actually the recirculating flow must offer some resistance which is Reynolds number dependent.

0.03 is adopted as representative. This procedure does not account for upstream mass injection and therefore further conservatism is incurred in its application.

A turbulent separated flow is probable in some Apollo flight regimes. Chapman also considered this situation and predicted that the heating would be increased above the equivalent attached flow value for low supersonic Mach numbers. This prediction has not been borne out by experiment. Rather, the reverse has been observed - the heat transfer is reduced (Refs. 2.131, 2.134). In view of this discrepancy, reliance should be placed on empirical methods for description of the turbulent, separated-flow heating. Unfortunately, results obtained with the Apollo configuration have not been found. A very crude and probably conservative prediction may be made by assuming that the local separated flow heating is equal to the heating just upstream of the separation point. This assumption yields a value for the distribution function,  $F_T$ , of approximately 0.06 for the separated flow region on Apollo.

#### Summary

Theoretical description of the afterbody flow field and heat transfer is difficult and uncertain. The techniques which are conventionally applied have been briefly described and then discarded in favor of semi-empirical methods. It is expected that these latter procedures will yield results which are the more realistic.

#### 2.5 ENVIRONMENTAL HISTORIES

The various phenomena affecting the heat transfer to a vehicle reentering the atmosphere at superorbital velocity have been studied in the foregoing sections. Prediction techniques accounting for most of the important effects have been presented and sample results for the inviscid flow field, radiative heat transfer, and convective heat transfer have been separately shown. In this section, the character of the reentry environment is further illustrated by presentation of total heating histories together with shield

ablation histories. First, the computational process for generation of environmental histories is reviewed. Then the influence of entry condition on total heating history is examined and finally detailed results are presented for a few selected situations.

#### 2.5.1 Unified Calculation Procedure

The heating histories presented here have been computed via the ENVIRONMENT code. As described in Volume II, this code incorporates correlated results from the STREAMTUBE, STAG-RADS, STRADS-AIR, and VORTICITY codes. It calculates instantaneous shock-layer conditions and provides a history of all environmental parameters required in evaluation of heat shield response.

The order in which the several computer codes are applied to obtain the desired end result is indicated by the information-flow diagram of Fig. 2-79. The analysis process is initiated by a STREAMTUBE solution for the inviscid flow field. The resultant data on the shock wave configuration, pressure distribution, and flow pattern form the input data for the remaining of codes. The VORTICITY program yields the convective-heat-transfer-coefficient distribution for a three-dimensional flow accounting for shock-generated vorticity effects and the STRADS-AIR code provides the radiative heat transfer distribution accounting for radiative energy losses and self-absorption. Both the convection and radiation distributions are only weakly dependent on flight condition and may be assumed frozen. Hence, the STRADS-AIR and VORTICITY codes need be applied only once for a given flow configuration. The results, when properly normalized, are entered as input distribution factors in the ENVIRONMENT code. The convective heating level is determined in this latter program by a correlation equation. The radiative heating level is obtained as a tabular function of the altitude-velocity condition. This function is provided by parametric application of the STAG-RADS code which solves for the stagnation point flux. Non-equilibrium and wake radiation are computed in the ENVIRONMENT code by empirical formulae. The ENVIRONMENT program yields the non-blowing convection coefficient. The actual convective heat transfer can be

determined only upon simultaneous solution for the heat shield response. The TRANSIENT code provides an efficient, but approximate means for evaluation of material response. An alternative and more rigorous technique, involving finite-difference integration of the conduction equation, is available in the CHIRP program.

This system of codes enables expeditious calculation of heating and material response. Once the fundamental heating parameters for a given configuration are computed and introduced into the ENVIRONMENT program, the heating may be computed for any trajectory simply by entering the appropriate trajectory data (altitude and velocity histories). The results account for three-dimensional flow geometry, vorticity, boundary-layer transition, radiative energy loss, and self-absorption. They are in a form suitable for subsequent material response calculations. The equation incorporated in the several codes have been developed in the preceding sections and are concisely summarized in Volume II.

### 2.5.2 Entry Heating

Heating histories have been computed for the three trajectories described in Section 1. It may be recalled that Trajectory I is representative of the early development-test flights. Trajectories II and III correspond approximately to the overshoot and undershoot extremes for lunar return. In all cases, the Apollo is assumed to be at 25 deg angle-of-attack.

#### Trajectory Influence

The geometric center position of the Apollo vehicle is considered a representative location for the purpose of examining the trajectory influence on heating. Figure 2-80 compares the radiative and convective heating histories at this location for the three aforementioned trajectories. The convective heating is shown for a cold, non-ablating wall. Transition is assumed to occur at a momentum thickness Reynolds number of 165, according to the empirical criterion previously discussed. The upper and lower dashed lines, respectively, are used to indicate the convective

heating which would occur if transition were earlier or later. The radiation results shown in the figure include both equilibrium and non-equilibrium contributions.

In all of the trajectories, the major heat load is delivered during the initial pullout maneuver. The heating during the final descent is relatively low because of the reduced flight velocity. The qualitative differences in heating history among the three trajectories are marked. As would be expected, radiation is relatively small for Trajectory I due to the low entry velocity (about 27,000 ft/sec). A short period of intense radiation is experienced in Trajectory II prior to pullout at 150,000 ft altitude. In Trajectory III, radiative heating persists for a much longer period due to the more gradual deceleration. Non-equilibrium radiation is predominant in both Trajectories I and III whereas most of the radiation in Trajectory II emanates from the equilibrium zone of the shock layer.\*

The convective heating histories for Trajectories I and II are similar in temporal distribution, but the levels for these trajectories differ by about a factor of two. A short period of turbulent flow at about the time of peak heating is predicted in both cases. The Reynolds number remains relatively low in Trajectory III due to the high pullout altitude and it is predicted that laminar flow will prevail until final descent. The prolonged deceleration period results in high total heat transfer, however.

#### Forebody Heating

Trajectory III is selected for more detailed examination. It is an interesting one as a consequence of the relatively high radiation levels and the greater probability of transition. Figure 2-81 again presents the heating history at the geometric center location, but now the actual convective

\* The empirically-derived non-equilibrium radiation law may overestimate the non-equilibrium contribution. The equation was selected to fit the upper envelope of the available experimental results.

heating rate accounting for mass injection is shown. Also indicated in the figure is the course of heat shield ablation. By comparison with the results of Fig. 2-80, it is seen that the mass transpiration effect is very pronounced. When the surface strata of the heat shield begins to decompose (at about 15 seconds) the mass injection causes a rapid drop-off in the convective heat flux. The radiative heat flux is sufficient to maintain a high charring rate and the flux of ablation products forces the thermal boundary layer off the surface. As the vehicle penetrates to the denser regions of the atmosphere, the mass injection becomes less effective and convection heating begins again. When the boundary layer transits to turbulent flow, the mass injection effect is further reduced.

It may be seen from Fig. 2-81 that the char front progresses into the material at a relatively constant rate during the period of peak heating. Conversely, the surface erosion rate varies significantly. At early times (prior to 40 seconds), the diffusion boundary layer is also blown off the surface and hence oxygen is unavailable for reaction with the char. During the period of turbulent flow, diffusion-controlled oxidation occurs at a relatively rapid rate.

Heating and shield ablation histories are shown in Figs. 2-82 and 2-83 for positions on opposite sides of the geometric center. The location  $S/R = 0.75$  is in the region of peak radiative heating whereas the location  $S/R = -0.96$  is on the far lee side where radiative heating is low. Radiative heating predominates at the former location due in part to the predicted absence of transition. At the latter position, radiative heating is almost an order of magnitude less than convection. It is interesting to note the difference in shield behavior at the two locations. In the region of high radiation a thick char layer develops and little surface erosion occurs. The trend reverses on the lee side.

The influence of boundary-layer transition criterion on total heating and shield ablation has been studied. Figure 2-84 depicts the location of the



transition position as a function of time for the adopted, Mach-number-dependent Reynolds number criterion and for a constant transition Reynolds number of 200. With the former criterion the duration of turbulence is somewhat less, but the transition position moves further forward. With the constant Reynolds number, the geometric center remains laminar during the initial pullout maneuver. The heating and ablation histories for this case are shown in Fig. 2-85 for comparison with the results of Fig. 2-81. The total convective heat transferred during the initial pullout maneuver in the laminar flow case drops to about the same level as the total radiative heat transfer. Although the total heat transfer during pullout is diminished by about 35 percent, the amount of ablation during this phase is reduced by less than 15 percent. Also observe in Fig. 2-85 that the amount of ablation occurring during the final descent is large relative to the heat transferred during this period. While the recovery enthalpy is relatively low, the convection coefficient becomes large and therefore surface erosion proceeds at a fast rate. These results demonstrate the sensitivity of ablator effectiveness to the environmental conditions.

Figure 2-86 shows the variation of total heat transfer and shield ablation (both during the pullout maneuver and final descent periods) as a function of location along the plane of symmetry. The individual contributions of radiation and convection are shown. Also indicated is the effect of transition criterion. It may be seen that convective heating predominates along most of the surface. Total heat transfer is maximum on the windward corner where the large pressure gradient leads to high laminar heating. The heating does not vary greatly along the spherical surface when transition is assumed to occur at a Reynolds number of 200. However, for the limit case of laminar flow throughout reentry, the heat transfer drops by more than a factor of five from one corner to the other. The shield ablation pattern shown in Fig. 2-86 generally reflects the heat transfer distribution.

### Afterbody Heating

Predicted heating histories for two positions on opposite sides of the afterbody are described in Fig. 2-87 for Trajectory I. The windward side receives no appreciable radiation from the contaminated wake because of its orientation. Radiative heat transfer is small even on the lee side due to the relatively low entry velocity. The convective heating is shown for the case of a cold non-ablating wall. The convective heating level on the windward side is high relative to that on the lee side since the boundary layer remains attached only on the windward side. Further results for the windward position are presented in Figs. 2-88 and 2-89. These were obtained assuming that laminar flow prevails. It may be seen that surface temperature remains low and that the extent of shield decomposition is slight. Even so, mass injection is sufficient to significantly reduce the convective heating level.

### 2.6 SUMMARY

The problem of predicting the heat transfer experienced by manned vehicles during entry at superorbital velocity has been investigated. The various phenomena affecting heat transfer have been identified and their relative importance has been quantitatively assessed. Existing theoretical and experimental works have been reviewed to determine their relevance to the problem and analysis techniques which account for most of the major effects have been formulated. A series of computer programs which may be used for detailed calculations of the aerothermal environment or for routine heating history computations have been developed.

The results have direct application to the Apollo Command Module and may be used in analysis of extended mission capabilities. The theoretical techniques and numerical methods have wide utility. The phenomenological review enables identification of problems for future research.

### 2.6.1 Conclusions

Consideration has been given to means for description of the inviscid flow field, radiative heat transfer, convective heating, and shield material behavior. The phenomena of non-equilibrium chemistry, radiative energy loss, self-absorption, foreign-species injection, shock-generated vorticity, boundary-layer transition, surface protuberance interactions, and flow separation have been examined.

#### Inviscid Flow Field

Because the Apollo vehicle operates at large angle of attack, the shock layer flow field is highly asymmetric. For the flight regimes of primary interest, the effects of non-equilibrium chemistry on the gross characteristics of the flow are small. Viscous displacement, even the mass injection considered, is not significant except at very high altitudes. Radiative energy transport alters the shock layer structure slightly at lunar return velocity.

Computation procedures for determining in detail the complete three-dimensional flow field are available. However they require large computation times and are subject to significant truncation errors. A relatively efficient numerical procedure employing the streamline coordinate system has been developed. At present it is limited in application for three-dimensional flows to the plane of symmetry and treats the shock layer as an inviscid flow in chemical equilibrium. Non-adiabatic effects are accounted for. Accuracy of the method has been demonstrated by comparing results with experimental data and alternate numerical solutions.

#### Radiative Heating

Radiative heat transfer to the Apollo will be significantly influenced by radiative energy loss and by self-absorption. Optical thicknesses of the shock layer are large in the vacuum ultraviolet region of the spectrum and small in the visible region. It appears that ablation products injected into the shock layer will have only second-order effect on Apollo forebody

heating. Absorption and emission from the contaminated boundary layer may become important for different conditions, however. The non-equilibrium contribution to the total radiative flux will be significant for Apollo, especially along the overshoot trajectory.

In order to enable realistic prediction of the equilibrium shock-layer radiation, two complementary numerical techniques for solution of the radiation-coupled flow field with self-absorption have been formulated. Flow similarity is assumed in one approach to obtain a stagnation region solution. A streamtube technique is used in the second approach to compute radiative heat transfer distribution about the body. The results obtained in exercise of these techniques indicate that energy loss and self-absorption may reduce radiation by an order of magnitude at Apollo conditions. They also show that the radiative heat transfer distribution is almost frozen.

The influence of ablation products may be theoretically estimated if the assumption of chemical equilibrium within the boundary layer is admitted. However, the reliability of results is adversely affected by large uncertainties in spectral absorption coefficient data.

Radiation from the non-equilibrium zone is most reliably predicted by empirical methods. The experimental data scatter is large, however, and as a result the empirically predicted level is uncertain.

#### Convective Heating

The three-dimensional flow pattern over Apollo appreciably influences the convective heat transfer distribution, but direct effects of cross-flow are small. Shock-generated vorticity will cause a slight increase in convective heating level at the higher altitudes. Mass injection will have a first order effect. Non-equilibrium chemistry and radiation coupling effects appear to be of second-order importance for Apollo. Boundary layer transition, with attendant large increase in convective heat flux, is probable for undershoot trajectories.

A large body of literature exists on the convective heating of blunt bodies at high speeds. Almost all important phenomena have been theoretically studied, but the various effects have generally been treated separately. Simple formulae accurately correlating numerical results of first-order laminar boundary layer analyses are available and relations enabling corrections for certain of the second-order effects have been derived for laminar flow. Turbulent boundary layer theory is not far advanced.

Techniques which may be simply applied have been selected for prediction of convective heat transfer. These incorporate approximate theoretical means for establishing the influence of three-dimensional flow and vorticity. The mass transfer boundary condition is theoretically modeled, but the transpiration effect is treated semi-empirically. An approximate criterion for boundary layer transition has been obtained by correlation of flight test data. The basic procedures for prediction of convective heating distribution and coupled material response have been validated by comparison of predictions with experimental data.

Application of the adopted techniques for flight predictions indicates that convective heating will generally predominate over radiation in Apollo trajectories. The total convective heat load is strongly influenced by mass injection. During periods of intense radiation, the injection rate of gaseous ablation products is sufficient to separate the thermal boundary layer from the surface and convection ceases.

#### Afterbody Heating

Heat transfer to afterbody regions is relatively low. This is fortunate since there are many complications which make accurate predictions of the environmental conditions very difficult. The flow will be separated over a large portion of the Apollo afterbody and non-equilibrium chemistry will prevail. The downstream viscous wake may be an important source of radiation as a consequence of its large volume and high content of ablation products.

Existing theoretical models for prediction of convective heat transfer in separated flow regions are not well suited for application to the Apollo. The use of semi-empirical procedures is favored. First order predictions are made possible by correlation of the large body of experimental data.

Empirical prediction of the radiative heating is highly uncertain due to a paucity of test results and to the lack of substantiation of scaling relationships. However, no sound theory for quantitative prediction of wake emission is available at present and the empirical procedures must suffice.

#### 2.6.2 Recommendations

##### Flow Field

The effects of precursor radiation on the flow field have not been investigated. A substantial fraction of the energy assumed to be lost to space will in reality be absorbed in the immediate free stream and will be convected back into the shock layer. The bow shock configuration may be altered and radiative heat transfer will be increased. While it is anticipated that all of these effects will be small at Apollo flight conditions, quantitative analyses should be performed.

The numerical procedure devised for computation of the inviscid flow field is relatively efficient, but its application is limited due to the simplifying assumptions which have been incorporated. Its utility would be greatly extended by removal of thin shock-layer assumptions and by accounting more precisely for normal pressure gradients. The basic computation technique is ideally suited for non-equilibrium chemistry calculations. Conventionally, the flow pattern is solved independently of the chemical kinetics. The present procedure could be modified for coupled study of flow chemistry effects.

### Radiation

The numerical techniques developed for evaluation of radiative heat transfer treat self-absorption considering air as a multi-band radiator. The continuum atomic and molecular band absorption coefficients are accommodated, but atomic line radiation is not. Because the atomic lines are very strong and numerous, the line contribution to radiation may be significant. Numerical procedures enabling a realistic accounting for line radiation should be developed.

The theoretical estimates of the influence of ablation products on radiation transport through the boundary layer are uncertain. Consideration of additional absorption processes and finite chemical kinetics may alter the conclusions. It is desirable that the theoretical estimates be validated by comparison of prediction with measurements for the range of temperature-pressure conditions of interest. The effect of ablation products on wake radiation is not well-defined. Further experimental work is required to establish the importance of contaminated wake radiation at flight conditions. Valuable information could be obtained by properly instrumenting the Apollo vehicle.

### Convection

The techniques selected for evaluation of convective heating employ the assumption of local similarity and furthermore they treat the various influencing phenomena in uncoupled fashion. While these approximations appear justified for engineering predictions of the heat transfer, the development and exercise of more rigorous procedures is recommended. In particular, diffusion, finite chemical reaction rate, and radiative coupling effects with injection of gaseous ablation products should be studied using realistic compositions and properties.

Criteria for boundary-layer transition are not well established. The acquisition and correlation of further experimental data for ablating bodies is necessary. Both ground and flight test programs would be useful.

Turbulent heating from dissociated and ionized boundary layers with foreign species injection has not been theoretically treated and the available experimental data are very sparse. Again, further experimental work is recommended. In this regard, the incorporation of accurate and reliable instrumentation on development-test vehicles is highly desirable.

Theoretical models for evaluation of the heat transfer in the separated-flow region should be refined and extended to include detailed consideration of the recirculating flow. There is some limited experimental evidence of a Reynolds number dependence for laminar, separated-flow heating distinct from that predicted by the Chapman model. This effect should be further explored.



## REFERENCES

- 2.1 Vinokur, M., Nicolet, W. E., Buckingham, A. C., and Hoshizaki, H., Project Fire Flow Field Prediction and Analysis - Final Report, Lockheed Missiles & Space Co., Report M-12-65-1, March 1965
- 2.2 Dunn, M. G., Daiber, J. W., Lordi, J. A., and Mates, R. E., Estimates of Nonequilibrium Ionization Phenomena in the Inviscid Apollo Plasma Sheath, CAL No. A1-1972-A-1, Cornell Aeronautical Laboratory, Inc., September 1965
- 2.3 Stulov, V. P., and Telenin, G. F., Nonequilibrium Supersonic Air Flow Around a Sphere, Izv, AN SSSR, OTN, Mekhanika, No. 1, 1965
- 2.4 Dunn, M. G., private communication
- 2.5 Kaattari, George E., The Effect of Simulated Ablation-Gas Injection on the Shock-Layer of Blunt Bodies at Mach Numbers of 3 and 5, NASA TN D-2954, August 1965
- 2.6 Kaattari, George E., Shock Envelopes of Blunt Bodies at Large Angles of Attack, NASA TN D-1980, December 1963
- 2.7 Swigart, R. J., Hypersonic Blunt Body Flow Fields at Angle-of-Attack, AIAA Journal, Vol. 2, No. 1, 1964
- 2.8 Webb, H. E. Jr., Study of Flow Fields About Axisymmetric Blunt Bodies at Large Angle-of-Attack, Report No. SID65-1353, North American Aviation Inc., Space & Information Systems Division, 29 October 1965

- 2.9 Waldman, George, Flow Field Computer Program - Final Report, RAD TR 64-17, AVCO Corp.
- 2.10 Bohachevsky, Ivor O., Rubin, Ephraim L., and Mates, Robert E., A Direct Method for Computation of Non-equilibrium Flows with Detached Shock Waves, AIAA Paper No. 65-24, AIAA 2nd Aerospace Sciences Meeting, New York, N.Y., January 25-27, 1965
- 2.11 Cooke, J. C., and Hall, M. G., Boundary Layers in Three Dimensions, AGARD Report 273, North Atlantic Treaty Organization, April 1960
- 2.12 Hayes, Wallace D., and Probstein, Ronald F., Hypersonic Flow Theory, Academic Press, New York, 1959
- 2.13 Chin, J. H., and Hearne, L. F., Shock Layer Radiation for Sphere Cones with Radiative Decay, AIAA Journal, 2, No. 7, 1345-1347, July 1964
- 2.14 Inouya, Mamoru, Blunt Body Solutions for Spheres and Ellipsoids in Equilibrium Gas Mixtures, NASA TN D-2780, May 1963
- 2.15 Bertin, John J., The Effects of Protuberances, Cavities, and Angle-of-Attack on the Wind Tunnel Pressure and Heat Transfer Distribution for the Apollo Command Module, to be published as NASA TM
- 2.16 Garberoglio, J. E., Hypersonic Shock Tunnel Pressure and Heat Transfer Tests of the Apollo Reentry Vehicle for North American Aviation, CAL Report No. AA-1712-Y-2 and AA-1805-Y-1, Cornell Aeronautical Laboratory Inc., December 1962 and September 1963
- 2.17 Wilson, K. H., and Hoshizaki, H., Inviscid Non-adiabatic Flow About Blunt Bodies, AIAA Journal, 3, No. 1, 67-74, January 1965

- 2.18 Chin, Jin H., Radiation-Coupled Flow Field Around Bodies, I. STRADS-AIR and II. STRADS-ABLATION, Lockheed Missiles & Space Co., Report Y-75-65-11, 30 September 1965
- 2.19 Chin, J. H., Inviscid Radiating Flow Around Bodies, Including the Effect of Energy Loss and Self-Absorption, Lockheed Missiles & Space Co., Report 668005, 12 October 1965
- 2.20 Kivel, B. and Bailey, K., Tables of Radiation from High Temperature Air, AVCO, Research Report 21, December 1957
- 2.21 Meyerott, R. E., Sokoloff, J. and Nicholls, R. W., Absorption Coefficients of Air, Geophysics Research Paper No. 68, Air Force Cambridge Research Center, Bedford, Mass. (1960)
- 2.22 Armstrong, B. H., Sokoloff, J., Nicholls, R. W., Holland, D. H. and Meyerott, R. E., Radiative Properties of High Temperature Air, J. Quant. Spectrosc. Radiat. Transfer 1, 145-162 (1961)
- 2.23 Nardone, M. C., Breene, R. G., Zeldin, S. S. and Riethof, T. R., Radiance of Species in High Temperature Air, General Electric R 63 SD3, June 1963
- 2.24 Churchill, D. R., Hagstrom, S. A. and Landshoff, R. K. M., The Spectral Absorption Coefficient of Heated Air, Quant. Spectrosc. Radiat. Transfer 4, 291-321 (1964)
- 2.25 Gilmore, F. R., Approximate Radiation Properties of Air Between 2000 and 8000<sup>o</sup>K, Rand Corp. Memorandum RM 3997-ARPA, March 1964
- 2.26 Armstrong, B. H., Johnston, R. R. and Kelly, P. S., Opacity of High-Temperature Air, AFWL TR 65-17, June 1965

- 2.27 Hahne, G. E., The Vacuum Ultraviolet Radiation from  $N^+$  - and  $O^+$  - Electron Recombination in High Temperature Air, NASA TN D 2794 (June 1965)
- 2.28 Allen, R. A., Air Radiation Graphs: Spectrally Integrated Fluxes Including Line Contributions and Self-Absorption, AVCO Everett Research Laboratory, Research Report 230, September 1965
- 2.29 Churchill, D. R., Armstrong, B. H. and Mueller, K. G., Absorption Coefficients of Heated Air: A Compilation to 24,000<sup>o</sup>K, AFWL-TR 65-132, Vols. 1 and 2, October 1965
- 2.30 Losev, S. A. and Osipov, A. I., The Study of Non-Equilibrium Phenomena in Shockwaves, Soviet Physics-Uspekhi, Russian Vol. 74, Nos. 3-4, 393-434, July 1961, Translation January-February 1962
- 2.31 Lin, S. C. and Teare, J. D., Rate of Ionization Behind Shockwaves in Air II. Theoretical Interpretation, AVCO-Everett Laboratory, Research Report 115, September 1962
- 2.32 Allen, R. A., Rose, P. H. and Camm, J. C., Nonequilibrium and Equilibrium Radiation at Super-Satellite Re-entry Velocities, AVCO-Everett Laboratory, Research Report 156, September 1962
- 2.33 Page, W. A., Shock-Layer Radiation of Blunt Bodies Travelling at Lunar Return Entry Velocities, IAS Paper No. 63-41, IAS Annual Meeting, January 21-23, 1963, New York
- 2.34 Allen, R. A., Rose, P. H. and Camm, J. D., Non-equilibrium and Equilibrium Radiation at Super-Satellite Re-entry Velocities, IAS Paper No. 63-77, IAS Annual Meeting, January 21-23, 1963, New York

- 2.35 Teare, J. D., Georgiev, S. and Allen, R. A., Radiation from the Non-equilibrium Shock Front, AVCO Everett Research Laboratory, Research Report 112, October 1961
- 2.36 Lees, L., Laminar Heat Transfer over Blunt-Nosed Bodies at Hypersonic Flight Speeds, Jet Propulsion, Vol. 26, No. 4, pp 259-269, 1956
- 2.37 Emmons H. W. and Leigh, D., Tabulation of the Blasius Function with Blowing and Suction, Combustion Aerodynamic Laboratory, Interim Technical Report No. 9, Harvard University, November 1953
- 2.38 Lees, L., Convective Heat Transfer with Mass Addition and Chemical Reactions, Third AGARD Combustion and Propulsion Colloquium, 1958
- 2.39 Weisner, J., Private communication
- 2.40 Hoshizaki, H. and Wilson, K. H., Convective and Radiative Heat Transfer During Superorbital Entry, AIAA Paper 66-106, January 1966
- 2.41 2.41 Yoshikawa, K. K. and Chapman, D., Radiative Heat Transfer and Absorption Behind a Hypersonic Normal Shock Wave, NASA TN D 1424, September 1962
- 2.42 Goulard, R., The Coupling of Radiation and Convection in Detached Shock Layers, Bendix Product Div., Applied Science Lab., RN 23, December 1960
- 2.43 Wick, B. H., Radiative Heating of Vehicles Entering the Earth Atmosphere, Fluid Mechanics Panel, AGARD, Brussels, Belgium, April 1962
- 2.44 Howe, J. T. and Viegas, J. R., Solution of the Ionized Radiating Shock Layer, Including Reabsorption and Foreign Species Effects, and Stagnation Region Heat Transfer, NASA TR R-159, 1963

- 2.45 Hoshizaki, H. and Wilson, K. H., The Viscous Radiating Shock Layer About a Blunt Body, AIAA Entry Technology Conference, Williamsburg and Hampton, Va., October 12-14, 1964, pp 65-76
- 2.46 Hearne, L. F., Chin, J. H. and Lefferdo, J. M., Reentry Heating and Thermal Protection of a Mars-Mission Earth-Reentry Module, AIAA Entry Technology Conference, Williamsburg and Hampton, Va., October 12-14, 1964, pp 118-135
- 2.47 Chin, J. H. and Hearne, L. F., Shock-Layer Radiation for Yawed Cones with Radiative Decay, AIAA Journal 3, No. 6, 1205-1207 (June 1965)
- 2.48 Kennet, H. and Strack, S. L., Stagnation Point Radiative Heat Transfer, ARS Journal, Vol. 31, No. 9, 374, 1961
- 2.49 Biberman, L. M., Vorobev, V. S., Norman, G. E. and Iakubov, I. T., Radiation Heating in Hypersonic Flow, Kosmich, Issled. 2, No. 3, 441-454 (1964)
- 2.50 Bird, G. A., The Effect of Thermal Radiation on the Inviscid Hypersonic Flow Over a Blunt Body, J. Aerospace Sciences 27, No. 9, 713-714 (September 1960)
- 2.51 Hilsenrath, Joseph, and Beckett, Charles W., Tables of Thermodynamic Properties of Argon Free Air to 15,000°K, TN 56-12, Arnold Engineering Development Center, September 1956
- 2/52 Study of Heat Shielding Requirements for Manned Mars Landing and Return Missions, Report 4-74-64-1, Lockheed Missiles & Space Co., December 1964

- 2.53 Viegas, J. R., and Howe, J. T., Thermodynamic and Transport Property Correlation Formulas for Equilibrium Air from 1000°K to 15,000°K, NASA TN D-1429, October 1962
- 2.54 Howe, J. T., and Sheaffer, Y. S., Effects of Uncertainties in the Thermal Conductivity of Air on Convective Heat Transfer for Stagnation Temperature up to 30,000°K, NASA TN D-2678, February 1965
- 2.55 Hansen, C. F., Approximations for the Thermodynamic and Transport Properties of High-Temperature Air, NASA TR R-50, 1959; and NACA TN 4150, 1958
- 2.56 Schultz, E. D., Holland, A. C., and Marmo, F. F., Planetary Aeronomy VIII. A Congeries of Absorption Cross Sections for Wavelengths Less than 3000A, NASA CR-15, Sept. 1963
- 2.57 Gilmore, F. R., Equilibrium Composition and Thermodynamic Properties of Air to 24,000°K, Rand Corporation Memorandum RM-1543, August 1955
- 2.58 Evans, J. S., and Schexnayder, C. J., Jr., An Investigation of the Effect of High Temperature on the Schumann-Runge Ultraviolet Absorption Continuum of Oxygen, NASA TR R-92, 1961
- 2.59 French, E. P., Approximate Absorption Coefficients for Vibrational Electronic Band Systems, AIAA Journal 2, No. 12, 2209-2211, Dec. 1964
- 2.60 Emanuel, G., Problems Underlying the Numerical Integration of the Chemical and Vibrational Rate Equations in Non-Equilibrium Flow, AEDC TDR 63-82, 1963
- 2.61 Hall, J. G., Eschenroader, A. Q., and Marrone, P. V., Inviscid Hypersonic Air Flows with Coupled Non-Equilibrium Processes, Journ. Aero. Sci. (29), 1962, p. 1038

- 2.62 Bortner, M. H., Chemical Kinetics in a Reentry Flow Field, G. E. Res. Rept. R63SD63, August 1963
- 2.63 Gilmore, F. R., Energy Levels, Partition Functions, and Fractional Electronic Populations for Nitrogen and Oxygen Atoms and Ions to 25,000°K, Rand Corp., Res. Memo RM-3748-PR, 1963
- 2.64 Moore, C. E., Atomic Energy Levels, N.B.S. Circ. 467, 1948
- 2.65 Herzberg, G., Molecular Spectra and Molecular Structure, I. Spectra of Diatomic Molecules, 2nd Ed., D. van Nostrand Co., J. J., 1950
- 2.66 Marrone, P. V., Normal Shock Waves in Air: Equilibrium Composition and Flow Parameters for Velocities from 26,000 to 50,000 ft/sec, C.A.L. Tech. Rept. AG-1729-A-2, August 1962
- 2.67 Chisnell, R. G., Hoshizaki, H., and Lasher, L. E., Stagnation Point Flow with Radiation, Lockheed Tech. Rept. 4-43-65-4, October 1965
- 2.68 Kivel, B., Hammerling, P. and Teare, J. D., Radiation from the Non-Equilibrium Region of Normal Shocks in Oxygen, Nitrogen, and Air, Planetary and Space Science, Vol. 3, February 1961, pp. 132-137
- 2.69 Hansen, C. F., and Chapin, C. E., Non-Equilibrium Radiation from the Stagnation Region of High-Velocity Bodies, presented at the Third Conference on the Performance of High Temperature Systems, Pasadena, California, 7-9 December 1964
- 2.70 Wray, K. L., and Teare, J. D., Excitation Mechanism for the N<sub>2</sub> (1+) Band System in Shock Heated Nitrogen, Atomic Collision Processes, M.R.C. McDowell (Ed.), Amsterdam, North-Holland Publishing Col, 1964, pp. 1123-1132



- 2.71 Page, W. A., and Arnold, J. O., Shock-Layer Radiation of Blunt Bodies at Reentry Velocities, NASA TR R-193, April 1964
- 2.72 Beckwith, Ivan E., Similarity Solutions for Small Cross Flows in Laminar Compressible Boundary Layers, NASA TR R-107, Langley Research Center, 1961
- 2.73 Van Dyke, M., Second-Order Boundary-Layer Theory for Blunt Bodies in Hypersonic Flow, Proc. ARS International Hypersonic Conference at MIT, August 16 to 18, 1961
- 2.74 Maslen, S. H., Second-Order Effects in Laminar Boundary Layers, AIAA Journal, Vol. 1, pp. 33-40, 1963
- 2.75 Ho, H. T., and Probst, R. F., The Compressible Viscous Layer in Rarefied Hypersonic Flow, Brown University ARL TN 60-132, August 1960
- 2.76 Herring, T. K., The Boundary Layer Near the Stagnation Point in Hypersonic Flow Past a Sphere, J. Fluid Mech., Vol. 7, pp. 257-272, 1960
- 2.77 Cheng, H. K., Hypersonic Shock-Layer Theory at the Stagnation Region at Low Reynolds Number, Cornell Aeronautical Laboratory, Inc., Report AF-1285-A-7, April 1961
- 2.78 Ferri, Antonio, Zakkay, Victor, and Ting, Lu, Blunt Body Heat Transfer at Hypersonic Speed and Low Reynolds Number, Polytechnic Institute of Brooklyn, ARL TN 60-140, June 1960
- 2.79 Fay, J. A., and Riddell, F. R., Theory of Stagnation Point Heat Transfer in Dissociated Air, J.A.S., Vol. 25, No. 2, pp. 73-85, February 1958

- 2.80 Goulard, Robert, On Catalytic Recombination Rates in Hypersonic Stagnation Heat Transfer, Presented at ARS 12th Annual Meeting, New York, N. Y., December 2-5, 1957
- 2.81 Clutter, Darwin W.; and Smith, A. M. O., Solution of the General Boundary-Layer Equations for Compressible Laminar Flow, Including Equilibrium Dissociation, Presented at the 6th BOWACA Symposium on Aeroballistics, Washington, D. C., 31 October - 1 November 1963
- 2.82 Rose, P. H.; and Stankevics, J. O., Stagnation-Point Heat-Transfer Measurements in Partially Ionized Air, AIAA Journal, Vol. 1, No. 12, pp. 2752-2763, December 1963
- 2.83 Bortner, M. H., Chemical Kinetics in a Reentry Flow Field, Report R63SD63, General Electric, August 1963
- 2.84 Bates, D. R., Atomic and Molecular Processes, p. 249, Academic Press, New York, New York, 1962
- 2.85 Goodwin, G.; and Chung, P. M., Effects of Nonequilibrium Flows on Aerodynamic Heating During Entry into the Earth's Atmosphere from Parabolic Orbits, Advances in Aeronautical Science, Vol. 4, Pergamon Press, 1961
- 2.86 Inger, C. R., Correlation of Surface Temperature Effect on Non-Equilibrium Heat Transfer, ARS Journal, Vol. 32, No. 11, pp. 1743-1745, November 1962
- 2.87 Rosner, D. E.; and Allendorf, H. D., High-Temperature Kinetics of Graphite Oxidation by Dissociated Oxygen, AIAA Journal, Vol. 3, pp. 1522-1524, August 1965
- 2.88 Goldstein, H. W., The Reaction of Active Nitrogen with Graphite, J. Phys. Chem., Vol. 68, p. 39, 1964

- 2.89 Zimman, W., Planetary Space Science, Vol. 3, p.46, 1961
- 2.90 Fay, J. A.; and Kemp, H. N., Theory of Stagnation-Point Heat Transfer in a Partially Ionized Diatomic Gas, AIAA Journal, Vol. 1, No. 12, pp. 2741-2541, December 1963
- 2.91 Fenster, S. J., Stagnation-Point Heat Transfer for a New Binary Air Model Including Dissociation and Ionization, AIAA Journal, Vol. 3, No. 12, pp. 2189-2196, December 1965
- 2.92 Libby, P. A., The Homogeneous Boundary Layer at an Axisymmetric Stagnation Point with Large Rates of Injection, JAS, Vol. 20, No. 1, January 1962
- 2.93 Pallone, A.; and Van Tassel, W., Stagnation Point Heat Transfer for Air in the Ionization Regime, ARS Journal, Vol. 32, No. 3, pp. 436-437, March 1962
- 2.94 Burggraf, Odus R., Asymptotic Solutions for the Viscous Radiating Shock Layer, Presented at AIAA 3rd Aerospace Sciences Meeting, New York, N. Y., January 24-26, 1966
- 2.95 Hoshizaki, H.; and Wilson, K. H., Convective and Radiative Heat Transfer During Superorbital Entry, Task II, LMSC 4-43-65-5, Lockheed Missiles and Space Company, November 1965
- 2.96 Ness, N.; and Lew, H. G., Turbulent Boundary Layer Equations with Binary Diffusion, Aerophysics Memo. 23, General Electric Missile and Space Vehicle Department, May 1958
- 2.97 Hoshizaki, H., Heat Transfer in Planetary Atmospheres at Super-Satellite Speeds, ARS Journal, Vol. 132, No. 10, pp. 1544-1551, October 1962

- 2.98 De Rienzo, Philip, and Pallone, Adrian, Convective Stagnation Point Heating for Reentry Speeds up to 70,000 feet/sec Including Effects of Large Blowing Rates, RAD-TM-65-58, AVCO Corporation, 5 January 1965
- 2.99 Scala, S. M., and Gilbert, L. M., Sublimation of Graphite at Hypersonic Speeds, AIAA Journal, Vol. 3, No. 9, 1965
- 2.100 Howe, John T., and Sheaffer, Yvonne S., Mass Addition in the Stagnation Region for Velocity up to 50,000 Feet per Second, NASA TR R-207, Ames Research Center, August 1964
- 2.101 Lees, L., Laminar Heat Transfer Over Blunt-Nosed Bodies at Hypersonic Flight Speeds, Jet Propulsion, Vol. 26, No. 4, pp. 259-269, April 1956
- 2.102 Kemp, Nelson H., Rose, Peter H., and Detra, Ralph W., Laminar Heat Transfer around Blunt Bodies in Dissociated Air, Journal of the Aerospace Sciences, Vol. 26, No. 7, pp. 421-430, July 1959
- 2.103 Cohen, Nathaniel B., Boundary Layer Similar Solutions and Correlation Equations for Laminar Heat-Transfer Distribution in Equilibrium Air at Velocities up to 41,000 Feet per Second, NASA TR R-118, Langley Research Center, 1961
- 2.104 Blottner, F. G., Non-Equilibrium Laminar Boundary Layer Flow of Ionized Air, Presented at AIAA Aerospace Sciences Meeting, New York, New York, January 20-22, 1964
- 2.105 Pallone, Adrian J., Moore, Jeffrey A., and Erdos, John I., Non-Equilibrium, Nonsimilar Solutions of the Laminar Boundary Layer Equations, presented at AIAA Aerospace Sciences Meeting, New York, New York, January 20-22, 1964

- 2.106 Eckert, E. R. G., Survey on Heat Transfer at High Speeds, WADC TR 54-70, 1954
- 2.107 Bromberg R.; Fox, J. L.; and Ackerman, W. O., A Method of Predicting Convective Heat Input to the Entry Body of a Ballistic Missile, Ramo-Wooldridge Corporation
- 2.108 Denison, M. R., Turbulent Boundary Layer on Blunt Bodies of Revolution at Hypersonic Speeds, Research Memorandum, Lockheed Missiles and Space Company, April 13, 1956
- 2.109 Burggraf, O. R., The Compressibility Transformation and the Turbulent-Boundary Layer on a Flat Plate, JAS, Vol. 28, No. 8, pp. 645-654, August 1961
- 2.110 Ness, Nathan, Foreign Gas Injection into a Compressible Turbulent Boundary Layer on a Flat Plate, JAS, Vol. 28, No. 8, pp. 645-654, August 1961
- 2.111 Denison, M. Richard, The Turbulent Boundary Layer on Chemically Active Ablating Surfaces, JAS, Vol. 28, No. 6, pp. 471-479, June, 1961
- 2.112 Chung, P. M.; Liu, S. W.; and Mirels, H., Effect of Discontinuity of Surface Catalycity on Boundary Layer Flow of Dissociated Gas, Int. J. Heat Mass Transfer, Vol. 6, pp. 193-210, 1963
- 2.113 Pallone, H., Nonsimilar Solutions of the Compressible Laminar Boundary Layer with Application to the Upstream Transpiration Cooling Problem, JAS, Vol. 2B, No. 6, pp. 449-492, June, 1961
- 2.114 Rubesin, M. W.; and Inouye, M., A Theoretical Study of the Effect of Upstream Transpiration Cooling on the Heat-Transfer and Skin-Friction Characteristics of a Compressible, Laminar Boundary

Layer, NACA TN 3969, May 1947

- 2.115 H rtnett, J. P., Eckert, E.R.G., Birkebak, R., and Sampson, R. L., Simplified Procedures for the Calculation of Heat Transfer to Surfaces with Non-Uniform Temperatures, WADC Tech. Report 56-373, December 1956
- 2.116 Reshotko, Eli, Heat Transfer to a General Three-Dimensional Stagnation Point, Jet Propulsion, Vol. 28, No. 1, 58-60, 1958
- 2.117 Braslow, A. L., Review of the Effect of Distributed Surface Roughness on Boundary Layer Transition, AGARD Report 254, April 1960
- 2.118 Klebanoff, P. S., Schubauer, and Tidstrom, Measurements of the Effects of Two-Dimensional and Three-Dimensional Roughness Elements on Boundary Layer Transition, JAS, November 1955
- 2.119 Mickley, H. S., Ross, R. C., Squyers, A. L., and Steward, W. D., Heat, Mass, and Momentum Transfer for Flow over a Flat Plate with Blowing or Suction, NACA TN 3208, July 1954
- 2.120 Pappas, Constantine C., and Okuno, Arthur F., Measurements of Skin Friction of the Compressible Turbulent Boundary Layer on a Cone with Foreign Gas Injection, JAS, May 1960
- 2.121 Stetson, Kenneth F., Boundary-Layer Transition on Blunt Bodies with Highly Cooled Boundary Layers, JAS, February 1960
- 2.122 Kratsch, K. M., Hearne, L. F., and McChesney, H. R., Theory for the Thermophysical Performance of Charring Organic Heat Shield Composites, Report 803099, Lockheed Missiles and Space Company, 18 October 1963

- 2.123 Meyer, M. G., Charring in Reinforced Plastics (CHIRP) - An IBM 7094 Digital Computer Program, (Internal Report) Lockheed Missiles and Space Company, November 1963
- 2.124 Hearne, L. F., Coleman, W. D., and Foiles, S. R., Flight Test Corroboration of an Analytical Model for the Thermophysical Behavior of Char-Forming Organic Polymers, Paper presented at the Sixth U. S. Navy Symposium on Aeroballistics, Washington, D. C., 31 October and 1 November 1963
- 2.125 Woodruff, L. W., Transpiration Effects on Heat Transfer, Report D2-22202, The Boeing Company, 1962
- 2.126 Chapman, D. R., A Theoretical Analysis of Heat Transfer in Regions of Separated Flow, NASA TN 3792, October 1956
- 2.127 Korst, H., Page, R., and Childs, M., A Theory for Base Pressure in Transonic and Supersonic Flow, TN 392-2, University of Illinois Engr. Exp. Sta., March 1965
- 2.128 Baum, E., King, H. H., and Denison, M. R., Recent Studies of the Laminar Base-Flow Region, AIAA Journal, Vol. 2, No. 9, September 1964
- 2.129 Stephenson, Jack D., Measurement of Optical Radiation from the Wake of Ablating Blunt Bodies in Flight at Speeds up to 10 KM per Second, NASA TN D-2760, Ames Research Center, April 1965
- 2.130 Sprinks, T., A Review of Work Relevant to the Study of Heat Transfer in Hypersonic Separated Flows, U.S.A.A. Report 138, University of Southampton, Hampshire, England, June 1960
- 2-131 Larson, Howard K., Heat Transfer in Separated Flows, Journal of the Aerospace Sciences, Vol. 26, No. 11, November 1959

- 2-132 Lee, George, Correlation of Heat-Transfer Data for the Apollo Afterbody at Mach Numbers 8 to 20, NASA TM X-855, Ames Research Center, February 1964
- 2-133 Murphy, John, Flight Test Aerodynamic Heating Data for the Afterbody of the Project Mercury Spacecraft with Comparisons to Available Prediction Methods, to be published as NASA CR
- 2-134 Seban, R. A., Emery, A., and Levy, A., Heat Transfer to Separated and Reattached Subsonic Turbulent Flows Obtained Downstream of a Surface Step, Journal of the Aerospace Sciences, Volume 26, No. 12, December 1959
- 2-135 Rubin, I., Shock Curvature Effects on the Outer Edge Boundary Condition of a Laminar Boundary Layer, AIAA Journal, Vol. 1, pp. 2850-2852, December 1963
- 2-136 Summary Analysis of X-17 RTV Program, Aerodynamic Heating and Boundary Layer Transition, LMSD 2161, Lockheed Missiles and Space Company, 2 July 1957
- 2-137 Bradshaw, W., Evaluation of Four Unidentified Ablating Composites, Internal Memorandum, Lockheed Missiles and Space Company, 30 November 1964
- 2-138 Goldstein, H. E., Pyrolysis Kinetics of Nylon Phenolic and Composites, TXN 1492, Lockheed Missiles and Space Company, 6 December 1963
- 2-139 Thermochemical and Air Arc Data for Typical Heat Shield Material, Private Communication from NASA Manned Spacecraft Center, October 1964



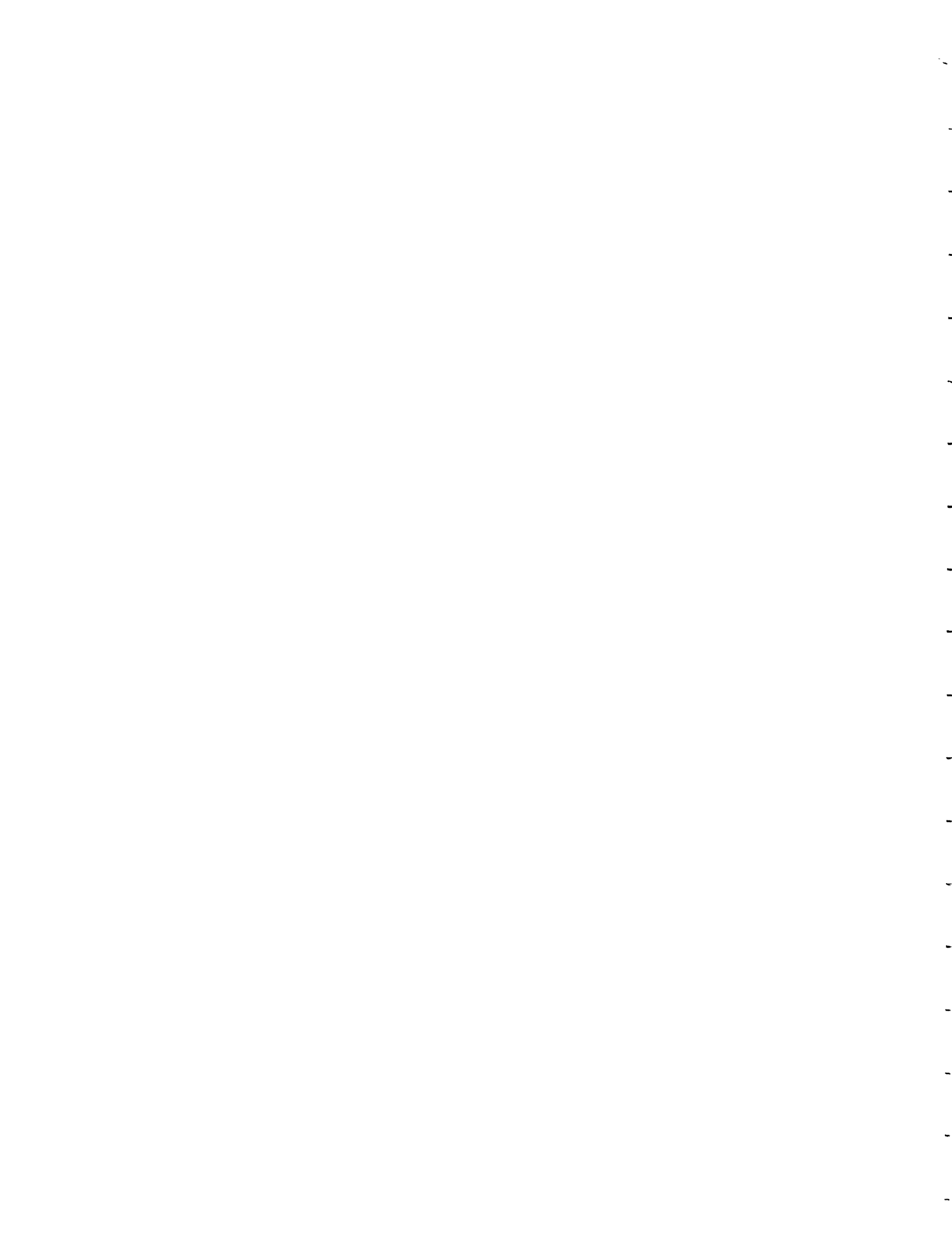
- 2.140 Gross, J. F., Hartnett, J. P., Masson, D. J., and Gazley, Carl, A Review of Binary Boundary Layer Characteristics, RAND Report P-1729, June 1959
- 2.141 Baron, J. R., and Scott, P. B., The Laminar Diffusion Boundary Layer in the Presence of External Flow Field Pressure Gradients, AFOSR TN 60-830, December 1959
- 2.142 Vojvodich, N. S., and Pope, R. B., The Influence of Ablation on Stagnation Region Convective Heating for Dissociated and Partially Ionized Boundary-Layer Flows, Proceedings of the 1965 Heat Transfer and Fluid Mechanics Institute, Stanford University Press
- 2.143 Gollnick, A. F., Thermal Effects on a Transpiration Cooled Hemisphere, ARS, 29, 5, May 1962
- 2.144 Hoshizaki, H., and Smith, H. J., Axisymmetric Stagnation Point Mass-Transfer Cooling, Lockheed Missiles & Space Co., TR LMSD-48381, January 1959
- 2.145 Scott, C. J., Integral Laminar Boundary Layer Solutions Using the Crocco Variables, AFOSR TN 59-1304, Engin. Memo No. 86, Univ. of Minnesota Institute of Technology, Rosemount Aero. Lab., August 1959
- 2.146 Chung, P. M., Effect of Localized Mass Transfer Near the Stagnation Region of Blunt Bodies in Hypersonic Flight, NASA TN D-141, May 1960
- 2.147 Low, G. M., The Compressible Laminar Boundary Layer with Fluid Injection, NACA TN 3404, March 1955

- 2.148 Brown, W. B., and Donoughe, P. L., Tables of Exact Laminar Boundary-Layer Solution When the Wall is Porous and Fluid Properties are Variable, NACA TN 2479, 1951
- 2.149 Reshotko, E., and Cohen, C. B., Heat Transfer at the Forward Stagnation Point of Blunt Bodies, NACA TN 3513, July 1965
- 2.150 Libby, P. A., and Pierucci, M., The Laminar Boundary Layer with Hydrogen Injection Including Multicomponent Diffusion, ARL 64-40, March 1964
- 2.151 Hartnett, J. P., et al., Mass Transfer Cooling in a Turbulent Boundary Layer, IAS Paper No. 60-66, 1960
- 2.152 Leadon, B. M., The Status of Heat Transfer Control by Mass Transfer for Permanent Surface Structure, Proceedings of a Conference on Aerodynamically Heating Structure, Prentice Hall, Inc., Englewood Cliffs, New Jersey, 1962
- 2.153 Rubesin, M. W., An Analytical Estimation of the Effect of Transpiration Cooling on the Heat Transfer and Skin-Friction Characteristics of a Compressible, Turbulent Boundary Layer, NACA TN 3341, 1954
- 2.154 Van Driest, E. R., On Mass Transfer Near the Stagnation Point, RAND Symposium on Mass-Transfer Cooling for Hypersonic Flight, June 1957
- 2.155 Rubesin, M. W., and Pappas, C. C., An Analysis of the Turbulent Boundary Layer Characteristics on a Flat Plate with Distributed Light-Gas Injection, NACA TN 4149, February 1958
- 2.156 Mickley, H. S., et al., Heat, Mass, and Momentum Transfer for Flow over a Flat Plate with Blowing or Suction, NACA TN 3208, 1954

- 2.157 Rubesin, M. W., Pappas, C. C., and Okuno, A. F., The Effect of Fluid Injection on the Compressible Turbulent Boundary Layer -- Preliminary Tests on Transpiration Cooling of a Flat Plate at M = 2.7 with Air as the Injected Gas, NACA RM A55119, December 1955
- 2.158 Chauvin, Leo T., and Charter, Howard S., Exploratory Tests of Transpiration Cooling on a Porous 8° Cone at M = 2.05 Using Nitrogen Gas, Helium Gas, and Water as the Coolants, NACA RM L55C29, 1955
- 2.159 Scott, C. J., Anderson, G. E., and Elgin, D. R., Laminar, Transitional, and Turbulent Mass Transfer Cooling Experiments at Mach Numbers from 3 to 5, Univ. of Minnesota Institute of Technology, AFOSR-TN-1305 (ASTIA AD 231974), August 1959
- 2.160 Bartle, E. R., and Leadon, B. M., Experimental Evaluation of Heat Transfer with Transpiration Cooling in a Turbulent Boundary Layer at M = 3.2, J. Aerospace Sci., 27, 78-79, 1960
- 2.161 Bartle, E. R., and Leadon, B. M., The Compressible Turbulent Boundary Layer on a Flat Plate with Transpiration Cooling. I. Measurements of Heat Transfer and Boundary Layer Profiles, CSRL RR No. 11, May 1961
- 2.162 Rashis, B., Exploratory Investigation of Transpiration Cooling of a 40° Double Wedge Using Nitrogen and Helium as Coolants at Stagnation Temperatures from 1295° to 2910°F, NASA TN D-721, May 1961
- 2.163 Tewfik, O. E., Eckert, E. R. G., and Jurewicz, L. S., Measurement of Heat Transfer from a Circular Cylinder to an Axial Stream with Air Injection, Univ. of Minnesota Institute of Technology, HTL TR No. 38, (ASTIA AD 266568), August 1961

- 2.164 Walton, T. E., and Rashis, B., Measurement and Empirical Correlation of Transpiration-Cooling Parameter on a 25° Cone in a Turbulent Boundary Layer in Both Free Flight and Hot Gas Jet, NASA TN D-967, October 1961
- 2.165 Bartle, E. R., and Leadon, B. M., The Effectiveness as a Universal Measure of Mass Transfer Cooling for a Turbulent Boundary Layer, Proceedings of the 1962 Heat Transfer and Fluid Mechanics Institute, Stanford Univ. Press, pp. 27-41
- 2.166 Pappas, C. C., and Okuno, A. F., Measurement of Heat Transfer and Recovery Factor of a Compressible Turbulent Boundary Layer on a Short Cone with Foreign Gas Injection, NASA TN D-2230, April 1964
- 2.167 Bloom, M. H., and Pallone, A., Heat Transfer to Surfaces in the Neighborhood of Protuberances in Hypersonic Flow, Preprints from Heat Transfer and Fluid Mech. Inst., June 19-21, 1957
- 2.168 Burbank, P. B., and Strass, H. K., Heat Transfer to Surfaces and Protuberances in Supersonic Turbulent Boundary Layer, NACA Research Memo 158EO 1a, July 1958
- 2.169 Wisniewski, R. J., Turbulent Heat Transfer Coefficients in the Vicinity of Surface Protuberances, NASA Memo 10-1-58E, October 1958
- 2.170 Yip, P. S., Summary Report for the Aerodynamic Heating Test at the NASA Langley Unitary Plan Wind Tunnel, Convair Rept. No. AE 60-0574, July 1960
- 2.171 Seban, R. A., Heat Transfer and Flow with Separated and Reattached Boundary Layers as Produced by Surface Irregularities, Univ. of California at Berkeley, Rept. No. WADC TR 56-217, May 1956

- 2.172 Charwat, A. F., Dewey, C. F., Roos, J. N., and Hitz, J. A., An Investigation of Separated Flows - Part II: Flow in the Cavity and Heat Transfer, JAS, July 1961, pp. 513-527
- 2.173 Lighthill, M. J., On Boundary Layers and Upstream Influence I. A Comparison Between Subsonic and Supersonic Flows, Proceedings of the Royal Society, Series A, 1953
- 2.174 Gadd, G. E., Boundary Layer Separation in the Presence of Heat Transfer, AGARD Rept. 280, April 1960
- 2.175 Curle, N., The Effects of Heat Transfer on Laminar-Boundary Layer Separation in Supersonic Flow, Aeronaut. Quart. XII, November 1961, pp. 309-336



NOTATION

a	sonic velocity
A	$1 + y/R_c$
B	Planck function for radiation intensity
$B'_w$	mass transfer parameter, $\rho_w v_w / \bar{c}_H$
$B'_{i_w}$	partial mass transfer parameter, $(\rho v)_{i_w} / \bar{c}_H$
c	velocity of light
$c_p$	specific heat
$\bar{c}_p$	total specific heat
$c_s$	solid specific heat
$\tilde{C}_i$	mass fraction of $i^{\text{th}}$ element in pyrolysis gas
$C_c$	compressibility correction
$C_f$	non-blowing skin friction coefficient
$C_H$	non-blowing value of convection coefficient
$\bar{C}_H$	blowing value of convection coefficient
D	Damkohler number, diffusion coefficient
E	activation energy
$E_n(5)$	$n^{\text{th}}$ exponential integral
f	transformed stream function, $\Psi / \mu_o (2\tilde{s})^{1/2}$ ; $-\rho v \sqrt{R_c / u_{\infty}} (L + 1)$ ; f - number
F	$-\rho v / \rho_{\infty} u_{\infty}$

$F_M$	momentum thickness Reynolds number distribution function, Eq. (2.167)
$F_T$	turbulent heating distribution function, Eq. (2.164)
$g$	$H/H_s$
$h$	static enthalpy, Planck constant
$h_1$	length parameter
$h_2$	length parameter, or spreading coordinate
$H$	total enthalpy
$H_D$	heat of decomposition
$k$	Boltzmann constant, mass absorption coefficient, thermal conductivity
$k_f$	forward reaction rate coefficient
$k_r$	reverse reaction rate coefficient
$\bar{k}$	total conductivity; Planck-mean mass absorption coefficient
$k_o$	reaction rate constant
$K$	surface curvature, $1/R_c$ , or molecular species concentration
$\tilde{K}_i$	mass fraction of $i^{\text{th}}$ element
$l$	element of length, or surface distance measured normal to meridional line
$L$	0 for two dimensional, 1 for axisymmetric; Loschmidt number
$Le$	Lewis number
$\dot{m}$	mass injection rate
$m$	distance measured along meridional line
$M$	molecular weight



$\bar{M}$	average molecular weight
$n$	curvilinear coordinate on body surface; curvilinear coordinate measured normal to streamline direction; reaction order
$N$	particle density
$p$	pressure
$Pr$	Prandtl number
$\bar{Pr}$	Prandtl number based on total properties
$q$	heat flux; radiative terms for differential layer
$q_{re}$	equilibrium radiative flux
$q_{rn}$	non-equilibrium radiative flux
$q_{rt}$	total radiative flux
$Q$	radiative terms for finite streamtube or layer
$Q_{co}$	heat liberated in carbon monoxide production reaction per unit mass of carbon reactant
$r$	radial distance from axis of symmetry
$rf$	recovery factor
$R$	characteristic body dimension
$R_c$	body surface radius of curvature
$R_M$	maximum body radius
$R_{EFF}$	effective radius of curvature, Eq. (2E.1)
$R_o$	initial radial distance at stagnation point
$R_s$	geodetic radius of curvature of streamline
$Re_\theta$	momentum thickness Reynolds number
$Re_s$	surface distance Reynolds number

$A$	distance along arbitrary streamline
$s$	curvilinear coordinate on body surface, or curvilinear coordinate measured along streamline wetting body surface
$\bar{s}$	distance along surface from geometric center of body
$St$	Stanton number
$\tilde{s}$	$\frac{1}{\mu_0^2} \int_0^s \rho_w \mu_w^u e^{h^2} dA$
$T$	absolute temperature
$Tr_\theta(\xi)$	$\begin{cases} e^{-\xi/\cos\theta} & , \text{ for oblique parallel beam at angle } \theta \\ E_2(\xi) & , \text{ for isotropic volume source} \end{cases}$
$Trw_\theta(\xi)$	$\begin{cases} e^{-\xi/\cos\theta} \cos\theta & , \text{ for oblique parallel beam at angle } \theta \\ E_3(\xi) & , \text{ for isotropic volume source} \end{cases}$
$u$	velocity component parallel to body
$U$	total velocity
$v$	velocity component normal to body
$V$	specific volume
$\dot{w}$	chemical production rate
$x$	mole fraction
$y$	distance from body surface
$z$	rectangular coordinate measured from plane of symmetry; distance behind shock wave
$Z$	compressibility
$\alpha$	power law exponent, Eq. (2.30); stoichiometric coefficient
$\beta$	power law exponent, Eq. (2.30); stoichiometric coefficient
$\beta_0$	stagnation point velocity gradient in plane of symmetry

$\beta_s$	tangential velocity gradient immediately behind shock in plane of symmetry
$\beta_z$	stagnation point velocity gradient in direction normal to plane of symmetry
$\tilde{\beta}$	transformed pressure gradient parameter, Eq. (2.139)
$\gamma$	power law exponent, Eq. (2.29); stoichiometric coefficient; isentropic exponent
$\Gamma$	ratio of radiative flux to limiting radiative flux; normalized enthalpy gradient (Eq. 2.140)
$\Gamma_a$	ratio of transparent, adiabatic shock layer radiative flux to limiting radiative flux
$\Gamma_e$	ratio of total radiative flux to limiting radiative flux
$\Delta$	shock layer thickness
$\delta^*$	boundary layer displacement thickness
$\delta_*$	transformed turbulent boundary layer thickness
$\Delta_e$	thickness of equilibrium layer
$\Delta_n$	thickness of non-equilibrium layer
$\Delta_p$	distance from shock wave to radiation peak location
$\epsilon$	shock density ratio, $\rho_{\infty}/\rho_s$
$\xi$	$(L + 1) \int_0^z \frac{\rho}{\rho_{\infty}} \frac{dz}{R_c}$ , Eq. (2.101)
$\eta$	$\frac{u_s}{\sqrt{2\xi}} \left(\frac{r}{A}\right)^L \int_0^y A^L \rho dy$ , Eq. (2.87)

$\theta$	time; angle
$\theta_B$	angle between body-surface normal and free-stream wind vector at plane of symmetry
$\theta_s$	angle between shock-surface normal and free-stream wind vector
$\lambda$	rectangular coordinate; wavelength
$\mu$	absorption coefficient; viscosity
$\nu$	frequency; kinematic viscosity
$\xi$	rectangular coordinate, defined in Fig. 2-9; Eq. (2.86)
$\rho$	density
$\rho W$	mass flux
$\sigma$	Stefan-Boltzmann constant
$\tau$	optical thickness
$\psi$	stream function; angle between local body surface normal and flight vector
$\emptyset$	angle between flight vector and normal; angle between streamline and meridional line

#### Subscripts

a	undissociated air
c	fully charred; carbon
co	carbon monoxide
e	local; local boundary layer edge
g	pyrolysis gases
i	shock entry position; $i^{\text{th}}$ streamtube or layer; $i^{\text{th}}$ element

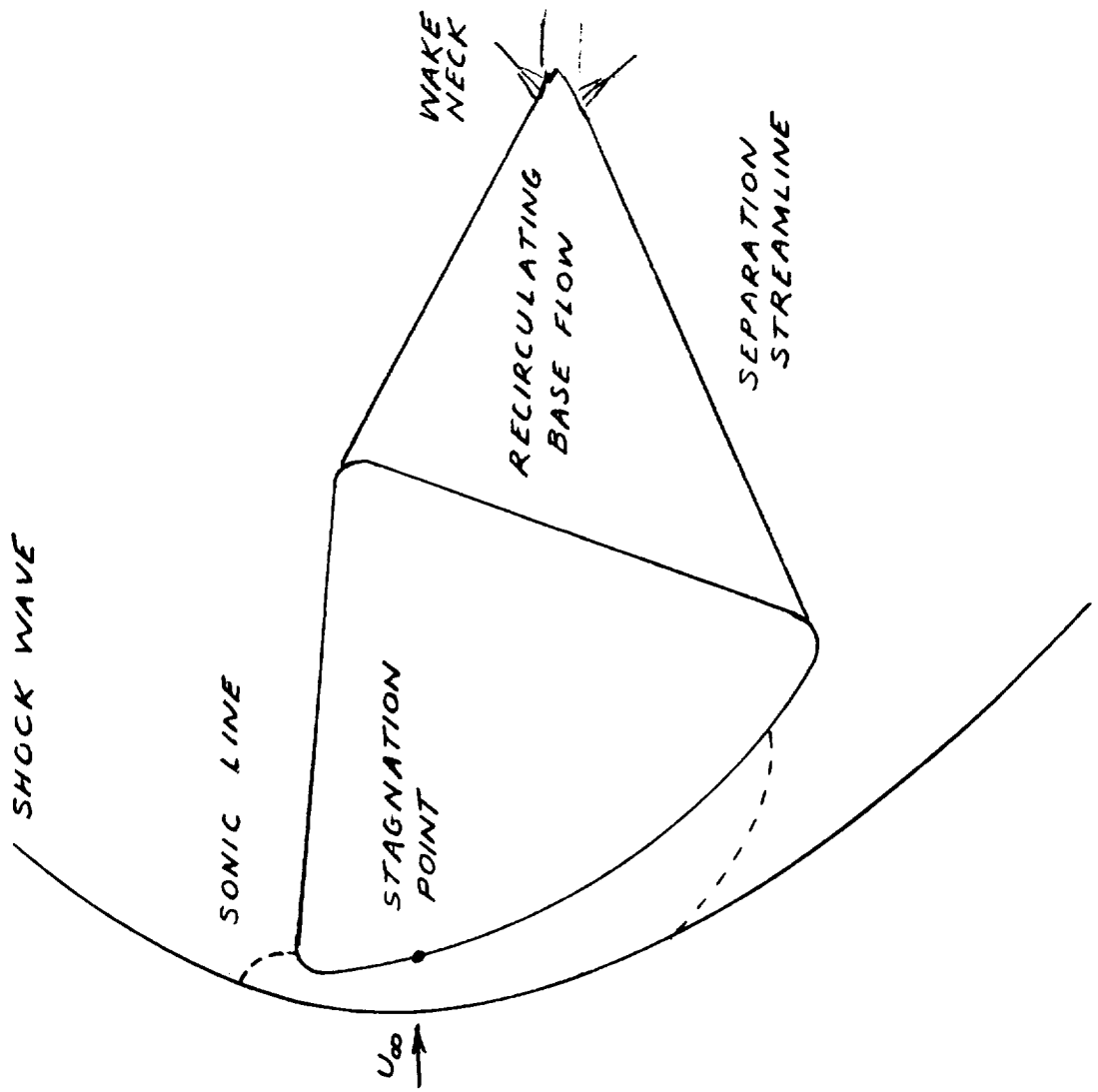
inj	injectant
inv	inviscid
j	$j^{\text{th}}$ streamline; $j^{\text{th}}$ chemical specie
k	$k^{\text{th}}$ surface station; $k^{\text{th}}$ chemical specie
<i>l</i>	<i>l</i> <sup>th</sup> surface station; <i>l</i> <sup>th</sup> chemical specie
m	$m^{\text{th}}$ surface station
n	$n^{\text{th}}$ surface station
o	stagnation point; body surface value for plane of symmetry; oxygen
r	recovery
s	immediately behind shock; solid material
SL	sea-level conditions
t	stagnation point
w	wall conditions
z	body surface value for direction normal to plane of symmetry
$\theta$	at angle $\theta$
$\nu$	at frequency
$\infty$	ambient conditions
l	body surface streamline
*	reference

#### Superscripts

'	denotes derivative
*	effective edge
-	with blowing, average; total property



FIG 2-1  
APOLLO FLOW FIELD CHARACTERISTICS



FOREBODY SURFACE  
STREAMLINE PATTERN

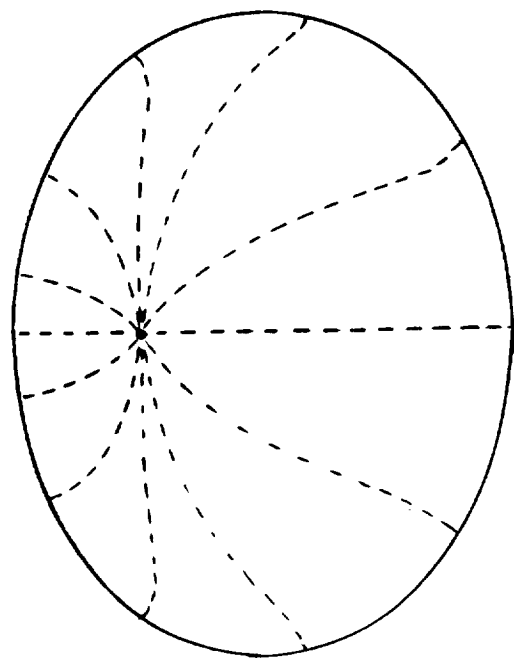


FIGURE 2-2 INFLUENCE OF NON-EQUILIBRIUM ON THERMODYNAMIC STATE  
 TRAJECTORY III, STAGNATION POINT

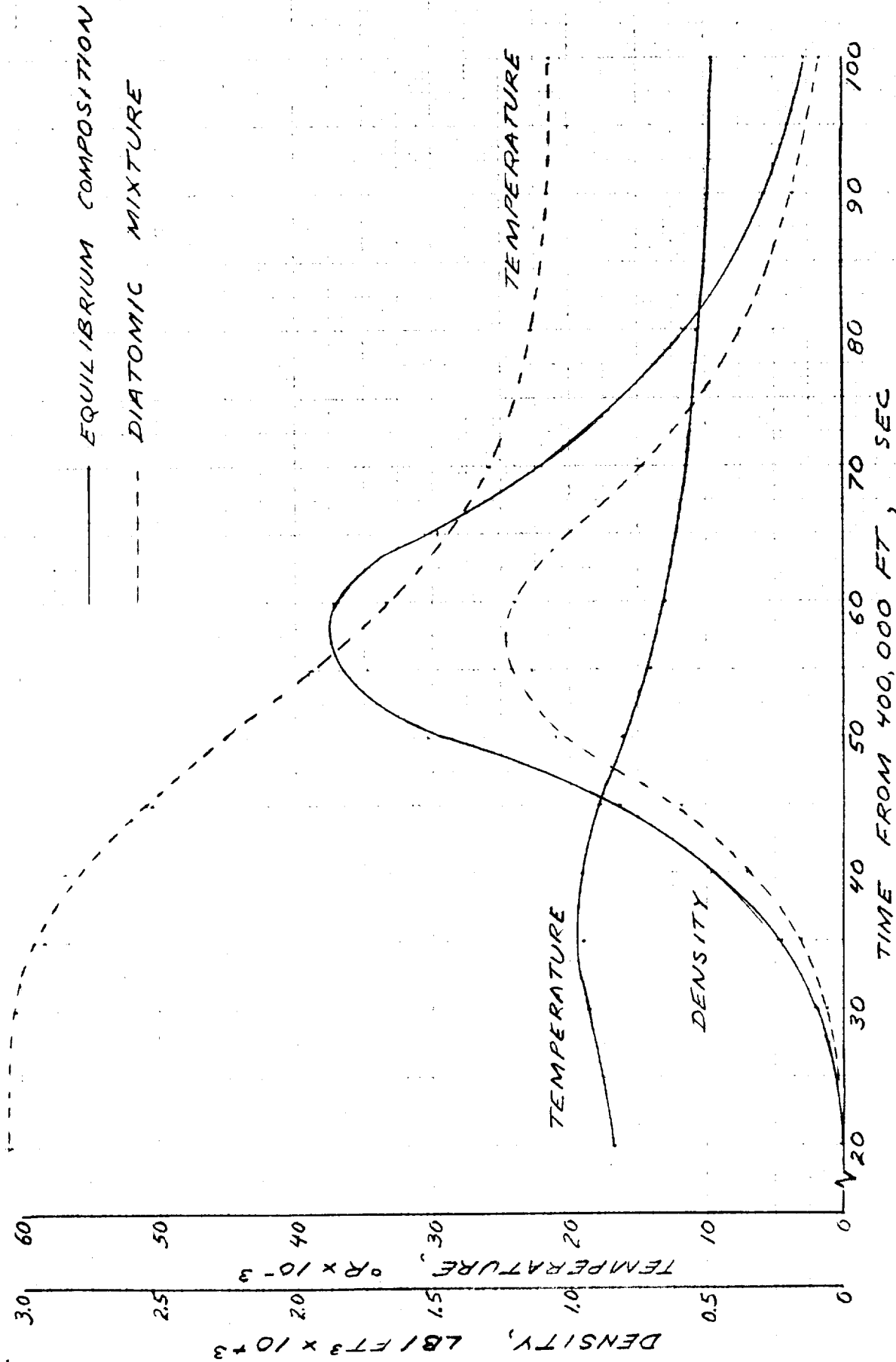




FIGURE 2-3  
INFLUENCE OF SHOCK DENSITY RATIO  
ON SHOCK LAYER THICKNESS

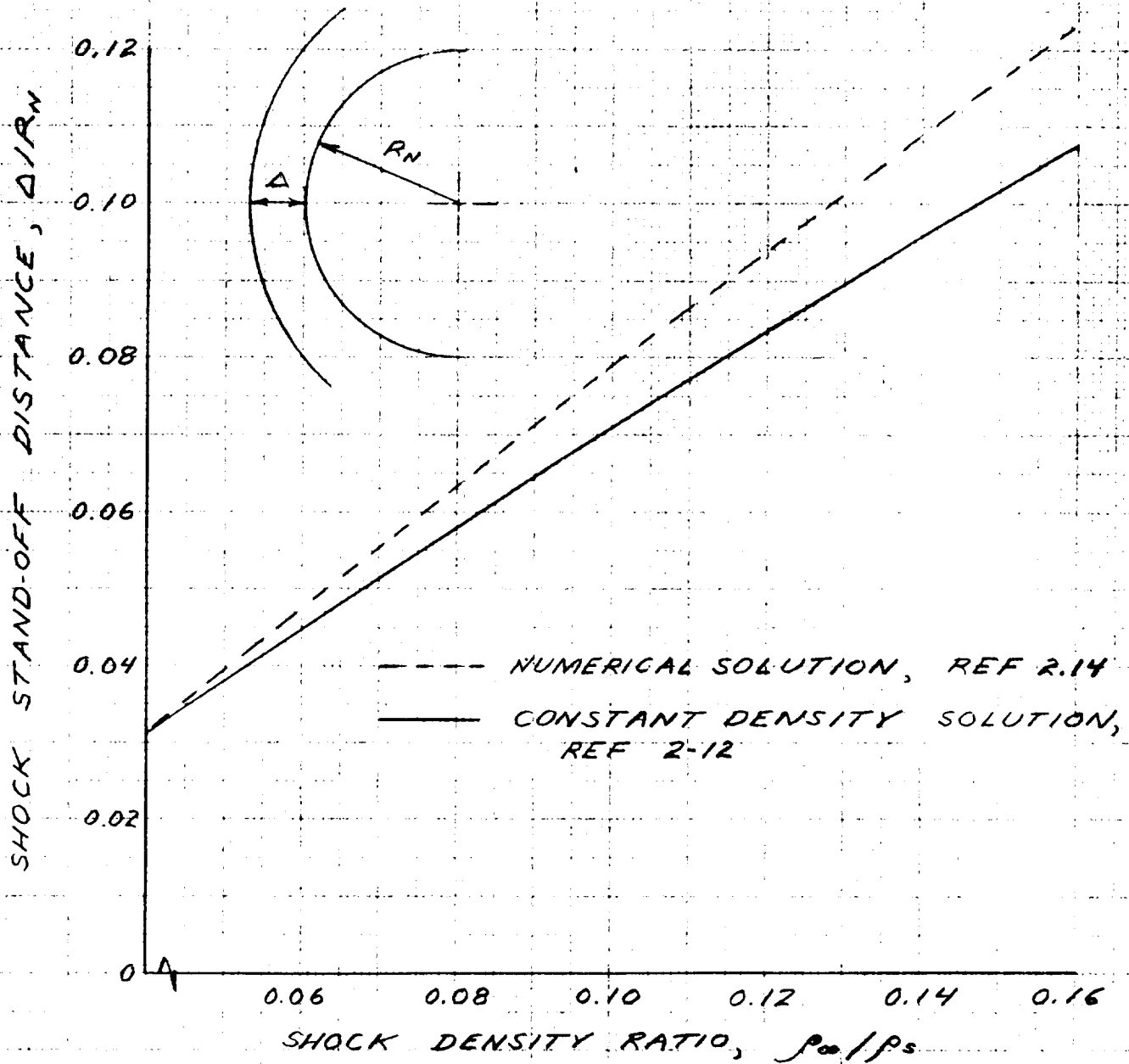


FIG 2-4

CHEMICAL HISTORY FOR NON-EQUILIBRIUM FLOW  
 ALTITUDE 200,000 FT, VELOCITY 30,000 FT/SEC

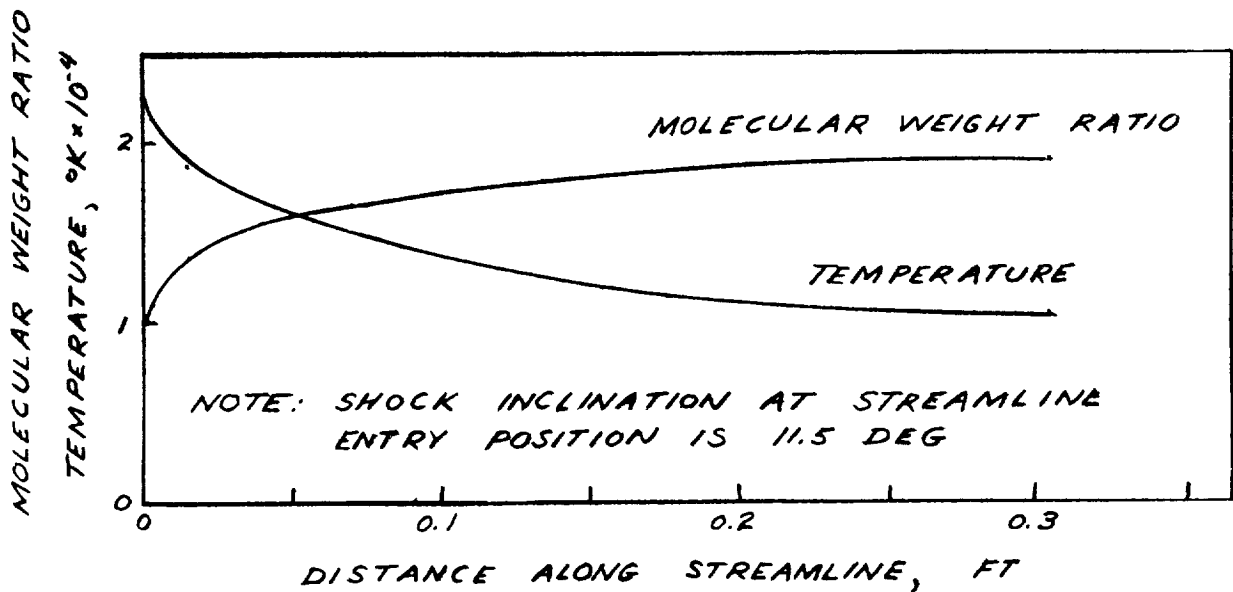
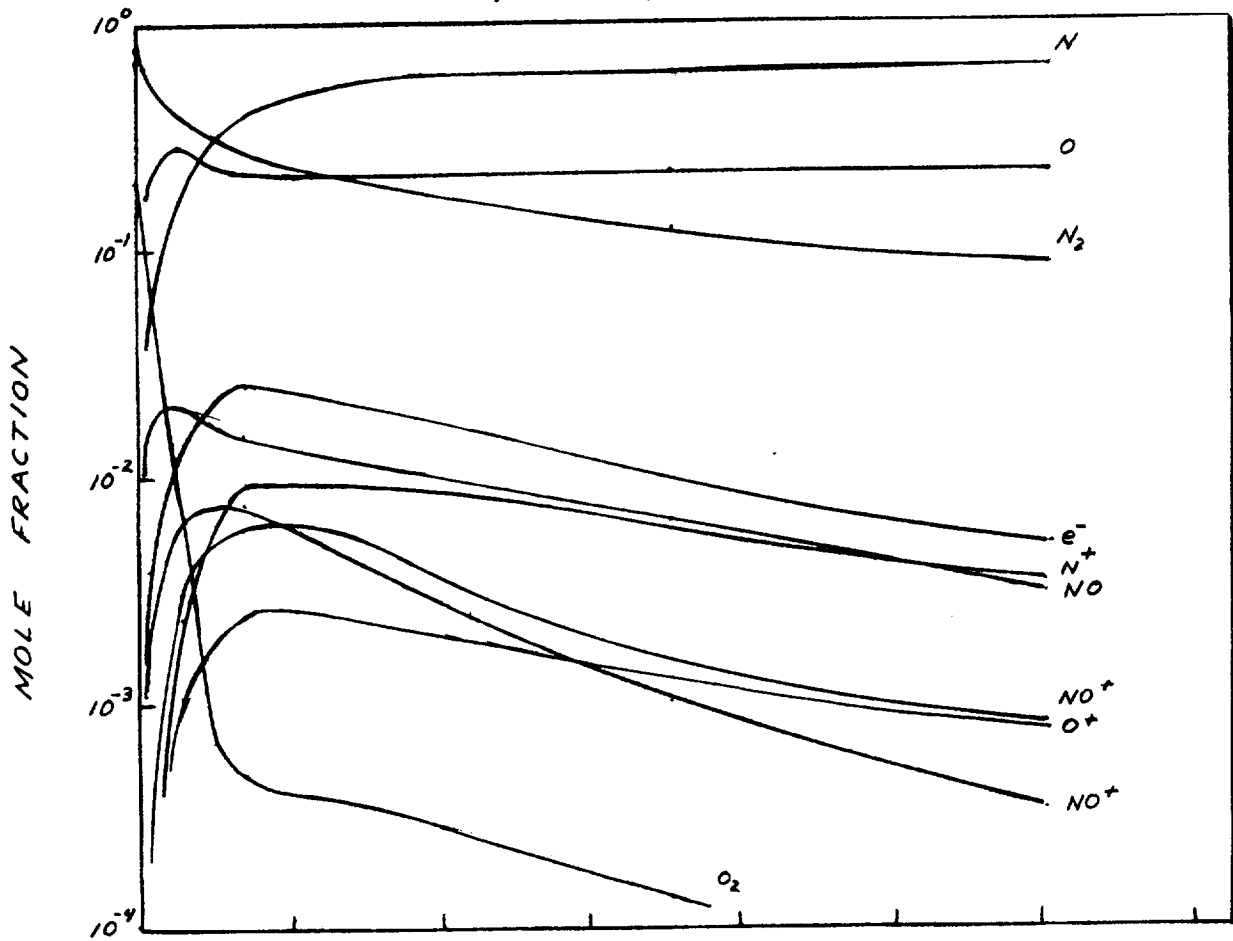


FIGURE 2-5  
VARIATION OF NON-EQUILIBRIUM ZONE  
THICKNESS WITH ALTITUDE

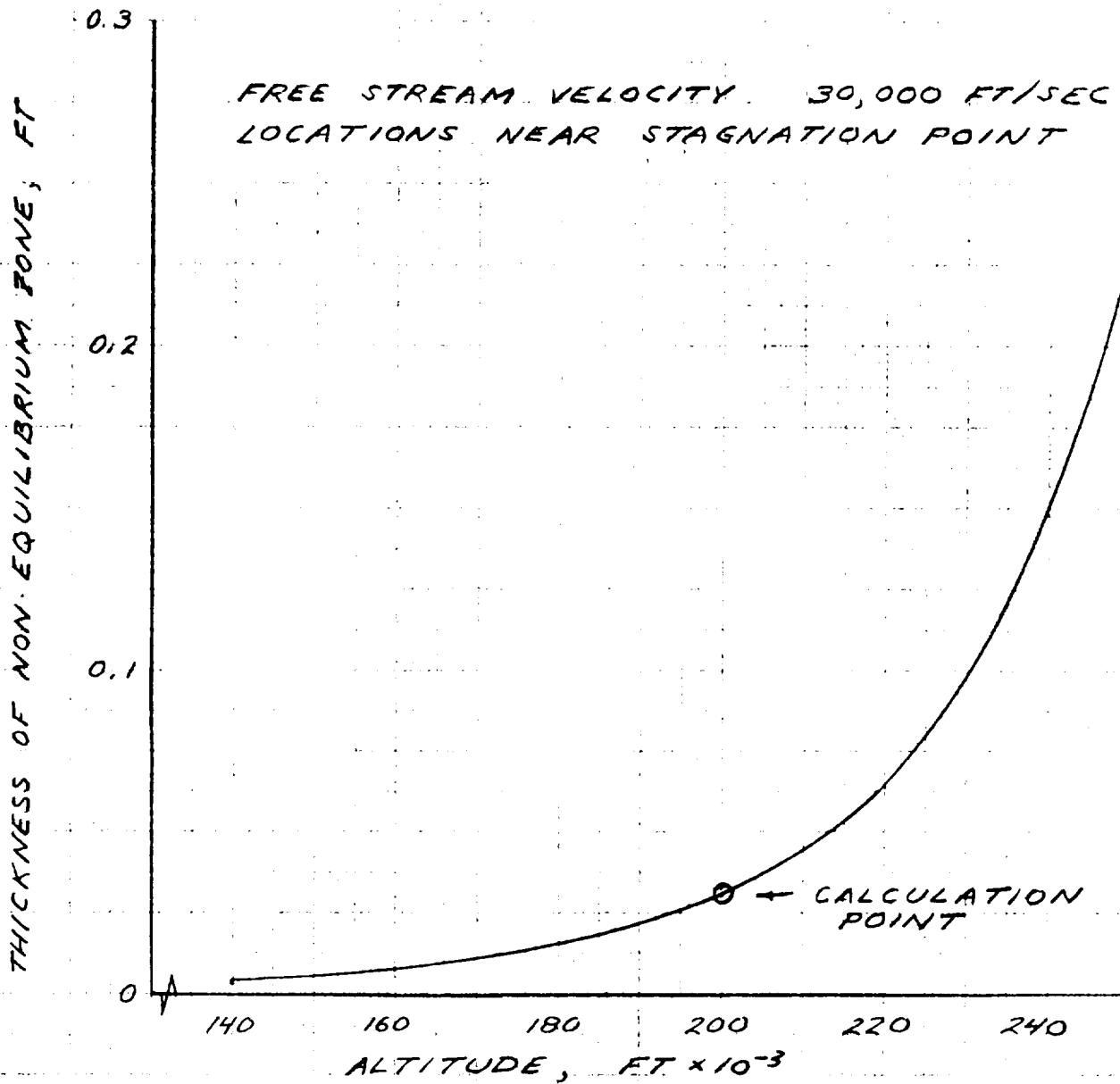


FIG. 2-6  
BOUNDARY-LAYER DISPLACEMENT THICKNESS  
TRAJECTORY III, GEOMETRIC CENTER

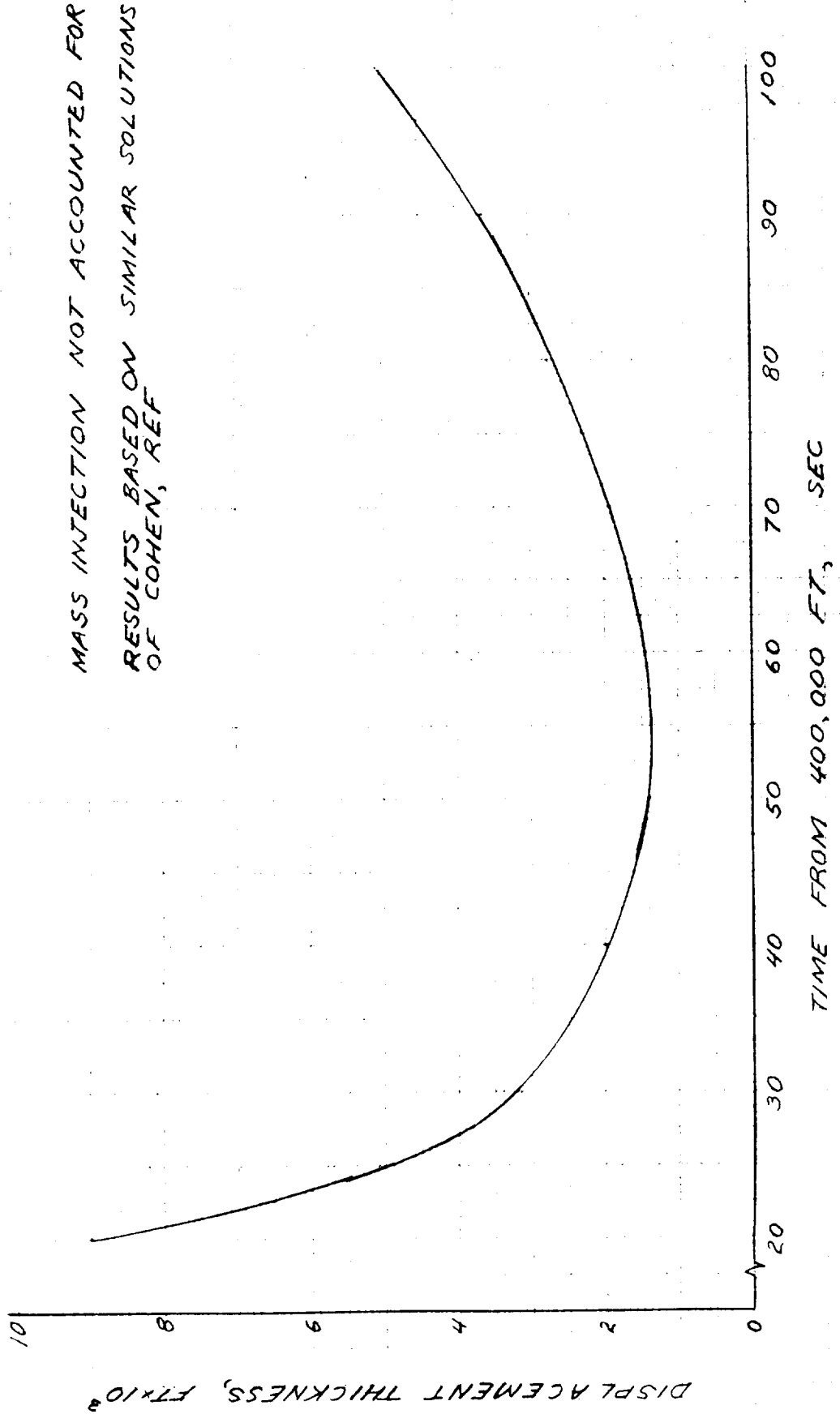
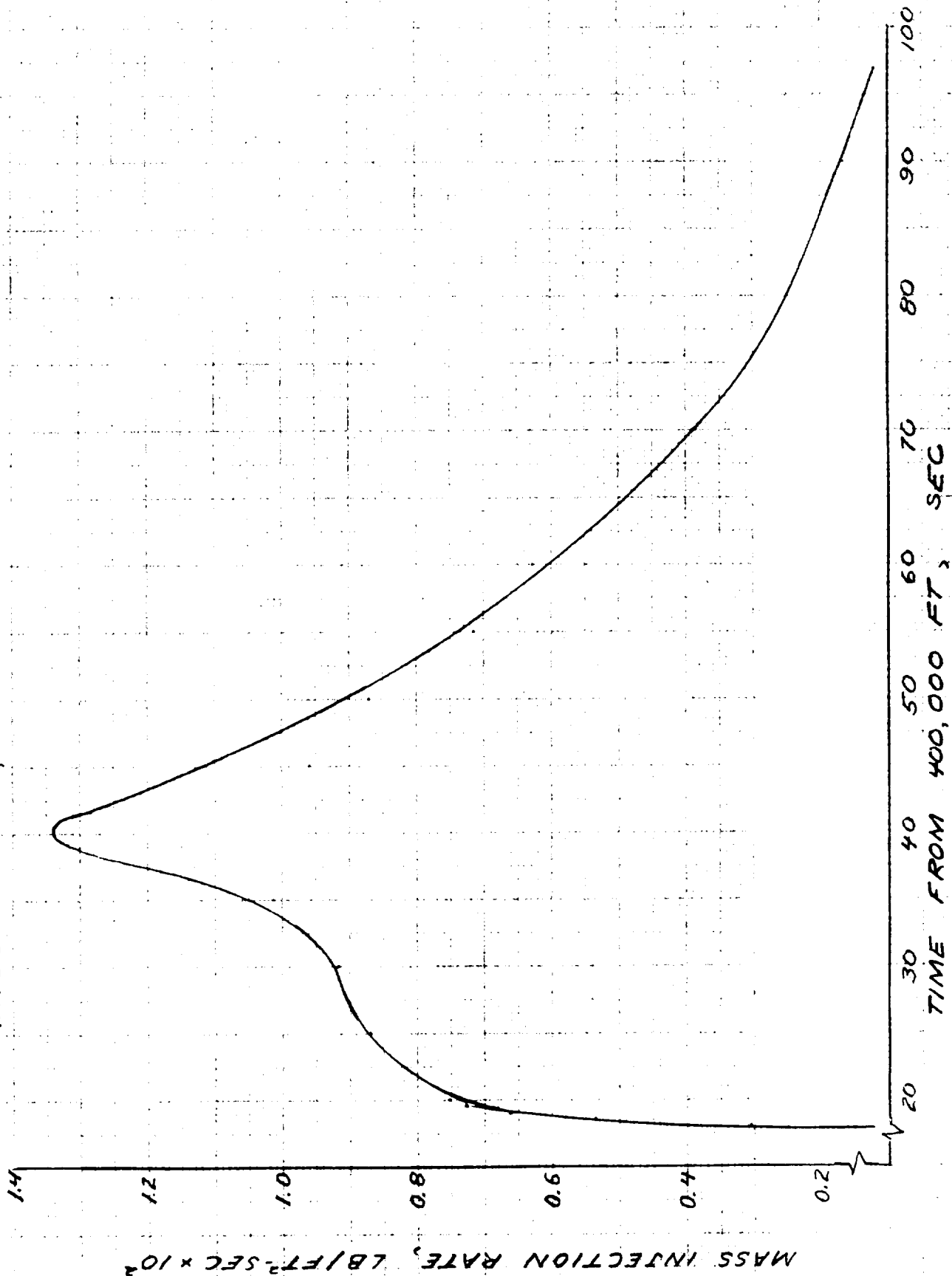


FIGURE 2-7 ABLATION HISTORY OF HEAT SHIELD  
TRAJECTORY III, GEOMETRIC CENTER



ENGINE 208  
 MASS INJECTION PARAMETER HISTORY  
 TRANSDUCER, GEOMETRIC CENTER

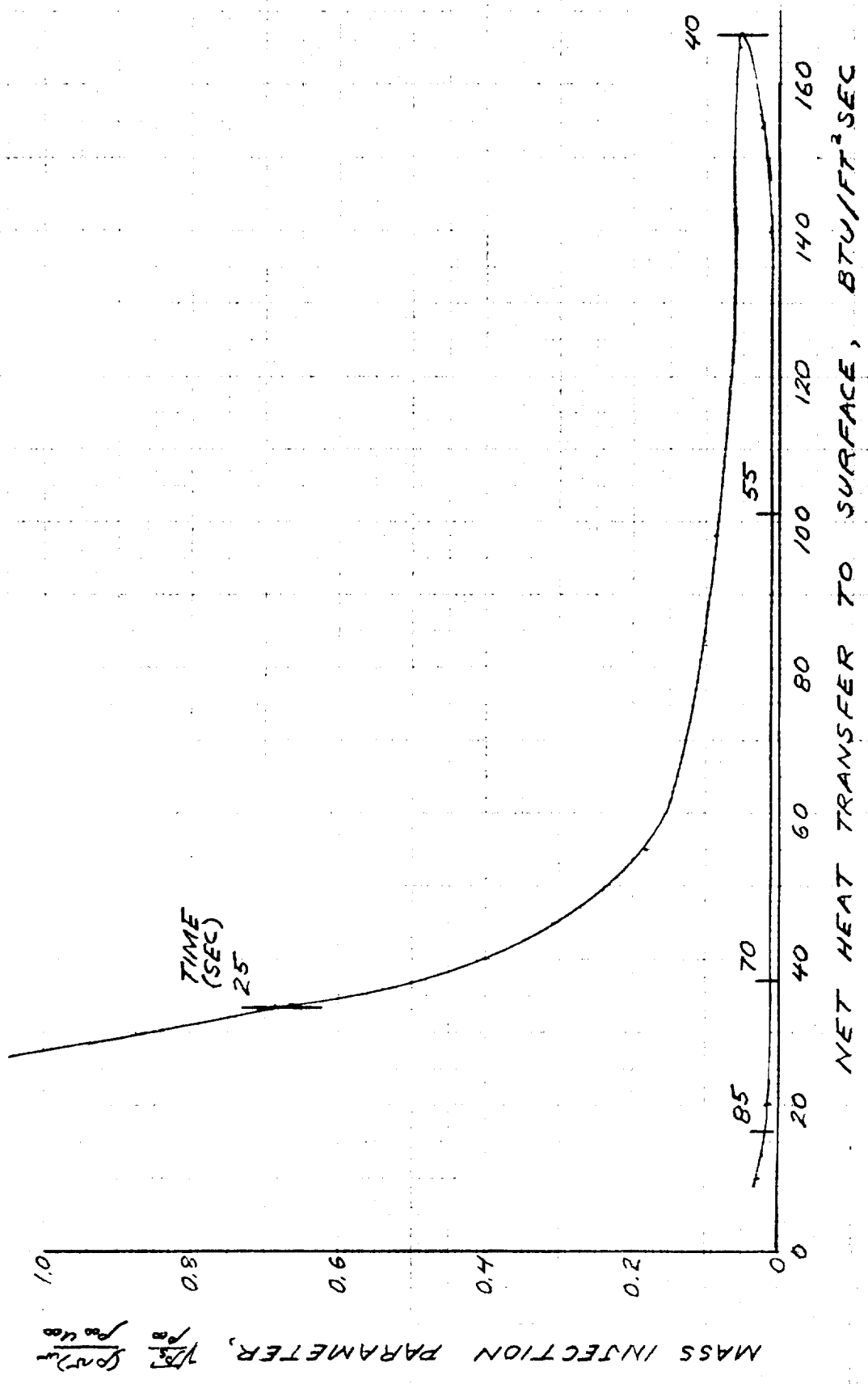
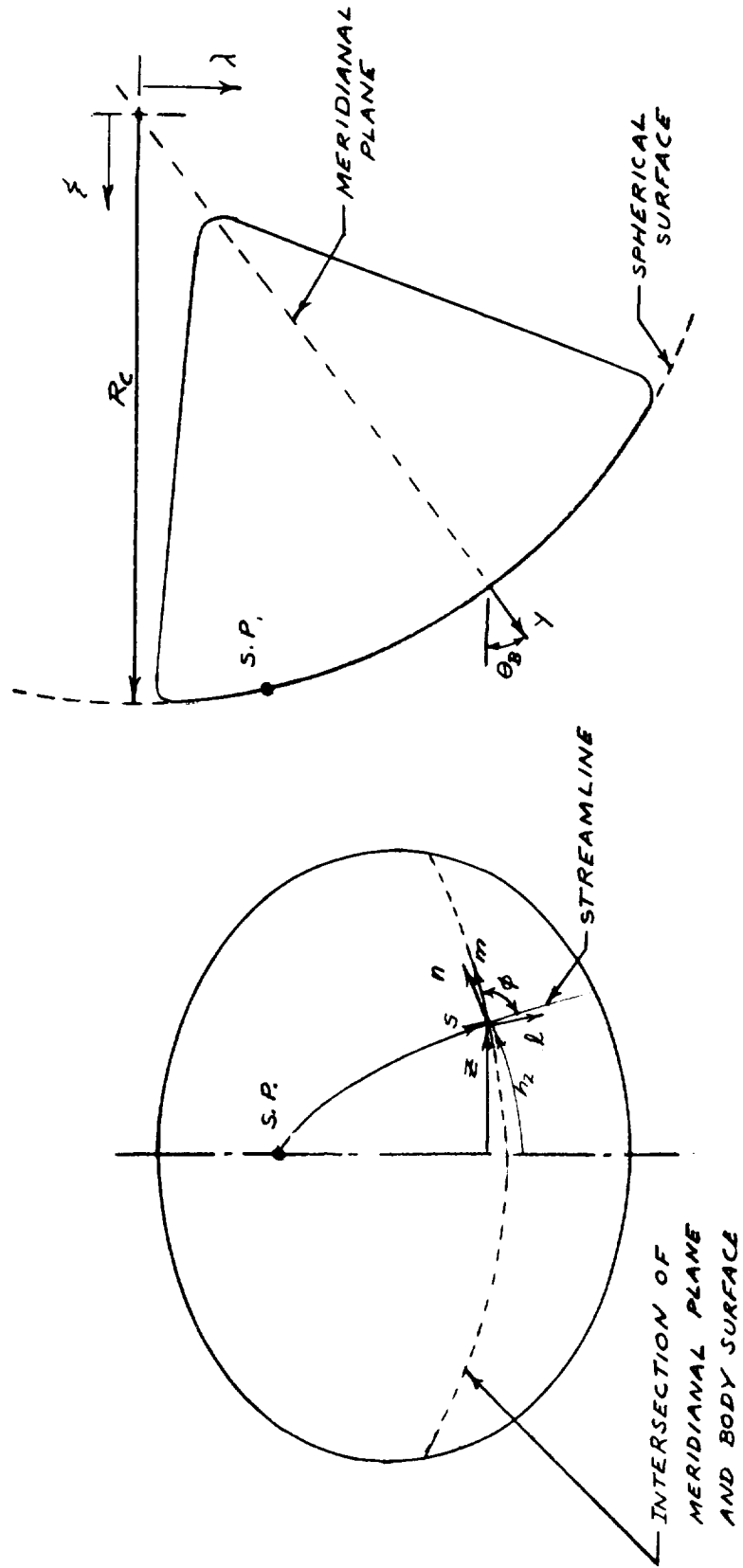
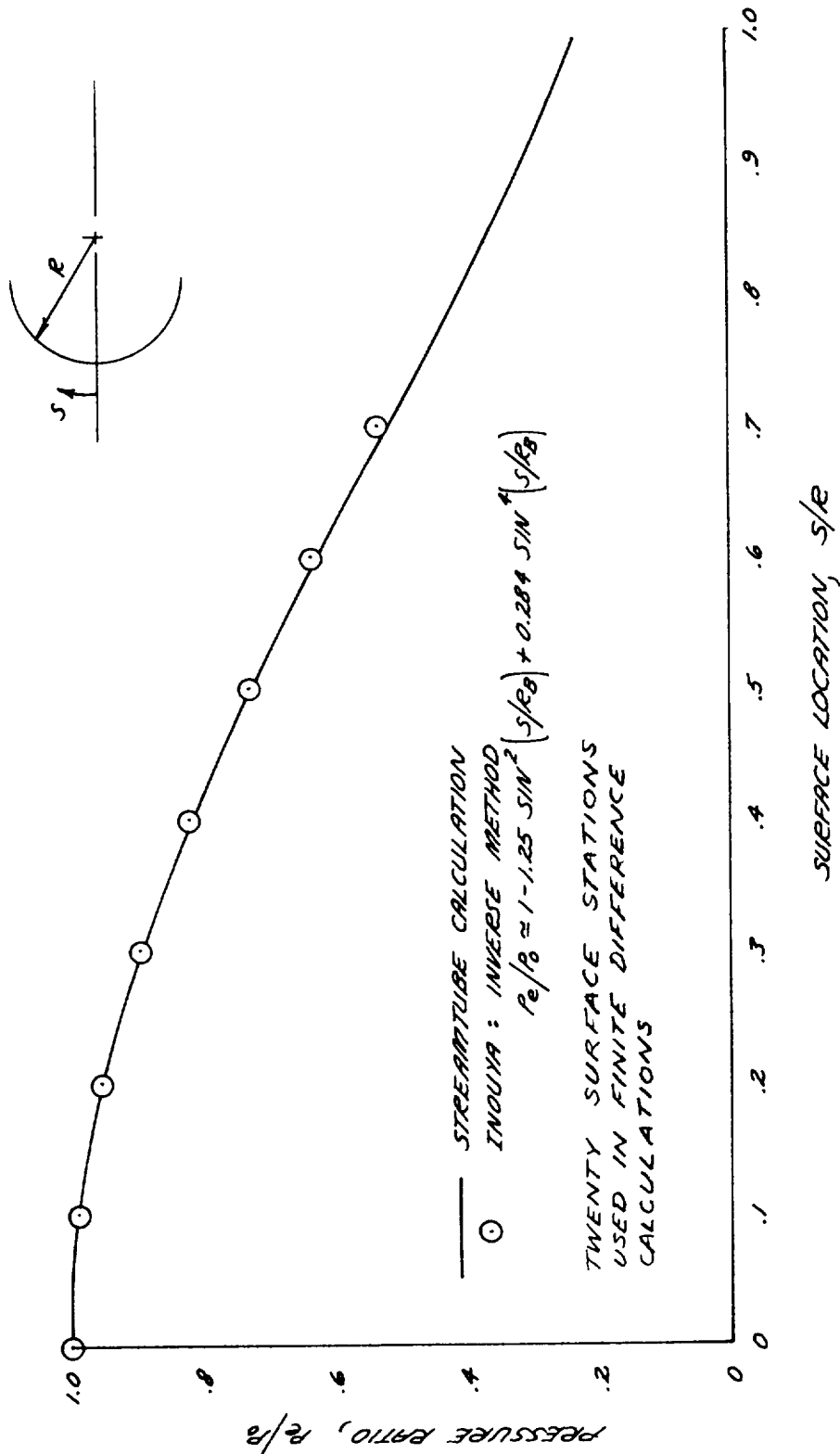


FIG 2-9  
 GEOMETRY FOR SPREADING COORDINATE CALCULATION



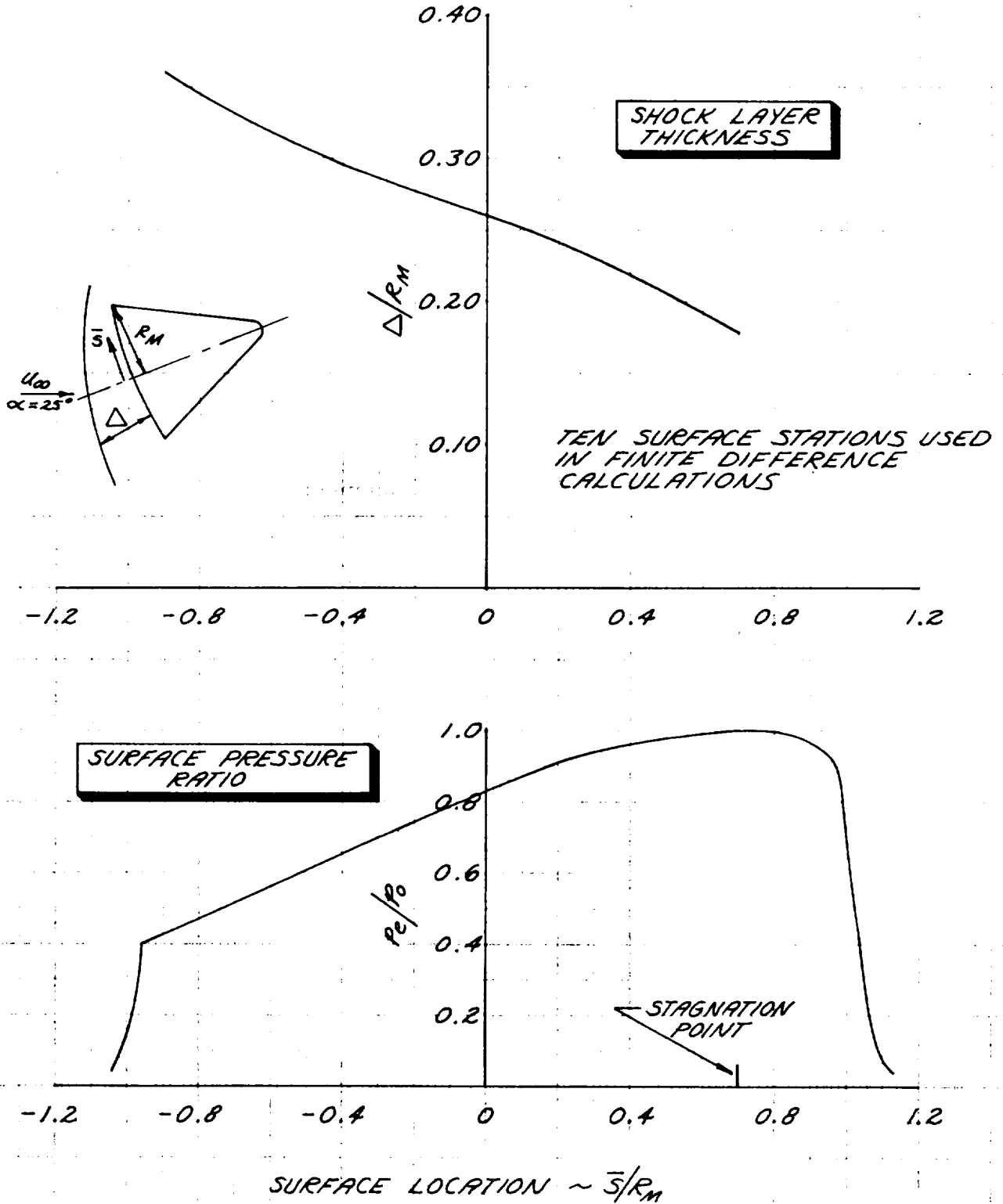
Prepared	NAME <i>[Signature]</i>	DATE	LOCKHEED MISSILES & SPACE COMPANY A GROUP DIVISION OF LOCKHEED AIRCRAFT CORPORATION	Page	TEMP	PERM
Checked			TITLE	Model		
Approved				Report No.		

FIGURE 2-10  
COMPARISON OF SURFACE PRESSURE DISTRIBUTION PREDICTIONS  
FOR A HEMISPHERE





**FIGURE 2-11**  
**SHOCK LAYER THICKNESS AND SURFACE**  
**PRESSURE DISTRIBUTION FOR APOLLO,**  
**IDEAL GAS FLOW**



**FIGURE 2-12**  
**SHOCK LAYER CHARACTERISTICS FOR**  
**A SPHERICALLY-BLUNTED BODY**  
**AT 20 DEG ANGLE OF ATTACK**

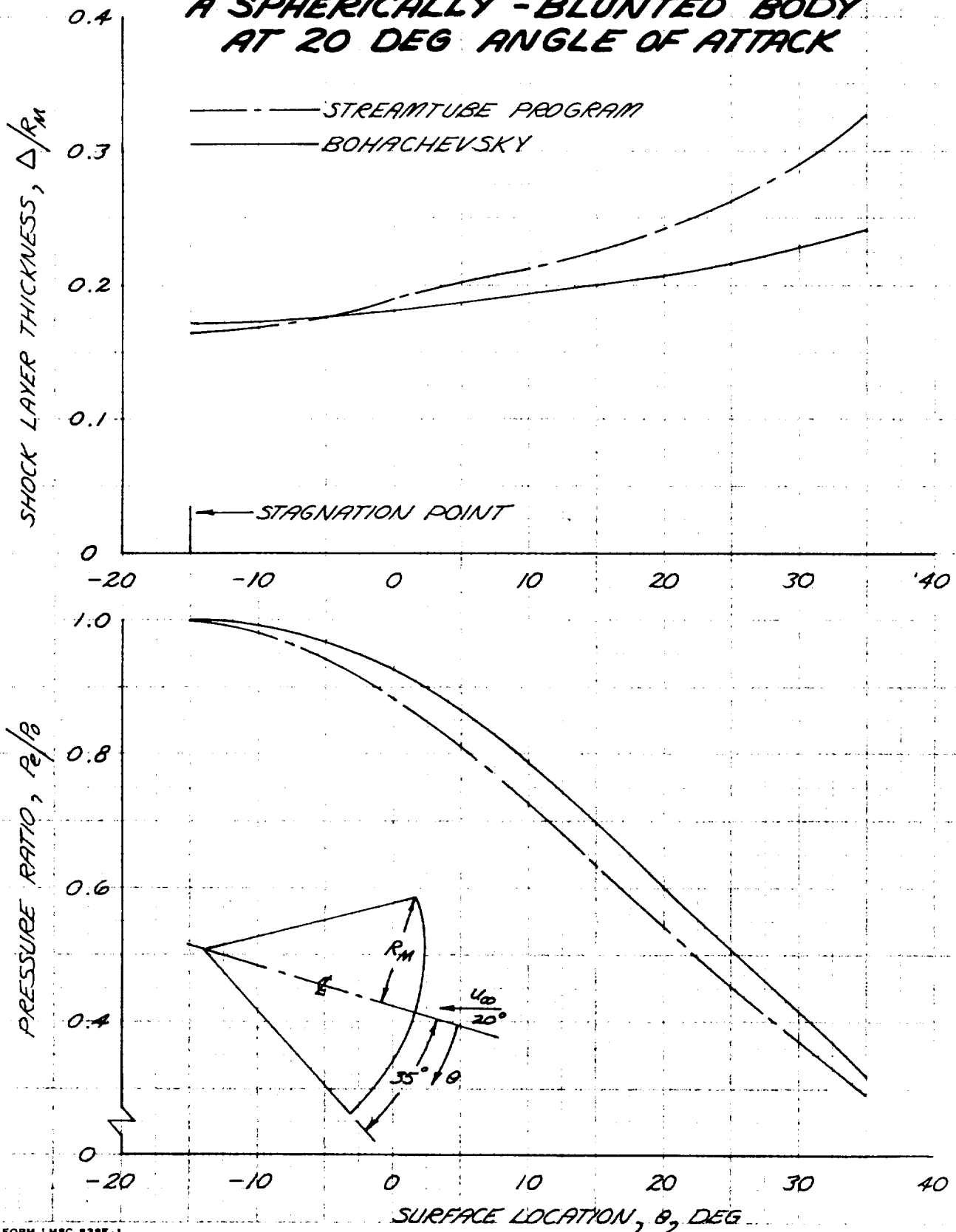
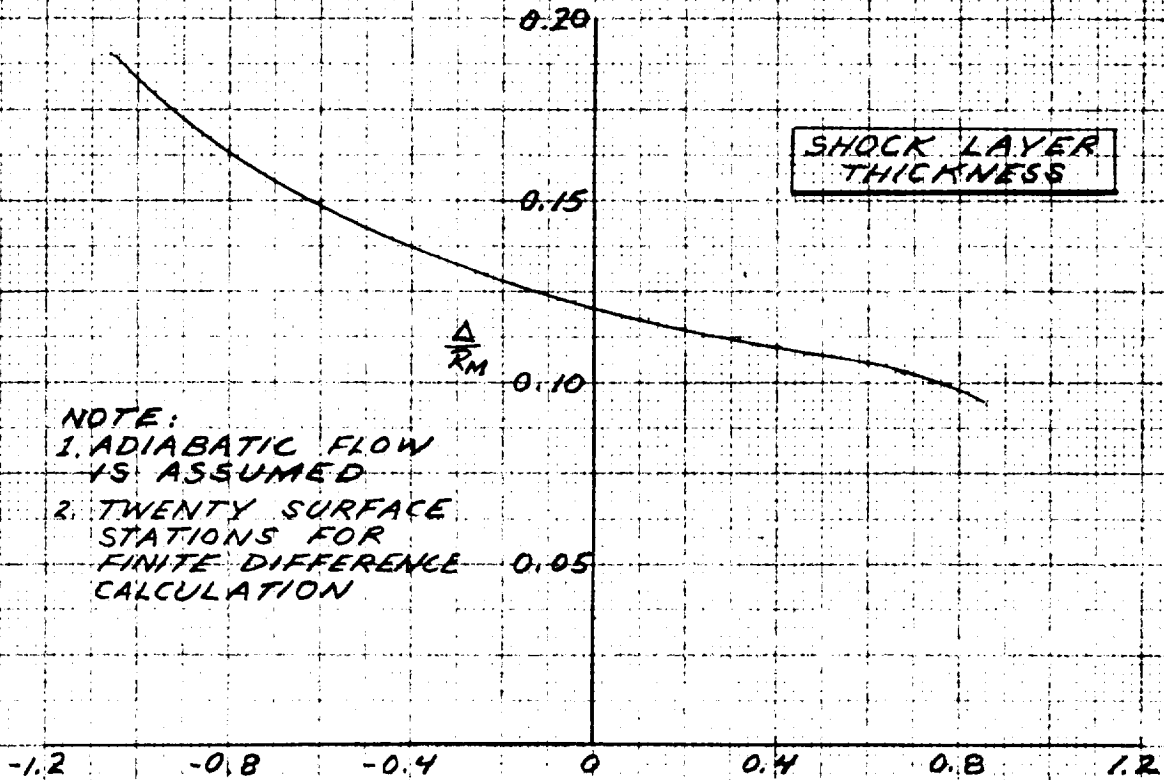


FIGURE 2-13

PREDICTED SHOCK LAYER CONDITIONS  
FOR APOLLO  
VELOCITY 35,000 FT/SEC, ALTITUDE 200,000 FT



NOTE:  
1. ADIABATIC FLOW IS ASSUMED  
2. TWENTY SURFACE STATIONS FOR FINITE DIFFERENCE CALCULATION

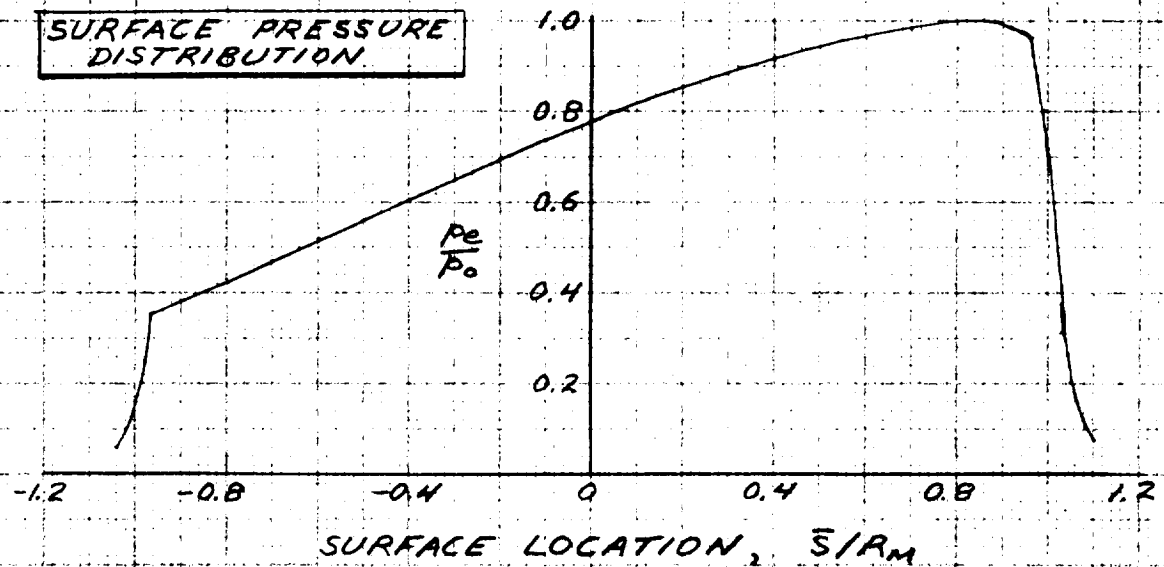


FIG. 2-14 SHOCK CONFIGURATION IN PLANE OF SYMMETRY

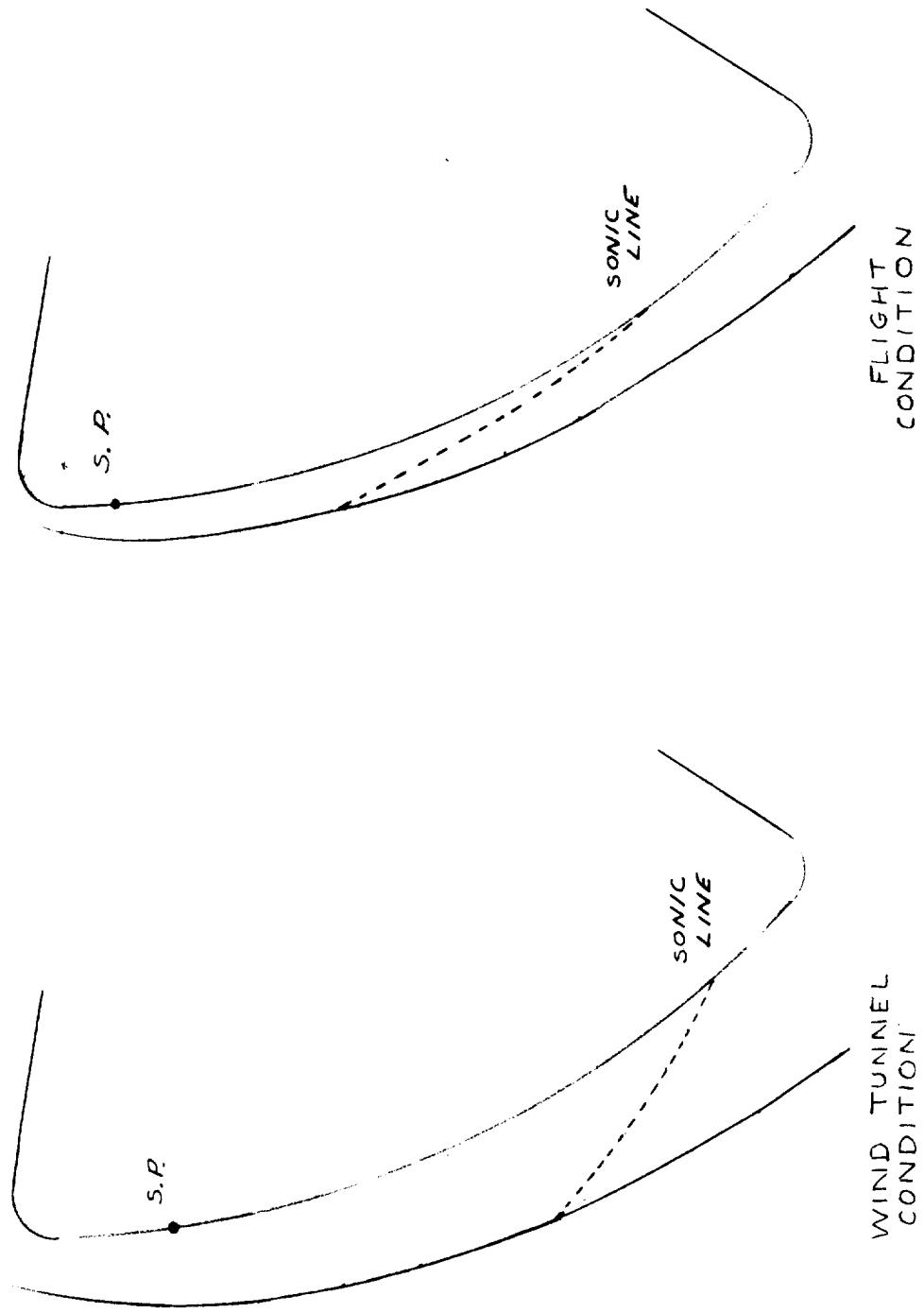


FIGURE 2-15  
INFLUENCE OF FLIGHT CONDITION ON SHOCK LAYER FLOW PROFILES  
GEOMETRIC CENTER OF APOLLO

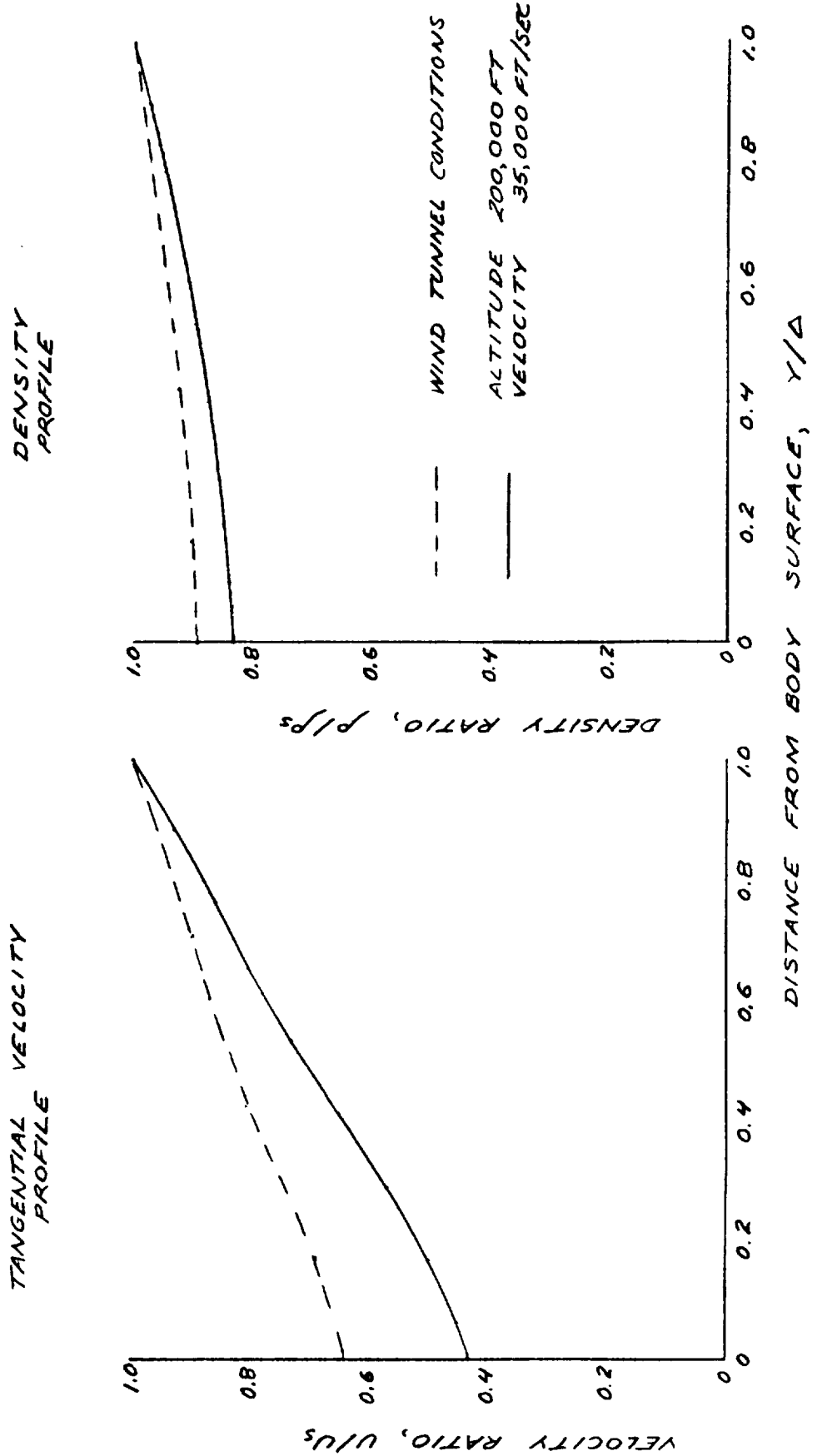


FIGURE 2-16  
 SPREADING COORDINATE FOR APOLLO  
 25 DEG ANGLE OF ATTACK

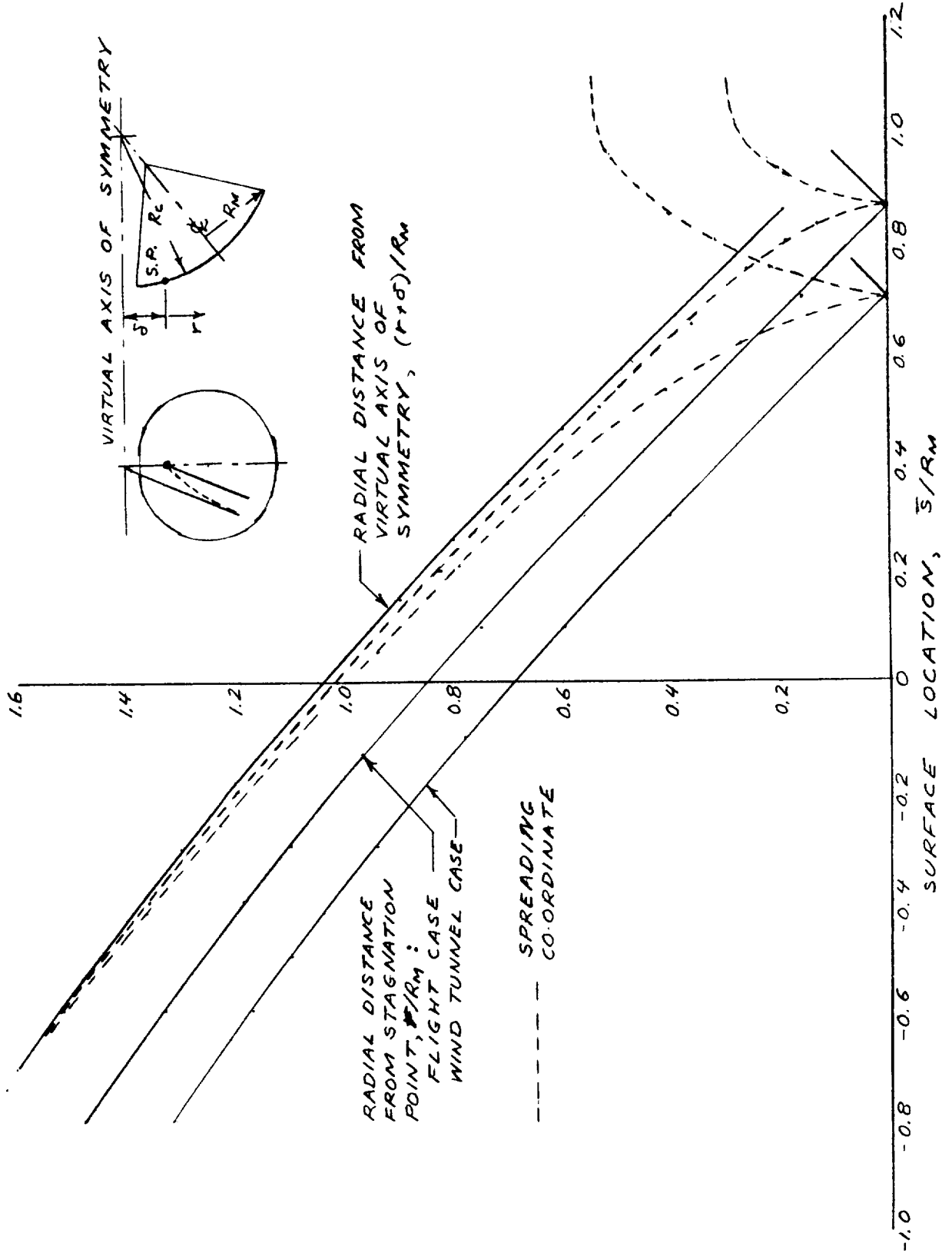
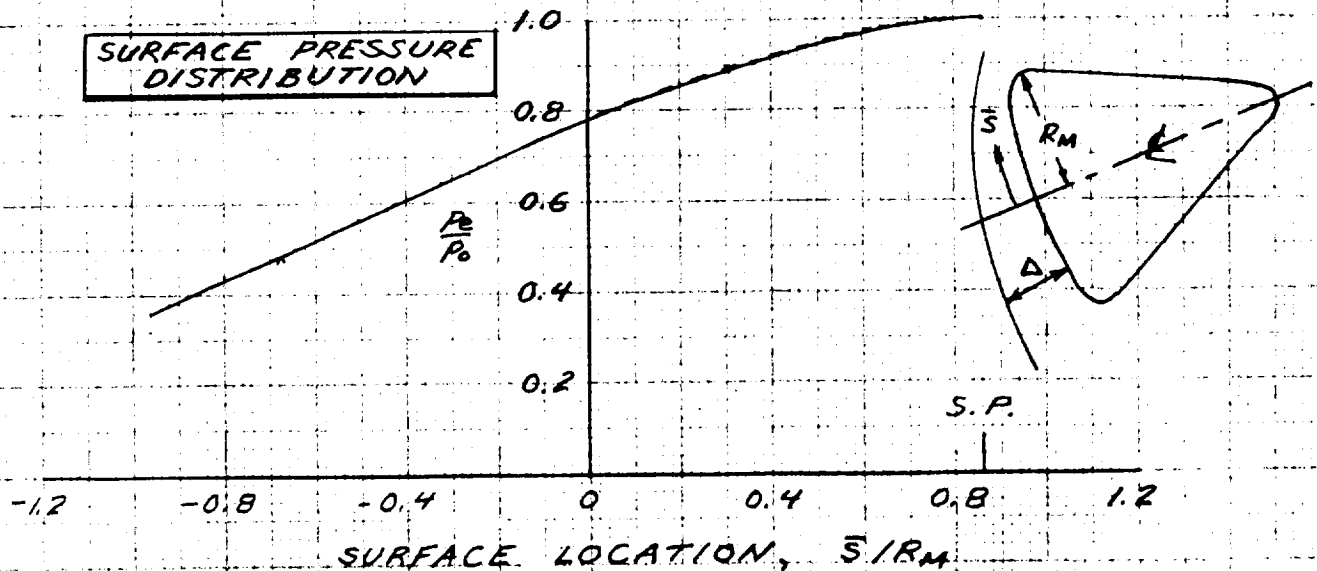
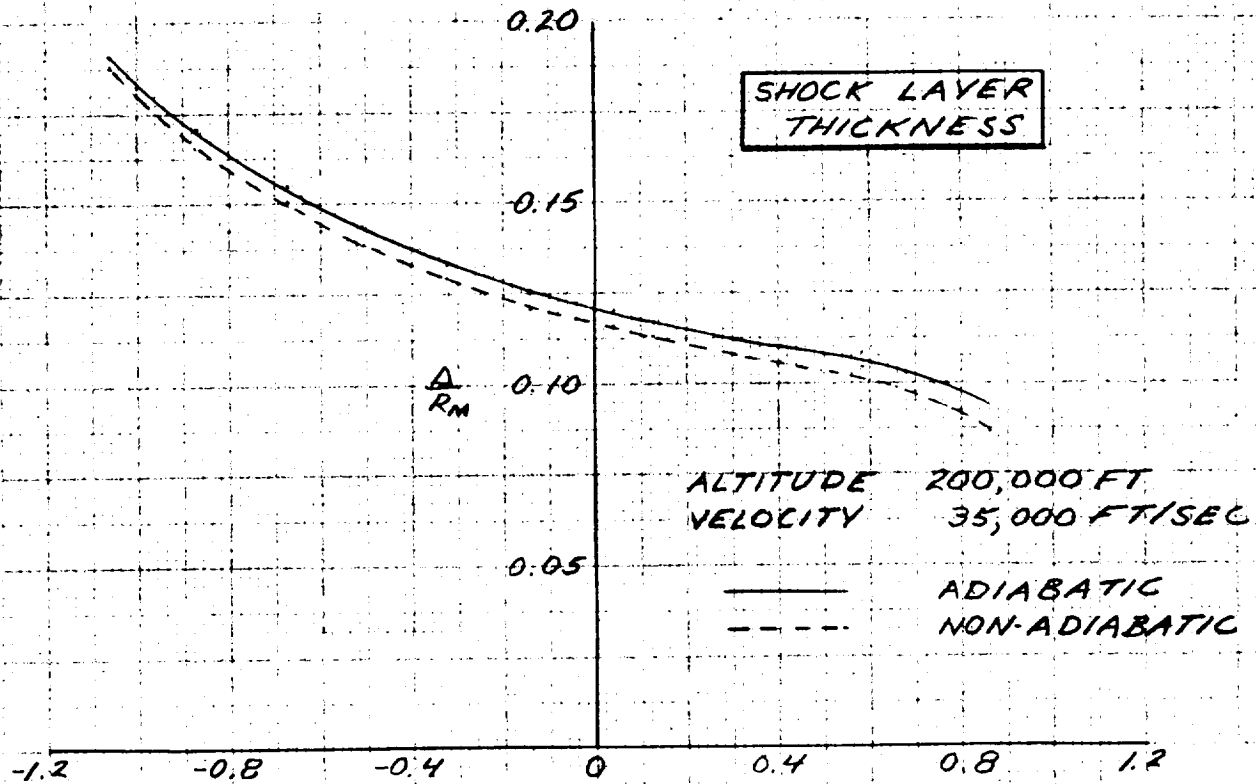
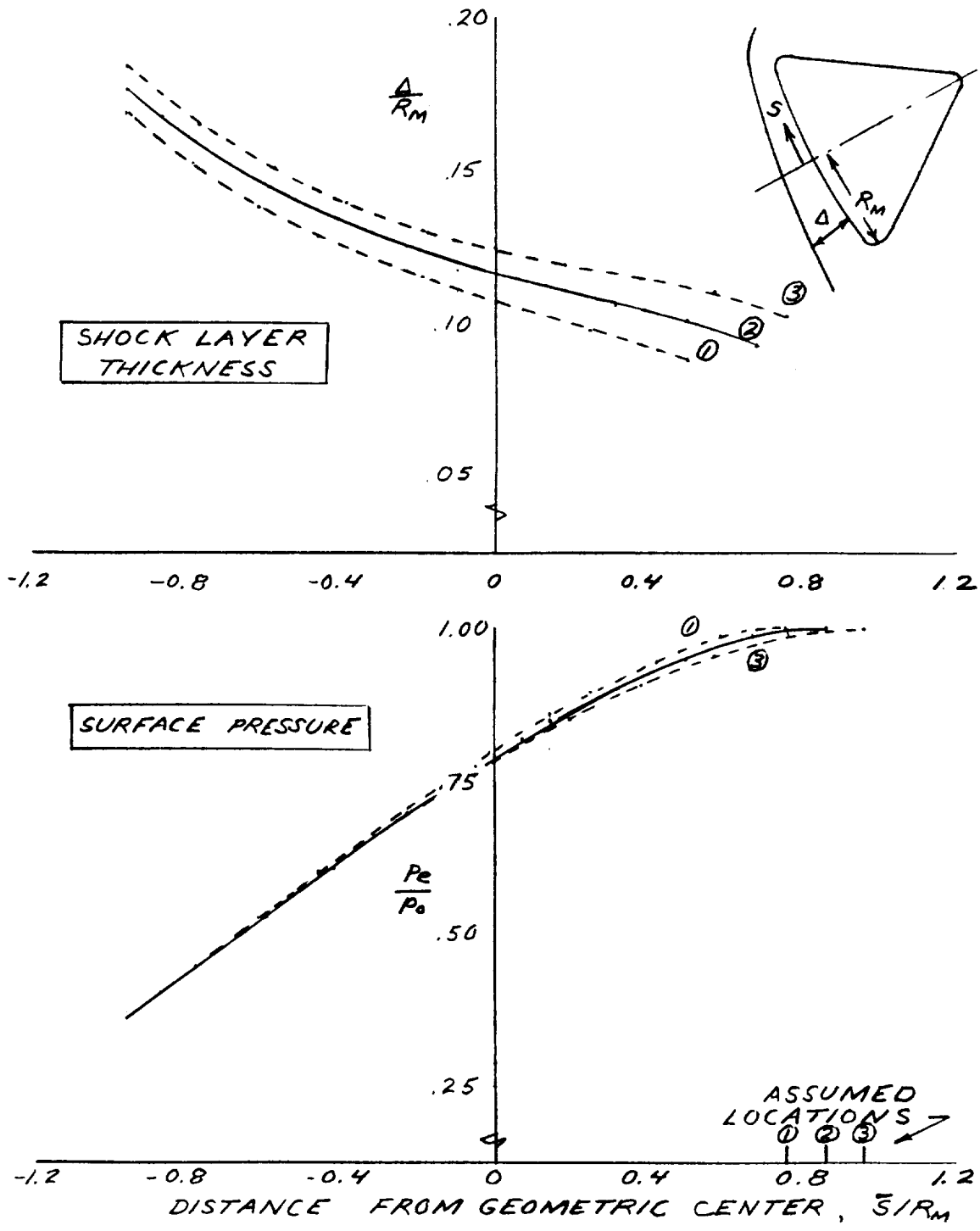


FIGURE 2-17  
 INFLUENCE OF ENERGY LOSSES  
 ON SHOCK LAYER CONDITIONS  
 APOLLO, 25 DEG ANGLE-OF-ATTACK



Prepared	NAME	DATE	LOCKHEED MISSILES & SPACE COMPANY A GROUP DIVISION OF LOCKHEED AIRCRAFT CORPORATION	Page	TEMP	PERM
Checked			TITLE FIGURE 2-19	Model		
Approved				Report No.		

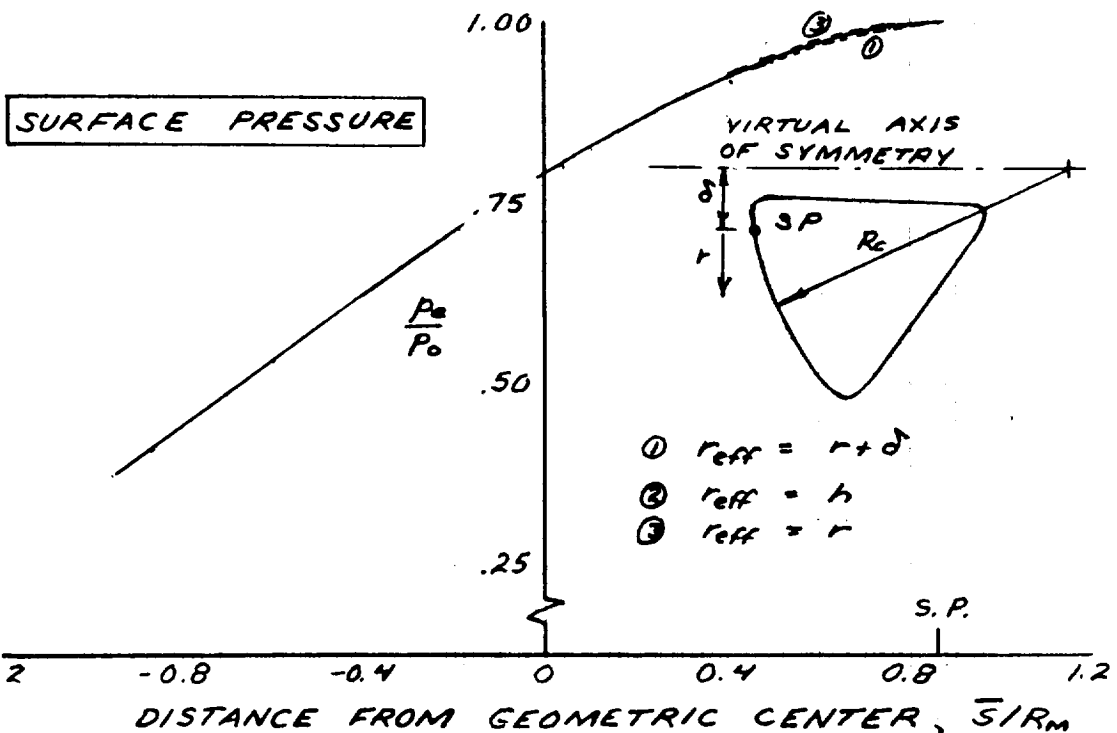
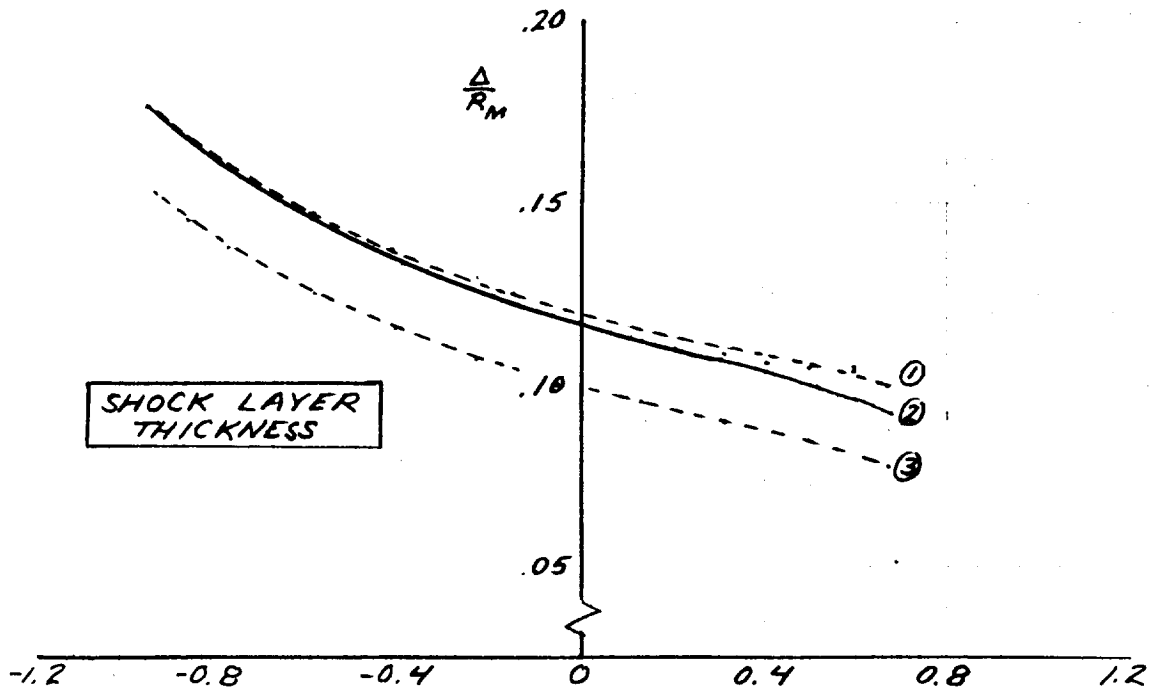
INFLUENCE OF UNCERTAINTY IN STAGNATION POINT LOCATION





Prepared	NAME	DATE	LOCKHEED MISSILES & SPACE COMPANY A GROUP DIVISION OF LOCKHEED AIRCRAFT CORPORATION	Page	TEMP	PERM
Checked			TITLE FIGURE 2-19	Model		
Approved				Report No.		

INFLUENCE OF SPREADING COORDINATE



MODEL

DATE

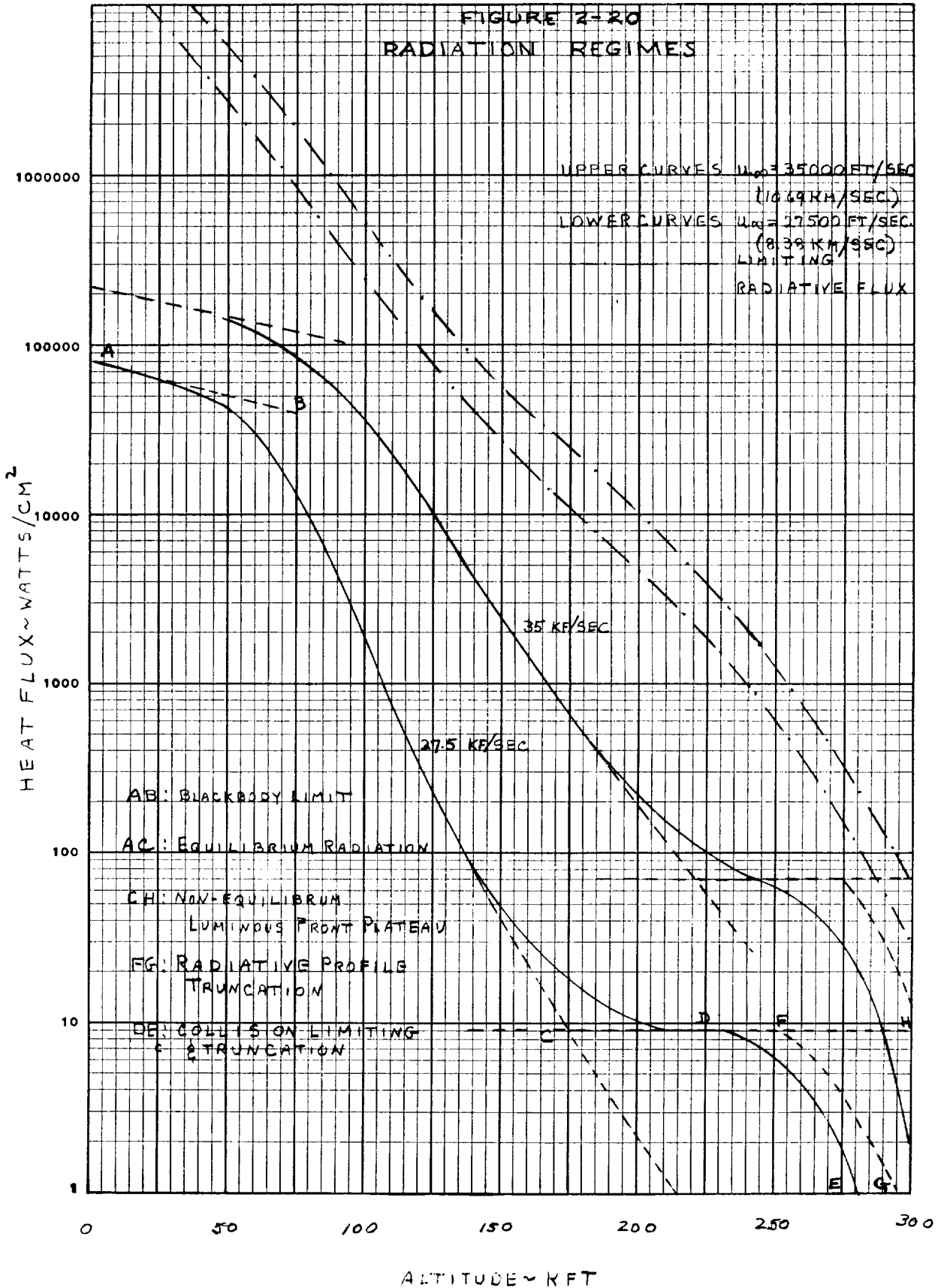


FIGURE 2-21

INFLUENCE OF RADIATIVE ENERGY LOSS  
ON SHOCK LAYER RADIATION

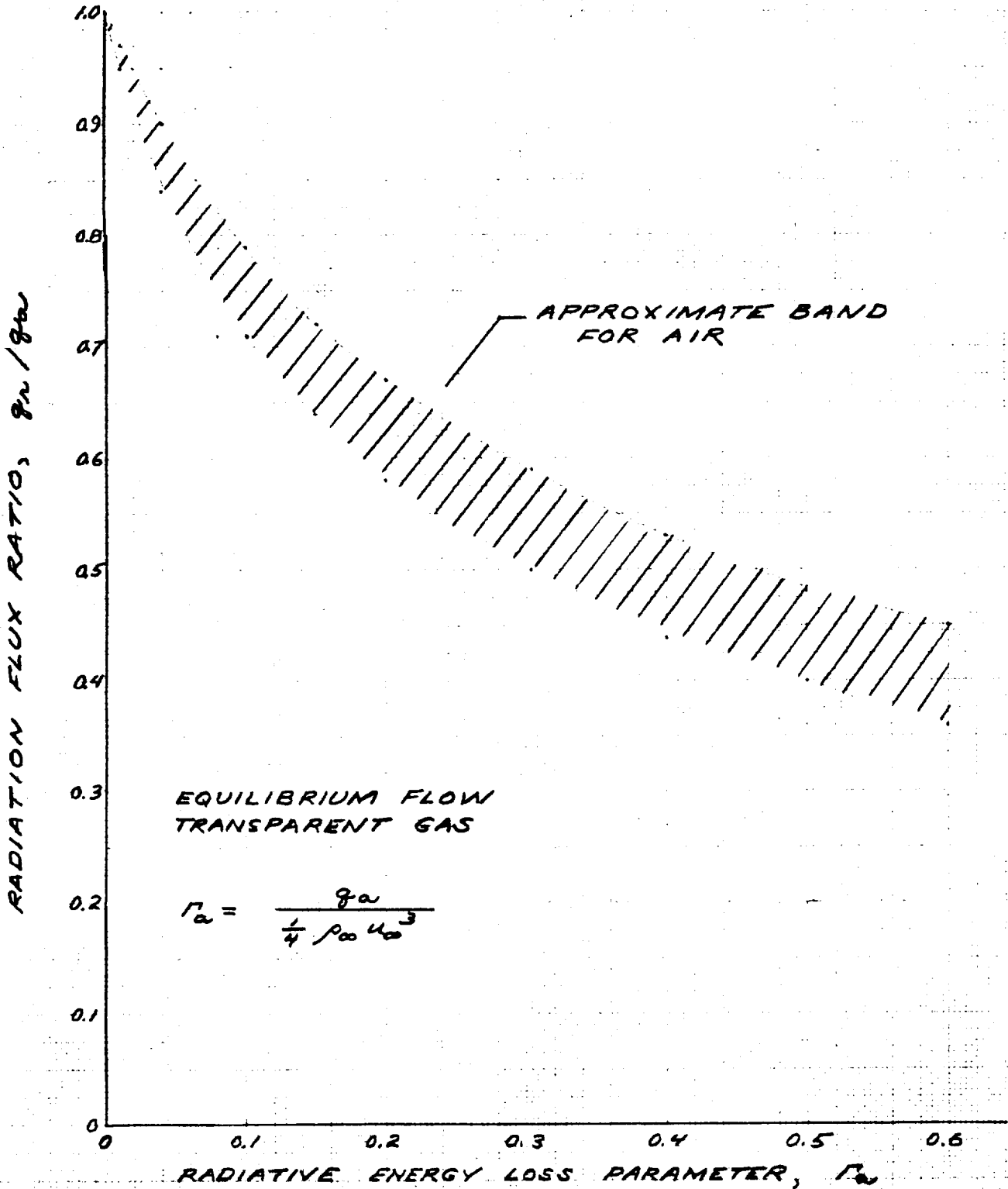
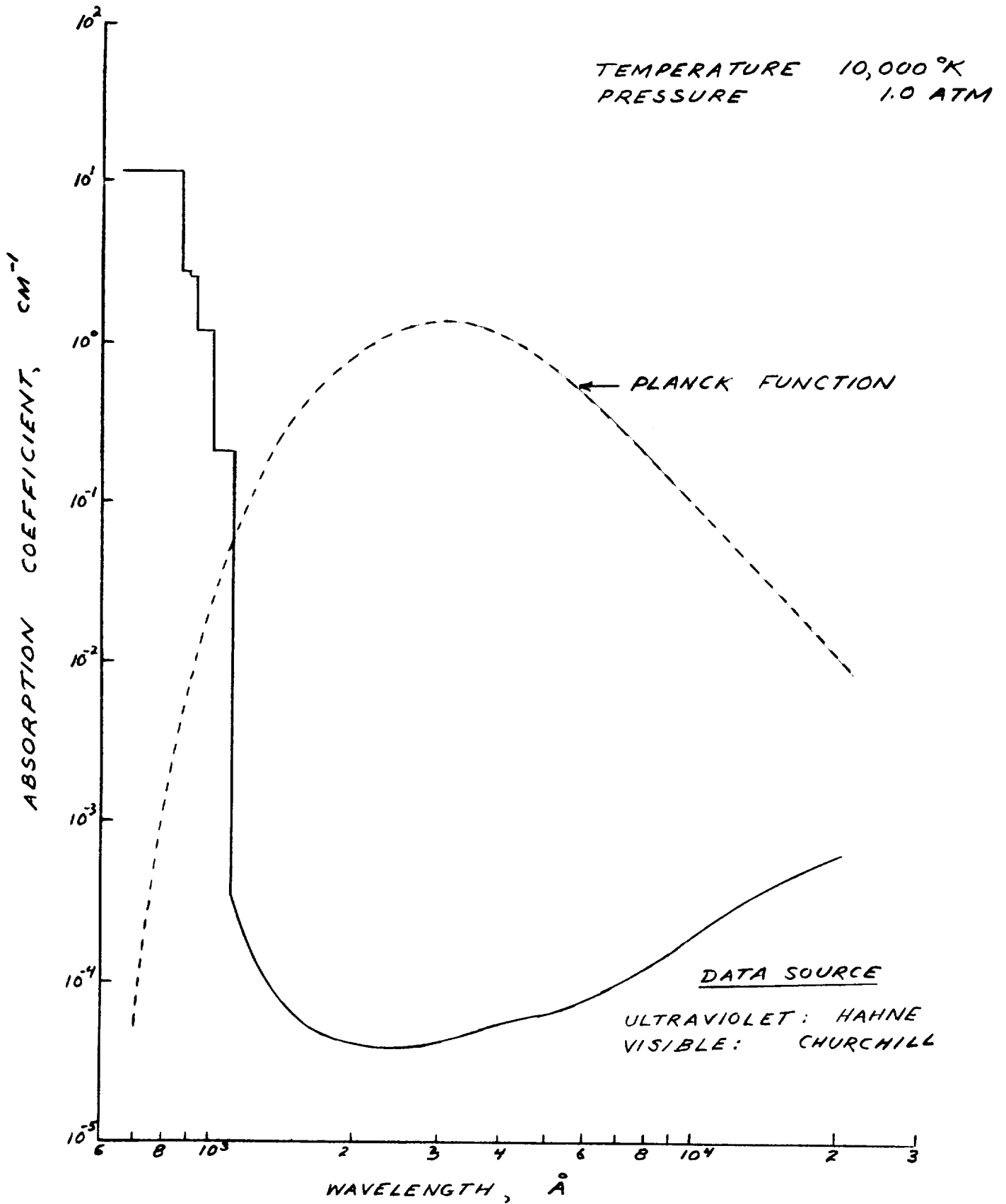


FIGURE 2-22  
ABSORPTION COEFFICIENT OF  
HEATED AIR



MODEL

DATE

FIGURE 2-23  
EQUILIBRIUM COMPOSITION OF  
BOUNDARY LAYER

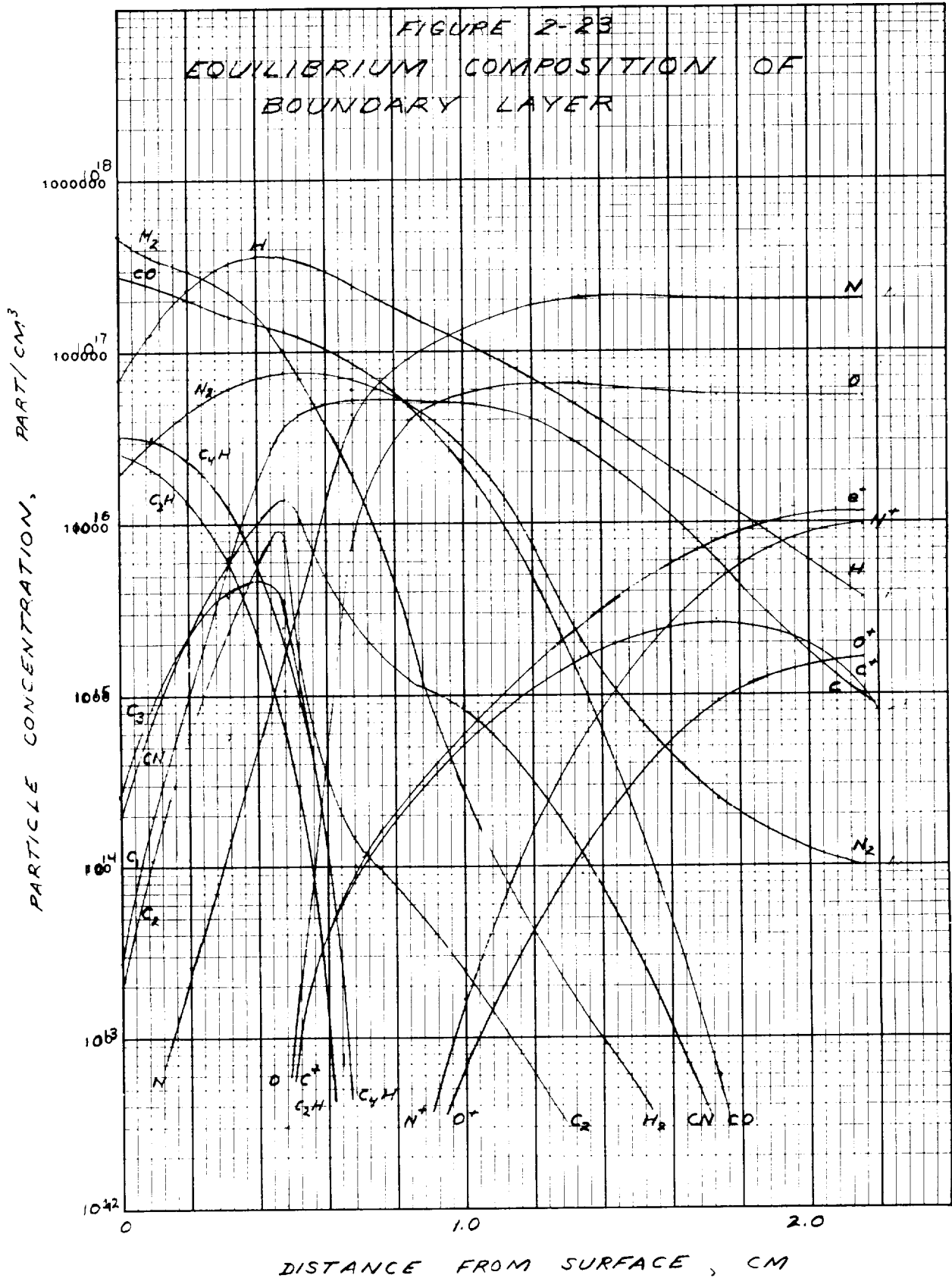


FIGURE 2-24

APOLLO BOUNDARY LAYER PROFILE WITH  
 INJECTION OF ABLATION PRODUCTS

GEOMETRIC CENTER LOCATION  
 TRAJECTORY III, TIME 40 SEC

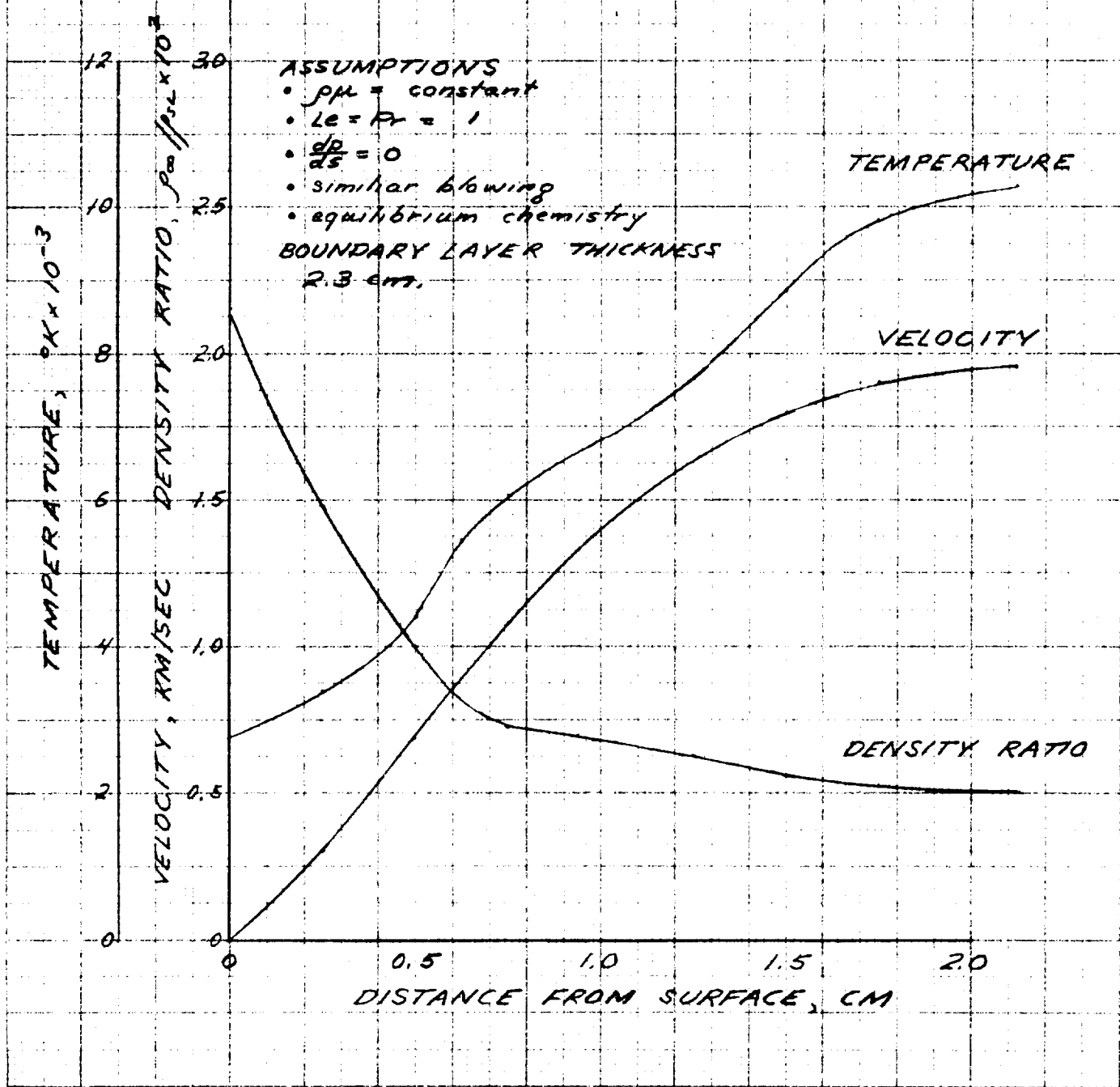
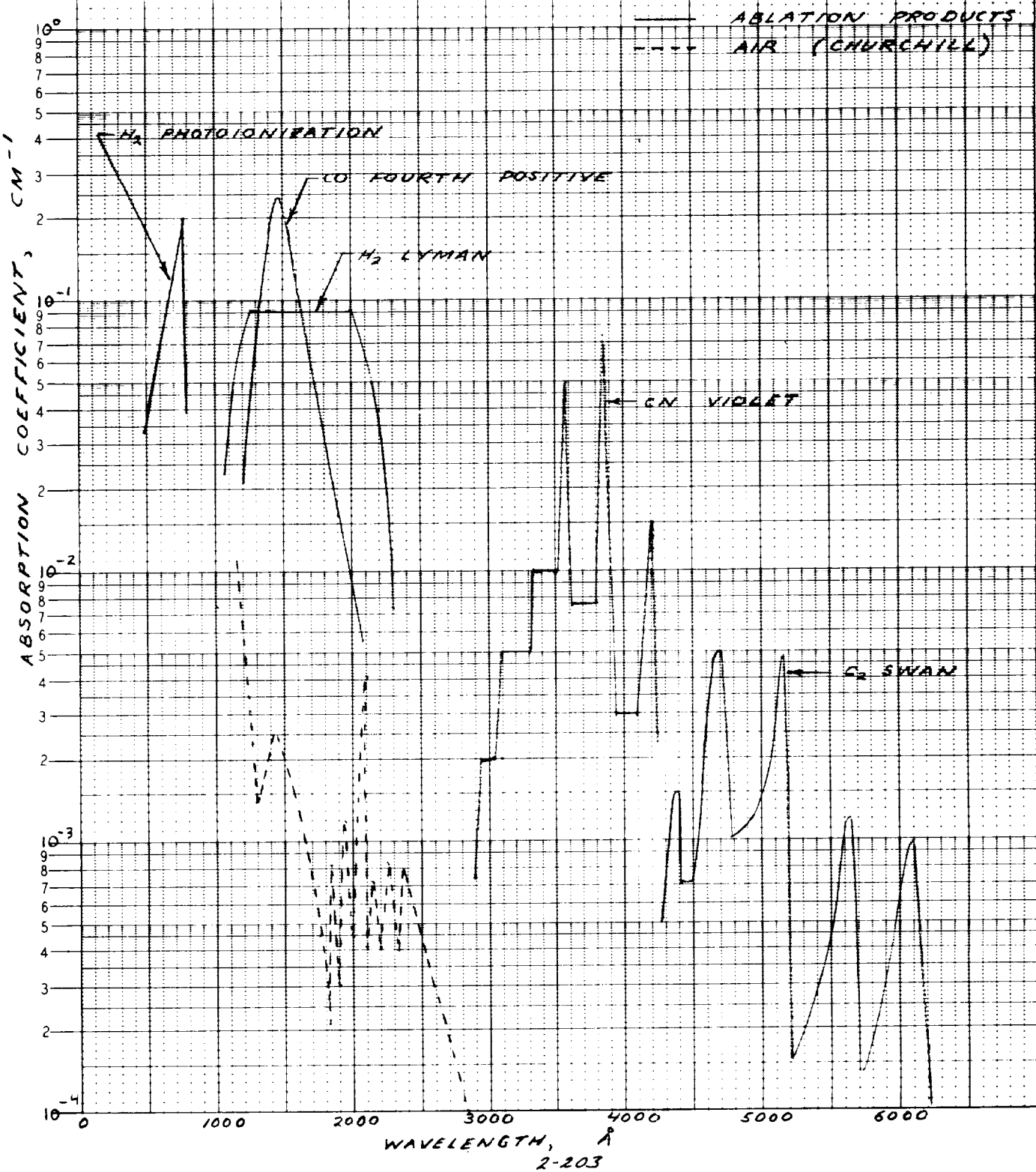


FIGURE 2-25  
ABSORPTION COEFFICIENT FOR THE  
CONTAMINATED BOUNDARY LAYER

LOCATION,  $y = 0.6$  CM.  
TEMPERATURE, 5000°K  
PRESSURE, 0.39 ATM



10<sup>5</sup>

FIGURE 2-26  
STAGNATION POINT HEAT FLUX

STAGNATION HEAT FLUX, WATTS/CM<sup>2</sup>

10<sup>4</sup>

10<sup>3</sup>

ADIABATIC  
TRANSPARENT

ADIABATIC  
ABSORBING

NONADIABATIC  
ABSORBING

ADIAB TRANS	ADIAB ABS	NONAD ABS
----------------	--------------	--------------

$u_{\infty} = 15.24 \text{ KM/SEC}$   
 $\rho_{\infty} / \rho_{SL} = 1.8 \times 10^{-4}$

TWO BAND	—	—	—
SIX BAND	↗	↗	↗

$u_{\infty} = 16.78 \text{ KM/SEC}$   
 $\rho_{\infty} / \rho_{SL} = 1.8 \times 10^{-4}$

▲	▲	■
---	---	---

$u_{\infty} = 19.8 \text{ KM/SEC}$   
 $\rho_{\infty} / \rho_{SL} = 8.1 \times 10^{-5}$

△	△	□
---	---	---

10<sup>2</sup>

40                      80                      120                      160                      200                      240

NOSE RADIUS, CM  
2-204



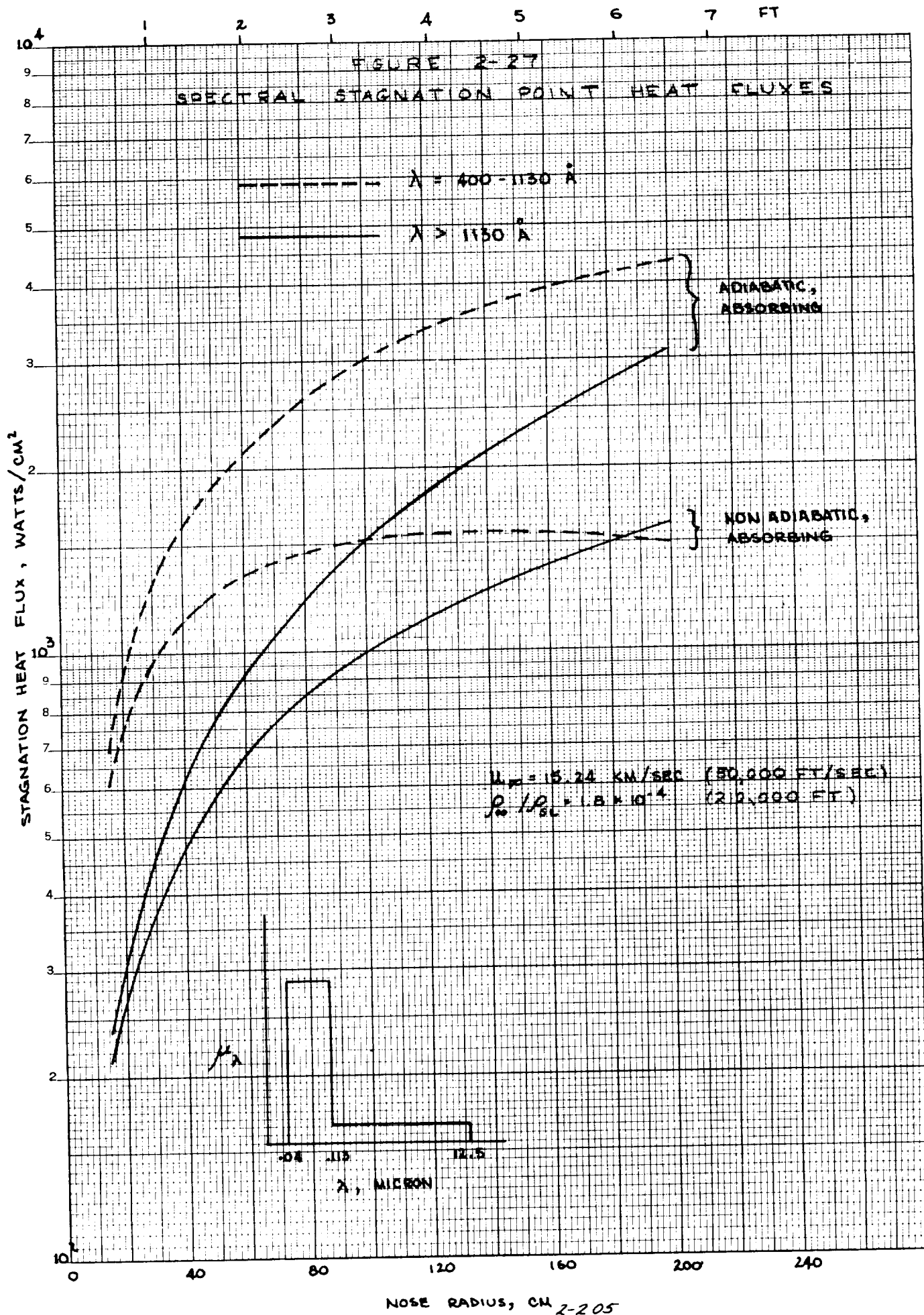


FIGURE 2-28

STAGNATION REGION SHOCK LAYER THICKNESSES

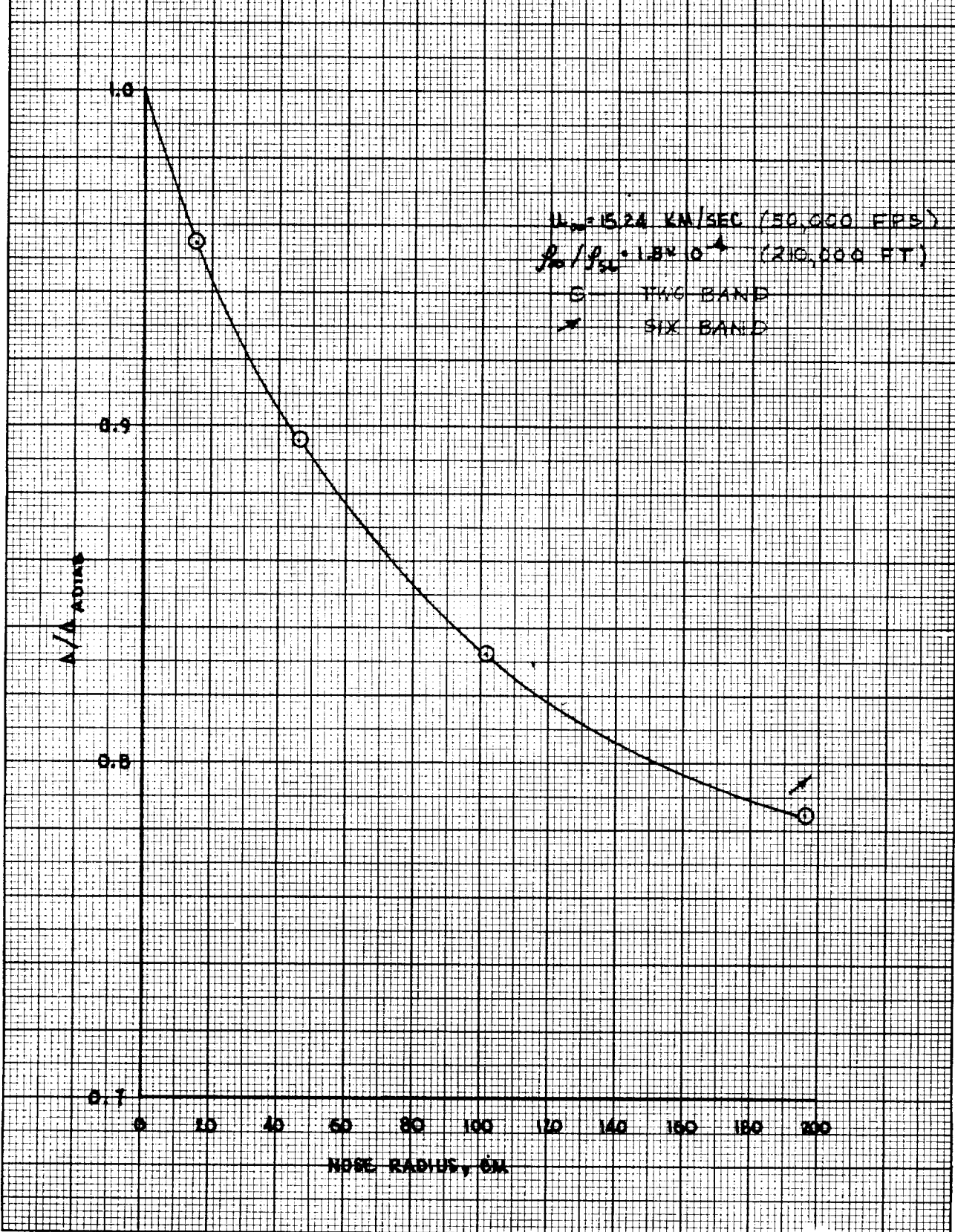
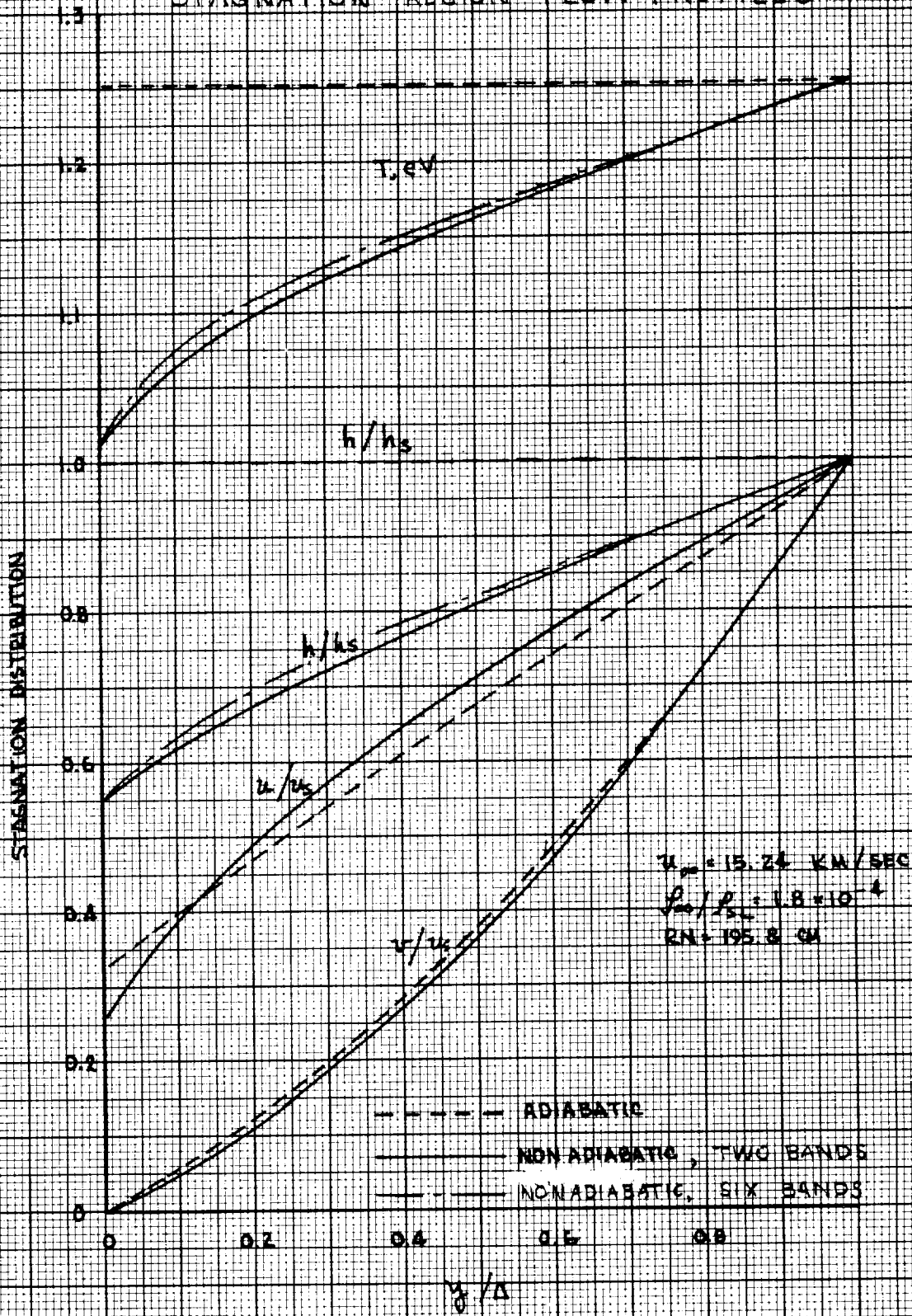


FIGURE 2-29  
STAGNATION REGION FLOW PROFILES



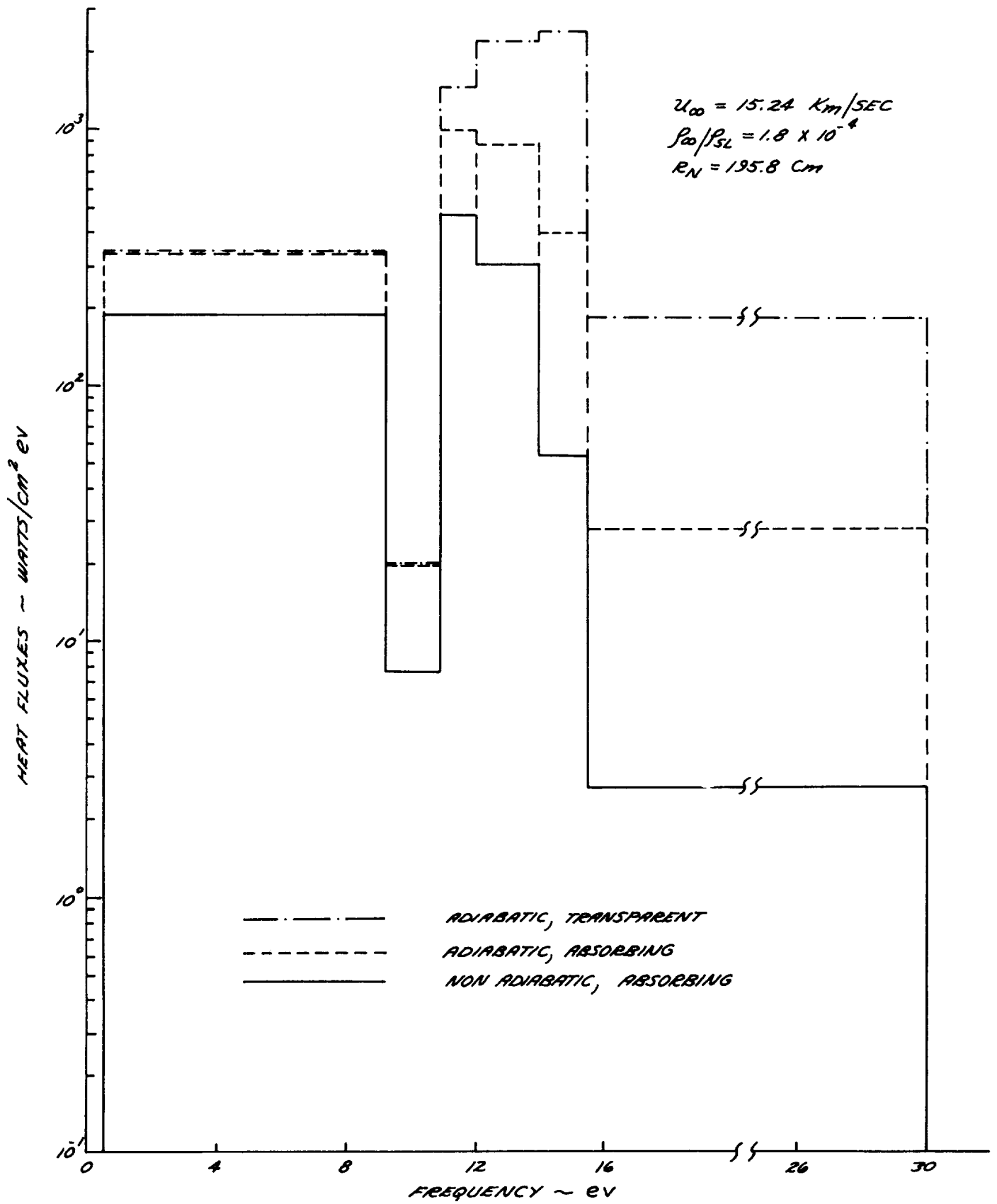


Figure 2-30 Spectral Stagnation Heat Fluxes, Six-Band Model

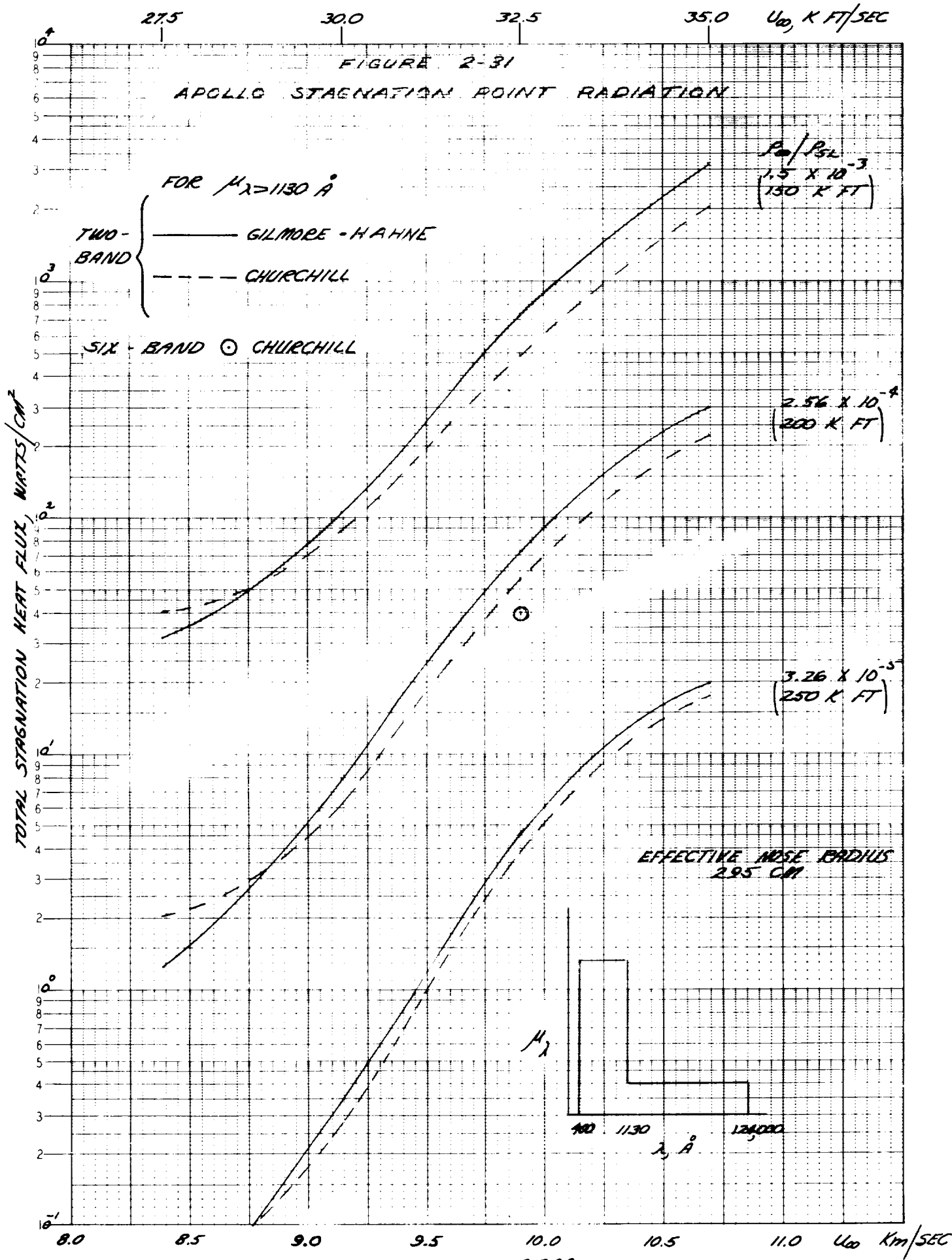
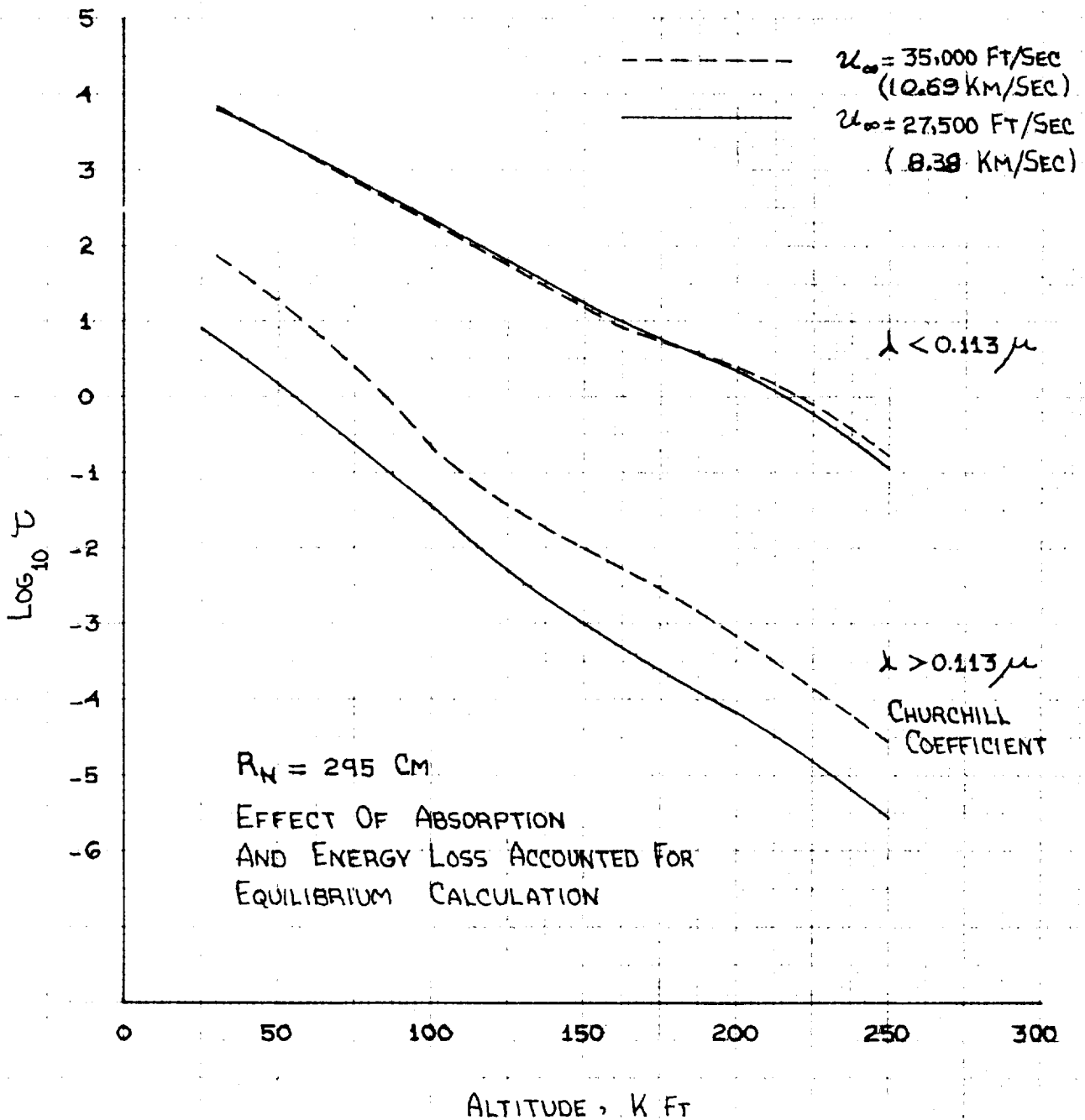


FIGURE 2-32

APOLLO SHOCK LAYER OPTICAL THICKNESSES, TWO BANDS  
STAGNATION REGION



MODEL

DATE

FIGURE 2-38

# APOLLO RADIATION LOSS PARAMETER

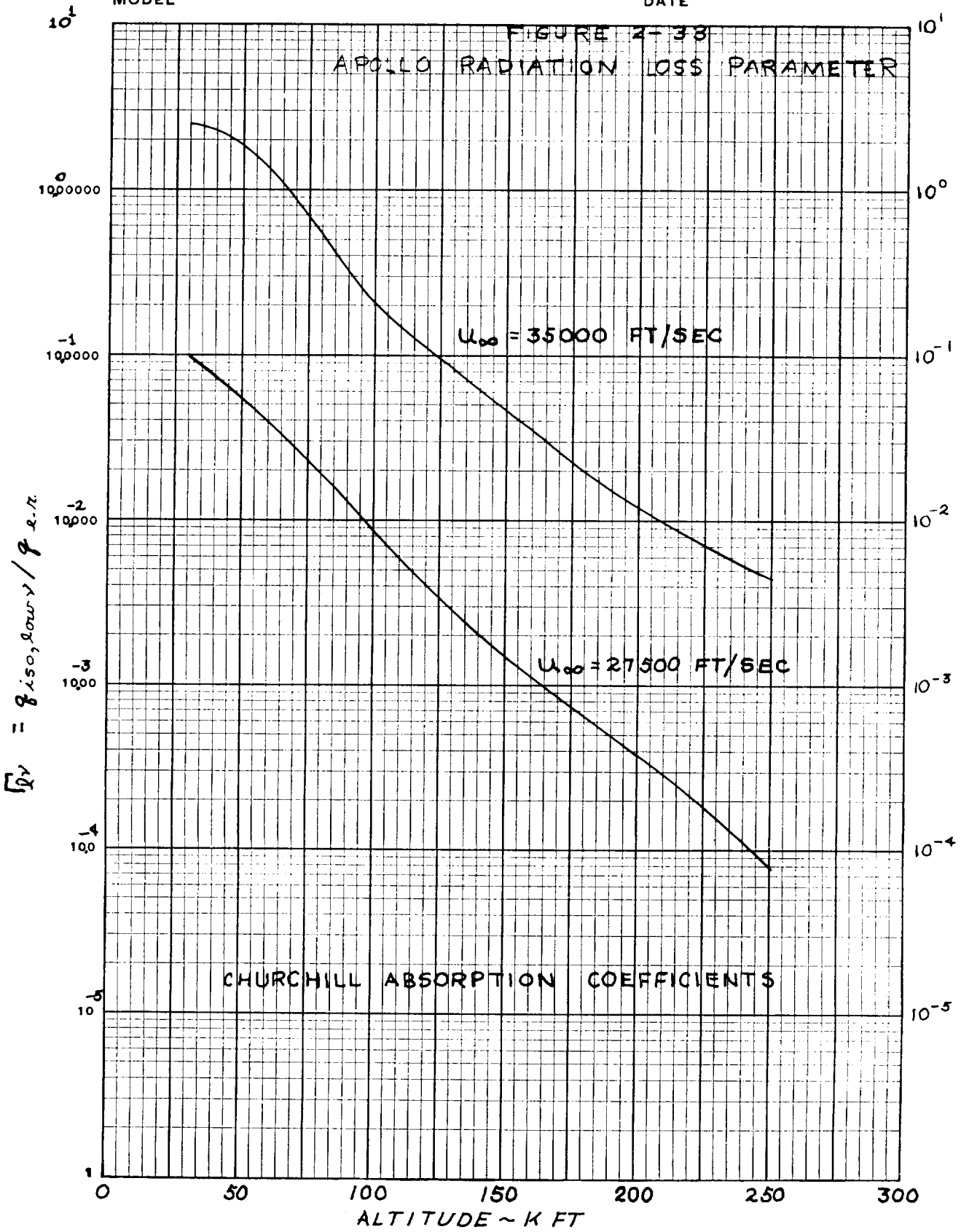


FIGURE 2-34

APOLLO RADIATION LOSS PARAMETER

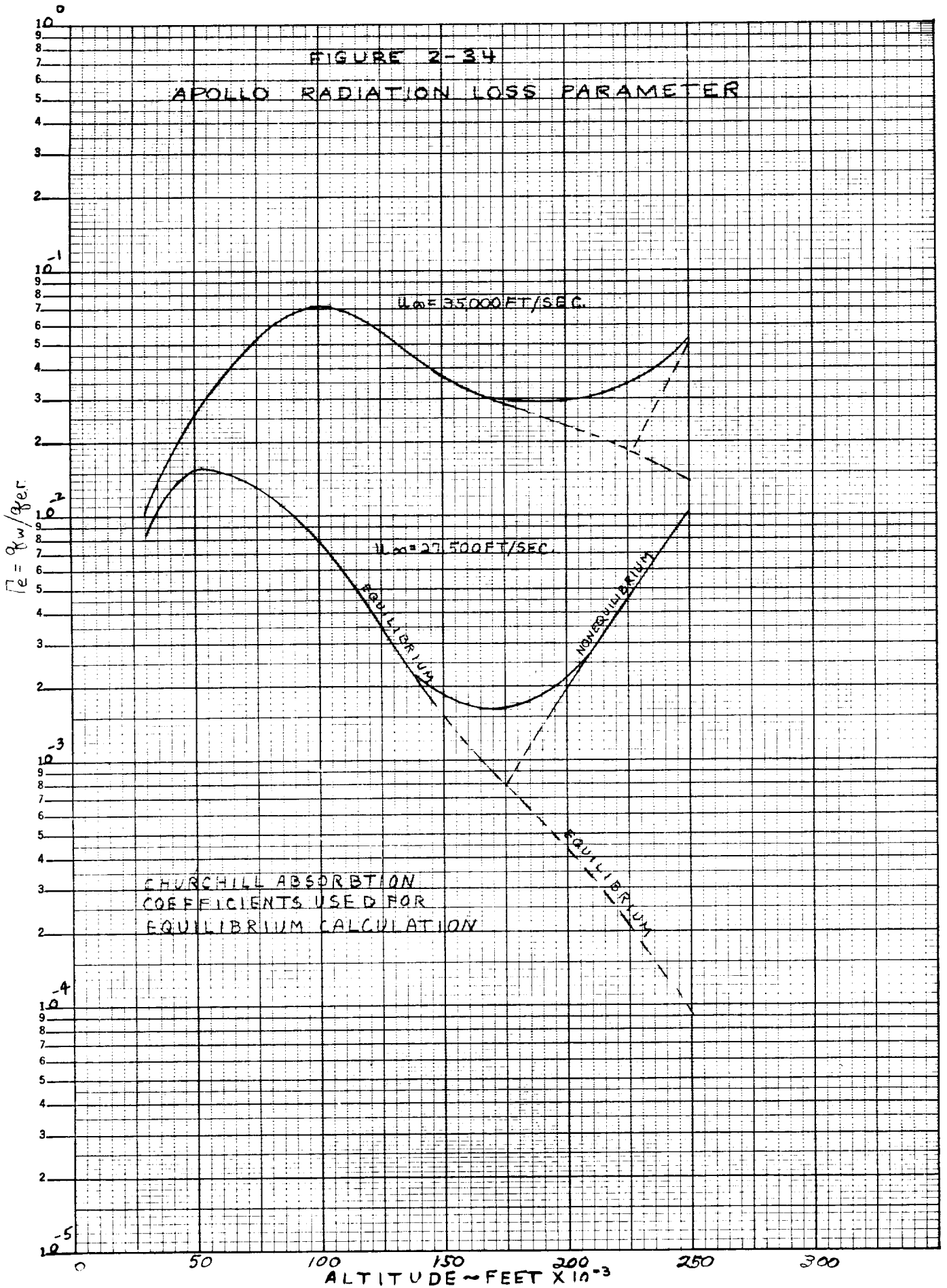
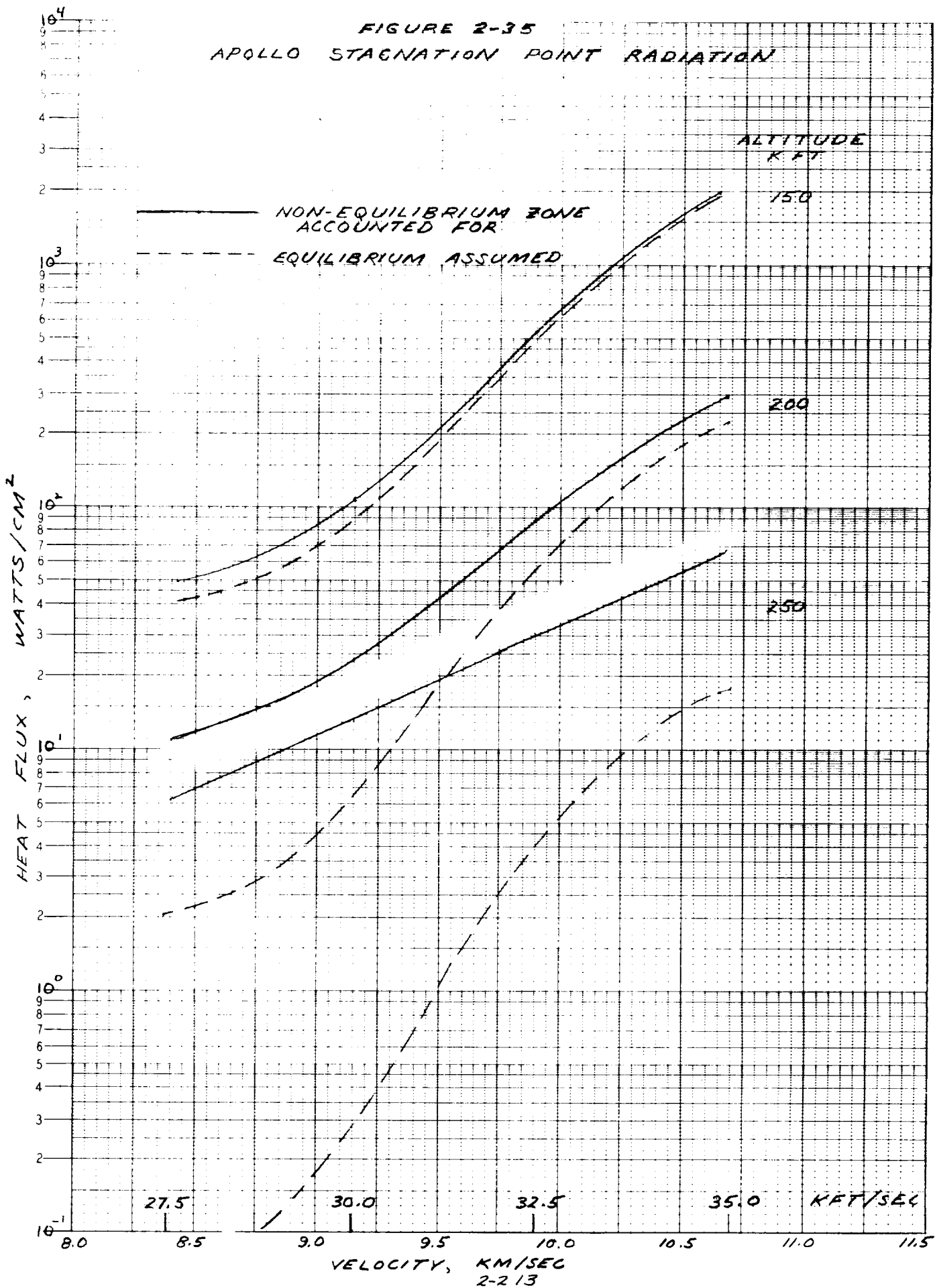




FIGURE 2-35  
 APOLLO STAGNATION POINT RADIATION



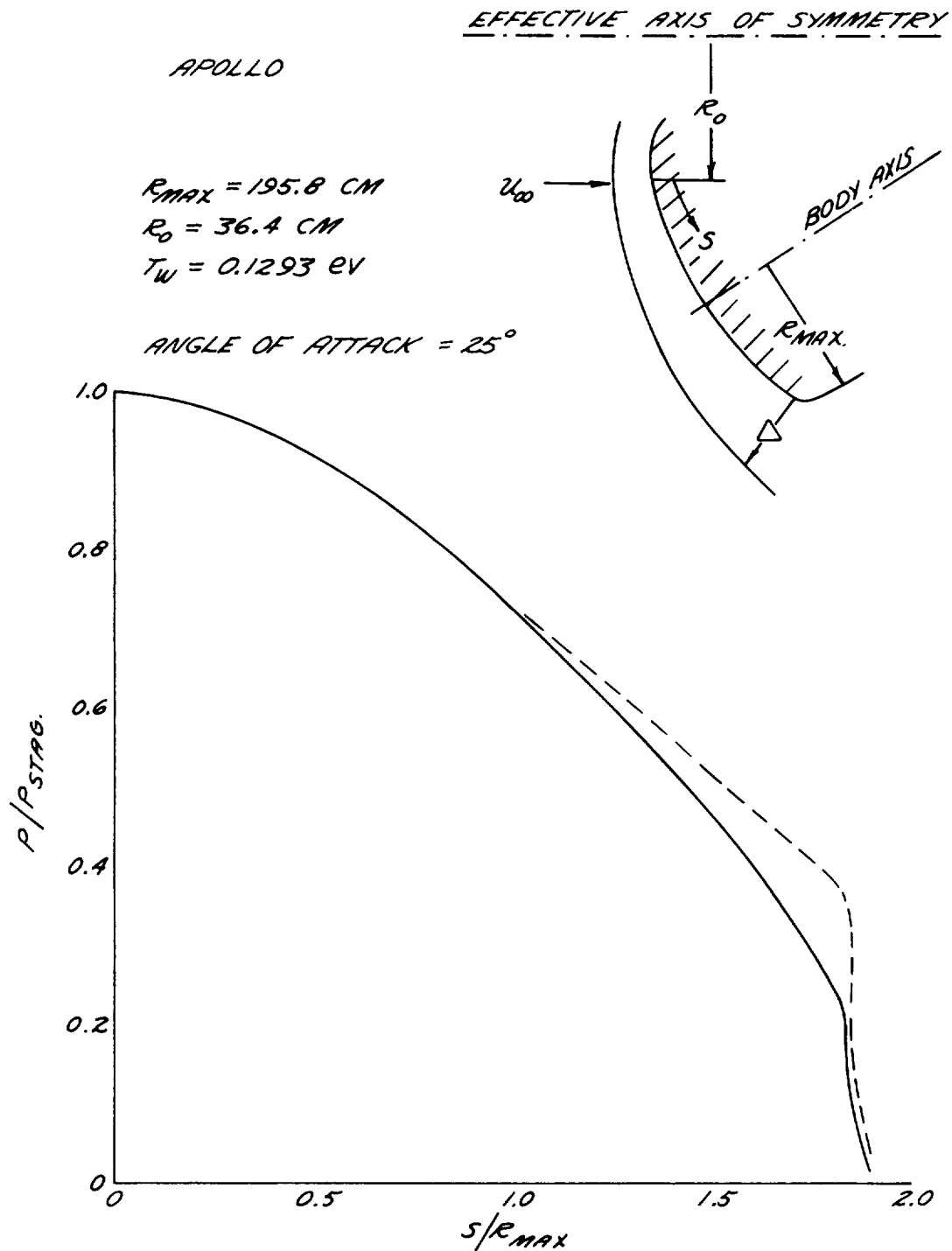


Figure 2-36 Apollo Configuration and Surface Pressure Distribution

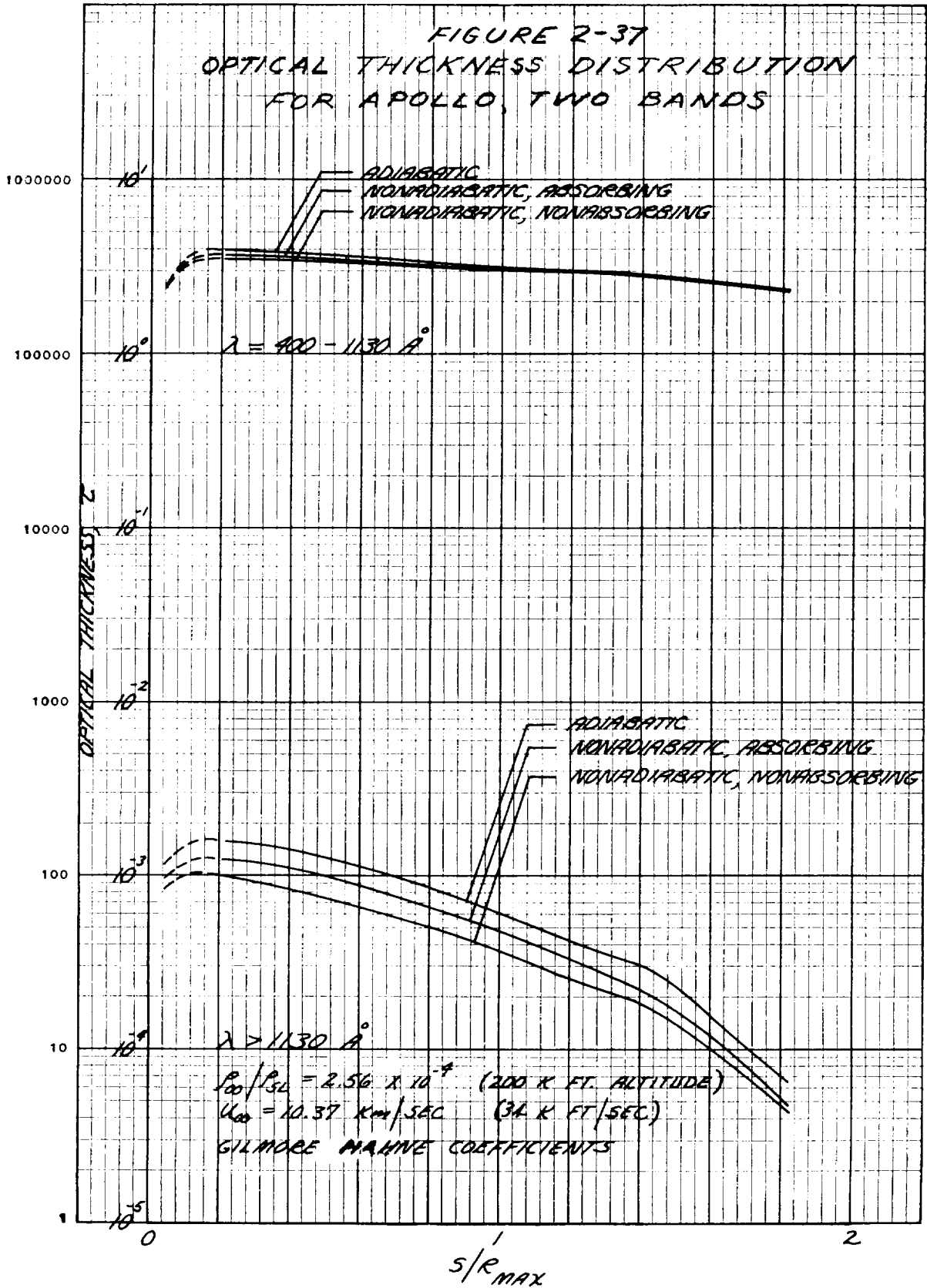


FIGURE 2-38

TOTAL HEAT FLUX DISTRIBUTION FOR APOLLO,  
TWO BANDS

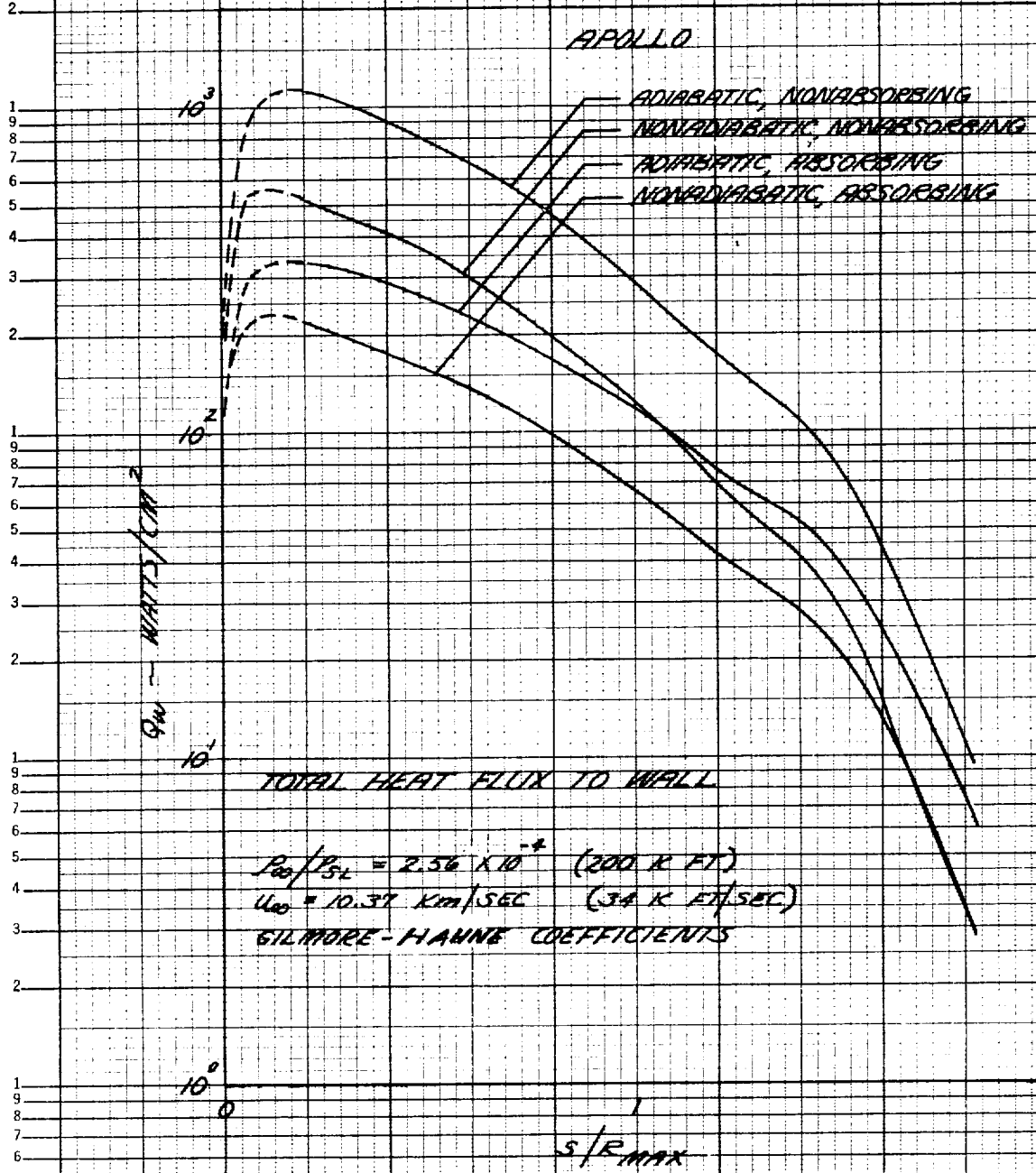


FIGURE 2-39

HIGH FREQUENCY HEAT FLUX DISTRIBUTIONS FOR APOLLO  
TWO BAND MODEL

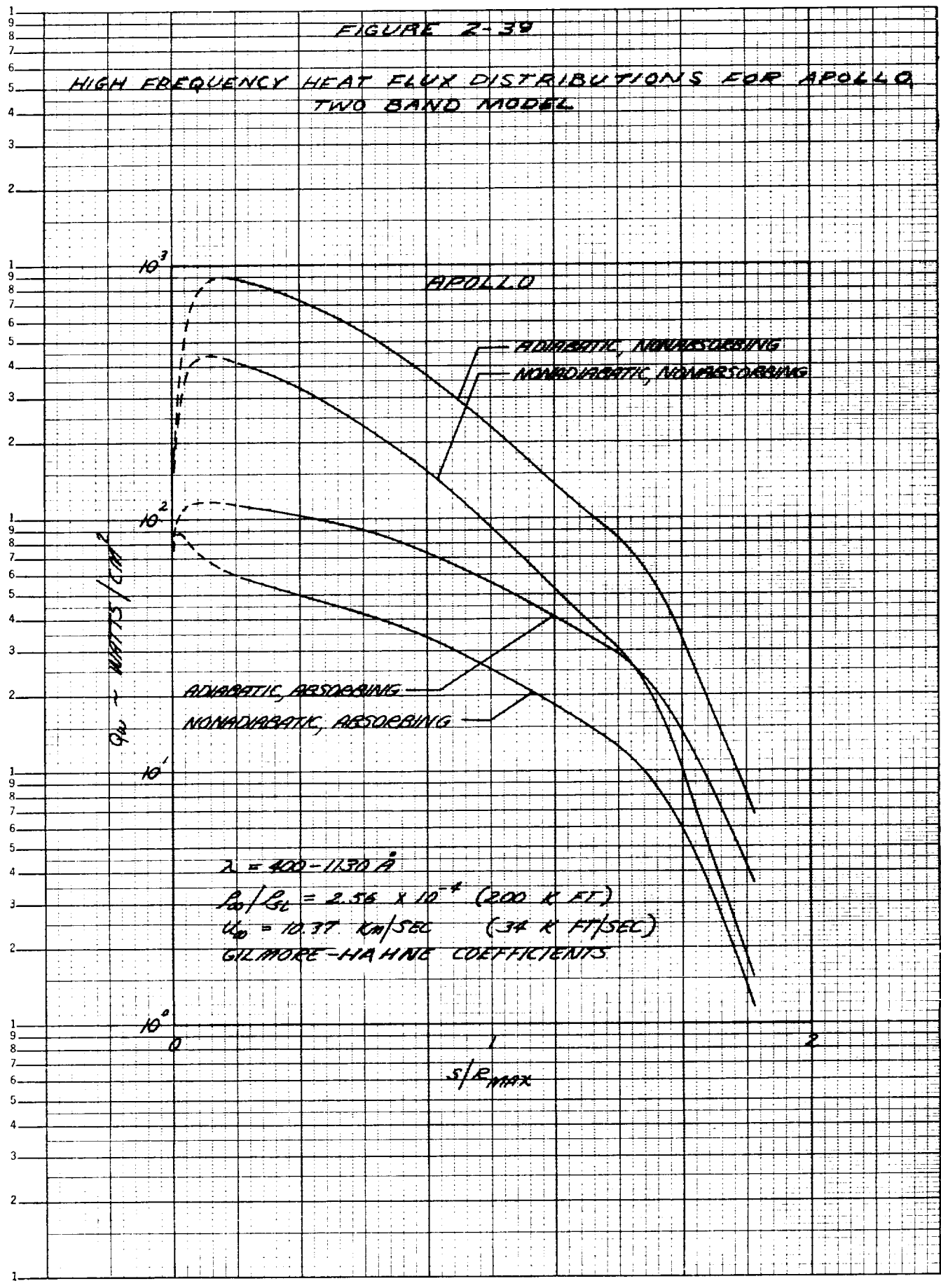


FIGURE 2-40

LOW FREQUENCY HEAT FLUX DISTRIBUTIONS FOR APOLLO,  
TWO BAND MODEL

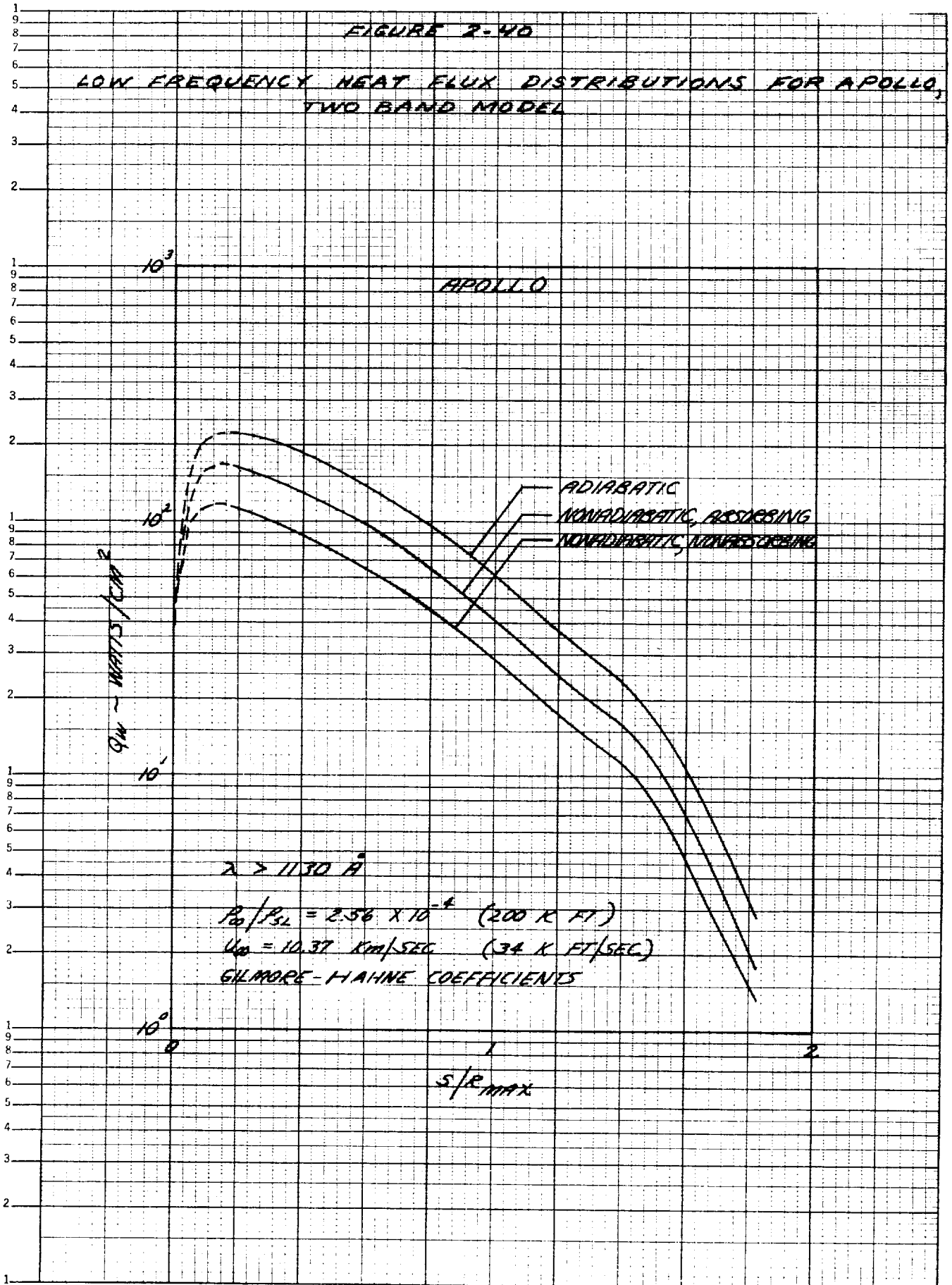


FIGURE 2-41

TEMPERATURE PROFILES FOR APOLLO,  
 $S/R_{MAX} = 0.25$

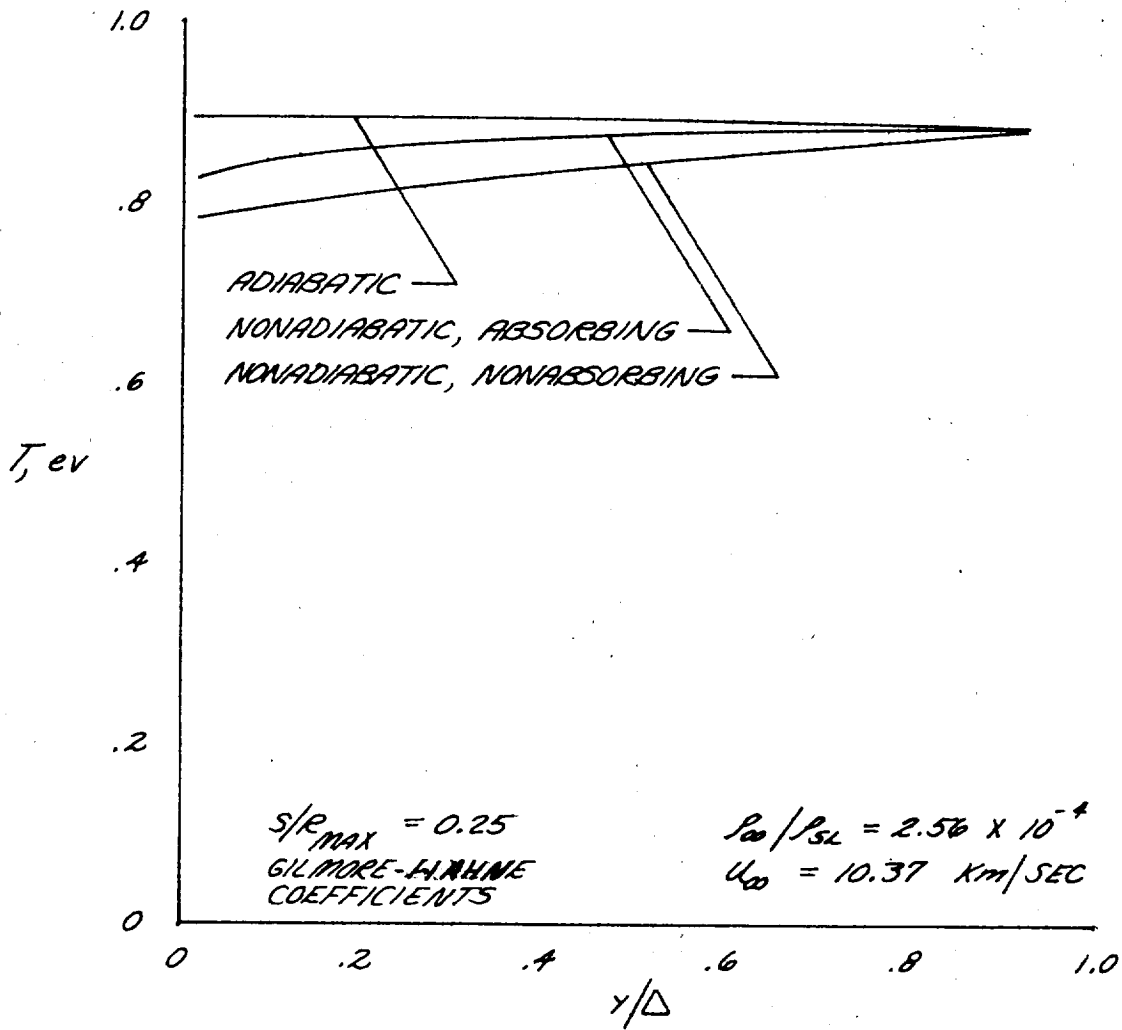


FIGURE 2-42

TEMPERATURE PROFILES FOR APOLLO,  
 $S/R_{MAX} = 1.61$

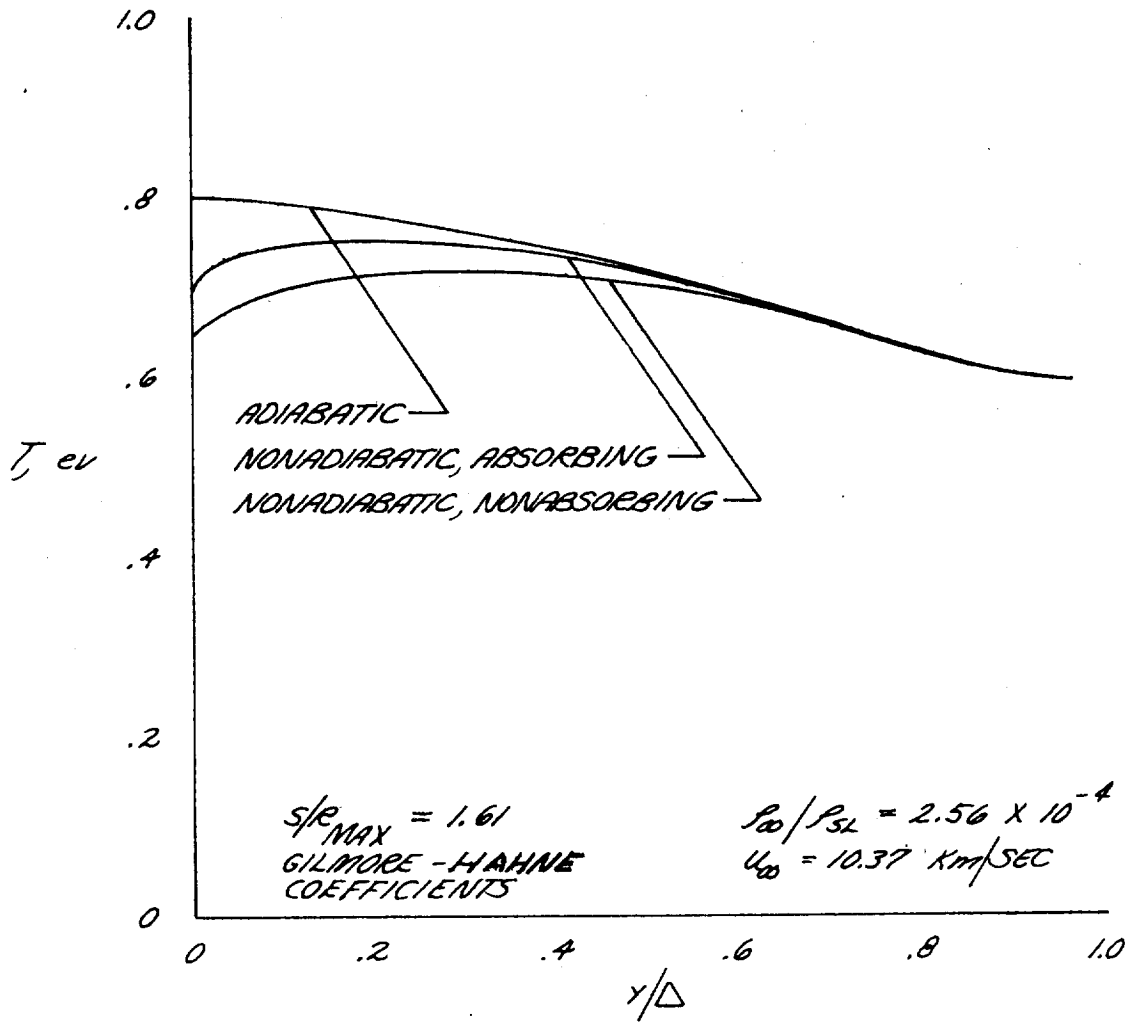
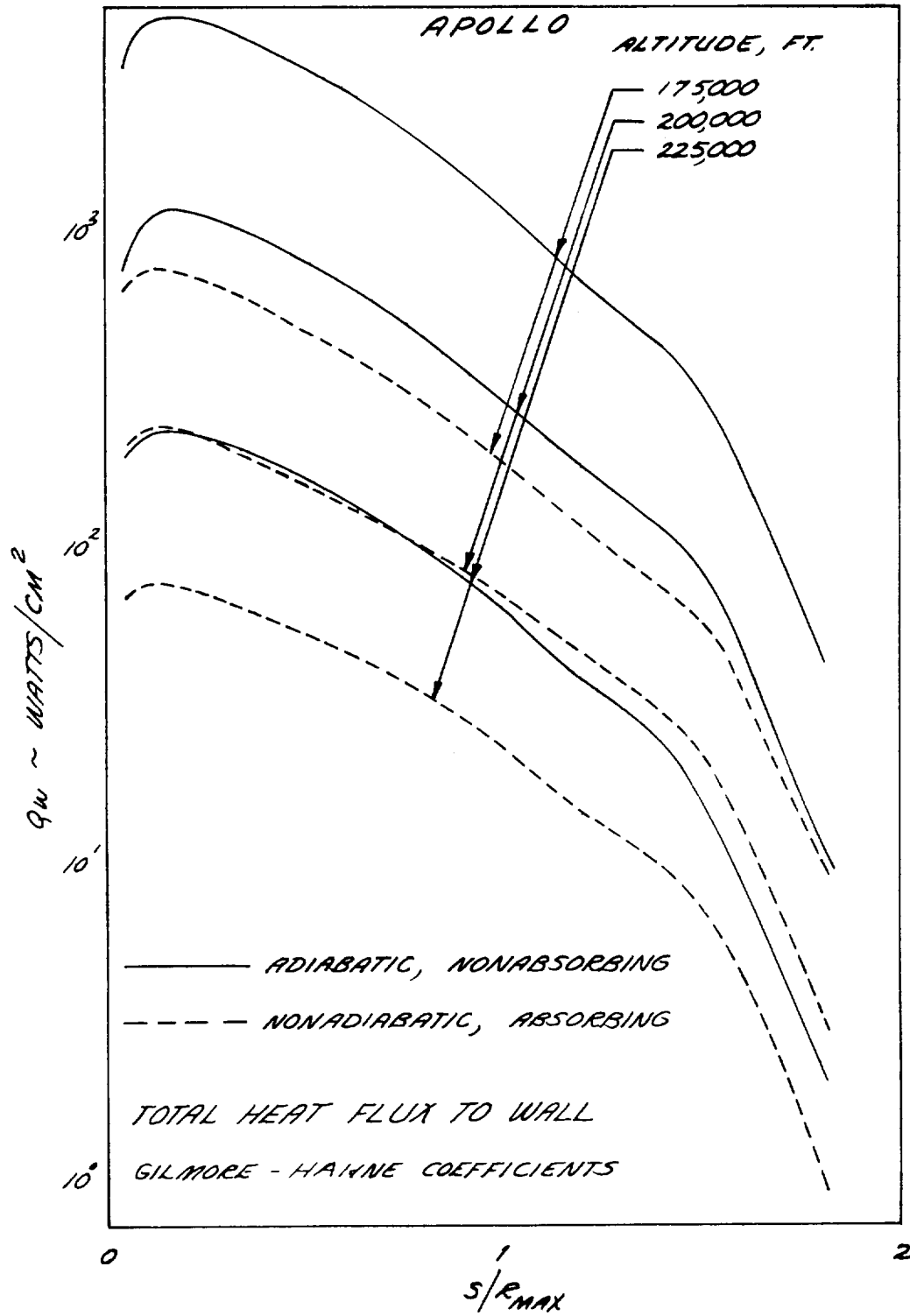




FIG 2-43

EFFECT OF ALTITUDE ON  
TOTAL HEAT FLUX FOR APOLLO,  
TWO BAND MODEL



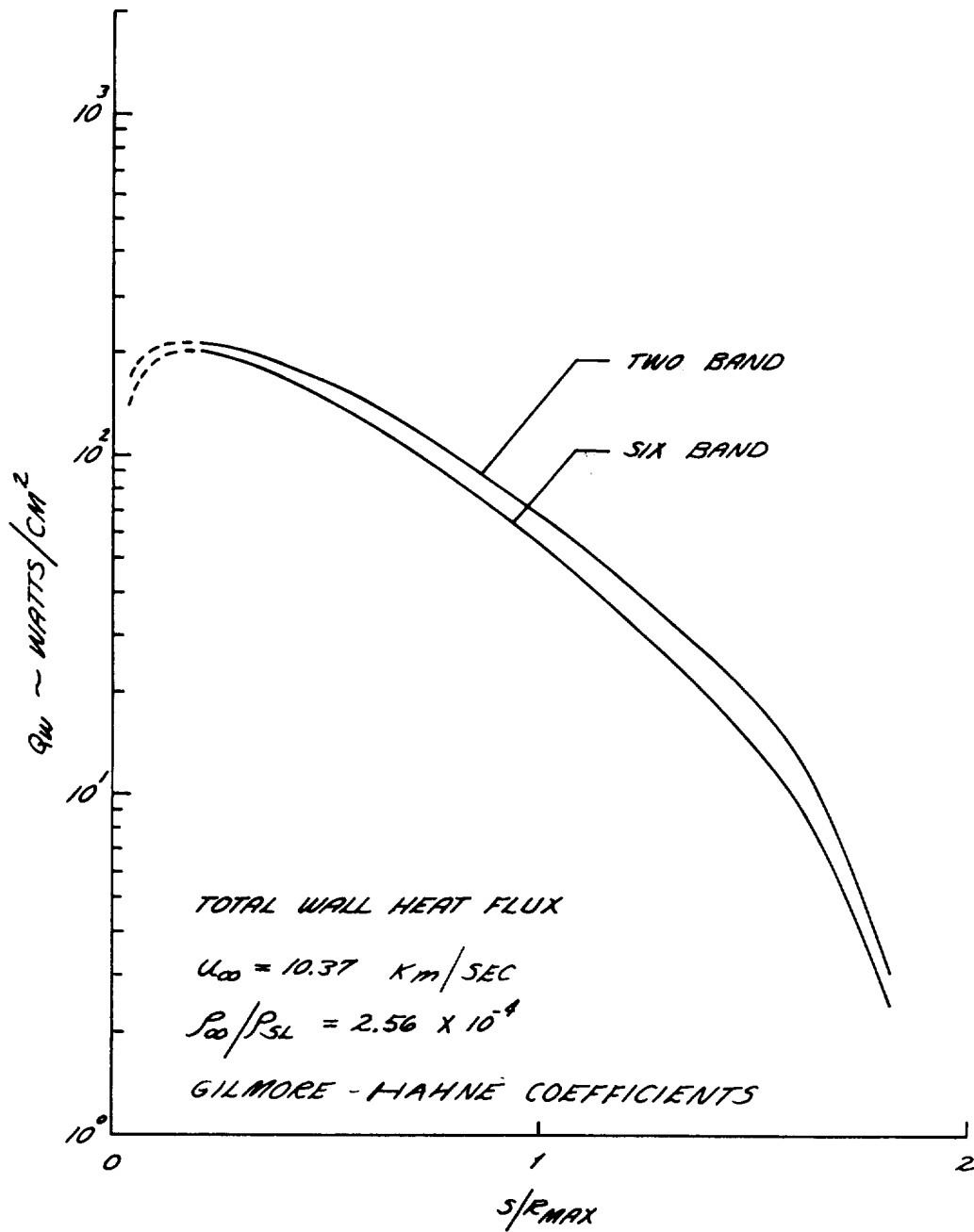


Figure 2-44 Comparison of Two-Band and Six-Band Heat Fluxes, Apollo

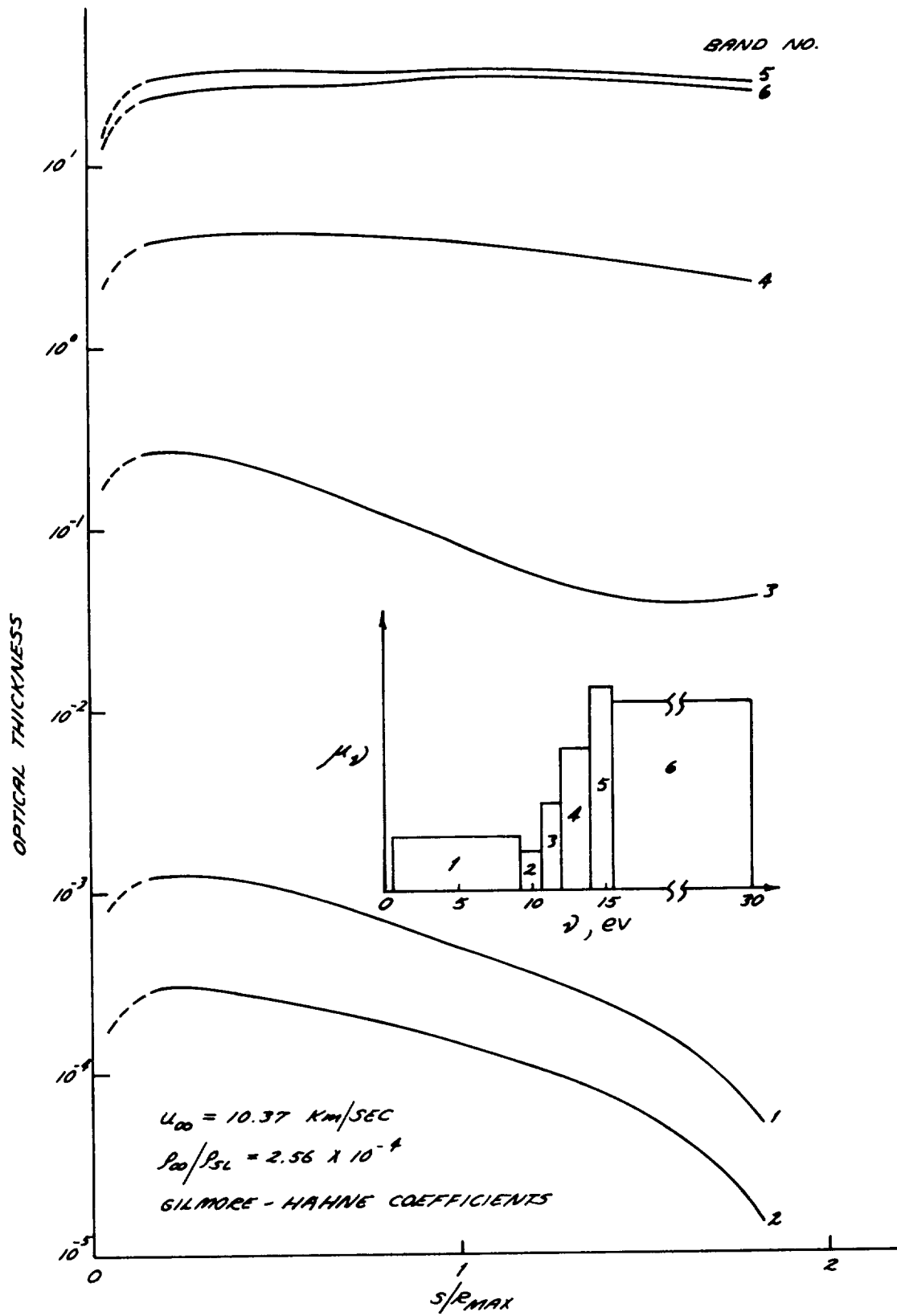


Figure 2-45 Optical Thickness Distribution, Apollo, Six-Band Model

FIGURE 2-46  
 EFFECT OF PRESSURE DISTRIBUTION AND  
 ABSORPTION COEFFICIENTS ON APOLLO HEAT FLUX

STAG. PT.  
 SOLN.  
 $R_N = 295 \text{ CM}$

APOLLO

$R_{max} = 195.8 \text{ CM}$   
 $U_{\infty} = 9.9 \text{ KM/SEC}$   
 $\rho_{\infty}/\rho_w = 2.56 \times 10^{-4}$   
 $T_w = 0.1293 \text{ TW}$

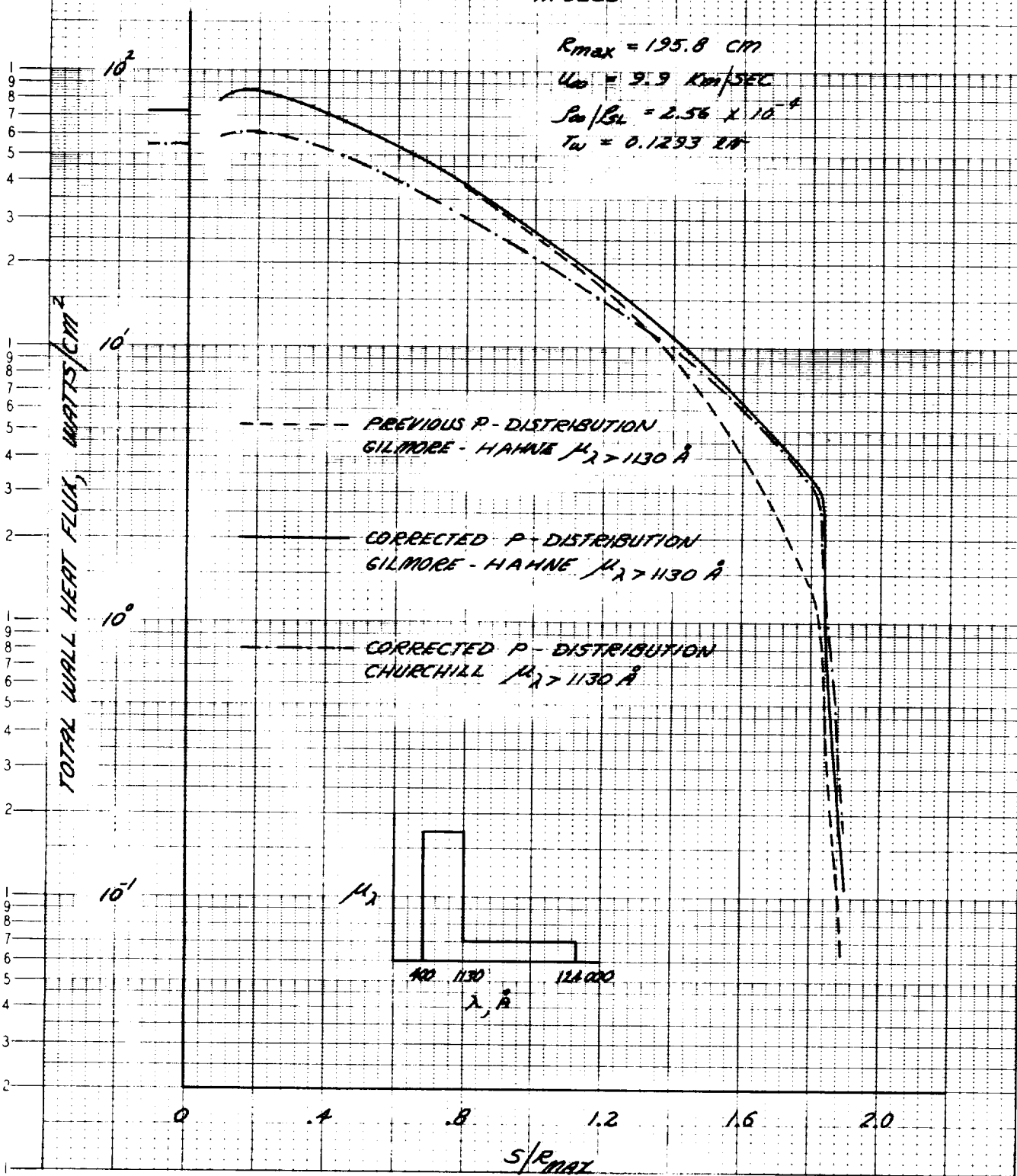
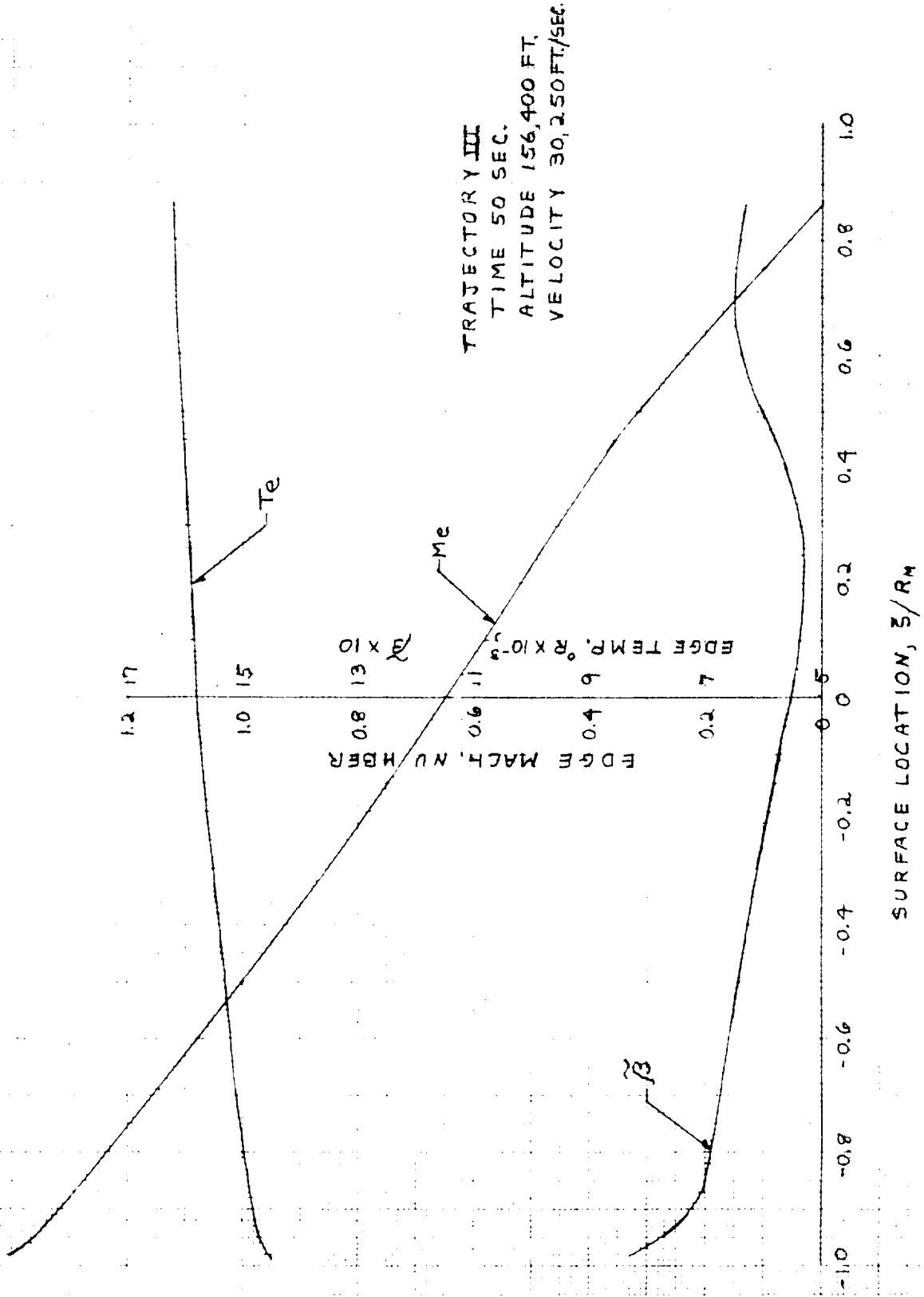


FIGURE 2-47  
 OUTER-EDGE CONDITIONS FOR APOLLO BOUNDARY LAYER



2-225

FIGURE 2-48  
 INNER-EDGE CONDITIONS FOR APOLLO BOUNDARY LAYER

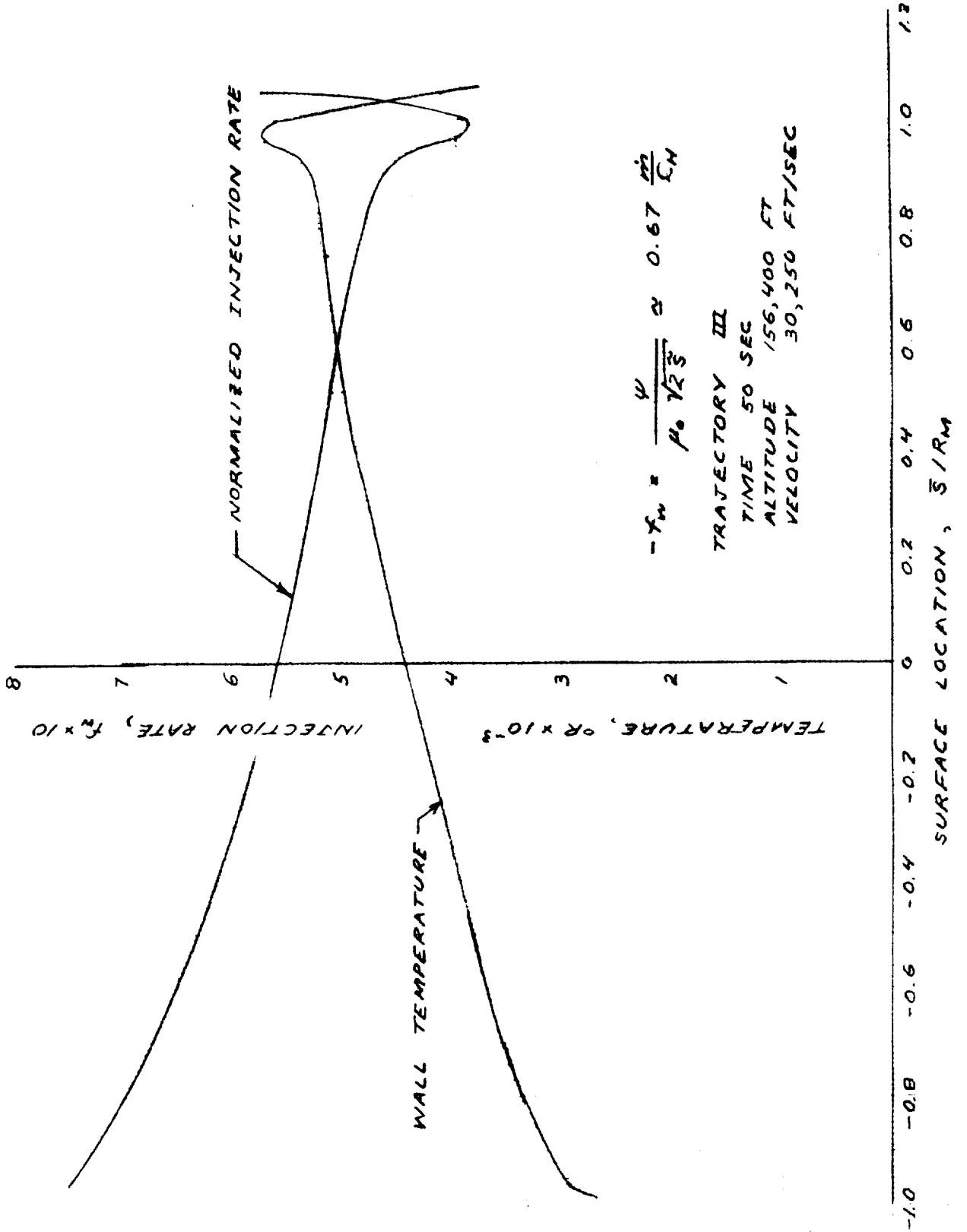
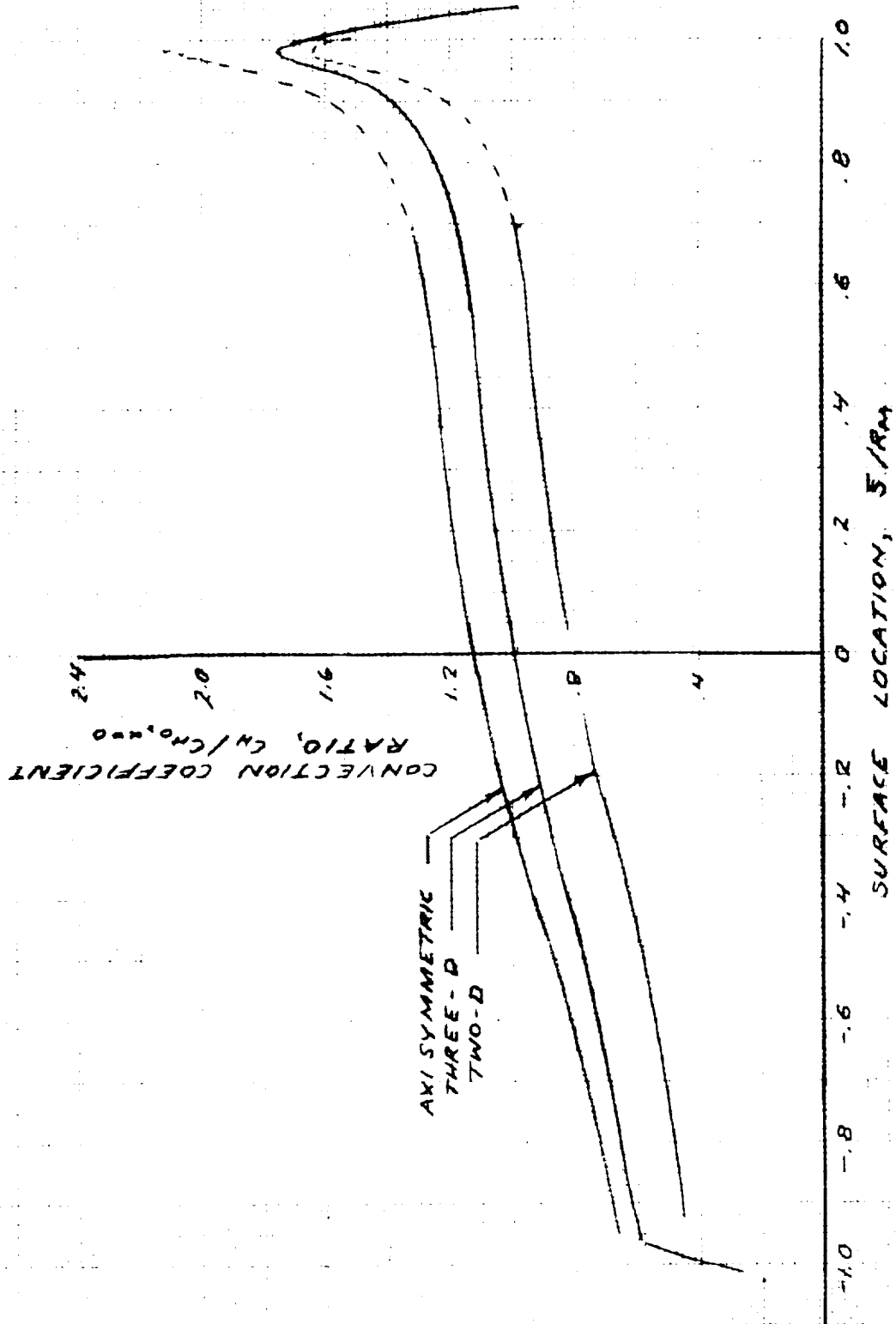


FIGURE 2-49

INFLUENCE OF FLOW GEOMETRY  
ON ARO110 CONVECTIVE HEATING DISTRIBUTION



**FIGURE 2-50**  
**CHARACTERISTICS OF PROTUBERANCE - BOUNDARY LAYER INTERACTION**

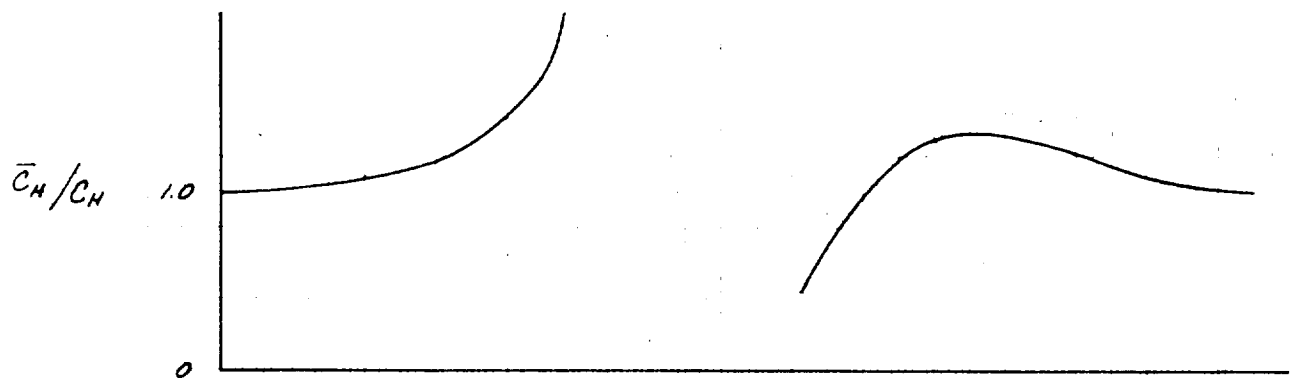
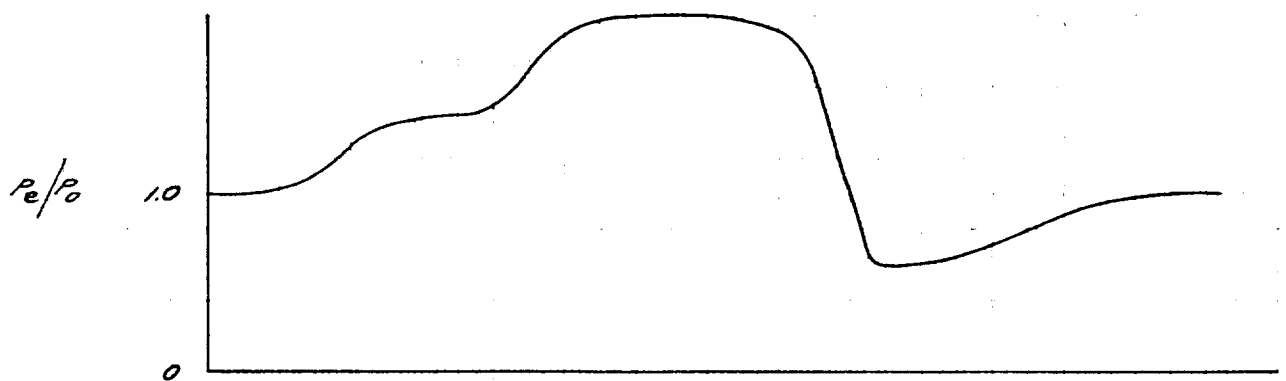
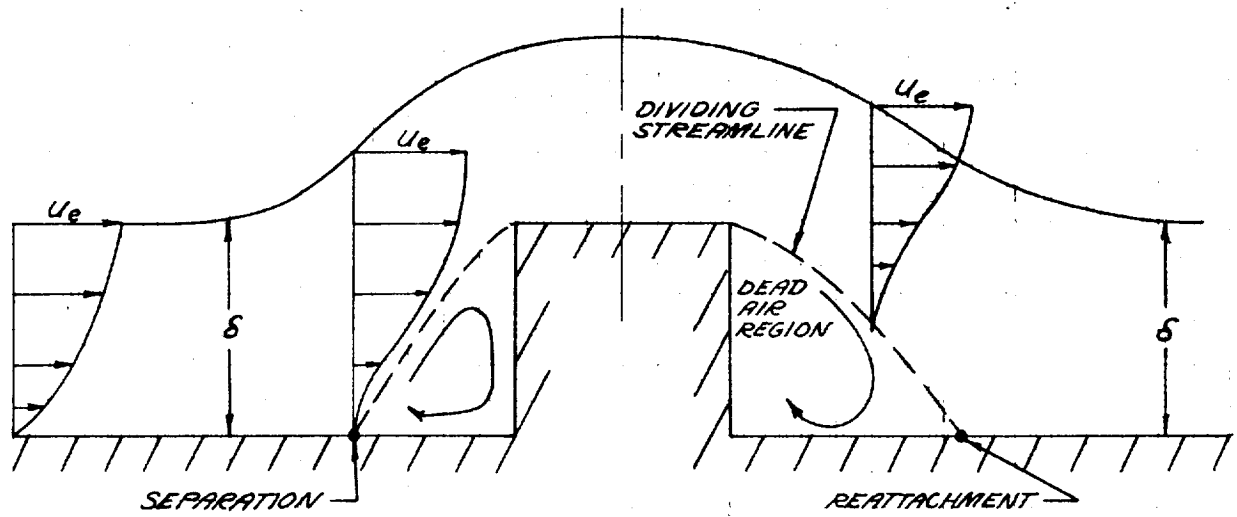




FIGURE 2 - 51  
COMPARISON OF VORTICITY INTERACTION SOLUTIONS

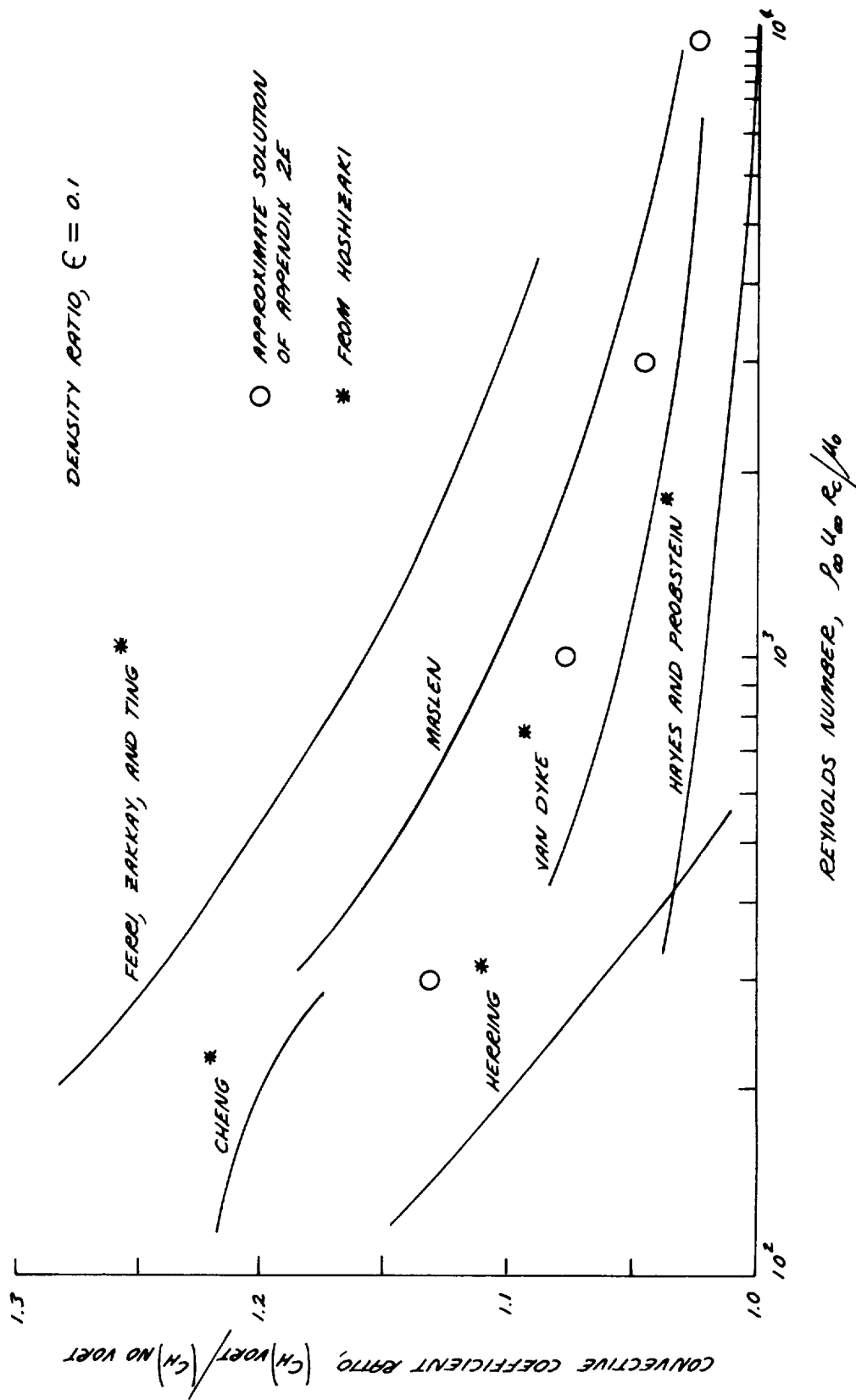
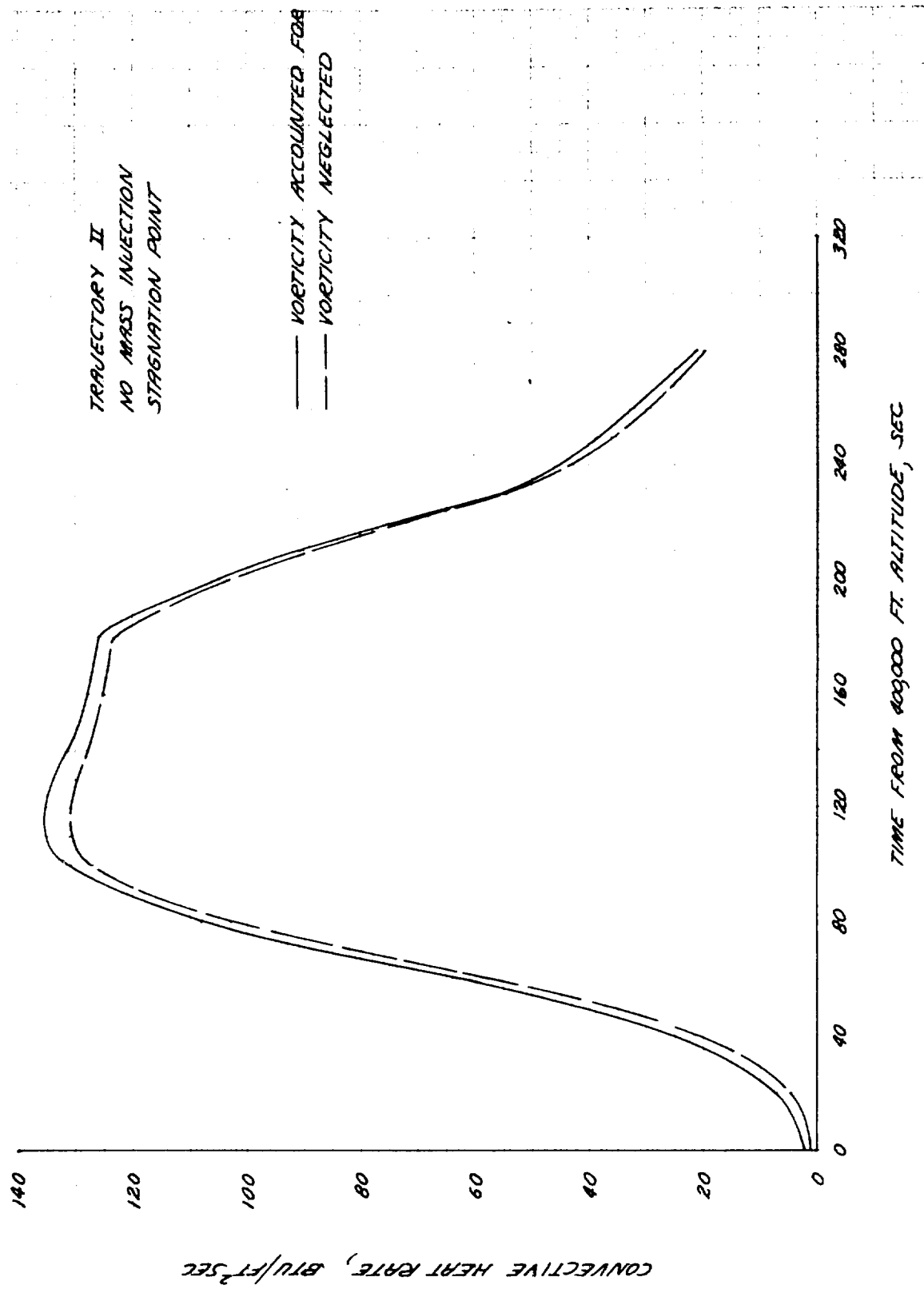
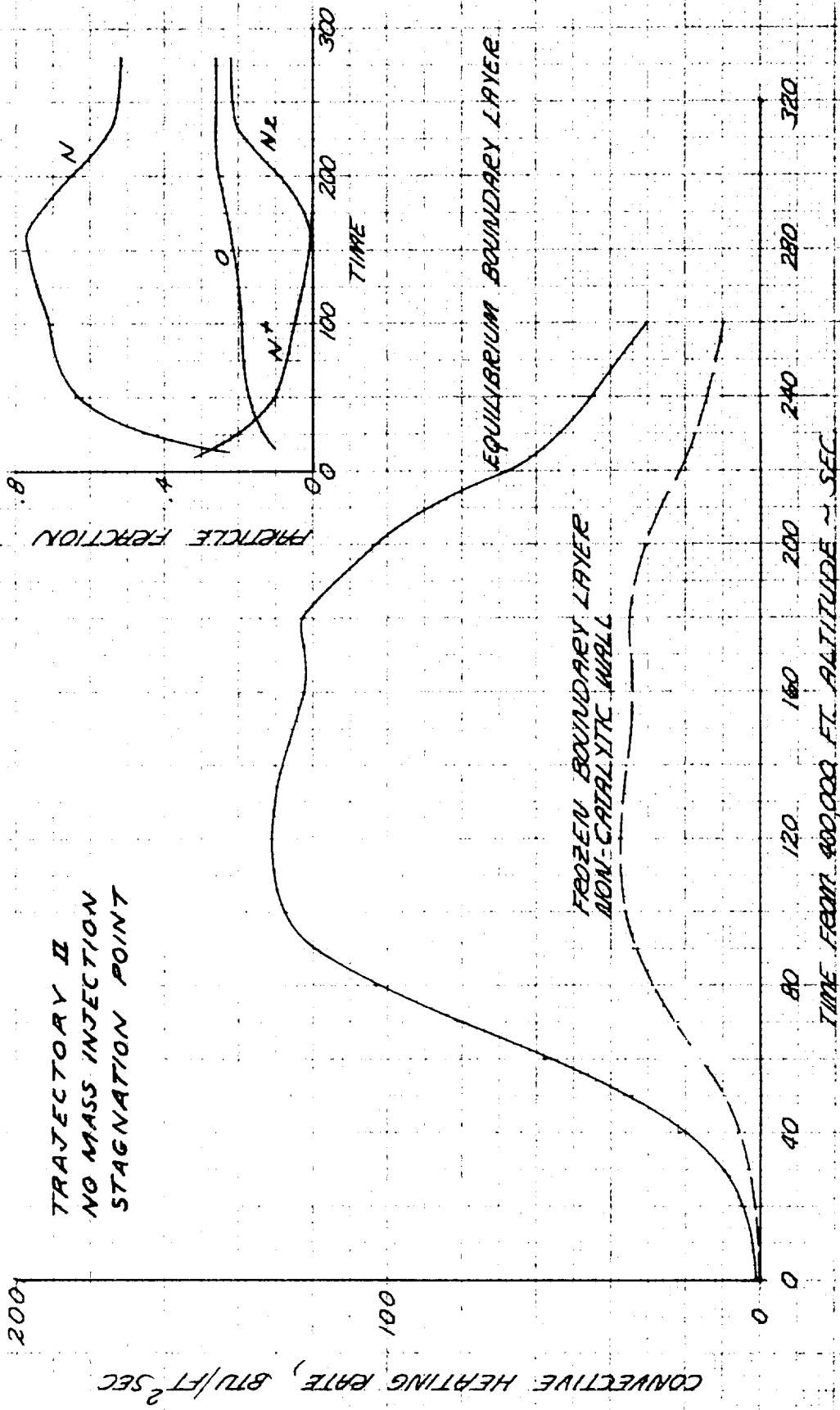


FIGURE 2-52  
INFLUENCE OF SHOCK-GENERATED VORTICITY ON  
APOLLO HEATING



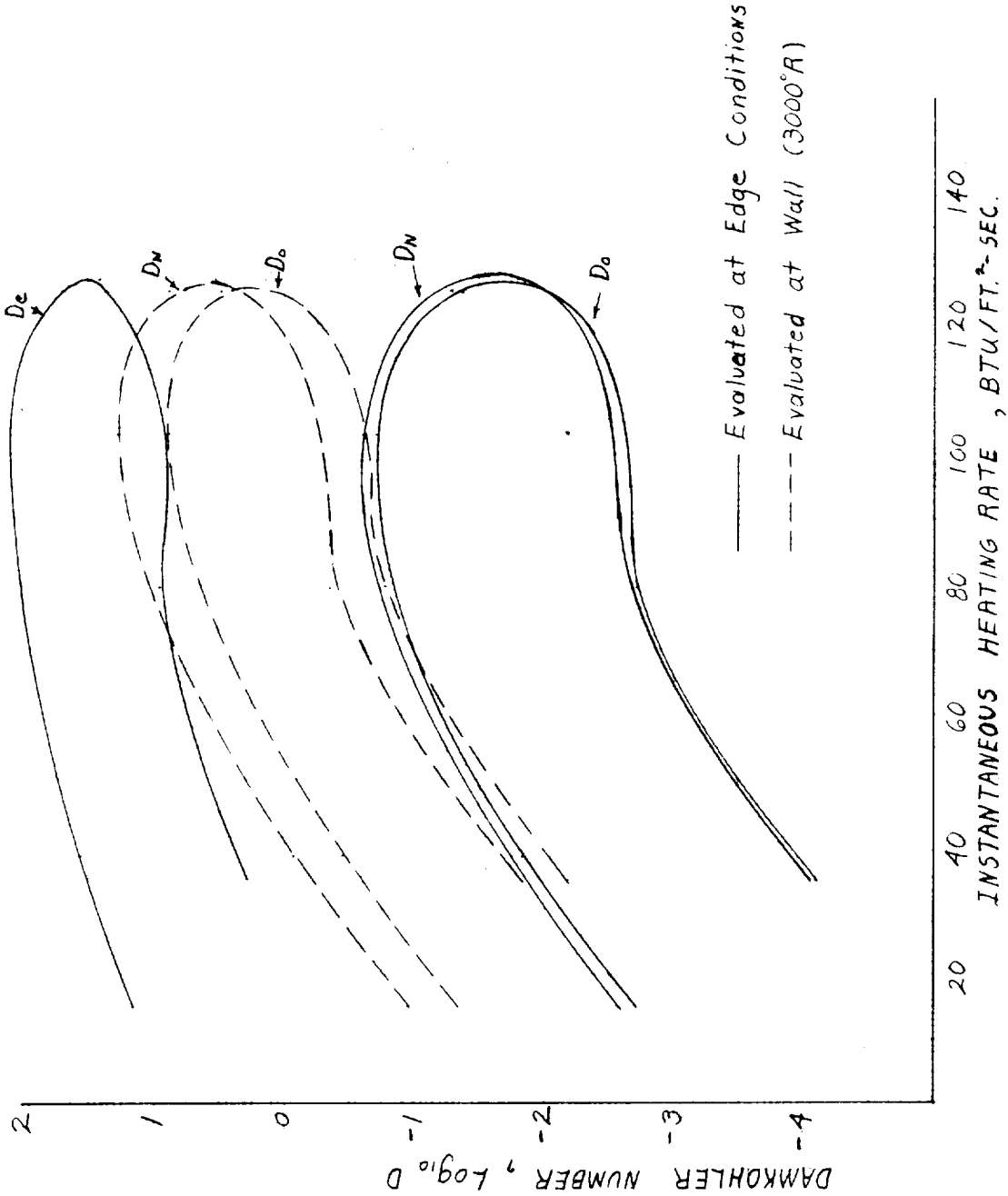
**FIGURE 2-53**  
**LIMITING EFFECTS OF WALL CATALYTICITY ON APOLLO HEATING**  
**WITH FROZEN BOUNDARY LAYER**



Prepared	NAME	DATE	LOCKHEED MISSILES & SPACE COMPANY A GROUP DIVISION OF LOCKHEED AIRCRAFT CORPORATION	Page	TEMP.	PERM.
Checked				Model		
Approved				Report No.		

FIGURE 2-54  
DAMKOHLE R NUMBERS FOR APOLLO BOUNDARY LAYER

Trajectory II



2-232

FIGURE 2-55  
 EXTENT OF DEPARTURE FROM CHEMICAL EQUILIBRIUM

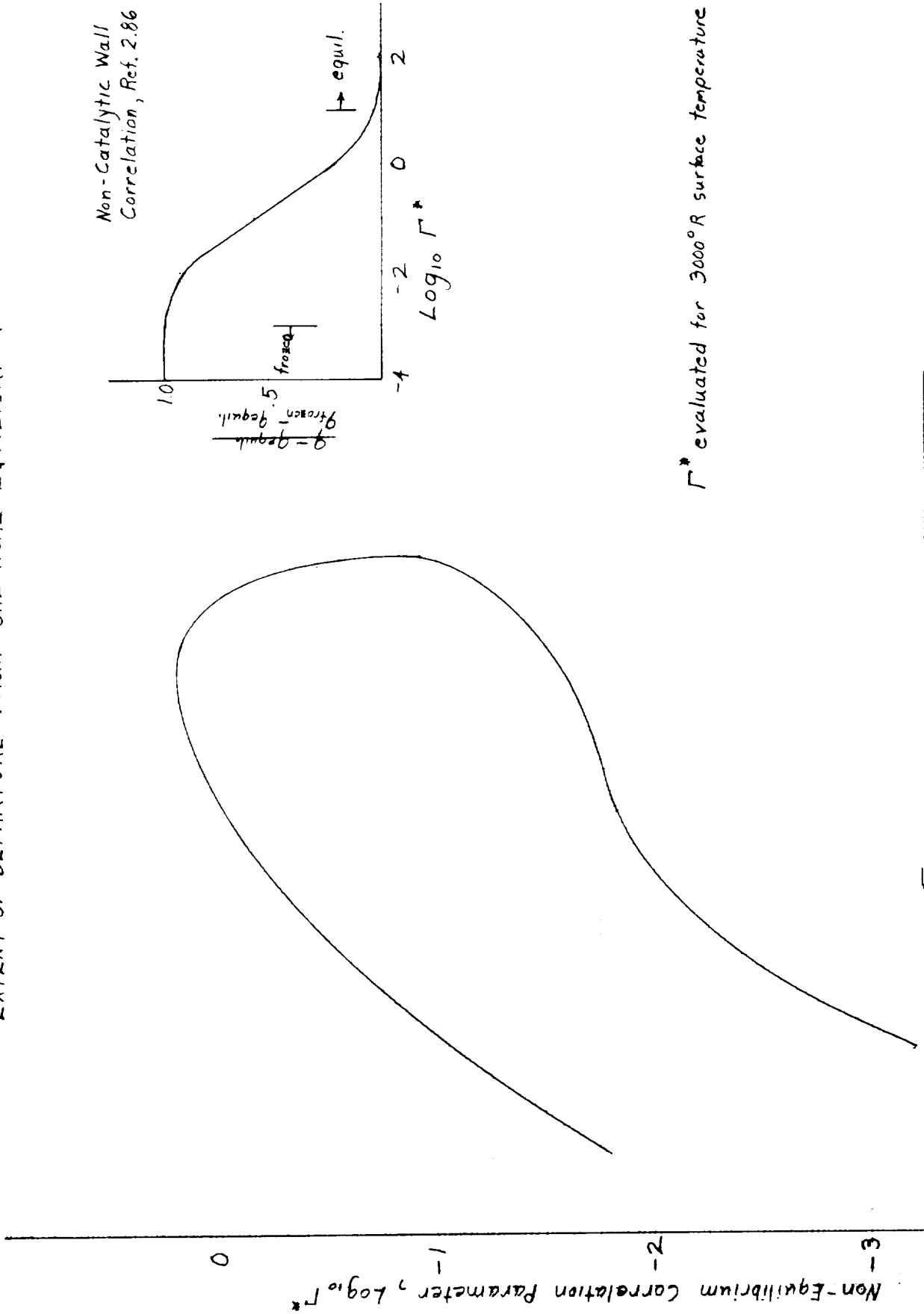
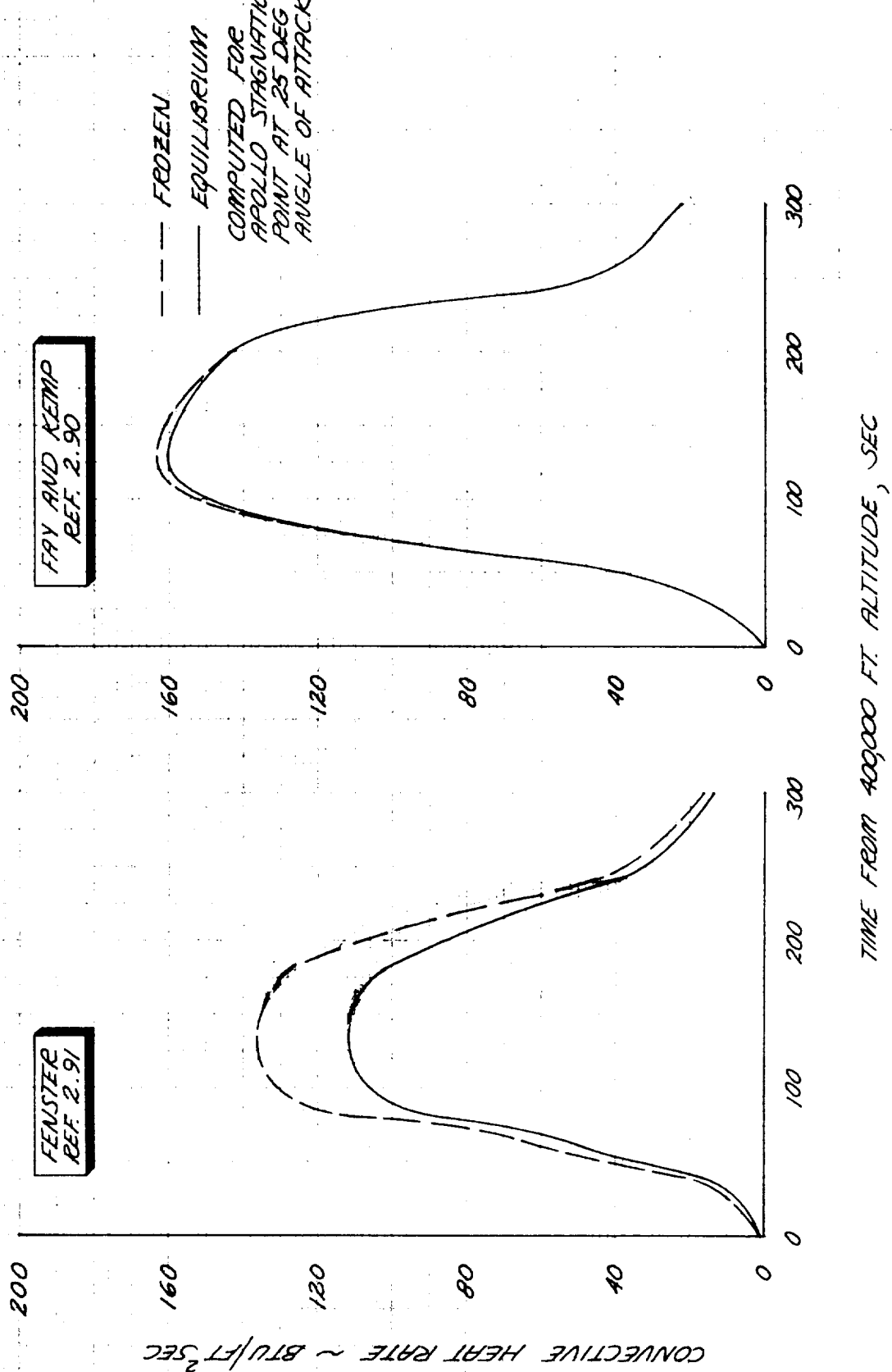


**FIGURE 2-56**  
**INFLUENCE OF NON-EQUILIBRIUM ON APOLLO HEATING**  
**WITH A HIGHLY CATALYTIC WALL**



Prepared	NAME	DATE	LOCKHEED MISSILES & SPACE COMPANY A GROUP DIVISION OF LOCKHEED AIRCRAFT CORPORATION	Page	TEMP	PERM
Checked			TITLE	Model		
Approved				Report No.		

FIGURE 2-57

ABLATION PRODUCT INJECTION HISTORY  
GEOMETRIC CENTER, TRAJECTORY III

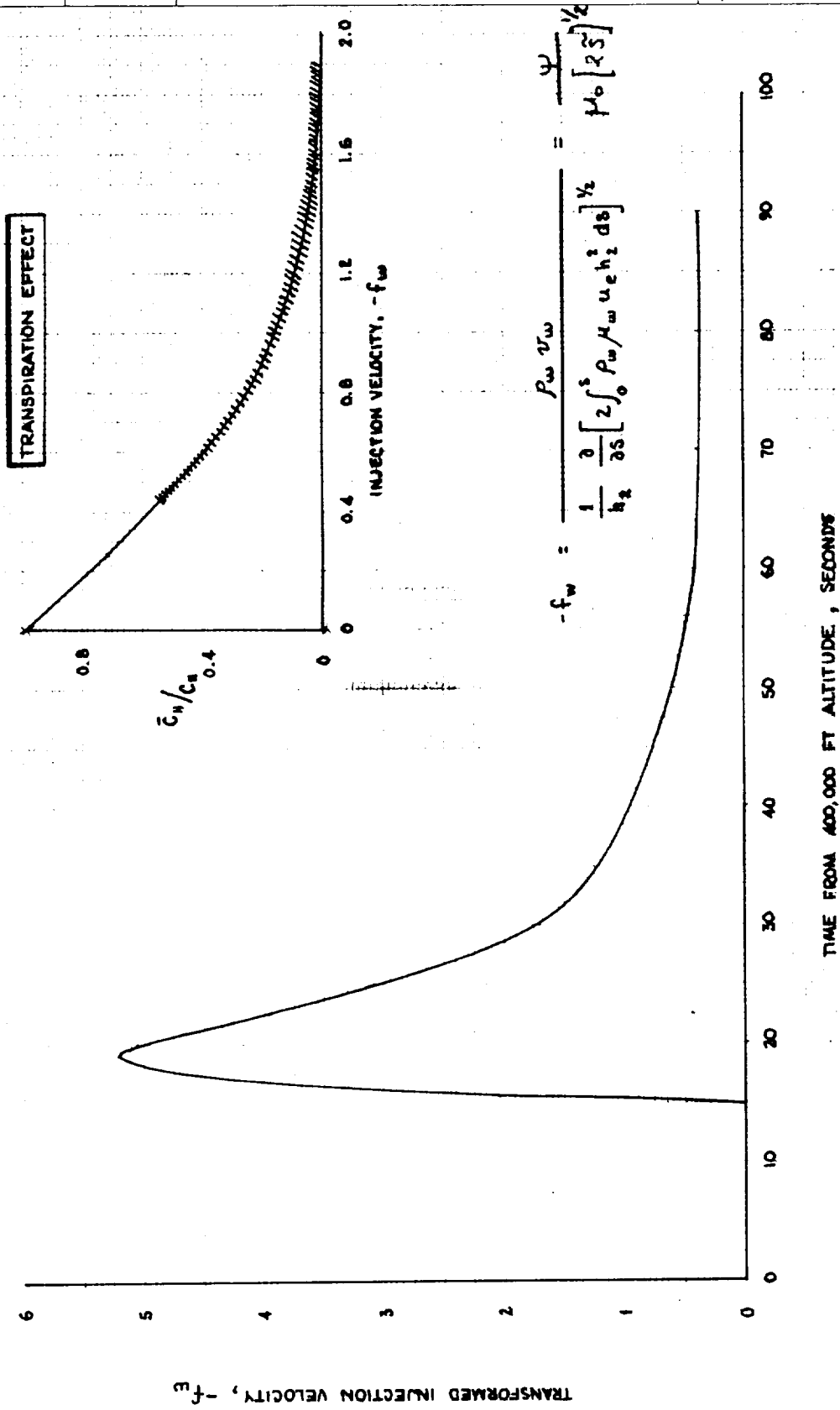


FIGURE 2-58  
INFLUENCE OF MASS INJECTION ON APOLLO HEATING  
GEOMETRIC CENTER, TRAJECTORY III

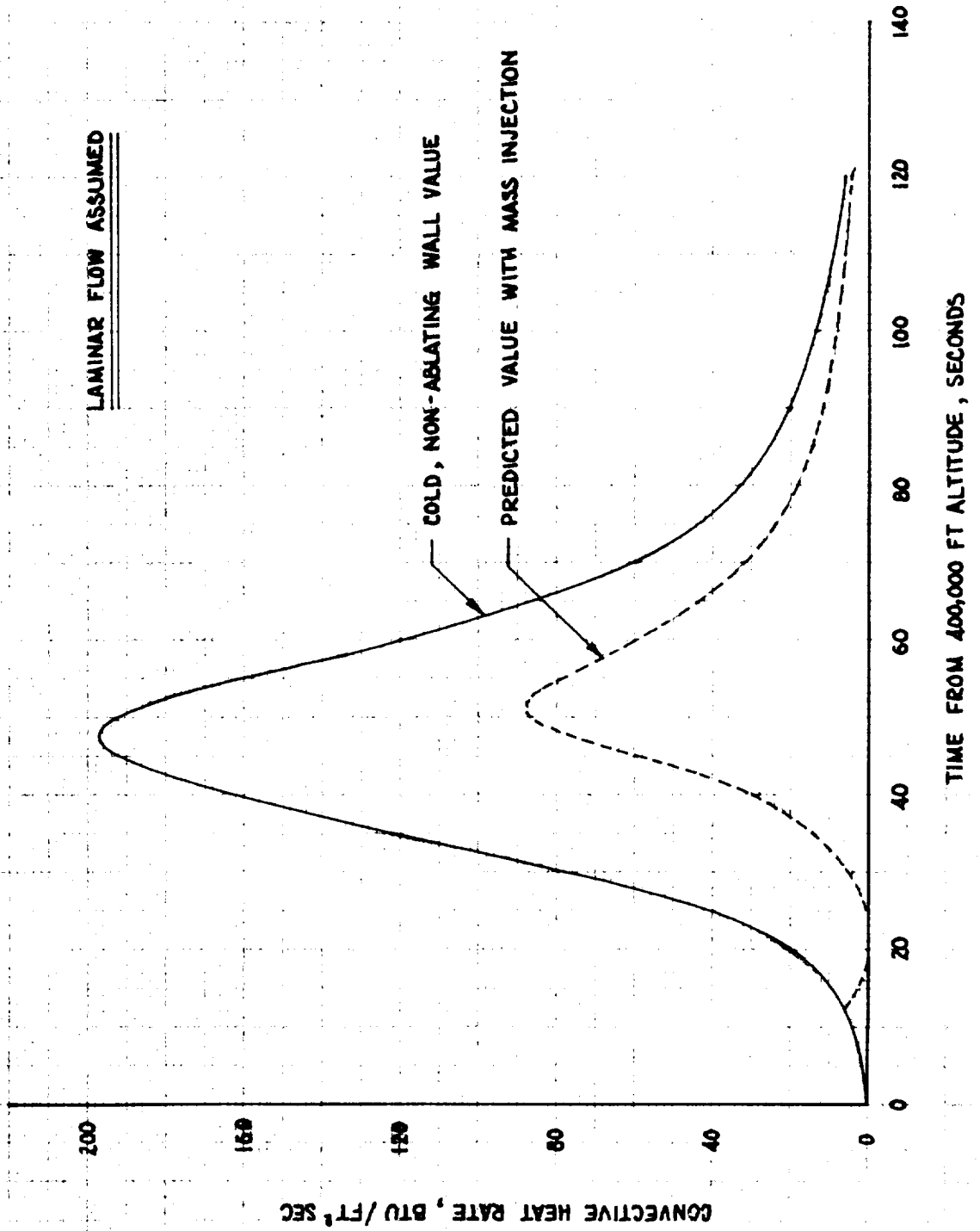




FIGURE 2-59

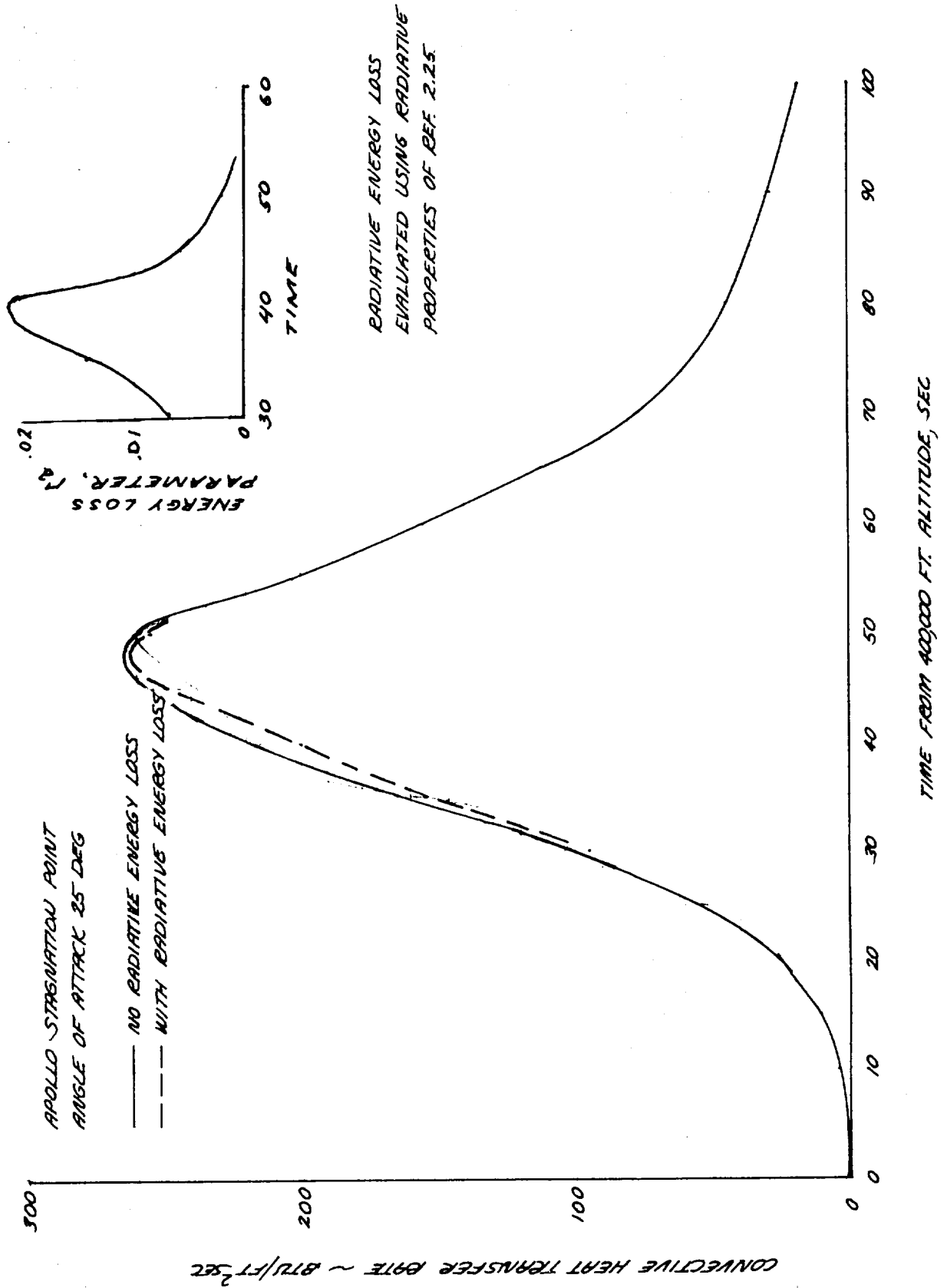
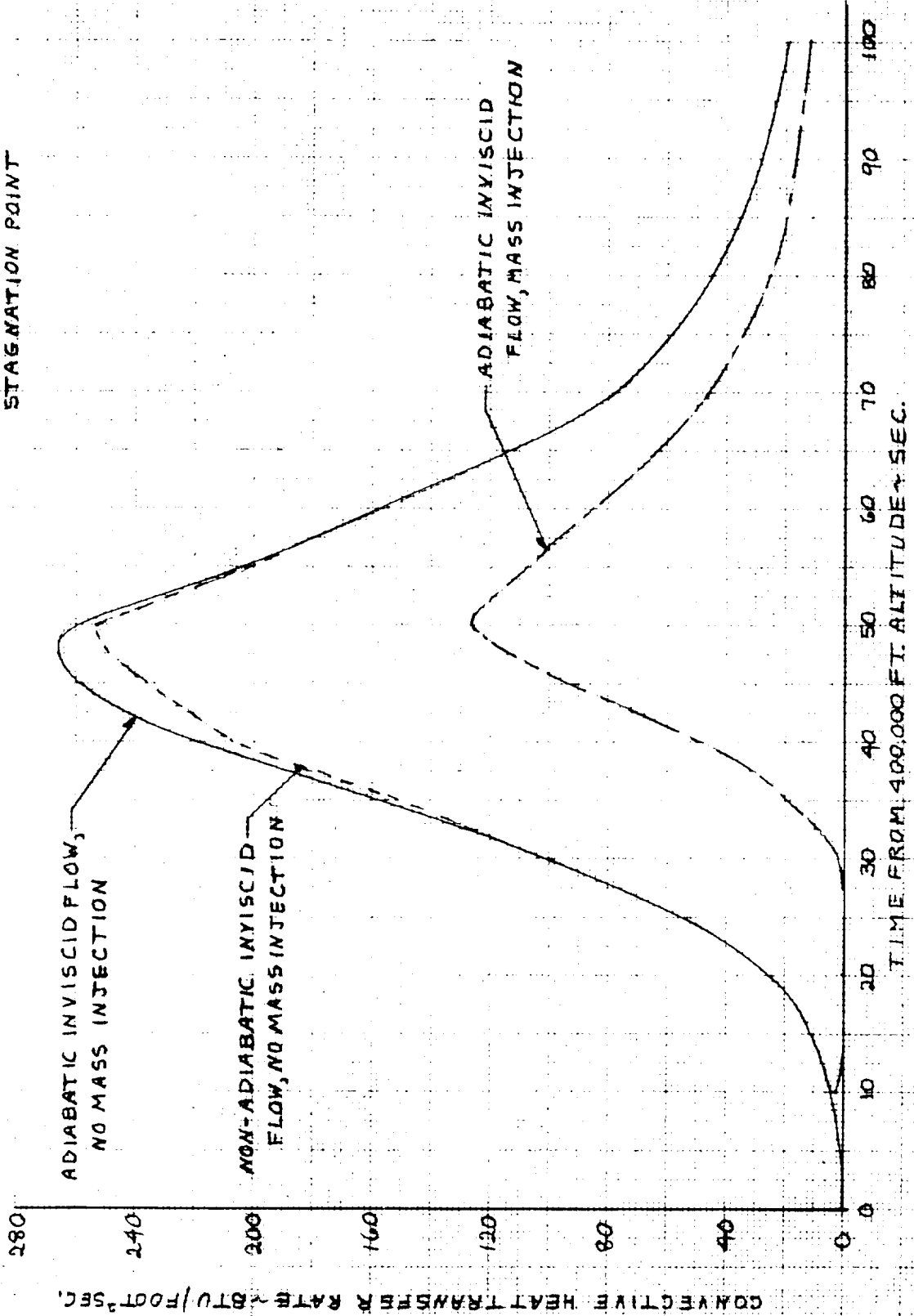


FIGURE 2-60

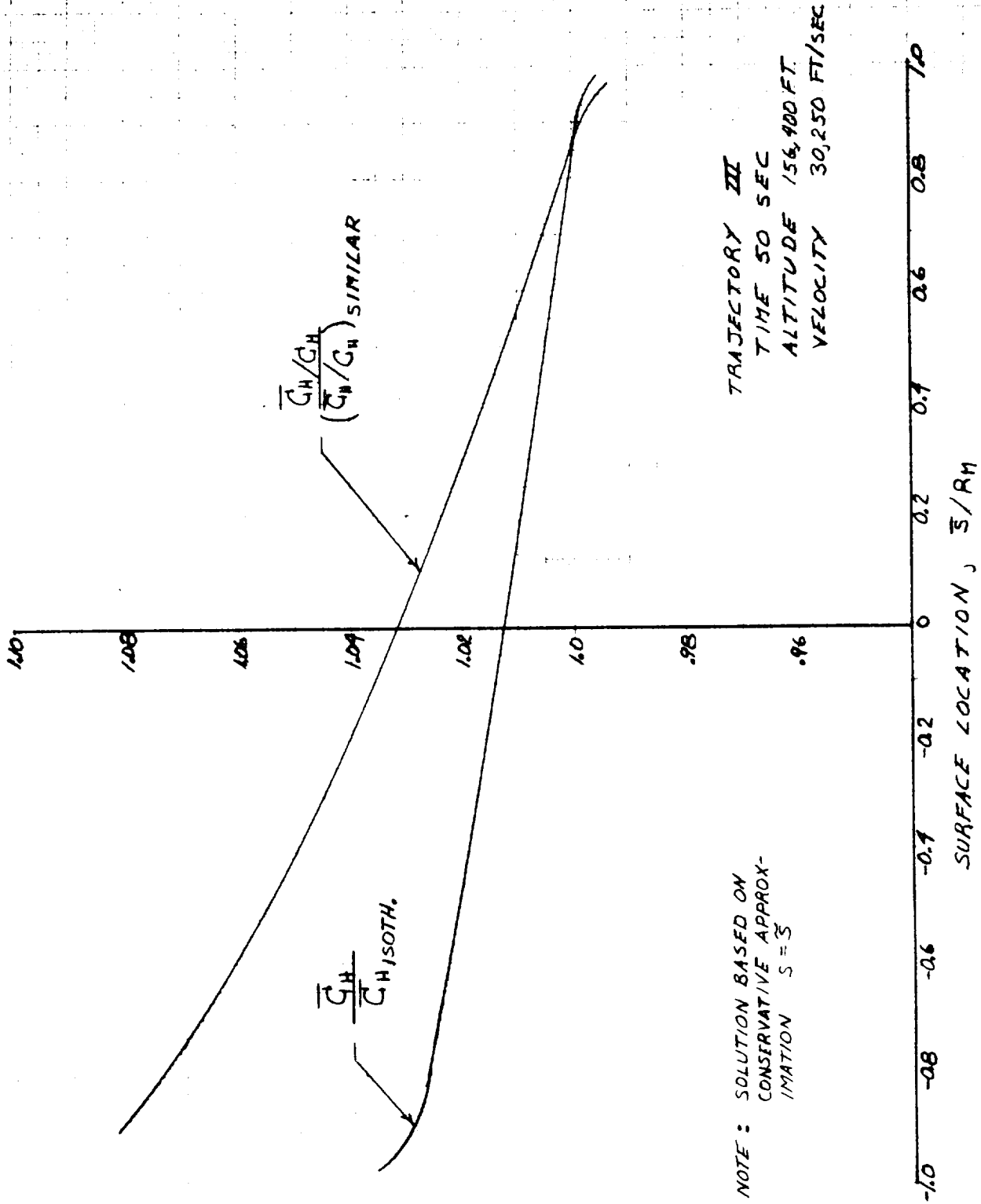
COMPARISON OF THE EFFECTS OF MASS INJECTION AND RADIATIVE ENERGY LOSS ON APOLLO HEATING

TRAJECTORY III  
STAGNATION POINT



832-2

FIGURE 2-61  
 INFLUENCE OF NON-SIMILAR WALL CONDITIONS ON  
 APOLLO HEATING



2-239

FIGURE 2-6E  
COMPARISON OF LAMINAR AND TURBULENT HEAT  
TRANSFER RATES FOR APOLLO

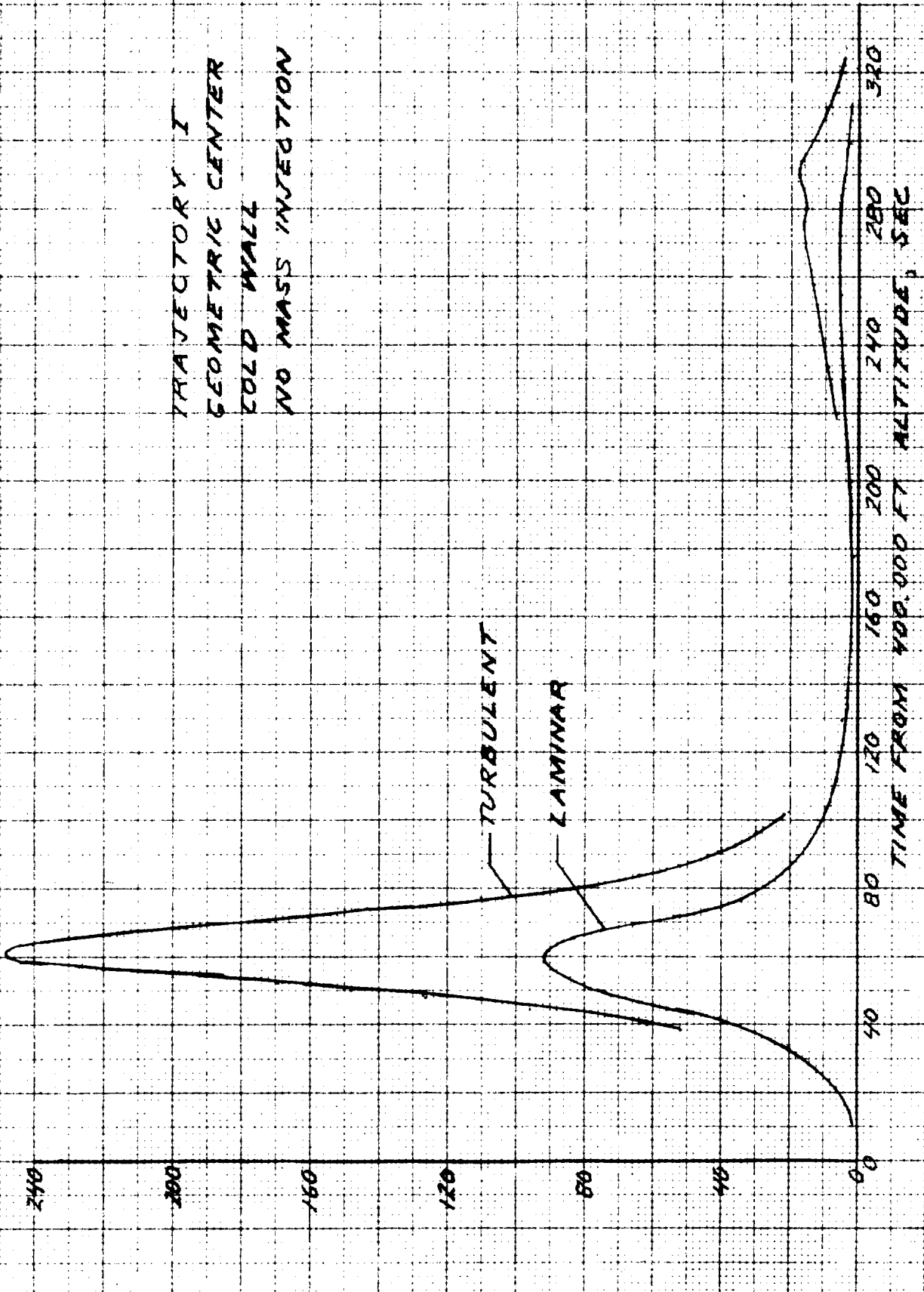


FIGURE 2-68  
 TURBULENCE PATTERN FOR SEVERAL ASSUMED  
 TRANSITION REYNOLDS NUMBERS

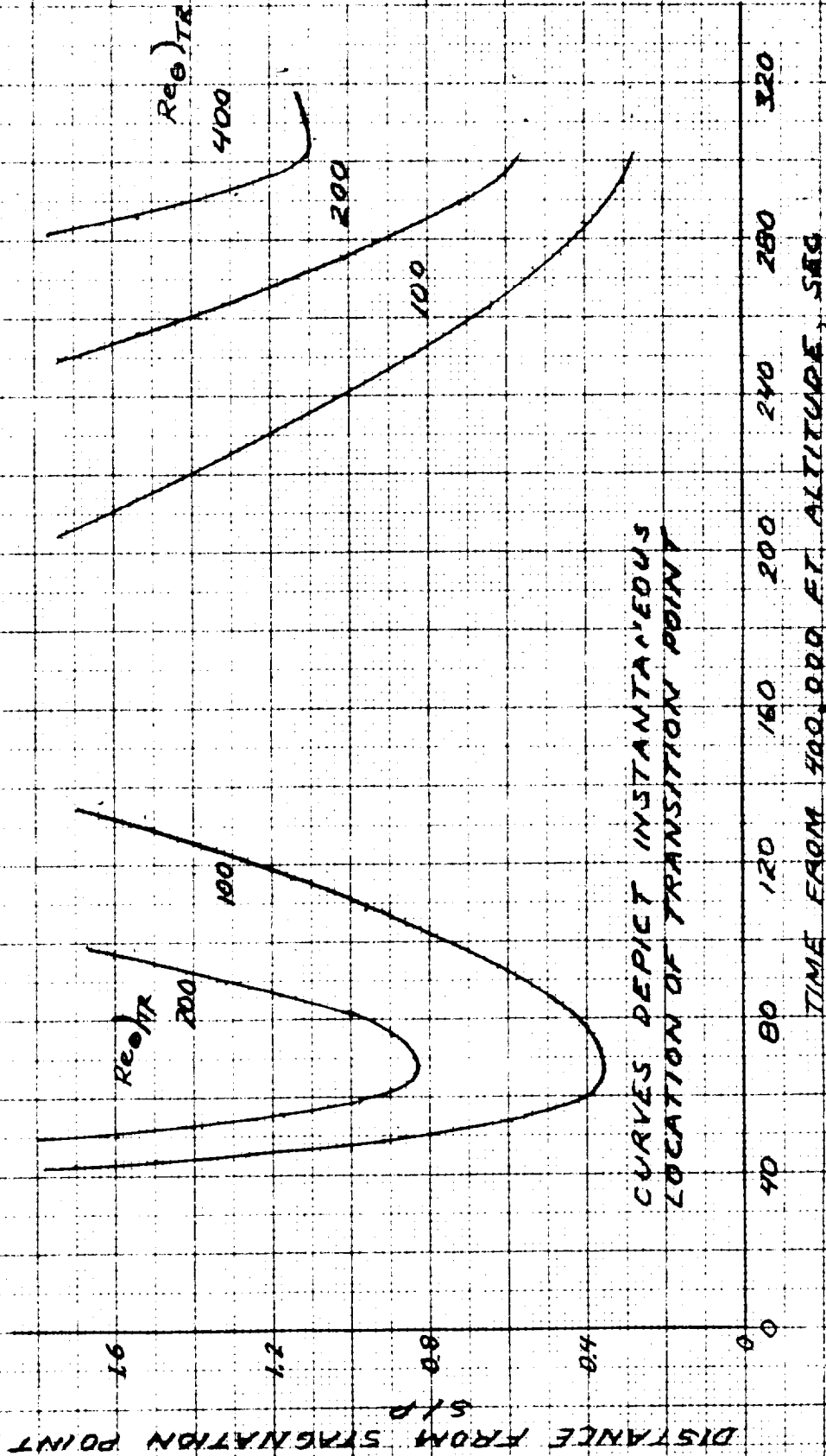


FIGURE 2-64  
 INFLUENCE OF TRANSITION CRITERION  
 ON TOTAL HEAT TRANSFER

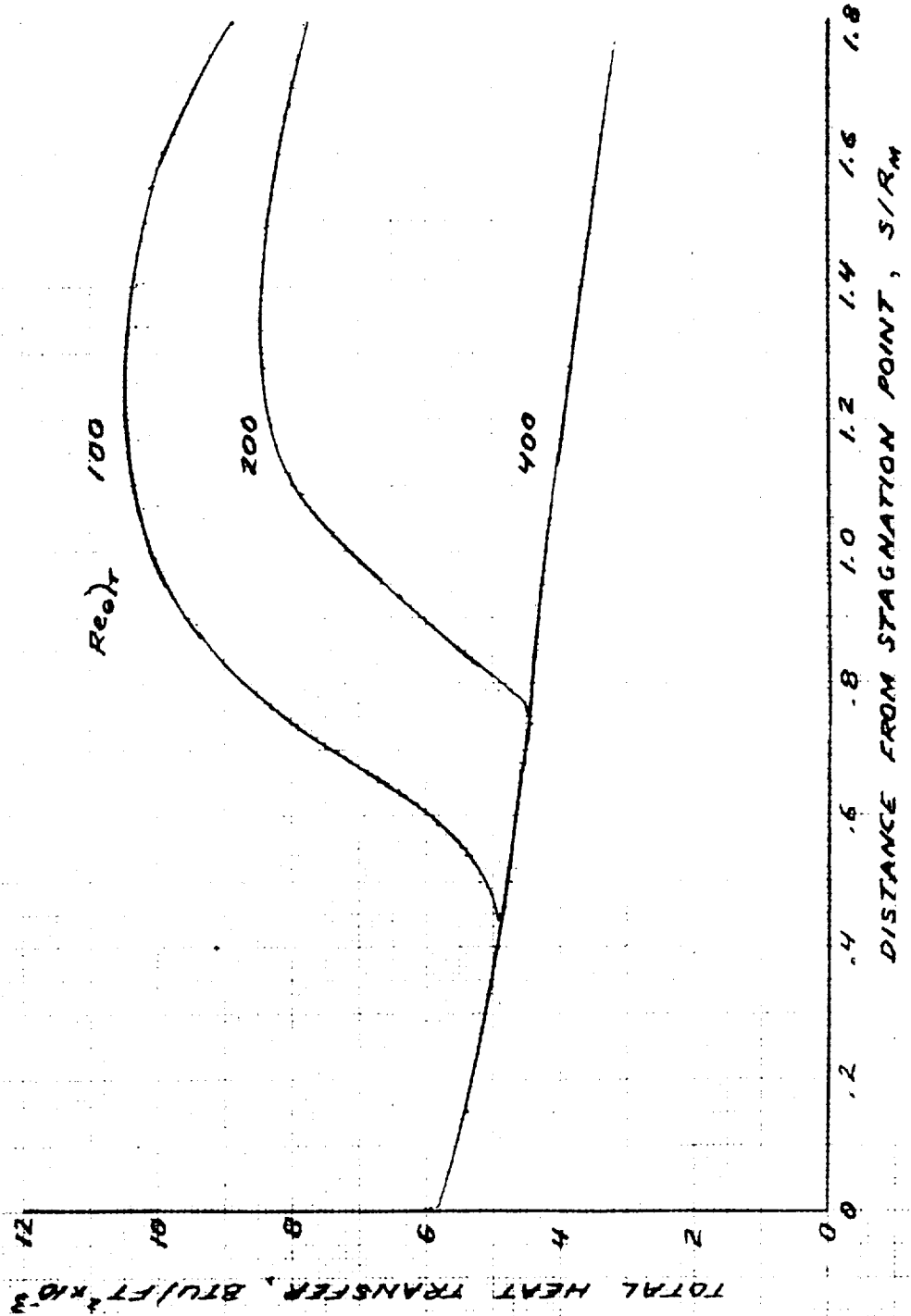


FIGURE 2-65 VARIATION OF TRANSITION REYNOLDS NUMBER WITH LOCAL MACH NUMBER

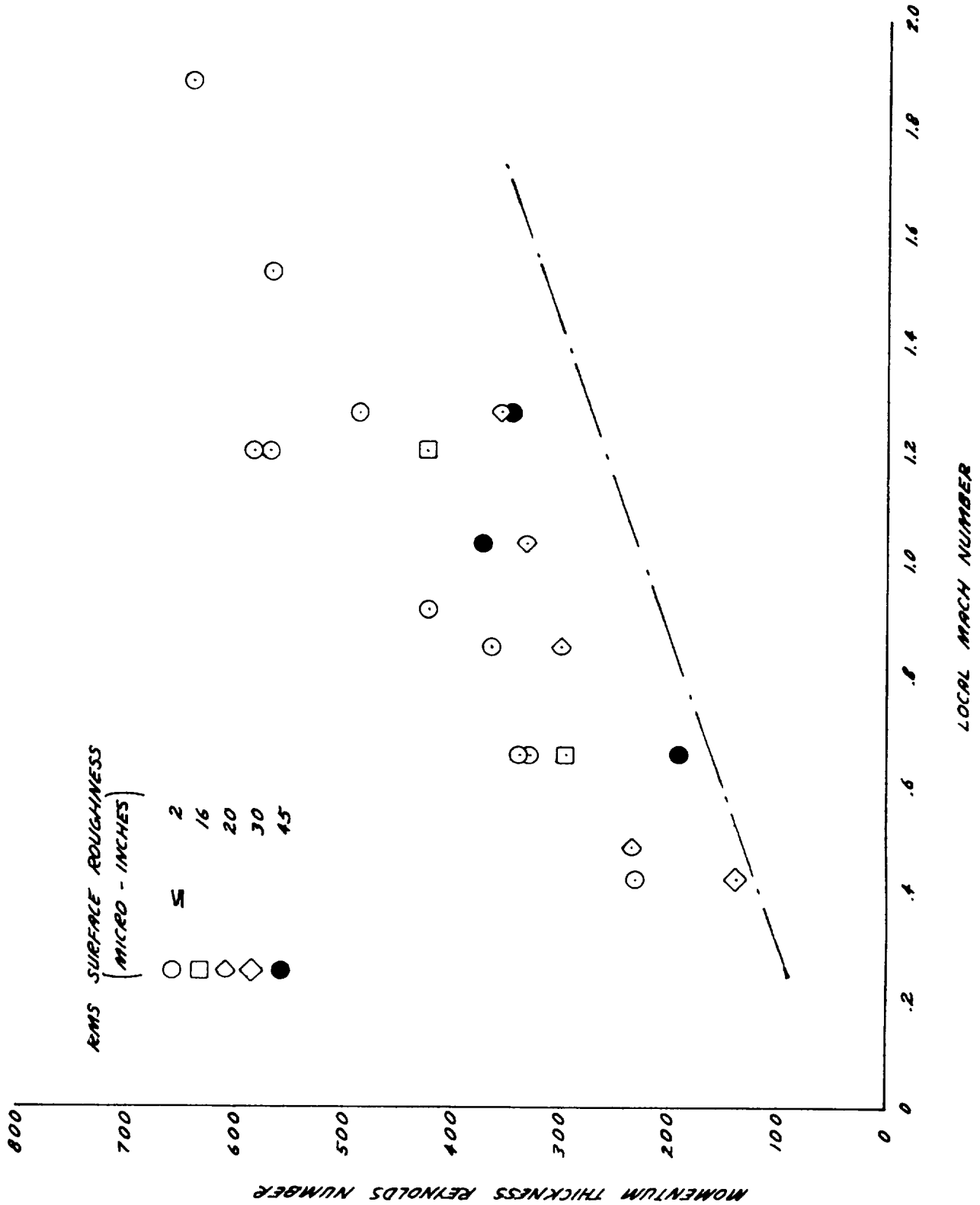


FIGURE 2-66  
 TRANSPIRATION UNCERTAINTY

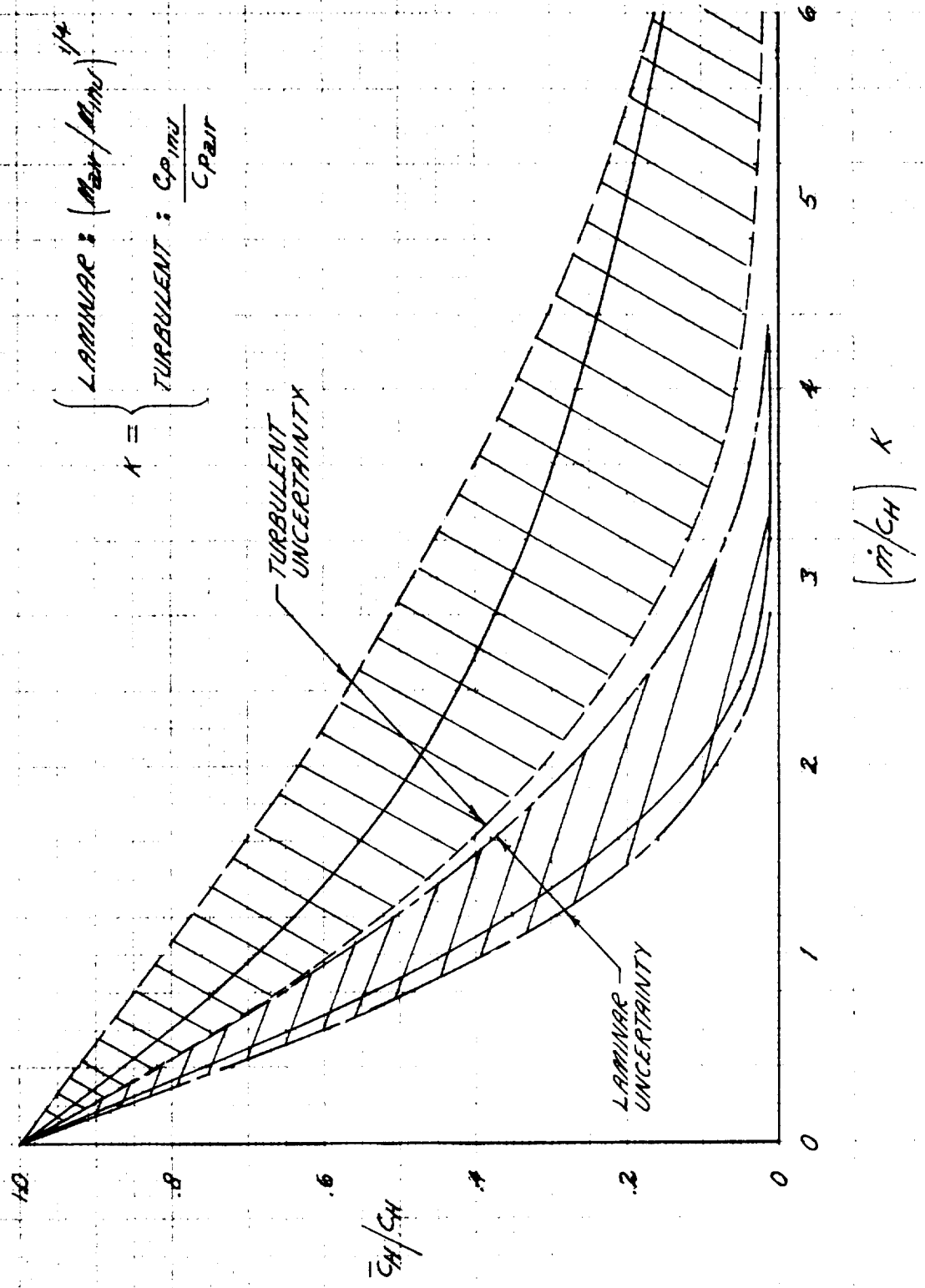
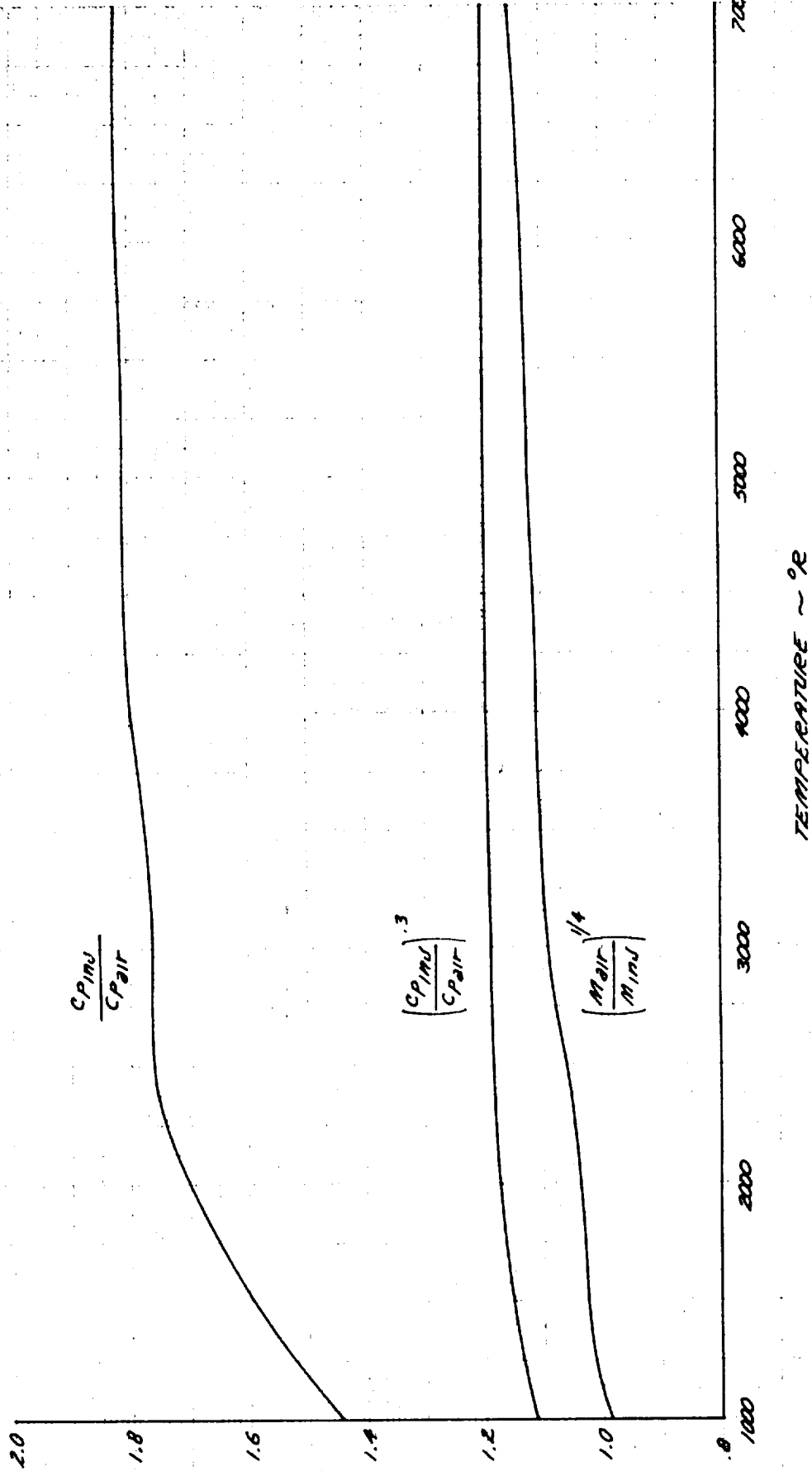




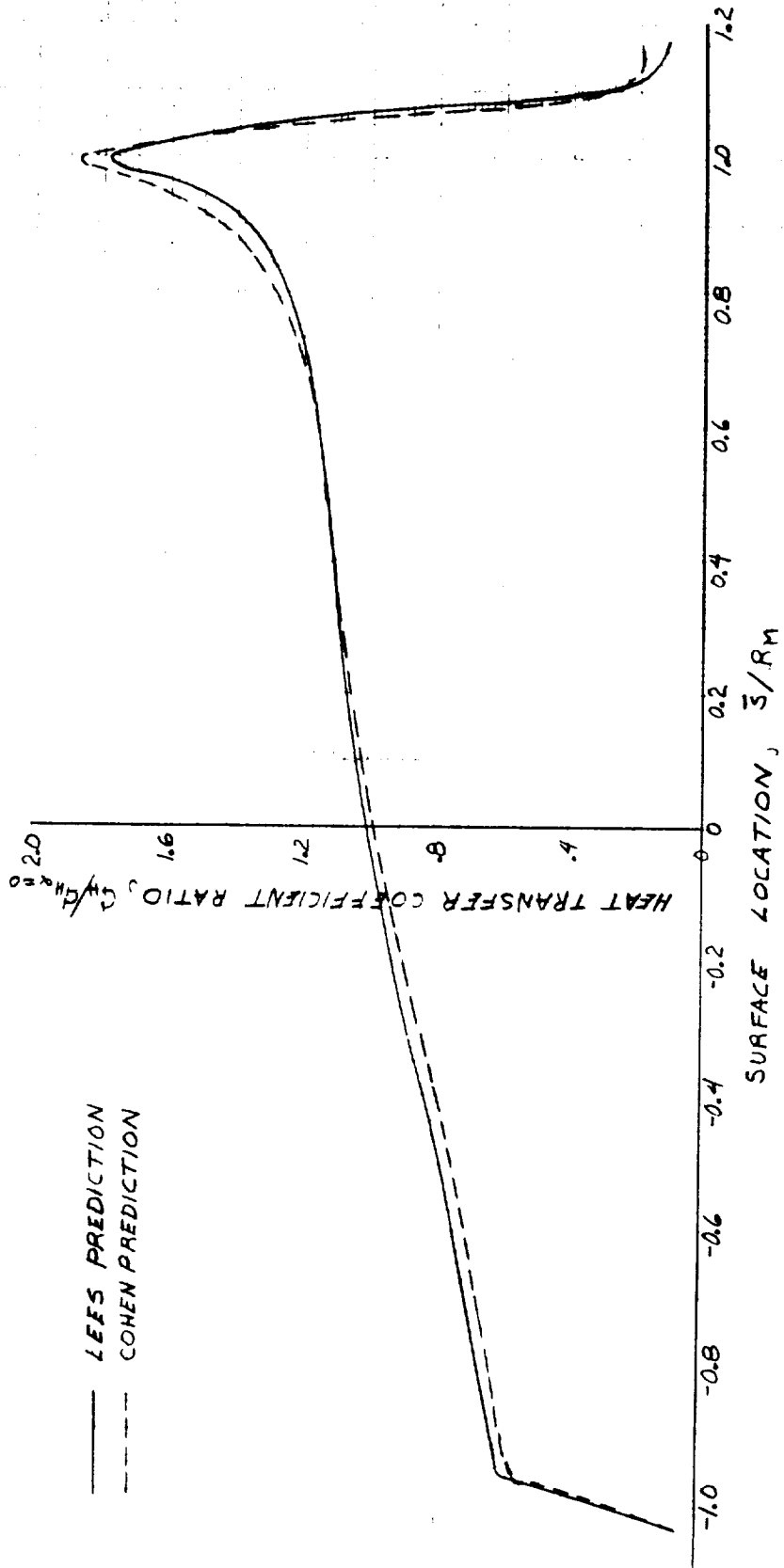
FIGURE 2-67  
**CORRELATING FUNCTIONS FOR FOREIGN GAS INJECTION**



2-245

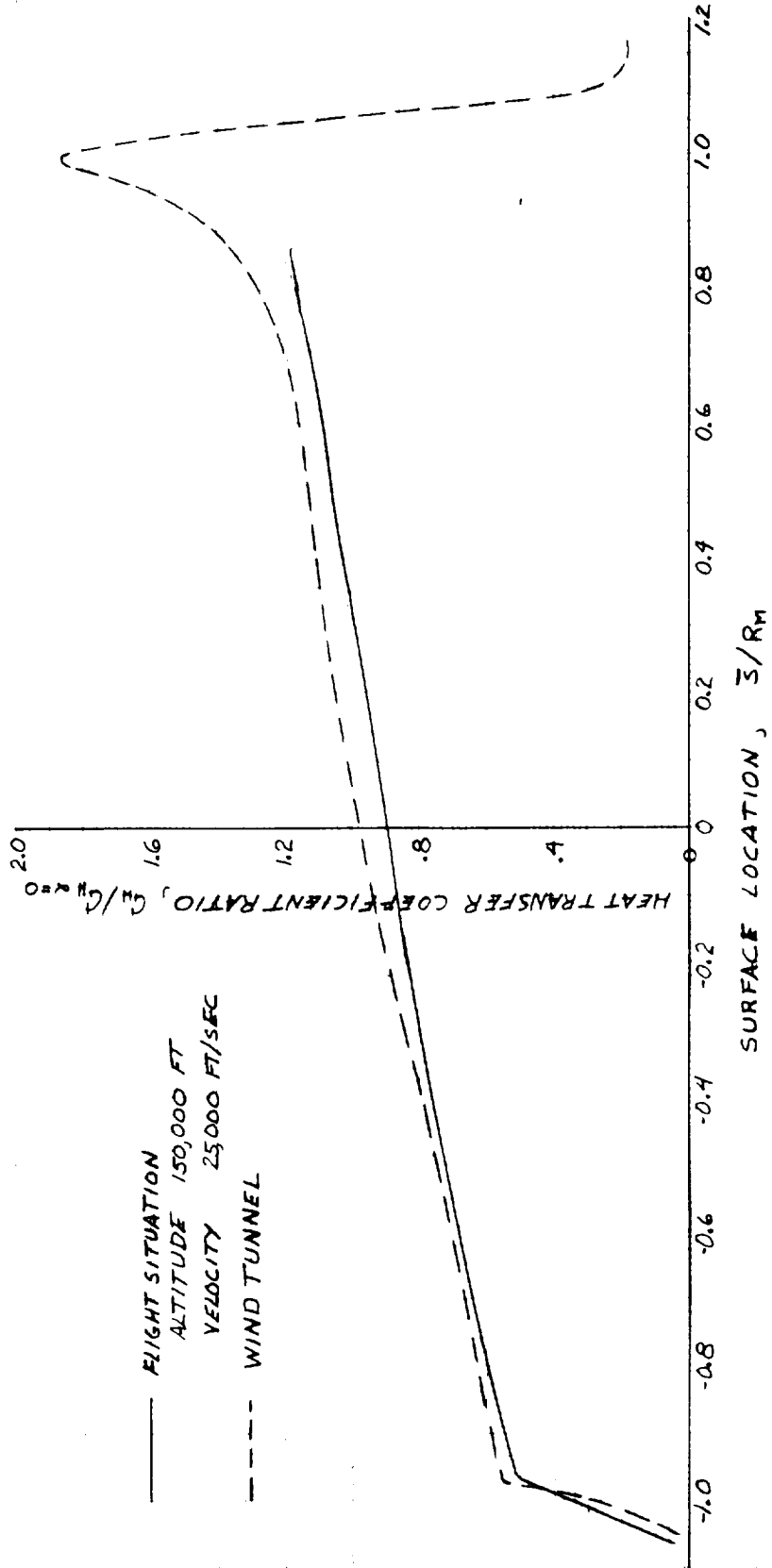
FIGURE 2-68

PREDICTED LAMINAR HEATING DISTRIBUTION  
FOR APOLLO AT WIND TUNNEL CONDITIONS



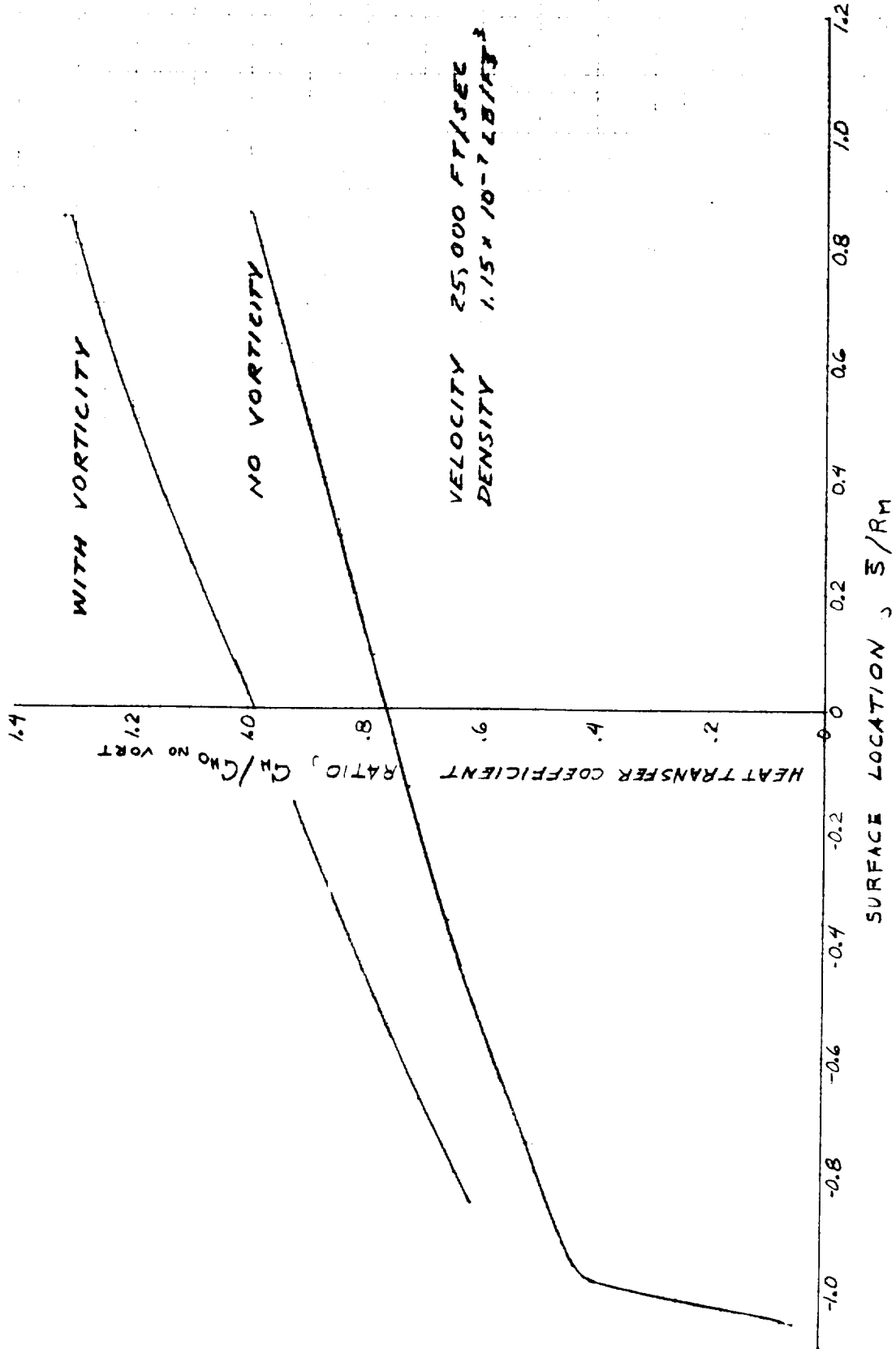
2-246

FIGURE 2-69  
INFLUENCE OF FLIGHT CONDITIONS ON LAMINAR  
HEAT TRANSFER DISTRIBUTION



2-247

FIGURE 2-70  
 INFLUENCE OF SHOCK GENERATED VORTICITY  
 ON THE HEAT TRANSFER DISTRIBUTION



2-248

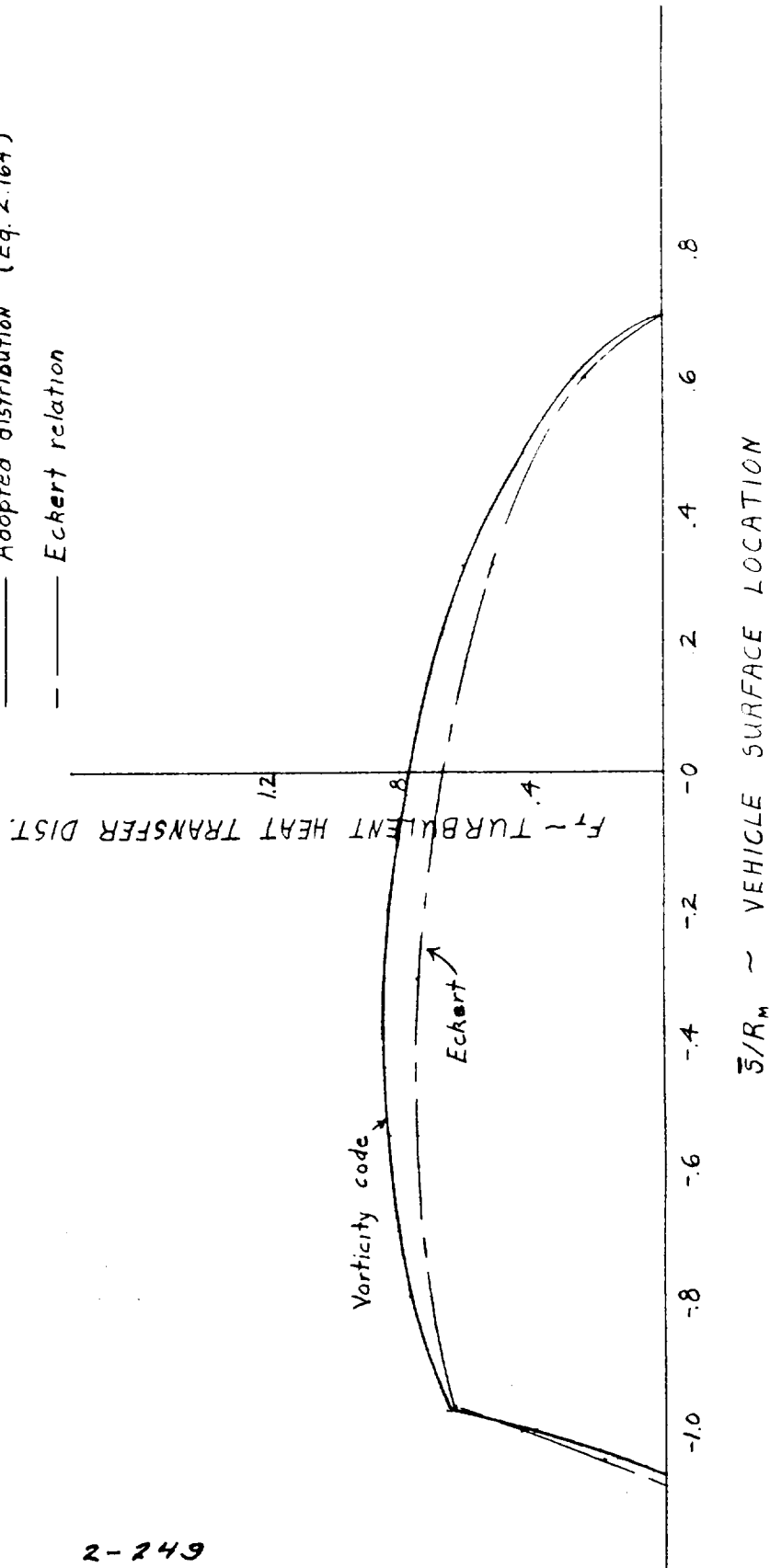
Prepared	NAME	DATE	LOCKHEED MISSILES & SPACE COMPANY A GROUP DIVISION OF LOCKHEED AIRCRAFT CORPORATION	Page	TEMP.	PERM.
Checked			TITLE	Model		
Approved				Report No.		

FIGURE 2-71

PREDICTED TURBULENT HEAT TRANSFER DISTRIBUTION FOR APOLLO AT WIND TUNNEL CONDITIONS

$$F_{T, Eckert} = 1.02 \frac{(\rho_0 u_0)^{0.8} \mu_0^{0.2} / (S/R_m)^{0.2}}{(\rho_0 \theta_0)^{0.4} \mu_0^{0.2}}$$

— Adopted distribution (Eq. 2.164)  
 - - - Eckert relation



2-249

FIGURE 2-72  
INFLUENCE OF FLIGHT CONDITIONS ON TURBULENT HEAT TRANSFER DISTRIBUTION

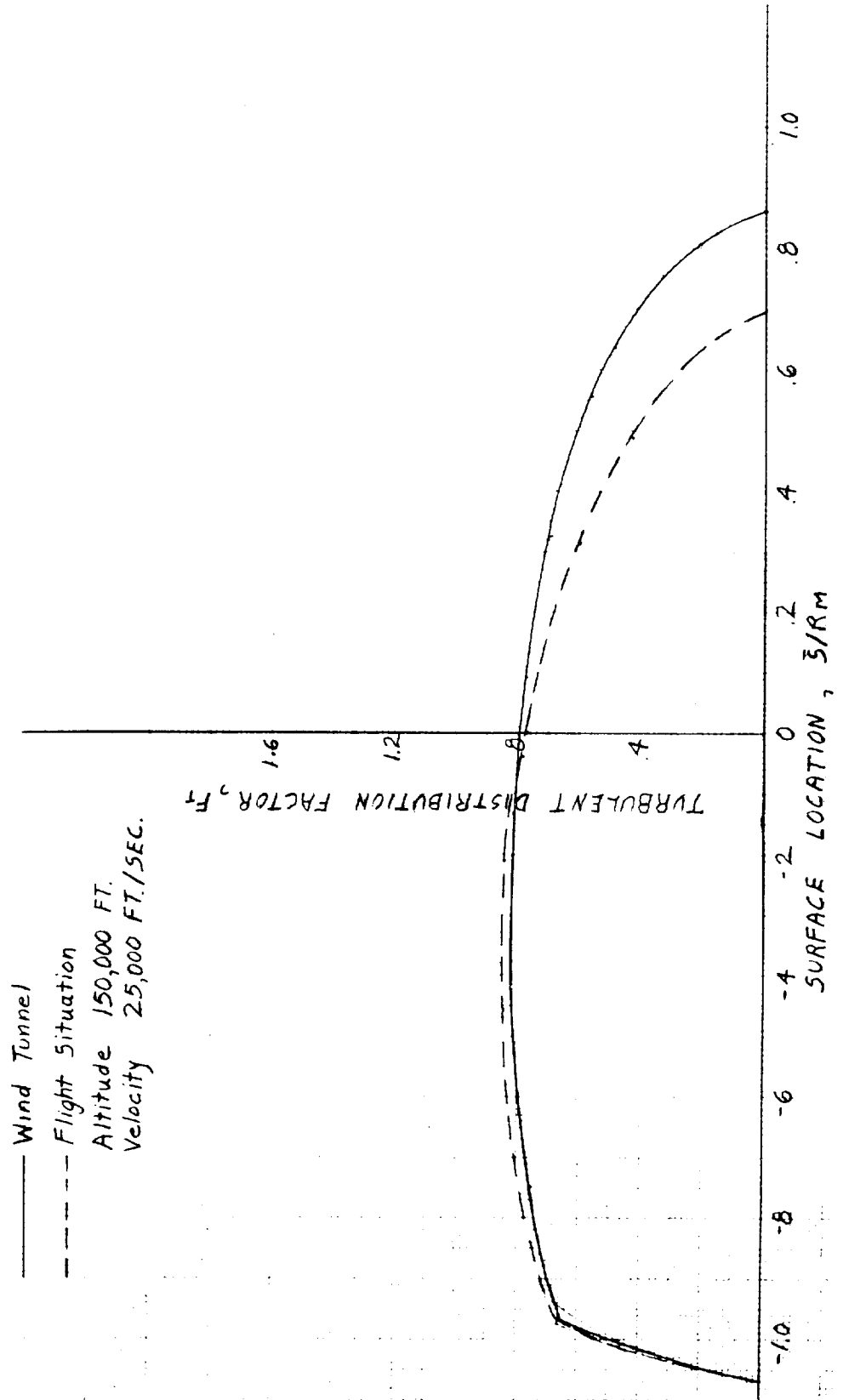
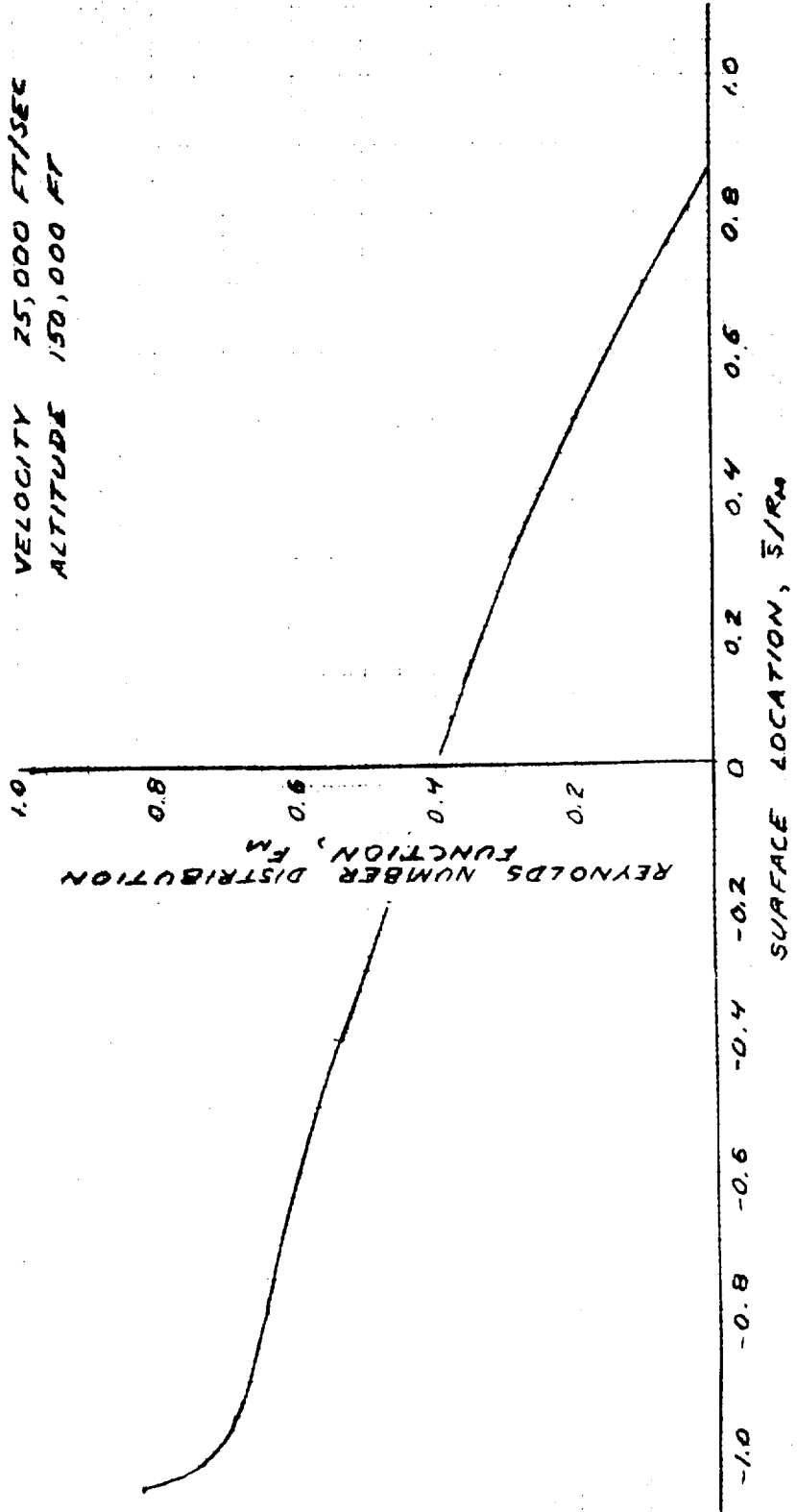


FIGURE 2-73

MOMENTUM-THICKNESS REYNOLDS-NUMBER  
DISTRIBUTION FACTOR FOR APOLLO

VELOCITY 25,000 FT/SEC  
ALTITUDE 150,000 FT



2-251

FIGURE 2-74  
TRANSITION SENSITIVITY TO ALTITUDE

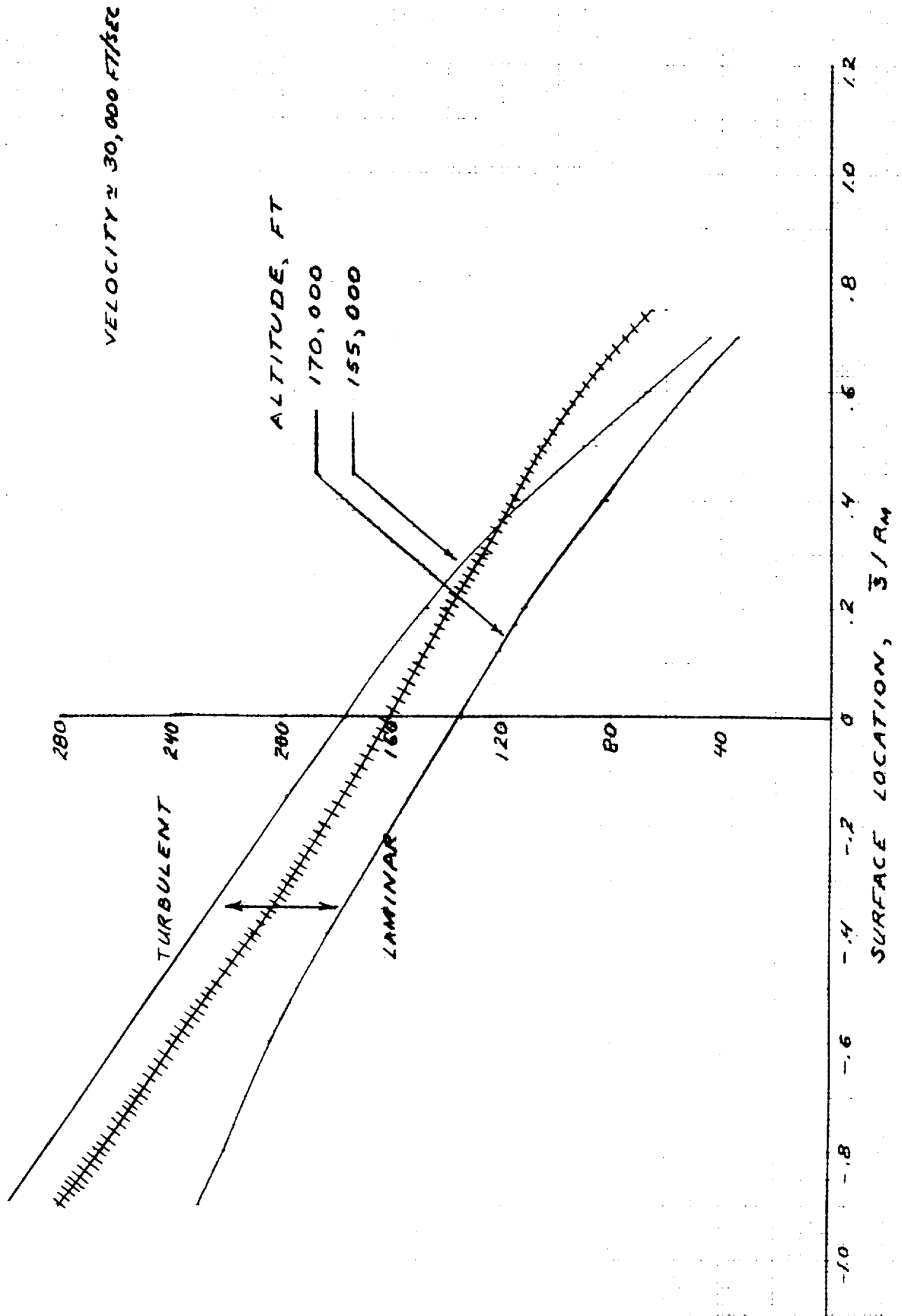




FIGURE R-75  
EMPIRICAL PRESSURE DISTRIBUTION FOR AFTERBODY  
WINDWARD SIDE

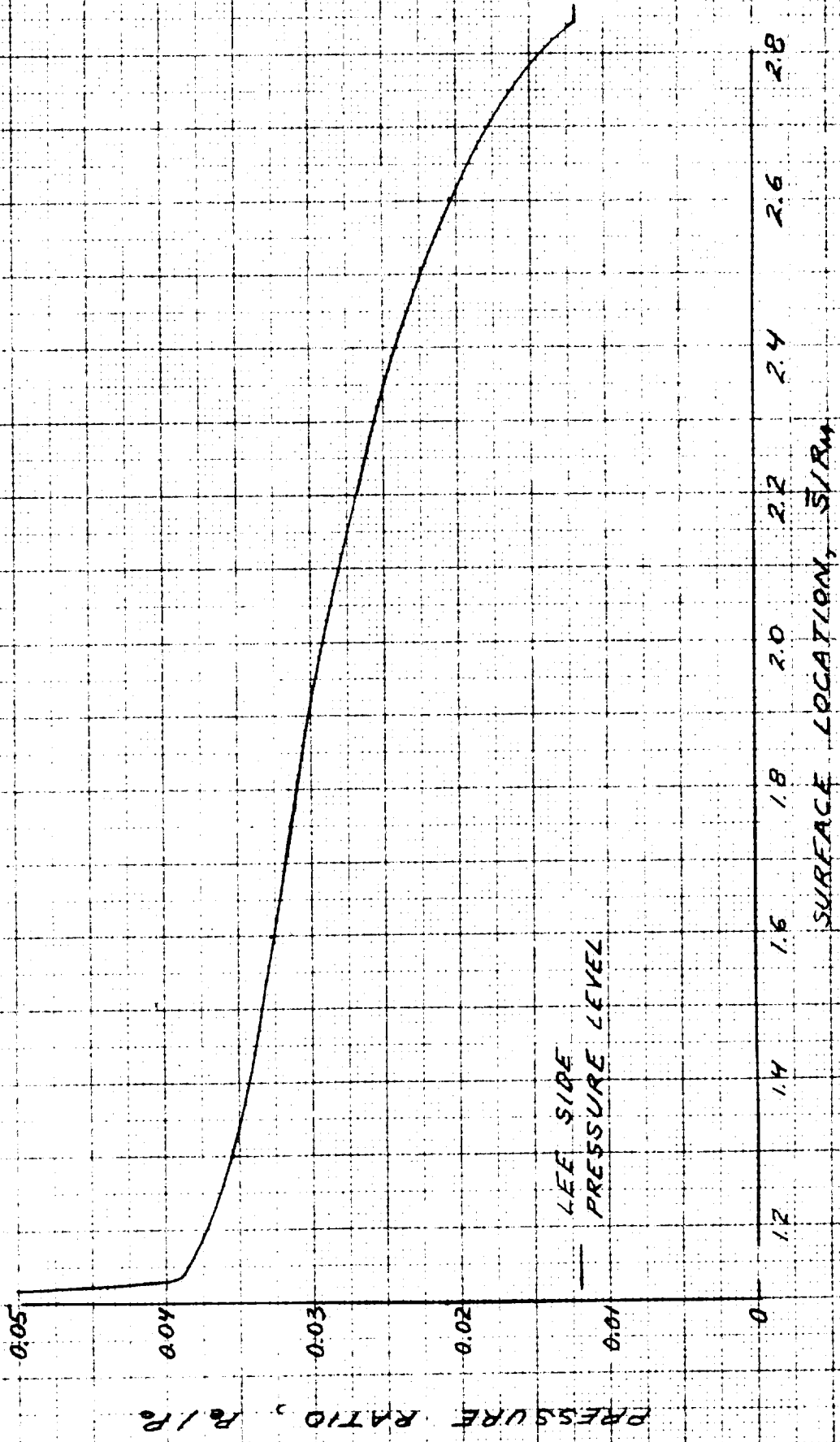
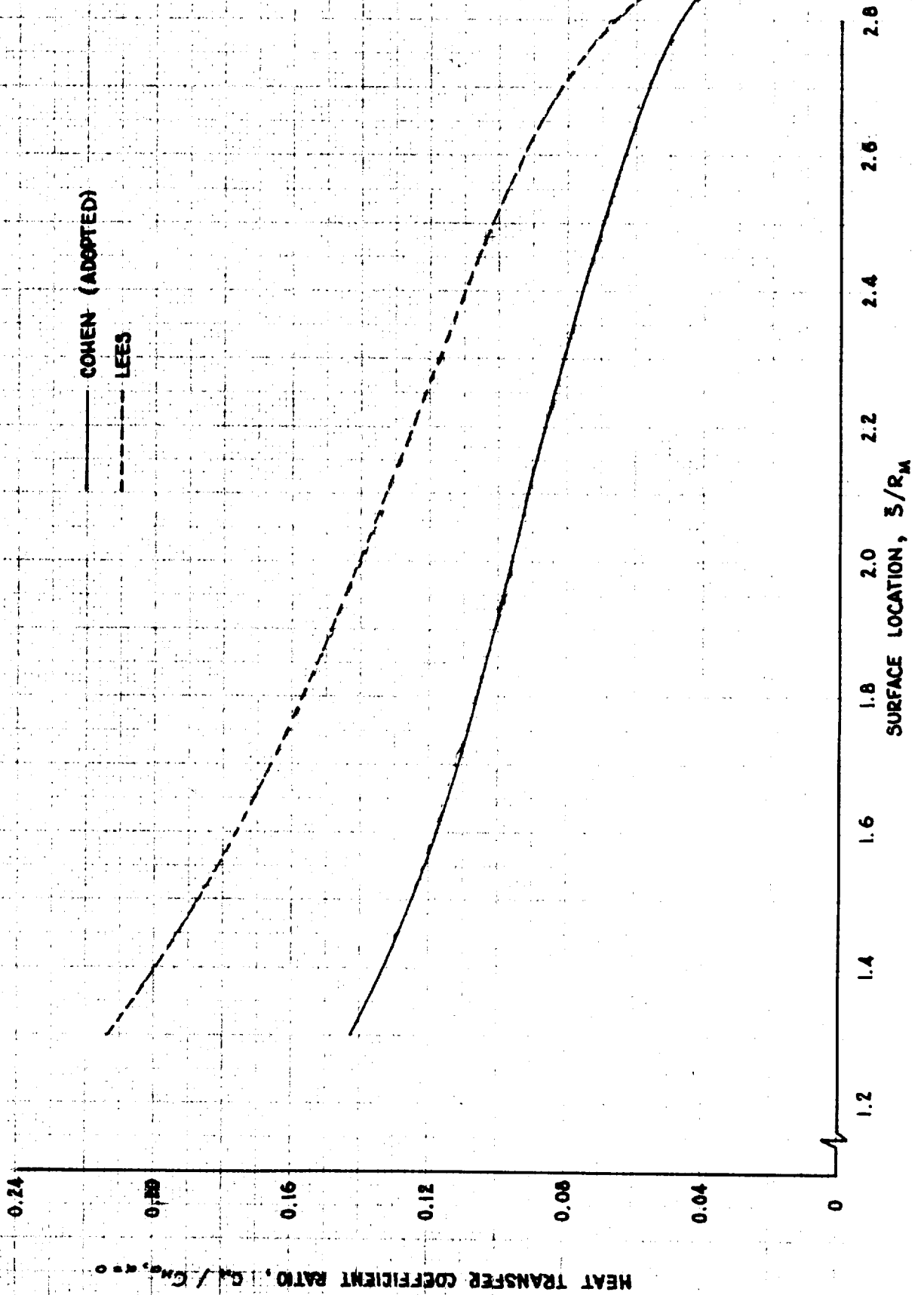


FIGURE 2-76

PREDICTED HEAT TRANSFER DISTRIBUTION OVER APOLLO AFTERBODY



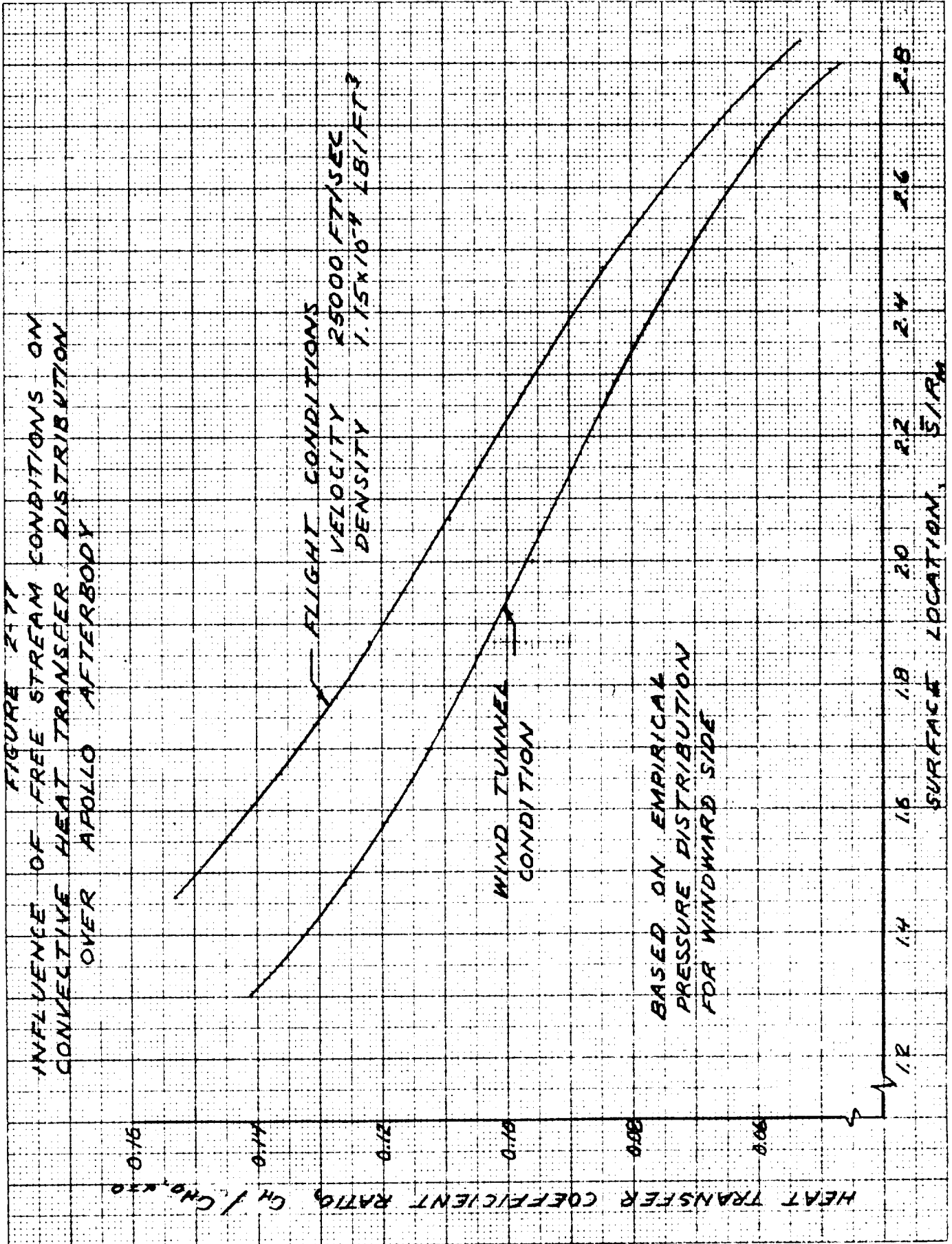


FIGURE 2-78  
 TURBULENT HEAT TRANSFER DISTRIBUTION OVER APOLLO AFTERBODY,  
 WINDWARD SIDE

FLIGHT CONDITIONS  
 VELOCITY 25000 FT/SEC  
 DENSITY  $1.15 \times 10^{-4}$  LB/FT<sup>3</sup>

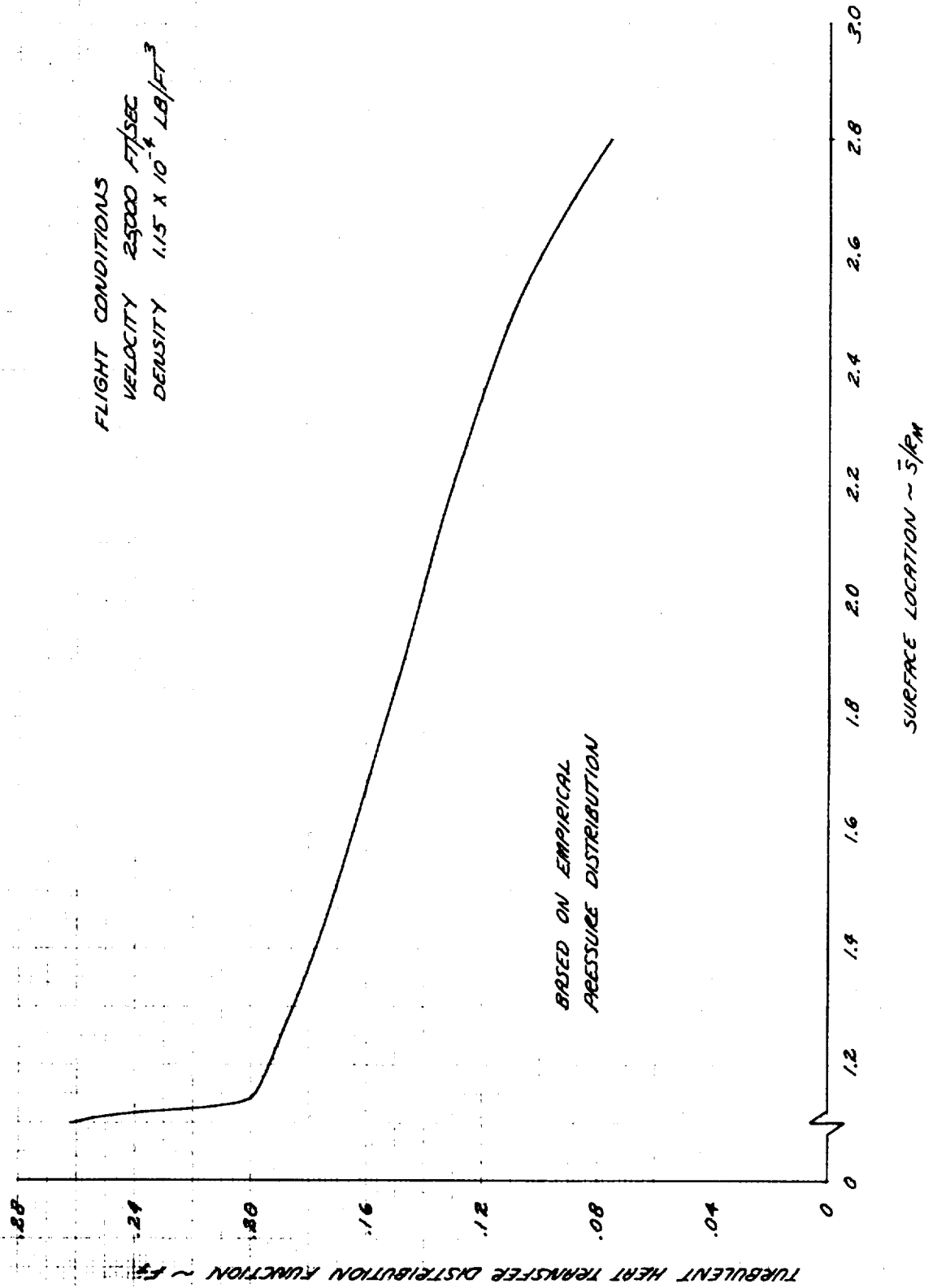


FIGURE 2-79

COMPUTER CODES FOR PREDICTION OF ENVIRONMENT

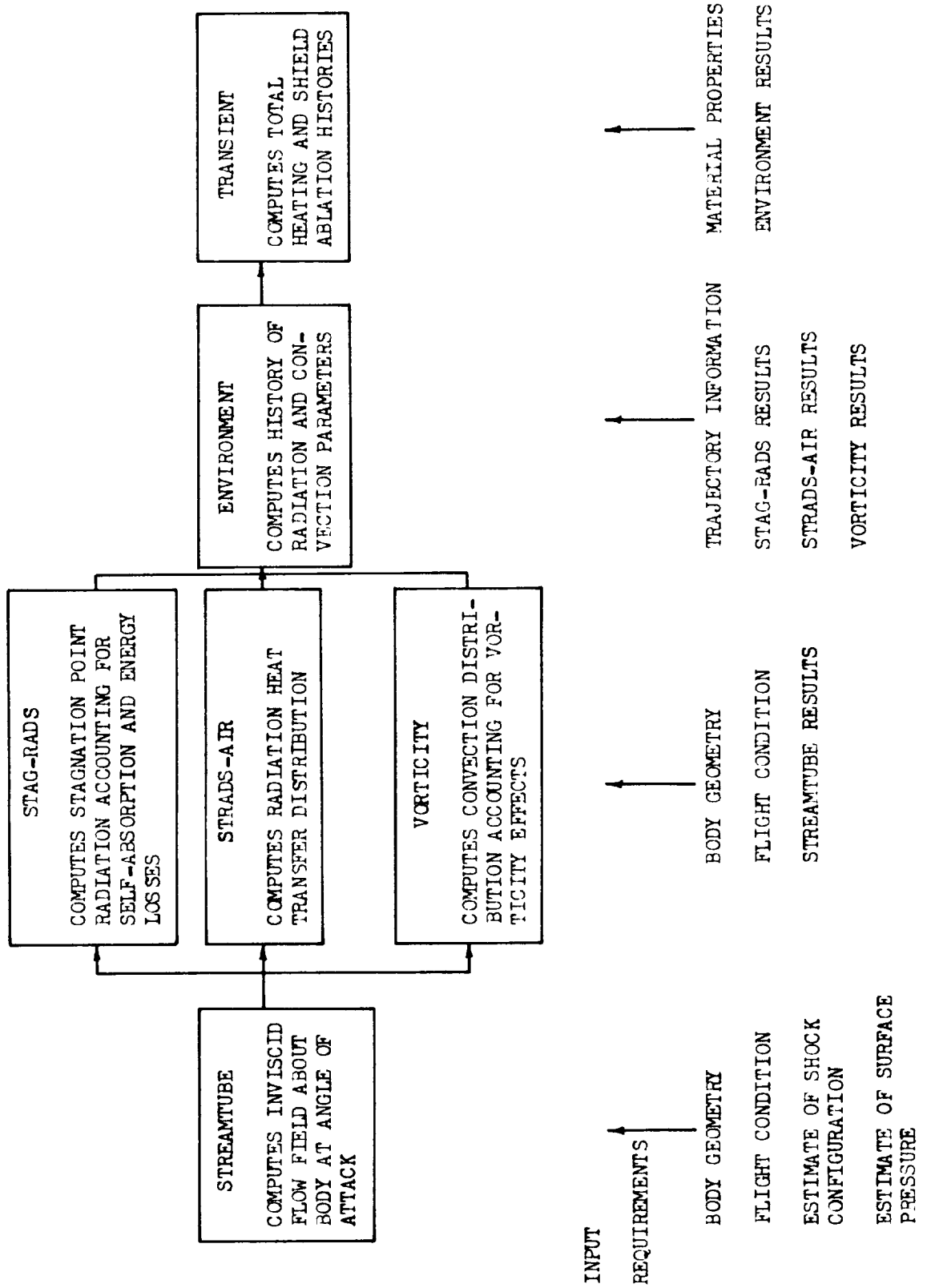


FIGURE 2-80  
INFLUENCE OF ENTRY CONDITION ON APOLLO HEATING  
AT GEOMETRIC CENTER LOCATION

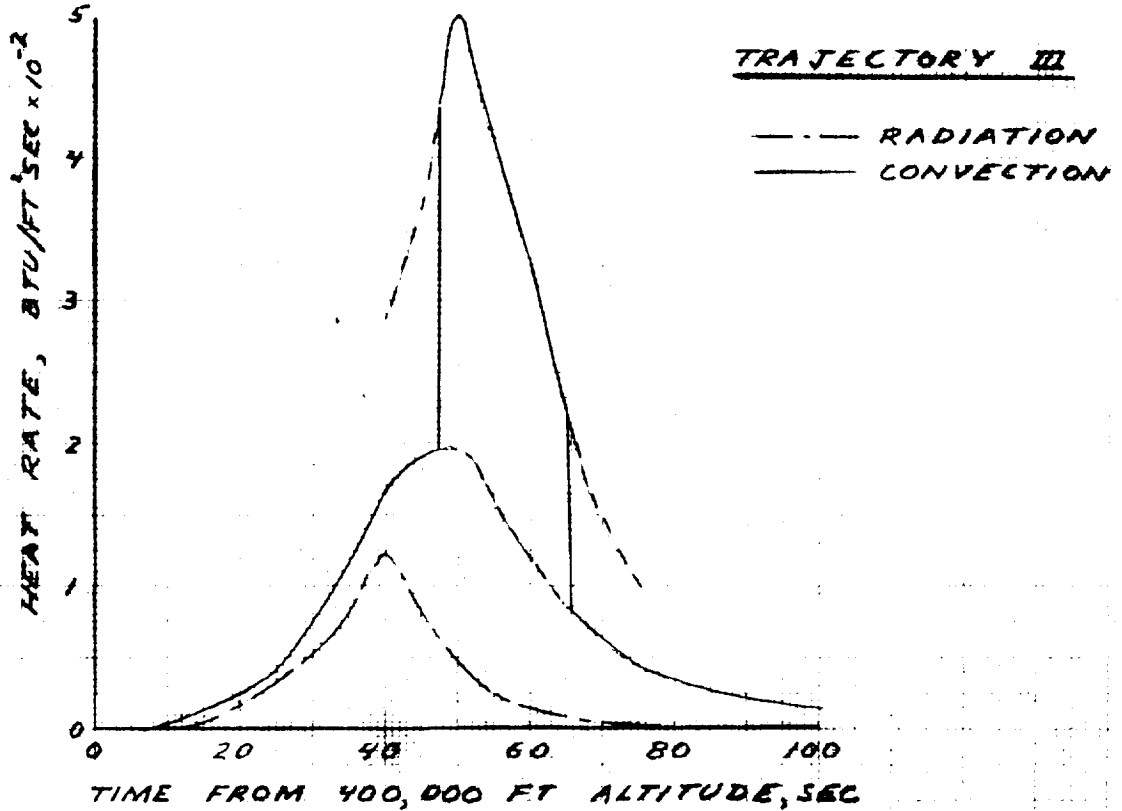
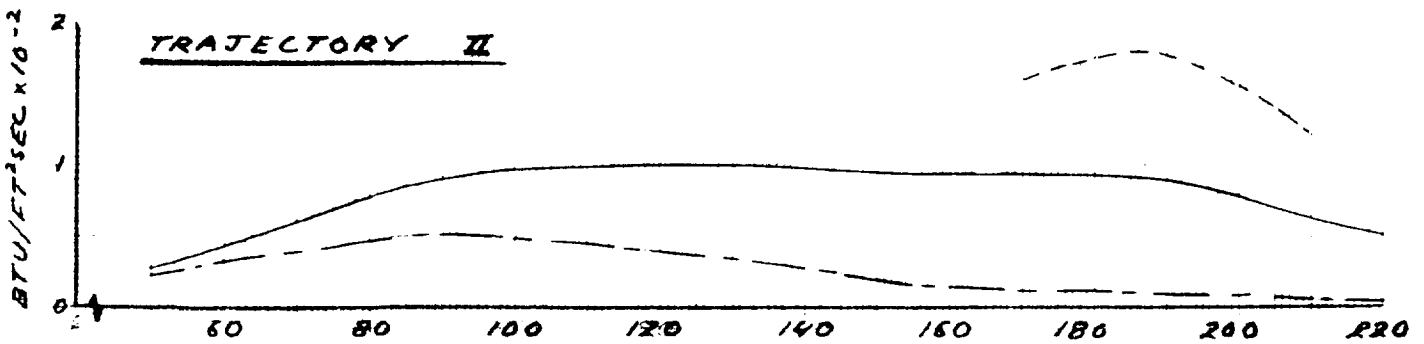
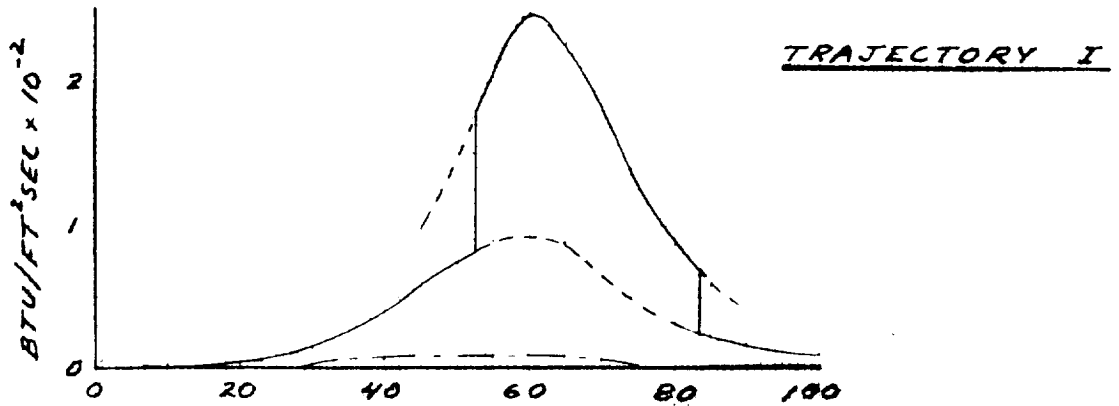
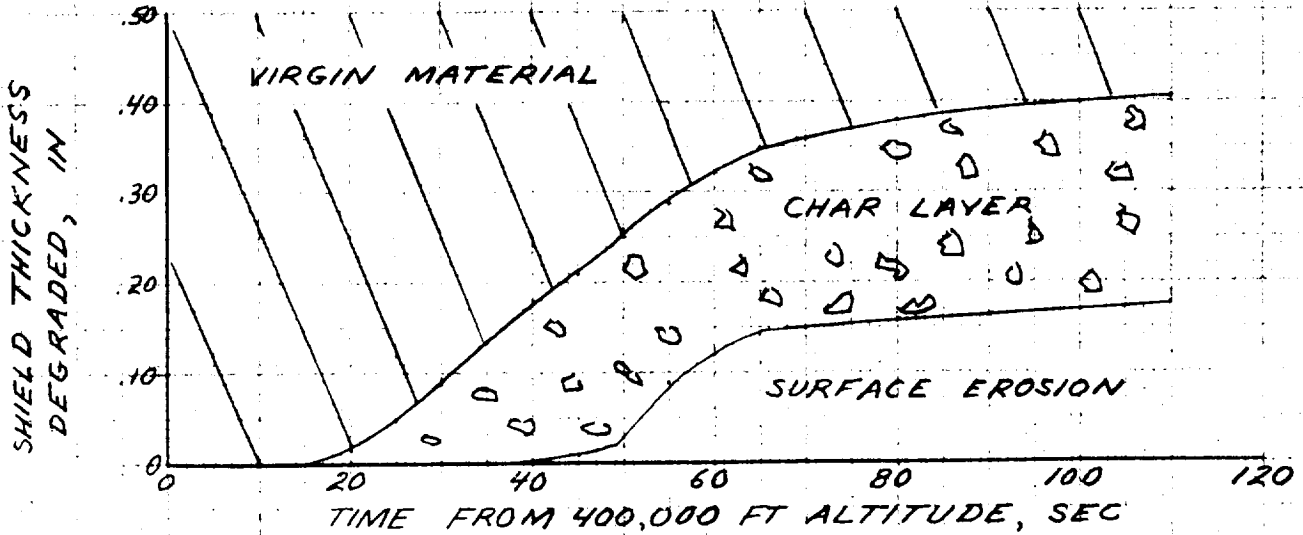
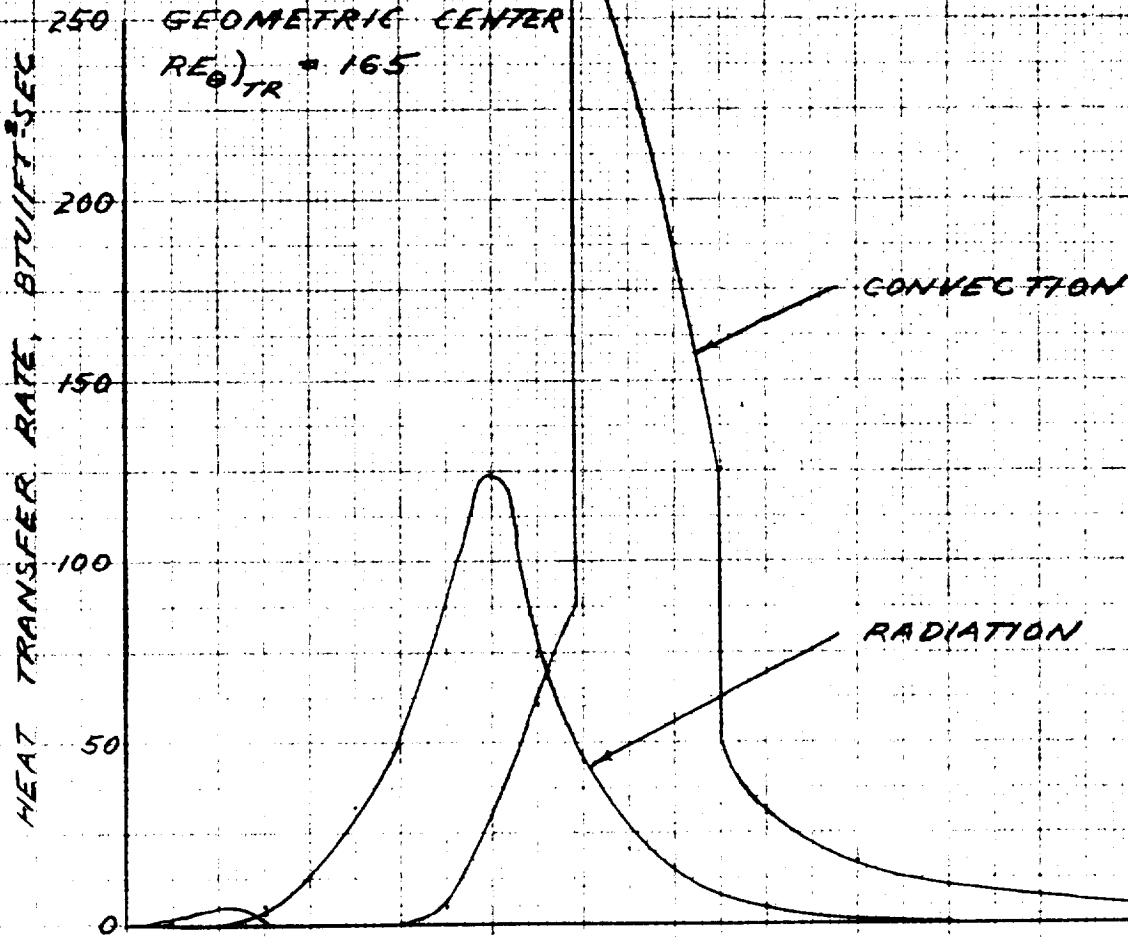
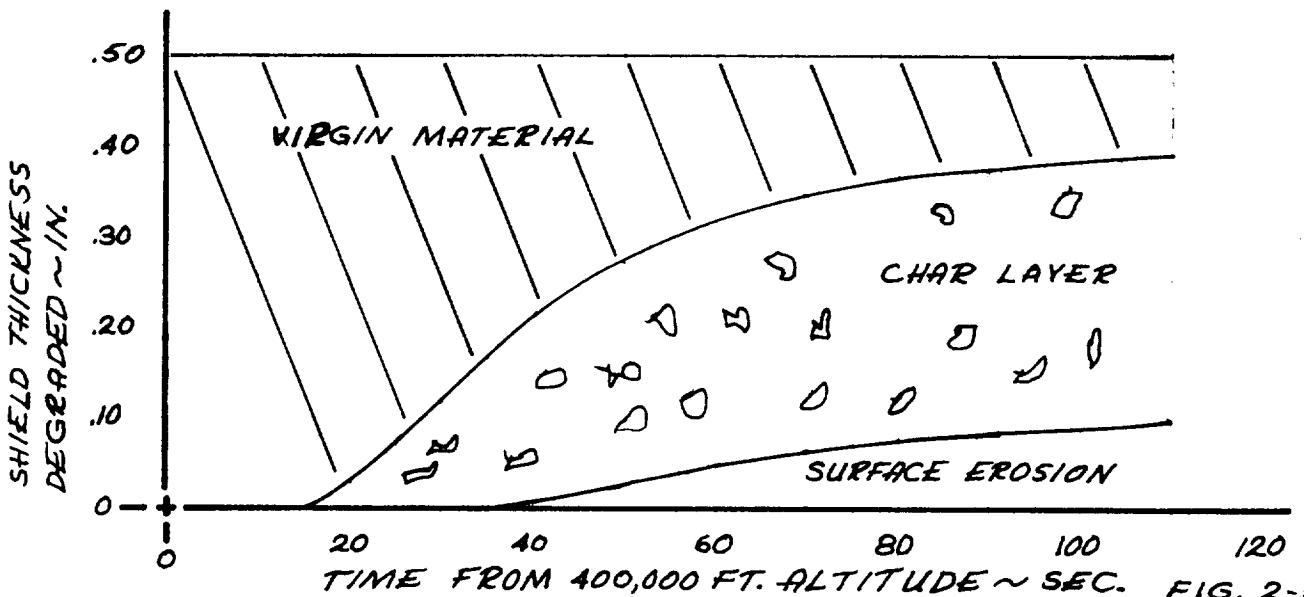
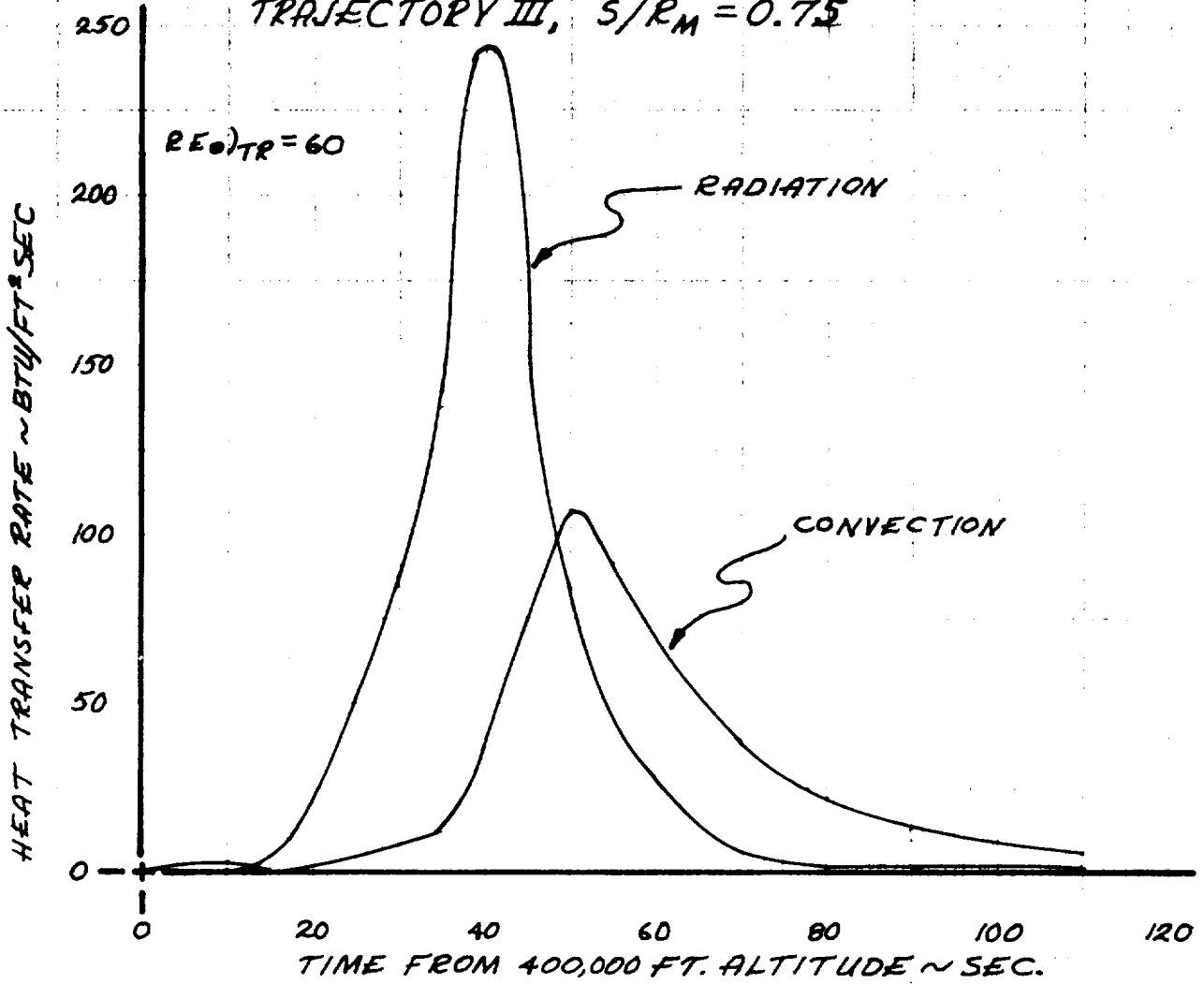


FIG 2-81 HEAT TRANSFER AND SHIELD ABLATION TRAJECTORY III



### HEAT TRANSFER AND SHIELD ABLATION TRAJECTORY III, $\bar{S}/R_M = 0.75$





# HEAT TRANSFER AND SHIELD ABLATION TRAJECTORY III, $S/R_M = -0.96$

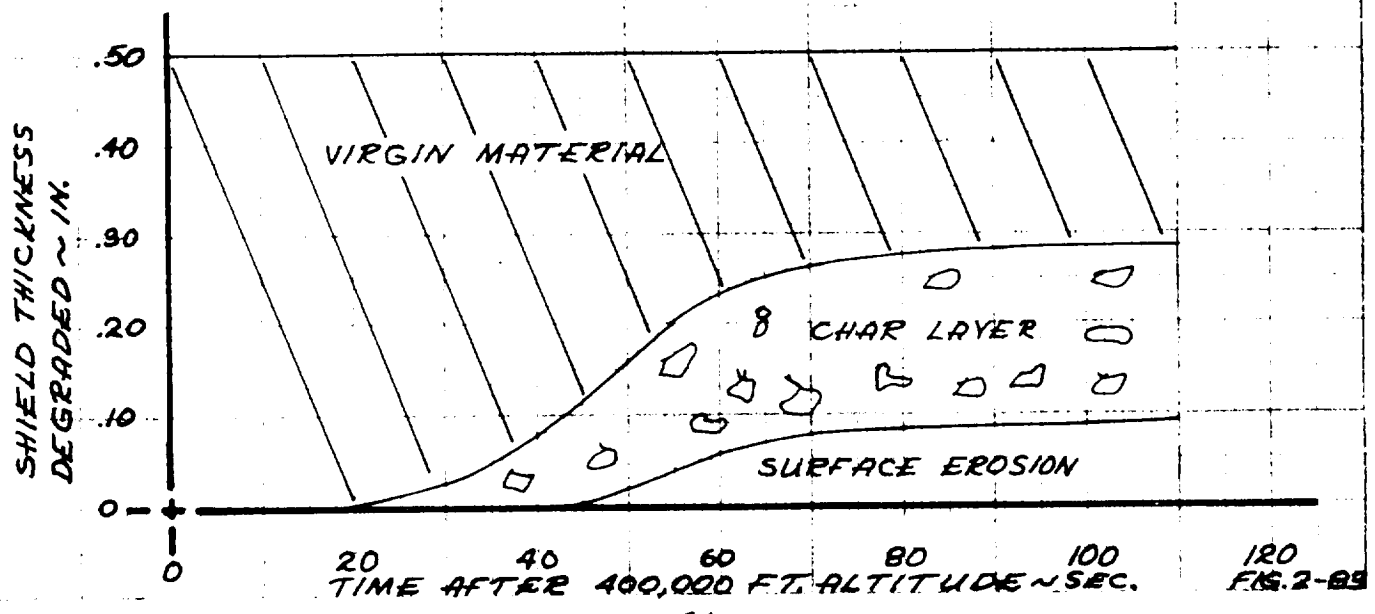
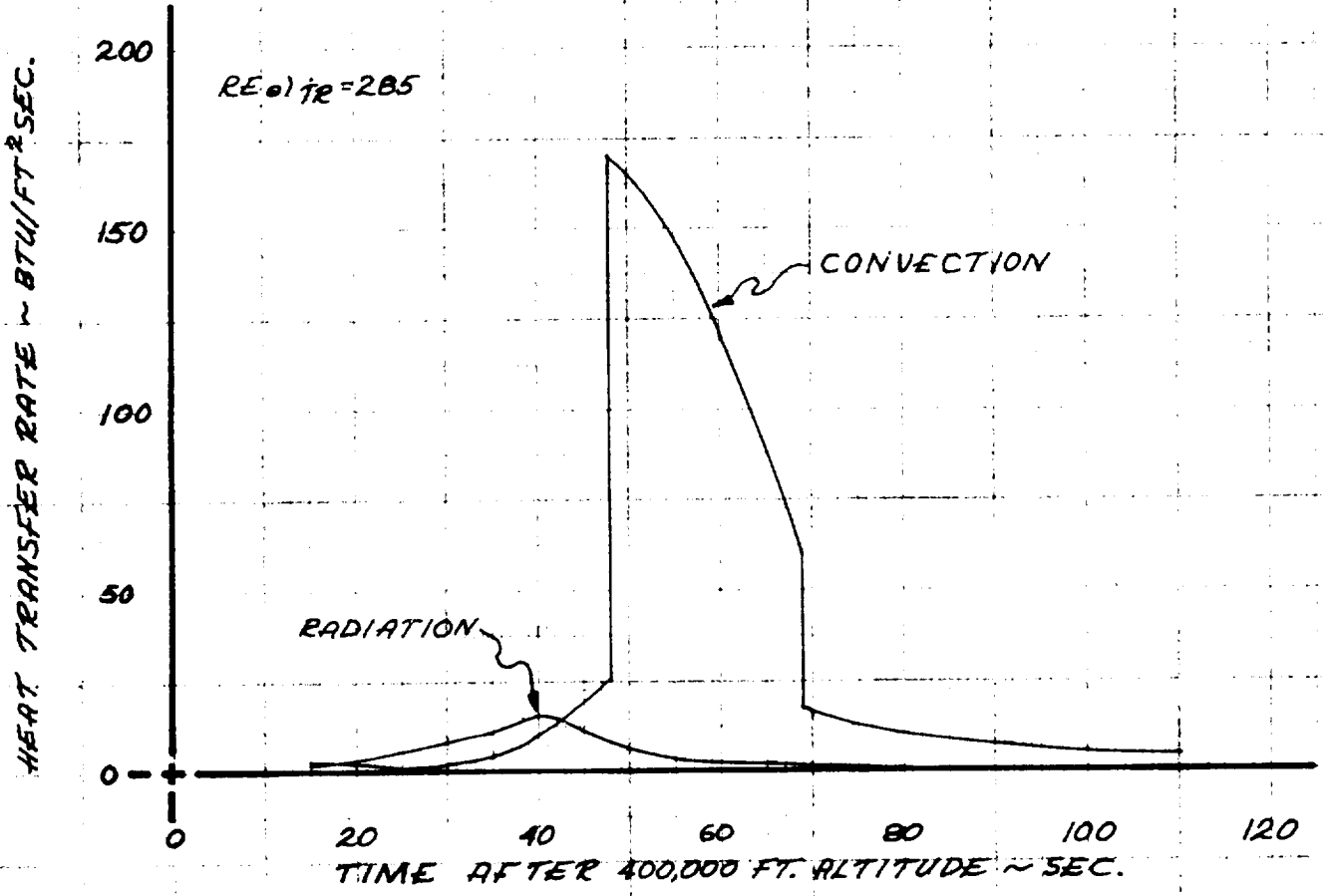


FIGURE 2-84  
 PREDICTED MOVEMENT OF  
 TRANSITION LOCATION

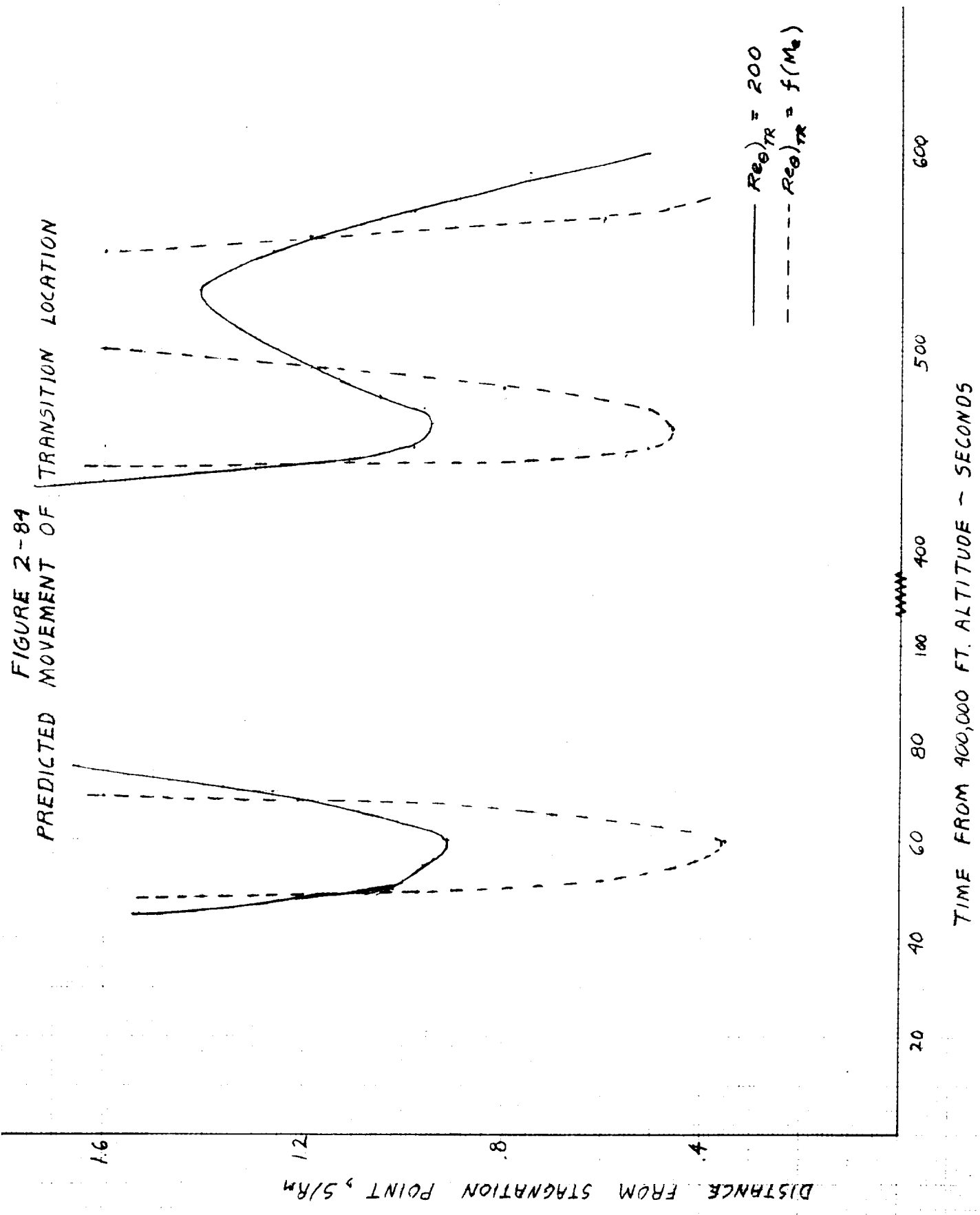


FIGURE 2-85  
HEAT TRANSFER AND SHIELD ABLATION  
TRAJECTORY III, GEOMETRIC CENTER  
LAMINAR FLOW

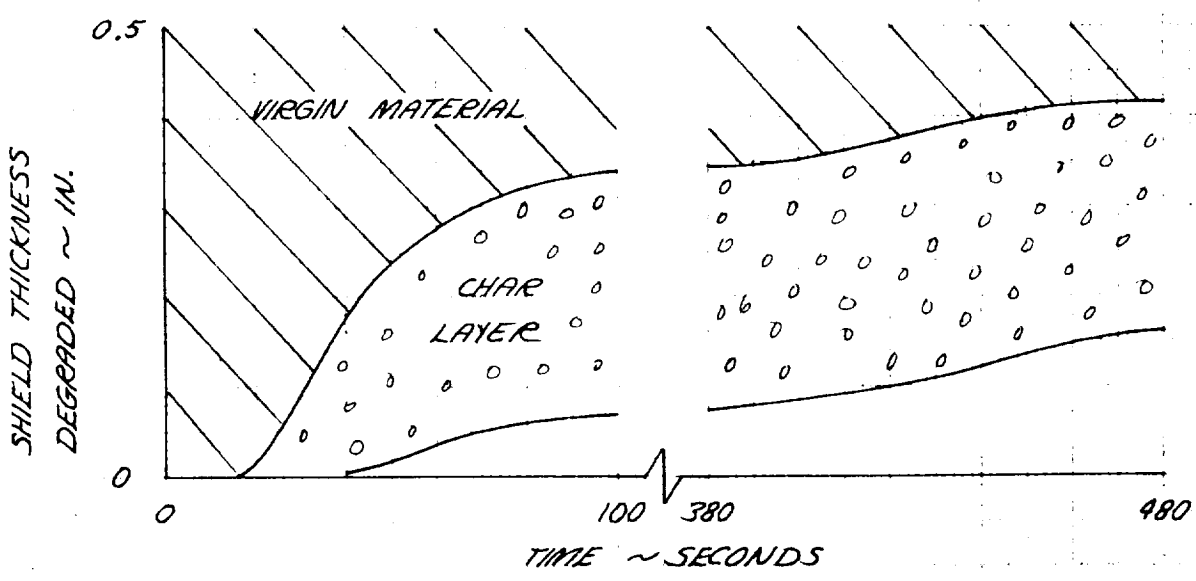
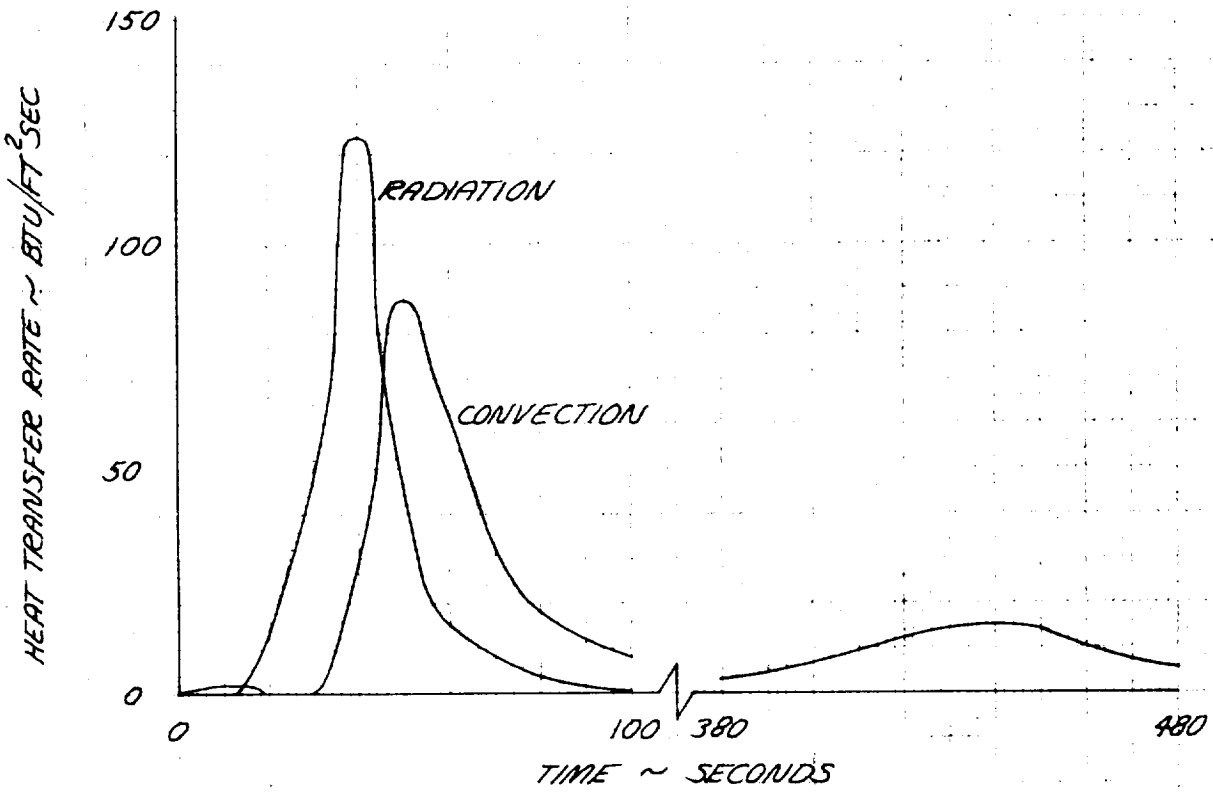
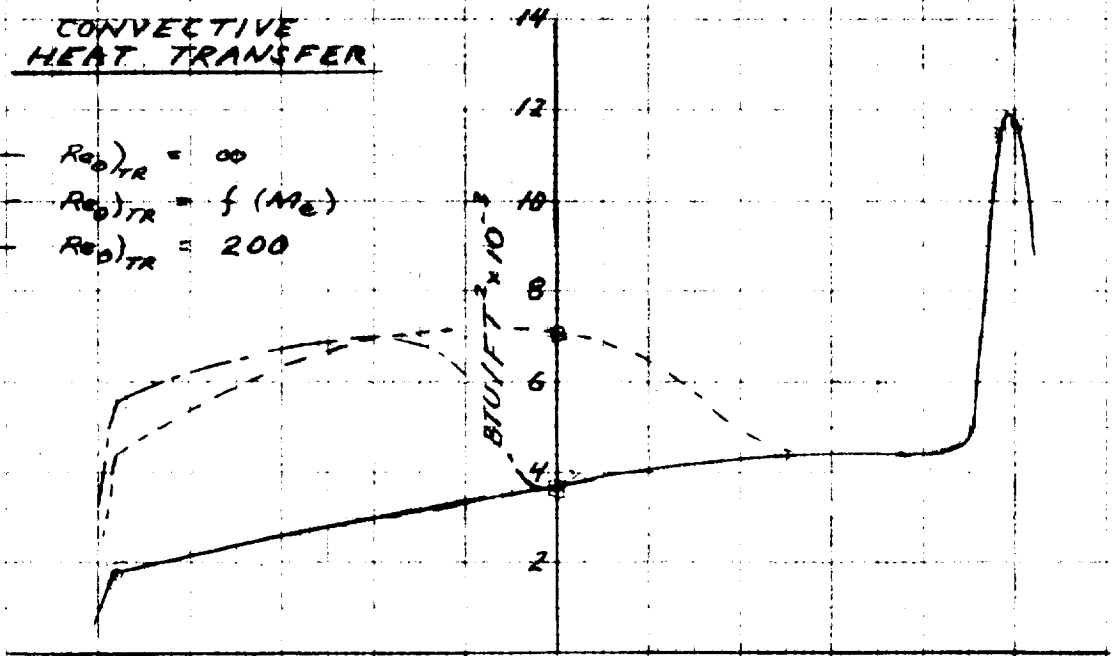


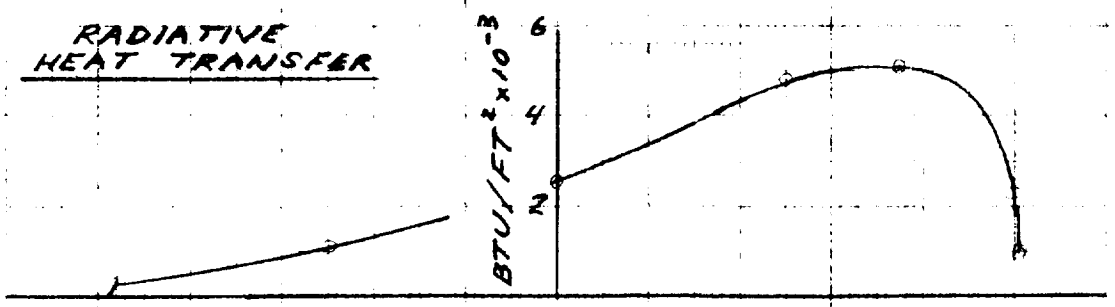
FIG 2-86 INFLUENCE OF TRANSITION CRITERION ON TOTAL HEAT TRANSFER AND SHIELD ABLATION

CONVECTIVE HEAT TRANSFER

- $Re_D)_{TR} = \infty$
- - -  $Re_D)_{TR} = f(Ma_e)$
- - -  $Re_D)_{TR} = 200$



RADIATIVE HEAT TRANSFER



SHIELD ABLATION

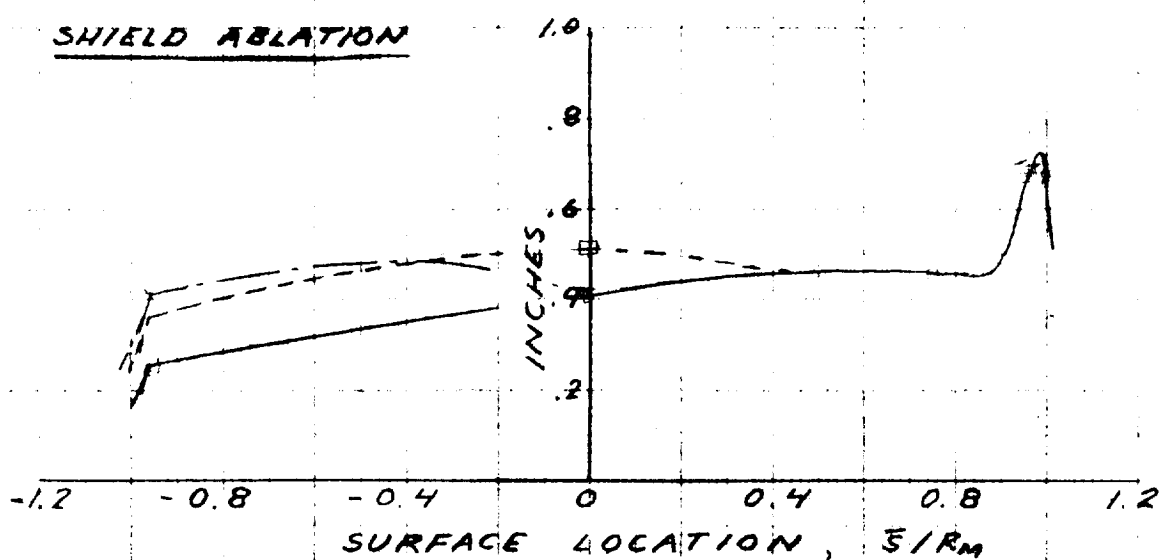
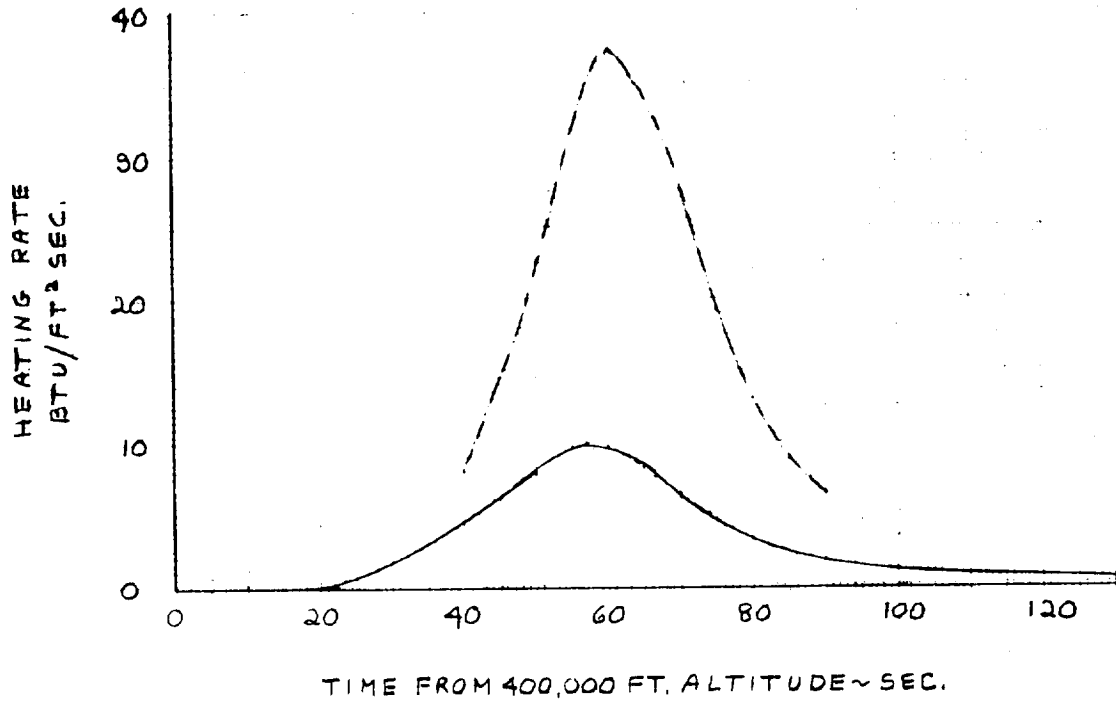
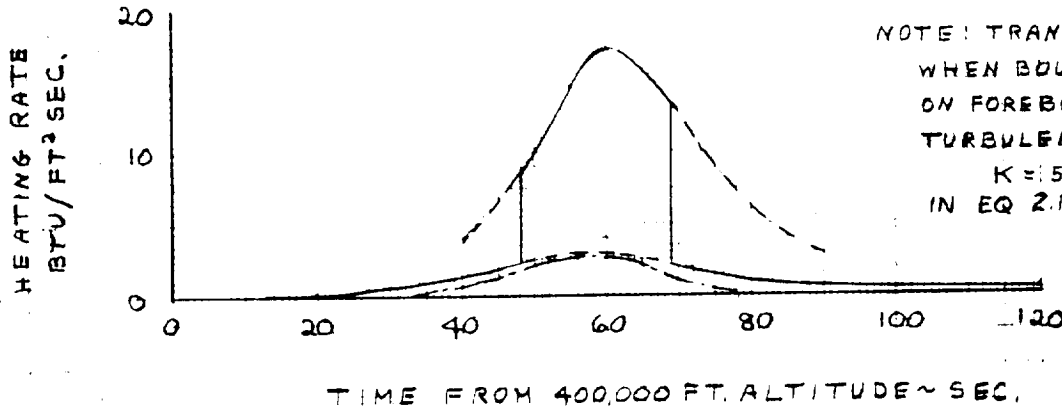


FIGURE 2-87  
PREDICTED AFTERBODY HEATING HISTORIES  
TRAJECTORY I

WINDWARD SIDE  
 $\bar{S}/RH = 2.2$

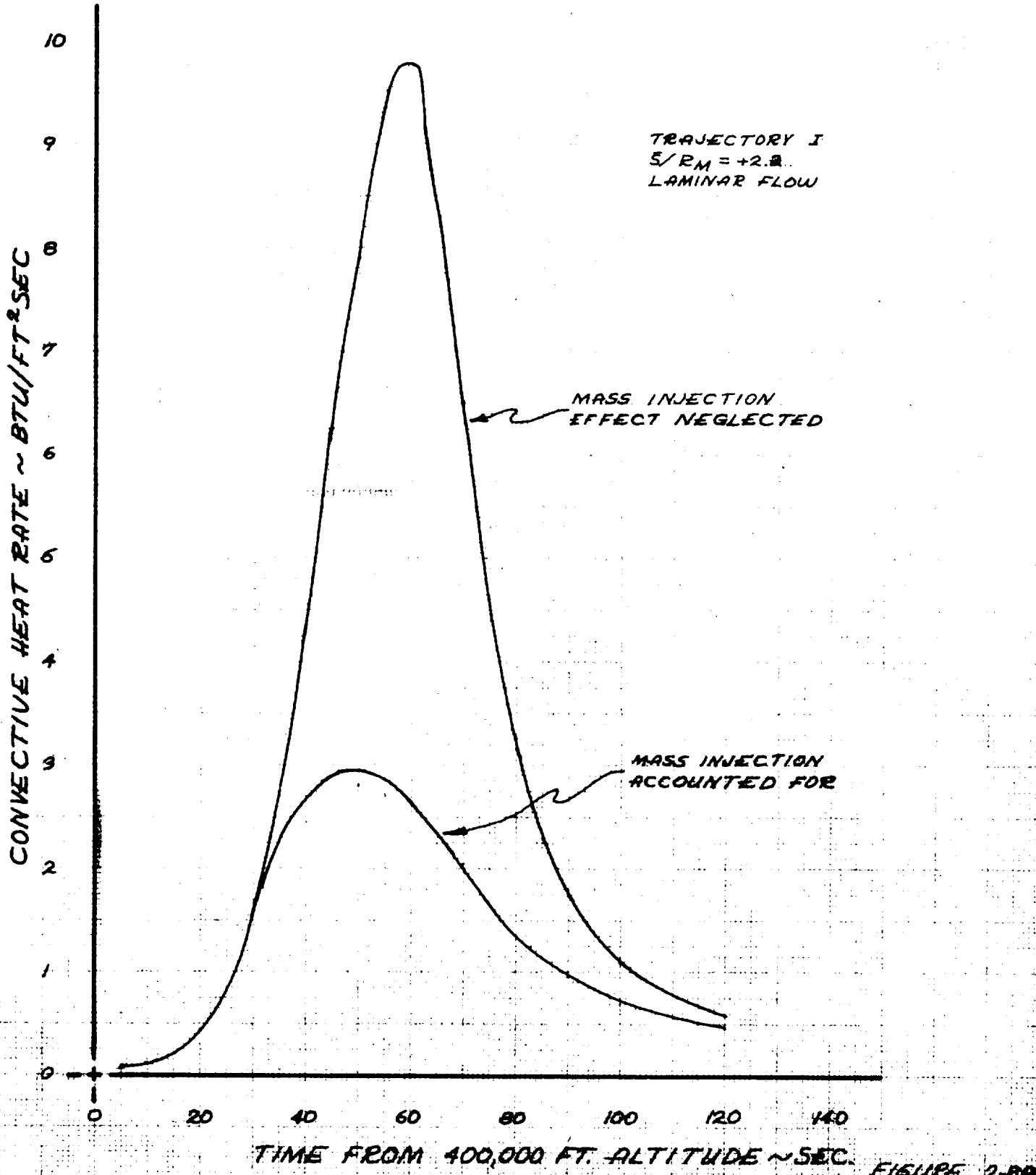


LEEWARD SIDE  
—— CONVECTION  
- - - RADIATION



NOTE: TRANSITION OCCURS  
WHEN BOUNDARY LAYER  
ON FOREBODY BECOMES  
TURBULENT  
 $K = 53 \text{ BTU/LB}_m\text{-SEC.}^{\frac{65}{7}} \text{ FT}^7$   
IN EQ 2.183 FOR RADIATION

# INFLUENCE OF SHIELD ABLATION ON AFTERBODY HEATING, WINDWARD SIDE



# HEAT SHIELD RESPONSE FOR WINDWARD AFTERBODY LOCATION

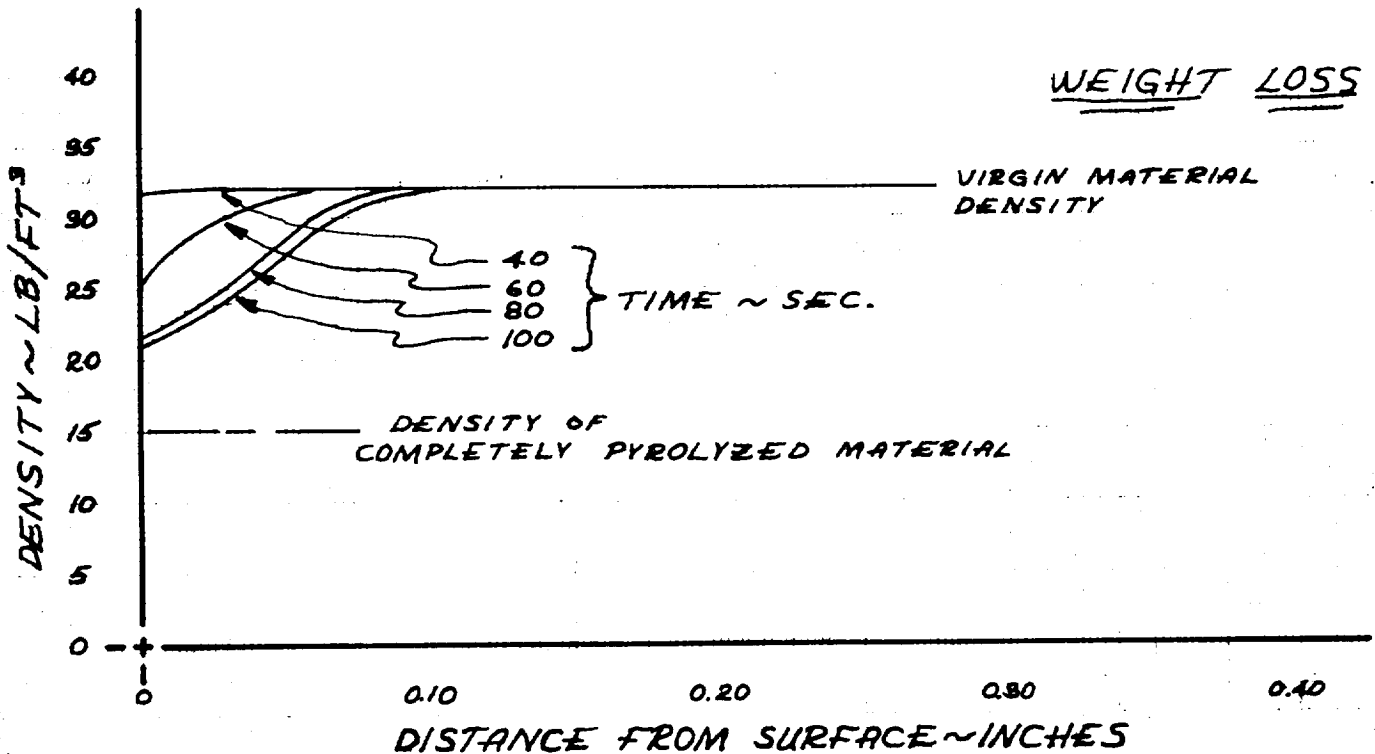
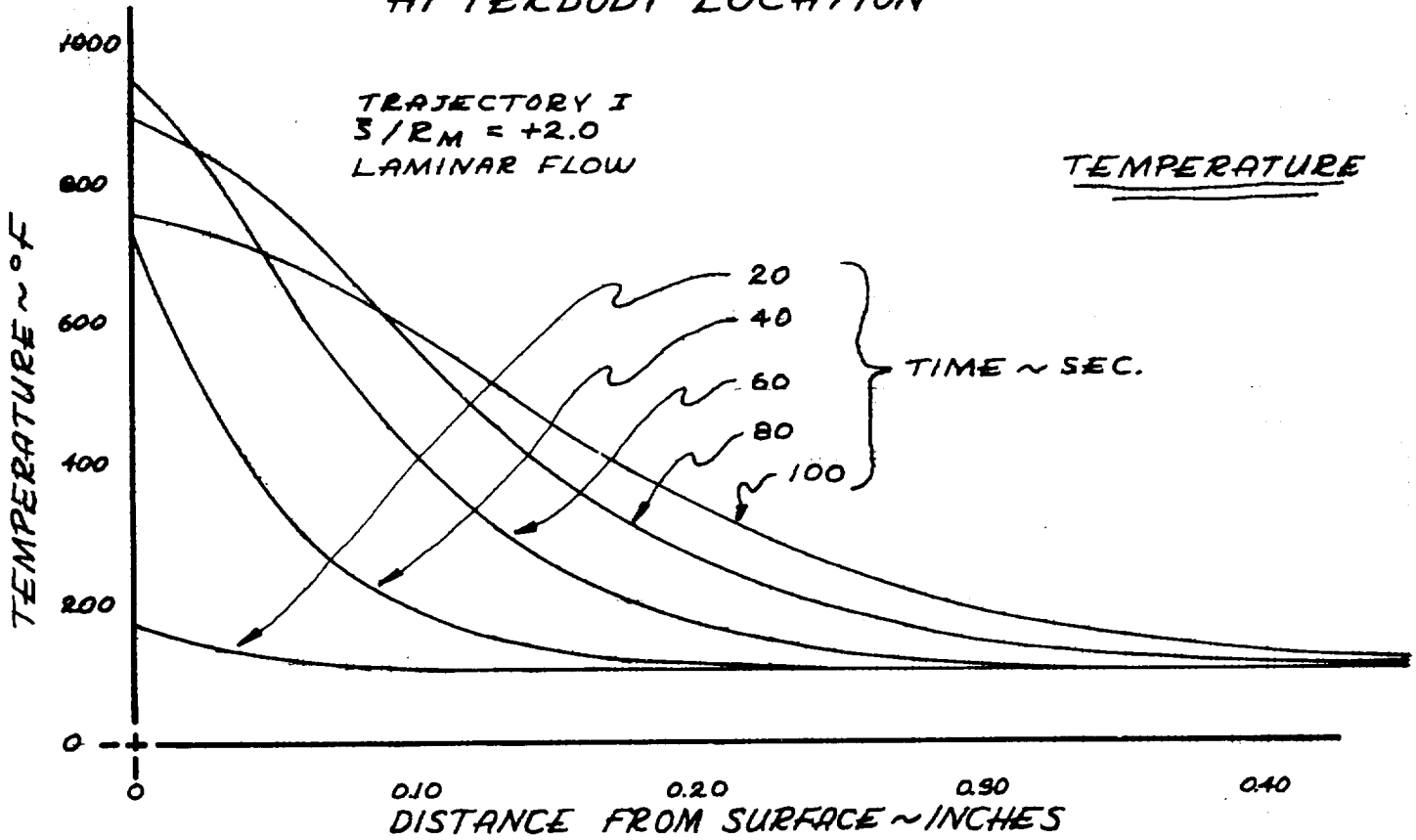


FIGURE 2-B9





Appendix 2A  
SPREADING CO-ORDINATE

The length element,  $h_2$ , appearing in the mass conservation equation (2.6) accounts for divergence of streamlines in the three-dimensional flow over the body surface. It provides a measure in the orthogonal, body-oriented co-ordinate system of the distance between (or spreading of) streamlines on the body surface. Thus it plays the same role as does the radial co-ordinate in rotationally symmetric flows. This length element, which is termed the spreading co-ordinate, may be evaluated provided that the pressure gradient transverse to the streamline direction is specified. The relations necessary for such an evaluation near the plane of symmetry are developed in this appendix.

The geometry of the problem is described in Fig. 2-9. The body surface consists of a spherical sector of radius  $R_c$ . A particle emanating from the stagnation point diverges from the plane of symmetry as it moves along a streamline to the point P. It is desired to determine the variation of the co-ordinate  $h_2$  with the streamwise distance,  $s$ . The local curvature of the streamline in the plane tangent to the body surface,  $R_s$ , is simply given by the centrifugal equation

$$\frac{1}{R_s} = \frac{1}{\rho u^2} \frac{\partial P}{\partial n} \quad (2A.1)$$

The normal pressure gradient,  $\frac{\partial P}{\partial n}$ , is not known a priori and in this analysis it must be estimated. The estimate is made by resolution of gradients in the  $m$ - and  $l$ -directions.

$$\frac{\partial P}{\partial n} = \sin \varphi \frac{\partial P}{\partial m} - \cos \varphi \frac{\partial P}{\partial l} \quad (2A.2)$$

It is assumed, with some empirical justification, that the pressure gradient along the body surface in the  $m$ -direction is Newtonian. That is the pressure gradient along the line formed by the intersection of the body surface and the meridional plane is assumed to be

$$\frac{\partial P}{\partial m} = \rho_t \frac{\partial \cos^2 \psi}{\partial m} \quad (2A.3)$$

where  $\psi$  is the angle between the local surface normal and the free stream wind vector. Considering next the  $\lambda$ -direction pressure gradient, it is noted that only streamlines very close to the plane of symmetry are to be treated. Then, the  $\lambda$ -direction pressure gradient is closely approximated by the  $s$ -direction pressure gradient which is independently determined. With this approximation, Eqs. (2A.1, 2A.2, and 2A.3) may be combined to yield

$$\frac{1}{R_s} = \frac{1}{\rho U^2} \left[ \rho_t \sin \varphi \frac{\partial \cos^2 \psi}{\partial m} - \cos \varphi \frac{\partial P}{\partial s} \right] \quad (2A.4)$$

In order to proceed further, geometrical transformations must be introduced. Vector algebra is used to define the radius of curvature,  $R_s$ , and angles,  $\varphi$  and  $\psi$ , in terms of the rectangular co-ordinates  $(\xi, \lambda, z)$ .

The equations of the spherical surface and meridional plane are, respectively

$$\left( \frac{\xi}{R_c} \right)^2 + \left( \frac{\lambda}{R_c} \right)^2 + \left( \frac{z}{R_c} \right)^2 = 1 \quad (2A.5)$$

$$\xi = \lambda \cot \theta_3 \quad (2A.6)$$

Thus, the meridional line (line formed by the intersection of the two surfaces) is

$$\left(\frac{\lambda}{R_C}\right)^2 \csc^2 \theta_B + \left(\frac{z}{R_C}\right)^2 = 1 \quad (2A.7)$$

The unit vectors giving directions of the local surface normal,  $\vec{F}$ , and the meridional line,  $\vec{m}$ , are from the above relations

$$\vec{F} = \left[1 - \left(\frac{z}{R_C}\right)^2\right]^{1/2} \left[\cos \theta_B i + \sin \theta_B j\right] + \left(\frac{z}{R_C}\right) k \quad (2A.8)$$

and

$$\vec{m} = -z/R_C \cos \theta_B i - z/R_C \sin \theta_B j + \left[1 - \left(\frac{z}{R_C}\right)^2\right]^{1/2} k \quad (2A.9)$$

The unit vector giving the streamline direction is (for  $z \ll s$  or  $\frac{dz}{ds} \ll 1$ )

$$\vec{s} = -\sin \theta_B i + \cos \theta_B j + \frac{dz}{ds} k \quad (2A.10)$$

The geodetic radius of curvature,  $R_S$ , may be determined from the relation

$$\frac{1}{R_S} = -\left(\vec{F} \times \vec{s} \cdot \frac{d\vec{s}}{ds}\right) \quad (2A.11)$$

Substituting the results of Eqs. (2A.8 and 2A.11) into Eq. (2A.11) and performing the indicated operation yields

$$-\frac{1}{R_S} = \frac{z}{R_C^2} + \frac{d^2 z}{ds^2} \left[1 - \left(\frac{z}{R_C}\right)^2\right]^{1/2}$$

which for small  $z$  reduces to

$$-\frac{1}{R_S} = \frac{z}{R_C^2} + \frac{d^2 z}{ds^2} \quad (2A.12)$$

The angles  $\psi$  and  $\phi$  may be determined from scalar products of the vectors defined above, according to

$$\cos \psi = \vec{r} \cdot \vec{i} \quad (2A.13)$$

$$\cos \phi = \vec{m} \cdot \vec{s} \quad (2A.14)$$

The results are

$$\cos \psi = \left[ 1 - \left( \frac{z}{R_c} \right)^2 \right]^{1/2} \cos \theta_B \quad (2A.15)$$

$$\cos \phi = \left[ 1 - \left( \frac{z}{R_c} \right)^2 \right]^{1/2} \frac{dz}{ds} \quad (2A.16)$$

The meridional pressure gradient can now be determined in terms of  $z$ . From Eqs. (2A.3 and 2A.15), noting that  $\theta_B$  is constant along the meridional line

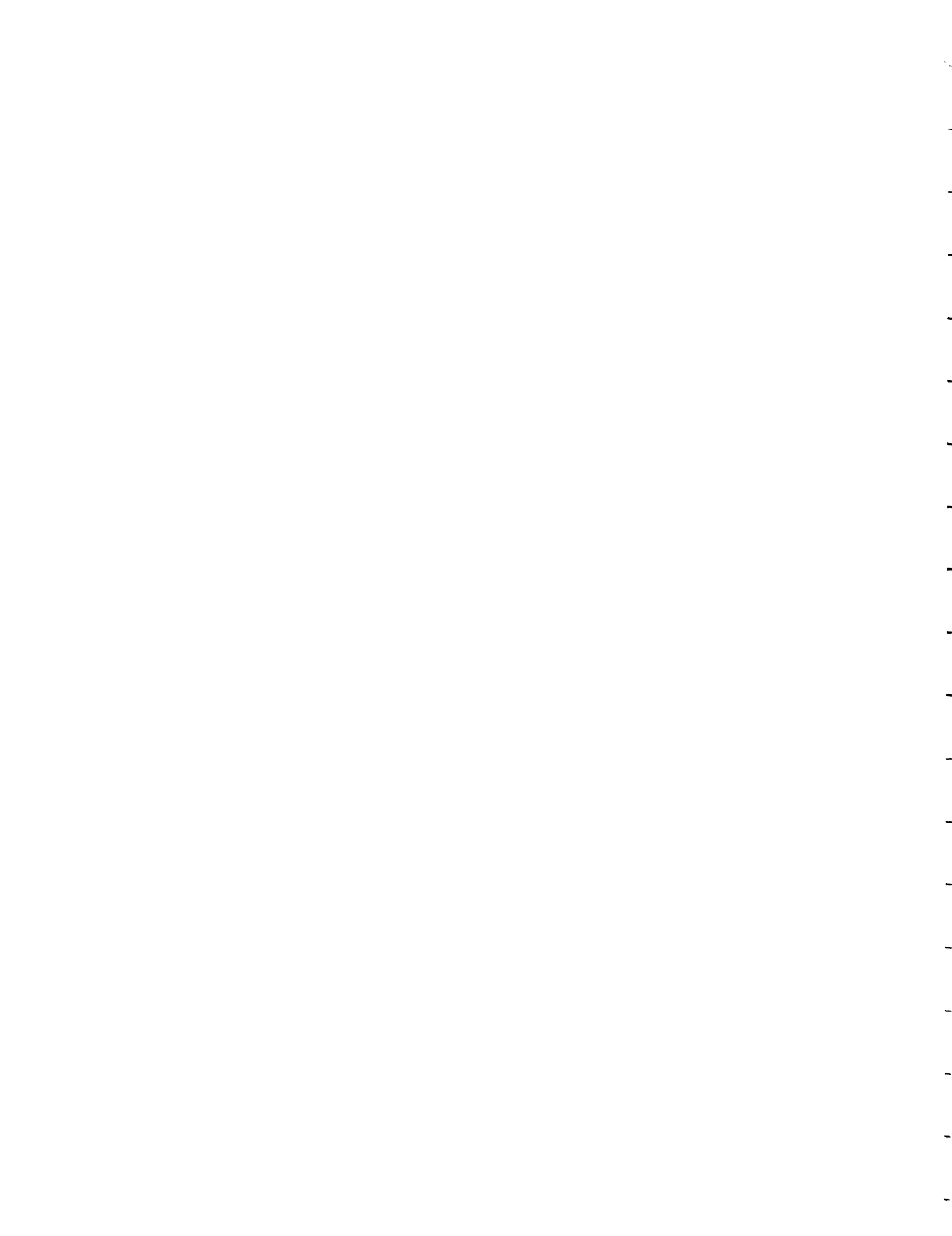
$$\begin{aligned} \frac{\partial p}{\partial m} &= \frac{\partial z}{\partial m} \left( \frac{\partial \cos \psi}{\partial z} \right) \\ &= -2 \frac{z}{R_c^2} \frac{\partial z}{\partial m} \end{aligned} \quad (2A.17)$$

For small  $z$  the partial derivative  $\frac{\partial z}{\partial m}$  approaches unity and thus this term may be eliminated from Eq. (2A.17).

The results of Eqs. (2A.12, 2A.15, 2A.16, and 2A.17) may be substituted in Eq. (2A.4) to obtain a relation for the variation of the  $z$  co-ordinate with distance  $s$  along a streamline. For small  $z$ , such that  $\left[ 1 - \left( \frac{z}{R_c} \right)^2 \right]^{1/2} \approx 1$ , this relation is

$$\frac{d^2 z}{ds^2} = - \frac{z}{R_c^2} + \frac{1}{\rho u^2} \left[ \rho \frac{z z}{R_c^2} \cos^2 \theta_B + \frac{dz}{ds} \frac{\partial p}{\partial s} \right] \quad (2A.18)$$

The co-ordinate  $z$  is equivalent to the spreading co-ordinate  $h_2$  for small  $z$ . Thus, Eq. (2A.18) provides a means for computing the spreading co-ordinate in the vicinity of the plane of symmetry. The equation may be directly integrated given the streamwise pressure gradient. The manner in which this is accomplished is discussed in Section 2.1.2.



Appendix 2B  
THERMODYNAMIC AND TRANSPORT PROPERTIES

The several computer codes discussed in Section 2 have been designed to use real gas properties. This appendix describes the data adopted for sample calculations. Thermodynamic properties, including chemical composition, and radiative properties are presented.

THERMODYNAMIC PROPERTIES

For a given composition of elementary species, two state variables are sufficient to specify the thermodynamic properties of a gaseous mixture in thermodynamic equilibrium. The state properties may be put in a tabular form so that property calculations may be made by table look-up and interpolation. This system is employed in several of the computer codes including STREAMTUBE, VORTICITY, and ENVIRONMENT. Alternately, curve fits of one state variable versus a second at several levels of a third may be used. Such fits are used in the STAGRADS and STRADS-AIR programs.

For both systems, the basic thermodynamic data have been obtained from Ref. 2.51 for temperatures to 15,000°K and from Ref. 2.52 for higher temperatures. Correlation equations were available from Refs. 2.52 to 2.54. However, for the purpose of reducing the computer time required, new correlations with a more suitable set of units have been generated. The correlations express the variation of the dependent state property with enthalpy at fixed pressure. The division of enthalpy ranges was selected in such a manner that interpolation of the coefficients in the correlations between adjacent pressure levels could be conveniently made.

The units selected for correlation purposes are:

P , pressure in atm

T , temperature in ev, 1 ev = 11605.7°K

H , enthalpy ratio,  $h/h_{\text{satellite}}$ ,  $h_{\text{satellite}} = 12,484 \text{ Btu/lb}_m$

$PV/V_{SL}$  , in atm,  $V_{SL}$  = sea-level (1 atm, 288.16°K) air specific volume

The correlation formula coefficients for air are given in Table 2B-1.

Also indicated in the table is the accuracy of the fits.

For calculation of radiative properties, the species particle concentrations are required. The particle number density N is given by Eq. (2B.1).

$$N = xZ \left( \rho / \rho_* \right) L \quad (2B.1)$$

where x = mole fraction, Z = compressibility,  $\rho_*$  = air density at standard conditions (1 atm and 0°c), and L = Loschmidt number =  $2.687 \times 10^{19}$ .

Another form of Eq. (2B.1) is

$$N = xZ \left( V_{SL} / V \right) 2.542 \times 10^{19} \quad (2B.2)$$

The mole fractions may be readily calculated if Hansen's (Ref. 2.55) simplified model of air chemistry is used. Hansen's simplified model involves the following assumptions:

- (1) The ratio of  $N_2$  and  $O_2$  in normal air is taken as 4 to 1.
- (2) As temperature increase,  $O_2$  begins to dissociate alone to form O without the formation of NO.
- (3)  $N_2$  begins to dissociate to form N after the dissociation of  $O_2$  is complete.
- (4) N and O begin to ionize simultaneously to form  $N^+$  and  $O^+$  after the dissociation of  $N_2$  is complete.
- (5) Double ionization begins after N and O become complete singly ionized.



With the simplified model of air chemistry, the product xZ is given by the following equations:

For  $1 \leq Z \leq 1.20$

$$(xZ)_{N_2} = 0.8 \quad (2B.3)$$

$$(xZ)_{O_2} = 1.2 - Z \quad (2B.4)$$

$$(xZ)_O = 2(Z - 1) \quad (2B.5)$$

$$(xZ)_N = (xZ)_{N^+O^+} = (xZ)_{N^{++}O^{++}} = 0 \quad (2B.6)$$

For  $1.20 \leq Z \leq 2.0$

$$(xZ)_{N_2} = 2 - Z \quad (2B.7)$$

$$(xZ)_N = 2(Z - 1.2) \quad (2B.8)$$

$$(xZ)_O = 0.4 \quad (2B.9)$$

$$(xZ)_{O_2} = (xZ)_{N^+O^+} = (xZ)_{N^{++}O^{++}} = 0 \quad (2B.10)$$

For  $2.0 \leq Z \leq 4.0$

$$(xZ)_N = 0.8(4 - Z) \quad (2B.11)$$

$$(xZ)_O = 0.2(4 - Z) \quad (2B.12)$$

$$(xZ)_{N^+O^+} = Z - 2 \quad (2B.13)$$

$$(xZ)_{N_2} = (xZ)_{O_2} = (xZ)_{N^{++}O^{++}} = 0 \quad (2B.14)$$

For  $4.0 \leq z \leq 6.0$

$$\left(\chi z\right)_{N^+O^+} = 6 - z \quad (2B.15)$$

$$\left(\chi z\right)_{N^{++}O^{++}} = z - 4 \quad (2B.16)$$

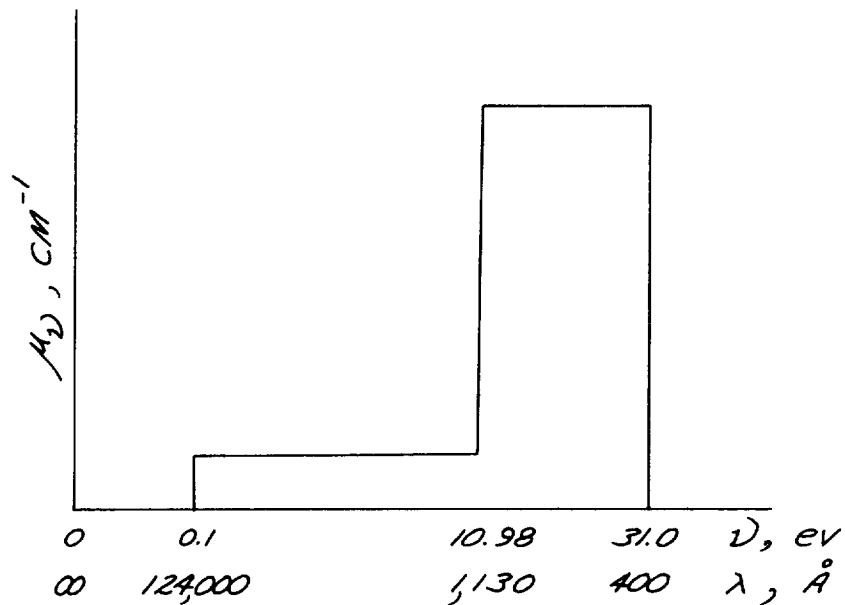
$$\left(\chi z\right)_{N_2} = \left(\chi z\right)_{O_2} = \left(\chi z\right)_N = \left(\chi z\right)_O = 0 \quad (2B.17)$$

#### AIR ABSORPTION COEFFICIENTS

As discussed in Section 2.2.2, many sets of calculated equilibrium air absorption coefficients are available. However, differences among results of different investigators exist. These differences are due to the different models and approximations used in the calculations and to the different values of oscillation strengths or cross sections employed. For estimate of the effects of the different radiative phenomena, a consistent set of radiative properties must be selected.

The radiative properties employed may be from one extreme the detailed spectral absorption coefficients including the line-shape effects to the other extreme the Planck-mean absorption coefficients. For radiative transport calculations involving the radiation-coupled flow field around blunt bodies, the spectral resolution of absorption coefficients cannot be very fine; otherwise excessive computer time is required. The spectral absorption coefficients for air employed in STAGRADS and STRADS-AIR are based on a "two-band" model and a "six-band" model.

The "two-band" model, sketched below, assumes a two-level spectral absorption coefficient -- a low level at low frequencies and a high level at high frequencies. The levels of the two "bands" are functions of temperature and density and are "extracted" from the data given in Refs. 2.22, 2.23, 2.25, 2.27, and 2.56. Figure 2B-1 shows the Planck-mean absorption coefficients in the low-frequency region from Nardone, Breene, et al (Ref. 2.23), Gilmore (Ref. 2.25), and Armstrong (Ref. 2.22). The numerical



values of the low-frequency coefficients used in the computer code correspond essentially to the line curves in Fig. 2B-1. A different set of the Planck-mean absorption coefficients in the low frequency region based on the spectral absorption coefficients of Churchill (Ref. 2.29) has also used for this study (see Section 2.2.3)

Figure 2B-2 shows the high-frequency ( $\lambda = 400 - 1130\text{Å}$ ) absorption coefficients for air. At high temperatures, the dominant contribution is due to the photoionization of N and O (e.g.,  $N + h\nu \rightarrow N^+ + e$ ). The values of the coefficients in this range are essentially based on the results of Hahne (Ref. 2.27). At low temperatures, the dominant contribution is due to the photoionization of undissociated molecules. According to the compilation of Schultz (Ref. 2.56), the linear ultra-violet absorption coefficients for air-component molecules at standard conditions are in excess of  $100 \text{ cm}^{-1}$ . An "average" value of  $200 \text{ cm}^{-1}$  is selected here for calculation purposes. Assuming that the absorption cross section is insensitive to temperature changes, the linear ultra-violet absorption coefficients for

molecules may be calculated for other than the standard conditions using species concentration tables for high temperature air (e.g., Gilmore, Ref. 2.57).

The "six-band" model, depicted below, provides more bands in the ultra-violet region. The contributions included in the six bands are summarized in Table 2B-2.

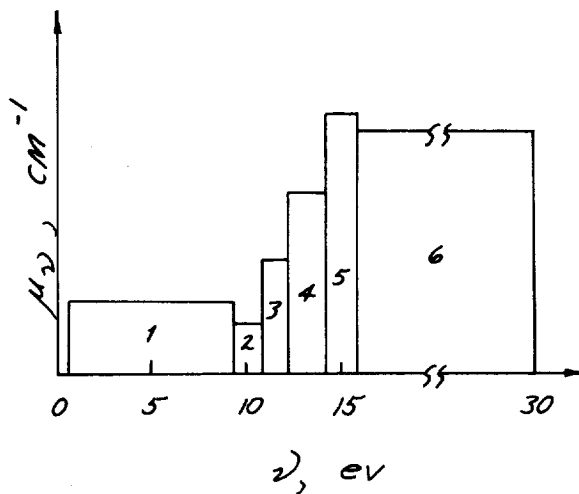


Table 2B-2  
SPECTRAL RANGES AND ABSORPTION PROCESS FOR "SIX-BAND" MODEL

Band Number (Region)	Frequency, ev		Absorption Process
	Lower	Upper	
1	0.5	9.2	processes included in Fig. 2B-1
2	9.2	10.9	O <sub>2</sub> S-R continuum, N continuum
3	10.9	12.0	N <sub>2</sub> B-H band, N continuum
4	12.0	14.0	N <sub>2</sub> B-H band, N cont., O <sub>2</sub> photoionization
5	14.0	15.5	N <sub>2</sub> B-H band, N cont., O <sub>2</sub> photoionization
6	15.5	30.0	N cont., O <sub>2</sub> + N <sub>2</sub> photoionization

The contribution from  $O_2$  Schumann-Runge continuum is calculated according to the Sulzer-Wieland formula (see Evans and Schexnayder, Ref. 2.58).

The Sulzer-Wieland is not accurate at high temperatures but is considered adequate for the present study. The  $N_2$  Birge-Hopfield band system

$(x' \sum_g^+ \rightarrow b' \sum_u^+)$  is calculated according to an approximate model due to French (Ref. 2.59); the f number used is 0.10. The approximate model yields the following expression for the spectral absorption coefficient of  $N_2$  B-H band systems:

$$\mu_\nu = 1456 \left[ Z x_{N_2} \left( \rho / \rho_{SL} \right) \right] \left( 1 - e^{-0.29245/T} \right) e^{-E_n(\nu)/T} \quad (2B.18)$$

where

- $x_{N_2}$  = mole fraction of  $N_2$
- Z = compressibility factor
- T = temperature in ev
- $E_n(\nu)$  = vibrational energy (ev) of the lower state
- $\mu_\nu$  = spectral absorption coefficient,  $cm^{-1}$

In the above equation,  $E_n(\nu)$  is the only frequency-dependent variable, as given in Fig. 2B-3.

The contribution of atomic N continuum in the high-frequency regions is based on the results as calculated by Armstrong (Ref. 2.26) et al. The absorption coefficients for regions ("bands") 2 to 6 per  $2.542 \times 10^{19}$  particles (particle number/ $cm^3$  at sea-level conditions) are given in Fig. 2B-4.

The contribution due to photoionization of  $N_2$  and  $O_2$  is based on the approximate estimate of Weisner (Ref. 2.39). The photoionization cross-sections are assumed to be insensitive to temperature changes with the following values:

$$O_2 \text{ photoionization} = \begin{cases} 4.45 \times 10^{-18} \text{ cm}^2, & \text{region 3} \\ 3.82 \times 10^{-18} \text{ cm}^2, & \text{region 4} \\ 2.0 \times 10^{-17} \text{ cm}^2, & \text{region 5} \end{cases}$$

$$N_2 \text{ photoionization} = 2.5 \times 10^{-17} \text{ cm}^2, \text{ region 6}$$

The species concentrations required to calculate the six-band air spectral absorption coefficients are calculated according to the simplified model of air chemistry discussed previously.

The use of a more approximate radiative property model is permissible in the STREAMTUBE program since the program is used to describe the flow field characteristics rather than the radiation transfer to the surface. The STREAMTUBE program does not account for absorption and hence the total radiancy of air is used rather than spectral absorption coefficients. Data on the radiancy,  $\bar{k}\sigma T^4$ , are entered in tabular form as a function of the density-enthalpy or pressure-enthalpy state conditions. Values utilized have been derived from the results of Churchill (Ref. 2.29).\* As indicated in Section 2.1 the decay of radiancy along a streamline is obtained in the STREAMTUBE calculation from a power law expression.

$$\frac{\bar{k}\sigma T^4}{\bar{k}_i\sigma T_i^4} = \left(\frac{p}{p_i}\right)^\alpha \left(\frac{h}{h_i}\right)^\beta \quad (2.30)$$

The exponents are obtained by numerical differentiation of the input radiancy values at the  $(p_i, h_i)$  condition. The pertinent relations are

\* Photoionization contributions to the radiation are not included by Churchill. The emission due to photoionization is a large fraction of the total emission from heated air. However it is strongly absorbed as shown by the results of Section 2.2. For a thick shock layer, it is more accurate to neglect the photoionization contribution when transparency is assumed.

$$\alpha = \frac{\partial \ln \rho \bar{k} \sigma T^4}{\partial \ln \rho} - \frac{\partial \ln \rho}{\partial \ln \rho} \quad (2B.19)$$

$$\beta = \frac{\partial \ln \rho \bar{k} \sigma T^4}{\partial \ln H} - \frac{\partial \ln \rho}{\partial \ln H} \quad (2B.20)$$

Table B-1  
CORRELATION FORMULA COEFFICIENTS, AIR

Property y	H <sub>lower</sub>	H <sub>upper</sub>	P (atm)	a <sub>0</sub>	a <sub>1</sub>	a <sub>2</sub>	a <sub>3</sub>	a <sub>4</sub>	a <sub>5</sub>	a <sub>6</sub>	Accuracy (%)
T, °v	0	0.0785	.01-10	1.1835678-1	6.5812617-1	9.3439634-1	-3.053483	2.4147548	-5.8669396-1	6.4	
	0.0785	1.50	0.01	1.0487607-1	9.5327098-1	3.2467991-3	-1.5121987	1.3027109	-3.0545366-1	6.4	
			1.0	9.6979514-2	1.1433893	-3.5657184-1	-1.0256385	1.0029850	-2.4502322-1	6.2	
			10.0	1.1613734-1	1.0843619	1.1034320-1	-1.6526663	1.3729724	-3.3199664-1	3.9	
	1.50	5.50	0.01	-1.5819349	3.3455871	-1.8624081	5.2266841-1	-7.2395315-2	3.9710259-3	1.0	
	5.50	9.9	0.1	-1.9378666	3.8547943	-2.0904657	5.7519457-1	-7.8194046-2	4.2031918-3	1.0	
	5.50	7.43	1.0	-1.8226109	3.4983767	-1.7229472	4.3881665-1	-5.5808967-2	2.8371443-3	1.0	
	5.50	6.78	10.0	-1.2891001	2.5154559	-1.0005790	2.1112489-1	-2.2369219-2	9.6330532-4	1.3	
			0.01	1.9205406	-5.1167326	2.2507384	-3.7221565-1	2.7302427-2	-7.470516-4	2.2	
	5.50	9.9	0.10	1.9295706+2	-1.3286946+2	3.5826885+1	-4.7588249	3.1126795-1	-8.0365421-3	1.0	
	5.50	7.43	1.0	2.8774962+1	-1.3385786+1	2.1445183	-1.1088207-1			1.0	
	5.50	6.78	10.0	-7.3068604-2	9.3749066-1	-1.9204991-1	1.5081737-2			1.0	
T (alternate)	0.0361	0.36	0.01	-9.5098987-3	2.7438727	7.6381683-1	-1.2213621+2	5.5486666+2	-7.1270858+2	1.3	
			0.10	3.5647251-2	2.4819323-1	4.7476579+1	-3.0754271+2	2.1908001+3	-4.2729834+3	1.0	
			1.0	-1.9368604-3	2.3758528	3.8650062	-9.1807305+1	3.2603521+2	-3.4814249+2	1.3	
			10.0	1.7905563-2	1.15133458	1.4744230+1	-1.3762337+2	4.0607364+2	-3.9627689+2	1.0	
	0.36	1.50	0.01	-9.1095707-1	1.0041215+1	-3.1187126+1	5.0529627+1	-4.4270302+1	1.9837832+1	1.0	
			0.10	-1.1822706-1	2.8525348	-5.5224045	5.6209047	-2.9035087	6.1978861-1	1.0	
			1.0	6.5851264-2	1.5634838	-1.7494294	8.5083235-1	-1.1486050-1		1.0	
			10.0	-9.2106463-2	2.4273938	-3.0304437	1.7403332	-3.4802097-1		1.0	
	5.50	11.0	0.01	3.5245559+2	-2.8068595+2	9.1419875+1	-1.5572593+1	1.4670453	-7.2599443-2	1.4	
PV/V <sub>S,L</sub> (atm)	0	0.0785	.01-10	4.1466486	3.1607714+1	7.0980384+1	-1.7031562+2	1.2768093+2	-2.9994045+1	5.7	
	0.0785	1.50	0.01	3.4124600	4.5715655+1	2.2263377+1	-8.3560087+1	6.3467061+1	-1.3608969+1	5.4	
			1.0	3.1948184	5.0919528+1	1.6362194+1	-7.3823562+1	5.7745495+1	-1.2956107+1	4.0	
			10.0	3.7750871	4.8311173+1	3.6479840+1	-9.8644062+1	7.2579584+1	-1.6722378+1	2.6	
	1.50	5.50	0.01	-1.2724814+2	2.5536017+2	-1.3807613+2	4.0678168+1	-5.8880258	3.3852882-1	1.0	
			0.10	-1.4284936+2	2.7319929+2	-1.4179943+2	4.0460512+1	-5.6722231	3.1539598+1	1.0	
			1.0	-1.3549011+2	2.488272+2	-1.1659636+2	3.1199285+1	-4.1153845	2.173742-1	1.0	
			10.0	-7.3263048+1	1.3473468+2	-3.6334966+1	6.1591101	-4.2335399-1	9.2513935-3	1.3	
	5.50	11.0	0.01	-6.3540412+2	-1.7310820+2	1.8382531+2	-3.6014227+1	2.8527773	-8.1544380-2	1.9	
	5.50	9.9	0.10	2.5708608+4	-1.7743649+4	4.8244025+3	-6.4277878+2	4.2158865+1	-1.0911418	1.0	
	5.50	7.43	1.0	3.6719114+3	-1.7467849+3	2.8518962+2	-1.4827085+1			1.0	
	5.50	6.78	10.0	1.1714926+2	1.7900484+1	-2.9186889	7.5179851-1			1.0	
PV/V <sub>S,L</sub> (alternate)	0.0361	0.36	0.01	-2.9150224-1	1.0816331+2	1.8632507	-4.0867975+3	1.9336595+4	-2.5392588+4	1.1	
			0.10	-3.9293492-1	1.1212841+2	-9.4952171+1	-2.5456987+3	1.2088268+4	-1.505385+4	1.5	
			1.0	-7.9702854-2	9.8552205+1	4.7099724+1	-2.5586988+3	9.8867488+3	-1.1004687+4	1.1	
			10.0	5.5855155-1	7.0821747+1	3.9679145+2	-4.0339294+3	1.2486950+4	-1.2649987+4	1.0	
	0.36	1.5	0.01	6.9132261	2.5195433+1	5.9373260+1	-1.3021310+2	9.3944820+1	-2.0886602+1	1.6	
			0.10	1.3690118	7.0848172+1	-5.9618294+1	2.5006220+1			1.0	
			1.0	2.1078820	6.9536693+1	-5.0323748+1	2.0157349+1			1.0	
			10.0	-4.1878757	1.0303833+2	-9.9332450+1	5.6323946+1	-1.0105138+1		1.0	
	5.5	11.0	0.01	4.6079518+4	-3.6897522+4	1.2067170+4	-2.0617303+3	1.9472368+2	-9.6571384	1.3	



Table B-1 (Cont)

Property $y$	$H_{lower}$	$H_{upper}$	$P$ (atm)	$a_0$	$a_1$	$a_2$	$a_3$	$a_4$	$a_5$	$a_6$	Accuracy (%)
$Z$	0	0.0785	.01-10		$Z = 1.0$						
	0.0785	1.50	0.01	0.90204210	1.3765963	-1.5847662	1.5546703	-0.51615931			1.3
			0.10	0.89964231	1.3061862	-1.4626525	1.4298675	-0.46987220			1.3
			1.0	0.90237909	1.1686618	-1.1587565	1.1151654	-0.36066937			1.7
			10.0	0.88730931	1.1296640	-1.0581270	0.95701218	-0.29414222			1.3
	1.50	5.50	0.01	1.2736413	0.50509824	-0.54156490-2					1.1
			0.10	1.3301822	0.44379041	0.97737477-3					1.0
			1.0	1.3685294	0.39338470	0.48567735-2					1.0
			10.0	1.4055444	0.33971451	0.82709458-2					1.0
	5.50	11.0	0.01	2.8602478	0.16921459	.25806779-2					1.0
	5.50	9.9	0.1	2.8614600	0.15494900	.32019459-2					1.0
	5.50	7.43	1.0	-1.38604584	1.0478795	-0.6454679-1					1.0
	5.50	6.78	10.0	-0.64086440	1.1224999	-0.66709173-1					1.0

$$y = a_0 + a_1 x + a_2 x^2 + a_3 x^3 + \dots$$

$$x = H = h/h_{satellite} \cdot h_{satellite} = 12464 \text{ Btu/lb}_m \cdot V_{SL} \text{ for air at 1 atm \& 288.15}^\circ\text{K}$$

Data Sources:

- (1) Hansen, C.F. NACA TR R-50 for  $1,000 \leq T^\circ\text{K} \leq 12,000$
- (2) LMSC Report 4-74-64-1, for  $12,000 \leq T^\circ\text{K} \leq 25,000$

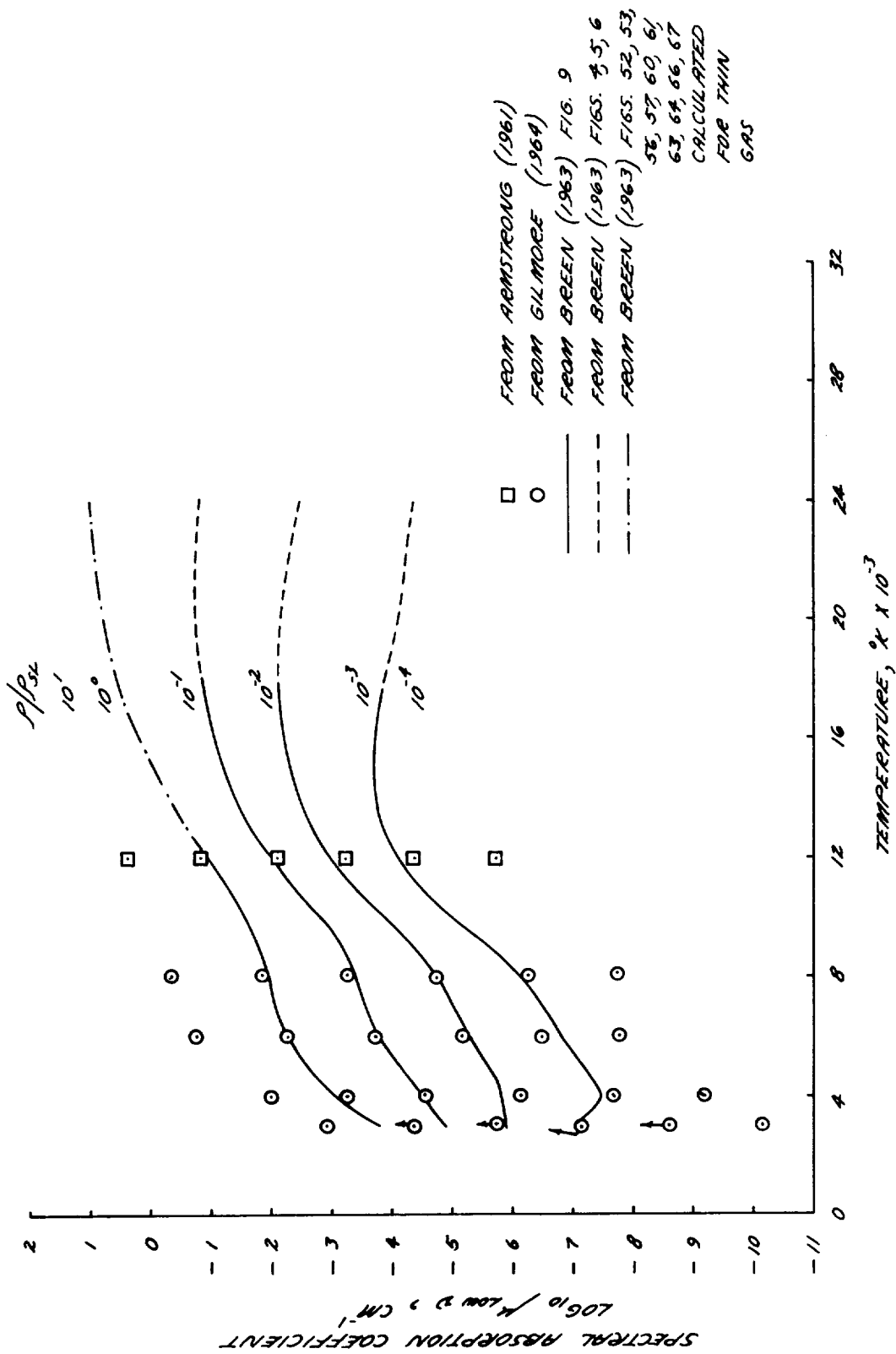


Figure 2B-1 Low-Frequency Air Absorption Coefficients

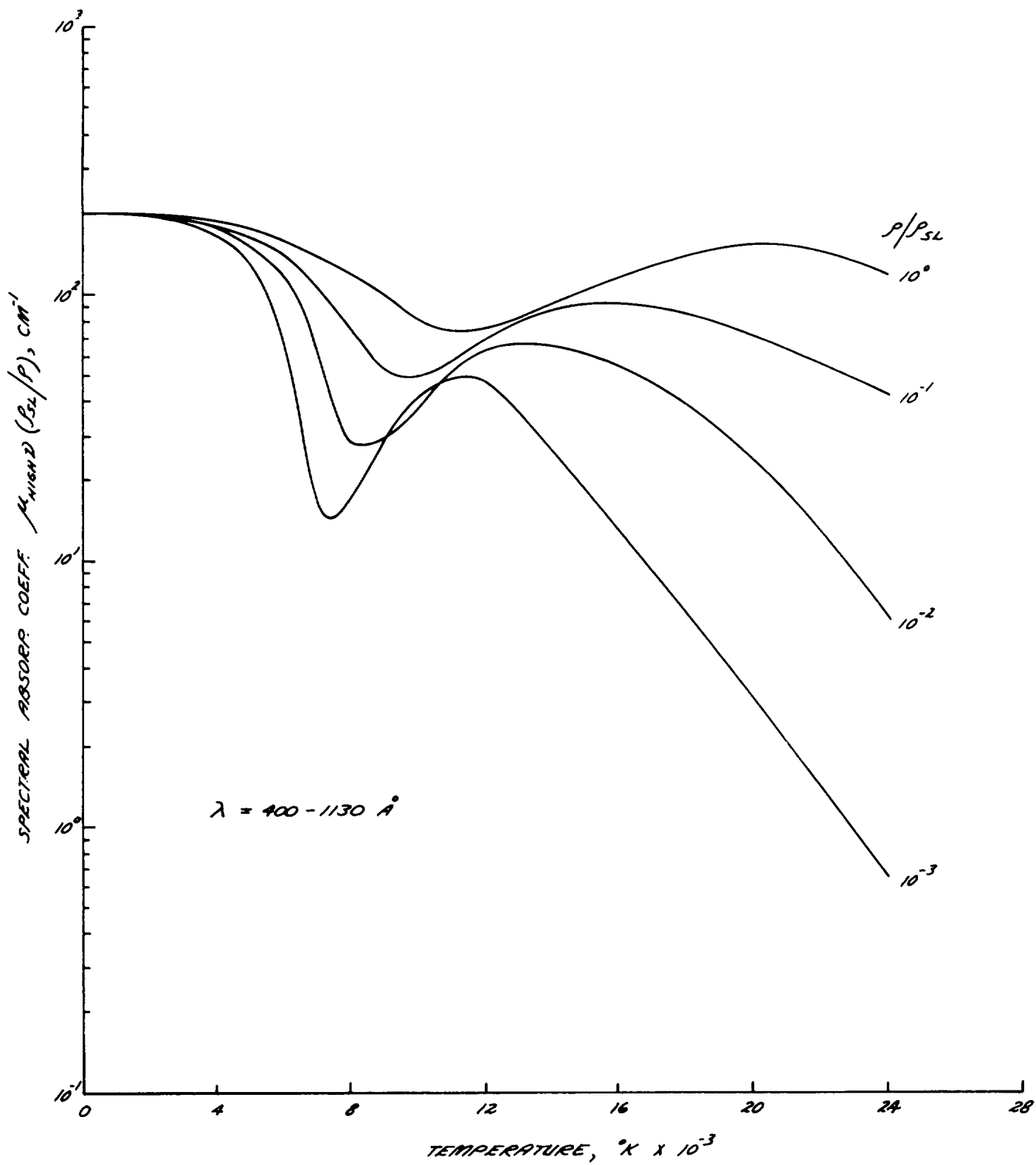


Figure 2B-2 High-Frequency Air Absorption Coefficients, Two-Band Model

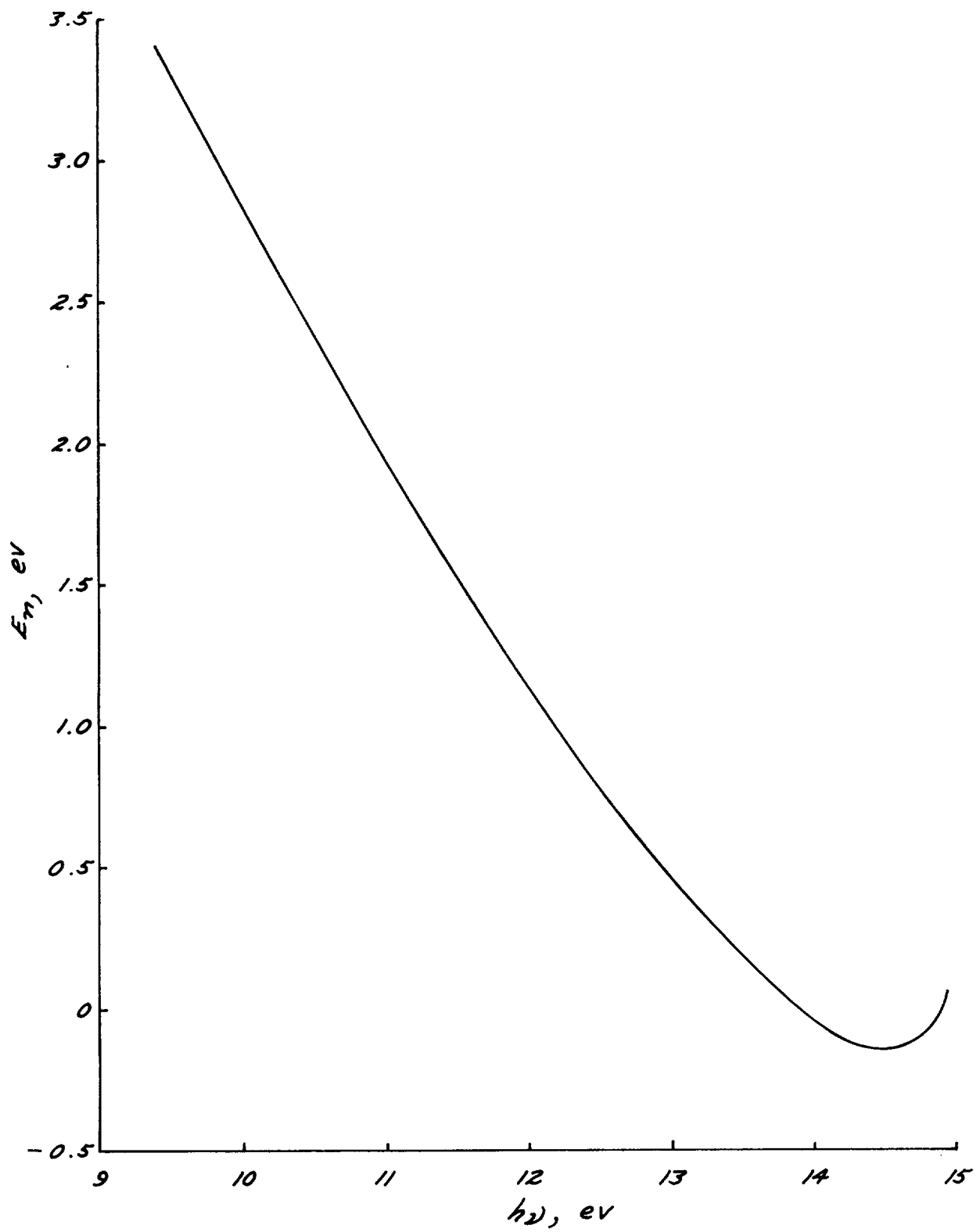


Figure 2B-3  $N_2$  Birge-Ropfield Band System Frequency-Dependent Factor

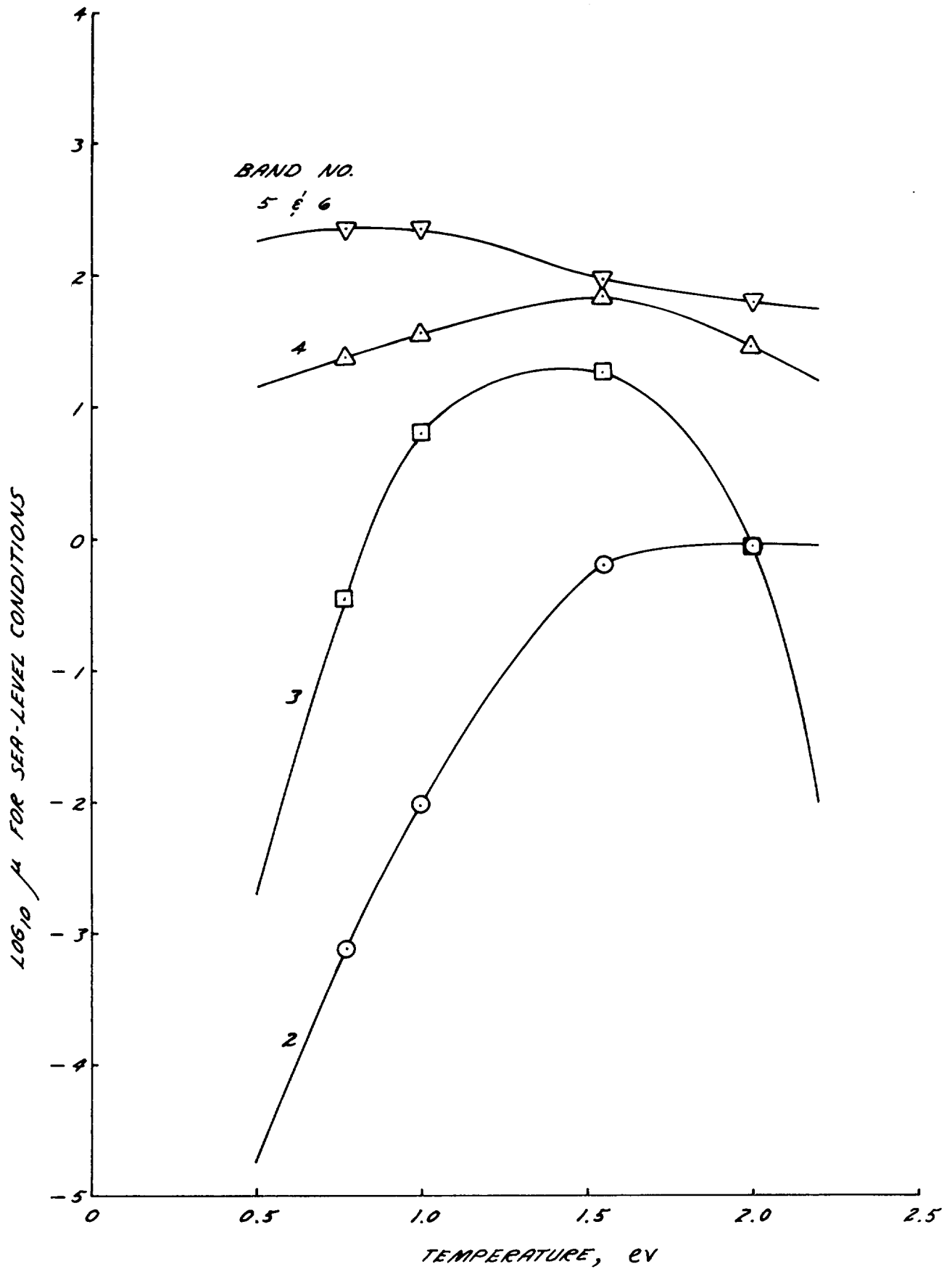


Figure 2B-4 N Continuum Spectral Absorption Coefficients, Six-Band Model



Appendix 2C  
NON-EQUILIBRIUM EFFECTS

By  
W. E. Nicolet and A. C. Buckingham

INTRODUCTION

As the nonequilibrium flow passes through the shock front and progresses downstream, collisions between particles excite the electronic states and initiate dissociation, ionization and other chemical processes. The kinetic temperatures drops monotonically (in a uniform flow) from a high value at the shock front to its fully equilibrated value some distance downstream. Those states which excite rapidly are soon populated in a quasi-equilibrium manner at the local kinetic temperature (hence they are overpopulated in relation to the equilibrium temperatures). If such states are active radiators they emit radiation as though they are at the local kinetic temperature. This is the phenomenon which accounts for the so-called "overshoot" radiation. It is clear that the more rapidly an excited state is populated the more significant will be the overshoot radiation.

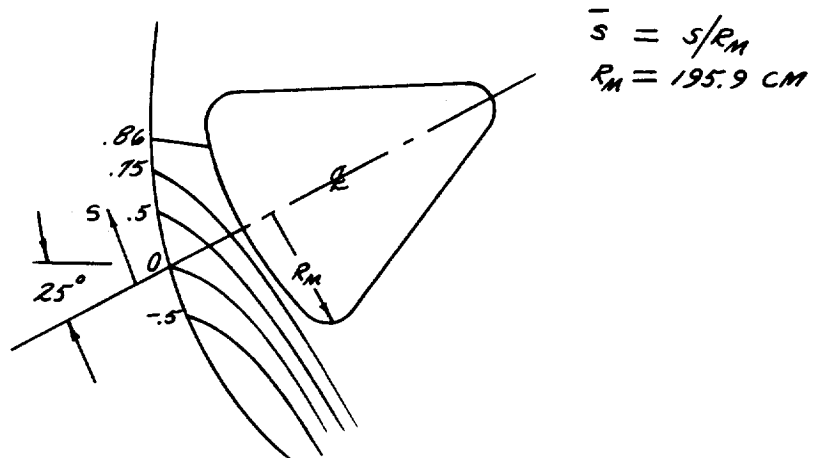
The kinetic temperature and the species concentrations are essentially uncoupled from the radiation field at Apollo conditions. Accordingly they are calculated independently by the flow rate chemistry calculation described in the following section. Using the data obtained from this calculation, the radiation properties and transport are determined.

FLOW RATE CHEMISTRY

General

The flow region analyzed is the shock layer flow field adjacent to the front face of the Apollo vehicle. The conceptual altitude is 260 kft.

The corresponding velocity is 35 kfps. The analysis is directed to the asymmetric flow associated with a vehicle pitched at  $25^\circ$  angle of attack with respect to the incident stream. The general geometrical characteristics of the flow field and the relative position of the 5 streamlines treated in the nonequilibrium analysis are sketched below.



The necessary flow variables, shock layer geometry, and streamline pattern were obtained from an equilibrium STREAMTUBE calculation and an assumed pressure distribution between shock front and body. While the pressure distribution governs, to first order, the transit time of the reacting fluid element in the subsequent analysis the error from this simplified treatment probably does not penalize the results severely. This is because the principal nonequilibrium effects occur in a limited region near the shock front where the pressure distribution is primarily governed by the shape of the shock front itself. On the other hand, the general shock front geometry (curvature and distortion) is a critical characteristic of the preliminary flow analysis since the subsequent chemistry calculations directly respond to variations in shock front strength in terms of variations to initial energetic excitation of the reacting fluid elements.

An additional assumption was made with respect to the ultimate behavior of the maximum entropy streamline (that streamline entering the shock at



normal incidence). This streamline was assumed to stagnate at the body surface. This essentially calls for two assumptions which are theoretically debatable: (1) The maximum entropy streamline in asymmetric flow may not actually reach or wet the body surface (Ref. 2.7), (2) The distortion of the shock front caused by asymmetry of the flow at large angles of attack makes the assumed concentricity of local body and shock curvature less probable (Ref. 2.12). These restrictions are considered of minor significance in the present analysis, however, since the ultimate stagnation of this particular streamline ( $S/R = 0.86$ ) is used only to estimate the effects of the nonequilibrium density vis-a-vis local shock stand-off. The approximation is used to provide a qualitative estimate of the relative effects of nonequilibrium flow on further distortion of the shock layer. The assumption of literal stagnation at the body or merely a close approach to it by this streamline is quantitatively insignificant with respect to the chemistry.

#### Stream Tube Chemistry Treatment

An IBM computer code developed at Lockheed (Ref. 2.1) was used to calculate the concentration profiles of the component species along each of the 5 streamlines previously discussed. The basic rate chemistry code is formulated in terms of the stream tube approximation. That is, a specified streamline geometry (constant area tube) and streamline pressure (or velocity) distribution govern the transit of a fluid element through an appropriate one-dimensional streamline momentum equation. Streamline position and pressure (or velocity) distributions are obtained from an equilibrium flow field solution.

Using the input data previously indicated, the rate chemistry code generates solutions to the following set of  $j+3$  equations:

$$u \frac{du}{dx} = - \frac{1}{\rho} \frac{dp}{dx} \quad \left( \text{MOMENTUM} \right) \quad (2C.1)$$

$$T(x) = \frac{H_{TOTAL} - \frac{[u(x)]^2}{2} - \sum_j n_j(x) \{e_{Dj} - e_{Ij}\}}{\sum_j n_j(x) c_{pj}} \quad (ENERGY) \quad (2C.2)$$

$$\frac{\rho(x)}{P(x)} = \sum_j n_j(x) T(x) \quad (STATE) \quad (2C.3)$$

$$\frac{dn_j}{dx} = \sum_{i \neq j} \frac{L_i}{\theta_i} (T) \quad (SPECIES PRODUCTION) \quad (2C.4)$$

where Eq. (2C.4) allows the properties to be spatically dependent.

The quantities in the foregoing equations signify the physical entities: streamline velocity, pressure, density and distance  $(u, p, \rho, x)$ ; static and total enthalpy,  $j^{th}$  species molar mass fraction, specific heat capacity, kinetic temperature, dissociation and ionization energies  $(h(x), H_{total}, n_j(x), c_{pj}, T(x), e_{Dj}, e_{Ij})$ .

The complete formulation of the rate processes is described in detail in a separate report (Ref. 2.1). The formulation is based on the method developed by G. Emanuel (Ref. 2.60). The contributions of the several rate processes, to the production of species,  $n_j$ , are written symbolically as:

$$\frac{L_i}{\theta_i} = \rho^N K_{Fi} \prod_k^N n_k - \rho^M K_{Ri} \prod_k^M n_k \quad (2C.5)$$

where the forward rate constants,  $K_{Fi}$ , were taken from Hall et al (Ref. 2.61) and Bortner (Ref. 2.62), while the reverse rate constants are computed from the equilibrium constants for the components,  $K_{Ri} = \frac{K_{Fi}}{K_{Ci}}$ .

The  $K_c$  are, in turn, calculated at every step from partition functions for the components developed from spectroscopic data listed in Gilmore (Ref. 2.63), Moore (Ref. 2.64), and Herzberg (Ref. 2.65). A total of 20 effective rate processes were used (applying preferential 3rd body collisions) for the production of 10 component species considered. Three algebraic equations were used which express the conservation of parent molecules and charge conservation thus reducing the number of differential equations of the form of Eq. (2C.4) to  $j-3$ .

The coupled system of equations was solved numerically by forward integration along each streamline using a 4<sup>th</sup> order Runge-Kutta system. The following species were considered:  $O_2$ ,  $N_2$ ,  $NO$ ,  $O$ ,  $N$ ,  $NO^+$ ,  $N_2^+$ ,  $O^+$ ,  $N^+$ ,  $e^-$ . Output of the code includes enthalpy, temperature, pressure, velocity, density, molecular compressibility, species molar fraction and number density, all as a function of streamline position,  $x$ . The initial conditions behind the shock for each of the streamlines were based on the data of Marrone (Ref. 2.66) with appropriate calculations for the local shock strength using the known shock angle. The Lockheed code solutions were based on an initial "state" of the gas fully excited in available vibrational and rotational modes, equilibrated to translational mode, but initially chemically inert. The ambient "air" model in the code is considered a molar mixture nitrogen and oxygen, 79 and 21 parts per 100, respectively.

#### The Stagnation Streamline

The nonequilibrium effects along the stagnation streamline were obtained from a separate calculation. The numerical solution to Eqs. (2C.1) - (2C.4) cannot be obtained for this streamline because of their well-known singularity at the stagnation point. Computationally, one finds ever-shrinking step sizes (hence ever-increasing computational times) as the flow nears the stagnation point. A method developed by Vinokur (Ref. 2.1) based on the work of Chisnell (Ref. 2.67) was used to circumvent this problem in the present study.

Vinokur shows that time can be related to actual physical distance along the stagnation streamline by the equation:

$$\rho u = \frac{dz}{dt} = (1 - z^2), \text{ WITH SOLUTION } t = \frac{z}{1-z^2} \quad (2C.6)$$

$$(t \rightarrow 0 \text{ AT THE SHOCK WAVE})$$

The quantity,  $Z$ , is a transformed coordinate defined by the Dorodnitsyn relation:

$$z = \int_0^x \rho dx \quad (2C.7)$$

The actual distance may then be obtained (valid to 1st order) using a nonequilibrium density profile calculated by the stream tube code using a constant pressure flow field solution. With this information and Eq. (2C.6) the real physical distance,  $x(z)$ , is found by a single quadrature, inverting Eq. (2C.7)

$$x(z) = \int_0^z \frac{dz}{\rho[t(z)]}$$

with the computed density distribution and its relation to  $t$  given by Eq. (2C.6).

The above method was also used to estimate the change in the shockwave standoff distance caused by nonequilibrium effects. The corrected standoff distance was found to be 9.8 cm or a 43% larger value than the equilibrium standoff distance.

### Results

The general results of the nonequilibrium calculations were used to predict the spatial distribution of the species number densities for input into the subsequent calculations predicting the radiation characteristics of the shock layer gas and ultimately the radiation flux itself. In general, the

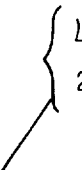
onset of steepest gradients (evolution) in dissociation processes occurred near the shock front (distances of 1 cm or less) while the corresponding steep ionization onset gained significance at distances of around 3 to 10 cm. The dissociation and ionization along the several streamlines (other than the stagnation streamline) reached relatively constant levels at from 10 to 30 cm behind the shock. Changes to the number density of the species populations were relatively insignificant past this point with the exception of the nitric oxide and molecular nitrogen ions which generally underwent a sharp reversal and gradually disappeared near this streamline location.

The comparative behavior between the various streamlines showed the expected strong dependence on local shock geometry (the behavior consistently reflected the relative energetic excitation implied by the comparative shock strength). Illustrative characteristics of the chemical evolution on the streamlines may be seen in Table 2C.1. The table is arranged sequentially from the most energetic (S/R = 0.86) to the least energetic (S/R = -0.50) streamlines for ease in systematic comparison.

Table 2C.1

NON-EQUILIBRIUM CHARACTERISTICS OF THE STREAMLINES TRACED

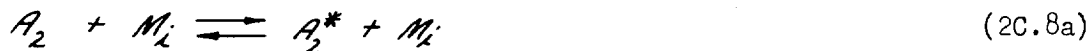
STREAMLINE (S/R <sub>M</sub> ) <sub>i</sub>	INITIAL KINETIC	MAX. ELECTRON NO.		TEMPERATURE AT	
	TEMPERATURE (°K)	Density (CM <sup>-3</sup> )	Position (CM)	STREAMLINE LIMIT T(°K)	Position(CM)
0.86	4.4 <sup>+4</sup>	1.9 <sup>+15</sup>	9.8	9.7 <sup>+3</sup>	9.8
0.75	4.3 <sup>+4</sup>	4.0 <sup>+14</sup>	4.5 <sup>+1</sup>	1.6 <sup>+4</sup>	4.5 <sup>+1</sup>
0.50	4.2 <sup>+4</sup>	1.65 <sup>+14</sup>	2.25 <sup>+2</sup>	1.45 <sup>+4</sup>	2.25 <sup>+2</sup>
0	3.7 <sup>+4</sup>	4.4 <sup>+13</sup>	4.0 <sup>+1</sup>	1.1 <sup>+4</sup>	1.55 <sup>+2</sup>
-0.50	3.0 <sup>+4</sup>	2.97 <sup>+13</sup>	1.3 <sup>+1</sup>	9.3 <sup>+3</sup>	6.8 <sup>+1</sup>


 Overshoot, followed by decay on these two, "coolest" streamlines

RADIATION PROPERTIES AND TRANSPORT

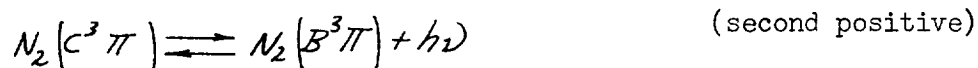
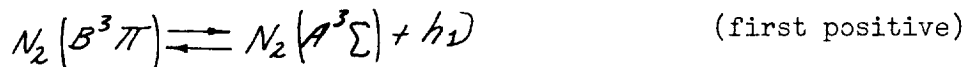
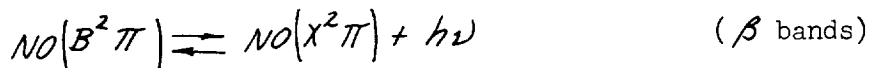
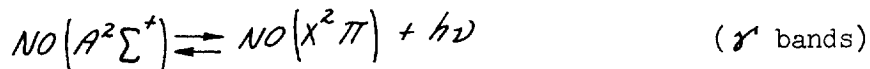
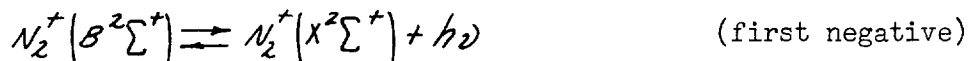
Radiation Properties

For air the overshoot radiation comes from overpopulated electronic states of the constituent molecules. The general reaction governing this phenomena is



where  $A_2$  is a molecule in its ground state,  $A_2^*$  and  $A_2'$  are the same molecule in different excited states,  $M_i$  is a non-interacting (neutral or charged) particle and  $h\nu$  designates the emission of radiation. Excitations by collisions as given by Eq. (2C.8a) tend to dominate the populating rate of the excited state  $A_2^*$ ; consequently, Eq. (2C.8a) can be solved independently of Eq. (2C.8b) and the populations then used to calculate the emission rate associated with Eq. (2C.8b).

The radiative reactions for air which are considered to be important enough to evaluate are the following:



where it has been assumed that the  $O_2$  Shumann-Runge bands do not radiate significantly in the nonequilibrium region. This assumption is subsequently discussed.

It was shown in Ref. (2.1) that the emission coefficient for a radiative reaction can be related to the usual forward rate coefficient through the equation

$$j_{\nu} = \frac{N_{A_2^*} k_{mf}(\nu)}{4\pi} \quad (2C.9)$$

It was also shown that the rate coefficient could be calculated from fundamental data by the relation

$$k_{mf}(\nu) = \frac{8\pi\nu^2}{c^2} \frac{W_{A_2^*}}{W_{A_2}} \frac{\pi e^2}{mc} f_{A_2^* - A_2} g'(\nu) \quad (2C.10)$$

where the quantities  $f_{A_2^* - A_2}$ ,  $W_{A_2^*}$  and  $W_{A_2}$  are the electronic oscillator strength and the statistical weights of the interacting electronic states and are given in Table 2C.2. The quantity  $g'(\nu)$  is the effective Franck Condon factor given by the relation

$$g'(\nu) = \frac{1}{5\nu} \sum_{v''} \sum_{v'} \frac{N_{A_2^*, v'}}{N_{A_2^*}} g_{v'' v'} \quad (2C.11)$$

which can be evaluated using the Franck Condon factors  $(g_{v'' v'})$  tabulated by Nicholls (see the references quoted in Ref. 2.1) and the populations of the vibrational levels  $N_{A_2^*, v'}$  of the excited electronic levels.

Table 2C.2

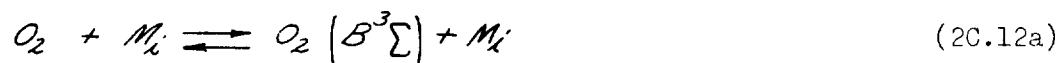
## OSCILLATOR STRENGTHS AND STATISTICAL WEIGHTS

Species	Transition	$f_{A_2^* - A_2^*}$	$W_{A_2^*}$	$W_{A_2^*}$
NO	$B^2\pi \rightarrow X^2\pi$	0.0008	4	4
	$A^2\Sigma \rightarrow X^2\pi$	0.0025	4	2
$N_2^+$	$B^2\Sigma \rightarrow X^2\Sigma$	0.0348	2	2
$N_2$	$B^3\pi \rightarrow A^3$	0.02	3	6
	$C^3\pi \rightarrow B^3\pi$	0.07	6	6

Non-Equilibrium Populations

The evaluation of Eqs. (2C.9) and (2C.11) requires that the species populations as calculated by the flow rate chemistry code be subdivided into the populations of their constituent electronic and vibrational states. This calculation is relatively straightforward in the case of the vibrational states, as it is consistent with the assumptions of the species concentration to assume that the vibrational levels are in equilibrium with the kinetic temperature. In the case of the electronic levels, however, the required rate coefficients are not known and even the excitation mechanisms have not been established. Any techniques presently available for the calculation of these quantities require drastic assumptions which cast doubt on their validity.

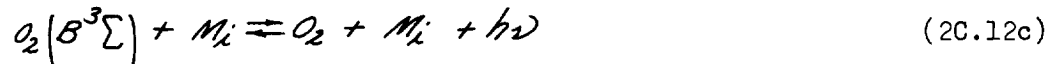
Insight into the excitation mechanism of  $O_2$  is particularly limited. It has been suggested by Kivel, Hammerling and Teare (Ref. 2.68) that the population rate of the level of  $O_2$  (the upper level in the Shuman-Runge transition) is determined by competition between the reactions







and



They performed a series of experiments at relatively low Mach number flows (equilibrium temperatures were less than about 5000°K) and observed that oxygen emission did not overshoot its equilibrium value. They concluded that the forward reaction rates for Eq. (2C.12b) are fast enough to keep the  $O_2(B^3\Sigma)$  level depleted and severely limit emission. This result is to be contrasted with the calculations of Hansen and Chapin (Ref. 2.69) where they found that  $O_2$  emission dominated the overshoot region. Little is known about the rate coefficients associated with Eq. (2C.12b); consequently, its effect cannot be accurately ascertained. However, the approach taken in the present study was to neglect  $O_2$  emission entirely.

For the  $N_2^+$ , NO and  $N_2$  bands, it was assumed that the excited electronic levels are in equilibrium with each other. This is consistent with the approach taken by Wray and Teare (Ref. 2.70). The experimental results of Allen, Rose and Camm (Ref. 2.32) were used to determine the ratio of the time required for the molecular emission to reach its peak  $\tau_m$  to the time required for it to decay to equilibrium  $\tau_e$ . Assuming that the time for the decay in emission is the same as the time required to dissociate  $N_2$ , one can obtain  $\tau_e$  (hence  $\tau_m$ ) from the results of the flow chemistry calculation.

For times equal to or greater than  $\tau_m$ , the required populations were obtained from an equilibrium calculation based on the local kinetic temperature. For times earlier than  $\tau_m$ , the populations were estimated by fairing a linear, monotonic electronic temperature curve between the

boundary condition value at the shock and the kinetic temperature calculated at  $\tau_m$ . The populations were calculated from an equilibrium calculation at the local electronic temperature ( $\theta$ ) by the following equation

$$\frac{N_{A_2}^*}{N_{A_2}} = \frac{W_{A_2}^*}{W_{A_2}} \frac{Q_{A_2}^*(T_i)}{Q_{A_2}(T_i)} e^{-\frac{E_{A_2}^*}{k\theta}} \quad (20.13)$$

where  $E_{A_2}^*$  is the energy difference between the excited and ground electronic states, and  $Q_{A_2}^*(T_i)$  and  $Q_{A_2}(T_i)$  are the partition functions of the excited and ground states, respectively, and are based on the local kinetic temperature  $(T_i)$ .

#### Radiative Heating to the Apollo Vehicle

About 10 values of  $j$  were calculated along each streamline. These values were then crossplotted as a function of the distance behind the shock along normals to the surface of the vehicle. This plot is shown in Fig. 20-1 with the peak emission coefficients shown in parenthesis. The radiative heating was obtained by applying the plane slab approximation locally, viz

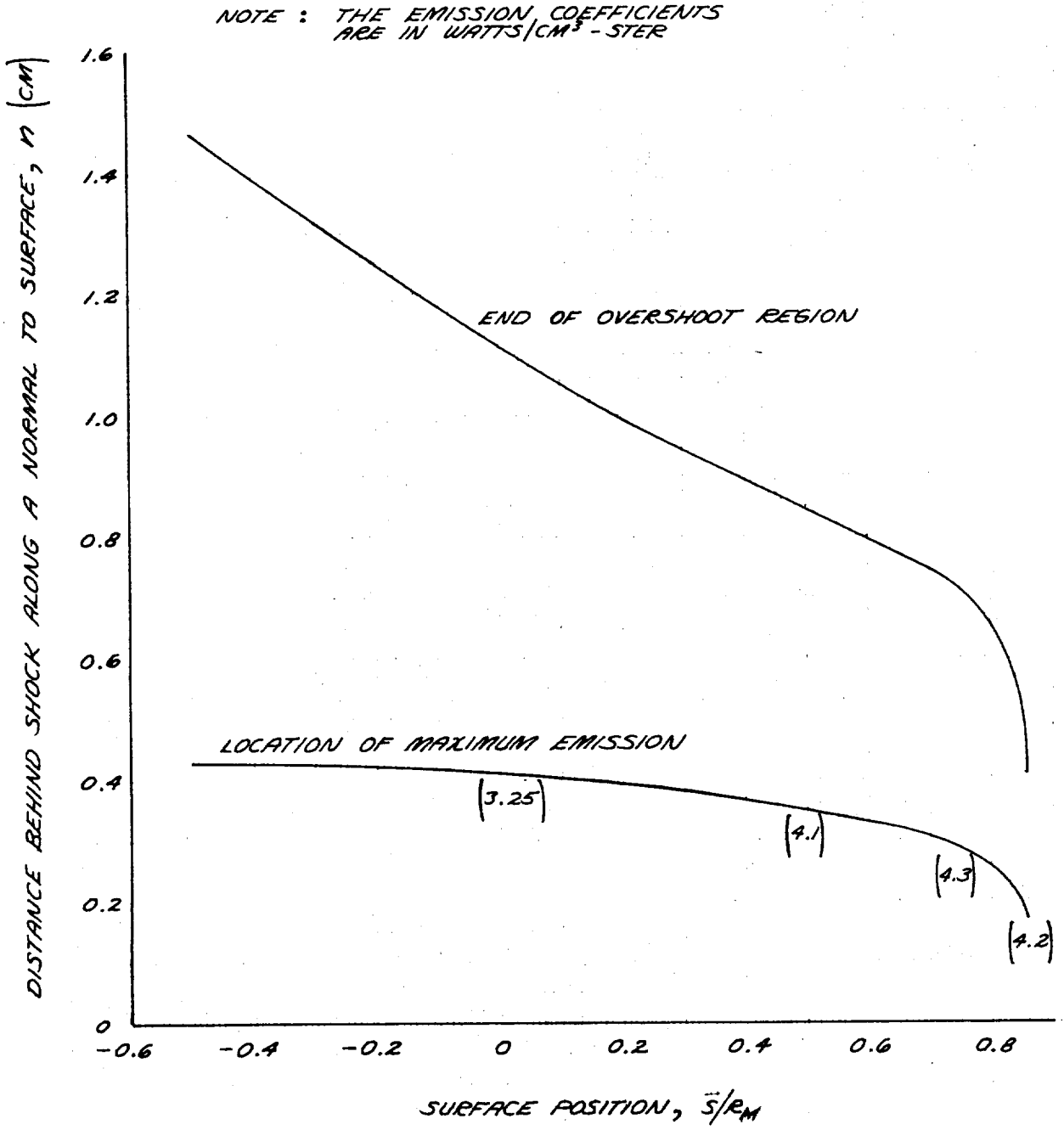
$$q_r(s/R) = 2\pi \int \int \int_{\text{OVERSHOOT REGION}} j_v d\nu dn \quad (20.14)$$

where  $n$  is the geometrical distance normal to the surface of the vehicle. The resulting radiative heating distribution is shown in Fig. 20-2.

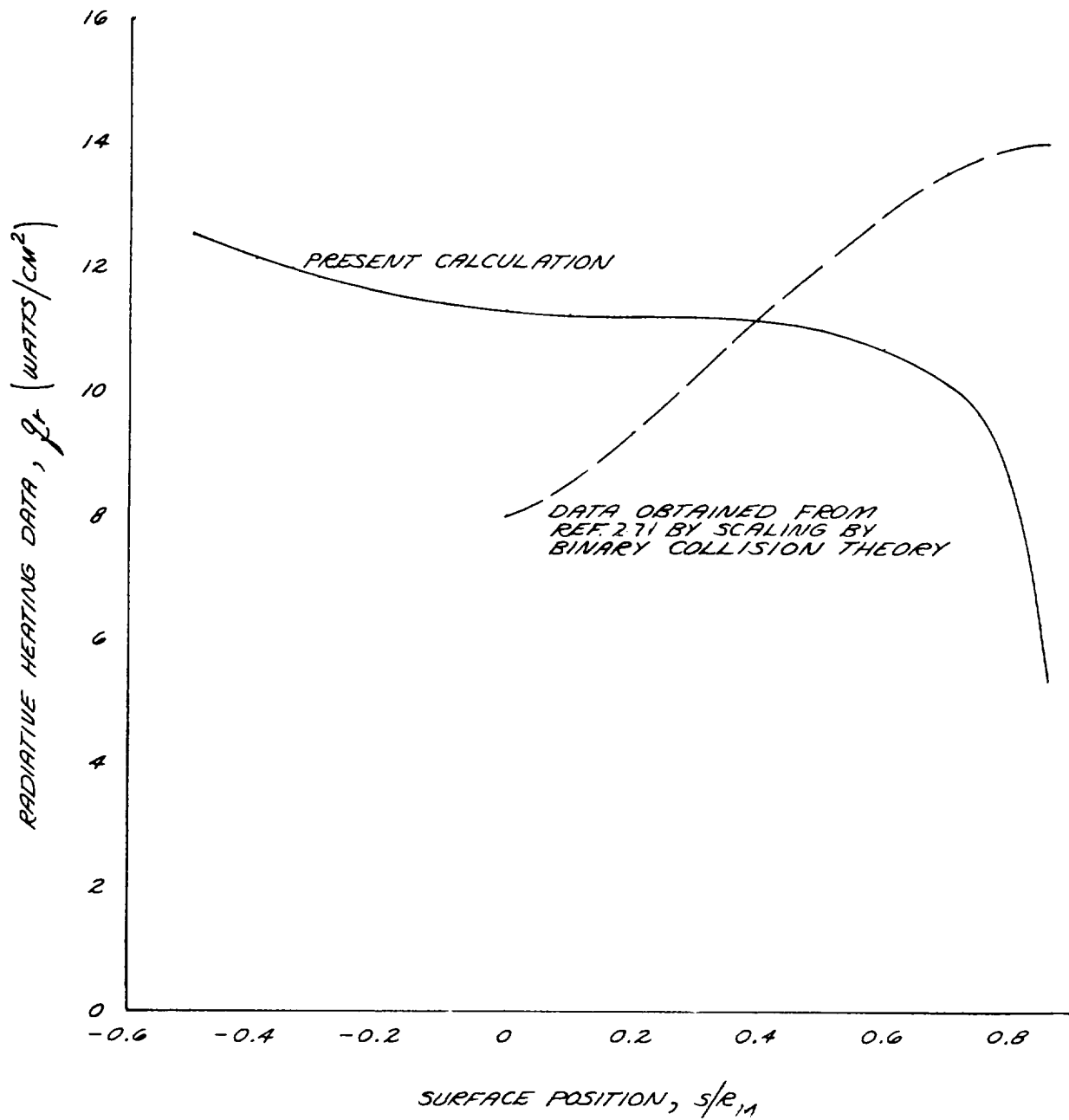
If one uses binary collision theory to scale the measurements given in Ref. (2.32) to the Apollo flow conditions, one finds that the calculated locations of the maximum and equilibrium emission coefficients are situated somewhat closer to the shock front than are the scaled values. This indicates that the dissociation rates which were used in the flow chemistry calculation are too high. It also indicates that the overshoot region

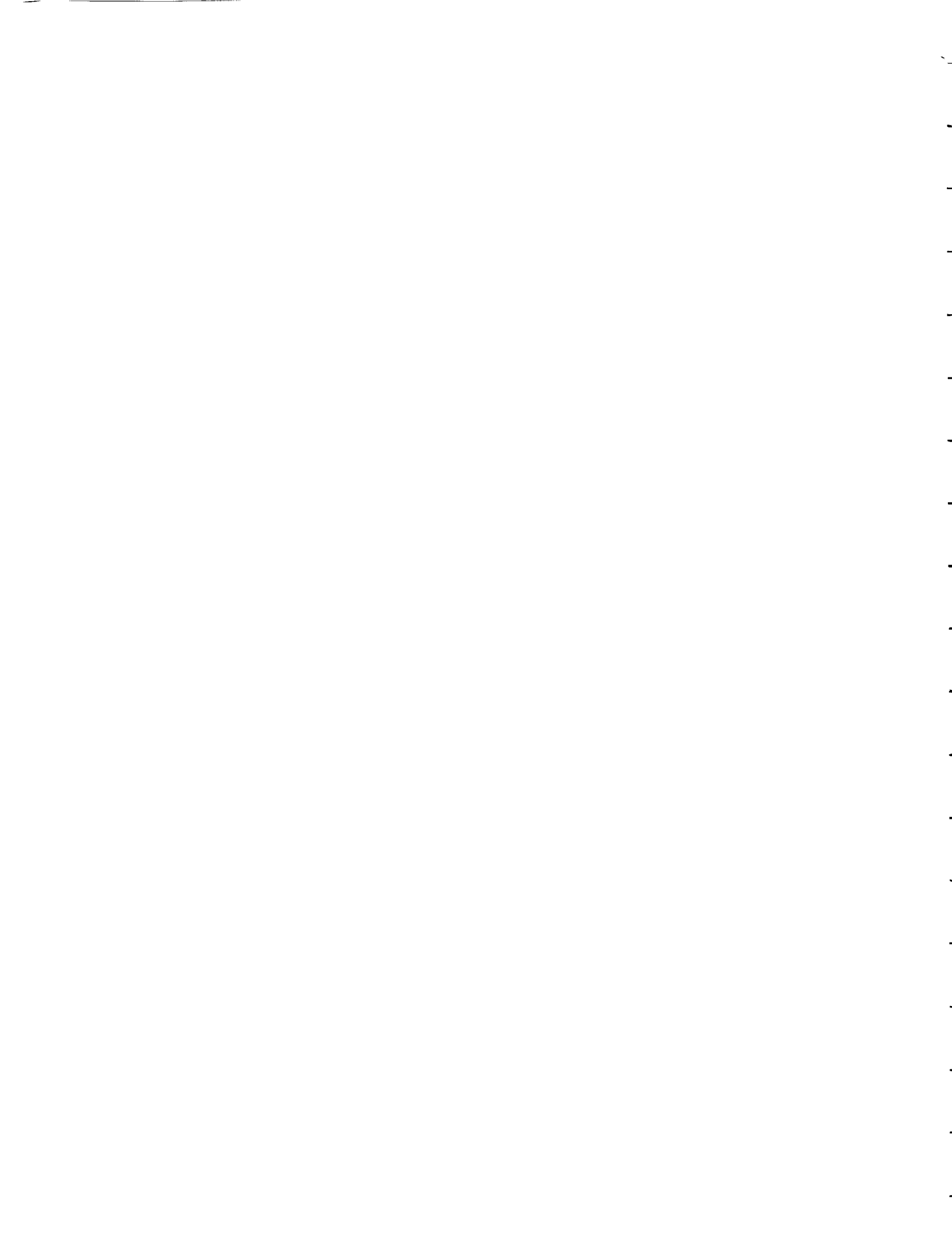
is too thin, and, consequently, the radiative heating is too small. If one uses binary collision theory to scale the radiative heating measurements of Ref. (2.71) to Apollo conditions, it is, indeed, found that the scaled values are somewhat higher than the calculated values (see Fig. 2C-2). The discrepancy is significantly greater using the measurements of Ref. (2.32).

**FIGURE 2C-1**  
**LOCATION OF THE OVERSHOOT REGION**



**FIGURE 2C-2**  
**RADIATION HEATING DATA**





## Appendix 2D

### CONVECTIVE HEATING WITH THREE-DIMENSIONAL FLOW

For the case with small cross-flow, the conservation equations governing three-dimensional boundary-layer flow may be put in a form identical with those for axially symmetric flow. This is accomplished using the spreading coordinate discussed in Section 2.1 and defined in Appendix 2A. It may be recalled that the coordinate provides a measure of the divergence of adjacent streamlines. Thus it is analogous to the radial coordinate used for axially symmetric flows. It appears in the mass conservation equation in place of the radial coordinate.

The application of the spreading coordinate in evaluation of convective heat transfer is described in this appendix. In particular, a relation for determining three-dimensional stagnation point heating is developed. Also formulated is an equation for the heat transfer distribution. These developments follow along the general lines suggested by Cohen ( Ref. 2.103). It is assumed that the boundary layer flow is in chemical equilibrium and that mass injection is absent. Furthermore, local similarity is assumed.

#### BASIC RELATIONS

In order to proceed, the conservation equations (2.127 - 2.130) are reduced to similar form. First, it is noted for the assumed chemical equilibrium condition that the species conservation equation is superfluous and that diffusion terms may be eliminated from the energy equation by use of the total (or effective) property concept. With these simplifications the conservation equations reduce to

$$\frac{\partial}{\partial s} (\rho u h_2) + \frac{\partial}{\partial y} (\rho v h_2) = 0 \quad (2D.1)$$

$$\rho u \frac{\partial u}{\partial s} + \rho v \frac{\partial u}{\partial y} = - \frac{dp}{ds} + \frac{\partial}{\partial y} \left( \mu \frac{\partial u}{\partial y} \right) \quad (2D.2)$$

$$\rho u \frac{\partial H}{\partial s} + \rho v \frac{\partial H}{\partial y} = \frac{\partial}{\partial y} \left[ \frac{\mu}{\bar{Pr}} \frac{\partial H}{\partial y} + \frac{\mu}{\bar{Pr}} \left( \bar{Pr} - 1 \right) \frac{\partial u^2/2}{\partial y} \right] \quad (2D.3)$$

where  $\bar{Pr}$  denotes the Prandtl number based on total conductivity and specific heat. Following Cohen's development for the analogous axisymmetric case, the following coordinate transformation is made

$$\tilde{s} = \frac{1}{\mu_0^2} \int_0^s \rho_w \mu_w u_e h_2^2 ds \quad (2D.4)$$

$$\eta = \frac{u_e h_2}{\mu_0 \sqrt{2\tilde{s}}} \int_0^y \rho dy \quad (2D.5)$$

and a stream function satisfying the continuity equation is introduced

$$\frac{\partial \psi}{\partial y} = \rho u h_2 \quad (2D.6)$$

$$\frac{\partial \psi}{\partial s} = \rho v h_2 \quad (2D.7)$$



The similarity variables are

$$f(\eta) = \frac{\psi}{H_0 \sqrt{2S}} \quad (2D.8)$$

$$g(\eta) = \frac{H}{H_e} \quad (2D.9)$$

The momentum and energy equations transform to

$$\left( \frac{\rho\mu}{\rho_w\mu_w} f'' \right)' + ff'' = \tilde{\beta} \left[ (f')^2 - \frac{\rho_e}{\rho} \right] \quad (2D.10)$$

$$\left( \frac{1}{Pr} \frac{\rho\mu}{\rho_w\mu_w} g' \right)' + fg' = \left[ \frac{\rho\mu}{\rho_w\mu_w} \left( \frac{1-\bar{Pr}}{Pr} \right) \left( 1 - \frac{h_e}{H_e} \right) (f')^2 \right]' \quad (2D.11)$$

where the transformed pressure gradient parameter is related to the physical velocity gradient by

$$\tilde{\beta} = \frac{2H_e}{h_e} \frac{\tilde{s}}{u_e} \frac{ds}{d\tilde{s}} \frac{du_e}{ds} \quad (2D.12)$$

The transformed boundary layer equations and associated boundary conditions are formally identical with those for axially symmetric flow. Thus the axially symmetric solutions for  $f'$  and  $g$  may be directly applied if the pressure gradient parameter  $\tilde{\beta}$  and the enthalpy ratio  $h_e/H_e$  are correctly evaluated.

With a solution of the transformed energy equation for  $g'_{\eta=0}$ , the convective

heat flux may be determined from Eqs. (2D.5) and (2D.9)

$$q = \left( \frac{\bar{k}_w}{\bar{c}_{pw}} \frac{dH}{dy} \right)_{y=0} = \frac{\bar{k}_w \rho_w U_e h_2}{\bar{c}_{pw} \mu_0 \sqrt{2} S} He(q)_{\eta=0} \quad (2D.13)$$

#### STAGNATION POINT SOLUTION

The foregoing equation may be simplified somewhat for the stagnation point. In the stagnation region

$$U_e = \left. \frac{dU_e}{ds} \right|_{s=0} s = \beta_0 s \quad (2D.14)$$

and the spreading coordinate is given in Section 2.1 as

$$h_2 \sim s^{\beta_2/\beta_0} \quad (2D.15)$$

Thus, the transformed streamwise coordinate of Eq. (2D.4) reduces to

$$\tilde{s} = \frac{\rho_w \mu_w \beta_0 s^{2(1+\beta_2/\beta_0)}}{2(1+\beta_2/\beta_0) \mu_0^2} \quad (2D.16)$$

Substitution of these results in Eq. (2D.13) yields

$$q = \frac{1}{\bar{P}_{rw}} \left[ \left( \frac{\beta_2}{\beta_0} + 1 \right) \rho_w \mu_w \beta_0 \right]^{1/2} He(q)_{\eta=0} \quad (2D.17)$$

For rotationally symmetric flow,  $\beta_2/\beta_0 = 1$  and thus

$$\frac{q_{3D}}{q_{AXI}} = \left\{ \frac{\left[ 1 + \frac{\beta_2}{\beta_0} \right]^{1/2}}{2} \right\} \frac{(q'_{\eta=0})_{3D}}{(q'_{\eta=0})_{AXI}} \quad (2D.18)$$

The transformed stagnation point enthalpy gradient for given external and wall conditions is dependent only on the transformed pressure gradient

parameter. Cohen has obtained the following correlation for results obtained in numerical solution of Eqs. (2D.10) and 2D.11)

$$\frac{q'(\tilde{\beta})}{q'(\tilde{\beta}=1)} = \frac{1 + 0.527 \tilde{\beta}^{.686}}{1.116 + 0.411 \tilde{\beta}^{.686}} \quad (2D.19)$$

From Eqs. (2D.12), (2D.14) and 2D.16), the values of the pressure gradient parameter for axially symmetric and three-dimensional flows are found to be  $1/2$  and  $(1 + \beta_z/\beta_o)^{-1}$ , respectively. Thus, equations (2D.18) and 2D.19) may be combined to obtain the following simple relation for the effect of three-dimensional flow.

$$\frac{q_{3D}}{q_{AXI}} = \left[ \frac{1}{2} \left( 1 + \beta_z/\beta_o \right) \right]^{1/2} \left[ \frac{1.033}{1.116 + 0.411} \left( \frac{1 + \beta_z/\beta_o}{1 + \beta_z/\beta_o} \right)^{-.686} \right] \quad (2D.20)$$

#### CONVECTIVE HEAT TRANSFER DISTRIBUTION

It is convenient in heat transfer calculations to work with the ratio of local heating to stagnation point heating. This ratio may be obtained from Eq. (2D.13) and 2D.17). After substitution for the local value of  $\tilde{S}$ , the result is

$$\frac{q}{q_o} = \frac{\rho_w \mu_w u_e h_2}{\left[ 2(\beta_z + \beta_o) \left( \rho_w \mu_w \right)_{s=0} \right]^{1/2} \left[ \int_0^s \rho_w \mu_w u_e h_2^2 ds \right]^{1/2}} \frac{\left( q'_{\eta=0} \right)_s}{\left( q'_{\eta=0} \right)_{s=0}} \quad (2D.21)$$

As explained in Section 2.3.2, the ratio of the transformed enthalpy gradients may be obtained from Cohen's local similarity solutions.



## Appendix 2E

It has been suggested by Rubin (Ref. 2.135) and others that the influence of shock-generated vorticity on boundary-layer flow may be approximately accounted for by utilizing an "effective" outer-edge velocity in application of existing first-order boundary layer solutions. The primary difficulty in such an approach is definition of the proper point in the inviscid flow at which to evaluate the effective edge velocity. In Reference 2.52, it was assumed that this point could be defined in terms of the transformed stream function,  $f = \psi/\mu_0 \sqrt{25}$ .<sup>\*</sup> A unique value, 1.06, of this function was selected by requiring the correct asymptotic behaviour of the wall shear stress in the limit as the vorticity approaches infinity. The basic technique is appealing in its simplicity and, with the effective edge definition of Ref. 2.52, it appears to yield results in good agreement with second-order boundary-layer-theory solutions. The method is therefore adopted in spite of its lack of rigor.

The stagnation-point solution of Ref. 2.52, is reformulated in this appendix for the case of three-dimensional flow. Also described is a procedure for evaluating the effect of vorticity on the convective heat transfer distribution.

### STAGNATION POINT SOLUTION

An approximate model of the inviscid flow field is developed prior to consideration of the boundary layer. The basic relations are obtained

---

\* The coordinate transformation defined in Appendix 2D is used throughout this work.

from Section 2.1.2. The tangential velocity immediately behind the shock wave in the plane of symmetry is from Eq. (2.45) and (2.47)

$$\frac{u_s}{u_\infty} = \frac{d\theta_s}{ds} s \equiv \frac{s}{R_{EFF}} \quad (2E.1)$$

where  $R_{EFF}$  is the radius of curvature of the shock at the stagnation point. Provided that the density ratio,  $\epsilon$ , is small, Eq. (2.50) for the inviscid surface velocity may be approximated by

$$\frac{u_0}{u_\infty} \approx \sqrt{2\epsilon} \frac{u_s}{u_\infty} = \sqrt{2\epsilon} \frac{s}{R_{EFF}} \quad (2E.2)$$

Maintaining the assumption of Section 2.1.2 that the velocity varies linearly with distance from the surface, the local inviscid velocity is given by

$$\frac{u_{inv}}{u_\infty} = \frac{u_0}{u_\infty} + \left[ \frac{u_s}{u_\infty} - \frac{u_0}{u_\infty} \right] \frac{y}{\Delta} \quad (2E.3)$$

The continuity equation is

$$\frac{\partial \rho u h_2}{\partial s} + \frac{\partial \rho v h_2}{\partial y} = 0 \quad (2E.4)$$

which can be alternately expressed in terms of the stream function as (Eq. 2.20)

$$\psi = \int_0^y \rho u h_2 dy = \rho_\infty u_\infty \int_0^{\pi/2} h_2 dx \quad (2E.5)$$

The spreading coordinate in the immediate vicinity of the stagnation point was given by Eq.(2.53) as

$$h_2 = s \beta_z / \beta_0 \quad (2E.6)$$

For the previously assumed condition of a thin shock layer and small density ratio, the velocity gradient ratio can be approximated as

$$\frac{\beta_z}{\beta_0} \approx \frac{R_{EFF}}{R_C} \quad (2E.7)$$

Thus, with the approximation of uniform density, Eq. (2E.5) may be integrated after substitution of Eqs. (2E.3) and (2E.6) to obtain the following result for the shock layer thickness

$$\frac{\Delta}{R_{EFF}} = \frac{2E}{(1 + \sqrt{2E})(1 + R_{EFF}/R_C)} \quad (2E.8)$$

The same equations provide a relation between the stream function and the local inviscid velocity.

$$\psi = \frac{\rho_0 \Delta}{2} \frac{u_{inv}^2 - u_0^2}{u_s - u_0} s \frac{R_{EFF}}{R_C} \quad (2E.9)$$

This relation may be put in a form more convenient for later use.

$$\psi = \frac{\rho_0 \Delta}{2} \left[ \frac{\left(\frac{u_s}{u_0}\right)^2 - 1}{\frac{u_s}{u_0} - 1} \right] \frac{du_0}{ds} s \frac{R_{EFF}}{R_C} + 1 \quad (2E.10)$$

Equation (2E.10) is the final result required for the inviscid flow. The boundary layer may now be considered.

The boundary-layer equations and similarity transformations were described in Appendix 2D. Using these results, the mass flow at any point,  $y$ , within the boundary layer is given by

$$\psi = \int_0^y \rho u h_2 dy = \mu_0 \sqrt{2\tilde{s}} f \quad (2E.11)$$

where, near the stagnation point

$$\tilde{s} = \frac{\rho_w \mu_w}{\mu_0^2} \frac{du_{inv}^*}{ds} \frac{(s)^2 \left(\frac{R_{EFF}}{R_C} + 1\right)}{2 \left(\frac{R_{EFF}}{R_C} + 1\right)} \quad (2E.12)$$

In this latter relation  $U_{inv}^*$  denotes the effective edge velocity. It was found in Ref. 2.52 that a suitable point for evaluation of this velocity was at  $f = 1.06$ . Then, equating (2E.10) and (2E.11) and rearranging

$$\frac{u_{inv}^*}{u_0} = \left\{ 1 + \frac{2 \left( 1.06 \right)}{\left( 1 + \frac{R_{EFF}}{R_C} \right)^{1/2}} \left( \frac{\rho_w \mu_w}{\rho_0^2 \frac{du_0}{ds} \Delta^2} \right)^{1/2} \left( \frac{du_{inv}^*}{ds} / \frac{du_0}{ds} \right)^{1/2} \right\}^{1/2} \quad (2E.13)$$

The velocity gradient term within the braces is approximated as unity to simplify evaluation of the expression. Furthermore, the density-viscosity product is assumed constant through the boundary layer. Then, with the aid of Eqs. (2E.8) and (2E.2), Eq. (2E.13) reduces to



$$\frac{U_{inv}^*}{U_0} = \left\{ 1 + \frac{3}{2} \left( 1 + \frac{R_{EFF}}{R_C} \right)^{1/2} \left( \frac{\mu_0}{\rho_0 U_0 R_{EFF}} \right)^{0.5} \frac{1-2\epsilon}{(2\epsilon)^{5/4}} \right\}^{1/2} \quad (2E.14)$$

The convection coefficient as determined from a first-order boundary layer solution varies directly as the square root of the stagnation-point velocity gradient. Noting that

$$\frac{dU_{inv}^*}{ds} / \frac{dU_0}{ds} = \frac{U_{inv}^*}{U_0}$$

the influence of vorticity is given by

$$\frac{C_{H VORT}^*}{C_{H NO VORT}} = \left( \frac{dU_{inv}^* / ds}{dU_0 / ds} \right)^{1/2} = \left\{ 1 + \frac{3}{2} \left( 1 + \frac{R_{EFF}}{R_C} \right)^{1/2} \left( \frac{\mu_0}{\rho_0 U_0 R_{EFF}} \right)^{1/2} \frac{1-2\epsilon}{(2\epsilon)^{5/4}} \right\}^{1/4} \quad (2E.15)$$

This result indicates that flow geometry weakly influences the extent of the vorticity interaction. The formula shows that the vorticity effect will decrease as the flow approaches a two-dimensional pattern. However, the indicated effect may not be correct. The previously introduced assumption of a linear inviscid-velocity profile is justified only for axially symmetric flow. It underpredicts the surface velocity gradient for two-dimensional flows. Elimination of this assumption would tend to compensate for the flow geometry effect indicated by Eq. (2E.15).

In order to assess the validity of Eq. (2E.15) it may be compared with second-order boundary-layer solutions. For this purpose, the axially-symmetric stagnation-point solution of Maslen (Ref. 2.74) is examined. His result, which applies to a cold wall, may be expressed as

$$\frac{C_{H \text{ VORT}}}{C_{H \text{ NO VORT}}} = 1 + \frac{2}{0.664 \sqrt{\rho \frac{d_{40}}{d_5}} / M_0} \left[ -\frac{0.02}{R_c} + 0.13 \left( \frac{d_{11,v}}{d_0} \frac{dy}{dx} + \frac{1}{R_c} \right) + 0.06 \frac{H_w}{H_e} \right] \quad (2E.16)$$

The terms within the brackets account for surface curvature, vorticity, and slip, respectively. It may be seen that the vorticity interaction is the predominant one. Then, neglecting the small curvature and slip effects, Eq. (2E.16) may be put in a form similar to that of Eq. (2E.15) by utilizing Eqs. (2E.1) to (2E.3) and (2E.8). The result is

$$\frac{C_{H \text{ VORT}}}{C_{H \text{ NO VORT}}} = 1 + \frac{0.26}{0.664} \left[ \frac{M_0}{\rho_{\infty} u_{\infty} R_c} \right]^{1/2} \left[ \frac{1 - 2\epsilon}{(2\epsilon)^{3/4} (\epsilon)^{5/4} + 1} \right] \quad (2E.17)$$

For small  $\epsilon$ , this becomes

$$\frac{C_{H \text{ VORT}}}{C_{H \text{ NO VORT}}} = 1 + 0.55 \left( \frac{M_0}{\rho_{\infty} u_{\infty} R_c} \right)^{1/2} \left[ \frac{1 - 2\epsilon}{(2\epsilon)^{5/4}} \right] \quad (2E.18)$$

The approximate solution may be expanded in a power series for direct comparison. If only the first term is retained (corresponding to small vorticity effect) the solution specialized for the axially symmetric case is

$$\frac{C_{H \text{ VORT}}}{C_{H \text{ NO VORT}}} = 1 + 0.53 \left( \frac{M_0}{\rho_{\infty} u_{\infty} R_c} \right)^{1/2} \left[ \frac{1 - 2\epsilon}{(2\epsilon)^{5/4}} \right] \quad (2E.19)$$

It may be seen that the approximate solution is in very close agreement with the result obtained by rigorous means. It is concluded that the

solution can be applied with some confidence.

#### CONVECTION DISTRIBUTION

The foregoing procedure is readily extended for locations downstream of the stagnation point. The problem is to prescribe the local, effective edge velocity as a function of distance from the stagnation point. Since the total enthalpy and local static pressure are known quantities for a given flight condition, the edge velocity may be determined if edge entropy is defined. The entropy of an inviscid streamline is dependent upon the point on the shock,  $r_1$ , from which the streamline has emanated. This position may be found by application of Eqs. (2E.5) and (2E.11). Retaining the value of 1.06 for the transformed stream function at the effective edge, the entry point is given by solution of

$$\rho_{\infty} u_{\infty} \int_0^{r_1} h_2 dr = 1.06 \mu_0 \sqrt{2 \tilde{S}} \quad (2E.20)$$

where now

$$\tilde{S} = \left( \frac{1}{\mu_0} \right)^2 \int_0^s \rho_w \mu_w u_{inv}^* h_2^2 ds \quad (2E.21)$$

These equations may be simply solved by numerical integration techniques as discussed in Volume II. Once the streamline entry point is located and the entropy determined, the inviscid velocity can be obtained by application of an equation of state and the energy conservation law. The functional relations in consecutive order of use are

$$\begin{aligned} r_1 &= f(\tilde{S}) \\ \text{entropy} &= f(r_1) \\ h_{inv}^* &= f(\text{entropy}, p_e) \\ u_{inv}^* &= f(H, h_{inv}^*) \end{aligned}$$

The effective edge velocity is utilized in Eq. (2.144) to obtain the convective heating distribution accounting for vorticity. It is noted that in computing the distribution using Eq. (2.144), an effective stagnation-point velocity gradient as defined by Eq. (2E.14), must be used.

## Appendix 2F

### EMPIRICAL CRITERION FOR BOUNDARY LAYER TRANSITION

At sufficiently high Reynolds number, the boundary layer flow transits from laminar to turbulent. The phenomenon depends in a complicated manner upon local Mach number, degree of wall cooling, surface roughness, pressure gradient, and mass injection rate. While the affecting parameters have been individually studied, no comprehensive correlation has been achieved. In order to accurately predict the occurrence of transition, experimental data obtained at conditions closely simulating those of interest are required. Unfortunately, results applicable to Apollo are meager. Data obtained in the X-17 flight test program have been utilized to provide an estimate of the transition Reynolds number. The X-17 series of flight tests were conducted for the specific purpose of acquiring heating level and transition data.

#### EXPERIMENTAL DATA CORRELATION

The RTV X-17 flight test program is described in Reference 2.136. Heat transfer results are also summarized in this document. In the majority of the RTV X-17 flights, a hemispherical nose configuration was used. Nose diameter was nine inches. The heat shield consisted of a thick-walled, metal heat sink. The shield was instrumented with thermocouples imbedded near the surface and mounted at intervals along the surface on rays emanating from the stagnation point. Surface finish was controlled to enable data acquisition for varying degrees of roughness. The vehicles were propelled during the reentry phase. Maximum velocities of approximately 12,000 ft/sec were attained at altitudes in the vicinity of 40,000 feet.

A typical heat transfer history, as deduced from thermocouple measurements

is shown in Figure 2F-1. Although the data scatter and data reduction process produce some extraneous oscillations in the heat transfer results, the approximate time of boundary-layer transition may be inferred from comparison of the heat transfer data with the laminar and turbulent boundary-layer heat flux predictions.

The heat transfer results from five flights have been examined in order to provide sufficient data for study of the transition phenomena. Typical results for local transition times are shown in Figure 2F-2. Each graph shows data for a different azimuthal ray; symbols indicate the apparent transition time. It is evident from comparison of these results that surface roughness has an appreciable effect on the occurrence of transition. It is further evident that in some instances turbulence flashes forward over the surface, rather than gradually creeping forward as free stream Reynolds number increases. This indicates the boundary layer to be more stable at positions further away from the stagnation point.

The conditions existing at the observed transition times in the several flights have been evaluated in the attempt to provide some degree of correlation. Momentum thickness Reynolds number, wall cooling ratio, surface roughness and position (Mach number) were considered as important parameters. Wall cooling ratios generally ranged between 0.07 and 0.2. There did not appear to be a sensitivity to wall cooling within this range. Momentum thickness Reynolds numbers at transition covered a wide range. The results are summarized in Figure 2F-3. The different symbols represent differing surface roughnesses. There is a general trend for reduced  $Re_{\theta}$  at transition with increase in surface roughness, but the influence is not strong. It is clear that the boundary-layer becomes more stable with increasing distance from the stagnation point. In this regard, the flight test results are very similar to the ground test results reported by Stetson (Ref. 2.121).

The observed variation of the transition Reynolds number with position might be attributed to Mach number or pressure gradient effects. How-

ever, the pressure gradient parameter,  $\tilde{\beta}$ , varies only slightly along the surface of the X-17 nose and therefore it is presumed that Mach number is the influential factor. To exhibit the effect of Mach number, the data of Fig. 2F-3 have been replotted in Fig. 2-65. The transition Reynolds number varies almost directly with the Mach number.

The effect of surface roughness should correlate as a function of the ratio of surface roughness to some characteristic boundary-layer dimension. Figure 2F-4 shows for two surface positions the variation of the transition Reynolds number with the ratio of surface roughness to boundary layer momentum thickness. The roughness ratio appears to influence the transition Reynolds number, but the data scatter is too large to accurately establish the dependence.

#### APPLICATION TO APOLLO

The relevance of the X-17 data depends on the degree to which Apollo boundary-layer conditions were simulated. The Apollo wall is highly cooled; at peak heating the ratio of wall enthalpy to boundary layer edge enthalpy is about 0.05. The surface roughness is estimated to be about 0.01 inch. Momentum thickness, Mach number, and Reynolds number distributions are depicted in Fig. 2F-5. The normalized mass injection rate at the time of peak heating is  $\dot{m}/C_H \approx 0.7$ .

With an estimated surface roughness of 0.01 inch for the Apollo vehicle, the ratio of surface roughness to momentum thickness will be about 0.1 in the altitude region of primary interest. This is somewhat in excess of roughness ratios for the RTV X-17 data. Hence, from this consideration, application of the X-17 data could result in some optimism. The destabilizing influence of mass transpiration is absent in the X-17 results. Therefore, further optimism could result from this difference. Wall cooling ratios do not differ significantly and therefore should not be an important factor. Inviscid flow Mach numbers on the Apollo forebody are within the range covered by the X-17 data. The values of the

pressure gradient parameter for X-17 and the spherical sector of the Apollo forebody are almost identical. In view of these circumstances it seems reasonable to utilize the X-17 data correlations to establish an approximate upper bound on the transition Reynolds numbers for Apollo. The lower envelope of results presented in Figure 2-65 are considered adequate for this purpose.



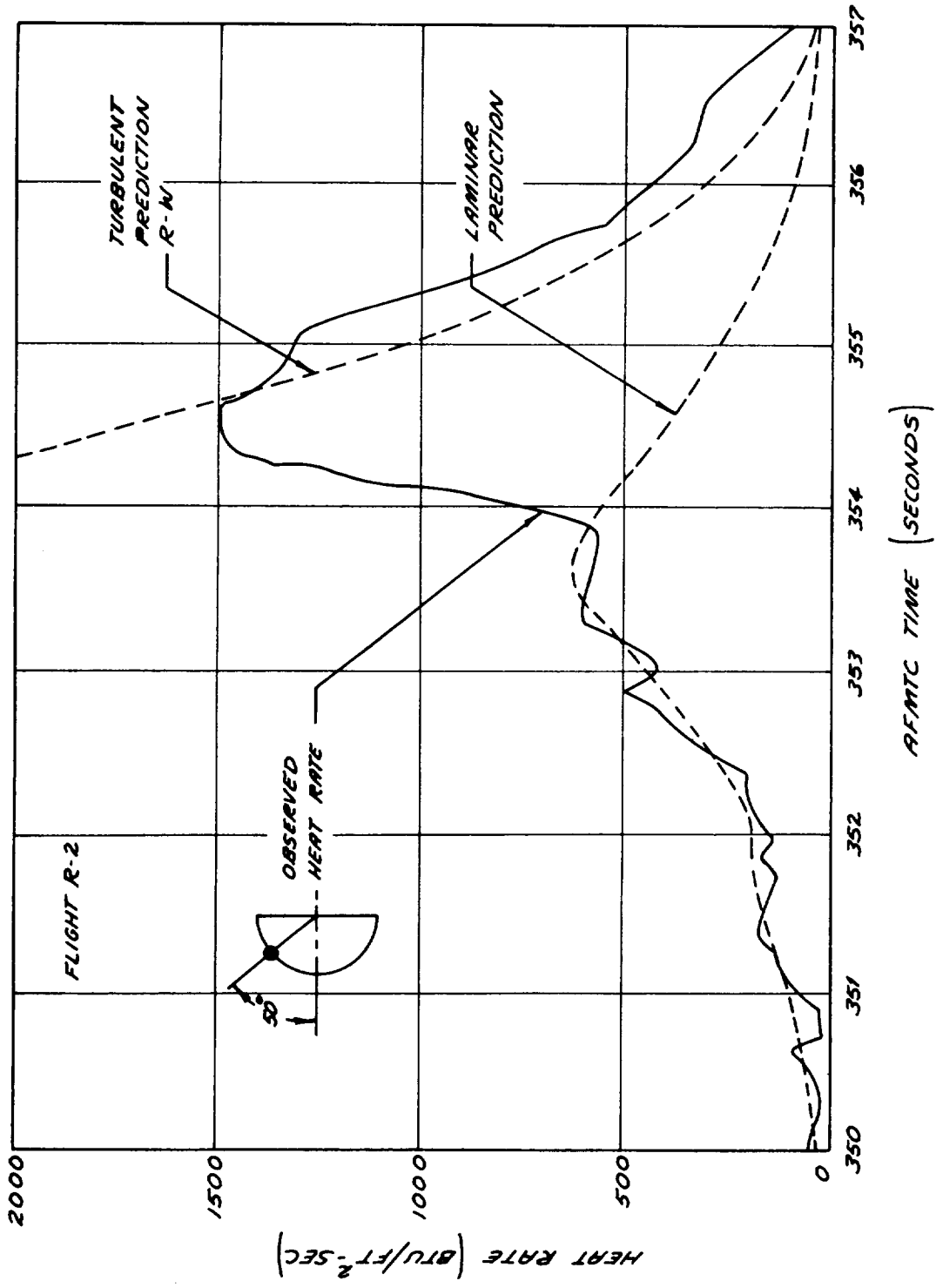


FIGURE 2F-1 COMPARISON OF OBSERVED AND PREDICTED HEAT RATES  
X-17 FLIGHT R-2

FIGURE 2F-2 APPARENT BOUNDARY LAYER TRANSITION TIMES,  
 RTV X-17 VEHICLE, FLIGHT R-26

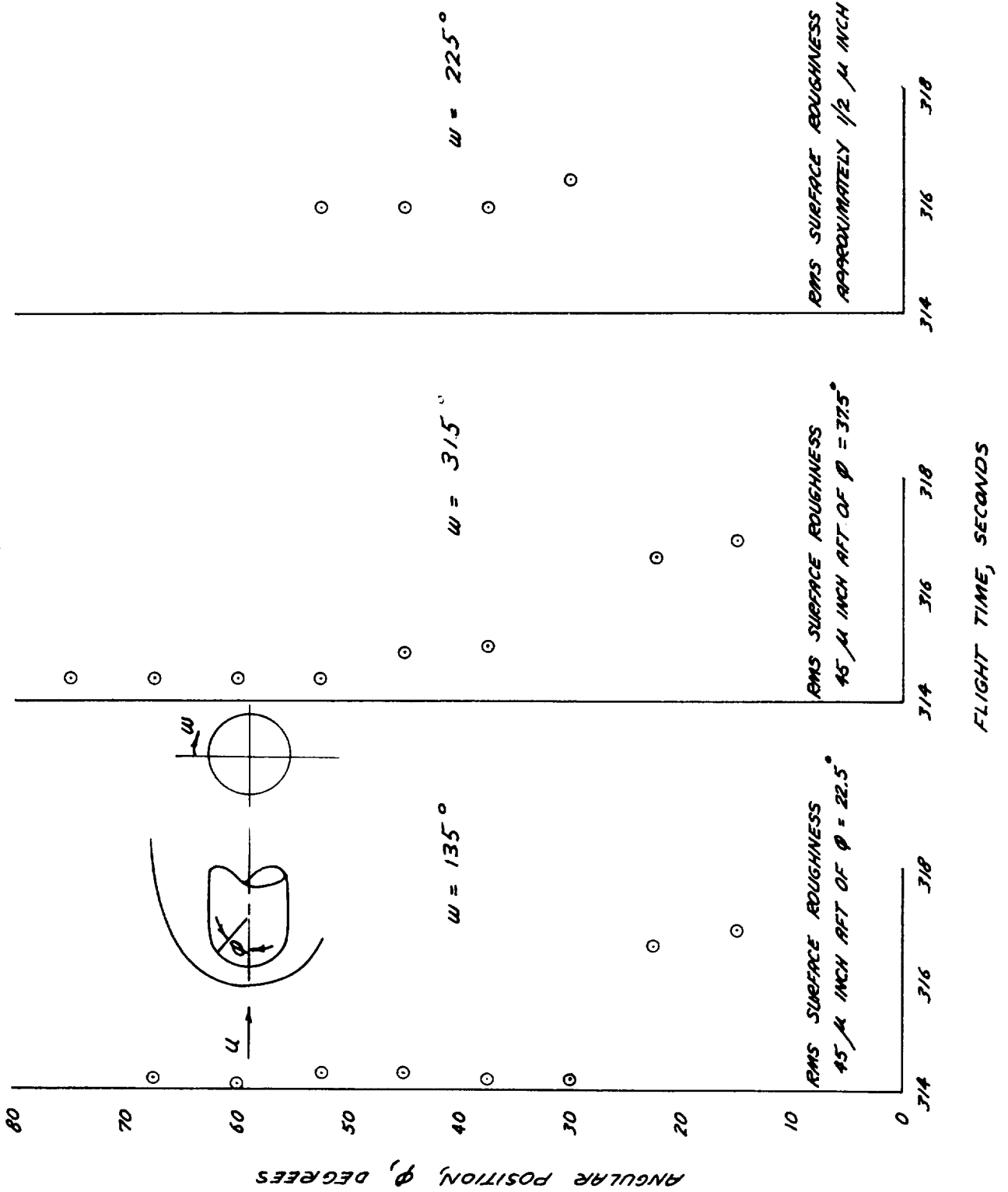


FIGURE 2F-3 REYNOLDS NUMBER AT TIME OF BOUNDARY LAYER TRANSITION

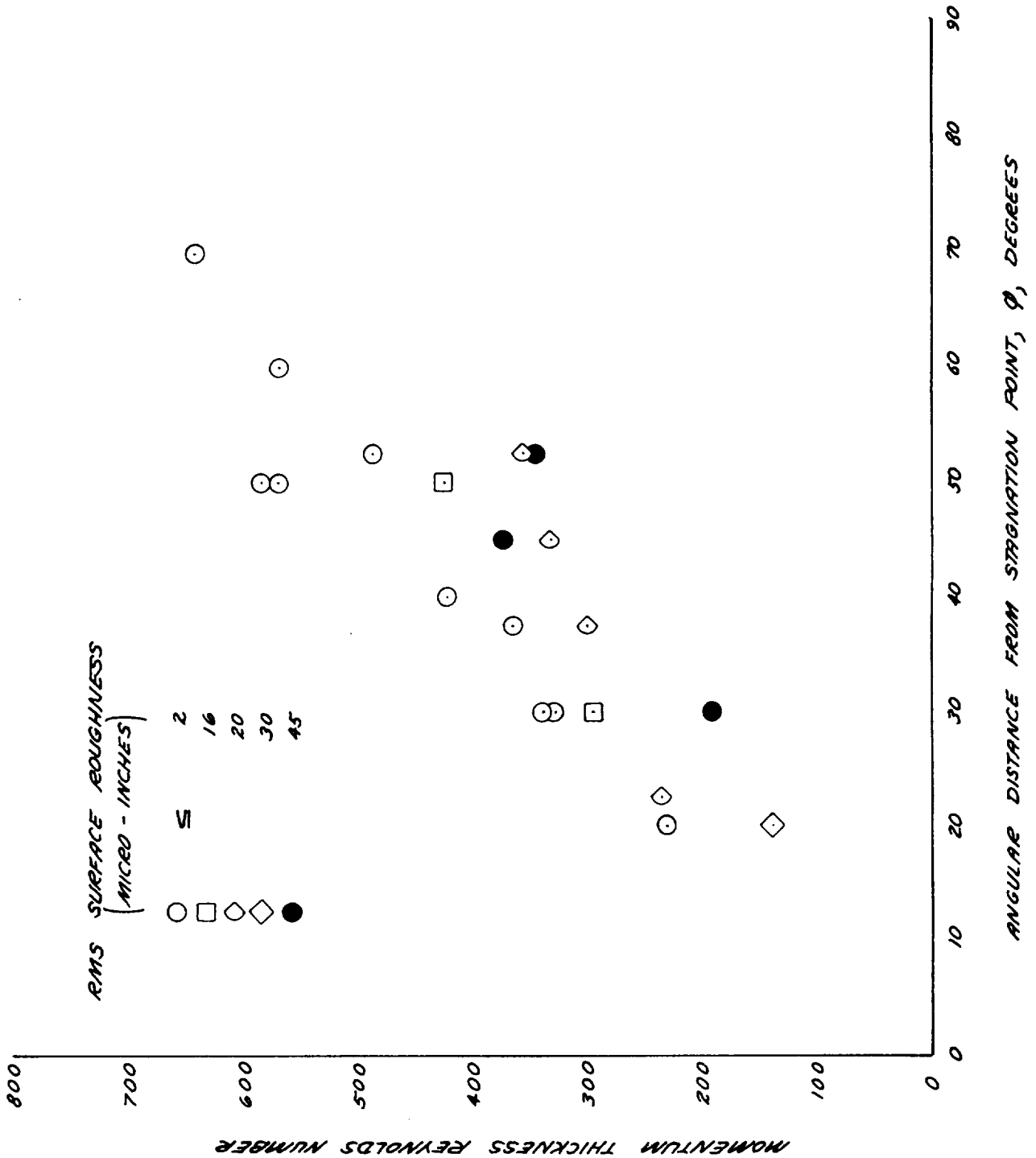
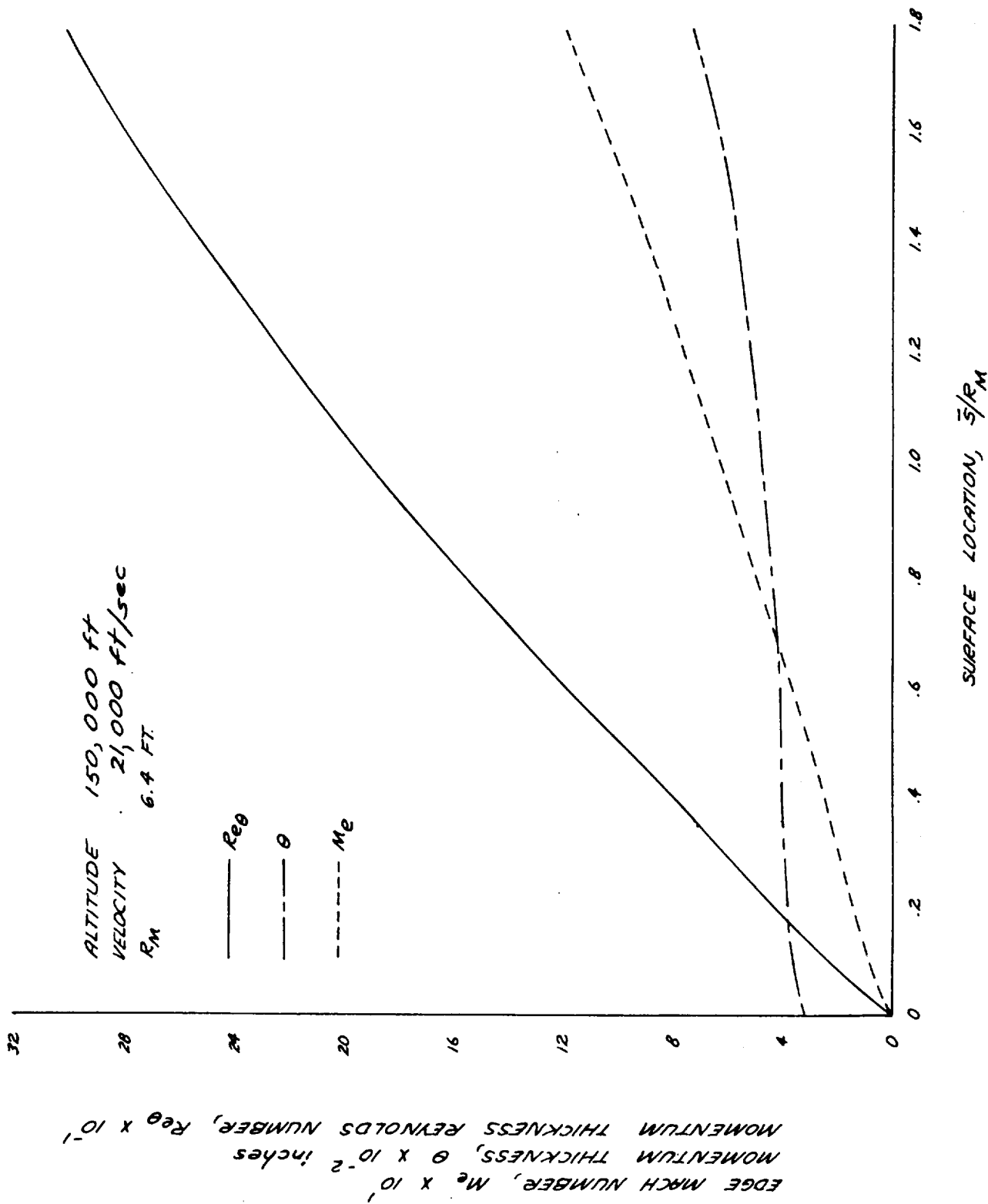




FIGURE 2F-5 BOUNDARY LAYER CONDITIONS ON APOLLO VEHICLE  
 AT APPROXIMATE TIME OF PEAK HEATING





Appendix 2G  
PERFORMANCE MODEL FOR HEAT SHIELD MATERIAL

by

H. E. Goldstein and W. D. Coleman

Consideration must be given to heat-shield-material behaviour in detailed analysis of the heating experienced by an entry vehicle. Injection of gaseous ablation products significantly affects the convective heat transfer. Radiative heat transfer may also be appreciably influenced if the injected species are strong absorbers. An investigation of the Apollo heat shield material and its performance characteristics was therefore undertaken as a part of this study. The investigation was not intended to yield techniques and data for evaluation of the shield design. Rather, its purpose has been to provide realistic information for use in study of the heat-shield/environment interactions.

The material which is treated can only be considered representative of the actual Apollo material. A small sample of this representative material was obtained from NASA and subjected to laboratory analysis in order to determine composition and certain of its properties. The experimental results enabled theoretical estimation of properties not directly measured. Thermochemical performance of the material is determined by an approximate, theoretical model. Validity of the model has been assessed by comparison of performance predictions with experimental data provided by NASA.

#### MATERIAL PROPERTIES

##### Virgin Material Composition

The material sample received from NASA was determined after analysis to be a composite of silica fibers and phenolic microballoons bonded together

by an epoxy resin. It has been assumed, based on available information, that the material is used as a filler in a honeycomb matrix. It was further assumed that the honeycomb is refrasil-phenolic in 40-60 weight ratio and that the mass fraction of the honeycomb in the final composite is 0.10.

The elemental composition and density of the filler, honeycomb and composite is given in Table 2G-1. These results and the filler formulation were obtained from infrared analysis, photomicrographs, and elemental analysis (Ref. 2.137).

#### Char Composition

The filler material was pyrolyzed in an inert atmosphere to determine the characteristics of the fully-charred material. The residual weight fraction (ratio of char weight to virgin material weight) was 0.444. Chemical analysis of the char was not performed since it can reliably be assumed that all the silica is retained and that the remainder of the residual material is carbon. The residual weight fraction for the honeycomb material was estimated from the results of Ref. 2.138 to be 0.7. The honeycomb char was also assumed to consist of only silica and carbon.

The residual weight fraction and char composition for the composite of honeycomb and filler material are simply obtained from the above results. The results are given in Table 2G-1.

#### Thermophysical Properties

The specific heat of the heat shield material and its char can be estimated by summing the known specific heats of the components. Fig. 2G-1 shows the results of this calculation for the virgin material and char. Also plotted is the data reported by NASA for these materials. The agreement indicates that the components determined are probably correct.



Using these specific heats, the sensible enthalpies of the virgin plastic and char were calculated and are shown in Fig. 2G-2.

The thermal conductivity was determined by analysis of transient temperature response data as subsequently discussed. Fig. 2G-3 shows the results.

### Thermochemical Properties

Necessary for prediction of material ablative behaviour are the heat of decomposition of the virgin material and the pyrolysis gas enthalpy. The energy absorbed by pyrolysis of the heat shield material  $H_D$  can be calculated with the following equation (Ref. 2.138):

$$H_D = f_c H_c + (1 - f_c) H_g - H_{vp} \quad (2G.1)$$

where  $f_c$  is the fraction of virgin material retained as char,  $H_g$  is the enthalpy of the pyrolysis gas,  $H_c$  and  $H_{vp}$  are the enthalpies of the virgin plastic and char defined as follows:

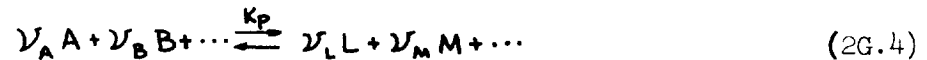
$$H = \Delta H_{f_0} + \int_0^T C_p dT \quad (2G.2)$$

The heats of formation which were obtained for the virgin and char materials by standard estimation techniques are given in Fig. 2G-2 together with the sensible enthalpy terms.

The enthalpy of the pyrolysis gases is defined by the following equation

$$H_g = \sum_j K_j \left[ \int_0^T C_p dT + \Delta H_{f_j} \right] \quad (2G.3)$$

It is apparent from this equation that the pyrolysis gas composition must be known in order to calculate the enthalpy of the pyrolysis gases. The pyrolysis products of this material have not been determined experimentally. Therefore, the gas enthalpy cannot be calculated exactly. The enthalpy may be estimated, however, by assuming that all the pyrolysis gases are in thermodynamic equilibrium. If this assumption is made the following equation may be used to describe a multi-component chemical reaction system.



where  $\nu_A$ ,  $\nu_B$ , and  $\nu_L$ ,  $\nu_M$  are the numbers of moles of A, B, and L, M, respectively, and  $K_P$  is the equilibrium constant as defined below.

$$K_P = \prod_j p_j^{\nu_j} \quad (2G.5)$$

The change in Gibb's free energy for such a system in terms of the equilibrium constant is

$$\ln K_P = -\sum_j \frac{\nu_j G_j}{RT} \quad (2G.6)$$

where the  $\nu_j$ 's are positive for reactants and negative for products. Since Gibbs' free energy approaches a minimum as the system approaches equilibrium, one need only determine the concentration of species that give a minimum of Gibbs' free energy to specify the system thermodynamically. This can be accomplished in practice by solving a set of nonlinear equations on a high speed digital computer with the free energy minimization program (FEMP, Ref. 2.122). To use this program the atom ratios of the material must be known.

Using the preceding estimates for the virgin material and char compositions, the elemental composition of the pyrolysis gases was found by differencing to be

C	.614
H	.093
O	.293

The enthalpies of the pyrolysis gases and specie concentrations were then calculated using FEMP. Fig. 2G-4 shows the gas enthalpies from 1000°R to 8000°R and from 0.01 to 100 atmospheres pressure, and Fig. 2G-5 shows the specie concentrations from 1000°R to 8000°R at 1 atmosphere pressure.

The heat of decomposition may now be calculated using the gas enthalpies shown in Fig. 2G-6 and the thermo-chemical properties of the virgin material and char previously derived. Figure 2G-6 shows the heat of decomposition for 0.01, 1.0 and 10 atmospheres.

It is noted that pyrolysis will occur primarily in the temperature range below 2000°R. The negative heat of decomposition in this range indicates that the pyrolysis reaction is exothermic. Thus the heat absorption capability of this material should be somewhat inferior to materials such as nylon-phenolic which undergo endothermic pyrolysis reactions (Ref. 2.122).

### Pyrolysis Kinetics

The pyrolysis of the filler material may be described by the following equation (Ref. 2.138).

$$\frac{W}{W_0} \xrightarrow{K_f} \frac{W_g}{W_0} + \frac{W_c}{W_0} \quad (2G.7)$$

where the initial weight of virgin material ( $W_o$ ) is converted to gas ( $W_g$ ) and char ( $W_c$ ).

For an irreversible reaction the rate equation may be written in terms of the density as

$$\frac{d\rho_s/\rho_o}{d\theta} = -k_f f\left(\frac{\rho_s - \rho_c}{\rho_o}\right) \quad (2G.8)$$

where  $\rho_s$  denotes the instantaneous solid density,  $\rho_o$  and  $\rho_c$  are the virgin material and fully-charred densities, respectively, and

$$f\left(\frac{\rho_s - \rho_c}{\rho_o}\right) = \left(\frac{\rho_s - \rho_c}{\rho_o}\right)^n \quad (2G.9)$$

$$k_f = k_o e^{-\frac{E}{RT}} \quad (2G.10)$$

Substituting into Eq. (2G.8)

$$\frac{d\rho_s/\rho_o}{d\theta} = -k_o e^{-\frac{E}{RT}} \left(\frac{\rho_s - \rho_c}{\rho_o}\right)^n \quad (2G.11)$$

The rate constant ( $k_o$ ), activation energy ( $E$ ), and reaction order ( $n$ ) may be determined by correlation of data obtained in thermogravimetric analysis. In this procedure the material is heated at constant rate of temperature rise, i.e.,

$$\frac{dT}{d\theta} = c$$

For analysis of the test data, Eq. 2G.11 may then be rewritten as

$$\frac{d\rho_s/\rho_o}{dT} = -\frac{k_o}{c} e^{-\frac{E}{RT}} \left(\frac{\rho_s - \rho_c}{\rho_o}\right)^n \quad (2G.12)$$

One TGA of the material at a rate of temperature rise of 23°C/min was obtained (Fig. 2G-7). In order to completely analyze the kinetics considerably more data is necessary. A fairly simplified approach was therefore taken. First a char weight fraction ( $\rho_c/\rho_o$ ) of 0.47 was assumed. The Arrhenius equation was then used to determine the activation energy, rate constant, and reaction order. This equation is obtained by rearranging Eq. (2G.12) and taking logarithms to obtain the following

$$\log \left[ \frac{\left( \frac{dT}{d\theta} \right) \left( - \frac{d\rho_s/\rho_o}{dT} \right)}{\left( \frac{\rho_s - \rho_c}{\rho_o} \right)^n} \right] = - \frac{E}{R} \log \left( \frac{1}{T} \right) + \log k_o \quad (2G.13)$$

For constant E,  $k_o$  and n a plot of the left side of Eq.(2G.13) versus  $1/T$  gives  $-E/R \log e$  as the slope and  $\log k_o$  as the intercept. To use this equation one of the three parameters, E,  $k_o$  or n must be known or assumed. Since so little data were available the reaction order n was arbitrarily assumed to be 1, 2, or 3. An Arrhenius relation using each of these orders was then plotted. A reaction order of 3 was found to give the best correlation. The resulting Arrhenius plot (Fig. 2G-8) gives an activation energy of 40,871 BTU/lb-Mole and a rate constant of  $9.31 \times 10^5 \text{ sec}^{-1}$ .

To verify the rate parameters the experimental data must be compared to the predictions obtained with the rate equation. Equation 2G.12 can be rearranged as follows:

$$\frac{d\rho_s/\rho_o}{\left( \frac{\rho_s - \rho_c}{\rho_o} \right)^n} = - k_o e^{-\frac{E}{RT}} dT \quad (2G.14)$$

Integrating the left side of the equation with respect to  $\rho_s/\rho_o$  and the right side with respect to T and rearranging, the following result is obtained (Ref. 2.138):

$$\frac{\rho_s}{\rho_o} = \left[ -(n-1) \frac{k_o}{c} \int_0^T e^{-\frac{E}{RT}} dT + \frac{\rho_s - \rho_c}{\rho_o} \right]^{1/1-n} + \frac{\rho_c}{\rho_o} \quad (2G.15)$$

The integral

$$\int_0^T e^{-\frac{E}{RT}} dT \quad (2G.16)$$

is obtained graphically by determining the area under the curve from a plot of  $e^{-E/RT}$  versus T. Figure 2G-9 shows Eq. (2G.15) plotted against the experimental results. The plot shows that excellent correlation is obtained for the major part of the pyrolysis.

#### ABLATION MODEL

The foregoing properties are sufficient to predict performance of the material in the entry heating environment provided that a realistic mathematical model of the energy and mass transfer processes active in ablation can be formulated. The theory developed by Kratsch, Hearne, and McChesney (Ref. 2.122) for charring materials has been applied to mathematically describe material behaviour. The essential features of the theory are outlined here and its application to the Apollo shield material is described.

Upon exposure to heat, the long-chain organic molecules in the material decompose into high molecular weight gaseous products and a porous carbonaceous char. This decomposition occurs in a reaction layer which is generally physically thin. The porous structure remaining upon completion of pyrolysis acts as a particle bed in heating the pyrolysis gases as they diffuse to the surface. At the surface, chemical reactions occur between the residual char and the boundary-layer species with the result that the char surface gradually recedes.

### Internal Response

Energy transfer within the material is given by a modified conduction equation. Generally, temperature and density gradients parallel to the surface are small and the following one-dimensional equation may be used

$$\rho_s c_s \frac{\partial T}{\partial \theta} = \frac{\partial}{\partial y} \left( k \frac{\partial T}{\partial y} \right) + (\rho v)_g \frac{\partial H_g}{\partial y} + \frac{d\rho_s}{d\theta} H_D \quad (2G.17)$$

The terms in this equation, respectively, account for sensible enthalpy change of the solid material, conduction, convection by the pyrolysis gases, and enthalpy production in pyrolysis. The local flux of pyrolysis gases is obtained by integration of the pyrolysis rate equation (2G.11) from the local position to the inner surface

$$(\rho v)_g = - \int_y^{\delta} \frac{d\rho_s}{d\theta} dy \quad (2G.18)$$

This equation is a simple mass conservation statement. That is, the local production rate of gases per unit volume is equal to the rate of change of the solid density. The flux of pyrolysis gases past a given point is equal to total rate of production beyond that point, assuming that the gas flow is quasi-steady.

The pyrolysis gases are assumed to be in chemical equilibrium. Furthermore, they are assumed to be in thermal equilibrium with the surrounding char. Pressure gradient through the char is neglected. With these assumptions the local gas enthalpy,  $H_g$ , and heat of decomposition, may be obtained from the results shown in Figs. 2G-4 and 2G-6 as a function of the local temperature and the surface (or boundary layer edge) pressure. In application of this model, it is found that the pyrolysis gases absorb a significant portion of the incident heat flux both through sensible enthalpy rise and chemical cracking.

The conduction equation is solved by standard, explicit-finite difference procedures. The computer program which is utilized is described in Ref. 2.123.

The boundary conditions impressed in solution of the conduction history equation are the net heat transfer rate and surface recession. The net heat transfer is determined accounting for the blowing value of the convection heat flux, shock-layer radiation, heat liberated by surface reactions (char combustion), and reradiation from the surface. Evaluation of the surface recession boundary condition is accomplished by considering the surface chemical reaction system discussed subsequently.

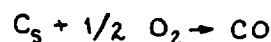
Before proceeding with the development of a surface erosion model, it was necessary to infer from transient temperature response data the thermal conductivity of the virgin and charred materials. Parametric computations with conductivity as a variable were made for comparison with temperature history data. The selection of a conductivity variation with temperature was guided by results available for other materials. The transient temperature data were obtained from air-arc test results supplied by NASA (Ref. 2.139). In order to avoid interference of uncertainties in the surface erosion phenomena with in-depth material response characteristics, a test run with minimal surface recession was chosen for data correlations. The cumulative effort of these correlations resulted in the definition of the conductivities which were shown in Fig. 2G-3. The correlation achieved with this conductivity is shown in Fig. 2G-10 by comparison of observed and predicted temperature histories at selected depths. These results are for a test sample exposed to a cold wall heat rate of approximately  $25 \text{ BTU/ft}^2 \text{ sec}$ . The initial temperature rise correlation confirms the adopted value of the virgin material conductivity. Near the surface the observed temperature is under-predicted; however, the discrepancy can be largely attributed to the fact that surface erosion, which totaled 0.05 inches, was not accounted for in the predictions. In view of the uncertainties in thermocouple depths and air-arc heating levels, the degree of correlation is considered good.



## Surface Erosion

The char layer of the material under consideration consists of carbon and silica in approximately equal amounts by weight. The silica component is in fiber form and because of its higher density occupies a small fraction of the char layer volume relative to the carbon component. In view of this, a reasonable approach is to assume that the silica component is suspended in a continuous carbonaceous structure and that surface recession is governed by the rate at which the carbon is oxidized. The silica component of the char is assumed to be mechanically removed as the carbon surface recedes. Melting with subsequent flow or direct loss of the fibers is possible. For the environmental conditions of interest, silica vaporization temperatures will not be attained, however.

The combustion reaction with the char is assumed to occur by



Two separate reaction regimes may be identified. In the first, the rate-limited regime, combustion is incomplete and controlled by reaction kinetics. The rate of solid carbon removal is given by

$$(\rho v)_E = k_o e^{-\frac{E}{RT_w}} (P_{O_2})_w^n \quad (2G.19)$$

where  $P_{O_2}$  is the partial pressure of oxygen at the wall and  $T_w$  is the wall temperature. The adopted rate constants are

$$\begin{aligned} n &= 1/2 \\ k_o &= 1.74 \times 10^5 \text{ lb}_m/\text{ft}^2 \text{ sec atm}^{1/2} \\ E/R &= 36,200^\circ\text{R} \end{aligned}$$

Char erosion rates become significant at wall temperatures of roughly  $2000^\circ\text{R}$ . As reaction rates increase, concentration of oxygen at the wall

is reduced. Finally, as reaction kinetics become very fast, all of the oxygen at the wall is consumed and transition to the diffusion-controlled oxidation regime is accomplished. In this regime, the oxidation rate is dictated by the rate at which boundary layer oxygen is diffused to the wall. With the use of appropriate assumptions this rate may be expressed as a function of the blowing value of heat transfer coefficient. For the trajectories of interest, the majority of surface erosion occurs in the diffusion limited regime. The role of the reaction rate limited regime is essentially one of determining the initiation and cessation of oxidation. Between these two points, surface temperatures and, hence, reaction rates are sufficiently high such that the diffusion of oxygen to the wall prescribes erosion rates.

The mathematical boundary layer model employed to describe the surface combustion rate is exactly that described in Ref. 2.122. The development and final results are reviewed here. In this treatment the pyrolysis gases are assumed to act as an inert diluent. The Lewis and Prandtl numbers are taken equal to one.

The net flux of an element,  $i$ , normal to the surface is the sum of the convection and diffusion fluxes

$$(\rho v)_{i_w} = (\rho v \tilde{K}_i)_w - \left( \rho D \frac{\partial \tilde{K}_i}{\partial y} \right) \quad (2G.20)$$

where the elemental concentrations,  $K_i$ , are related to the specie concentrations,  $K_j$ , by

$$\tilde{K}_i = \sum_j \frac{\nu_i M_i}{M_j} K_j \quad (2G.21)$$

When the Lewis and Prandtl numbers are unity, Lees (Ref. 2.38) has shown that the concentration and enthalpy profiles are similar:

$$\left(\frac{\partial \tilde{K}_i}{\partial y}\right)_w = \left(\frac{\tilde{K}_{i_e} - \tilde{K}_{i_w}}{H_e - H_w}\right) \left(\frac{\partial H}{\partial y}\right)_w \quad (2G.22)$$

Furthermore, heat transfer to the wall by virtue of conduction and diffusion is

$$\left(\frac{k}{\bar{c}_p} \frac{\partial H}{\partial y}\right)_w = \bar{c}_H (H_e - H_w) \quad (2G.23)$$

Thus, with Lewis-number unity, the net flux of each element at the wall may be expressed as

$$(\rho v)_{i_w} = (\rho v \tilde{K}_i)_w - \bar{c}_H (\tilde{K}_{i_e} - \tilde{K}_{i_w}) \quad (2G.24)$$

For convenience, a mass transfer parameter is defined for each element:

$$B'_{i_w} = \frac{(\rho v)_{i_w}}{\bar{c}_H} \quad (2G.25)$$

and by summation over all elements

$$B'_w = \frac{(\rho v)_w}{\bar{c}_H} = \sum_i B'_{i_w} \quad (2G.26)$$

Thus the  $i$ -th mass transfer parameter is a simple function of the edge and wall concentrations of the  $i$ -th element.

$$B'_{i_w} = \tilde{K}_{i_w} (1 + B'_w) - \tilde{K}_{i_e} \quad (2G.27)$$

The edge concentrations are by definition those for air.

In accordance with the previously stated assumptions, the pyrolysis gases are treated as an inert diluent and their contribution to species and elemental concentrations neglected in determination of the extent of surface reactions.\* The ablation flux is then considered as having two components, one due to erosion of the char surface and the other due to injection of the inert diluent pyrolysis gases:

$$B'_w = B'_E + B'_g \quad (2G.28)$$

The pyrolysis gas contribution is given by Eq. (2G-18 ):

$$B'_g = - \frac{1}{\rho_e u_e c_H} \int_{y_w}^{\delta} \frac{d\rho_s}{d\theta} dy \quad (2G.29)$$

A relation for  $B'_E$  is obtained by applying Eqs. (2G.21) and (2G.27). In particular, for the stated reaction system,

$$\begin{aligned} B'_C &= B'_E = \tilde{K}_{C_w} (1 + B'_E + B'_g) \\ B'_O &= 0 = \tilde{K}_{O_w} (1 + B'_E + B'_g) - \tilde{K}_{O_e} \\ \tilde{K}_{C_w} &= \frac{3}{7} K_{CO_w} \\ \tilde{K}_{O_w} &= \frac{4}{7} K_{CO_w} + K_{O_2_w} \end{aligned} \quad (2G.30)$$

---

\*This omission simplifies the presentation; it is not necessary to the development of the end relations for mass transfer.

and there results

$$B'_E = \frac{3/4 \left[ \tilde{K}_{O_e} - K_{O_2w} (1 + B'_g) \right]}{1 + 3/4 K_{O_2w}} \quad (2G.31)$$

This equation must be augmented to obtain the wall concentration of un-reacted oxygen. The kinetic equation (2G.19) for the carbon monoxide production reaction is used for this purpose. This equation may be rewritten using the mass transfer parameter definition and a partial pressure-mass fraction relation as

$$B'_E = \frac{1}{\bar{C}_H} k_0 e^{-\frac{E}{RT_w}} \left[ K_{O_2w} \frac{M_w}{M_{O_2}} P_e \right]^n \quad (2G.32)$$

The two preceding equations may be combined to yield an implicit relation for the wall concentration of oxygen.

$$\frac{3/4 \tilde{K}_{O_e} P_e u_e \bar{C}_H}{k_0 e^{-\frac{E}{RT_w}} \left[ \tilde{K}_{O_e} \frac{M_w}{M_{O_2}} P_e \right]^n} = \frac{\left( \frac{K_{O_2w}}{\tilde{K}_{O_e}} \right)^n \left[ 1 + 3/4 \tilde{K}_{O_e} \left( \frac{K_{O_2w}}{\tilde{K}_{O_e}} \right) \right]}{1 - (1 + B'_g) \left( \frac{K_{O_2w}}{\tilde{K}_{O_e}} \right)} \quad (2G.33)$$

The result obtained for the wall concentration of oxygen may be substituted in either Eq. (2G.31) or (2G.32) to obtain the surface erosion rate. When the reaction rate becomes very fast and diffusion is the controlling factor, the solution is much simpler. In this limit, practically all oxygen at the wall is consumed ( $K_{O_2w} \rightarrow 0$ ), and thus the mass transfer parameter equation (2G.32) reduces to

$$B'_E = \frac{3}{4} \tilde{K}_{O_e} = 0.174 \quad (2G.34)$$

Erosion rates predicted by this model have been compared with air-arc data for which the quasi-steady ablation situation is approximated (Ref. 2.129). The comparison is presented in tabular form in Table 2G-3. The method 1 prediction corresponds to diffusion-controlled oxidation of the char with a carbon/density of 6.32 lbs/ft<sup>3</sup>. The comparison between predicted and observed rates is not completely satisfactory. The rates are underpredicted by as much as 40%. This result may have been anticipated since the silica in the char was assumed not to enter into any chemical reaction.

The possible effect of silica reactions was examined in a limit analysis employing the same mass transfer theory. Retaining the assumption that the surface recession is governed by carbon oxidation, it was postulated that reactions within the char layer involving the carbon component might occur which effectively reduce the carbon fraction available for reaction with boundary layer oxygen. A preliminary consideration indicates the following reaction might occur:



If this reaction is assumed to continue to completion (i.e., the SiO<sub>2</sub> reactant is completely consumed), the remaining carbon density in the char is only 2.85 lbs/ft<sup>3</sup>. The resulting quasi-steady erosion rate predictions are labeled method 2 in Table 2G-2. The correlation with observed rates is good with the exception of one group of data.

Methods 1 and 2 are considered theoretical limits on the chemical behaviour of the char. A more refined prediction technique would perhaps enable consistent and accurate correlation of the experimental results. In

this regard, several difficulties could be encountered. The silica-carbon reaction might be inhibited by the formation of SiC around the silica fiber. A liquid layer at the surface would inhibit reactions between the carbon and boundary-layer oxygen. Significant mechanical erosion would compromise the chemical erosion model.

The relatively simple erosion model designated as Method 1 has been adopted in this study. It yields results in reasonable agreement with the experimental data and it is considered sufficiently detailed to enable a realistic assessment of the importance and nature of heat shield/environment interactions.

Table 2G-1  
MATERIALS PROPERTIES

	FILLER	HONEYCOMB	COMPOSITE	CHAR
COMPOSITION - %				
C	52.6	ND	ND	40
H	5.14			
O	16.24			
SiO <sub>2</sub>	<u>25.8</u>			60
	99.88			
DENSITY, lb/ft <sup>3</sup>	28.7	4.3*	32*	15
HEAT OF FORMATION				
BTU/lb at 536°R				
Virgin	-1870	-3200*	-2000	-3730
Char				

\* Estimate



Table 2G-2

COMPARISON OF AIR-ARC DATA - SURFACE RECESSON WITH PREDICTION  
RECESSON RATE, IN/SEC X 10<sup>3</sup>

TEST CASE	TEST CONDITIONS						RECESSON RATE, IN/SEC X 10 <sup>3</sup>					
	LB/FT <sup>2</sup> SEC X 10 <sup>2</sup>	h <sub>o</sub>	H <sub>o</sub> BTU/LB	P <sub>o</sub> ATM	Q <sub>cw</sub> BTU/FT <sup>2</sup> SEC	MEASURED	PREDICTED METHOD 1	% DEVIATION	PREDICTED METHOD 2	% DEVIATION		
140-2	1.107	10,028	0.012	110	110	3.40	2.57	24	3.80	12		
141-2	1.112	9,990	0.012	110	110	3.00	2.58	14	3.83	28		
142-2	1.108	10,032	0.012	110	110	3.20	2.57	20	3.81	19		
145-7	0.607	17,125	0.004	114	114	2.23	1.505	32	2.30	33		
146-7	0.674	16,885	0.004	113	113	2.60	1.561	40	2.32	11		
147-7	0.660	17,035	0.004	112	112	2.40	1.530	36	2.27	5		
149-7	0.663	17,000	0.004	112	112	2.46	1.539	37	2.28	7		
151-8	2.207	10,025	0.044	219	219	4.80	5.12	7	7.60	58		
152-8	2.210	9,965	0.044	218	218	6.00	5.13	15	7.60	27		
153-8	2.190	10,050	0.044	218	218	5.20	5.08	2	7.54	45		
158-3	1.284	16,985	0.018	217	217	4.80	2.98	38	4.42	8		
159-3	1.287	17,055	0.018	218	218	4.66	2.98	36	4.42	5		

NOTE: 1) Quasi-steady erosion assumed

2) Actual recession rate was obtained by dividing total erosion by exposure time

FIGURE 26-1  
SPECIFIC HEAT OF A TYPICAL HEAT  
SHIELD MATERIAL AND CHAR

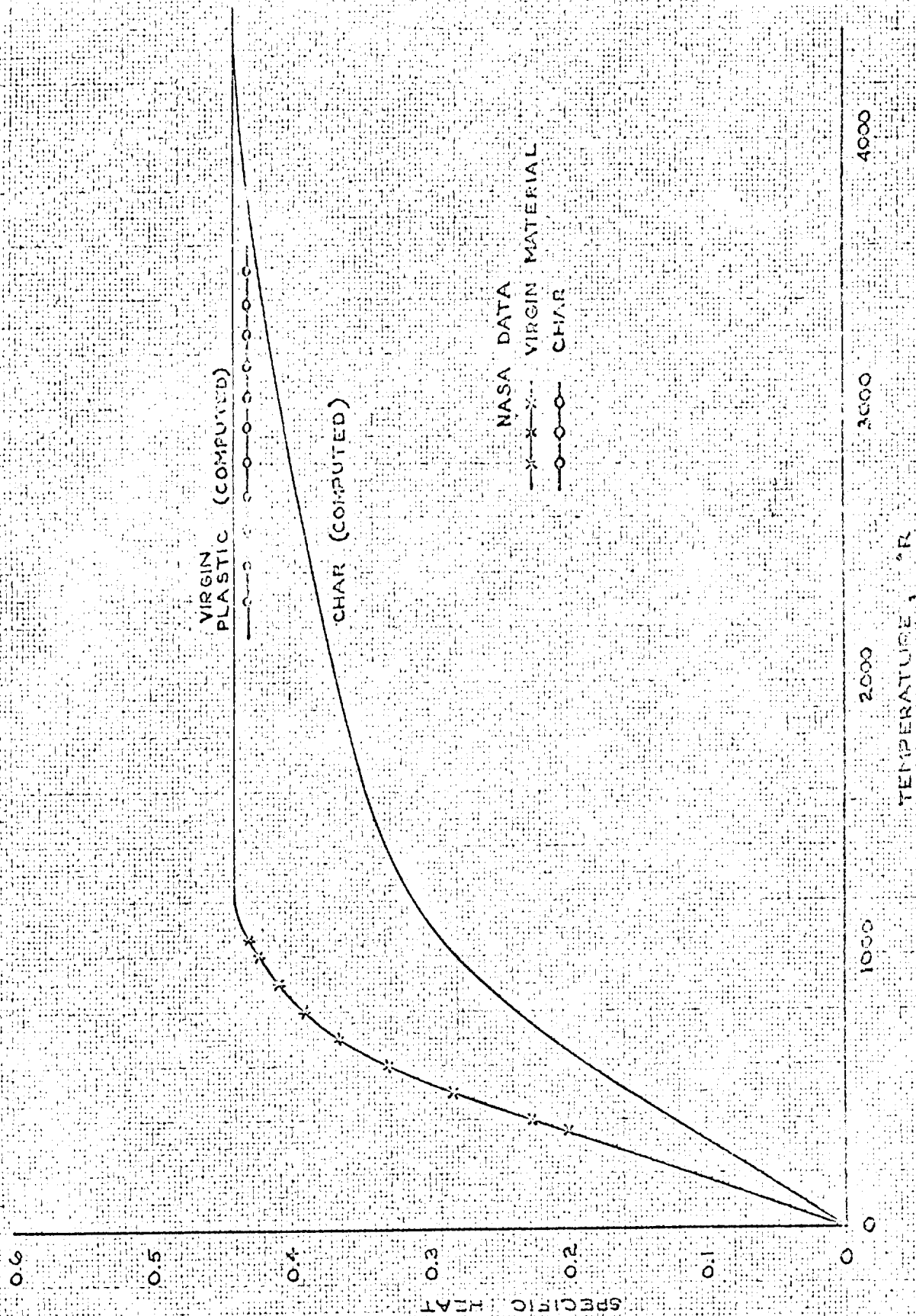


FIGURE 2G-2  
ENTHALPY OF A TYPICAL HEAT  
SHIELD MATERIAL AND CHAR

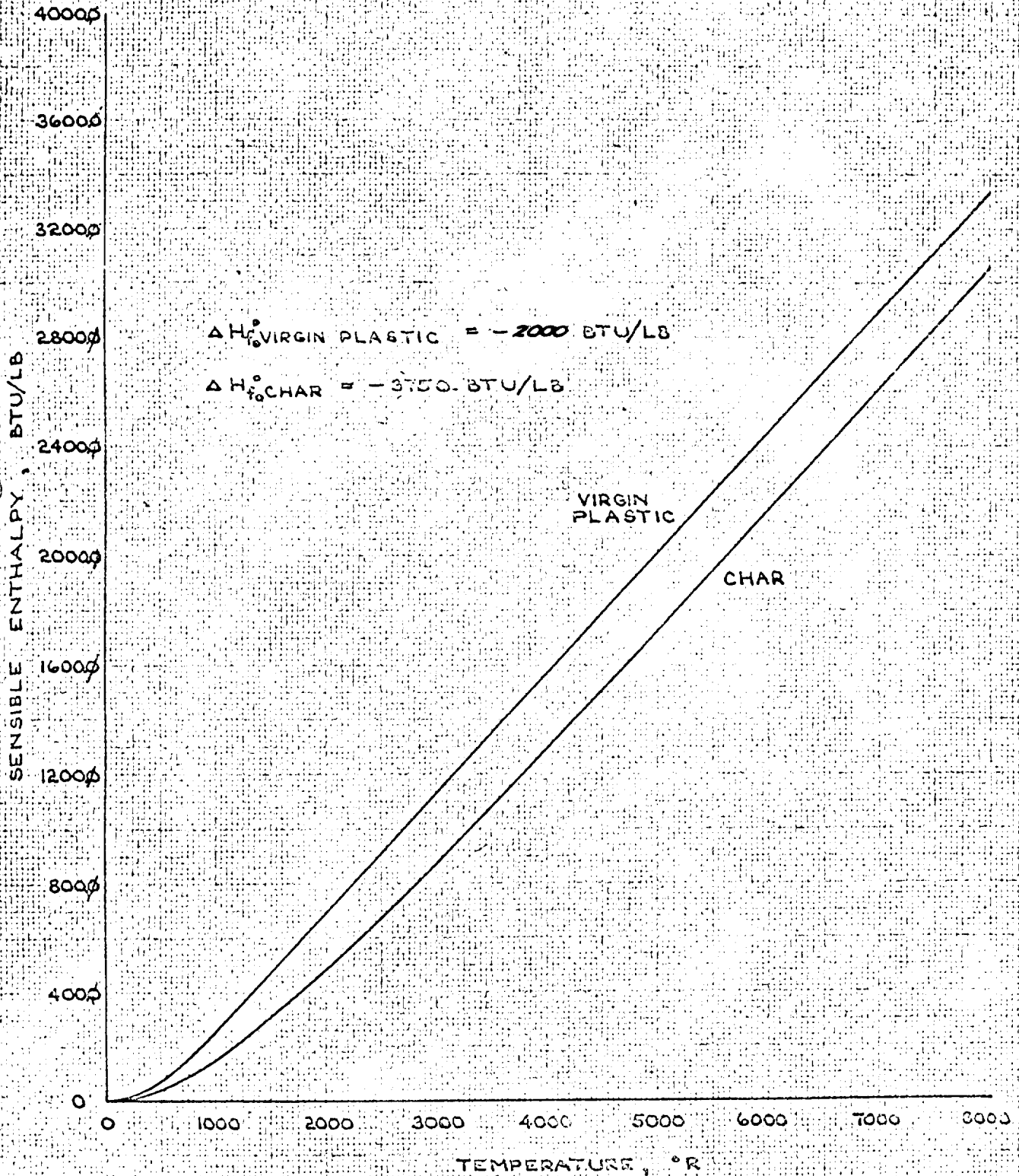
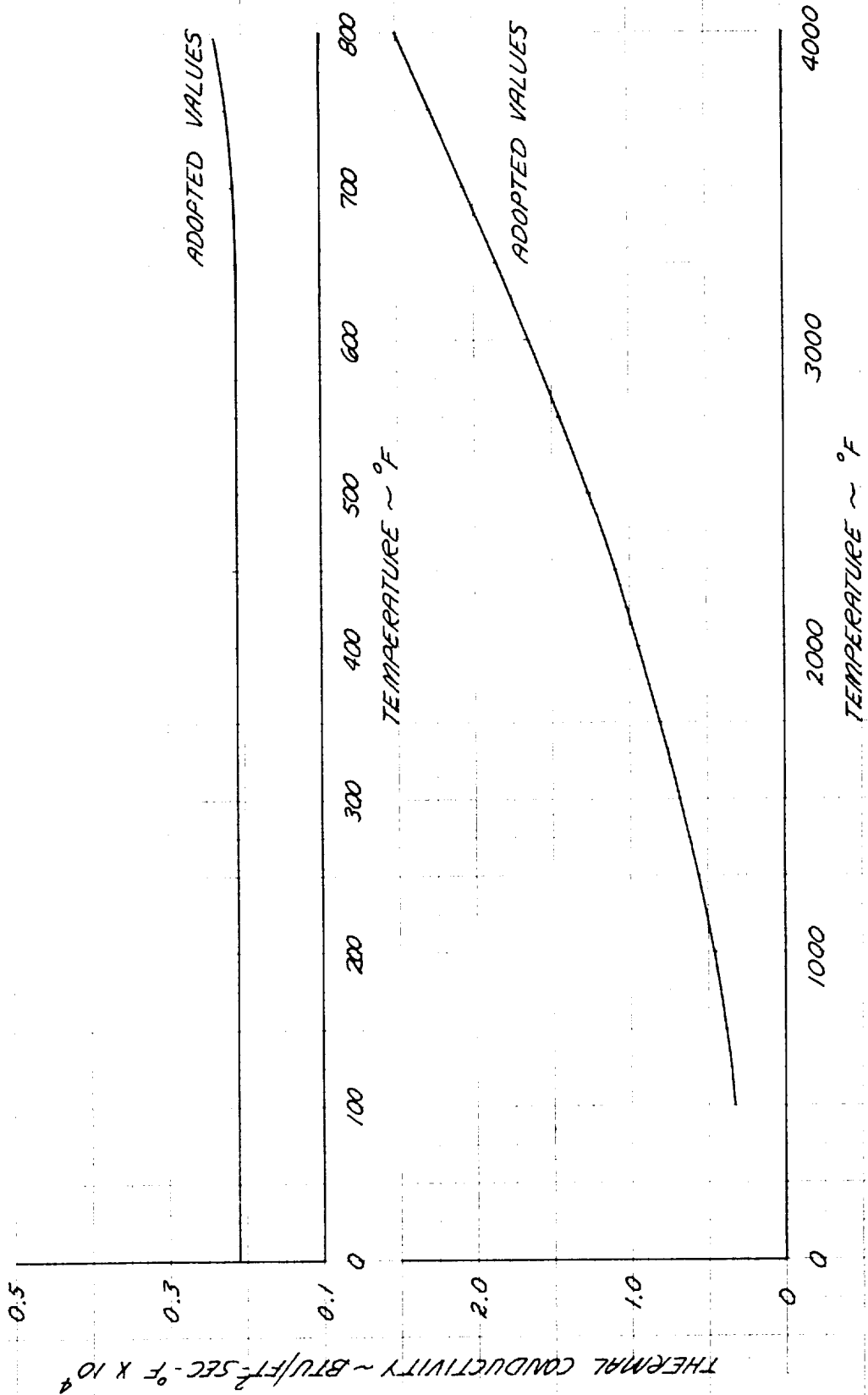


FIGURE 26-3  
 THERMAL CONDUCTIVITY OF A TYPICAL HEAT SHIELD MATERIAL



**FIGURE 26-4**  
**ENTHALPY OF A TYPICAL HEAT SHIELD**  
**MATERIAL PYROLYSIS GASES**

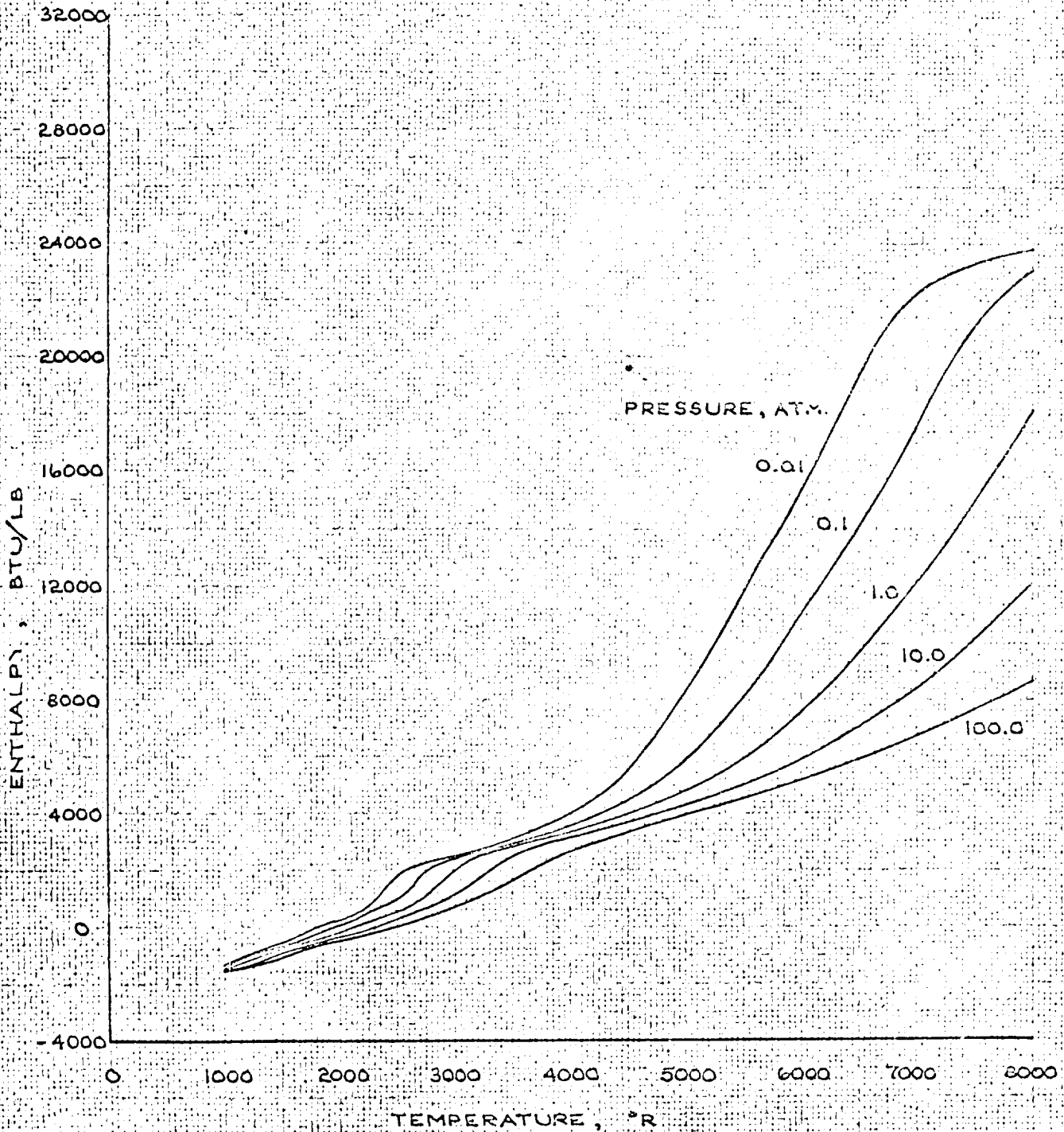
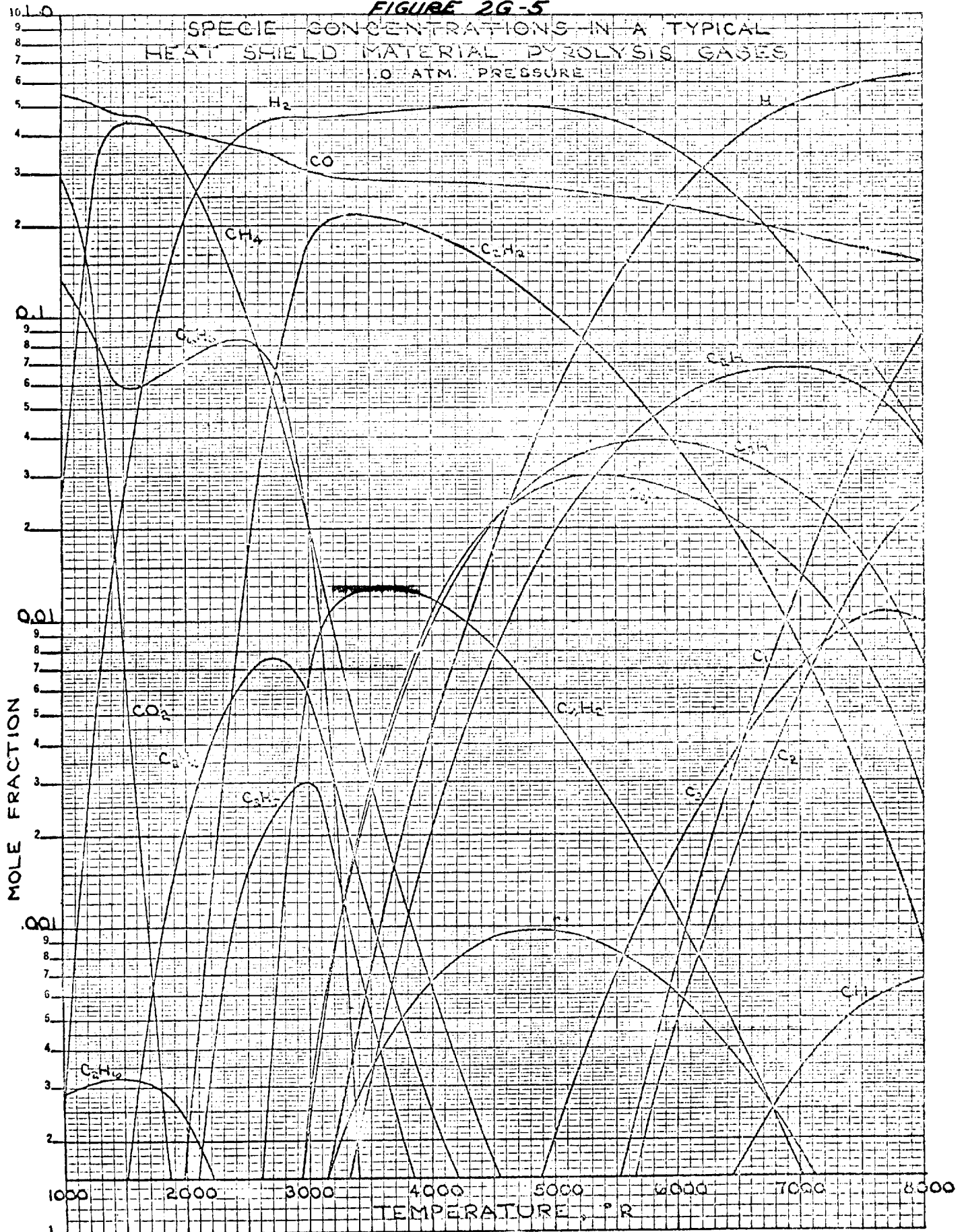
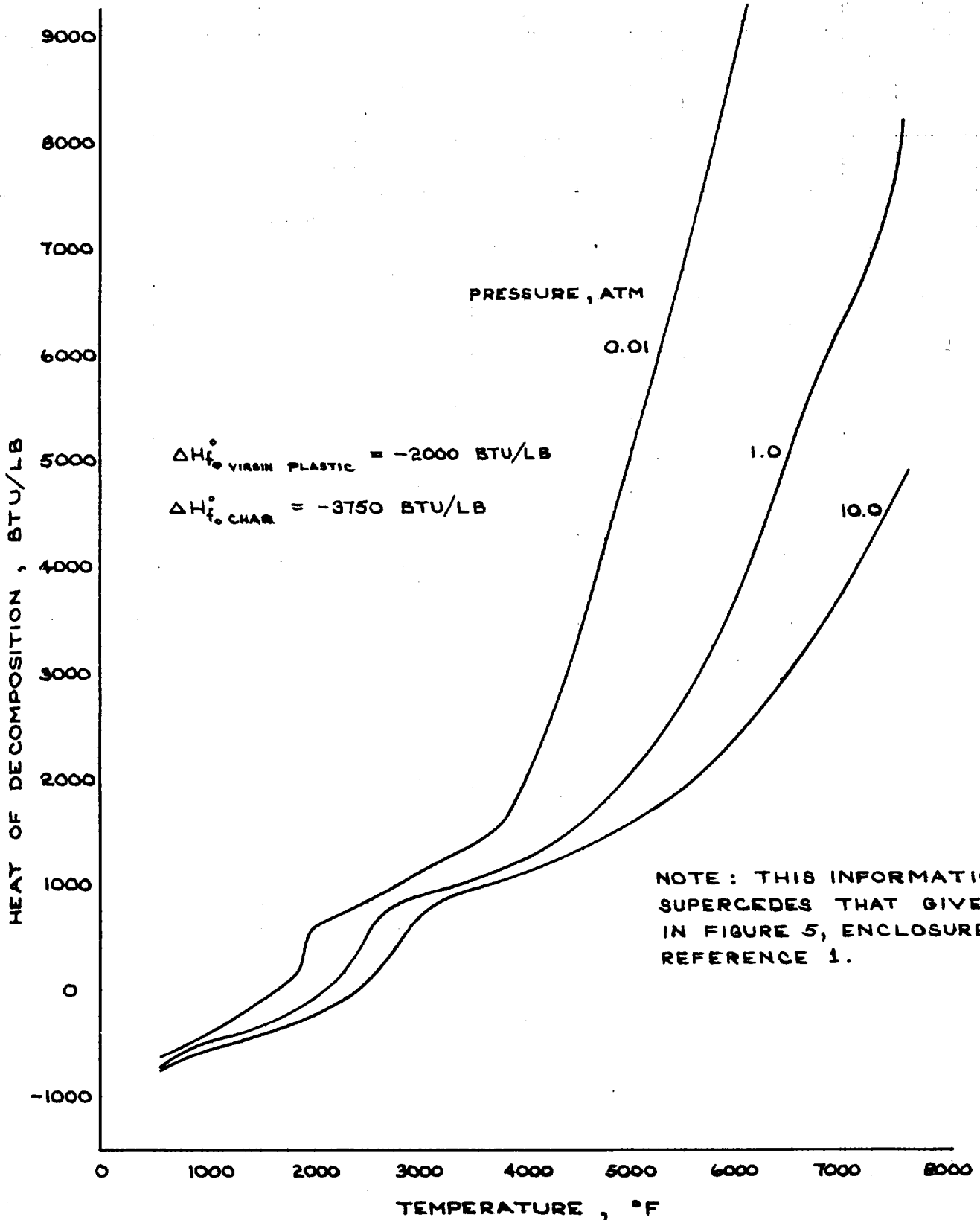


FIGURE 2G-5

SPECIE CONCENTRATIONS IN A TYPICAL  
HEAT SHIELD MATERIAL PYROLYSIS GASES  
1.0 ATM. PRESSURE

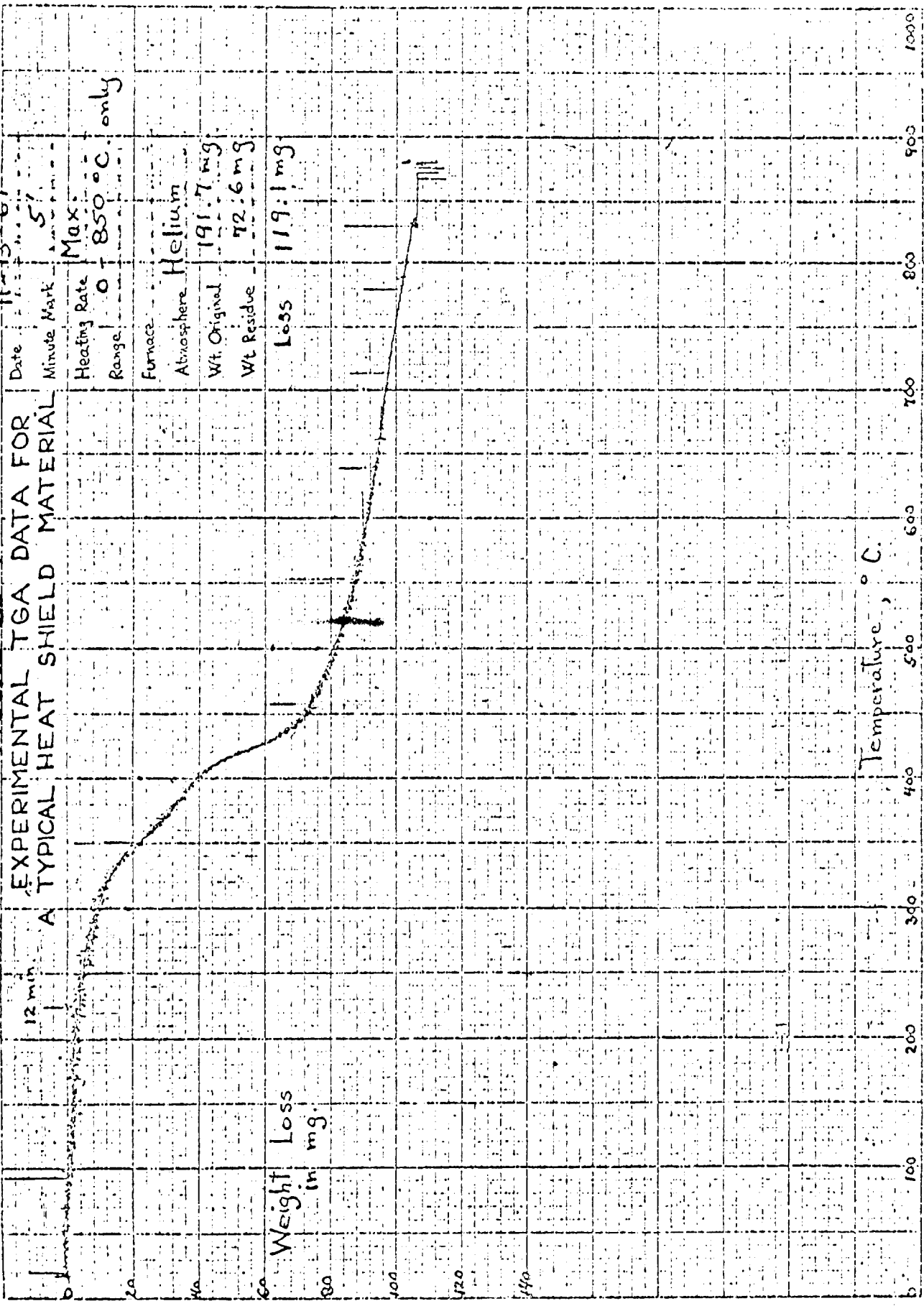


*FIGURE 2G-6*  
HEAT OF DECOMPOSITION OF A  
TYPICAL HEAT SHIELD MATERIAL



NOTE: THIS INFORMATION  
SUPERCEDES THAT GIVEN  
IN FIGURE 5, ENCLOSURE 3,  
REFERENCE 1.

FIGURE 2G-7

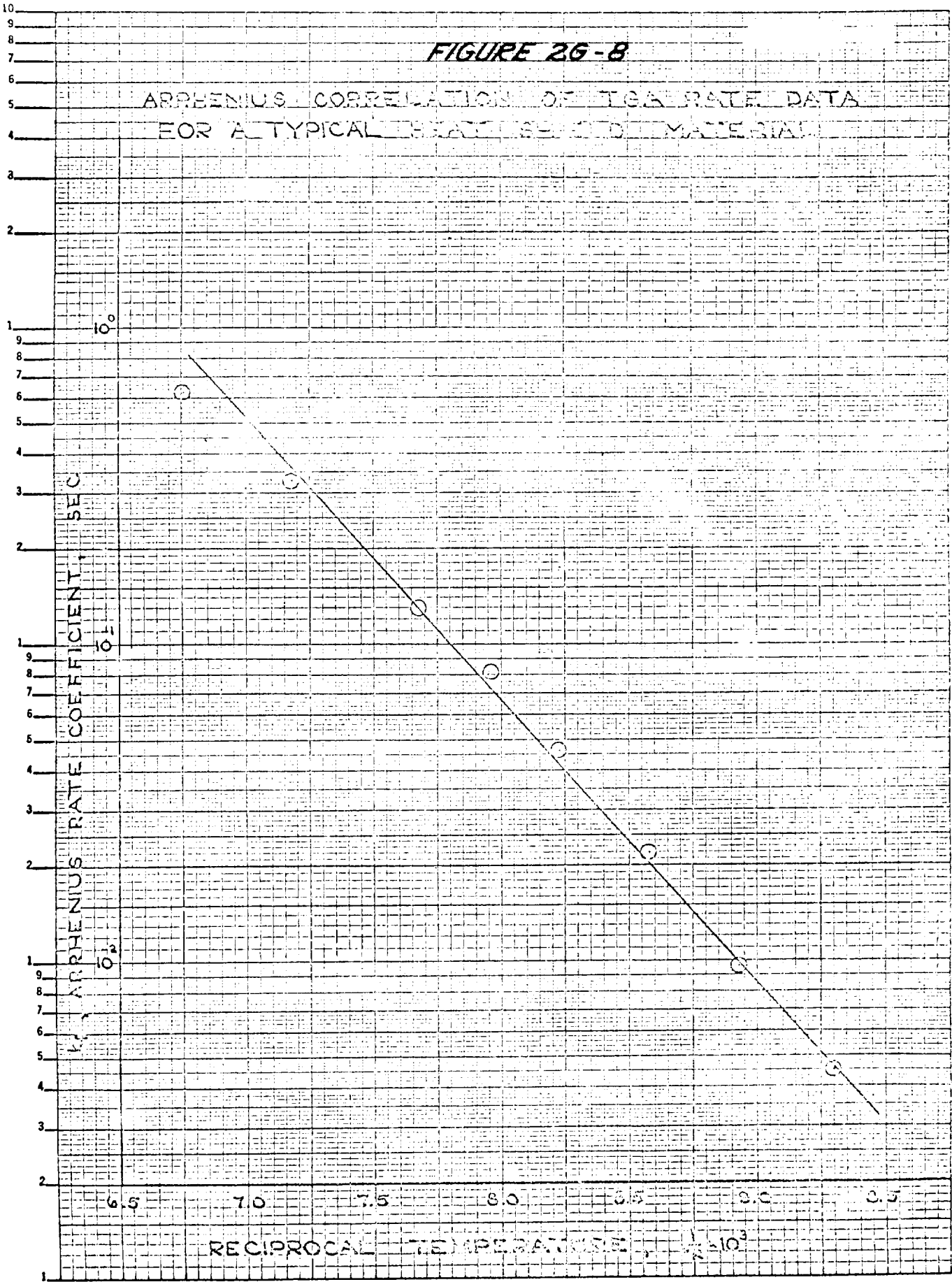


F. Witner - 110561-A

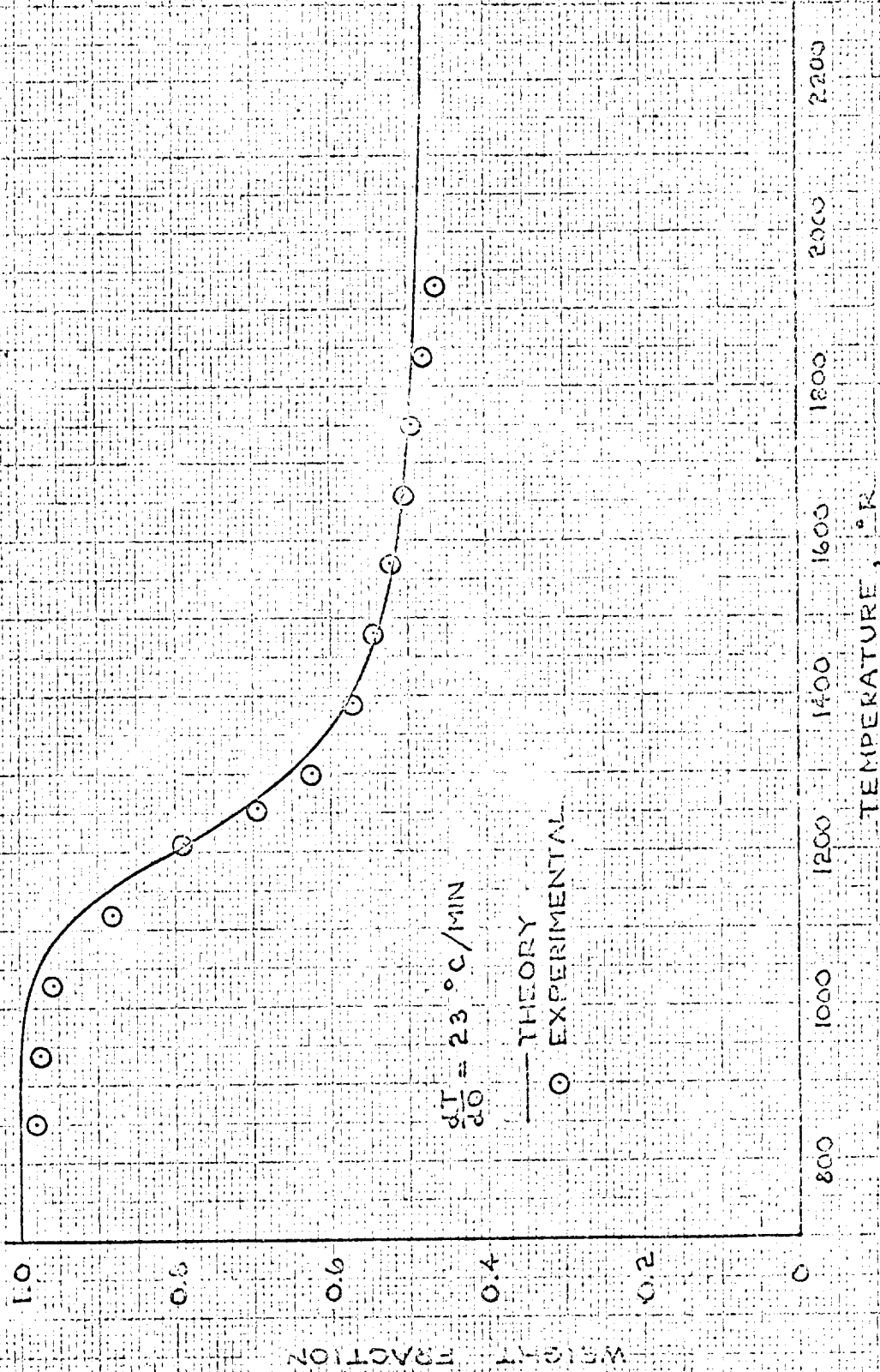


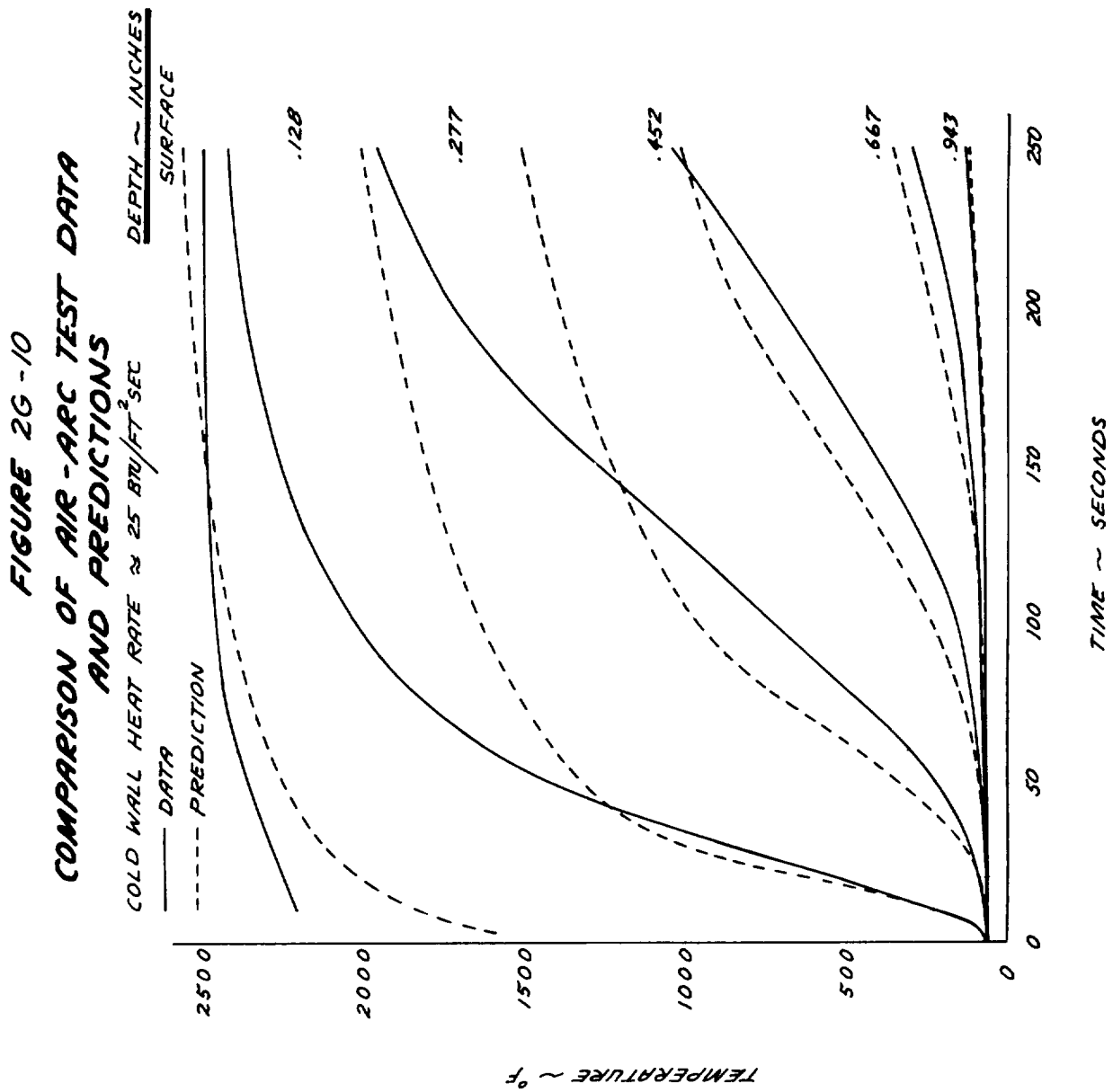
FIGURE 26-8

ARRHENIUS CORRELATION OF TGA RATE DATA  
FOR A TYPICAL BRITISH S-800 MATERIAL



**FIGURE 26-9**  
**TGA DATA FOR**  
**A TYPICAL HEAT SHIELD MATERIAL**







## Appendix 2H

### MASS TRANSPIRATION EFFECTS ON CONVECTIVE HEAT TRANSFER

Convective heating is appreciably reduced by the injection of gaseous-ablation products into the boundary layer. This effect is primarily attributable to a thickening of the boundary layer with a corresponding reduction of the enthalpy gradient at the wall.

Theoretical evaluation of the mass transfer effect for realistic ablation situations is difficult. It involves evaluation of transport properties for complex mixtures and solution of the multicomponent boundary layer equations accounting for diffusion. Fortunately, an adequate description of the effect may be obtained utilizing simple procedures. It is well known that the ratio of the heat transfer coefficient with transpiration to that without may be conveniently correlated in terms of a simple mass injection rate parameter (i.e., the ratio of the mass injection rate to the convection coefficient at zero mass transfer). The effect of injection of a gas other than air may be accounted for by the multiplying factors  $(M_a/M_{inj})^{1/4}$  for laminar flow and  $Cp_{inj}/Cp_e$  for turbulent flow.

The correlation functions which have been adopted for prediction of the mass transfer effect were shown in Fig. 2-66. The laminar mass transpiration correlation is based on the axisymmetric stagnation region analysis of Libby (Ref. 2.94). The turbulent method is empirically derived from experimental results. Justification of these methods is presented in this appendix. The results of both turbulent and laminar investigations of mass transfer cooling are reviewed. The influence of Mach number, Reynolds number and wall to freestream temperature ratio is considered. In general the experimental and analytical information employed corresponds to similar mass injection (implying the injection parameter is independent of location) at either a stagnation point or zero pressure gradient region with an isothermal wall. Uncertainties associated with laminar mass

transfer cooling are evaluated by comparing typical boundary conditions on the Apollo forebody with those inherent in the theoretical analysis. For turbulent flow the uncertainty is assessed by consideration of the accuracy of the experimental data forming the empirical basis. The resulting error band estimates are shown in Fig. 2-66 together with the adopted correlations.

#### LAMINAR BOUNDARY LAYER

Considerable information has evolved concerning injection into the laminar boundary layer as a result of the interest in stagnation region heating and the availability of reliable theoretical analysis techniques. The development of relations to predict the reduction in skin friction and heat transfer due to gas injection as well as a comprehensive survey of most of the existing literature is given in Refs. 2.140 and 2.125. The intent here is to summarize the information applicable for the conditions existing on the Apollo forebody. First the method used to predict the transpiration effect in the present study is justified by comparison with analytical and experimental results for the axisymmetric stagnation region. Then the influence of various complicating factors is examined.

The laminar transpiration correlation adopted here is compared with the axisymmetric stagnation region analysis of Ref. 2.92 and the high velocity results of Ref. 2.98 in Fig. 2H-1. The influence of wall to total temperature ratio and flight velocity on the heat transfer reduction is seen to be minimized when the results are presented in terms of the similarity blowing parameter,  $\frac{\dot{m}}{\rho_e u_e} \sqrt{Re_s}$  (this parameter is easily converted to the more convenient  $\dot{m}/C_H$ ). A similar conclusion is reached with respect to Reynolds number and Mach number when considering zero pressure gradient and low speed wedge flows. Fig. 2H-1 also demonstrates the applicability of the foreign gas correction  $(M_a/M_{inj})^{1/4}$ , at least for helium injection. Corroboration of the theoretical analyses is provided in Fig. 2H-2 by comparison with experimental results. In applying the correlation it is convenient to assume that transpiration effects on the recovery factor are negligible. This assumption is well

justified for the situation where the wall to total enthalpy ratio is small.

In predicting laminar transpiration cooling the degree to which the physical situation violates the theoretical model essentially determines the magnitude of uncertainty. In particular, the boundary conditions for the boundary layer downstream from the stagnation point will be inconsistent with those employed in the analyses upon which the present correlation is based. Therefore, the following conditions will be considered as to their effect in perturbing the transpiration curve:

1. non-similar mass injection
2. non-isothermal wall
3. pressure gradient
4. foreign gas injection.

The effect of a non-similar injection distribution and a non-isothermal wall on mass transfer cooling is investigated by obtaining a relatively simple integral solution of the homogeneous boundary layer equations. As an upper limit on the influence of non-similar injection a constant injection rate is assumed. Although integral solution for the complex flow situation of interest is somewhat questionable, the results are useful in indicating trends. The influence of the pressure gradient deviating from the stagnation point value and the applicability of the foreign gas correlation are assessed from the information available in the literature. The results of this work are combined with typical boundary conditions existing on the Apollo forebody to yield a band of uncertainty.

#### Non-Similar Boundary Conditions

The influence of non-similar blowing and a non-isothermal wall on laminar mass transfer cooling is investigated using the integral solution of Scott (Ref. 2.145). The general approach and applicable results are

indicated below. Only homogeneous injection is treated.

The analysis is initiated by specifying the boundary layer equations and appropriate boundary conditions. The solution is made considerably more tractable by using the hypersonic approximations of Lees. In this manner the relations describing a rotationally symmetric, compressible boundary layer may be reduced to those for incompressible flow over a flat plate by an appropriate transformation. It is also convenient to assume that the Lewis and Prandtl numbers are unity. This procedure which has been described by Chung (Ref. 2.146) and others yields the following conservation relations.\*

$$\text{Continuity: } \partial u / \partial \tilde{s} + \partial v / \partial \eta = 0 \quad (2H.1)$$

$$\text{Momentum: } u \partial u / \partial \tilde{s} + v \partial u / \partial \eta = \nu_{e0} \partial^2 u / \partial \eta^2 \quad (2H.2)$$

$$\text{Energy: } u \partial q / \partial \tilde{s} + v \partial q / \partial \eta = \nu_{e0} \partial^2 q / \partial \eta^2 \quad (2H.3)$$

where,

$$\tilde{s} = \int_0^s c_0 u_e r^{2L} ds$$

$$\eta = u_e r \int_0^y \frac{\rho}{\rho_{e0}} dy$$

$$u = u/u_e \quad q = H/H_e \quad (2H.4)$$

$$c_0 = \rho \mu / \rho_{e0} \mu_{e0}$$

\* It should be noted that the transformations utilized here differ slightly from those used elsewhere in this section.



The boundary conditions to be studied are

$$\begin{aligned}
 \text{at } \eta = 0 \\
 U &= 0 \\
 V &= v_w(s) \\
 q &= q_w(s)
 \end{aligned}
 \tag{2H.5}$$

$$\begin{aligned}
 \text{at } \eta = \infty \\
 U &= q = 1
 \end{aligned}
 \tag{2H.6}$$

where physically,

$$v_w/2e_0 = \frac{\rho_w \mu_w}{\mu_{e_0} C_0 U e r^2}
 \tag{2H.7}$$

The boundary layer equations are first transformed to the velocity-shear stress plane using the Crocco transformations. The relations are then solved by substitution of appropriate cubic polynomials representing shear stress and enthalpy. This approach furnishes accuracies comparable with fifth or sixth degree polynomials in the velocity versus normal distance formulation.

The transformed shear stress is defined by

$$\tau \equiv \partial u / \partial \eta
 \tag{2H.8}$$

where physically

$$\tau_w = \frac{\rho_e \rho_0}{\rho_w \mu_w r^2} \frac{\overline{C_f}}{2}
 \tag{2H.9}$$

Transformation to velocity space is obtained by replacing  $\eta$  by U as one of the independent variables while the shear stress  $\tau$  replaces U as one of the dependent variables.

Let

$$\xi = \tilde{\xi}, U = U(\tilde{\xi}, \tau) \quad (2H.10)$$

This results in the following conservation relations:

$$\text{Momentum:} \quad U \left( \frac{\partial \tau}{\partial \xi} \right)_U = \nu_{e0} \tau^2 \left( \frac{\partial^2 \tau}{\partial U^2} \right)_\xi \quad (2H.11)$$

$$\text{Energy:} \quad U \left( \frac{\partial q}{\partial \xi} \right)_U = \nu_{e0} \tau^2 \left( \frac{\partial^2 q}{\partial U^2} \right)_\xi \quad (2H.12)$$

with the boundary conditions at  $U = 0$

$$\tau = \tau_w, \quad q = q_w$$

$$\left( \frac{\partial \tau}{\partial U} \right)_w = \frac{V_w}{\nu_{e0}}$$

$$\left( \frac{\partial^2 \tau}{\partial U^2} \right)_w = \left( \frac{\partial^2 q}{\partial U^2} \right)_w = 0$$

$$\left( \frac{\partial q}{\partial U} \right)_w = S_w \quad (2H.13)$$

where

$$S_w = \frac{\rho_w \mu_w}{\rho_w} \frac{-\dot{q}}{He \tau_w} \frac{u_{er}^2}{\rho_{e0}} \quad (2H.14)$$

at  $U = 1$ :  $g = 1 \quad \tau = 0$  (2H.15)

The boundary conditions are employed to yield the following cubic polynomials.

$$\tau = \tau_w + \frac{V_w}{\nu_{e0}} U - \left( \tau_w + \frac{V_w}{\nu_{e0}} \right) U^3$$
(2H.16)

$$g = g_w + S_w U + (1 - g_w - S_w) U^3$$
(2H.17)

Substituting Eqs.(2H.16) and (2H.17) into the momentum and energy equations and integrating from  $U = 0$  to  $U = 1$  gives,

$$\left. \begin{aligned} \frac{3}{10} \frac{\partial \tau_w}{\partial \xi} + \frac{2}{15} \frac{1}{\nu_{e0}} \frac{\partial V_w}{\partial \xi} + \nu_{e0} \left( \tau_w + \frac{V_w}{\nu_{e0}} \right) \left\{ \frac{27}{20} \tau_w^2 \right. \\ \left. + \frac{11}{10} \tau_w \frac{V_w}{\nu_{e0}} + \frac{1}{4} \left( \frac{V_w}{\nu_{e0}} \right)^2 \right\} = 0 \end{aligned} \right\} \quad (2H.18)$$

$$\left. \begin{aligned} \frac{3}{10} \frac{\partial g_w}{\partial \xi} + \frac{2}{15} \frac{\partial S_w}{\partial \xi} + \nu_{e0} \left( g_w + S_w^{-1} \right) \left\{ \frac{27}{20} \tau_w^2 + \frac{11}{10} \tau_w \frac{V_w}{\nu_{e0}} \right. \\ \left. + \frac{1}{4} \left( \frac{V_w}{\nu_{e0}} \right)^2 \right\} \end{aligned} \right\} \quad (2H.19)$$

These equations constitute the solution of the boundary layer equations for an arbitrary distribution of surface enthalpy and injection rate.

The applicability of this simple integral solution may be assessed by comparison with more rigorous solutions for the situation of isothermal similarity injection. For the situation, the boundary conditions may be expressed as

$$\begin{aligned} \frac{V_w}{v_{e0}} &= A (v_{e0} S)^{-1/2} \\ \tau_w &= B (v_{e0} S)^{-1/2} \\ q_w &= \text{constant} \end{aligned} \quad (2H.20)$$

Equation 2H.18 may be integrated to yield

$$15A^3 + 81A^2B + 147AB^2 + 81B^3 - 9B - 4A = 0 \quad (2H.21)$$

The particular solution for zero injection ( $A = 0$ ) is  $B = 1/3$ , or

$$\frac{\bar{C}_f}{2} = \frac{1}{3} \frac{\rho_w \mu_w r^L}{\rho_e \mu_e} \left( v_{e0} \int_0^S C_0 u_e r^{2L} ds \right)^{-1/2} \quad (2H.22)$$

which agrees well with more exact solutions for flat plate or stagnation regions. The reduction in skin friction as a result of mass injection is readily obtainable from Eq.(2H-21), i.e.,

$$\bar{C}_f / C_f = B / B_{A=0}$$

$$A = \frac{\rho_w \mu_w}{\rho_e \mu_e u_e r^L} \sqrt{\frac{\int_0^S \rho_e \mu_e u_e r^{2L} ds}{C}} \quad (2H.23)$$

where  $C$  is the compressibility constant  $\rho_w \mu_w / \rho_e \mu_e$ . Chung suggests

$$C = \left( \rho_w \mu_w / \rho_e \mu_e \right)_0^{0.2}$$

Verification of the above result is provided in Fig. 2H-3 by comparison with the exact solutions of Ref. 2.37 and 2.147.

The transpiration effect for arbitrary injection and surface temperature

distributions may be determined by solving Eqs. (2H.18) and (2H.19). For example, following the procedure outlined in Ref. 2.145, it is possible to obtain the transpiration effect for the case of uniform injection, i.e.,

$$v_w / v_{e0} = \text{constant.}$$

This solution is also presented in Fig. 2H-3. It is seen that the transpiration effect for uniform injection is about the same as for the similarity case except at the higher blowing rates where the integral solution is less applicable.

#### Pressure Gradient

A simple correlation of the pressure gradient effect on mass transfer cooling was suggested by Eckert. Multiplying the injection parameter by the term  $\sqrt{1-\beta/2}$  was found to correlate the results for plane stagnation and flat plate flow. The pressure gradient parameter is defined by

$$\tilde{\beta} \equiv \frac{2\tilde{S}}{u_e} \frac{du_e}{d\tilde{S}} \quad (2H.24)$$

Corroboration of this method is given in Fig. 2H-4 where the theoretical mass transfer results for  $\tilde{\beta} = 0$  (zero pressure gradient),  $\tilde{\beta} = 1/2$  (axisymmetric stagnation point) and  $\tilde{\beta} = 1$  (2-dimensional stagnation line) are shown. Satisfactory correlation is obtained at all but the higher blowing rates. Therefore, the influence of the pressure gradient deviating from  $\tilde{\beta} = 1/2$  on the mass transfer cooling may be assessed directly from the blowing parameter:  $\frac{\dot{m}}{C_H} \sqrt{1-\tilde{\beta}/2}$

The applicability of this correlating function must be qualified. The

influence of a pressure gradient will be affected by the local and upstream conditions. In particular, the rate and distribution of mass injection and the degree of wall cooling may have significant effects. Therefore, the correlation probably only qualitatively indicates the pressure gradient effect for realistic flight condition.

### Foreign Gas Injection

The uncertainties associated with the molecular weight ratio correlation are attributable to two sources. First is the accuracy and generality of the correlation with respect to the injection of a single species into the boundary layer. Second is the error introduced by not considering the actual conditions of multicomponent injection with possible gas phase reaction.

The accuracy of the present correlation for single component injection may be assessed by comparison with the available theoretical information. The effectiveness of an injected species depends upon its energy storage capacity and its ability to move quickly into the hot outer portions of the boundary layer. The former is characterized by the specific heat and the latter by the molecular weight of the injectant. Approximate correlations have been obtained using both parameters. In Ref. 2.125 good correlations for a variety of injectants were obtained using the specific heat ratio. These results are repeated in Fig. 2H-5 for two flow situations: zero pressure gradient and two-dimensional stagnation regions. This information was drawn from a number of theoretical investigations for a wide variety of flow conditions. For the axisymmetric stagnation region the correlation for helium, shown in Fig. 2H-1, is essentially the same whether the molecular weight ratio or  $(C_{p_{inj}}/C_{p_{air}})^{0.30}$  is used. The results for Teflon ablation, shown in Fig. 2H-2, support the specific heat ratio correlation. Since Teflon decomposes to the monomer  $C_2F_4$  the associated specific heat is comparable with that of air. If molecular weight was controlling, Teflon ablation

would be less effective than air in transpiration cooling; a result not exhibited by Fig. 2H-2. It is suggested here that the uncertainty in the molecular weight correlation for single component injection is indicated by the difference between it and the specific heat correlation of Ref. 2.125,  $(Cp_{inj}/Cp_{air})^{0.30}$ .

The most significant uncertainty associated with foreign gas injection involves the question of multicomponent injection of reacting gases. For example, one of the few examinations of this effect (Ref. 2.150) studied hydrogen injection with subsequent oxidation resulting in four species in the boundary layer. This oxidation and multicomponent diffusion yielded mass transfer cooling results completely different from those obtained for an unreacting binary mixture. In considering ablation products, species such as hydrogen are present in enough quantity to make the thermochemical characteristics significantly different from air, although the average molecular weights are comparable. At present, insufficient information is available to provide any conclusions as to this effect. An investigation of this complex phenomenon was not within the scope of this study. Approximate methods are employed in the present study to account for this phenomenon. An average molecular weight or specific heat is employed in defining the foreign gas effect for a multicomponent mixture. Gas phase reactions are accounted for by basing the heat transfer on the enthalpy potential under the assumption of unity Lewis and Prandtl numbers (See Section 2.3).

#### Band of Uncertainty

Typical surface conditions existing on the leeward side of the Apollo forebody are shown in Fig. 2.48. The distributions of the pressure gradient parameter and the transformed distance are depicted in Figs. 2.47 and 2H-6, respectively. Correlating functions for foreign gas injection based on a mass average of the ablation products are presented in Fig. 2-67.

To ascertain the magnitude of the uncertainty resulting from the non-similar boundary conditions on the Apollo forebody, Eqs. (2H-18) and (2H-19) were numerically integrated for the representative surface conditions shown in Fig. 2-48. The effect on the transpiration effect is given in Fig. 2-61. It is concluded that negligible error is accrued if the adopted transpiration effect which is based on similar boundary conditions is applied. Therefore, the band of uncertainty for laminar mass transfer cooling is defined by the possible variation in the pressure gradient parameter and the foreign gas correlation. In this respect the pressure gradient parameter is considered to vary from 1/2 to 1,\* while the foreign gas correlating function ranges from 1.040 to 1.175.

#### TURBULENT BOUNDARY LAYER

The study of mass transfer cooling in the turbulent boundary layer has been hampered by the inability to solve the boundary layer equations in a direct manner. Solutions have been obtained under assumptions similar to those employed for laminar flow. Unfortunately, these solutions all require specifying certain ill-defined empirical constants (such as mixing length parameters). Because of these difficulties the majority of the investigations have been devoted to developing experimental information. In the following section an extensive review of existing information on turbulent mass transfer cooling is given. Emphasis is placed on the more current work. An excellent review of the literature through 1959 can be found in Ref. 2.151. This information is then employed to assess the possible error resulting from use of the turbulent curve of Fig. 2-66. In general these errors result from (1) the deviation of the actual surface and flight conditions from those of the experimental and analytical models and (2) the uncertainties associated with the basic investigations.

---

\*An upper limit of one for the pressure gradient parameter was selected since the correlation appears to be inapplicable for higher values.



## Theoretical Investigations

The majority of the analytical solutions for the turbulent boundary-layer equations with surface injection have been extensions of the usual mixing-length theories; a chronological list of these may be found in Ref. 2.152. All of these theories are based on scant experimental data.

Utilizing the concept of a laminar sublayer and a turbulent core, the theoretical analyses of Rubesin (Ref. 2.153) and Van Driest (Ref. 2.154) yielded essentially the same results for the effect of air injection on heat transfer. A comparison of Rubesin's results with experimental data is shown in Fig. 2H-7. Although the theory tends to slightly overpredict the reduction in Stanton number, the correct trend is present and, more importantly, the theory demonstrates that  $\bar{C}_H/C_H$  is almost a unique function of the blowing parameter  $\dot{m}/C_H$ . This choice of blowing parameter minimizes the influence of Mach number, stagnation temperature, and Reynolds number, at least for the ranges investigated :

$$0 < M \leq 8$$

$$1 < T_w/T_0 < 3$$

$$10^5 \leq Re \leq 10^8$$

It is shown in Fig. 2H-8 that the mass transfer cooling effect is only weakly dependent on the pressure gradient. Therefore, it can be assumed that the investigations for zero pressure gradient flow are applicable for the blunt body situation.

The two-layer mixing-length theory was also applied to the problem of foreign gas injection by Rubesin and Pappas (Ref. 2.155). Due to lack of experimental information on foreign gas injection, their theory yielded only qualitative information; hydrogen was shown to be a substantially better coolant than helium or air, and helium was found to be more

efficient than air.

### Experimental Investigations

There is a considerable amount of experimental information available on turbulent transpiration cooling. A chronological list of investigations is given in Table 2H-1. Before discussing the results, it is desirable to divide these investigations into ones for which the data can be assumed to be reliable and those for which the work was only exploratory. In the former category, Refs. 2.159-2.160, 2.163, 2.165 and 2.166 should probably be included. In many of the other investigations, the authors themselves have pointed out that their data should be treated as being only qualitative.

The effect of mass injection on the turbulent heat transfer coefficient and recovery factor as obtained from the aforementioned references is shown in Figs. 2H-7 and 2H-9. It should be noted that the data of Refs. 2.159 and 2.166 were taken from a mean curve drawn through the data. Several conclusions can be drawn from these results with respect to the reduction in heating.

1. The theory of Rubesin for air injection is in substantial agreement with the experimental results.
2. The influence of Mach number on the convective coefficient reduction is minimized if the data are correlated in terms of the blowing parameter  $\dot{m}/C_H$ .
3. As suggested by Bartle and Leadon (Ref. 2.165), the heat transfer reduction dependence on foreign gas injection is minimized if the injection parameter is modified by the specific heat ratio,  $c_{p_{inj}}/c_{p_e}$ .

A comprehensive investigation of foreign gas injection was made in Ref.

2.165. The data for a variety of gases and gas mixtures when presented in terms of an effectiveness parameter,  $R = \frac{T_W - T_{inj}}{T_{rf} - T_{inj}}$ , were found to agree closely to the correlating curve,

$$R = \left( 1 + \frac{1}{3} \frac{C_{p inj}}{C_{pe}} \frac{\dot{m}}{C_H} \right)^{-3} \quad (2H-24)$$

The effectiveness can be easily reconverted to the heat transfer coefficient reduction,  $\bar{C}_H / C_H$ ; this was done and the data and correlating curve are shown in Figure 2H-10. Although the data scatter in this form is more pronounced, it should be noted that the scatter is among data points for the same coolant and that, in general, elimination of this scatter would probably place the data for all of the coolants nearly on the same curve.

Since the heat transfer reduction appears to be under-predicted using Eq. 2H-24, prediction of the turbulent transpiration effect in this study is made using the correlating equation derived in Ref. 2.125:

$$\bar{C}_H / C_H = \left[ 1 + \frac{1}{10} \frac{C_{p inj}}{C_{pe}} \frac{\dot{m}}{C_H} \right]^{-4} \quad (2H-25)$$

This method is compared with the aforementioned theoretical and experimental information on Figs. 2H-7 and 2H-10.

#### Band of Uncertainty

The previously discussed data were obtained over a wide range of flow and surface conditions. These results should encompass all environmental conditions of present interest, and curves which bracket this data should therefore constitute an upper limit on the mass transfer cooling uncertainty. The uncertainty is then defined using the data of Figs. 2H-9 and 2H-10 for the upper boundary and Rubesin's results for the lower boundary.

This band is shown in Figs. 2-66 and 2H-7 and represents a conservative estimate as to the magnitude of uncertainty associated with predicting turbulent mass transfer cooling.

Year	Author(s)	Ref.	Geometry	Particle Description	Mach No.	Stagnation Temp. (°F)	Reynolds No. $\times 10^{-6}$	Coolant
1954	Miskely, et al.	2.156	Plate	Wire screen	0	530	2-3.3	Air
1955	Rubens, Pappas Okuno	2.157	Plate	Sintered stain- less steel powder	1.7	610	1.5 to 7	Air
1955	Casavin and Carter	2.158	30° Cone	Monel wire	2	1010	11	H <sub>2</sub> , He, H <sub>2</sub> O
1959	Scott, Anderson, and Eigin	2.159	Cone and Plate	Sintered stain- less steel wire	3.5	530	0.2 to 20	He, Air
1960- 61	Bartle and Leadin	2.160 2.161	Plate	Sintered stain- less steel powder	1, 3, 4	560	_____	N <sub>2</sub>
1961	Randall	2.162	45° Wedge	Sintered stain- less steel powder	1	1775 to 1370	0.5 to 8	He, N <sub>2</sub>
1961	Tewfik, Eckert, and Jurewicz	2.163	Cylinder	Sintered stain- less steel wire	0	560	0.1 to 2	Air
1961	Walton and Rackis	2.164	170° Cone	Sintered stain- less steel powder	0, 4.5	937 to 1490	_____	He, N <sub>2</sub>
1962	Bartle and Leadin	2.165	Plate	Sintered stain- less steel powder	3.0	560	_____	H, He, N <sub>2</sub> , O <sub>2</sub> , CO <sub>2</sub> , CO, COCl <sub>2</sub>
1964	Pappas and Okuno	2.166	Cone	Sintered stain- less steel powder	1.7, 3.07, 4.35	525, 640, 750	1-11.8	He, Air, CO, CO <sub>2</sub>

TABLE III-1. EXPERIMENTAL MEASUREMENTS OF THE EFFICIENCY OF GAS EXCHANGE IN THE TURBULENT HEAT TRANSFER

**FIGURE 2H-1**  
**CORRELATION OF FOREIGN GAS INJECTION FOR**  
**LAMINAR AXISYMMETRIC STAGNATION POINT FLOW**

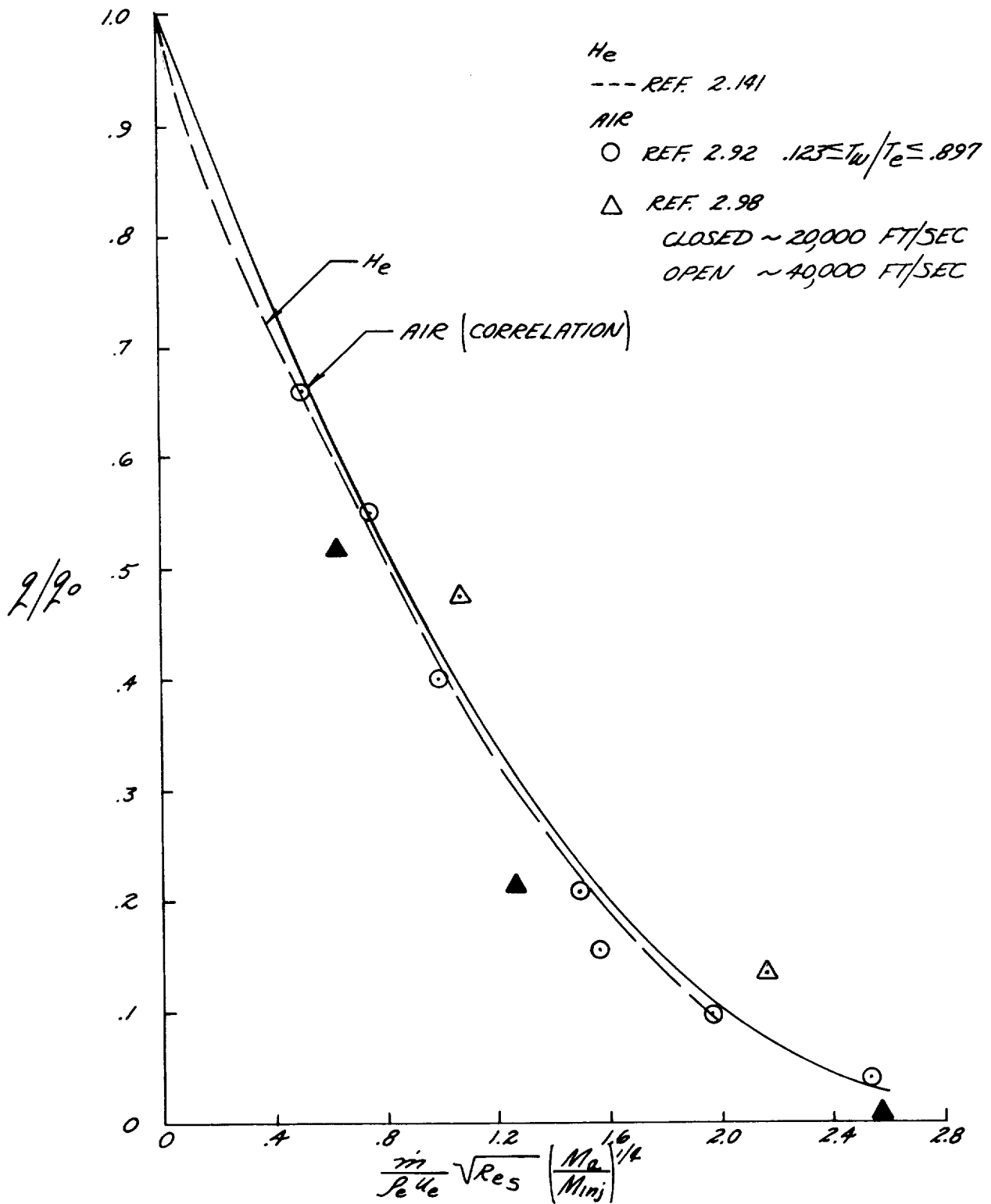
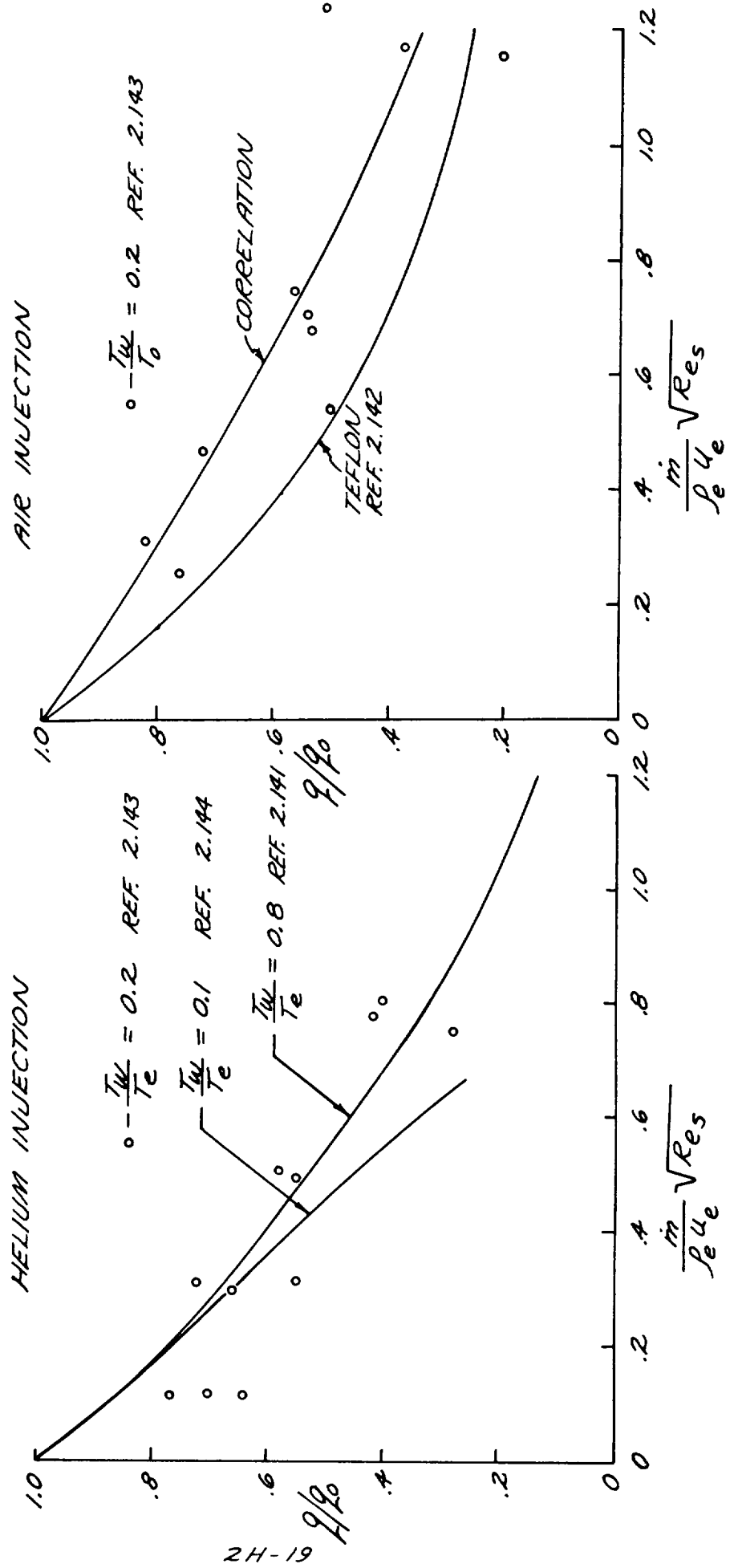
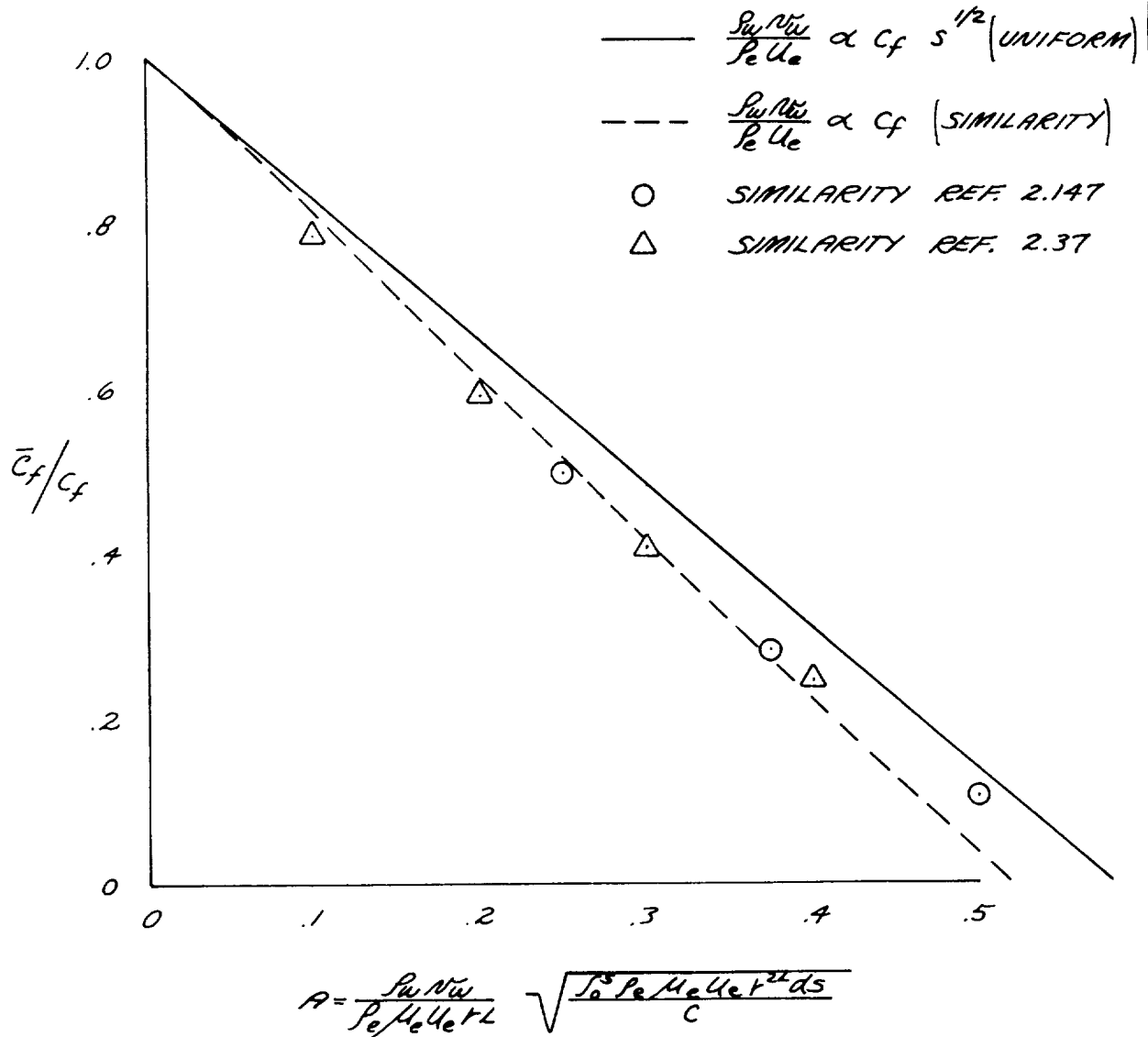


FIGURE 2H-2  
 COMPARISON OF EXPERIMENTAL AND THEORETICAL  
 LAMINAR MASS TRANSFER COOLING AT THE AXI-  
 SYMMETRIC STAGNATION POINT



Prepared	NAME <i>sjh</i>	DATE	LOCKHEED MISSILES & SPACE COMPANY A GROUP DIVISION OF LOCKHEED AIRCRAFT CORPORATION	Page	TEMP	PERM
Checked			TITLE	Model		
Approved				Report No.		

**FIGURE 2H-3  
INFLUENCE OF MASS INJECTION AND ITS  
DISTRIBUTION ON SKIN FRICTION**





**FIGURE 2H-4  
 INFLUENCE OF PRESSURE GRADIENT ON MASS  
 TRANSFER COOLING IN THE LAMINAR BOUNDARY  
 LAYER**

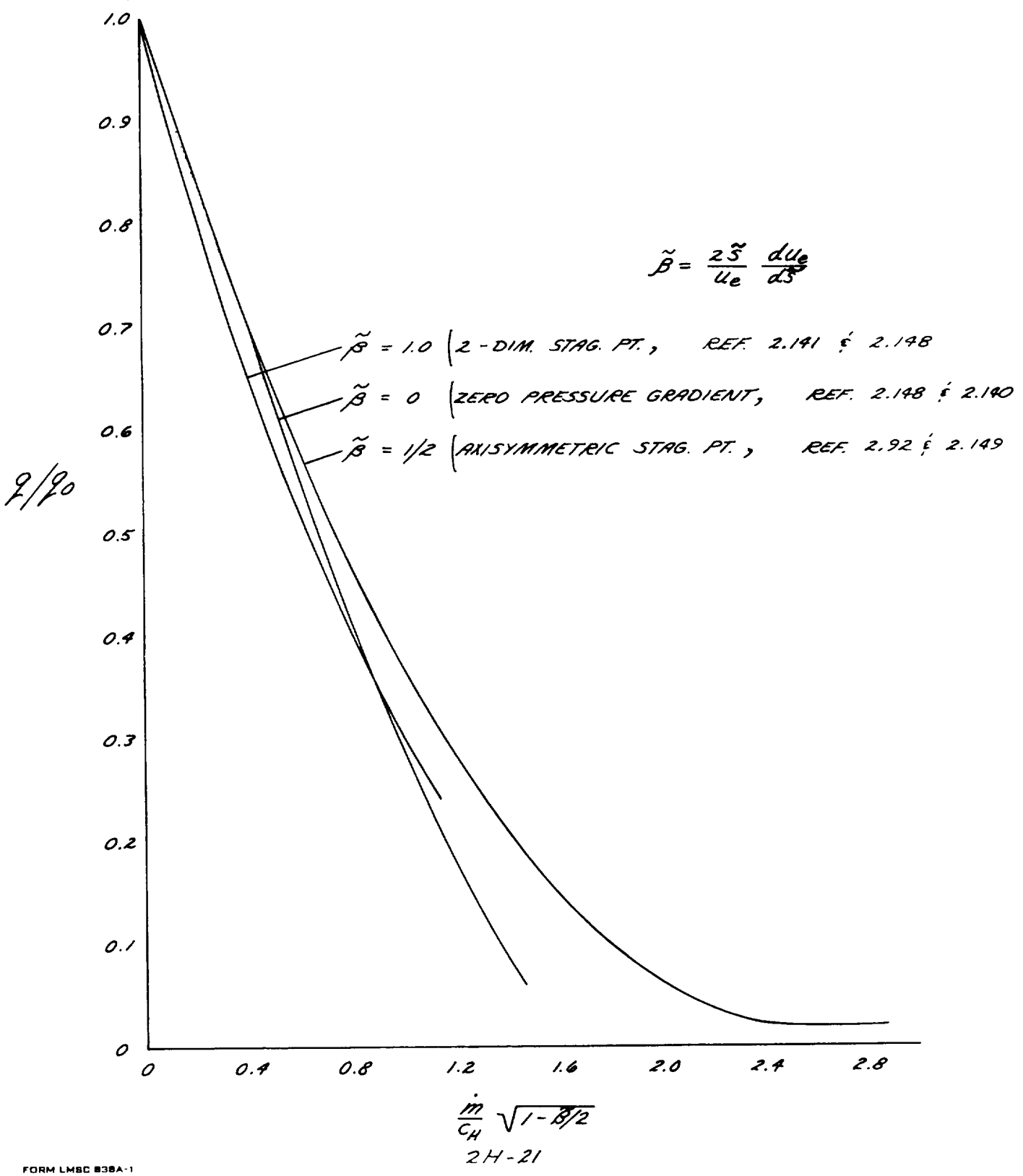
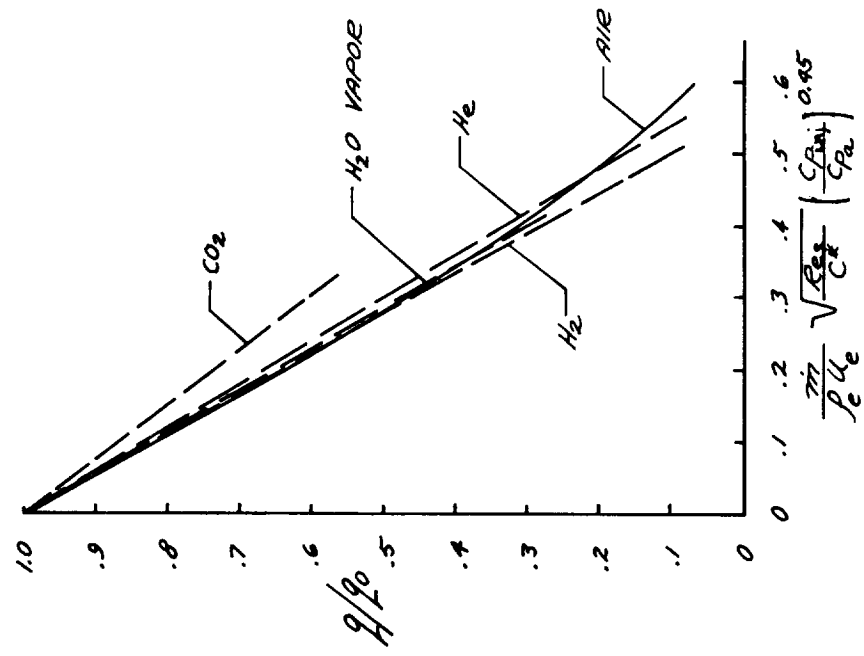


**FIGURE 2H-5**

**CORRELATION OF FOREIGN GAS INJECTION FOR THE LAMINAR, ZERO PRESSURE GRADIENT, BOUNDARY LAYER**



**CORRELATION OF FOREIGN GAS INJECTION FOR LAMINAR, TWO-DIMENSIONAL STAG. REGION FLOW**

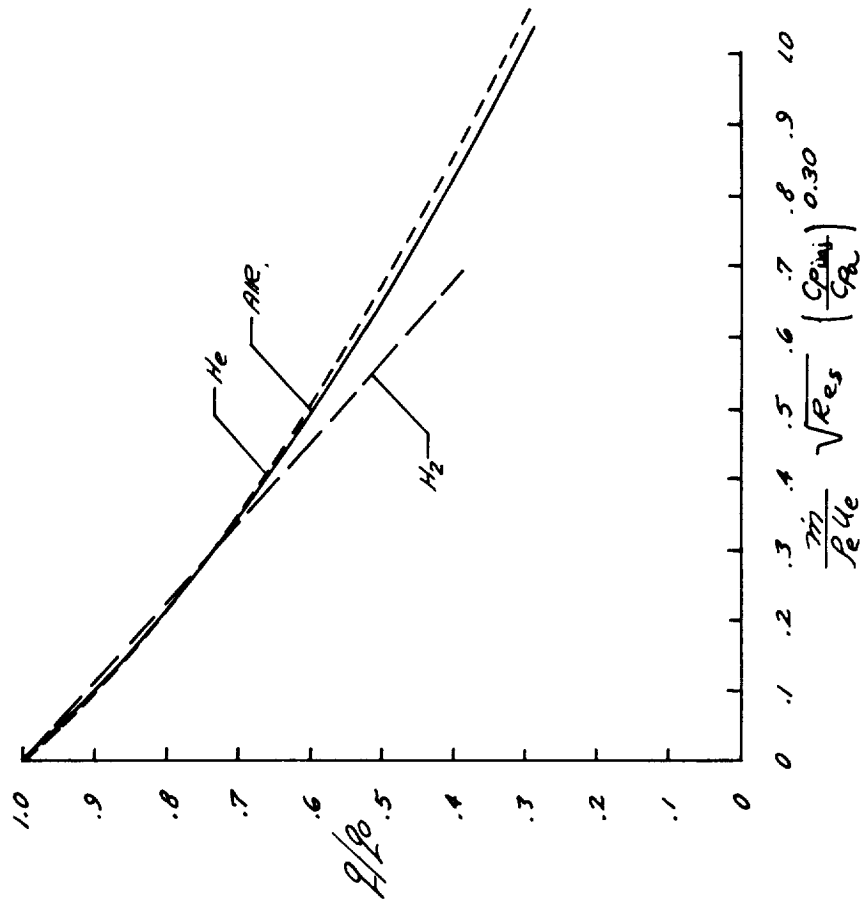
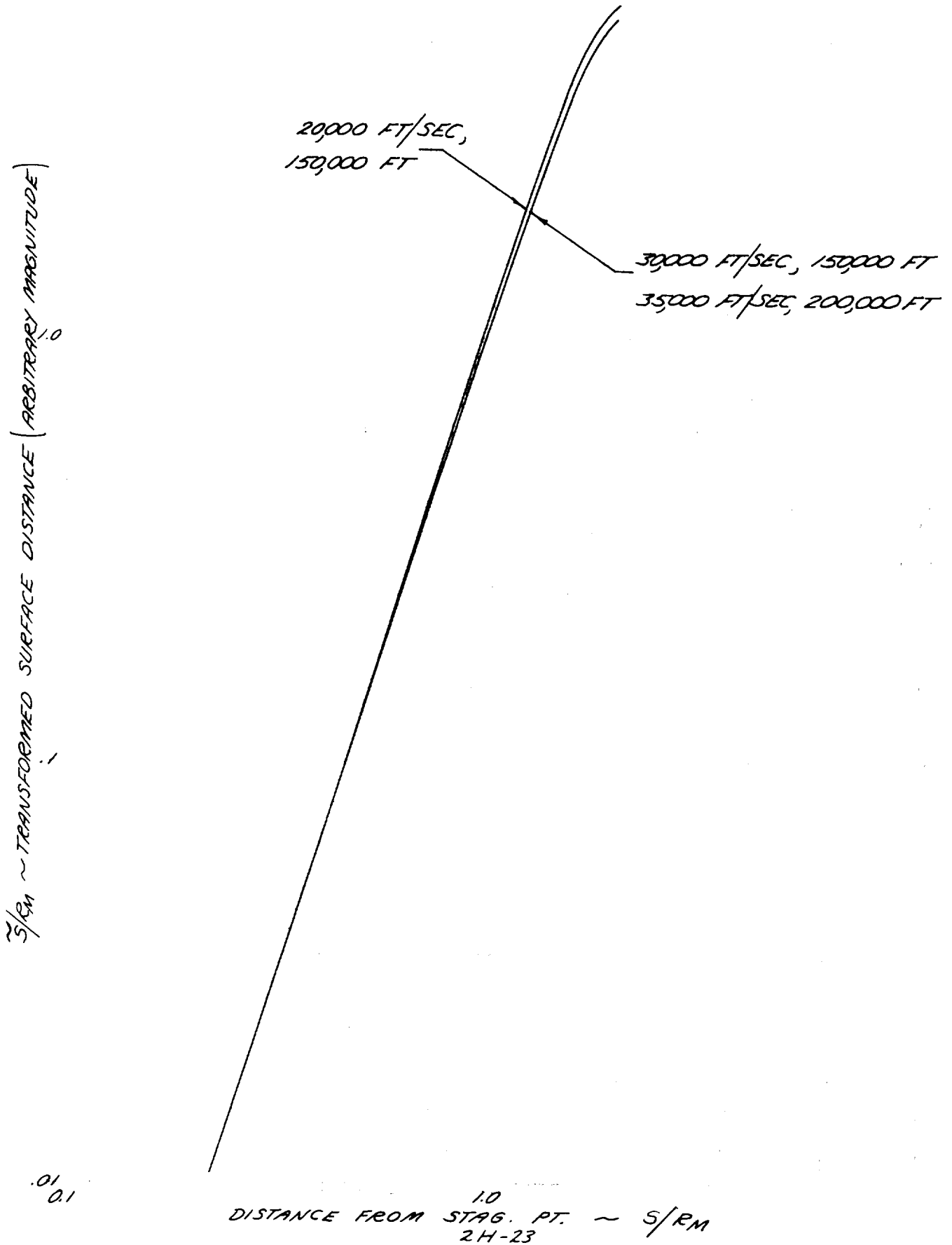
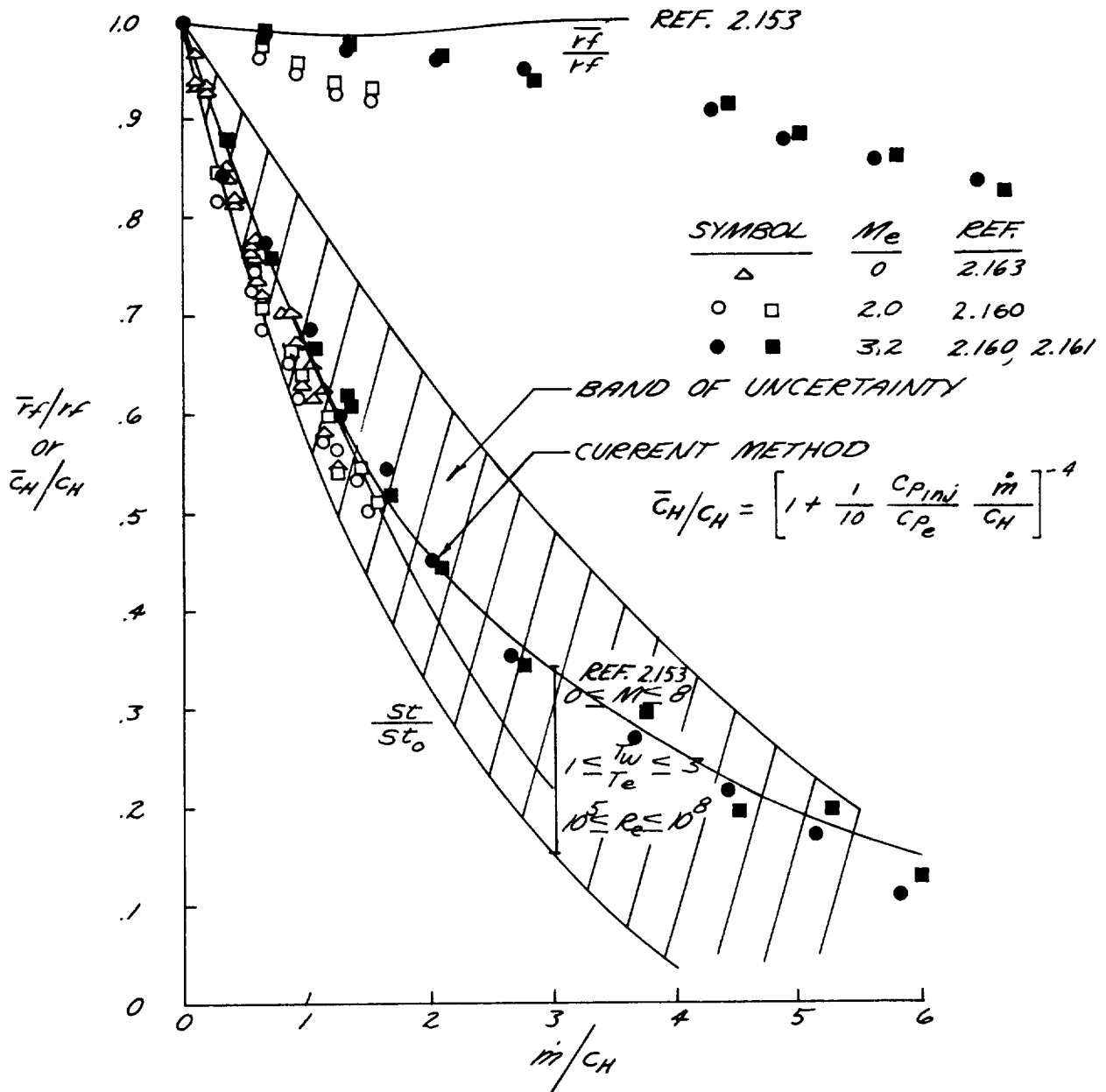


FIGURE 2H-6  
VARIATION OF TRANSFORMED SURFACE COORDINATE  
FOR APOLLO VEHICLE IN PLANE OF SYMMETRY



**FIGURE 2H-7**  
**EFFECT OF AIR INJECTION ON THE TURBULENT**  
**STANTON NUMBER AND RECOVERY FACTOR**



**FIGURE 2H-8**  
**INFLUENCE OF PRESSURE GRADIENT ON THE**  
**MASS TRANSFER COOLING IN TURBULENT FLOW**

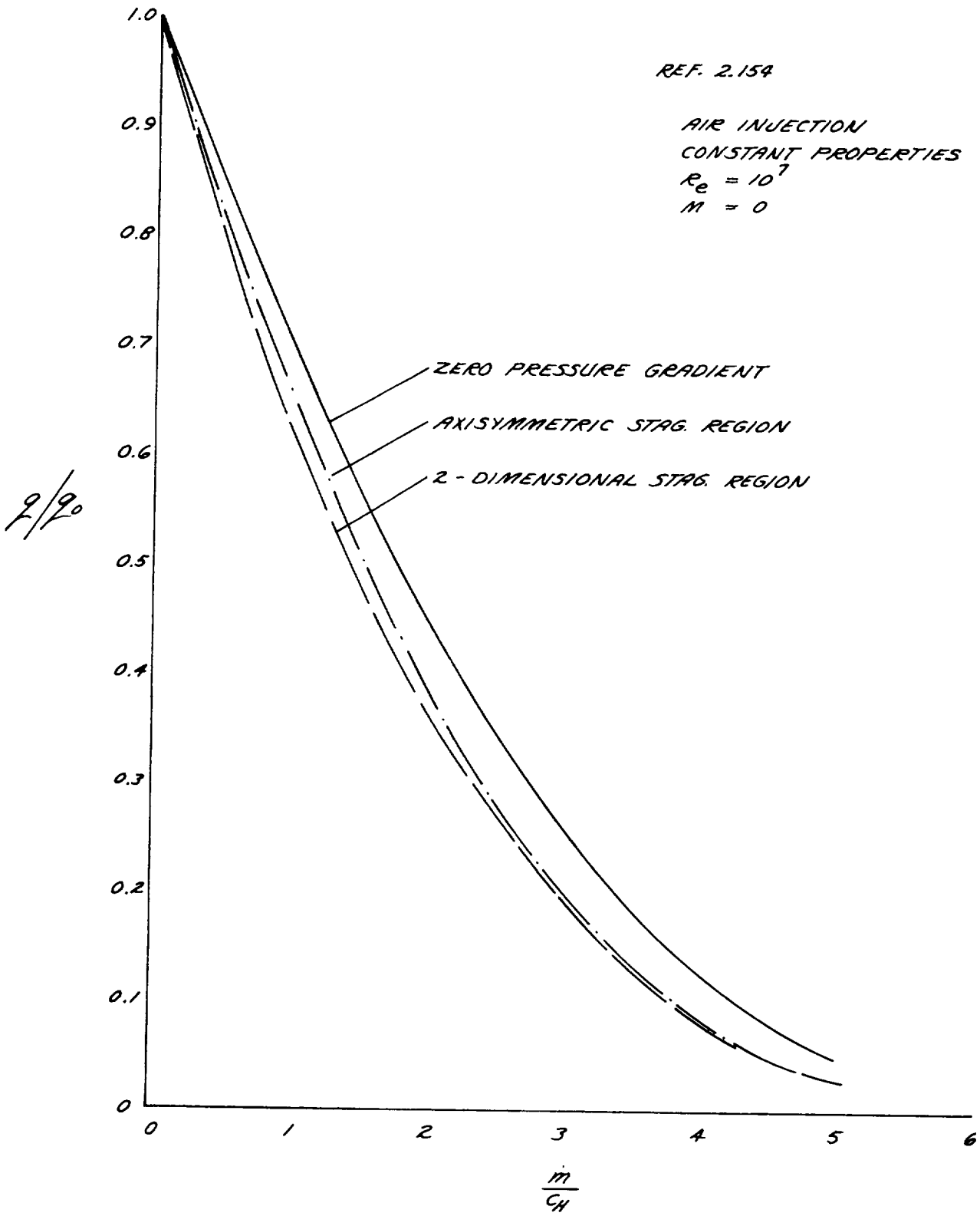


**FIGURE 2H-9  
EFFECT OF FOREIGN GAS INJECTION ON THE  
TURBULENT STANTON NUMBER**

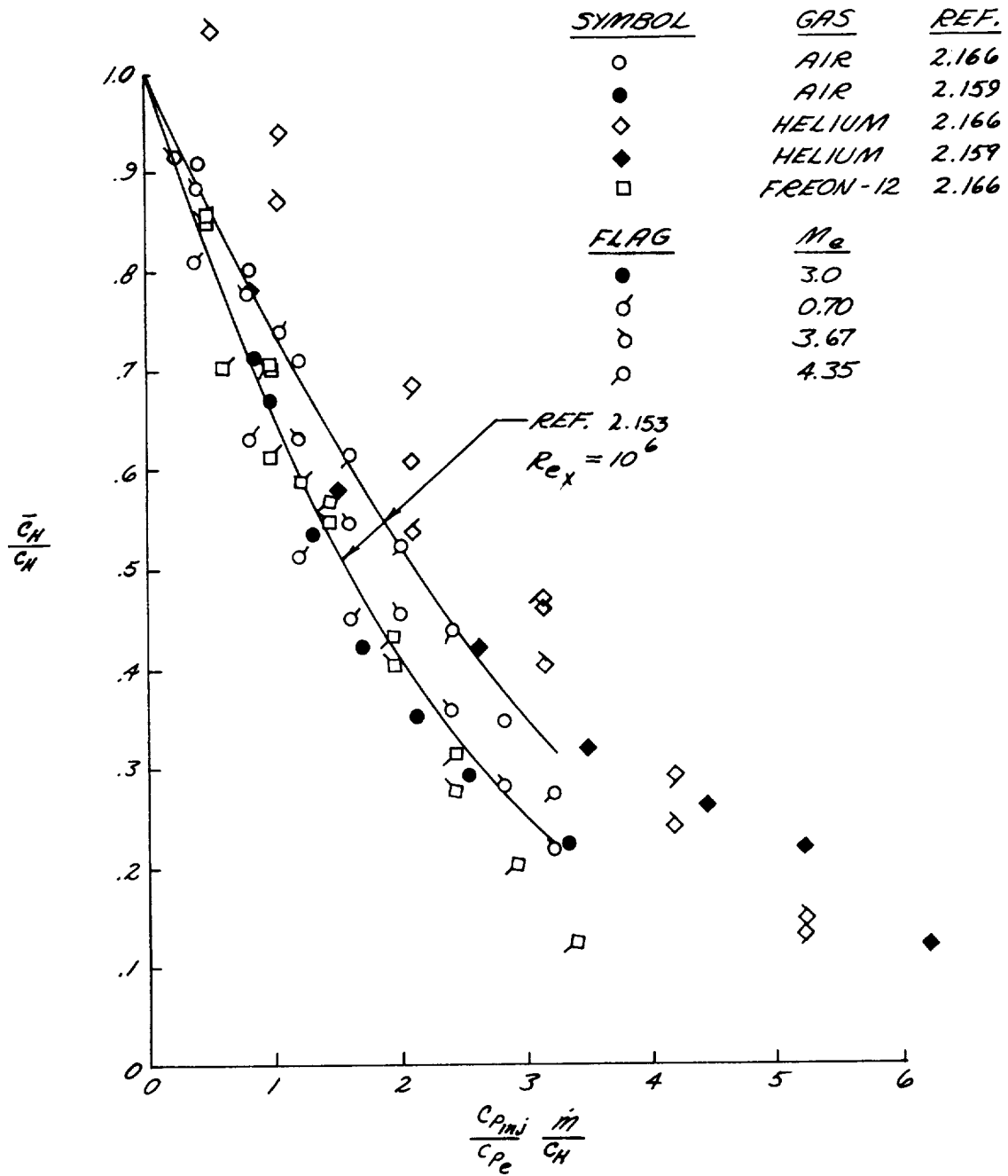
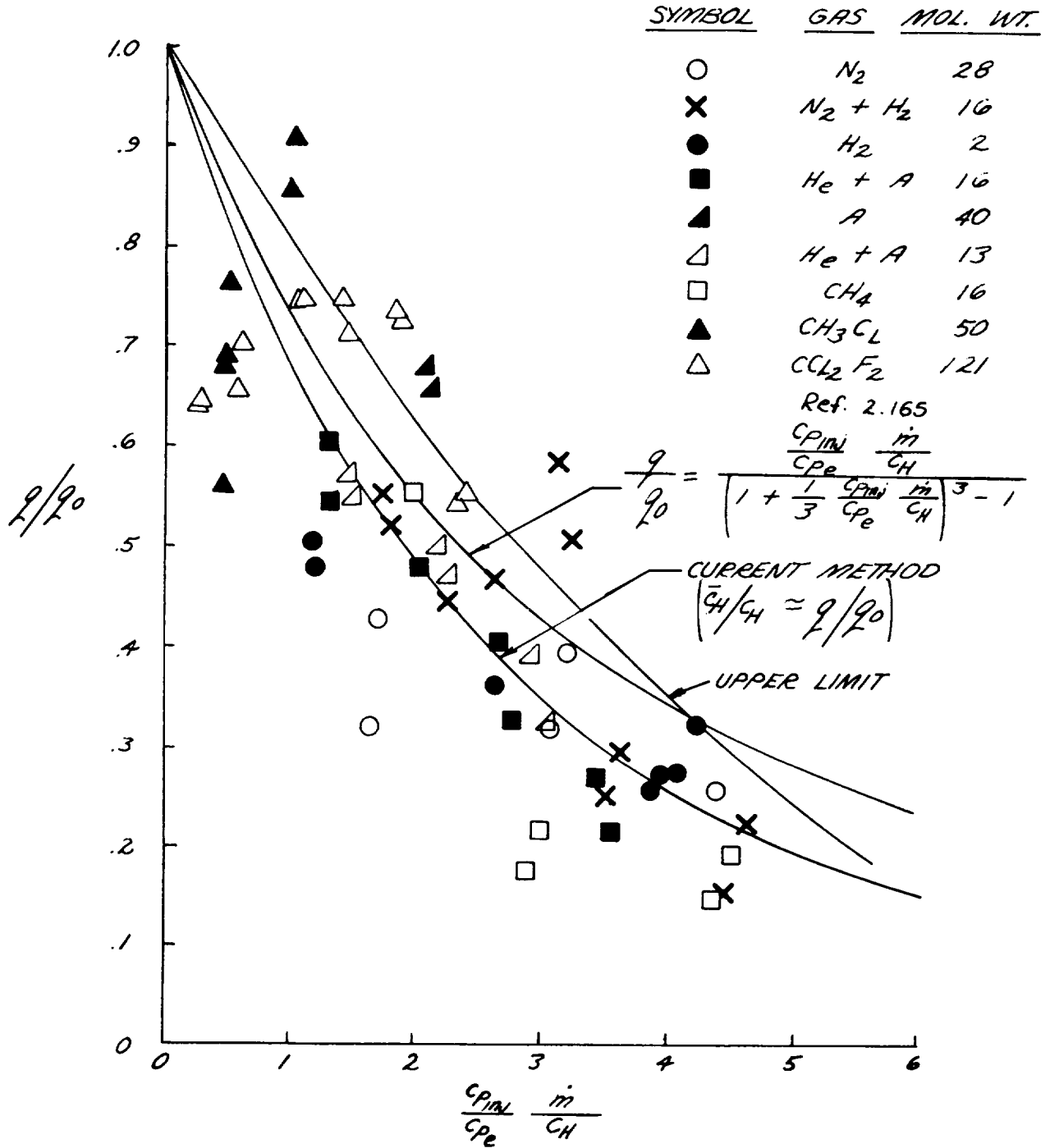


**FIGURE 2H-10**  
**EFFECT OF FOREIGN GAS INJECTION ON THE**  
**TURBULENT HEAT FLUX**







## Appendix 2I

### PROTUBERANCE EFFECTS ON CONVECTIVE HEAT TRANSFER

The influence of protuberances on the convective heat flux experienced by the Apollo vehicle is discussed in this section. Since the protuberance-boundary layer phenomenon is complex, recourse must be made to experimental data. Interference factors (ratio of disturbed to smooth surface heat transfer) for an Apollo scale model are available for two wind tunnel conditions. The primary objective here is to assess the applicability of the experimentally derived protuberance interaction factors at flight conditions.

Considerable attention, both experimental and analytical, has been devoted to the influence of surface irregularities on the boundary layer characteristics. The majority of these studies have been restricted to simple two-dimensional steps or impinging shock waves in zero pressure gradient flow. Emphasis has been given to the surface pressure distributions, although more recent investigations have been concerned with heat transfer. Experimental measurements of interference factors for three-dimensional protuberances are relatively scarce; Refs. 2.167, 2.168, 2.169 and 2.170 provide some applicable information. All of these studies are useful in understanding the basic nature of the problem and in defining the governing factors.

In the following discussion a qualitative description of the protuberance-boundary layer interaction is presented first. Characteristic parameters of the boundary layer and the protuberance which may influence their interaction are discussed, and available experimental and analytical information are used to delineate the relative effect of each parameter. Finally, flight and test conditions are compared and the applicability of the wind tunnel data is determined.

## DISTURBANCE PHENOMENON

In determining the scaling parameters it is helpful to understand the general nature of the flow over a protuberance. Consider the subsonic flow over the two-dimensional flange shown in Fig. 2-50. Since the boundary layer must thicken upstream and thin downstream in order to pass over the obstacle, a positive pressure gradient and a negative pressure gradient are propagated upstream and downstream, respectively. When the protuberance height becomes significant relative to the boundary layer thickness, separation may occur. Upstream boundary layer separation occurs when the kinetic energy of the fluid particles is insufficient as a result of viscous dissipation to overcome the pressure rise. When the pressure rise reaches a certain threshold, the wall shear is brought to zero and separation will occur. Downstream separation results when the streamline curvature necessary to follow the surface contour cannot be sustained by the pressure gradient normal to the surface. The separated or "dead air region" is characterized by recirculation of the flow. The heat transfer will tend to follow the pattern of the pressure distribution. In the upstream compression region the heat transfer coefficient will increase relative to the undisturbed value. Downstream, the heat transfer ratio increases from an initial value less than one to greater than one at reattachment before decaying to its undisturbed value.

A similar pattern is to be expected for the flow characteristics around a three-dimensional disturbance. As an example, the interference factors for supersonic flow about a cylinder are presented in Fig. 2I-1. The center line distribution is similar to that for two-dimensional protuberances: upstream compression followed downstream by an expansion through a short separated region and reattachment.

## INFLUENCING PARAMETERS

Variations in flow condition and protuberance geometries can be expected

to have a significant influence on the boundary layer-protuberance interaction. The following parameters are deemed to be the most fundamental in this respect: (1) protuberance geometry, (2) Reynolds number, (3) Mach number, (4) flow regime, (5) wall cooling, (6) mass injection, (7) pressure gradient, and (8) interaction between protuberances. The relative influence of each of those parameters can be inferred from the applicable information found in the literature. In the following discussion general observations are made as to the effect each parameter has on the interference factor; whenever possible quantitative criteria are presented.

#### Protuberance Geometry

Obviously, the most critical parameter is the geometry of the protuberance. Geometrical considerations can be divided into two parts: (1) shape and (2) the projected characteristic dimensions in the plane perpendicular to the flow direction.

Heat transfer measurements with various shapes (Refs. 2.167, 2.169, and 2.170) suggest that both streamlined and swept-back obstacles will reduce the interference factor markedly; the opposite trend is observed with swept-forward protuberances. The nature of this effect is too complex to permit defining quantitative criteria.

The relative size of the protuberance with respect to the boundary layer thickness appears to be of major importance. In Fig. 2I-2 the interference factors for protruding cylinders, as obtained from three separate investigations, are presented. The height of the cylinders is much greater than the boundary layer thickness resulting in the diameter being the characteristic dimension. The data constitutes measurements made over a moderate range of Mach numbers and Reynolds numbers and for two diameters. The particular data presented was selected on the basis of having approximately equal ratios of momentum thickness to diameter. Although it is difficult to conclusively separate out the influence of

the diameter it does appear that the interference factors are essentially independent of the characteristic dimension when the ratio of momentum thickness to diameter is invariant. It is logical to expect a similar conclusion to hold with respect to other pertinent dimensions.

#### Unit Reynolds Number

The data presented in Fig. 2I-2 also indicates no discernable influence of Reynolds number per foot provided that  $\theta/D$  is maintained constant. The independence of the interference factor from the unit Reynolds number was also observed for two-dimensional disturbances in Ref. 2.171 (low speed turbulent flow) and Ref. 2.169 (supersonic axial flow over a cylinder). Further substantiation can be inferred from Refs. 2.172 and 2.131 where interference factors were measured in a cavity for both laminar and turbulent boundary layers.

#### Mach Number

There is substantial difference in the interference factor results between subsonic and supersonic flow. For Mach numbers greater than one, Lighthill (Ref. 2.173) points out that the extent of the interaction region is reduced relative to that for the subsonic case, but that pressure gradients in general are greater for supersonic flow. Similarly the extent of the separated region in supersonic flow is decreased. Accordingly, it can be expected that the region where the heating is influenced will be reduced while the magnitude of the interference factor will be increased when the local Mach number exceeds one.

Since the Mach number influences the shock shape and location some dependence of the interference factor distribution on Mach number would be expected. The data cited previously are either for two-dimensional disturbances or are concerned only with the centerline distribution for protruding cylinders. The data presented in Fig. 2I-2 indicates

that the interference factor-Mach number dependence is a relatively weak one. Insufficient information is available to determine the influence of Mach number on the lateral distribution of the interference factor.

### Flow Regime

A similar effect occurs when the boundary layer goes from laminar to turbulent as when the flow goes from subsonic to supersonic velocity. A turbulent boundary layer with its inherently greater kinetic energy has a more limited boundary layer-protuberance interaction region. Much greater disturbances are required to separate a turbulent boundary layer. One serious problem associated with surface irregularities is the possibility of tripping the flow. Transition may occur within the interaction region or following reattachment, accompanied by a marked increase in heat transfer. Subsequently, downstream, the boundary layer may return to a laminar condition or turbulence may envelop the remaining downstream surface.

### Wall Cooling

An increase in the boundary layer kinetic energy will accompany an increase in heat transfer (wall cooling) as the velocity profile becomes fuller. The extent of the boundary layer-protuberance interaction region will therefore decrease but the pressure gradient and associated interference factor will increase. In investigating separation it was observed in Refs. 2.174 and 2.175 that the extent of the separated region varies as the wall temperature while the pressure gradient is inversely proportional to it. No such quantitative criteria has been determined with respect to the interference factor although a similar trend would be expected.

### Mass Injection

Since no applicable information is available, the influence of mass injection can only be qualitatively indicated. Small rates of surface mass injection are known to significantly reduce the surface skin friction and heat transfer. This reduction in the velocity gradient at the wall should tend to increase the extent of the perturbed region and reduce the magnitude of the interference factor. A trend of this nature is also suggested by the fact that surface mass transfer promotes separation.

### Pressure Gradient

The influence of a pressure gradient on the boundary layer characteristics has been discussed previously in terms of the protuberance generated pressure gradient. The relative effect of the pressure gradient derived from the body contour can be inferred by superimposing the two distributions. That is, a favorable pressure gradient,  $dp/ds < 0$ , will tend to reduce the influence of the protuberance, the converse being true for a positive pressure gradient.

### Interaction Between Protuberances

As a result of the perturbed flow field closely located protuberances will influence one another. The interaction between two protuberances was investigated experimentally in Refs. 2.168 and 2.170 for supersonic flow over a flat plate. Measurements of interference factors indicated that the relative location of the downstream protuberance is critical. When the protuberance is in line (in the flow direction) with the upstream disturbance interference factors were generally reduced. As the distance between the two decreases the interference factors for the downstream protuberances approach one. Conversely, locating the protuberance in the vicinity of the shock generated by the upstream

disturbance resulted in an appreciable rise in the local interference factors. The applicable information is insufficient to do more than note these two trends.

#### INTERFERENCE FACTORS FOR APOLLO

All of the aforementioned parameters influence the interference factors for the Apollo. It is evident that the available information is insufficient to predict even approximately the interference factors for such a complex situation. Recourse must be made to scale model testing.

Experimentally determined interference factors on a 0.09 scale model have been obtained at angles of attack of  $22^\circ$  and  $33^\circ$  for two wind tunnel conditions:

$$A: M_\infty = 10.19, \quad Re_D = 2.56 \times 10^6$$

$$B: M_\infty = 10.14, \quad Re_D = 1.37 \times 10^6$$

The intent here is to assess their applicability for flight conditions. The flight conditions for discussion purposes are selected as those corresponding to the time of peak heating during entry along Trajectory I; the vehicle is assumed to be at 25 deg. angle of attack.

#### Influencing Parameters

It is evident from the previous discussion that if test results are to be applicable for free flight condition the following correspondence must exist between the local flow conditions:

1. the flow is subsonic in both cases or supersonic
2. pure laminar flow exists throughout the interaction region for both cases or fully developed turbulent flow.

If these criteria are satisfied then in extrapolating the results from

a scale test model, as a first approximation, the only parameters that need be considered are: (1) characteristic dimensions of the protuberance, (2) wall cooling, and (3) mass injection.

The interference factor is independent of the protuberance size if the ratio of boundary layer thickness to the characteristic dimensions of the protuberance is fixed. Similarly wall cooling will be inconsequential if the ratio of wall to total temperature is matched. No applicable information is available for extending the interference factors obtained without mass injection to the situation of an ablating surface. Certainly the influence will be significant and further study of the phenomenon is required.

#### Comparison of Flight and Test Conditions

The boundary layer conditions on the Apollo forebody for both the flight and wind tunnel situations are presented in Fig. 2I-3. The flight condition selected is representative of those existing during the period of peak heating. The local Mach number and the ratio of the momentum thickness to protuberance height are shown to be roughly the same for the flight and wind tunnel conditions. Similar correspondence can be expected to exist on the windward side of the afterbody. Wall cooling for the two situations should also be comparable (wall to total temperature ratios are approximately 1/3). Therefore, if the influence of mass injection is neglected the interference factors obtained in the wind tunnel tests are directly applicable to the flight conditions for the majority of the forebody and windward afterbody locations.

Unfortunately, the transition location can be expected to differ considerably, depending on the surface conditions, and mass injection. The only recourse is to establish the limits of this influence by performing scale model testing over a range of Reynolds number. In this manner local interference factors for both laminar; transitional, and turbulent flow can be determined.



A better definition of the influence of wall cooling can also be evaluated by a wider range of test conditions.

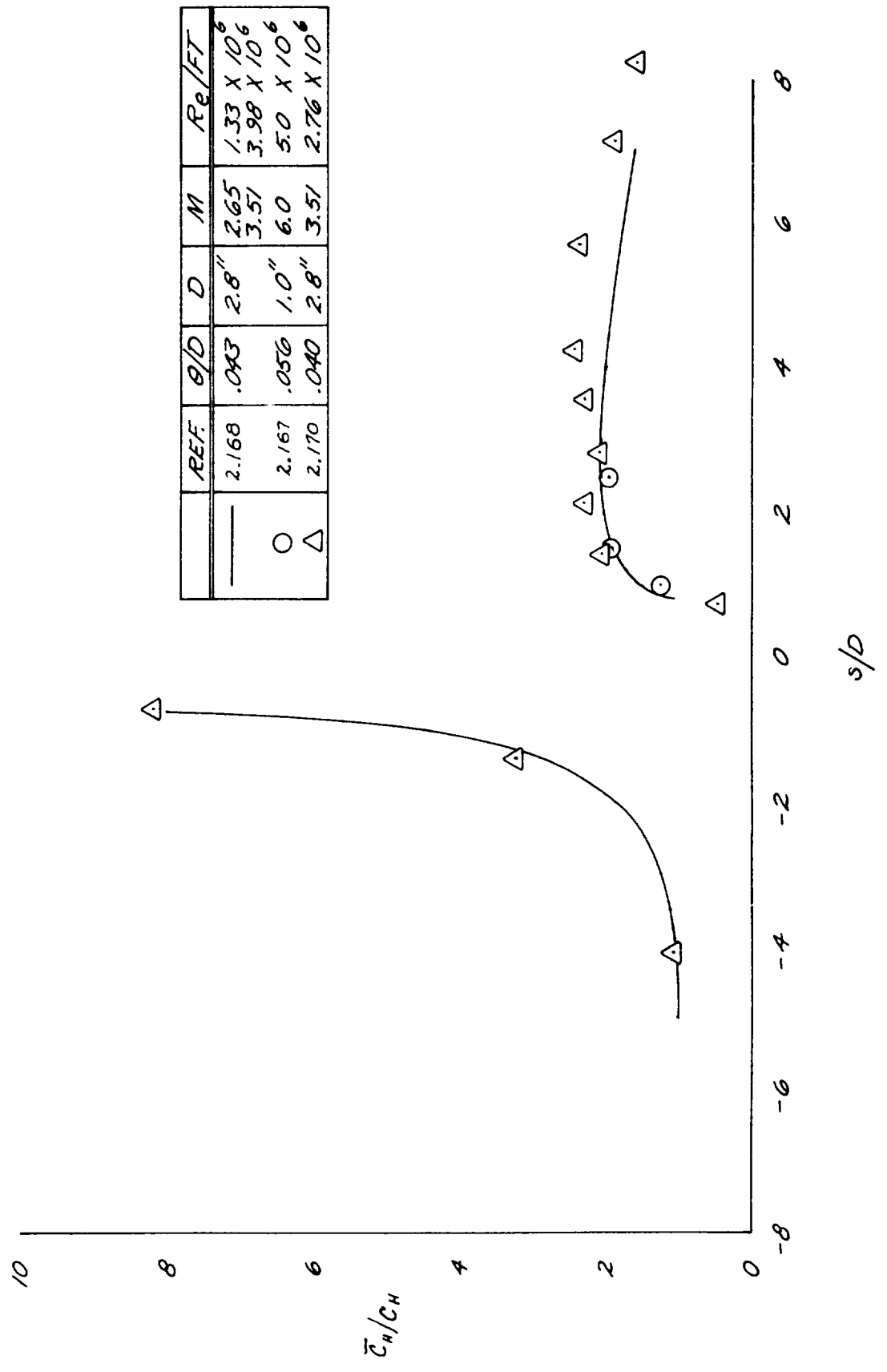
The influence of mass injection may only be assessed from additional experimental information. Ideally, scale model testing under wind tunnel conditions similar to those reported here should be undertaken using a model capable of surface mass transfer.

#### SUMMARY

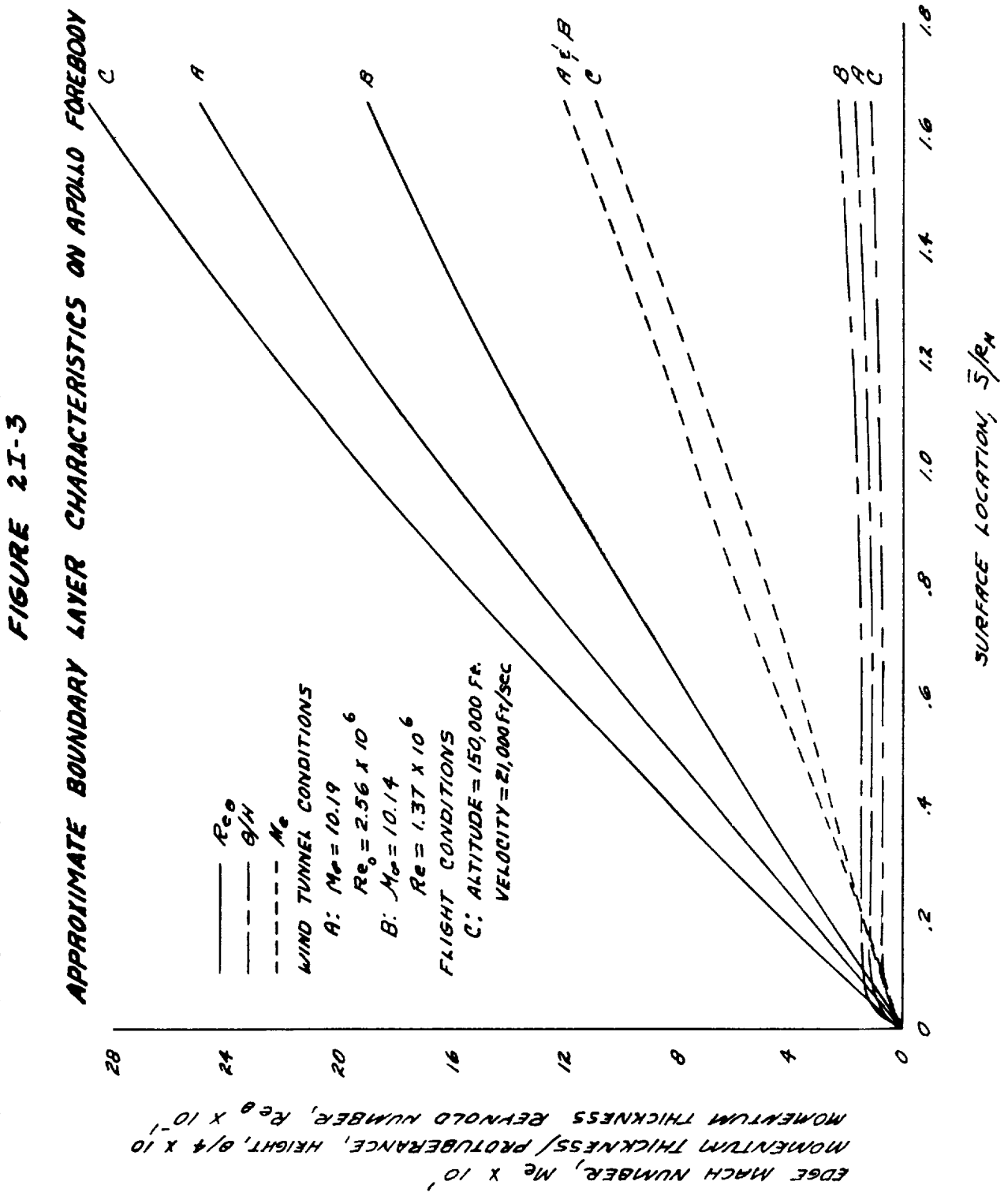
1. Neglecting the mitigating influence of mass injection, the experimentally determined interference factors should prove reasonably applicable for the flight conditions investigated.
2. The critical regions where appreciable error may be incurred in flight are those where transition occurs.
3. Further scale model testing over a wider range of conditions must be performed in order to assess the influence of transition, and wall cooling; it is also necessary from the standpoint of supplying applicable data for a wider range of flight conditions.
4. Experimental and analytical investigations of the influence of mass injection on the interference factors should be undertaken.



FIGURE 2I-2  
 CORRELATION OF CENTER LINE INTERFERENCE FACTORS  
 FOR A PROTRUDING CYLINDER IN FLAT PLATE  
 TURBULENT FLOW



Prepared	NAME	DATE	LOCKHEED MISSILES & SPACE COMPANY A GROUP DIVISION OF LOCKHEED AIRCRAFT CORPORATION	Page	TEMP	TERM
Checked			TITLE	Model		
Approved				Report No.		



Section 3.0  
AERODYNAMIC HEATING MEASUREMENT

In view of the uncertainties associated with theoretical predictions of the aerothermal environment experienced by the reentering vehicle, in-flight measurement of the actual heat transfer appears highly desirable. Ideally, this may be accomplished by mounting calorimeters within the heat shield. In practice, sensor design and data interpretation problems arise. These problems are magnified with an ablative heat shield.

Installation of a heat flux sensor in a heat shield disturbs the homogeneity of both the surface and interior thermal conditions. Aerodynamic heating sensed by the calorimeter differs from that to the surrounding shield, but is strongly dependent on response of the shield. The principle coupling effects are as follows:

- upstream mass injection and surface combustion
- differential recession of the shield and sensor surfaces
- discontinuous surface temperature variation

Thermal isolation of the sensor is generally impracticable and thus internal heat exchange becomes important.

In this section, the measurement of aerodynamic heating in Apollo flight tests is considered. First the various interactions influencing sensor heating are delineated and procedures are developed to account for the important effects. Sensor design is discussed. The performance characteristics of both capacitance or slug and asymptotic calorimeters are then analyzed in detail and simplified models for determining their response are formulated. Finally, data reduction techniques yielding the unperturbed convective heating are developed. Two digital computer codes are provided. One predicts sensor temperature response given the unperturbed environmental conditions while the other solves the inverse problem of determining the environment from a pre-

scribed sensor temperature history. Results from both programs are presented to demonstrate their utility and to indicate the influence of basic uncertainties.

### 3.1 CALORIMETER ENVIRONMENT

Generalized methods are formulated which describe the thermal environment of idealized heat sensors mounted in an ablative heat shield. Radiation, convection, and surface combustion are considered in evaluating the net heat flux. To develop suitable analysis procedures, the various interactions are assumed uncoupled and boundary conditions are somewhat simplified. The error incurred in this assumption is examined and found to be relatively small. Emphasis is placed on accounting for the influence of streamwise variations in surface temperature, mass injection, and surface reactivity on the convective heating. An arbitrary wall enthalpy distribution and a discontinuity in mass transfer are treated by analytically extending the applicable information in the literature. Analysis of sensor surface combustion is accomplished by considering the limiting surface reaction rate situation. For the physical and thermal calorimeter characteristics of interest, these methods yield relatively simple expressions for evaluating the heat flux.

#### 3.1.1 Phenomenological Review

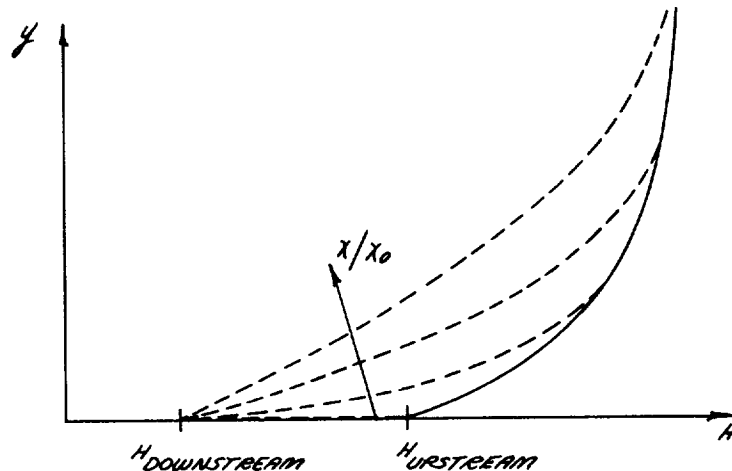
Except at early times the net heat transfer to the calorimeter will bear little resemblance to the unaffected heat flux. Reradiation and the distortion of the convection coefficient created by the disturbances in the surface conditions will be significant in altering the heat flux. Evaluation of the reradiation is straight forward since the data pertinent to its evaluation (sensor surface temperature and surface emissivity) will be known. However, determination of the convective heating requires that the complex influence of streamwise variations in surface conditions on the boundary layer characteristics be accounted for.

The surface boundary conditions associated with a slug calorimeter mounted in an ablative heat shield are typified in Fig.3-1. The calorimeter (denoting the entire assembly) is assumed to consist of a circular sensor surrounded

by concentric guard rings. (This model and the associated surface boundary conditions are easily modified so as to be applicable to a wide variety of asymptotic and slug type calorimeters.) The surface conditions are characterized by 1) two separate discontinuous changes in the wall temperature followed by an isothermal sensing element, 2) a step change in surface blowing, 3) a discontinuity in surface reactivity, and 4) protrusion of the sensor resulting in a pressure hump. It is noteworthy that the slug calorimeter presents a situation where finite values of the downstream surface mass addition and reactivity must be considered since the calorimeter may react with boundary layer gases. The mass injection and surface temperature discontinuity effects are relatively familiar. Streamwise variations in wall temperature are known to have an appreciable influence on convective heating, the severity of which is dependent on the magnitude and gradient of the temperature change. An abrupt decrease in the wall temperature will substantially increase the convection coefficient immediately downstream, relative to the value associated with the new surface temperature. On the other hand, a discontinuity in mass injection may be expected to exhibit a more gradual effect on the heating and persist further downstream. Over the relatively short length of the sensor the inference is that perturbations in the convective heating distribution associated with the non-isothermal wall must be carefully considered while the influence of a discontinuity in mass injection is of lesser importance. The surface reactivity discontinuity is critical in that it affects the rate of oxidation of the sensor surface and thus must be accounted for in evaluating surface combustion and calorimeter protrusion.

It is desirable to obtain a qualitative understanding of the way abrupt changes in the boundary conditions influence the heat transfer. This can be best achieved by examining the history of the boundary layer and considering the effect of events upstream on the total enthalpy, velocity and concentration profiles. Consider the surface distribution of enthalpy, elemental mass concentration and blowing. Upstream, where the surface conditions are constant, (or similar in the case of mass injection) the three profiles have similar shapes with their respective slopes at the wall being proportional to the

heat transfer, skin friction, and diffusional flux of the elements. If the surface conditions decrease in the flow direction the profiles will be stretched with an attendant rise in their surface gradient. Consider, for example, a step change in surface enthalpy. The downstream decay of the enthalpy profile is indicated in the following sketch:



Initially the enthalpy gradient and hence the heat transfer are infinite\*, decaying exponentially to an undisturbed value corresponding to the new surface condition far downstream. A similar phenomenon occurs with the cessation of surface injection; in this situation there is a downstream increase in the convective heating associated with the redistribution of the momentum and concentration gradients.

---

\* The occurrence of an infinite heating rate is analogous to the situation existing at the leading edge of an isothermal flat plate. Since the temperature gradient is infinite immediately downstream of the discontinuity boundary layer theory is invalid. Fortunately, it is known that this region may be neglected and boundary layer analyses become applicable a short distance downstream. In any case, the condition of a step change in temperature is physically unrealistic but does provide an applicable model when dealing with the abrupt changes.



It is evident from these considerations that streamwise variations in the boundary conditions have a profound influence on the slope of the profiles and consequently on the heat transfer, skin friction, and surface combustion. Evaluation of the pertinent fluxes, therefore, becomes a matter of solving the boundary layer equations in the streamwise direction. Conditions of this type preclude the use of the usual similarity transformations which yield easily solvable ordinary differential equations and recourse must be made to approximate analyses typified by integral solutions or to exact solutions using finite difference techniques. The integral technique is selected here as it readily yields reasonably reliable results as compared to the expensive and time consuming methods associated with the exact solution.

In order to show how the various interaction phenomena are accounted for it is necessary to examine the pertinent energy equations. Following the procedure outlined in Ref. 3.1 an energy balance at the surface of a charring ablator yields

$$q_w = k \frac{\partial T}{\partial y} + \rho D \sum_i H_i \frac{\partial K_i}{\partial y} + (\rho w)_p H_p + (\rho w)_c H_c - (\rho w)_w \sum_i K_i H_i - q_r + q_{sw} \quad (3.1)$$

where all terms are evaluated at the wall condition and the subscripts p and c refer, respectively, to the gaseous pyrolysis products and the solid char. The summations are carried out over all species in the gas at the wall. This relation is equally valid when applied to either the upstream ablator or to a downstream calorimeter (in which case  $(\rho w)_p$  is zero and  $(\rho w)_w = (\rho w)_c$  if carbon is present at the surface). It is now desirable to express the convective portion of the heat flux in terms of the conventional heat transfer coefficient defined by

$$h = \left( \frac{k}{c_p} \frac{\partial H_e}{\partial y} \right)_w / (H_e - H_w) \quad (3.2)$$

For the upstream ablator, it is now assumed that

- 1)  $Le = Pr = 1$
- 2) Similarity exists between elemental concentration and total enthalpy,

$$\frac{\partial \tilde{K}_i / \partial y}{\partial H_e / \partial y} = \frac{\tilde{K}_{ie} - \tilde{K}_{iw}}{H_e - H_w} \quad (3.3)$$

Then it is possible to rewrite the surface energy balance in the following convenient form,

$$q_w = (H_e - H_{2iw}) - (\rho w)_c q_c - q_r + q_{sw} \quad (3.4)$$

The importance of this relation is that the convective heating is determined by the air enthalpy potential independent of wall species concentration. In order to achieve a tractable boundary layer analysis it is assumed that Eq. (3.4) is also applicable for the downstream region. The validity of this assumption is questionable, since physically it would be expected that heat transfer would be a strong function of the wall species concentration. (Following the discontinuity in mass injection, the concentration profiles of such species as  $O_2$ ,  $N_2$ , and CO will undergo a streamwise redistribution as the pyrolysis gases diffuse away from the wall.) Eq. (3.4) is true downstream if 1) the injected species (from both pyrolysis and surface oxidation) can be treated as being thermally identical to air or 2) the upstream pyrolysis products are no longer present (a condition satisfied far downstream).

Basic to the analysis is the assumption that each interaction may be treated independently.\* For the calorimeter surface, Eq. (3.4) may then be written as

$$q_{wd} = h_0 \left( \frac{h}{h_0} \right)_D \left[ H_0 - H_w - f + B_D' q_c \right] - q_r + q_{sw} \quad (3.5)$$

---

\* The validity of this approximation is inferred from the coupled investigation of mass injection and non-isothermal wall presented in Section 3.1.2.2.

where

- H = enthalpy based on air
- $h/h_0$  = downstream reduction in the heat transfer coefficients as a result of mass injection (represents a perturbed value of the transpiration effect described in Appendix 2H)
- f = correction to the enthalpy potential accounting for the non-isothermal wall
- $B'_D$  = mass injection parameter accounting for a discontinuous change in surface reactivity

The relative effects of the different phenomena may be inferred from the convective heating curves for a slug type calorimeter depicted in Fig. 3-2. The unperturbed environment and the pertinent thermal and physical characteristics of the calorimeter are representative of Apollo reentry. These parameters and the methods necessary to generate the heating rates are delineated subsequently. The upper curve in Fig. 3-2 represents the convective heat which would be transferred to the calorimeter in the absence of any interactions and for a wall temperature identical to the ablator's. It is seen that mass injection drastically reduces the incident flux while wall temperature and surface reactivity exhibit a less significant influence. The effect of surface protrusion is not considered. Subsequently it will be shown that the transpiration effect has decayed very little from its upstream value. Thus the implication of Fig. 3-2 is that the calorimeter and surrounding heat shield experience very nearly the same convective heating.

A review of the effect of protuberances on the boundary layer characteristics and associated local heating was presented in Appendix 2I. It may be concluded from that review that 1) insufficient information is available to predict the local interference factor (ratio of disturbed to undisturbed convection coefficient), 2) relatively small surface irregularities may significantly alter the heating and 3) the simplest recourse is to experimentally determine the interference factors. The scope of this study does not warrant additional work in this area and therefore protuberance-boundary layer interactions have been neglected. The methods and programs proposed here may be

easily modified to account for the protruding sensor once the pertinent information becomes available.

### 3.1.2 Prediction Techniques

The influence of streamwise variations in surface conditions on the downstream heat flux is considered in detail. The objective is to develop realistic methods for predicting the heat transfer to a surface downstream of an ablative heat shield. To this end, relations have been developed for predicting the net heat flux to a non-isothermal surface with a step change in mass injection and wall reactivity. The derivations of these methods are reviewed in this section.

#### 3.1.2.1 State of the Art

Pertinent information available in the literature is reviewed here. The influence of surface variations in blowing and wall temperature on the convective heating is considered. A lack of applicable information concerning the effect of discontinuities in surface reactivity precludes its discussion.

#### Mass Injection Discontinuity

A considerable amount of information is available on the transpiration effect for the region of continuous injection (see Appendix 2H). Investigations dealing with regions downstream of a transpiring surface having zero or markedly different blowing rates are limited both in number and by their approximations (Ref. 3.2 - 3.5). Generally the approach is to obtain an integral solution of the laminar boundary layer equations for the zero pressure gradient compressible flat plate case in which the boundary layer profiles are approximated by polynomials beginning with known profiles at the discontinuity point. The results from these works are compared in Fig. 3-3. Since the majority of these studies solved only the momentum equation they are compared in terms of the skin friction reduction (a reasonable approximation is to equate the reduction in the convective coefficient with that of the skin friction). The more rigorous of these analyses are the finite difference solution of Ref. 3-5 and the modified Karman-Pohlhausen integral technique of Ref. 3.2. The analysis of Ref. 3.3 is selected for the present study since it is 1) in good

agreement with the more exact analyses), 2) easily applied to any blowing rate, 3) applicable for turbulent flow and 4) simply extended to the case of finite downstream injection. Further comparison of the exact solution and the results of Ref. 3.3 is afforded by Fig. 3-4 where the reduction in the convective coefficient is presented. The existence of the following restrictions in these results must be recognized and accounted for: 1) isothermal wall, 2) two-dimensional flow, 3) zero downstream injection, and 4) air injection.

#### Wall Temperature Discontinuity

A large body of information is available concerning the influence of a non-isothermal wall on the laminar and turbulent convective heating. In general these analyses have been restricted to zero pressure gradient, incompressible flow. The results of the most pertinent of these are summarized here.

Ref. 3.6 presents methods for both laminar and turbulent flows and justifies their use on the basis of comparison with an exact solution for the laminar case and comparison with experimental data for the turbulent case. Experimental data corroborating the turbulent theory for a step change in temperature may be found in Ref. 3.7. Of particular interest is the agreement between predicted and experimental results at locations just downstream of the jump ( $x/x_0 \sim 1.05$ ). The inference is that boundary layer theory is valid in these regions where the heating rate is tending to infinity.

The perturbation in the heat flux as a result of non-isothermal wall is given by

$$\frac{q(x)}{q_{isoth}(x)} = \frac{\int_0^x \frac{h(x, \xi)}{h(x, 0)} \frac{dT_w}{d\xi} d\xi + \sum_i \frac{h(x, \xi_i)}{h(x, 0)} [T_w(\xi_i^+) - T_w(\xi_i^-)]}{T_w(x) - T_f} \quad (3.6)$$

In this equation  $h(x, \xi)$  is the convective coefficient existing at the location  $x$ , where the surface is adiabatic upstream of position  $\xi$  and heated to a constant temperature downstream. The integral portion is evaluated with-

out taking into consideration any discontinuities in the wall temperature. Such discontinuities, denoted by  $T_w(\xi^+)$  downstream and  $T_w(\xi^-)$  upstream, are accounted for by the summation expression with each discontinuity giving a separate contribution to the local heat flux. The following expression for the reduction in the local laminar heat transfer coefficient when the adiabatic starting length is  $L$  was derived in Ref. 3.8 and 3.9 using an approximate integral techniques:

$$\frac{h(x, L)}{h(x, 0)} = \left[ 1 - \left( \frac{L}{x} \right)^{3/4} \right]^{-1/3} \quad (3.7)$$

For the turbulent case, Reynolds, et al (Ref. 3.7) assume one seventh power velocity and temperature distributions to obtain a solution of the integral energy equation. The result is

$$\frac{h(x, L)}{h(x, 0)} = \left[ 1 - \left( \frac{L}{x} \right)^{9/10} \right]^{-1/9} \quad (3.8)$$

This solution is very similar to that obtained by Rubesin (Ref. 3.10). A comparison of Eqs.(3.7)and(3.8)shows the non-isothermal wall effect to be more pronounced for the laminar case.

It is sometimes more convenient to represent the non-isothermal effect as a perturbation of the temperature or enthalpy potential. This is readily accomplished by rewriting Eq.(3.6)in the form

$$q(x) = h(x, 0) [T_r - T_u - f] \quad (3.9)$$

where

$$f = \sum_{i=1}^n \frac{h(x, \xi_i)}{h(x, 0)} [T_w(\xi_i^+) - T_w(\xi_i^-)] + \int_0^x \frac{h(x, \xi)}{h(x, 0)} \frac{dT_w}{d\xi} d\xi$$

For example, consider an aerodynamically heated flat plate with a single surface temperature discontinuity ( $T_{w_u} \rightarrow T_{w_D}$  at  $x = L$ ). Then the perturbation in the temperature potential is simply

$$f = (T_{wD} - T_{wU}) \frac{h(x, L)}{h(x, 0)}$$

In applying these relations in the present study it is necessary to account for 1) mass injection, 2) compressibility, and 3) pressure gradient.

### 3.1.2.2 Technique Development

The previous discussion reviewed the currently available means of accounting for the influence of streamwise variations in surface blowing and wall temperature on the convective heating. The limitations of these methods were delineated. Extension of these methods for application in the situation of interest is considered here and the effects of compressibility and pressure gradient are accounted for by repeating the aforementioned analyses using the transformed, hypersonic boundary layer equations. Relations for predicting the effect of mass transfer cooling on the downstream heat transfer are developed which account for downstream injection. The degree of coupling between the discontinuous mass injection and non-isothermal wall effects is determined in assessment of the error incurred in neglecting interactions. The influence of a discontinuous change in surface reactivity on surface combustion rates is examined and approximate means to account for this effect are developed. The methods are applicable for both laminar and turbulent flow.

The analysis begins by specifying the boundary layer equations and appropriate boundary conditions. Solutions are then obtained by extending analyses and results in the literature. Finally, these solutions are applied for the sensor configurations of interest and relatively simple, closed-form relations for evaluation of sensor heat flux are described.

#### Governing Relations

The hypersonic boundary layer equations and their transformation to the incompressible form are well known. (The notation of Chung (Refs.(3.11) and (3.12) is used here.) They are

$$\text{Continuity} \quad \partial u / \partial s + \partial v / \partial t = 0 \quad (3.10)$$

$$\text{Momentum} \quad U \partial u / \partial s + v \partial u / \partial t = \nu_{e,0} \partial^2 u / \partial t^2 \quad (3.11)$$

$$\text{Energy} \quad U \partial I / \partial s + v \partial I / \partial t = \nu_{e,0} \partial^2 I / \partial t^2 \quad (3.12)$$

$$\begin{array}{l} \text{Continuity of} \\ \text{elemental species} \end{array} \quad U \partial \tilde{\kappa}_i / \partial s + v \partial \tilde{\kappa}_i / \partial t = \nu_{e,0} \partial^2 \tilde{\kappa}_i / \partial t^2 \quad (3.13)$$

where

$$s = \int_0^x c_0 u_e r^{2\epsilon} dx \quad (3.14)$$

$$t = u_e r^\epsilon \int_0^y \frac{\rho}{\rho_{e,0}} dy$$

$$U = u / u_e$$

$$I = H_t / H_{t,e}$$

$$c_0 = \rho \mu / \rho_{e,0} \mu_{e,0}$$

In obtaining these equations the following important assumptions were made,

- 1)  $Le = Pr = 1$
- 2) The boundary layer is highly cooled (pressure gradient term in momentum equations can be neglected.
- 3)  $\rho \mu$  independent of  $y$

These relations are equally valid for both laminar and turbulent flow if it is understood that for a turbulent boundary layer the equations are written in terms of the mean flow properties and that the turbulent transport coefficients (Reynolds terms) are included in the Prandtl and Lewis number (see Ref. 3.13).

For convenience in this investigation it will be assumed the turbulent boundary



layer equations for zero pressure gradient flow are applicable for blunt bodies.

There is considerable justification for this since it is well known that flat plate solutions adequately depict the boundary layer characteristics over blunt bodies providing local boundary layer edge properties are used (see Ref. 3.13). It will be seen that this approximation makes the present analysis considerably more tractable. Accordingly, for turbulent flow, Eq.(3.14) may be re-written as

$$\begin{aligned}
 s &= C u_e x \\
 t &= u_e \int_0^y \frac{\rho}{\rho_e} dy \\
 C_0 &= \rho \mu / \rho_e \mu_e = C
 \end{aligned}
 \tag{3.15}$$

The boundary conditions to be studied are:

$$\begin{aligned}
 \text{at } t &= 0 \\
 U &= 0 \\
 V &= V_{W_u} = V(s) \\
 I &= I_{W_u} = \text{constant} \\
 \tilde{K}_i &= \tilde{K}_{i_{W_u}} = \text{constant} \\
 \left. \begin{aligned}
 V &= V_{W_D} = V(s) \\
 I &= I_{W_D} = I(s) \\
 \tilde{K}_i &= \tilde{K}_{i_{W_D}} = \tilde{K}_i(s)
 \end{aligned} \right\} \begin{array}{l} \text{for } s \leq s_0 \\ \text{for } s > s_0 \end{array}
 \end{aligned}
 \tag{3.16}$$

$$\begin{aligned}
 \text{at } t &= \infty \\
 U &= I = 1 \\
 \tilde{K}_i &= \tilde{K}_{i_e} \quad (\tilde{K}_{o_e} = 0.233, \tilde{K}_{N_e} = 0.767)
 \end{aligned}
 \tag{3.17}$$

These discontinuous boundary conditions preclude an exact solution of the boundary layer equations except possibly through a laborious finite difference method. Approximate solutions may be obtained, however, if suitable assumptions, particularly with respect to the boundary conditions, are made. These solutions and associated approximations are presented in the following sections.

### Mass Injection Discontinuity

The influence of a step change in mass injection on the downstream heat transfer is analyzed using the method of Ref. 3.3. Only the case of air injection is considered. The procedure involves solving the momentum integral equation by approximating the growth of the integral thickness downstream of the discontinuity with a quadratic in terms of the reciprocal of the distance. The constants in the quadratic are determined by specifying the surface condition and integral thickness (skin friction and momentum thickness) at the point of discontinuity and at an infinite distance downstream. The assumptions of 1) a constant wall temperature and 2) similarity mass injection (mass injection rate is proportional to the non-blowing heat transfer coefficient) are made. The final solution yields the downstream heat transfer or skin friction once the mass injection rates and their influence on the heat transfer for the situation of continuous, similarity injection are known.

#### Analysis:

Under the assumption of a constant wall enthalpy the momentum and energy equations and their respective boundary conditions are identical and Reynolds analogy is valid,

$$\frac{C_f}{2} = St \quad (3.18)$$

Therefore, it is only necessary to deal with the momentum and continuity equations. Integrating the momentum equation across the boundary layer yields the Von Karman integral equation,

$$\frac{d\theta}{ds} = \tau_w + \frac{V_w}{V_{e,0}} \quad (3.19)$$

where

transformed shear stress

$$\tau_w \equiv \left( \partial u / \partial t \right)_w \quad (3.20)$$

momentum thickness

$$\theta \equiv \frac{1}{V_{e,0}} \int_0^{\infty} u(1-u) dt$$

Physically,

$$\tau_w = \frac{P_e P_{e,0}}{P_w \mu_w r^\epsilon} \frac{C_f}{2} \quad (3.21)$$

$$\frac{V_w}{\nu_{e,0}} = \frac{P_w \mu_w}{\mu_{e,0} C_o U_e r^\epsilon}$$

The integral equation assumes the following forms for the various regions of interest:

For  $s < s_0$

$$d\theta_U/ds = \tau_{wU} + \frac{V_{wU}}{\nu_{e,0}} \quad (3.22)$$

For  $s > s_0$

$$d\theta_D/ds = \tau_{wD} + \frac{V_{wD}}{\nu_{e,0}} \quad (3.23)$$

for  $V_w = 0$

$$d\theta_0/ds = \tau_{w0} \quad (3.24)$$

The integral thickness is now expressed by,

$$\theta_D/\theta_0 = a + b \frac{s_0}{s} + c \left( \frac{s_0}{s} \right)^2 \quad (3.25)$$

where the boundary conditions are specified as follows:

1. at the point of discontinuity in mass transfer,  $s_0/s = 1$ , the momentum thickness and skin friction are continuous:

$$\frac{\tau_{wU}}{\tau_{wD}} = \frac{\theta_U}{\theta_D} = 1 \quad (3.26)$$

2. far downstream,  $s_0/s = 0$ , the influence of the upstream blowing can be neglected:

$$\tau_{wD} = \bar{\tau}_w, \quad \theta_D = \bar{\theta} \quad (3.27)$$

(The boundary layer behaves as if the downstream similar injection existed from the stagnation point.) It should be noted that the assumption of continuous wall shear at the point of discontinuity is questionable; the finite difference solution of Ref. 3.5 showed a distinct but small jump in skin friction. This relatively minor jump in the wall shear suggests that Eq. (3.26) should be reasonably accurate at least for moderate blowing rates.

Substituting Eqs. (3.24) and (3.25) into Eq. (3.23) yields the following expressions for the downstream skin friction:

$$\left(\frac{\tau_w}{\tau_{w_0}} + B\right)_D = a + b \frac{s_0}{s} (1 - \sigma) + c \left(\frac{s_0}{s}\right)^2 (1 - 2\sigma) \quad (3.28)$$

where

blowing parameter

$$B = \frac{V_w / \nu_{e,0}}{\tau_{w_0}} \quad (3.29)$$

flow parameter

$$\sigma = \frac{\theta_0 / s}{\tau_{w_0}} \quad (3.30)$$

The boundary conditions now can be written as,

at  $s_0/s = 1$

$$\left(\theta/\theta_0\right)_u = a + b + c \quad (3.31)$$

$$\left(\tau_w/\tau_{w_0}\right)_u + B_D = a + b (1 - \sigma) + c (1 - 2\sigma) \quad (3.32)$$

at  $s_0/s = 0$

$$\left(\frac{\bar{\tau}_w}{\tau_{w_0}} + B\right)_D = \left(\frac{\bar{\theta}}{\theta_0}\right)_D = a \quad (3.33)$$

Eq. (3.33) is satisfied and Eq. (3.31) can be put into a more usable form under the assumption of similar injection. With similar injection

$$\frac{V_w}{D_{e,0}} \propto \tau_{w,0} \quad (3.34)$$

and the following approximation is reasonable:

$$\frac{\tau_w}{\tau_{w,0}} = f\left(\frac{V_w/D_{e,0}}{\tau_{w,0}}\right) \text{ only} \quad (3.35)$$

Then from Eqs. (3.19) and (3.24),

$$\left(\frac{\bar{\theta}}{\theta_0}\right) = \left(\frac{\bar{\tau}_w}{\tau_{w,0}} + B\right) \quad (3.36)$$

Therefore Eq. (3.31) can be rewritten as,

$$\left(\frac{\bar{\tau}_w}{\tau_{w,0}} + B\right)_u = a + b + c \quad (3.37)$$

The constants a, b, and c, are now obtained from Eqs. (3.32), (3.33), and (3.37), and then substituted into Eq. (3.28) to yield the final expression for the downstream skin friction,

$$\begin{aligned} \left(\tau_w/\tau_{w,0}\right)_D = & \left(\bar{\tau}_w/\tau_{w,0}\right)_D + \frac{S_e}{S} (1-\sigma) \left\{ 2 \left[ \left(\frac{\tau_w}{\tau_{w,0}}\right)_u - \left(\frac{\bar{\tau}_w}{\tau_{w,0}}\right)_D \right] \right. \\ & \left. + \left(B_u + B_D\right) \left(2 - \frac{1}{\sigma}\right) \right\} - \left(\frac{S_e}{S}\right)^2 (1-2\sigma) \left\{ \left(\frac{\tau_w}{\tau_{w,0}}\right)_u - \left(\frac{\bar{\tau}_w}{\tau_{w,0}}\right)_D \right. \\ & \left. + \left(B_u - B_D\right) \left(1 - \frac{1}{\sigma}\right) \right\} \end{aligned} \quad (3.38)$$

Reynolds analogy yields

$$\frac{\tau_w}{\tau_{w,0}} = \frac{h}{h_0} \quad (3.39)$$

and from Eqs. (3.21) and (3.29) the blowing parameter can be written,

$$B = \frac{\dot{m}}{h_0} \quad (3.40)$$

The flow parameter is easily determined, since

$$\tau_{w,0} \propto S^{-\alpha} \quad (3.41)$$

where

$$\begin{aligned}\alpha_{Lam} &= 1/2 \\ \alpha_{Turb} &= 1/5\end{aligned}\tag{3.42}$$

Eq. (3.24) yields,

$$\begin{aligned}\sigma_{Lam} &= 2 \\ \sigma_{Turb} &= 5/4\end{aligned}\tag{3.43}$$

Finally, Eq. (3.38) may be written in the form

$$\begin{aligned}\left(\frac{h}{h_0}\right)_D &= \left(\frac{\bar{h}}{h_0}\right)_D + \frac{S_0}{S} (1-\sigma) \left\{ 2 \left[ \left(\frac{h}{h_0}\right)_U - \left(\frac{\bar{h}}{h_0}\right)_D \right] + \left[ \left(\frac{\dot{m}}{h_0}\right)_U - \left(\frac{\dot{m}}{h_0}\right)_D \right] \left( 2 - \frac{1}{\sigma} \right) \right\} \\ &- \left(\frac{S_0}{S}\right)^2 (1-\sigma)^2 \left\{ \left(\frac{h}{h_0}\right)_U - \left(\frac{\bar{h}}{h_0}\right)_D - \left[ \left(\frac{\dot{m}}{h_0}\right)_U - \left(\frac{\dot{m}}{h_0}\right)_D \right] \left( 1 - \frac{1}{\sigma} \right) \right\}\end{aligned}\tag{3.44}$$

Eq. (3.44) relates local downstream heat transfer to the continuous similar blowing solutions upstream and far downstream. The heat transfer reduction for similar mass injection into the laminar and turbulent boundary layer is discussed in Appendix 2H. In applying these results to the present problem it is assumed that the foreign gas correction is still valid. The heat transfer reduction for similar injection is presented in Fig. 2-66 as a function of the modified injection parameter.

Typical laminar and turbulent convection coefficient distributions downstream of a transpiring surface are presented in Fig. 3-5. In this figure the rate of upstream injection corresponds to quasi-steady ablation of the assumed Apollo heat shield material. The finite downstream mass transfer rate corresponds to diffusion controlled carbon oxidation. It is seen that the local effect of mass injection may differ substantially from the upstream effect, depending on distance from the discontinuity. For locations close to the discontinuity the changes are small. The physical situation of interest in this study illustrates this point. For example, consider a graphite sensor of radius 0.27" located at the Apollo geometric centerline. The transformed surface distance ratio is found to be

$$s_s/s_o = \begin{cases} \text{laminar: } 1.015 \\ \text{turbulent: } 1.0044 \end{cases}$$

Evaluation of the transpiration effect yields the following table:

	h/ho	
	<u>laminar</u>	<u>turbulent</u>
Upstream	0.693	0.730
Downstream, $B'_D = 0.175$	0.6952	0.7342
Downstream, $B'_D = 0$	0.6957	0.7364

Evidently, for distance ratios very close to one, the effect of downstream injection can be neglected, and in fact very little error will be incurred if the upstream heat transfer reduction is used for the sensor.

#### Wall Temperature Discontinuity

In the following section an approximate solution of the transformed energy equation for laminar flow is used to extend the non-isothermal relations (Eqs. 3.7 - 3.9) to two-dimensional or axisymmetric bodies, with an arbitrary wall enthalpy distribution, accounting for upstream mass injection and compressible flow. The analysis is strictly applicable only for the laminar boundary layer. A simple analogy using Eqs. (3.7) and (3.8) will be used to obtain a turbulent expression. The effect of the injectant being different from air will be neglected in this analysis, an assumption commensurate with basing the enthalpy potential on the free stream species.

Analysis:

Consider the transformed energy equation,

$$U \frac{\partial I}{\partial s} + V \frac{\partial I}{\partial t} = \nu e_o \frac{\partial^2 I}{\partial t^2} \quad (3.45)$$

with the following boundary conditions:

$$\begin{aligned} \text{for } s < s_o, \quad t = 0 \\ I = I_{ww} = \text{CONSTANT} \\ V = V_{wu} \end{aligned} \quad (3.46)$$

$$\begin{aligned} \text{for } s > s_0, \quad t = 0 \\ I = I_{wD} = \text{CONSTANT} \\ V = 0 \end{aligned} \quad (3.47)$$

For the situation of an unheated upstream section:

$$\text{for } s < s_0 \quad : \quad I = 1$$

$$\begin{aligned} \text{for } s > s_0 \\ t = 0 : I = I_w = \text{CONSTANT} \end{aligned} \quad (3.48)$$

Now suppose a solution of the form

$$\phi(s, t, s_0) = \frac{I - I_w}{1 - I_w} \quad (3.49)$$

can be obtained, where

$$\begin{aligned} \phi(s, 0, s_0) &= 0 \\ \phi(s < s_0, t, s_0) &= 1 \\ \phi(s, \infty, s_0) &= 1 \end{aligned} \quad (3.50)$$

Then, because the energy equation is linear in total enthalpy, various solutions may be superimposed to satisfy desired boundary conditions. Therefore, once the solution for a single step change is obtained, it is relatively easy to extend it to the general case.

For a step change from 1 to  $I_{wU}$  at the stagnation point and  $I_{wU}$  to  $I_{wD}$  at  $s_0$  the appropriate solution which satisfies both the boundary conditions (Eqs. 3.46 and 3.47) and the energy equation is of the form,

$$I_D = I_{wD} + (1 - I_{wU})\phi(s, t, 0) + (I_{wU} - I_{wD})\phi(s, t, s_0) \quad (3.51)$$

For the upstream surface,  $\phi(s, t, 0)$  is found from the Crocco relation. Since the wall enthalpy is constant, the momentum and energy equations and their respective boundary conditions are identical, therefore,

$$\phi(s, t, 0) = U \quad (3.52)$$



The downstream enthalpy profile is found from the solution of the homogeneous energy equation,

$$u \frac{\partial \phi}{\partial s} + v \frac{\partial \phi}{\partial t} = \nu_{e,0} \frac{\partial^2 \phi}{\partial t^2} \quad (3.53)$$

The procedure is identical to that given in Ref. 3.4 for a surface temperature discontinuity in zero pressure gradient flow. The boundary layer velocity profile is approximated by a linear profile having the correct slope at the surface,  $\tau_{w,D}$ , where

$$\tau_{w,D} = \left( \frac{\tau_w}{\tau_{w,0}} \right)_D \tau_{w,0} \quad (3.54)$$

and  $(\tau_w/\tau_{w,0})_D$  is given by Eq. (3.38). The enthalpy profile is assumed to be a function of a single parameter  $\zeta$ ,

$$\phi = \phi(\zeta) \quad (3.55)$$

With these substitutions the energy equation is reduced to a form readily solved by separation of variables. The final solution as obtained in Ref. 3.4 is given by

$$\phi = \frac{1}{3^{1/3} \Gamma(4/3)} \int_0^\zeta e^{-\zeta^{3/3}} d\zeta \quad (3.56)$$

where

$$\zeta = \left( \tau_{w,D}^{1/2} t \left( 32 \nu_{e,0} \int_{s_0}^s \tau_{w,D}^{1/2} ds \right)^{-1/3} \right)$$

Since only air is being considered the heat transfer is proportional to the enthalpy gradient at the wall, and Eq. (3.51) yields the following expression for the influence of a wall enthalpy discontinuity on the downstream heat transfer:

$$\frac{q}{q_{isoch}} = \left( \frac{(1-I_{w,u}) \frac{d\phi(s,t,0)}{dt} + (I_{w,u} - I_{w,p}) \frac{d\phi(s,t,s_0)}{dt}}{(1-I_{w,D}) \frac{d\phi(s,t,0)}{dt}} \right)_{t=0} \quad (3.57)$$

or substituting Eqs. (3.52) and (3.55) gives

$$\frac{q}{h} / \frac{q}{h} \Big|_{s=0} = \frac{(1 - I_{wD}) + \tau_{wD}^{-1} (I_{wU} - I_{wD}) \left( \frac{d\theta}{ds} \frac{ds}{dt} \right) \Big|_{t=0}}{1 - I_{wD}} \quad (3.58)$$

where

$$q_{isoth} = h \left\{ H_{te} (1 - I_{wD}) \right\} \quad (3.59)$$

Differentiating Eq. (3.56) and substituting yields

$$\frac{q}{h} / \frac{q}{h} \Big|_{s=0} = \frac{1 - I_{wU} + (I_{wU} - I_{wD}) \left[ \left( \frac{\tau_{wD}}{\tau_{w0}} \right)^{1/2} \Gamma \left( \frac{4}{3} \right) \right]^{-1} \left[ 9 \nu_{e0} \int_{s_0}^s \tau_{wD}^{1/2} ds \right]^{-1/3}}{1 - I_{wD}} \quad (3.60)$$

This equation is analogous to Eq. (3.6) where the right hand term in the numerator is identifiable as the heat transfer coefficient ratio expressed in Eqs. (3.7) and (3.8):

$$\frac{h(s, L)}{h(s, 0)} = \left[ \left( \frac{\tau_{wD}}{\tau_{w0}} \right)^{1/2} \Gamma \left( \frac{4}{3} \right) \right]^{-1} \left[ 9 \nu_{e0} \int_{s_0}^s \tau_{wD}^{1/2} ds \right]^{-1/3} \quad (3.61)$$

They become mathematically identical for the case of laminar flow with zero injection. Since the transformed boundary layer equations are identical to those for incompressible, flat plate flow the unperturbed shear stress may be obtained from the Blasius solution:

$$\tau_{w0} = 0.332 \left( 2 \nu_{e0} s \right)^{-1/2} \quad (3.62)$$

Substitution of Eqs. (3.54) and (3.62) into (3.61) yields

$$\frac{h(s, L)}{h(s, 0)} = \left( \frac{s}{s_0} \right)^{1/4} \Gamma^{-1} \left( \frac{4}{3} \right) \left( \frac{\tau_{wD}}{\tau_{w0}} \right)^{1/2} \left\{ \int_{s_0}^s \left[ \frac{\tau_{wD}}{\tau_{w0}} \frac{D}{(s/s_0)} \right]^{1/2} d \frac{s}{s_0} \right\}^{-1/3} \quad (3.63)$$

Note now that for zero mass injection Eq. (3.63) becomes

$$\frac{h(s, L)}{h(s, 0)} = 1.02 \left[ 1 - \left( \frac{s_0}{s} \right)^{3/4} \right]^{-1/3} \quad (3.64)$$

which is almost identical to Eq. (3.77).

The assumption of a linear velocity profile for the turbulent boundary layer is too severe an approximation to yield a valid solution. The procedure used here is to assume that the turbulent non-isothermal effect can be obtained from a relation of the same form as Eq. (3.61), this laminar expression is modified in such a manner as to yield Eq. (3.8) when the mass injection rate is zero. Accordingly, it is assumed that for turbulent flow

$$\frac{h}{h} \left( \frac{S, L}{S, 0} \right) = C \tau_{w0}^{-1/2} \left[ \nu_e \int_{S_0}^S \tau_w^{1/2} ds \right]^{-1/9} \quad (3.65)$$

where C will be determined by comparing Eqs. (3.65) and (3.8) for zero mass injection. As with the laminar case the unperturbed, skin friction relation is used to make Eq. (3.65) more tractable. The turbulent pipe flow equation is known to satisfactorily predict the skin friction or heat transfer distribution on blunt bodies. Therefore the skin friction is given by

$$\frac{c_f}{2} = 0.0296 \left( \frac{\rho_e \mu_e x}{\mu_e} \right)^{-1/5} \quad (3.66)$$

or substituting Eqs. (3.15) and (3.21) and assuming a compressibility factor of unity ( $C_0 = 1$ ) yields

$$\tau_{w0} = .0296 \nu_e^{-4/5} S^{-1/5} \quad (3.67)$$

Substituting Eq. (3.67) into (3.65) gives

$$\frac{h}{h} \left( \frac{S, L}{S, 0} \right) = C \left( 7.1 \right) \left( \frac{\tau_w}{\tau_{w0}} \right)^{-1/2} \left( \frac{S}{S_0} \right)^{1/10} \left[ \int_1^{S/S_0} \left( \frac{\tau_w}{\tau_{w0}} \right)^{1/2} \left( \frac{S}{S_0} \right)^{-1/10} d \frac{S}{S_0} \right]^{-1/9} \quad (3.68)$$

For zero mass injection,

$$\frac{h}{h} \left( \frac{S, L}{S, 0} \right) = (70) \left[ 1 - \left( \frac{S_0}{S} \right)^{9/10} \right]^{-1/9} \quad (3.69)$$

Therefore, to be consistent with Eq. (3.8)

$$c = 1/7 \quad (3.70)$$

The final expressions for the heat transfer downstream of the step change in temperature with upstream mass injection are given by Eq. (3.60) in conjunction with Eqs. (3.63) for laminar flow and (3.68) for turbulent flow. These may be rewritten in the following form:

$$q/q_{150ch} = \frac{1 - I_{wU} + f' (I_{wU} - I_{wD})}{1 - I_{wD}} \quad (3.71)$$

where

$$f'_{Lam} = 1.12 \left( \frac{h}{h_0} \right)^{-1/2} \left( \frac{s}{s_0} \right)^{1/4} \left\{ \int_0^{s/s_0} \left[ \frac{h/h_0}{s/s_0} \right]^{1/2} d \frac{s}{s_0} \right\}^{-1/3} \quad (3.72)$$

$$f'_{Turb} = 1.02 \left( \frac{h}{h_0} \right)^{-1/2} \left( \frac{s}{s_0} \right)^{1/10} \left\{ \int_0^{s/s_0} \left[ \frac{h/h_0}{s/s_0} \right]^{1/5} d \frac{s}{s_0} \right\}^{-1/9} \quad (3.73)$$

These equations are easily extended to the situation of an arbitrary downstream wall enthalpy distribution. Eq. (3.51) for the boundary layer enthalpy may be rewritten in the following form for an arbitrary number,  $r$ , of surface temperature discontinuities,

$$I = I_{w_r} + (1 + I_{w_U}) \phi(s, \tau, 0) + \sum_{j=1}^{r-1} (I_{w_j} - I_{w_{j+1}}) \phi(s, \tau, s_0) \quad (3.74)$$

Again, this is permissible since the homogeneous energy equation is linear in enthalpy.

as  $r \rightarrow \infty$

$$I = I_{w_D} + (1 - I_{w_U}) \phi(s, \tau, 0) - \int_{s_0}^s \frac{dI_w(s_a)}{ds_a} \phi(s, \tau, s_0) ds_a \quad (3.75)$$

since

$$q \propto \left( \frac{\partial T}{\partial x} \right)_{t=0}$$

it can be shown that for laminar flow

$$\frac{q}{q_{isoth}} = \frac{1 - I_{WU} - \frac{1}{4/3} \int_{s_a}^s \frac{dI_w(s_a)/ds_a}{\tau_{WD}^{-1/2}} ds}{1 - I_{WD}} \quad (3.76)$$

(where  $s_a$  is the variable of integration) which is consistent with Eqs. (3.7) and (3.60). Therefore, following the same procedure as given previously for a single discontinuity yields the following expressions for the downstream heat transfer with an arbitrary wall enthalpy,

$$\frac{q}{q_{isoth}} = \frac{1 - I_{WU} - f}{1 - I_{WD}} \quad (3.77)$$

where

$$f_{lam} = 1.12 \left\{ \frac{(\xi)^{1/2}}{h/h_0D} \right\}_1^\xi \int_{\xi_a}^\xi \left[ \frac{dI_w(\xi_a)/d\xi_a}{\left\{ \frac{h/h_0D}{(\xi_b)^{1/2}} \right\}^{1/2}} \right]^{1/3} d\xi_a \quad (3.78)$$

$$f_{turb} = 1.02 \left\{ \frac{(\xi)^{1/5}}{h/h_0D} \right\}_1^\xi \int_{\xi_a}^\xi \left[ \frac{dI_w(\xi_a)/d\xi_a}{\left\{ \frac{h/h_0D}{(\xi_b)^{1/5}} \right\}^{1/2}} \right]^{1/9} d\xi_a \quad (3.79)$$

where

$$\xi = s/s_0$$

It is apparent that the maximum non-isothermal influence occurs under the situation of a wall enthalpy jump. Accordingly, the influence of a step change in wall enthalpy on the downstream heat transfer with the presence of upstream mass injection is shown in Fig. 3-6. The  $f'$  function is presented for both laminar and turbulent flow with zero mass injection and for the blowing situation used in Fig. 3-5 ( $B'_u = .643$ ,  $B'_D = .175$ ). As mentioned previously the non-isothermal effect increases rapidly as the position of the discontinuity is approached; the effect being enhanced in laminar flow. Neglecting downstream mass injection yields a laminar value of  $f' = 5.1$  for the distance

ratio of interest in this study ( $s/s_0 \simeq 1.015$ ). It is noteworthy that the net influence on the convective heating for the slug calorimeter is still relatively minor since the enthalpy jump is small compared to the enthalpy potential; this is evidenced in the comparison of the various interactions presented in Fig. 3-2. Upstream blowing is found to increase the laminar non-isothermal effect by about 20%, the effect is somewhat less for turbulent flow. The effect of downstream injection is incorporated in the theory by accounting for it in the transpiration effect. Subsequent analyses will show that the non-isothermal effect significantly influences interpretation of the asymptotic calorimeter data. Therefore in this situation the influence of mass injection may become important.

#### Surface Reactivity Discontinuity

The influence of a discontinuous change of surface reactivity on surface combustion rates is examined here. The governing relations are given by Eqs. (3.10) through (3.17). A solution may be determined following the procedure described by Chung (Ref. 3.12) for the analogous problem of surface recombination in the frozen dissociated boundary layer. However, this type of solution is extremely cumbersome. An alternate and more approximate approach is taken here. In particular, the following two limit solutions will be obtained.

- A. The reaction rate constant downstream of the discontinuity is infinite. Combustion is limited by the diffusion rate of oxygen to the surface. This assumption will provide an upper limit on the surface combustion rate.
- B. The downstream reaction rate constant is assumed to be zero in order to determine the maximum local wall concentration of oxygen. Then the finite reaction rate equation is used to compute surface oxidation rate. This solution also provides an upper limit on the combustion rate.

Of the two solutions, the one yielding the lowest value provides the more realistic result.

### Boundary Conditions

The surface boundary conditions which will be used in investigating the downstream combustion rate are

for  $t = 0$ :

$$\begin{aligned} u &= 0 \\ v_u &= v_D^* \end{aligned} \quad (3.80)$$

for  $s \leq s_0$

$$I = I_U, \quad \text{a constant} \quad (3.81)$$

$$\tilde{K}_i = \tilde{K}_{iU}, \quad \text{constants}$$

for  $s > s_0$

$$I = I_{wD}(s), \quad \tilde{K}_i = \tilde{K}_{iD}(s) \quad (3.82)$$

The oxygen concentration at the wall is determined by imposing a kinetic equation describing reaction rates

$$(P_N)_c = k \left[ K_{O_2w} \frac{M_w}{M_{O_2}} P_e \right]^{1/2} \quad (3.83)$$

To implement Eq. 3.83 for the downstream region, it is necessary to relate the concentration of oxygen to the elemental concentrations. This is readily accomplished by neglecting the presence of pyrolysis gases. Then, considering only the char-oxygen reaction,



yields the following conservation statements for a carbon-air system

---

\* The consequences of neglecting the discontinuity in surface injection, may be inferred from the non-isothermal wall analysis. Since it was shown that a discontinuity in mass injection had a relatively small effect on the influence of a step change in wall enthalpy and since the enthalpy and species conservation equations are similar, it is reasonable to neglect this effect in analyzing a discontinuity in wall concentration.

$$\tilde{K}_{Ow} + \tilde{K}_{Nw} + \tilde{K}_{Cw} = 1 \quad (3.85)$$

$$V_{Cw} = V_{Cw} \tilde{K}_{Cw} - \nu_{e,o} \left. \frac{\partial \tilde{K}_c}{\partial t} \right|_w \quad (3.86)$$

$$V_{Ow} = 0 = V_{Cw} \tilde{K}_{Ow} - \nu_{e,o} \left. \frac{\partial \tilde{K}_o}{\partial t} \right|_w \quad (3.87)$$

$$V_{Nw} = 0 = V_{Cw} \tilde{K}_{Nw} - \nu_{e,o} \left. \frac{\partial \tilde{K}_N}{\partial t} \right|_w \quad (3.88)$$

At the wall, the species present are  $O_2$ ,  $CO$ , and  $N_2$ . From stoichiometric considerations,

$$K_{O_2w} = \tilde{K}_{Ow} - \frac{M_o}{M_c} \tilde{K}_{Cw} \quad (3.89)$$

It is evident from Eqs. (3.13), (3.87), (3.88) and the boundary conditions that the elemental concentration distributions for oxygen and nitrogen are similar. That is

$$\tilde{K}_o / \tilde{K}_N = \tilde{K}_{oe} / \tilde{K}_{Ne} \quad (3.90)$$

Then, from (3.85), (3.89) and (3.90)

$$\tilde{K}_{O_2wD} = \tilde{K}_{OwD} - \frac{M_o}{M_c} \left[ 1 - \tilde{K}_{OwD} \left( 1 + \frac{\tilde{K}_{Ne}}{K_{oe}} \right) \right] \quad (3.91)$$

The surface concentration may be conveniently related to the mass transfer parameter

$$B' \equiv \frac{(Pw)_w}{h} \quad (3.92)$$

by noting the similarity between elemental concentration and total enthalpy, Eq. (3.3) or

$$\left. \frac{\partial \tilde{K}_i / \partial s}{\partial I / \partial s} \right|_w = \frac{\tilde{K}_{ie} - \tilde{K}_{iw}}{1 - I_w} \quad (3.93)$$



Then, the upstream concentration of oxygen is determined from

$$\tilde{K}_{OwU} = \frac{\tilde{K}_{Oe}}{1 + B'_U} \quad (3.94)$$

To be consistent with neglecting the pyrolysis gases and to yield a conservative value for the oxygen concentration it is appropriate to use

$$B'_U = B'_{carbonU} \quad (3.95)$$

which has a maximum value of .174 corresponding to the familiar diffusion-limited result.

Case A:  $k = \infty$

Downstream of the discontinuity, since  $k = \infty$ , it may be seen from Eq. (3.83) that

$$K_{O2w} = 0$$

Thus, from Eqs. (3.85), (3.89), and (3.90)

$$\tilde{K}_{OwD} = \frac{\tilde{K}_{Oe}}{1 + \frac{M_G}{M_O} \tilde{K}_{Oe}} \quad (3.96)$$

Therefore, the downstream wall concentration of oxygen is constant.

The solution of the species continuity equation for oxygen with a step change in wall concentration is analogous to the solution of the energy equation for a jump in wall enthalpy. Therefore, Eq. (3.51) for the downstream enthalpy is also applicable for the concentration, i.e.

$$\tilde{K}_O = K_{OwD} + (\tilde{K}_{Oe} - \tilde{K}_{OwU}) \phi(\xi, \tau, 0) + (\tilde{K}_{OwU} - \tilde{K}_{OwD}) \phi(\xi, \tau, S_0) \quad (3.97)$$

or

$$\left. \frac{\partial \tilde{K}_O}{\partial \tau} \right|_{\tilde{K}_{Ow} = \text{constant}} = \frac{\tilde{K}_{Oe} - \tilde{K}_{OwU} - f'(\tilde{K}_{OwD} - \tilde{K}_{OwU})}{\tilde{K}_{Oe} - \tilde{K}_{OwD}} \quad (3.98)$$

where  $f'$  is given by Eqs. (3.72) and (3.73) for  $h/h_0 = 1$ .

Eq. (3.98) may be conveniently rewritten in terms of the mass transfer parameter by substituting Eqs. (3.21), (3.85), (3.87), and (3.93), and the definition of the isothermal heat transfer coefficient:

$$h_{isoth} = \frac{(\partial T / \partial t)_w}{1 - I_w} \frac{\rho_w \mu_w U_e r^E}{\rho_{g_0}} \quad (3.99)$$

The final result for the downstream distribution of the surface oxidation is then

$$B'_{D_0} = \frac{\dot{m}}{(h_{isoth})_D} = \frac{\tilde{K}_{oe} - \tilde{K}_{owu} - f'(\tilde{K}_{owD} - \tilde{K}_{owu})}{\tilde{K}_{owD}} \quad (3.100)$$

where

$$f'_{lam} = \left[ 1 - \left( \frac{S_0}{S} \right)^\gamma \right]^\beta \quad (3.101)$$

$$\beta = \begin{cases} \text{LAMINAR} : -1/3 \\ \text{TURBULENT} : -1/9 \end{cases} \quad (3.102)$$

$$\gamma = \begin{cases} \text{LAMINAR} : 3/4 \\ \text{TURBULENT} : 9/10 \end{cases}$$

Case B:  $k = 0$

Downstream of the discontinuity, since  $k = 0$ , from Eqs. (3.83) and (3.87), it is seen that

$$V_{cw} = 0 = \left. \frac{\partial \tilde{K}_0}{\partial t} \right|_w \quad (3.103)$$

Again, the solution of the species equation is analogous to the solution of the energy equation but now for an arbitrary downstream distribution of enthalpy or concentration. The applicable solution is given by Eq. (3.77) or

$$\frac{\partial \tilde{K}_0 / \partial t}{(\partial \tilde{K}_0 / \partial t)_{\tilde{K}_{ow} = \text{CONSTANT}}} = \frac{\tilde{K}_{oe} - \tilde{K}_{owu} - f}{\tilde{K}_{oe} - \tilde{K}_{owD}} \quad (3.104)$$

where  $f$  is given by Eqs. (3.78) and (3.79) for  $h/h_0 = 1$

Therefore, substituting Eq. (3.103) yields the following expression for the downstream distribution of oxygen concentration:

$$\tilde{K}_{oe} - \tilde{K}_{owu} = \int_{\xi}^{\xi} \frac{d\tilde{K}_{ow}}{d\xi} \left[ 1 - \left( \frac{\xi_a}{\xi} \right)^\gamma \right]^\beta d\xi_a \quad (3.105)$$

A method of integration is outlined in Ref.(3.4). The final result is

$$\frac{\tilde{K}_{oe} - \tilde{K}_{owD}}{\tilde{K}_{oe} - \tilde{K}_{owu}} = \frac{B_r \left( 1 + \beta, -\beta \right)}{\Gamma(1 + \beta) \Gamma(-\beta)} \quad (3.106)$$

where the incomplete Beta function is defined as

$$B_r = \int_0^z \frac{(s_0/s)^\gamma - (\beta+1)}{z^\beta (1-z)} dz$$

from Eqs. (3.83) and (3.91), the surface combustion rate may now be evaluated using

$$(p_r)_{CD} = k \left[ \frac{M_w}{M_{O_2}} \rho_e \left( \tilde{K}_{owD} - \frac{M_{O_2}}{M_w} \left\{ 1 - \tilde{K}_{owD} \left( 1 + \frac{\tilde{K}_{Na}}{\tilde{K}_{oe}} \right) \right\} \right) \right]^{1/2} \quad (3.107)$$

The solution for Cases A and B (Eqs. (3.100) and (3.107) together with auxiliary relations provide two alternative upper limits for surface combustion. A qualitative comparison of these solutions with actual behavior is shown in Fig. 3-7. Of these solutions, that of Eq. (3.100) is presently the more important. It provides a realistic upper limit when the surface combustion effect contributes significantly to heat transfer. It may be conveniently used since the functions required are relatively simple and are used elsewhere (in evaluating the wall temperature discontinuity effect).

The result of Eq. (3.107) provides a rough approximation to the surface combustion rate for  $s/s_0$  close to unity. For  $s/s_0$  somewhat larger than unity it does not do very well. It requires tabulated values of the incomplete Beta function and thus cannot be directly applied. The result of Eq. (3.107) could be replaced by a more conservative limit (the asymptotic form of Eq. (3.107) as  $s/s_0 \rightarrow \infty$ , i.e.  $\tilde{K}_{ow} = \tilde{K}_{oe} = 0.233$ )

Specifically

$$(\rho v)_c = k \left[ \frac{M_w}{M_o} P_e (0.233) \right]^{1/2} \quad (3.108)$$

Eq. (3.107) is useful when surface combustion rates are not very large. It therefore seems that the more conservative Eq. (3.108) could be used instead without significant error. The results would be affected as shown in Fig. 3-8.

For the present purposes Eqs. (3.100) and (3.108) will be utilized. In application, for any given time  $(\rho v)_c$  is computed by both equations and the smaller of the two solutions used as an upper limit.

#### Calorimeter Heat Flux

The physical characteristics of representative slug type and asymptotic heat flux gages are shown in Fig. 3-9. The relative dimensions of the different elements are roughly to scale. The surface distribution in enthalpy, mass injection, and surface reactivity to be considered are indicated. Streamwise variations indicated by the dotted lines are probably more representative of the physical situation. Solid lines indicate the distributions employed in the present analysis to enable a tractable solution. The ramp temperature decrease across the insulation ring for the case of a slug calorimeter is carried into the analysis although it is evident that a step change is a valid approximation. This more complex temperature variation is employed initially to demonstrate the general technique involved in the non-isothermal correction.

The local convective heat transfer to the calorimeter surface is given by

$$q = h_o \left( \frac{h}{h_o} \right) \left[ H_o - H_u - f_s + B_s' q_c \right] \quad (3.109)$$

where

$h/h_o =$  downstream reduction in the heat transfer coefficient as a result of mass injection

$(H_o - H_u) - f =$  enthalpy potential based on air properties for the downstream heat transfer accounting for the non-isothermal wall effect

$h B' Q_c =$  heat transfer due to surface combustion including the effect of a discontinuity in surface reactivity.

Evaluation of the sensor response requires that alternate forms of Eq.(3.109) be applied to the particular configurations of interest. For the case of the slug type gage, since the sensor may be considered isothermal, determination of the temperature response requires specifying only the average heat flux. The asymptotic calorimeter response, represented by the temperature differential between the disk center and edge, must be computed using local values of the heat flux. In applying Eq. (3.109), the analysis is considerably simplified if the following approximations are made:

- 1) coupling between the interaction phenomena is negligible. (Validity of this is inferred from the previous analysis which indicated that discontinuous mass injection exerts only a minor influence on the non-isothermal wall correction.)
- 2) The sensor dimensions are small compared to the surface distance from the stagnation point.

In the following section the pertinent convective heat flux expressions for the slug type and asymptotic calorimeters are developed.

#### Slug Calorimeter

Subsequent calculations will show that the surface enthalpy distribution for the slug calorimeter is typified by a ramp decrease across the insulation ring, followed by a constant value on the guard with a step change at the sensor guard interface. The surface reactivity and blowing rate are approximated by a single step change.

The average heat transfer to the sensor surface is given by

$$\bar{q}_s = \frac{2}{\pi R_s} \int_0^{\pi/2} \cos \varphi \left[ \int_{x_2'}^{x_2' + 2R \cos \varphi} q \, dx \right] d\varphi \quad (3.110)$$

Consistent with the above approximations (1 and 2) it is possible to rewrite Eq. (3.109) as

$$\bar{q}_s = h_0 \frac{h}{h_0} \left\{ H_0 - H_u - \bar{E}_s + \bar{B}'_s q_c \right\} \quad (3.111)$$

where  $h_0 (h/h_0)$  is evaluated at  $s_s/s_0$  (the distance ratio: calorimeter center to edge). The sensor non-isothermal correction along any streamwise strip may be expressed in the form

$$f_s = \frac{H_6 - H_{wu}}{\xi' - 1} \int_1^{\xi'_1} \left[ 1 - \left( \frac{\xi'_a}{\xi'} \right)^\gamma \right]^\beta d\xi'_a + (H_5 - H_6) \left[ 1 - \left( \frac{s'_2}{s'} \right)^\gamma \right]^\beta \quad (3.112)$$

where

$$\xi' = s/s_0 \text{ AND}$$

$$\gamma = \begin{cases} \text{Laminar: } 3/4 \\ \text{Turbulent: } 9/10 \end{cases} \quad (3.113)$$

$$\beta = \begin{cases} \text{Laminar: } -1/3 \\ \text{Turbulent: } -1/9 \end{cases}$$

It is understood that the wall enthalpies are based on air.

Further simplification is achieved if

$$\xi'_a / \xi' \approx 1 \quad (\text{the calorimeter dimensions are small compared to its location}) \quad (3.114)$$

and noting that then

$$\frac{\xi'_1 - 1}{\xi' - \xi'_1} \ll 1$$

(that thickness of the insulation ring is small compared to the guard's; less than 1/3 for the present configuration)

Then

$$f_s \approx (H_6 - H_{wu}) \gamma^\beta \left( \frac{\xi'_1 - \xi'_1}{\xi'} \right)^\beta + (H_5 - H_6) \gamma^\beta \left( \frac{\xi'_1 - \xi'_2}{\xi'} \right)^\beta \quad (3.115)$$

It is evident that under these assumptions the ramp enthalpy decrease is reduced to a step-change. The analysis is made more tractable if the transformed coordinate is expressed as an analytic function of the surface distance. Over the relatively short surface distances associated with the sensor the relationship is adequately represented by,

$$S \propto (x-d)^N \quad (3.116)$$

In the laminar boundary layer case, the constants N and d are evaluated locally using the transformed coordinate distribution given in Fig. 2H-6 for the Apollo vehicle along the plane of symmetry. For turbulent flow: N = 1, d = 0.

The average non-isothermal effect for the sensor may now be obtained by substituting Eqs. (3.115) and (3.116) into (3.110). A number of approximations, such as Eq. (3.114) are required to perform the integration; in particular it is assumed the sensor diameter is small compared to the guard's in evaluating the effect of the ramp temperature distribution. The final result is given by Eq. (3.117).

$$\bar{f}_S = (H_G - H_{WU}) \left( \frac{NYR_G}{\chi_1 - d} \right)^\beta + \frac{H_S - H_G}{\beta + 1} \frac{2}{\sqrt{\pi}} \frac{(2R_S N)^\beta}{(\chi_2 - d)^\beta} \frac{\Gamma\left(\frac{\beta+3}{2}\right)}{\Gamma\left(\frac{\beta+4}{2}\right)} \quad (3.117)$$

There are two expressions for  $B'_D$ . Eq. (3.100), corresponding to an infinite reaction rate, is of the same form as the non-isothermal correction, Eq. (3.115) i.e.

$$B'_{SD} = \frac{\tilde{K}_{oe} - \tilde{K}_{owu} + (\tilde{K}_{owu} - K_{ows}) \gamma^\beta \left( \frac{\xi}{\xi_1} - 1 \right)^\beta}{\tilde{K}_{ows}} \quad (3.118)$$

therefore

$$\bar{B}'_{SD} = \frac{\tilde{K}_{oe} - \tilde{K}_{owu} + (\tilde{K}_{owu} - K_{ows}) \left( \frac{NYR_G}{\chi_1 - d} \right)^\beta}{\tilde{K}_{ows}} \quad (3.119)$$

where  $\tilde{K}_{ows}$  and  $\tilde{K}_{owu}$  are evaluated from Eqs. (3.96) and (3.94) respectively.

The other limit solution is given by Eq. (3.108) which, since it is invariant

with distance, is directly applicable

$$\bar{B}'_{S_0} = \frac{k}{h_5} \left[ 0.233 \frac{M_w}{M_{O_2}} P_e \right]^{1/2} \quad (3.120)$$

Both Eqs. (3.119) and (3.120) are to be evaluated, with the smaller combustion rate being used in the analysis.

Therefore, once the unperturbed heat transfer, upstream surface conditions, and the local pressure are known, Eq. (3.110) in conjunction with Eqs. (3.44), (3.117), (3.119), and (3.120) are sufficient to determine the average heating rate to the sensor.

The average heat transfer to the graphite guard is evaluated in the same manner as for the sensor. The non-isothermal problem is considerably simplified if the influence of the sensor is neglected. This approximation is justified noting that the sensor to guard area ratio is about  $\frac{1}{4}$  and the influence of the upstream and downstream temperature discontinuities associated with the sensor tend to cancel each other. The correction for the non-isothermal effect for the guard is therefore given by

$$\bar{f}'_G = \frac{H_G - H_{WU}}{\beta + 1} \frac{2}{\sqrt{\pi}} \left( \frac{2R_G N_U}{\lambda_1 - d} \right)^\beta \frac{\Gamma \left( \frac{\beta + 3}{2} \right)}{\Gamma \left( \frac{\beta + 4}{2} \right)} \quad (3.121)$$

Similarly the combustion rate for the guard is given by

$$\bar{B}'_{G\infty} = \frac{\tilde{K}_{Oe} - \tilde{K}_{Ows} + (\tilde{K}_{Owu} - \tilde{K}_{Owg})}{\tilde{K}_{Owg}} \frac{2}{(\beta + 1) \sqrt{\pi}} \left( \frac{2R_G N_U}{\lambda_1 - d} \right)^\beta \frac{\Gamma \left( \frac{\beta + 3}{2} \right)}{\Gamma \left( \frac{\beta + 4}{2} \right)} \quad (3.122)$$

and for the other limit solution by Eq. (3.120).

The following auxiliary equations are required to supplement the analysis:

- 1) the heat of formation of carbon is determined using the correlation equation

$$Q_c = 3788 + 0.13T \text{ BTU/LB} \quad (3.123)$$



2) the oxidation rate constant is

$$k = k_0 e^{-E/RT_{\text{SURFACE}}} \quad (3.124)$$

$$k_0 = 1.74 \times 10^5 \frac{\text{LB}}{\text{FT}^2 \text{SEC ATM}^{1/2}}$$

$$E/R = 36,200 \text{ } ^\circ\text{R}$$

#### Asymptotic Calorimeter

Consideration of the thermal properties of the foil disk and high thermal capacity of the calorimeter body indicates that the sensor temperature will be considerably lower than the ablator's or the guard's. Therefore, it is consistent to represent the streamwise variation in surface enthalpy by a single step change followed by a distorted parabolic temperature variation across the sensor surface. (The distortion in the surface temperature results from the rapid decay in the heat transfer coefficient following a discontinuity in wall enthalpy.) A step change in blowing is also present but the downstream surface erosion is zero. Therefore, the local convective heating to the sensor is given by

$$q_s = h_0 \left( \frac{h}{h_0} \right) [H_0 - H_w - f_s] \quad (3.125)$$

Correct interpretation of the calorimeter output requires that the radial temperature difference be expressed as a function of the convective heating. Only the non-isothermal effect need be studied, assuming a constant heat transfer coefficient.

For the prescribed enthalpy distribution the non-isothermal effect may be written in the following form (see Eq. (3.9) and Fig. 3-9)\*:

$$-f_s = [H_w - H_2] \left[ 1 - \left( \frac{s_2'}{s'} \right)^{\beta} \right] - \int_{s_2}^s \frac{dH_w}{ds_a} \left[ 1 - \left( \frac{s_a'}{s'} \right)^{\beta} \right] ds_a \quad (3.126)$$

\* The non-isothermal and transpiration are uncoupled to permit a tractable analysis although their interaction may be significant.

The first term on the right hand side represents the effect of the step change while the second term accounts for the local sensor temperature variation. It will now be shown that the latter effect is generally negligible compared to the former. Consider for the moment a similar one dimensional case where the sensor enthalpy profile is undisturbed by the upstream discontinuity and representable by the parabolic profile (see Section 3.2.2):

$$H_w = H_2 + \frac{H_5 - H_2}{R^2} \left[ R^2 - (R - x + x_2)^2 \right] \quad (3.127)$$

Differentiating Eq. (3.127) and substituting into Eq. (3.126) and noting that  $R/x \ll 1$  yields,

$$-f_{s, 1-D} = (H_u - H_2) \gamma^\beta \left( \frac{r}{x_2} \right)^\beta - 2(H_5 - H_2) \gamma^\beta \left( \frac{r}{x_2} \right)^\beta \left\{ \frac{r/R}{\beta+1} - \frac{(r/R)^2}{(\beta+2)(\beta+1)} \right\} \quad (3.128)$$

where

$$r = x - x_2$$

For comparison purposes the average value of  $f_s$  across the sensor is evaluated.

$$-\bar{f}_s = (H_u - H_2) \frac{\gamma^\beta}{\beta+1} \left( \frac{2R}{x_2} \right)^\beta - (H_5 - H_2) \gamma^\beta \left( \frac{R}{x_2} \right)^\beta \left\{ \frac{\binom{2}{\beta+1} \binom{\beta+2}{\beta+2}}{\binom{2}{\beta+1} \binom{\beta+2}{\beta+2} \binom{\beta+3}{\beta+3}} - \frac{\binom{2}{\beta+1} \binom{\beta+3}{\beta+2} \binom{\beta+3}{\beta+3}}{\binom{2}{\beta+1} \binom{\beta+2}{\beta+2} \binom{\beta+3}{\beta+3}} \right\} \quad (3.129)$$

or

$$-\bar{f}_s = (H_u - H_2) \frac{\gamma^\beta}{\beta+1} \left( \frac{2R}{x_2} \right)^\beta \left[ 1 - A \frac{H_5 - H_2}{H_u - H_2} \right] \quad (3.130)$$

where

$$A = \frac{4}{\beta+2} - \frac{\beta}{\binom{\beta+2}{\beta+2} \binom{\beta+3}{\beta+3}}$$

or

$$A = \begin{cases} 0.60 & \text{(LAMINAR)} \\ 0.651 & \text{(TURBULENT)} \end{cases}$$

The second term within the brackets of Eq. (3.130) reflects the effects of the parabolic temperature distribution whereas the first term accounts for the step change at the leading edge. It is apparent for the situation where

$$\frac{H_s - H_2}{H_u - H_2} \ll 1$$

that only the step change need be considered in evaluating the convective heating.

Therefore, the local convective heating to an asymptotic sensor is given by

$$q_s = \left\{ h_0 \left( \frac{h}{h_0} \right) \right\}_s \left\{ H_0 - H_u + (H_u - H_2) \left[ 1 - \left( \frac{S_2'}{S'} \right)^\gamma \right]^\beta \right\} \quad (3.131)$$

where the transpiration effect is evaluated at the center of sensor using Eq. (3.44).

### 3.2 CALORIMETER PERFORMANCE

Consideration is given here to two types of calorimeters which have found wide application. These are the asymptotic and capacitance types. The function of these gages is the measurement of the net heat transfer; they do not distinguish the mechanism of heat transfer, be it radiative or convective.

Interpretation of calorimeter data requires an accurate accounting of all the means of energy storage and transfer. In general, the net heat transfer to the exposed surface is related to the calorimeter output (sensor temperature measurement) by means of an energy balance on the system. The simplest relationship between the output, physical characteristics and the input heat flux is illustrated in Fig. 3-10. Ideally the heat input to a slug calorimeter is either stored in a constant temperature sink or reradiated. Additional energy losses are not present and the thermocouple is assumed to read the true temperature. Thermal and physical properties of the sensor are invariant and the heating rate is independent of surface location. An energy balance on this system yields the relation,

$$q_{in} = \rho c_p \delta \frac{dT_s}{d\theta} + \epsilon_s \sigma_{SB} T_s^4 \quad (3.132)$$

The asymptotic calorimeter operates on a different principle, all of the incoming heat is assumed to flow radially through a thin surface disk to a constant temperature sink at its edge. The ideal model assumes no other radiation or conduction losses are present, the surface heating is invariant with location, disk temperatures are constant in the axial direction, and zero contact resistance exists at the sensor edge. In this situation, the differential temperature drop (center to edge) is directly related to the heat input through the expression,

$$q_{in} = \frac{4k\delta}{R^2} (T_s - T_2) \quad (3.133)$$

In actual applications of these devices perturbations in these idealized models will occur. The extent of the deviation is dependent on the particular physical characteristics of the meter and on the thermal environment to which it is exposed. Accordingly, most calorimeters are designed in such a manner as to correspond as closely as possible to the aforementioned models. Even so, rarely will the final meter design or the thermal environment be such as to eliminate all possible errors and thus means of accounting for the perturbing effects must be developed to reduce the calorimeter data.

In the present study interest is centered on the slug and asymptotic designs shown in Fig. 3-11\*. The objective is to develop means for accurately reducing

---

\* These designs are not necessarily current but are those applied at the initiation of the study. A modified design for the slug calorimeter has also been examined and is discussed in a separate memo.

Slug calorimeter: "Calorimeter Heat Transfer Study", Drwg. No. 1D015, High Temperature Instruments Corp.

Asymptotic Calorimeter: Asymptotic Calorimeter Model: 1170", Drwg. No. A-1902, Hy-Cal Engineering.

Apollo type calorimeter data. Emphasis is placed on developing relatively simple analytical methods, accounting for all significant modes of energy storage and transfer, which can be reliably used to evaluate the heat input-temperature response relationship. The approach is to carefully study the thermal response characteristics of the calorimeters for representative heating conditions. Effects which perturb the idealized models are delineated and means to account for them are developed. A subsidiary task involves assessing the flux errors attributable to the temperature measurement uncertainties associated with the thermocouple installation. Finally a critique of the calorimeter designs is made and suggestions are given as to their possible improvement. Because the slug calorimeter is somewhat more complex, primary attention is focused on this type.

### 3.2.1 Slug Calorimeter

Slug calorimeters afford a convenient means of making meaningful heat flux measurements for situations where a wide spectrum of heating rates and surface temperatures are expected. Some of the advantages of this type of calorimeter which make it uniquely qualified for Apollo forebody application are

- high heat rate capability
- transient heating capability
- structural integrity
- minimum disturbance of the homogeneity of the surrounding thermal environment

The disadvantages of a slug calorimeter rest in obtaining a reliable interpretation of the data. Rigorous reduction of the sensor temperature history requires performing a detailed energy balance on the calorimeter assembly and consequently involves lengthy and complex computational schemes. For example, the following effects must be analytically described and accounted for if they are present:

- conduction and radiation heat losses
- axial and radial temperature gradients
- surface erosion
- contact resistance
- thermocouple effects and errors

Recourse is often made to experimental calibration with the intent of grossly accounting for these effects. An alternate procedure is to examine in detail the influence of each error source for the particular calorimeter and then incorporate those corrections which are pertinent into a simpler analytical model.

Determination of experimental calibration curves requires a comprehensive test program. The thermal response characteristics of a particular calorimeter assembly are dependent on both the instantaneous rate and past history of the heating. Accordingly, the expected Apollo aerothermal environment would have to be simulated, a difficult task.

Development of a simple two capacitance model for use in interpreting the calorimeter data is pursued in this study. Subsidiary objectives are to investigate temperature measurement errors and to suggest possible design improvements. First the effect of thermocouple-sensor interaction on the temperature measurement accuracy is examined. Second, the thermal response characteristics of the slug calorimeter shown in Fig. 3-11 are investigated in detail. Emphasis is placed on determining the conduction and radiation losses and on assessing the influence that the resulting axial and radial temperature gradients have on the heat rate determination. Third, this information is employed in formulating a simple data reduction model. The influence of surface erosion is accounted for and a scheme for handling contact resistances is incorporated. Finally calorimeter design features which would increase both the efficiency and accuracy of the data reduction procedure are delineated.

#### Temperature Measurement Errors

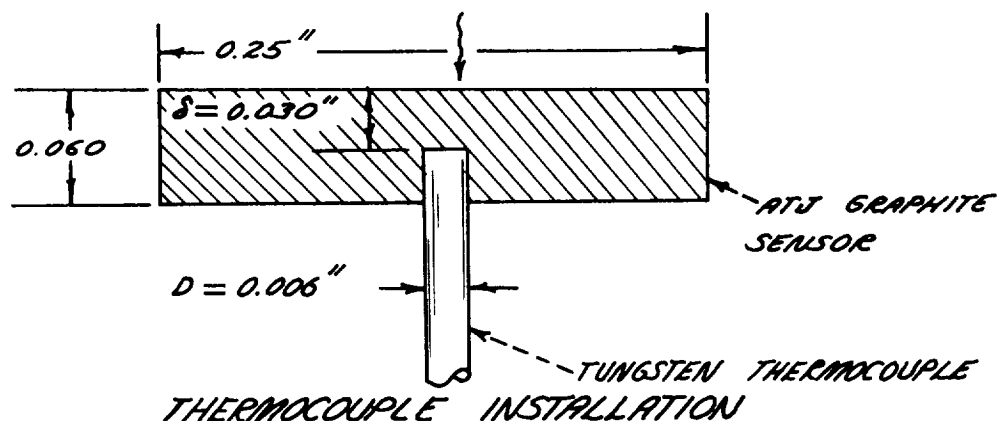
Perturbations in the predicted calorimeter thermal response or conversely in the reduced convection coefficients will arise as a result of temperature measurement errors. Measurement uncertainties will be associated with thermocouple-sensor interactions, thermocouple calibration, the telemetry system, etc., both random and ordered errors will occur. The identifiable sources of error in the temperature measurement due to sensor-thermocouple interaction are:

- Cavity effect due to TC installation hole:  
A hole drilled in the sensor wafer to receive the TC causes a local hot spot at the point of TC temperature measurement; as such, the surface flux inferred from the local temperature response is high.
- Drawn-down effect due to TC lead-wire conduction:  
If the TC lead wires are cooler than their junction, heat is conducted away from the measurement location; this causes a local cold spot and an underestimate of the inferred surface flux.
- Uncertainty in junction location:  
Errors in junction location lead to an overestimate or underestimate of surface flux depending on whether the junction location is closer or farther from the sensor surface than expected.
- Imperfect junction contact:  
Poor junction contact results in underestimating surface heat flux.

The contribution each of these effects makes to the uncertainty in the measured temperature and consequently the heat flux is assessed in the following section.

#### Geometry and Material Properties

The heat-flux sensor-thermocouple installation sketched below will be considered here. A central tungsten thermocouple is shown, although two symmetrically



placed TC's are to be used. The TC junction is assumed to be buried halfway in the sensor. The TC leads are of 3-mil diameter. Taken together, they are considered to require a 6-mil diameter hole.

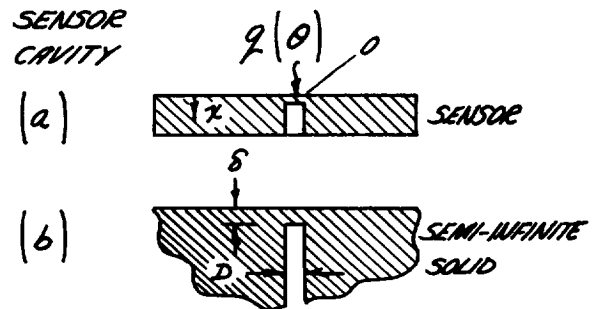
Nominal properties of ATJ graphite and tungsten are taken as follows:

	$\rho$ (lb/ft <sup>3</sup> )	$c_p$ (Btu/lb-°F)	$k$ (Btu/sec-ft-°F)	$\alpha$ (ft <sup>2</sup> /sec)
Graphite (ATJ)	108	0.47	0.00583	$115 \times 10^{-6}$
Tungsten	1210	0.032	0.0266	$668 \times 10^{-6}$

#### Cavity Effect

A bottom hole is drilled from the back sensor surface to accept a temperature-monitoring TC. Due to material removal, the temperature at point  $o$  will be higher than at other surface locations on

the sensor. This perturbed temperature is registered by the TC and will result in an error in inferred surface heat flux  $q$ . The effect is altered by inserting a TC. If the junction and lead wires do not completely fill the cavity (with perfect contact) or if the TC is of low conductivity relative to the wafer, then the disturbance is similar to that of a true cavity.



The cavity effect has been studied by Masters and Stein (Ref. 3.14) and later by Beck and Hurwicz (Ref. 3.15). Both papers considered a semi-infinite solid  $x \geq 0$ , containing an adiabatic cavity with either constant or time-varying surface heat flux  $q(\theta)$ . The latter paper determined that response times of cylindrical cavities associated with typical TC installations ( $\delta \approx D$ ) is

$$\theta \approx 30\delta^2/\alpha.$$

It was also found that if the heat flux does not vary appreciably in this response period (i.e., either slow variations in  $q$  or short  $\theta_r$  with rapid variations in  $q$ ), then steady-state results could be used to estimate the cavity



disturbance even though  $q = q(\theta)$ . For small  $g = D/2\delta$ , the steady state disturbance is

$$\left( T_0 - T_\infty \right) / \left( q D / k \right) = q / 4$$

where  $T_0$  is surface temperature directly above cavity (point 0) and  $T_\infty$  is surface temperature in absence of cavity (i.e.,  $\Delta T = T_0 - T_\infty$  is the absolute surface disturbance). In the present case  $g = 0.003/0.03 = 0.1$  and  $\Delta T = [0.1 (0.003/12)/2 \times 0.00583] q = 0.00215 q$ . Thus, even if  $q$  were 1000 Btu/sec-ft<sup>2</sup> the surface disturbance would only be of the order of 2°F.

The response time is  $\theta_r = 30 (0.030)^2 / 144 \times 0.000115 = 1.6$  sec. This is not low enough to be insignificant compared to characteristic times in  $q(\theta)$ . As such, the steady-state results of Ref. 3.15 are not strictly applicable. In the transient state the disturbance for  $q = \text{constant}$  (Ref. 3.15) is

$$e = \left( T_0 - T_\infty \right) / T_\infty = \left( q^2 / 4 \right) \sqrt{\pi / F_0} \operatorname{erfc} \left( 1 / \sqrt{F_0} \right), \quad (3.134)$$

where  $F_0 = \alpha \theta / \delta^2$ . Fig. 3-12 shows the time variation in error  $e$  expressed as a percentage. The maximum surface-temperature error (assuming constant  $q$ ) is seen to be less than 1/10 percent; it reaches this peak within a fraction of a second and thereafter slowly decays. If variable flux is considered, then approximately  $\Delta T = 0.00215 q$ . Since  $q_{\max}$  is only of the order of 100, the surface disturbance under variable flux is also negligible.

In summary, the cavity effect is not regarded as a major source of error for the values of  $g$  in the present design. However, it is expected that actual sensor fabrication will result in different cavity sizes. Three-mil TC wire is very small to work with. If the cavity diameter increases, the associated cavity error will increase.

#### Draw-Down Effect

The draw-down effect (cold spot) caused by conduction heat leak from the junction to cooled lead wires has been approximated by Burnett (Ref. 3.16). In this investigation backface mounted thermocouples were considered. This model is

therefore conservative with respect to the present study where the initial portion of the thermocouple lead is contained within the sensor body. Application of these results to the present configuration is shown in Fig. 3-12. Maximum error can be -5% at very early times; at later times this error diminishes to about -1%.

#### Junction Location Uncertainty

Errors in inferred surface heat flux have been studied by Chin (Ref. 3.17) for a wall of finite thickness exposed to cosine pulse heat input. It is determined from these results that for the subject calorimeter with a TC located 0.0055" below the heated surface the maximum error in inferred surface heat rate (pulse of 100 sec) is  $e = 0.001 q_{\max}$  per mil. Thus, if  $q_{\max} = 100$  Btu/sec-ft, the maximum error at  $q_{\max}$  (i.e.,  $\theta = \text{period}/2$ ) is 0.1 Btu/sec-ft<sup>2</sup> per mil uncertainty in the thermocouple junction depth location. If the TC can be placed only to within +10mils then the maximum error in  $q_{\max}$  is only +1%.

#### Additional Uncertainties

An accumulation of errors will be associated with poor junctions (electrical and thermal), poor contact between junction and sensor, TC calibration, data readout, temperature gradient determination, etc.,. These uncertainties are not amenable to analytical interpretation, and for any particular sensor-thermocouple system, statistical methods are the only recourse. Certainly, they represent a major source of error.

#### Temperature Measurement Uncertainty

Excluding the undefined errors the following tabulation yields a band of uncertainty for the heat flux measurement.

Cavity effect + 0.1%		+ 1.1%
Conduction error -1%	Net =	- 2.0%
Location error <u>+ 1</u> %		

#### Conduction Solution

A detailed computer solution has been obtained for the thermal response of the

complete sensor assembly. The solution accounts for radial geometry, variable heat input, surface reradiation, variable material properties, and internal radiation across gaps, shields, and between consecutive (stacked) sensors. In this computation sensor-guard conduction interchange was neglected but radiation interchange was accounted for.

Heat input for the study is shown in Fig. 3-13. These data are representative of the Apollo forebody heating during entry along Trajectory 1. First order procedures were used to account for effects of upstream mass injection, local wall temperature discontinuity, and sensor surface mass injection.

Fig. 3-14 shows the geometry (to scale) of the calorimeter assembly. Location of 49 node points are indicated for numerical simulation of the sensor assembly. The LMSC ARBITRARY NODE TEMPERATURE PREDICTION PROGRAM (Ref. 3.18) was used to perform the numerical calculation. This program affords an accurate and efficient means of determining temperature distributions for complex shapes composed of the isotropic materials with temperature dependent thermal properties. The problem is geometrically defined by employing a network of up to 15 by 15 arbitrarily placed nodes. Local temperatures are computed using an explicit finite difference form of the Fourier heat diffusion equation. The thermal properties data utilized in the calculation were obtained from Ref. 3.19. To avoid excessive computation time for the present problem, the maximum-allowable finite difference time step was artificially increased by reducing conductivity of the graphite below its actual value. This results in overprediction of the magnitude of temperature gradients within the graphite. As will be seen the predicted gradients are small and hence the final results of the conduction solution are not significantly affected.

Anticipated performance of the rhodium shields for back-face guarding of the sensor is

$$q_{\text{Loss}} = \sigma_{SB} \left[ \frac{\epsilon}{n+1} \right] (2 - \epsilon) \left( T_1^4 - T_{n+2}^4 \right) \quad (3.135)$$

This represents steady-state heat loss from a system of  $n$  shields interposed between two surfaces when all shields and surfaces are of equal emissivity. Thermal guarding is thus proportional to  $1/(n+1)$ . A single shield reduces heat loss to  $\frac{1}{2}$ ; three shields reduce it to  $\frac{1}{4}$ . The performance of a single rhodium shield ( $\epsilon = 0.1$ ) between ATJ graphite ( $\epsilon = 0.8$ ) and zirconia ( $\epsilon = 0.6$ ) is indicated in Fig. 3-15. The axial heat loss  $q_1$  is

$$q_1 = \sigma \left[ \frac{1}{a+b} \right] (T_1^4 - T_3^4) \quad (3.136)$$

where  $a = 1/\epsilon_1 + 1/\epsilon_{21} - 1$  and  $b = 1/\epsilon_3 + 1/\epsilon_{23} - 1$ . At  $2000^\circ\text{F}$  sensor temperature this amounts to only  $0.45 \text{ Btu/sec-ft}^2$ ; with three rhodium shields the heat leak would be roughly  $0.1 \text{ Btu/sec-ft}^2$ .

Fig. 3-16 shows the instantaneous surface temperature distributions along the calorimeter assembly up to near peak heating (initial temperature uniform throughout at  $100^\circ\text{F}$ ). Two calculation runs were performed, one for the actual case of a guarded sensor and the other assuming perfect radial and axial guarding. Several points are evident: the guarding is not perfect; heat leaks appear starting at about 30 sec and become quite pronounced near peak heating. Surface temperature of the avcoat sleeve is close to sensor surface temperature. The zirconia retainer runs considerably cooler than the sensor itself.

Fig. 3-17 shows a tabulation of surface and in-depth material temperatures at peak heating,  $\theta = 60 \text{ sec}$ . Radial and axial temperature drops in the sensor are quite small. In this sense the ATJ graphite may be considered to reasonably behave as an isothermal heat sink. The underlying calorimeter assembly (II) is well protected up to time of peak heating; the wafer temperature rise in this period is only  $10^\circ\text{F}$ .

The intent in this study is the development of an efficient data reduction model. Therefore, it is of interest to perform an energy balance applying first order data reduction procedures to the previously generated temperature history. The reliability of the approximate methods can then be inferred from comparison of the reduced and original (Fig. 3-13) heat inputs. Sample data reduction

was performed using temperature data from location (9) (Fig. 3-14) of the first computer run (with heat leaks). The following tabulation gives results of this analysis ( $\theta$  in sec,  $q$  in Btu/sec-ft<sup>2</sup>):

$\theta$	$q_{\text{sens}}$	$q_{\text{rerad}}$	$q_{\text{axial}}$	$q_{\text{radial}}$	$q_{\text{net}}$	$q_{\text{input}}$
5	0.41	0.041	0.000	0.001	0.45	0.5
10	1.19	0.053	0.000	0.006	1.25	1.0
15	2.42	0.088	0.001	0.022	2.53	2.8
20	2.93	0.165	0.002	0.063	3.16	3.7
25	2.75	0.258	0.003	0.116	3.13	2.5
30	3.28	0.381	0.005	0.189	3.86	4.3
35	4.44	0.473	0.008	0.211	5.13	4.5
40	6.79	0.923	0.014	0.487	8.21	8.0
45	10.98	1.73	0.03	0.92	13.7	13.0
50	15.50	3.72	0.06	1.85	20.7	20.0
55	17.93	7.53	0.12	3.66	29.2	30.1

Sensible heat absorption in the sensor was calculated as  $q_{\text{sens}} = \rho c \delta dT_0/d\theta$  using variable properties of ATJ. Flux reradiated to space was computed as  $q_{\text{rerad}} = \sigma_{\text{SB}} \epsilon T^4$  with  $\epsilon = 0.8$  for ATJ graphite. Axial and radial heat leaks were treated as radiation losses using computed data at points (9) and (33) (axial) and (2) and (3) (radial). The axial loss was independently checked from the sensible temperature rise of point (33) in the zirconia (treated as thermally thin). Net heat input is the sum of  $q_{\text{sens}}$  plus losses. This is seen to agree reasonably well with the assumed input of Fig. 3-13. The comparison is plotted in Fig. 3-18.

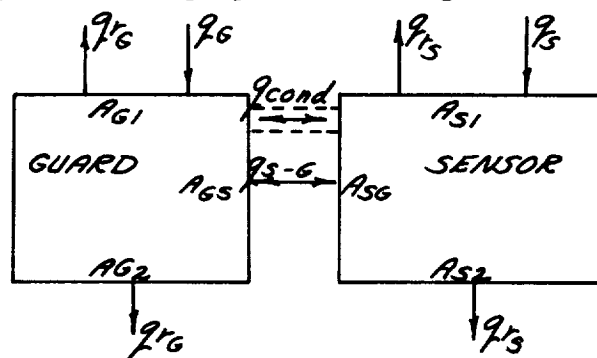
It is noteworthy that the axial heat leak is negligible (0.12 agrees with aforementioned prediction of shield performance which suggested an axial leak of 0.1), while the radial leak is large, almost half of the surface reradiation. Not included in the analysis is the effect of conduction heat losses through the retaining tabs joining the sensor and guard. Unfortunately, the conductance at the contacting surfaces cannot be accurately described without recourse to experimentation. For the purpose of assessing the appropriate influence of conduction heat losses, an average contact resistance over the

complete side surface of  $10 \text{ ft}^2 \text{ sec}^\circ \text{R/Btu}$  was selected. Fig. 3-19 indicates by a comparison the effect on the sensor element temperature history (pt 1). The influence is significant causing a further departure from the ideal sensor response (no radial losses).

The above analysis has considered in detail the thermal response characteristics of a representative slug calorimeter. The results of this study are to be used in formulating a simple but reliable data reduction model. In summary this model must account for energy storage, radial heat losses (radiation and conduction), and surface reradiation. Even for significant radial losses the sensor temperature gradients are not too severe. This means reduction of the sensor temperature data from a centrally located thermocouple will yield the energy storage with reasonable accuracy. Axial heat losses may be neglected for the present configuration.

#### Data Reduction Model

The previous results for the thermal response of the complete calorimeter were obtained by a multi-node, finite difference integration of the conduction equation. Such a solution requires large digital computer times and hence the utility of approximate representations of the conduction problem have been examined. A two node network in which the capacitance of the sensor and graphite guard are separately lumped evolved from this study. The system, which is described below, enables a proper accounting for the major effects.



A thermal balance for either the guard or the sensor yields

$$C_a \frac{dT_a}{d\theta} = \frac{T_b - T_a}{R_{ab}} + q_a - q_{ra} \quad (3.137)$$

where a may refer to either the guard or the sensor with b denoting the other element.

The capacitance is given by

$$C_a = K_a P_a A_a C_{Pa} \left( \frac{V_a}{A_a} - \int_0^\theta \dot{s}_a d\theta \right) \quad (3.138)$$

K is a correction for any additional capacitances or heat losses which may be present. The integral accounts for the volume reduction resulting from surface erosion.

The resistance may be written as

$$R_{SG} = R_{GS} = \frac{1}{\mathcal{F}_{SG} A_{SG} \sigma_{SB} (T_S + T_G) (T_S^2 + T_G^2) + \frac{1}{R_{CSG}}} \quad (3.139)$$

$\mathcal{F}_{SG}$  is the radiation interchange factor which for two concentric cylinders is given by

$$\mathcal{F}_{SG} = \frac{1}{\frac{1}{\epsilon_S} + \frac{A_{SG}}{A_{GS}} \left( \frac{1}{\epsilon_G} - 1 \right)} \quad (3.140)$$

$R_{CSG}$  denotes the contact resistance, accounting for the physical contact made between two elements.

The net axial radiation from an element is evaluated using the relation

$$Q_{ra} = \sigma_{SB} \sum_i \epsilon_a A_{ai} (T_a^* - T_i^*) \quad (3.141)$$

where i denotes axially located heat sinks (subsurface or freestream) with respect to element a.

Finally, the environmental heating is given by

$$Q_a = \bar{q}_a A_a + q_{swa} A_a \quad (3.142)$$

$\bar{q}$  and  $q_{sw}$  are the convective heat flux and shock layer generated radiation, respectively.

These relations were employed to determine the calorimeter response for the environmental situation previously examined by the more exact method. The only major energy exchange not accounted for in this energy balance is the conduction loss to the zirconia insulator. Since this loss may be treated as an equivalent capacitance, the guard capacitance was increased accordingly. It was found that a 26% increase in the guard volume ( $K = 1.26$ ) properly accounted for this effect. The other pertinent physical characteristics are given in Table 3-1. Corroboration of the two capacitance model is achieved in Fig. 3-20 where close agreement with the exact solution is shown.

#### Slug Calorimeter Critique

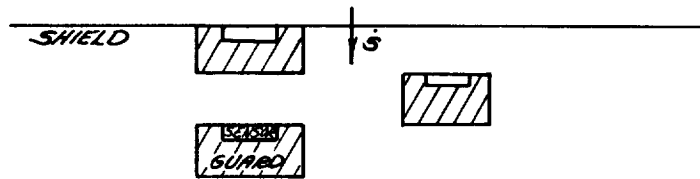
Ideally, the purpose of the Apollo calorimeter is the determination of the unperturbed heat transfer coefficient and/or the shock layer radiation. The relationship between the thermal environment and the actual heat received by sensors mounted in an ablative heat shield was discussed in Section 3.1. The previous discussion has been concerned with the energy interchange within the calorimeter assembly. A detailed study of the calorimeter response characteristics and the subsequent development of a data reduction model has been given. This model in conjunction with the aforementioned environment relations provides a means of determining the convection coefficient (assuming shock layer radiation is known).

The error in the reduced data represents an accumulation of the uncertainties in the temperature measurement and in predicting the sensor response, radiation, and sensor-environment interaction. These uncertainties can be minimized if appropriate design features are incorporated into the calorimeter. Desirable thermophysical characteristics which would enhance the data reduction are enumerated below and design features which promote each characteristic are delineated.



- Sensor Temperature Measurement
  1. Maximum Temperature Gradient,  $dT/d\theta$ 
    - a) low capacitance
    - b) minimum heat losses
    - c) high output thermocouple
  2. Good Sensor-Thermocouple Contact
    - a) welded thermocouple junction-sensor joint
    - b) compatible thermocouple-sensor thermal expansion coefficient
  3. Minimum Thermocouple Draw Down Effect (Conduction)
    - a) equal thermocouple-sensor thermal conductivities
    - b) horizontal mounting of thermocouple leads in sensor
    - c) minimum thermocouple diameter
  
- Sensor Response
  1. Minimum Radial Heat Leak (Minimum Radial Temperature Gradient)
    - a) sensor concentrically encased in a low conductivity sealant or
    - b) air gap between sensor and concentric guard; the guard side having a low emissivity coating and supporting tabs having a low thermal conductivity
    - c) equal capacitance per unit surface area of the sensor and guard (this could be accomplished by boring holes within the guard or increasing thickness of sensor).
  2. Minimum Axial Heat Loss
    - a) air gap - radiation shield sandwich arrangement
  3. Minimum Axial Temperature Gradient
    - a) maximum sensor thermal conductivity
    - b) minimum sensor thickness
    - c) maximum axial thermal guarding

- Shock Layer Radiation
  1. Isolate and Measure Shock Layer Radiation
    - a) cover calorimeter with an optically thin window
    - b) radiometer measurements, etc.
  
- Sensor-Environment Interaction
  1. Minimum Surface Temperature Variation (Minimum Reaction Rate Variation)
    - a) minimize radial temperature gradient (see above)
    - b) compatible calorimeter - ablator emissivity and effective capacitance.
  
  2. Minimum Calorimeter Protrusion
    - a) high calorimeter material porosity (equalize calorimeter and ablator erosion rates), or
    - b) stagger stacked calorimeters (expose new calorimeters before significant protrusion occurs) e.g.



- c) reduced abruptness of surface discontinuity, e.g.



In general, the proposed calorimeter configuration incorporates many favorable design characteristics. For example graphite for the sensor material is a particularly good choice with respect to reducing temperature gradients. The radiation shields are effective in reducing axial losses. The design also reflects a serious attempt to reduce radial heat losses through the use of concentric guard and insulator rings. It is evident from the previous discussions of the environment-ablator-calorimeter

interaction that certain design improvements are warranted. Consideration should be given to increasing the effectiveness of radial heat guarding; better insulation of the sensor should be possible employing a less complex configuration. Particular emphasis should be placed on reducing the calorimeter protrusion effect. This is one important phenomena which is not amenable to accurate analytical or experimental interpretation. Calorimetric measurements of the shock layer radiation is another critical problem which should be studied. Measurement errors, although not as critical, can also be reduced. For example, welding of the thermocouple-sensor junction (a compatible metal would have to be molecularly bonded to the graphite) would enhance the integrity of the temperature measurements.

A number of desirable design features and approaches have been indicated. In some cases they tend to conflict in promoting different favorable calorimeter characteristics. It is also evident that certain features are impractical from the fabrication standpoint. The ultimate design will represent a judicious trade-off between these considerations.

### 3.2.2 Asymptotic Calorimeter

Asymptotic calorimeters afford a relative simple means for measuring moderate heat fluxes. This instrument generates an emf which ideally is directly proportional to the heat input and its small time constant permits its application in highly transient environments. Since radiation and conduction losses are small, heat transfer occurs primarily in radial conduction through the disk and thus the heat flux-emf output can be theoretically predicted to first order accuracy. Calibration testing is conducted to provide corrections for the perturbations from ideal response arising from thermocouple conduction losses, thermophysical property variations, and manufacturing tolerances. The primary disadvantages of this instrument are the restriction to low surface temperatures (and consequently moderate heating rates), and the inherent parabolic surface temperature distribution. The latter effect, which causes difficulty in evaluating the convection coefficient when surface and recovery temperatures are comparable, is of

minor importance in the present situation (see Section 3.1.2.2). The magnitude of the surface temperature relative to the ablator's is what must be carefully considered here. In Apollo application the asymptotic calorimeter will be subjected to a rapid streamwise decay in heat flux as a result of the abrupt discontinuity in wall temperature experienced at the calorimeter edge. Since the theoretical predictions and calibration tests are based on uniform heating an appropriate correction must be made. Also since the temperature distribution is assumed to be quasi-steady possible perturbations to the theory arising in a highly transient environment should be examined.

In the following section the characteristic time constant for a representative asymptotic calorimeter (Fig. 3-11) is determined. The magnitude of the error in the heat flux attributable to a time lag is indicated. The temperature distribution associated with non-isothermal heating, specifically a step change in wall temperature, is analyzed. The differential equations describing the two-dimensional temperature distribution are solved to yield an explicit expression for the sensor output (center to edge temperature difference) in terms of the non-isothermal heating parameters. Finally a critique of the asymptotic calorimeter is given and suggestions are made as to its improvement.

#### Transient Response Characteristics

The time response associated with the instantaneous application of a constant heat flux was examined in Ref. 3.20. If the disk is considered thermally thin and the driving heat rate is independent of location the temperature distribution is described by the differential equation

$$\frac{\partial^2 T \left( \frac{r}{R}, \theta \right)}{\partial \left( \frac{r}{R} \right)^2} + \frac{1}{r/R} \frac{\partial T \left( \frac{r}{R}, \theta \right)}{\partial r/R} + \frac{R^2}{\alpha \delta T} q = \frac{R^2}{\alpha} \frac{\partial T \left( \frac{r}{R}, \theta \right)}{\partial \theta} \quad (3.143)$$

with the boundary conditions

$$T(1, \theta) = \text{constant}$$

$$T(r/R, 0) = T(1, \theta)$$

$$\frac{\partial T(0, \theta)}{\partial r/R} = 0$$

$$q(\theta < 0) = 0 \quad q(\theta > 0) = \text{constant}$$

Solutions were presented in Ref. 3.20 giving the unaccomplished temperature change (percent of temperature rise remaining to its time infinite value) as a function of time. These results are applied to the present configuration using the following properties:

$$\text{Disk radius} = 0.130''$$

$$\text{Thermal diffusivity (constantan)} = 0.237 \text{ ft}^2/\text{hr (Ref. 3.21)}$$

It is found that after 1 second of heating the center temperature is within 4.1% of its final value. Conversely, the time is 1.44 seconds if the criterion of a one percent error is used.

These results may be easily extended to the case of a time varying heat flux. To a first order approximation the unaccomplished change in the temperature differential following a step change in heat flux  $q_i$  at  $\theta_i$  is given by

$$T(\theta, \infty) - T(\theta, \theta) = \frac{q_i R^2}{4KS} e^{-\frac{(\theta - \theta_i)}{K}} \quad (3.144)$$

where  $K$  is the time constant for the calorimeter. For the particular configuration being considered, Eq. (3.144) yields results in good agreement with the exact solution of Ref. 3.20 if the time constant  $K = .31$  second is used. Now this equation is extended to a transient heat pulse by representing the heat flux history with a series of steps, so that

$$T(\theta, \infty) - T(\theta, \theta) = \sum_j \frac{R^2}{4KS} q_j e^{-|\theta - \theta_j|/K} \quad (3.145)$$

or, in differential form

$$T(\infty) - T(\theta) = \int_0^{\tau} \frac{R^2}{4k\delta} \frac{dq}{d\theta} e^{-\frac{1}{k}(\tau-\theta)} d\theta \quad (3.146)$$

The time response error in the asymptotic calorimeter measurements is most easily indicated by assuming a linear heat flux variation,  $q = \text{constant} \times \theta$ . Equation (3.146) can then be integrated from 0 to  $\tau$  to yield

$$T(\infty) - T(\theta) = \frac{R^2 k - q}{4k\delta} \left[ 1 - e^{-\tau/k} \right] \quad (3.147)$$

or the percent error in the measured heat flux is

$$\text{ERROR} = 100 \times \frac{T(\infty) - T(\theta)}{T(\infty) - T(0)} = 100 \frac{k}{\tau} \left[ 1 - e^{-\tau/k} \right] \quad (3.148)$$

For a time of 5 seconds a 6.2% error is incurred but by the time of peak heating ( $\theta \approx 60$  seconds) the error has decayed to 0.5%. Although this error is probably of secondary importance relative to other possible perturbations it should be considered in assessing the accuracy of the measured heating rates. If possible, the disk material should be one with a large thermal diffusivity thereby reducing the time lag.

#### Non-isothermal Heat Flux Analysis

The streamwise variation in the heat flux resulting from a non-isothermal surface condition was discussed in Section 3.1.2.2. It was shown that for the asymptotic calorimeter, the temperature distribution may be treated as a single step change at the calorimeter edge. As a consequence of the discontinuity a rapid decay in the surface heat flux is experienced. Following is a solution for the temperature distribution in an asymptotic calorimeter accounting for this heating distribution. Coupling between the transpiration and non-isothermal effects is neglected to permit a tractable analysis.

For steady-state heat conduction on the sensing disc the heat balance on the thermal sensing area is given by

$$\frac{\partial^2 T}{\partial (r/R)^2} + \frac{1}{r/R} \frac{\partial T}{\partial (r/R)} + \frac{1}{(r/R)^2} \frac{\partial^2 T}{\partial \phi^2} + R^2 \frac{q(r/R, \phi)}{k \delta} = 0 \quad (3.148)$$

with the boundary condition at  $r = R$  of  $T = \text{constant}$ . The effect of a non-isothermal wall on the heating rate was discussed in Section 3.1.2.2.

The resultant heat rate is given by Eq. (3.131):

$$q\left(\frac{r}{R}, \phi\right) = \left(\frac{h}{h_0} \frac{h}{h_0}\right)_s \left[ (H_0 - H_U) + (H_U - H_2) \left\{ 1 - \left(\frac{s_2}{s}\right)^\beta \right\} \right]$$

where the effect of three-dimensional compressible flow is accounted for by coordinate  $s$ . Employing Eq. (3.116):

$$s \propto (x-d)^N$$

the expression for the heating rate may be approximated by

$$q\left(\frac{r}{R}, \phi\right) = q_U + h(H_U - H_2) \left(\frac{\gamma N R}{x_2 + R - d}\right)^\beta \left\{ \left[ 1 - \left(\frac{r}{R} \sin \phi\right)^2 \right]^{1/2} - \frac{r}{R} \cos \phi \right\}^\beta \quad (3.149)$$

or

$$q\left(\frac{r}{R}, \phi\right) = A + B f\left(\frac{r}{R}, \phi\right) \quad (3.150)$$

where

$$A = q_U = h(H_0 - H_U) \quad (3.151)$$

$$B = h(H_U - H_2) \left(\frac{\gamma N R}{x_2 + R - d}\right)^\beta$$

$$f\left(\frac{r}{R}, \phi\right) = \left\{ \left[ 1 - \left(\frac{r}{R} \sin \phi\right)^2 \right]^{1/2} - \frac{r}{R} \cos \phi \right\}^\beta \quad (3.152)$$

Therefore the heat balance, Eq. (3.148), becomes

$$\frac{\partial^2 T}{\partial (r/R)^2} + \frac{1}{r/R} \frac{\partial T}{\partial r/R} + \frac{1}{(r/R)^2} \frac{\partial^2 T}{\partial \phi^2} = -\frac{AR^2}{k\delta} - \frac{BR^2}{k\delta} f\left(\frac{r}{R}, \phi\right) \quad (3.153)$$

The solution to this equation will be linear in A and B. Therefore it can be solved by superimposing the solution to the following two separate problems:

Problem A

$$\frac{\partial^2 T}{\partial (r/R)^2} + \frac{1}{r/R} \frac{\partial T}{\partial r/R} + \frac{1}{(r/R)^2} \frac{\partial^2 T}{\partial \phi^2} + R^2 \frac{A}{k\delta} = 0 \quad (3.154)$$

with  $T(1, \theta) = \text{constant}$ . The solution to Eq. (3.154) is easily shown to be

$$T\left(\frac{r}{R}, \phi\right) - T\left(1, \phi\right) = \frac{AR^2}{k\delta} \left[ \frac{1 - (r/R)^2}{4} \right] \quad (3.155)$$

at  $r = 0$ ,

$$T\left(0, \phi\right) - T\left(1, \phi\right) = \left(\Delta T\right)_A = \frac{AR^2}{4k\delta} \quad (3.156)$$

Problem B

$$\frac{\partial^2 T}{\partial (r/R)^2} + \frac{1}{r/R} \frac{\partial T}{\partial r/R} + \frac{1}{(r/R)^2} \frac{\partial^2 T}{\partial \phi^2} + \frac{BR^2}{k\delta} f\left(\frac{r}{R}, \phi\right) = 0 \quad (3.157)$$

The solution to this problem is of the form

$$T\left(\frac{r}{R}, \phi\right) - T\left(1, \phi\right) = \frac{BR^2}{k\delta} g_1\left(\frac{r}{R}, \phi\right) \quad (3.158)$$

Of particular interest is the solution at  $r = 0$ ,

$$\Delta T_B = T\left(0, \phi\right) - T\left(1, \phi\right) = \frac{BR^2}{k\delta} g_1\left(0, \phi\right) = g_2\left(\frac{BR^2}{k\delta}\right) \quad (3.159)$$



Equation (3.157) is not readily amenable to analytic solution and therefore finite difference techniques have been used. A particular solution was obtained employing representative conditions. The temperature correction was obtained as a function of location and  $BR^2/kS$  for each flow regime (since  $f(r/R, \theta)$  differs for laminar and turbulent flow). The results of the numerical solutions are shown in Fig. 3-21 for the center of the sensing disc.

The solution to the general problem is then

$$\Delta T \left( \frac{r}{R}, \theta \right) = \frac{AR^2}{kS} \left[ \frac{1 - (r/R)^2}{4} \right] + \frac{BR^2}{kS} g_1 \left( \frac{r}{R}, \theta \right) \quad (3.160)$$

at  $r = 0$ ,

$$\Delta T = \Delta T_A + \Delta T_B \quad (3.161)$$

The heating rate distribution along the centerline of the sensing disc is shown in Fig. 3-22 for a representative temperature discontinuity in both laminar and turbulent flows. The corresponding temperature distributions are shown in Fig. 3-23. Comparison to the results for a constant heat rate over the disc is also indicated. The departure from a symmetric temperature distribution is not large for the case considered, but temperature levels are significantly changed. This is manifested in Fig. 3-21 as a linear dependence of the temperature correction on the heat flux parameter,  $BR^2/kS$ . As the relative sensor size is reduced the heat flux gradient is increased causing the position of peak temperature to move upstream. This slightly reduces the non-isothermal effectiveness and the slope of the correction curve in Fig. 3-21 decreases. The distortion in the heating rate and surface temperature and hence the temperature correction are greater for laminar flow than turbulent flow. The difference arises primarily from the smaller values of  $B$  for turbulent flow at the same environmental conditions.

The results presented in Fig. 3-23 at the center of the disc,  $r = 0$  were obtained using Fig. 3-21 and Eq. (3.156). Similar data were used to determine the perturbation at the other points along the centerline. At  $r = 0$  the non-isothermal wall effect results in an increase in wall temperature of 47% for laminar flow, but only 10% for turbulent flow for the conditions assumed. These perturbations would directly affect any heat rate predictions made from these temperature differences. If the non-isothermal wall effect is neglected,  $B = 0$ , then Eq. (3.161) reduces to Eq. (3.156), i.e., the heat rate is directly proportional to temperature difference. Thus the heat rate would be overpredicted by the same amount the temperature difference is perturbed. It is clear that a knowledge of the type of flow that exists at the calorimeter location is of fundamental importance in determining the error in the temperature difference.

The foregoing material provides the influence of the non-isothermal wall conditions for an ideal calorimeter. In practice, complete reliance on the theoretical results is not permissible. Calibration test data must be utilized to determine the corrections to ideal behavior. Assume that the test data which are obtained for uniform heating may be conveniently put in the form

$$q = \Delta T \frac{4k\delta}{R^2} f_c \quad (3.162)$$

where  $f_c$  is a correction factor which is a weak function of  $\Delta T$ . Then, it should be permissible to use the same correction factor,  $f_c$ , in predicting calorimeter temperature response or reducing heat rates for the non-uniform flight heating situation. For example,

$$\Delta T = \frac{q_u R^2}{4k\delta f_c} + q_2 \left( \frac{BR^2}{k\delta f_c} \right) \quad (3.163)$$

#### Asymptotic Calorimeter Critique

Perturbations to the ideal calorimeter heat input-temperature response relation have been considered. It has been shown that the effect of a

time lag is of secondary importance and means have been developed to account for a streamwise decay in heat flux resulting from the discontinuity in surface temperature. Any additional perturbing phenomena are assumed to be included in the experimental calibration curve for the instrument. Since a perfect empirical accounting for these effects is impossible, the design of calorimeter should be such as to either reduce uncertainties or enhance the validity of the correction procedures. Accordingly, the following suggestions are made as to the design and calibration of the asymptotic calorimeter:

- The disc material should have a maximum thermal diffusivity compatible with the structural and emf output requirements; the purpose being to reduce the time lag.
- The disc-body-thermocouple lead material combination should be reviewed with the intent of obtaining the maximum emf output for a given heat input, i.e., minimum disc thermal conductivity in conjunction with maximum thermoelectric effect are desirable.
- The design should seek to reduce internal perturbations to ideal response. Desirable are:
  - a) minimum conduction losses to thermocouple (minimum wire diameter)
  - b) isothermal body (high conductivity, high capacity)
  - c) minimum radiation losses to cavity (high reflectivity surface)
- Calibration testing should be comprehensive enough to verify that internal perturbations are properly accounted for.

The calorimeter design and calibration should also be commensurate with its basic objective of obtaining the cold wall convection coefficient and/or shock layer radiation. Accordingly, many of the suggestions made with regard to the slug calorimeter are applicable here. Of particular significance are the types of installations that may be used to reduce the effect of gage protrusion.

The non-isothermal correction employed for the asymptotic calorimeter neglected perturbations arising from upstream mass injection. The effect of transpiration on the non-isothermal correction was studied in Section 3.1.2.2; the results indicate that the heating rate attributable to a step surface temperature change would be increased the order of 20%. Effort should be made to include this second order effect in the interpretation of calorimeter data. Since the analysis procedures employed in this investigation are necessarily approximate, further calibration testing to corroborate the theoretical corrections for perturbations in the surface heat flux (i.e. mass blowing, non-isothermal wall, etc.) is warranted.

### 3.3 DATA INTERPRETATION PROCEDURES

The foregoing sections have developed procedures for predicting the environment experienced by and response of heat flux sensors mounted in an ablative heat shield. Application of these procedures will enable pre-flight prediction of sensor measurements for subsequent comparison with flight test data. Such comparisons would provide early insight to the validity of theoretical predictions of the entry heating. However, they would provide no direct indication of the magnitude of heating differences. In order to obtain such information, the environment and response prediction techniques must be inverted. Specifically, a procedure for operating on the sensor response data to produce environmental information is desired. Ideally, this procedure would yield the radiation and convection heating histories given only the sensor output data and trajectory conditions.

This section first examines the sensor response predictions for the slug and asymptotic calorimeters. The intent is to delineate the important environment-gage interactions and to illustrate the application of the analysis procedures. Then the inverse problem is discussed with respect to the slug calorimeter. The basic procedure of obtaining non-blowing convection coefficients from the reduced heat input, being identical for both calorimeters. Finally, the possible uncertainties in response predictions and data reduction are discussed.

It is evident that the environment-calorimeter interactions are more complex for the capacitance type gage. Accordingly, the methods for describing the thermal response of and reducing data from a slug calorimeter have been coded for computer use. Three separate program have been developed:

- CALORIMETER RESPONSE
- SENSOR DATA REDUCTION - I
- SENSOR DATA REDUCTION - II

The formats for these programs are described in Volume II.

In the following section typical calorimeter temperature histories, generated for the slug calorimeter by the CALORIMETER RESPONSE program and by hand for the asymptotic type are discussed. The inverse problem of obtaining the convection coefficient from the sensor temperature history is illustrated by presenting results from SENSOR DATA REDUCTION. The aerothermal environment considered corresponds to that obtained on the Apollo forebody during entry along Trajectory 1. The particular calorimeter configurations studied are described in Fig. 3-11. (Numerical definition of the calorimeter characteristics may be obtained by referring to Table 3.1.

### 3.3.1 Prediction of Calorimeter Temperature Response

#### Slug Calorimeter

The governing equations describing the temperature response of a slug calorimeter were described previously. Given the physical constants of the system, the aerothermal environment and the response of the upstream ablator, the problem is completely specified. A summary of the pertinent equations is given in Volume II, and physical constants are given in Table 3.1. It should be noted that the guard capacitance is increased by 26% to account for conduction losses. For a different configuration this value may not be applicable and a new constant must be determined from a detailed solution for the thermal response characteristics. The ablator and environment histories necessary for the CALORIMETER RESPONSE program may be manually input or directly generated by the TRANSIENT program (see

Volume II. The following solution constitutes only a representative example in that first order methods were used in determining the Apollo aerothermal environment.

The heat flux to a calorimeter located at the geometric center of the Apollo forebody is shown in Fig. 3-2. The time variations of the parameters influencing the various shield-sensor interactions are presented in Fig. 3-24. The corresponding temperature and surface erosion histories are depicted in Figs. 3-25 and 3-26, respectively. The assumed occurrence of transition at about 66 seconds with associated abrupt changes in heating level is useful in illustrating the adaptability of the program. The upper curve in Fig. 3-2 represents the heat which would be transferred to the calorimeter in the absence of any interactions. Effects of the different interacting phenomena on the heat flux are indicated by the separations between the several curves. It is seen that mass injection drastically reduces the incident flux while the other phenomena exert a relatively minor influence. The implication is that the convective heating experienced by the calorimeter and heat shield are very nearly the same.

Guard and sensor temperatures are shown to agree closely, both initially lag behind the ablator temperature. Following peak heating, calorimeter temperature exceeds that of the upstream surface. Accordingly, the non-isothermal effect increases the heat flux prior to peak heating and decreases it thereafter.

Surface erosion results emphasize the need to examine further the effect of protuberances. With the occurrence of turbulent heating and the associated higher erosion rates for the ablator, the gage protrusion may be the order of 0.10 in. The thickness reduction of the sensor and guard are not particularly significant; the capacitances are changed only slightly. Surface combustion is seen to have a relatively significant effect, increasing the heat flux particularly at later times. The late time behavior results from the cessation of upstream surface combustion and the attendant

rise in oxygen concentration near the surface. With oxygen availability increased, sensor surface erosion is maximized. At very late times, the sensor surface temperature may be expected to drop to the point where reaction rates become very slow and surface combustion effectively ceases.

The influence of calorimeter location on the sensor temperature response may be inferred from Fig. 3-27. It is evident that transition is the dominant phenomenon. The sensor located at  $x/R_{\max} = 0.26$  experiences only laminar heating and initially will exhibit the highest temperature for the three locations. With the advent of turbulence at  $x/R_{\max} = 0.86$  the temperature levels for the two forward positions quickly become comparable. At distances further downstream the duration of turbulent heating is increased as evidenced by the increased magnitude of the sensor temperature at  $x/R_{\max} = 1.61$ .

It is necessary to qualify the validity of the results for times in excess of 120 seconds. Between approximately 120 seconds and 250 seconds, the TRANSIENT solutions are unavailable as a result of the low heating rates. A correct prediction of the calorimeter response requires judicious interpolation in specifying the upstream ablator conditions. The same comment also applies to the inverse problem of determining the heat transfer coefficient discussed later. The values presented in this time interval should not be considered reliable but only indicative of the trend.

The results presented here demonstrate the adaptability as well as the applicability of the calorimeter response program. The methods incorporated in the code are considered as realistic as the state-of-the-art permits.

#### Asymptotic Calorimeter

Methods for determining the differential temperature response of an asymptotic calorimeter accounting for perturbations to the ideal response were developed in Section 3.2.2. The temperature or emf output is given by Eq. (3.163).

$$\Delta T = \frac{q_u R^2}{k \delta f_c} + g_2 \left( \frac{BR^2}{k \delta f_c} \right) \quad (3.163)$$

The term  $g_2(BR^2/k \delta f_c)$  accounts for the non-uniform heating resulting from the discontinuity in surface temperature distribution. This temperature correction is presented in Fig. 3-21.  $f_c$  is a calibration constant accounting for miscellaneous phenomena which further perturb the ideal response. The procedure for determining the temperature response is similar to that employed for the slug calorimeter. The problem is completely specified once the physical characteristics of the sensor and the thermal response of the upstream ablator are known; in particular  $h_o$ ,  $h/h_o$ , and  $H_u$  are required. The enthalpy of the calorimeter body ( $H_2$ ) is assumed invariant and equal to its initial value. Since the heating rates will be relatively low, if the calorimeter body is large compared to the disc, this cold junction temperature will change very little during a reentry heating period of the order of 300 seconds. For environments which do not permit this assumption, it is necessary to know the surface temperature of the body either by direct measurement or by analytical determination.

Consideration is given here to the asymptotic calorimeter shown in Fig. 3-11. It is assumed that this instrument is located on the windward afterbody at  $x/R_{\max} = -0.79$ , measured from the stagnation point. The ablator response is evaluated using the CHIRP program discussed in Ref. 2.123. The manufacturer's specifications on this instrument yield

$$f_c \frac{k \delta}{R^2} = 0.833 \times 10^{-2} \frac{BTU}{FT^2 SEC ^\circ F} \quad (3.164)$$

The pertinent physical constants are given in Table 3.1. Applying the aforementioned procedure gives the differential temperature response curves presented in Fig. 3-28. For comparative purposes the ideal response associated with the upstream heating is also shown. It is seen that the non-isothermal effect contributes as much as 20 degrees to the calorimeter



output. For late times the percent deviation is increased as the step change in surface enthalpy becomes comparable with the enthalpy potential.

### 3.3.2 Prediction of Environment

The primary objective of a calorimeter is the measurement of the unperturbed heat flux given only the sensor temperature history. Ideally, both the non-blowing convection coefficient and shock layer radiation are desired. Unfortunately, reduction of the sensor temperature data provides only the net heat transfer to the surface. Further information can be obtained only if either the convective or radiative heat flux can be specified. For the early Apollo trajectories (entry at about orbital velocity) radiation will be relatively low. It has therefore been assumed throughout this study that radiation can be specified with sufficient accuracy to be subtracted from the net heat transfer. The unperturbed convection coefficient is then backed out employing correction methods developed previously. The various instrument-environment interactions which occur at the surface and internally preclude a closed form procedure for reducing the non-ablating convective coefficient from the temperature response of the sensor. A simple recourse is to evaluate the heat flux at a given time employing the current sensor temperature-time derivative and the results obtained at the preceding time step. In such a procedure an accurate solution requires a small time step. The calorimeter response program described in Volume II has been inverted employing such a procedure to enable evaluation of the convection coefficient. The inverted code is entitled SENSOR DATA REDUCTION. Response of the upstream ablator may be dealt with in two ways and thus two forms of the program have evolved:

- I. The program is coupled to TRANSIENT
- II. The ablator response is input

Program I is employed when insufficient information concerning the response of the ablator is available. This program provides a predicted history of shield ablation as well as the heat transfer coefficient. If sufficient quality flight data is obtained then SENSOR DATA REDUCTION II will yield the most credible interpretation of the sensor response.

Inputs to the program include the physical and thermal characteristics of the calorimeter and the smoothed temperature history of the sensor. Also required is the history of the shock layer radiation, total enthalpy, local pressure and enthalpy and the critical Reynolds number. Evaluation of the convection coefficient at a given time is determined from a thermal balance on the slug using the current sensor temperature gradient with all heating rate dependent quantities obtained from the previous time step. Having determined the convection coefficient the procedure is identical to that employed in CALORIMETER RESPONSE and TRANSIENT resulting in new conditions for the guard and upstream ablator. One simplification was made in the code: the local transpiration effect for the sensor is taken to be the same as for the upstream ablator.

An example result from this program is provided in Fig. 3-29 which depicts the unperturbed heat transfer coefficient ( $h_0$ ). The sensor temperature history corresponds to that shown in Fig. 3-27. The time step was 0.5 seconds for this example and yielded only a small error between the calculated and exact (corresponding to the values used to generate the temperature history) convection coefficients. One point should be emphasized concerning use of this program; it is imperative that the input sensor temperature be devoid of fluctuations; i.e., it must be smoothly varying. Crude representation of the temperature history was found to cause irregularities in the heat flux response.

### 3.3.3 Influence of Uncertainties

It is of practical interest to assess the possible uncertainties associated with predicting the calorimeter response or conversely in backing out the convection coefficient from measured temperatures. Accordingly, consideration is given to the influence of perturbations in the ablation model and in the transpiration effect. The following two limiting situations were studied:

1. the heat absorption capability of the pyrolysis gases is half the nominal value

2. the transpiration effect is represented by the upper limit in uncertainty (see Fig. 2-66).

Halving their heat absorption capability is to roughly represent the possible uncertainty in the thermophysical properties employed in describing the ablation mechanism. This is accomplished by decreasing the sensible and chemical enthalpy rise by a factor of 2 in computing the pyrolysis rate. Consequently the injection of pyrolysis gases increases by about 40%. Conversely perturbation of the transpiration effect constitutes an upper limit in ablation gas cooling of the convective heating.

The TRANSIENT and CALORIMETER RESPONSE programs were altered to incorporate these perturbations and the previous problem was rerun. The resulting perturbations in the sensor convective heating and temperature response are depicted in Figs. 3-30 and 3-31, respectively. Reduction of the transpiration effect is seen to increase the convective heating and consequently the sensor temperature. The opposite effect is evidenced when the heat absorption capability is perturbed. These trends are primarily attributable to the transpiration effect and the resulting heat transfer coefficient. It is interesting to observe that these relatively large perturbations have a rather small effect on the calorimeter temperature. The implication is that the interrelations between the various ablation phenomena tend to damp out any perturbations. Of more practical importance is the spread between the temperature curves, demonstrating the necessity of obtaining flight data with minimal distortion.

The SENSOR DATA REDUCTION - I program was used with the nominal pyrolysis gas enthalpy and transpiration effect data to generate convection coefficients from the perturbed temperature histories (Fig. 3-31). The environment prediction is presented in Fig. 3-29. The spread in the results is indicative of the uncertainty in the convection coefficient as reduced from flight data. For example, assume the nominal mass transfer cooling curve (Fig. 2-66) is overly optimistic and flight data yielded the upper curve in Fig. 3-21. Reduction of this temperature history would result in overprediction of the convection coefficient.

### 3.4 SUMMARY

The objective of this work has been to provide reliable procedures for reducing inflight calorimeter measurements. For this purpose, a comprehensive review of the factors affecting heat sensor environment and performance has been conducted and analysis techniques have been developed. Attention was devoted to determining the relation between the convective heating experienced by the shield and the sensor, and to describing the associated thermal response of representative calorimeters. It was assumed that shock layer generated radiation was either of minor importance or could be defined separately from theoretical or experimental means. Emphasis was placed on deriving general methods readily adaptable to various aerothermal environments and calorimeter configurations. In assessment of the aerodynamic heating, consideration was given to the following coupling effects between the upstream shield and calorimeter: upstream mass injection and surface combustion, and discontinuous surface temperature variation. The thermal exchange within the gages was carefully examined and subsequently a relatively simple numerical model was evolved which properly accounts for all significant modes of energy storage and transfer. The study was culminated in the presentation and discussion of calorimeter thermal response for a typical Apollo reentry situation.

#### 3.4.1 Conclusions

##### Calorimeter Environment

Techniques have been developed to account for the effects on sensor convective heating of streamwise variations in surface temperature and discontinuities in surface mass injection and reactivity. These methods are based on approximate solutions to the non-similar boundary layer equations. The convection heating was described by treating each interaction phenomena independently. Examination of the coupling between mass injection and the non-isothermal correction shows this to be a reasonable approximation for the slug calorimeter.

For abrupt changes in surface temperature the convection coefficient decays exponentially from an initial value which may approach infinity to an undisturbed value far downstream. The variation in the transpiration effect following a step change in surface injection is less severe as it decays from its upstream to downstream value. When the calorimeter dimensions are small relative to the upstream flow length little error is incurred if the upstream transpiration effect is employed in evaluating the sensor heating. An approximate approach was employed in assessing the effect of a discontinuity in surface reactivity on the downstream combustion rate.

Surface erosion is evaluated assuming the combustion rate is either:

(1) diffusion controlled following a step change in the surface oxygen concentration, or (2) reaction rate controlled with a maximum wall concentration of oxygen. Both solutions provide upper limits and thus the one yielding the lowest value provides the most realistic result.

The influence of gage protrusion resulting from differential surface recession would appear to be significant. Unfortunately this effect is not amenable to analytical interpretation and consequently it was neglected.

#### Calorimeter Performance

The thermal interchange within the slug calorimeter was carefully examined for a typical thermal environment. Effects which perturb the ideal response (the ideal calorimeter either stores the heat input in a uniform temperature sink or reradiates it) were delineated. It was shown that for the slug calorimeter of interest, axial heat losses, axial and radial temperature gradients, and temperature measurement errors are minor. Perturbations resulting from radial conduction and radiation are significant. Modifications which would enhance calorimeter performance were delineated. These included means for minimizing radial heat loss and possible techniques for reducing calorimeter protrusion effects.

A simple, two-capacitance thermal model of the complex slug calorimeter was devised in which guard-insulation conduction losses are accounted for

by using an effective capacitance. The model is expected to provide a reliable and efficient means for reducing temperature data.

The ideal asymptotic calorimeter generates an emf in direct proportion to the net heat input. Experimental calibration of this device yields a proportionality constant which accounts for perturbations in the thermophysical properties of the instrument. Perturbations arising from non-uniform, transient heating which are not accounted for in calibration testing were theoretically examined. The time lag for the calorimeter investigated is of secondary importance.

Non-isothermal heating resulting from the step change in surface temperature occurring at the shield-sensor interface will significantly distort the sensor temperature distribution. Accordingly, procedures were developed to account for this effect in interpreting the calorimeter output.

#### Data Interpretation Procedures

The results of this study yielded an analytic procedure for describing the relation between the aerothermal environment and calorimeter response. Applying these methods in a forward manner yields the thermal response of the calorimeter given the basic environmental conditions. Inversion of the procedure results in a means for flight data interpretation. For the slug calorimeter the relevant equations were coded for digital computer application.

The analysis procedures describing the thermal response of the slug and asymptotic calorimeters were applied for a representative Apollo reentry situation. For a slug calorimeter the dominant environment-sensor interaction is the transpiration effect; discontinuities in surface temperature and reactivity exert a minor influence. Gage protrusion becomes significant as the surrounding heat shield erodes. When the protrusion is small, the heat rate sensed by the slug calorimeter is very nearly that experienced by the ablator. The magnitude of the non-isothermal and transpiration

effects are comparable in perturbing the response of the asymptotic calorimeter. The discontinuity in surface temperature causes roughly a 20% change in output at peak heating and larger changes at later times. The influence of uncertainties in the transpiration effect and ablation model on interpretation of the flight measurements were indicated by exercising the data reduction program for the slug calorimeter. In particular, conservative limits on the transpiration effectiveness and the heat absorption capability of the gases were employed. The influence of these uncertainties on the reduced, unperturbed convection coefficient is significantly attenuated as a result of the interrelationship between the ablation phenomena.

### 3.4.2 Recommendations

#### Calorimeter Environment

- Experimentally determine the influence of gage protrusion on local heat transfer for environmental conditions of interest.
- Theoretically study the effect of gaseous ablation products on the downstream heat transfer.
- Develop fully-coupled, numerical (finite difference) solutions of the boundary layer equations for more accurate assessment of effects of non-similar boundary conditions.
- Devise calorimetry techniques for accurately distinguishing between radiation and convection heat transfer.

#### Calorimeter Design

- Reduce radial heat losses in the slug calorimeter. Experimentally measure the value of the contact resistances.
- Design and/or install calorimeter in such a manner as to reduce the protuberance effect.
- Validate theoretical model of slug calorimeter performance by comparing prediction against calibration test data.

### Data Interpretation Procedures

- o Code equations for asymptotic calorimeter for digital computer use. The non-isothermal correction for the asymptotic calorimeter should be extended to include coupling of the transpiration effect.

### 3.5 REFERENCES

- 3.1 Kratsch, K. M., Hearne, L. F., and McChesney, H. R., Theory for the Thermophysical Performance of Charring Organic Heat-Shield Composites, LMSC 803099, 2-60-63-7, 18 October 1963
- 3.2 Pallone, A., Nonsimilar Solutions of the Compressible-Laminar Boundary-Layer Equations with Applications to the Upstream Transpiration Cooling Problem, J. Aerospace Sci., Vol. 28, 449-456, June 1961
- 3.3 Woodruff, L. W., A Study of Discontinuous Mass Transfer Utilizing the Boundary Layer Integral Equations, Boeing Rpt D2-23556, September 1964
- 3.4 Rubesin, M. W., and Inouye, M., A Theoretical Study of the Effect of Upstream Transpiration Cooling on the Heat-Transfer and Skin-Friction Characteristics of a Compressible, Laminar Boundary Layer, NACA TN 3969, May 1957
- 3.5 Howe, J. T., Some Finite Difference Solutions of the Laminar Compressible Boundary Layer Showing the Effects of Upstream Transpiration Cooling, NASA Memo 2-26-59A, February 1959
- 3.6 Hartnett, J. P., Eckert, E. R. G., Birkebak, R., and Sampson, R. L., Simplified Procedures for the Calculation of Heat Transfer to Surfaces with Non-Uniform Temperatures, WADC Tech Rpt 56-373, December 1956



- 3.7 Reynolds, W. C., Kays, W. M., and Kline, S. J., Heat Transfer in the Turbulent Incompressible Boundary Layer II - Step Wall-Temperature Distribution, NASA Memo 12-2-58W, December 1958
- 3.8 Rubesin, M. W., An Analytical Investigation of the Heat Transfer Between a Fluid and a Flat Plate Parallel to the Direction of Flow Having a Stepwise Discontinuous Surface Temperature, M.S. Thesis, U. of California, Berkeley, 1945
- 3.9 Eckert, E. R. G., Introduction to the Transfer of Heat and Mass, McGraw-Hill Book Co., Inc., 1950
- 3.10 Rubesin, M. W., The Effect of an Arbitrary Surface Temperature Variation Along a Flat Plate on the Convective Heat Transfer in an Incompressible Turbulent Boundary Layer, NACA TN 2345, 1951
- 3.11 Chung, P. M., Effect of Localized Mass Transfer Near the Stagnation Region of Blunt Bodies on Hypersonic Flight, NASA TN D-141, May 1960
- 3.12 Chung, P. M., Liu, S. W., and Mirels, H., Effect of Discontinuity of Surface Catalycity on Boundary Layer Flow of Dissociated Gas, Int. J. Heat Mass Transfer, Vol. 6, 193-210, 1963
- 3.13 Phillips, R. L., A Summary of Several Techniques Used in the Analysis of High Enthalpy Level, High Cooling Ratio Turbulent Boundary Layer on Blunt Bodies of Revolution, GM-TM-194, September 1957
- 3.14 Masters, J. L., and S. Stein, Effect of an Axial Cavity on the Temperature History of a Surface Heated Slab, Review of Scientific Instruments, Vol. 27, 1965

- 3.15 Beck, J. V., and Hurdwicz, H., Effect of Thermocouple Cavity on Heat Sink Temperature, ASME Journal of Heat Transfer, February 1960
- 3.16 Burnett, D. R., Errors in Transient Temperature Measurements Due to Conduction Along Thermocouple Wires, LMSC TXN/308, 16 June 1960
- 3.17 Chin, J. H., Effect of Uncertainties in Thermocouple Location on Computing Surface Heat Fluxes, ARS Journal, February 1962
- 3.18 Collins, A., IBM 709 Arbitrary Node Temperature Prediction Program, LMSC Interdepartmental Communication, TIAD/188, August 1960
- 3.19 Goldsmith, A., Waterman, T. E., and Hirschhorn, H. J., Handbook of Thermophysical Properties of Solid Materials, The MacMillan Co., New York, 1961
- 3.20 Sheppard, T. D., The Determination of the Time Constant of an Asymptotic Calorimeter when the Heat Flux Variation Across the Surface is Small, LMSC Interdepartmental Communication, TIAD/341, March 1962
- 3.21 Eckert, E. R. G., and Drake, R. M., Heat and Mass Transfer, McGraw-Hill Book Co., New York, 1959

## NOTATION

A	area; constants
a,b,c,	constants, Eq. 3.25
B	blowing parameter, Eq. 3.29; constants
B'	blowing parameter, Eq. 3.92
$C_{\perp}$	capacitance, Eq. 3.138
C, $C_0$	compressibility constants, Eq. 3.14
$c_p$	specific heat at constant pressure
$C_f$	skin friction coefficient
d	surface distance parameter, Eq. 3.116
D	thermocouple diameter
e	temperature measurement error
$\mathcal{F}$	radiation interchange factor, Eq. 3.140
Fo	Fourier number
f	non-isothermal parameter for an arbitrary surface temperature distribution, Eq. 3.77
f'	non-isothermal parameter for a step change in surface temperature, Eq. 3.71
$f_c$	asymptotic calorimeter correction, Eq. 3.157
h	heat transfer coefficient
H	enthalpy
I	total enthalpy ratio, Eq. 3.14
k	forward reaction rate constant; conductivity
$K_i$	mass concentration
K	arbitrary constant
L	surface distance to temperature discontinuity
Le	Lewis number
$\dot{m}$	mass injection rate
M	molecular weight
N	surface distance parameter, Eq. 3.116
q	heat flux rate
Q	heat flux
$Q_c$	heat of combustion of carbon

Pr	Prandtl number
r	radial coordinate
R	radius; resistance, Eq. 3.139
s	transformed surface distance, Eq. 3.14
$\dot{s}$	surface recession rate
St	Stanton number
T	temperature
t	transformed coordinate normal to surface, Eq. 3.14
U,V	transformed components of velocity parallel and normal to surface
u,v	components of velocity parallel and normal to surface
x	surface distance from stagnation point
y	distance normal to surface
$\alpha$	proportional; flow constant, Eq. 3.42; thermal diffusivity
$\beta$	flow parameter, Eq. 3.102
$\gamma$	flow parameter, Eq. 3.102
$\delta$	sensor thickness
$\Gamma$	the Gamma function
$\epsilon$	surface emissivity; geometric index
$\zeta$	similarity coordinate, Eq. 3.55
$\theta$	momentum thickness, Eq. 3.20; time
$\mu$	viscosity
$\nu$	kinematic viscosity
$\xi$	normalized distance, $s/s_0$ ; integration variable
$\rho$	density
$\sigma_{SB}$	Stefan-Boltzmann constant
$\sigma$	flow parameter, Eq. 3.43
$\tau$	transformed shear stress, Eq. 3.20
$\vartheta$	dimensionless enthalpy profile, Eq. 3.49; angle

#### Subscripts

a	air
a,b	integration variables
C	carbon

Ch char  
 D region downstream of a surface discontinuity  
 e boundary layer edge  
 G guard  
 GS effective area for radiation interchange  $G \rightarrow S$   
 i species  
 k discontinuous wall concentration effect  
 N nitrogen  
 O oxygen  
 PG pyrolysis gas  
 r radiation; recovery  
 s sensor  
 sw shock layer radiation  
 t total conditions  
 T non-isothermal effect  
 U region upstream of all surface discontinuities  
 w wall  
 O with zero injection; at surface discontinuity; stagnation  
 1,2 geometric indicies

Superscripts

$\bar{\quad}$  average; assumes similarity conditions  
 $\sim$  elemental

Table 3.1  
 ASSUMED CALORIMETER'S THERMOPHYSICAL CONSTANTS

Properties	Slug Calorimeter		Asymptotic Calorimeter Sensor
	Sensor	Guard	
Radius	$1.04 \times 10^{-2}$	$2.08 \times 10^{-2}$	$1.08 \times 10^{-2}$
Surface Area	$3.41 \times 10^{-4}$	$9.95 \times 10^{-4}$	
Volume	$1.82 \times 10^{-6}$	$7.41 \times 10^{-6}$	
Capacitance Correction	1.0	1.26	
Radiation Interchange Area	$3.38 \times 10^{-4}$	$3.52 \times 10^{-4}$	
Density (Graphite)	112	112	
Emissivity (Graphite)	0.8	0.8	
Contact Resistance	$\infty$	$\infty$	
Thermal Diffusivity (Constantan)			.237
Laminar Distance Transformation Parameters			
	$x/R_{\max}$	0.26	0.86
d		0	0
N		3.17	3.0
			1.61
			-0.79
			0
			0.531

**FIGURE 3-1**  
**CALORIMETER - ENVIRONMENT INTERACTION**

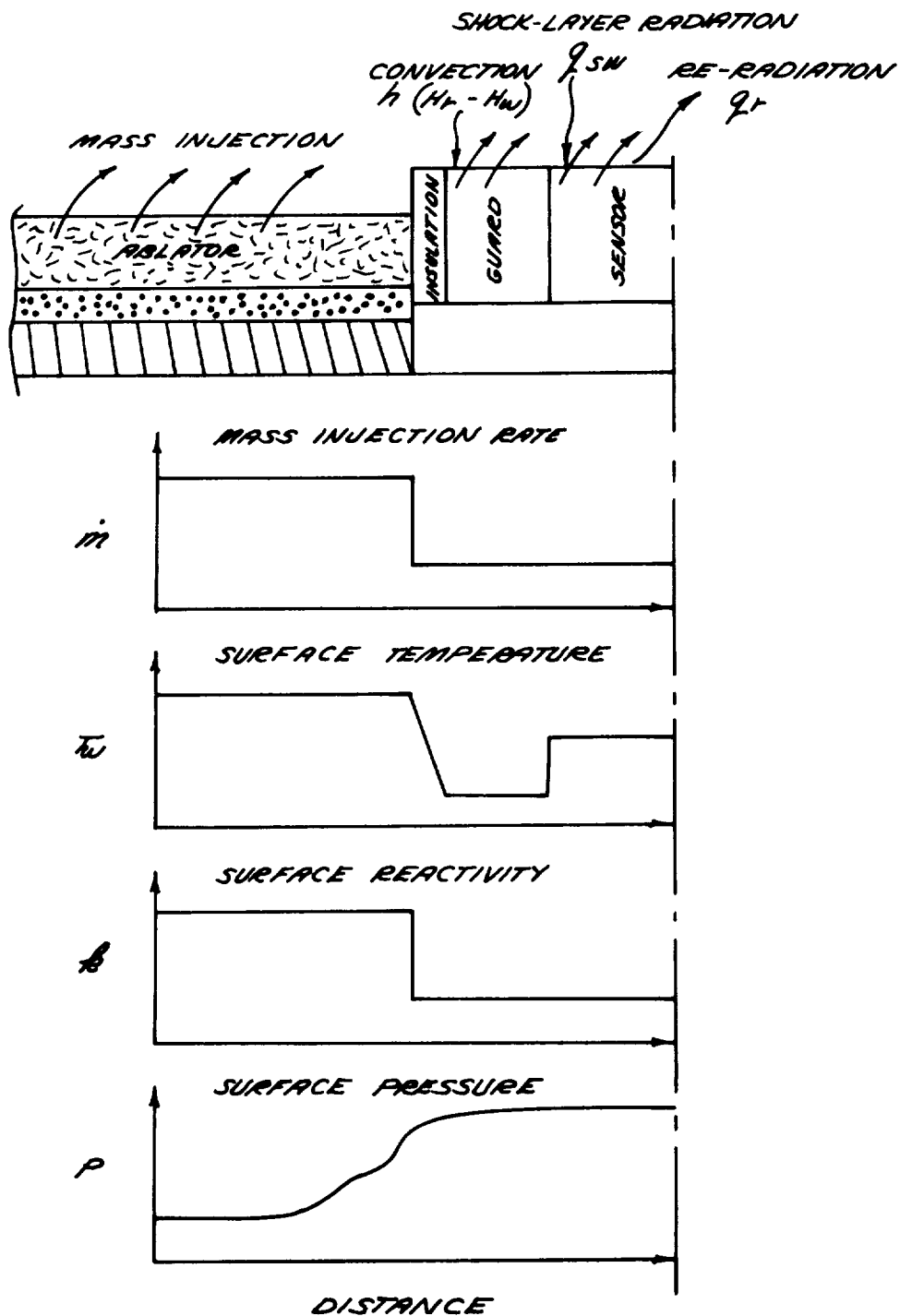


FIGURE 3-3

HEAT TRANSFER TO GROUND SENSOR

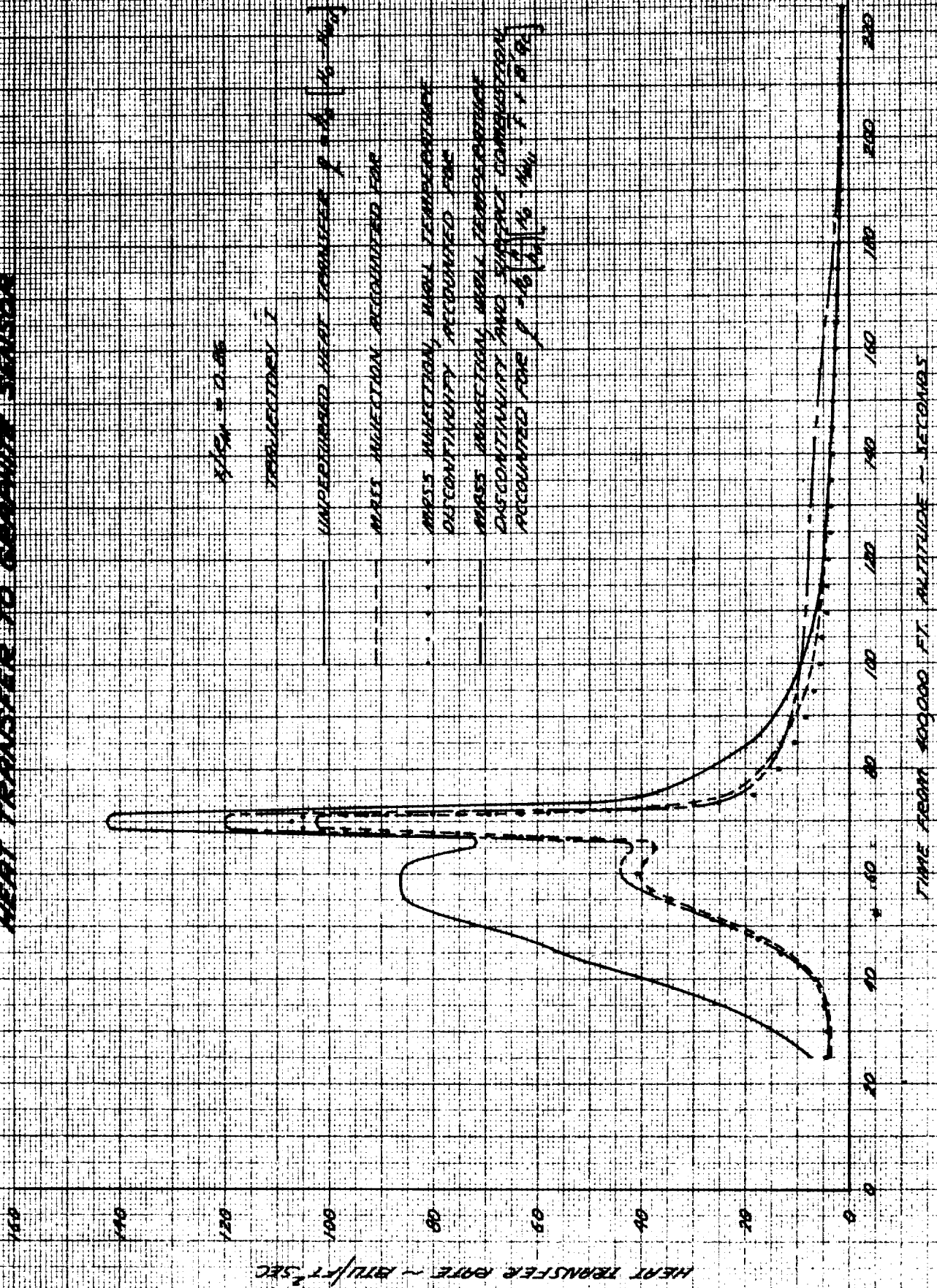
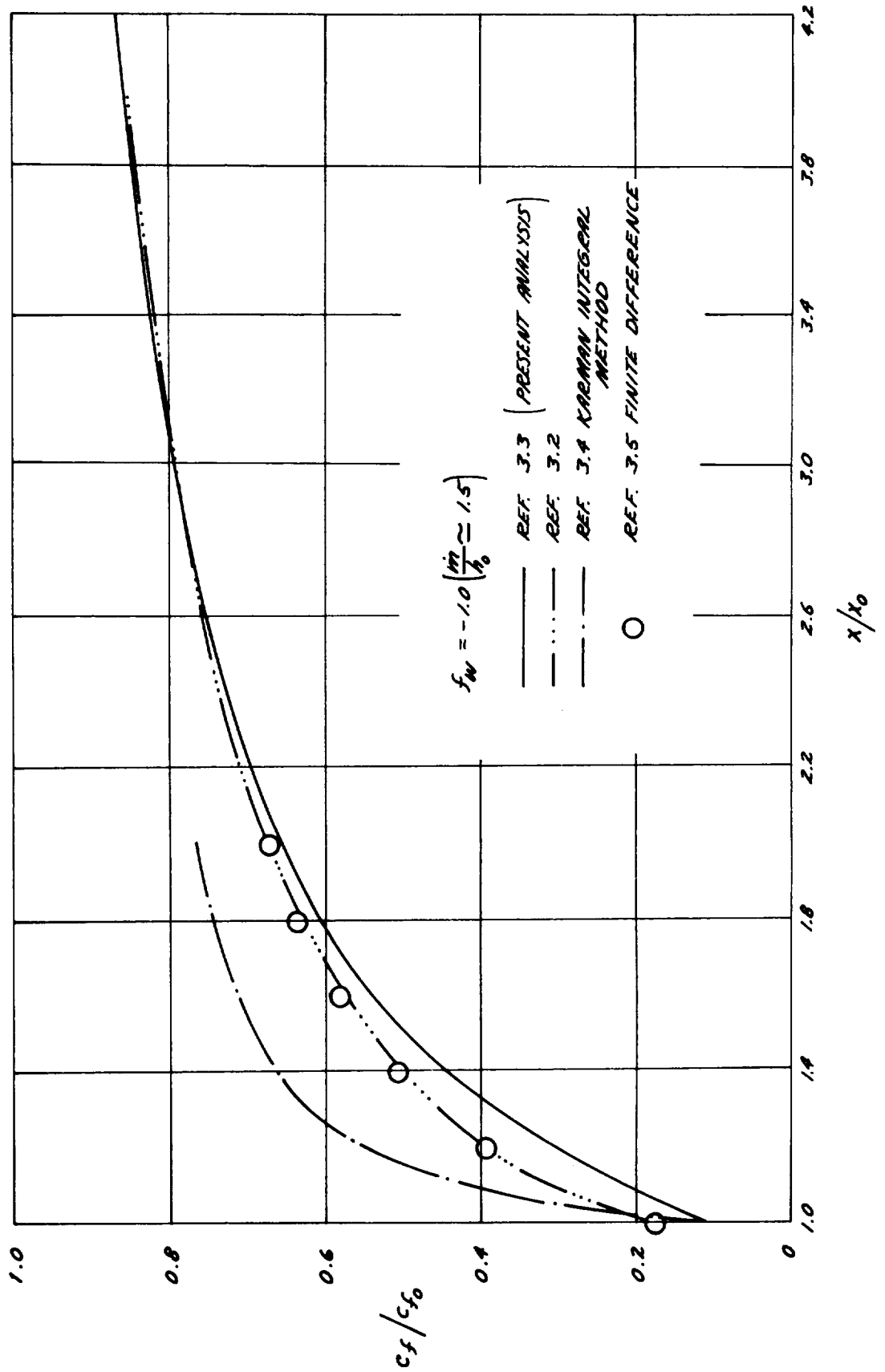




FIGURE 3-3

DECAY OF THE LAMINAR SKIN FRICTION REDUCTION DOWNSTREAM OF THE TRANSPIRATION REGION



**FIGURE 3-4**

**DECAY OF THE LAMINAR HEAT TRANSFER  
REDUCTION DOWNSTREAM OF THE  
TRANSPIRATION REGION-COMPARISON  
WITH EXACT SOLUTION**

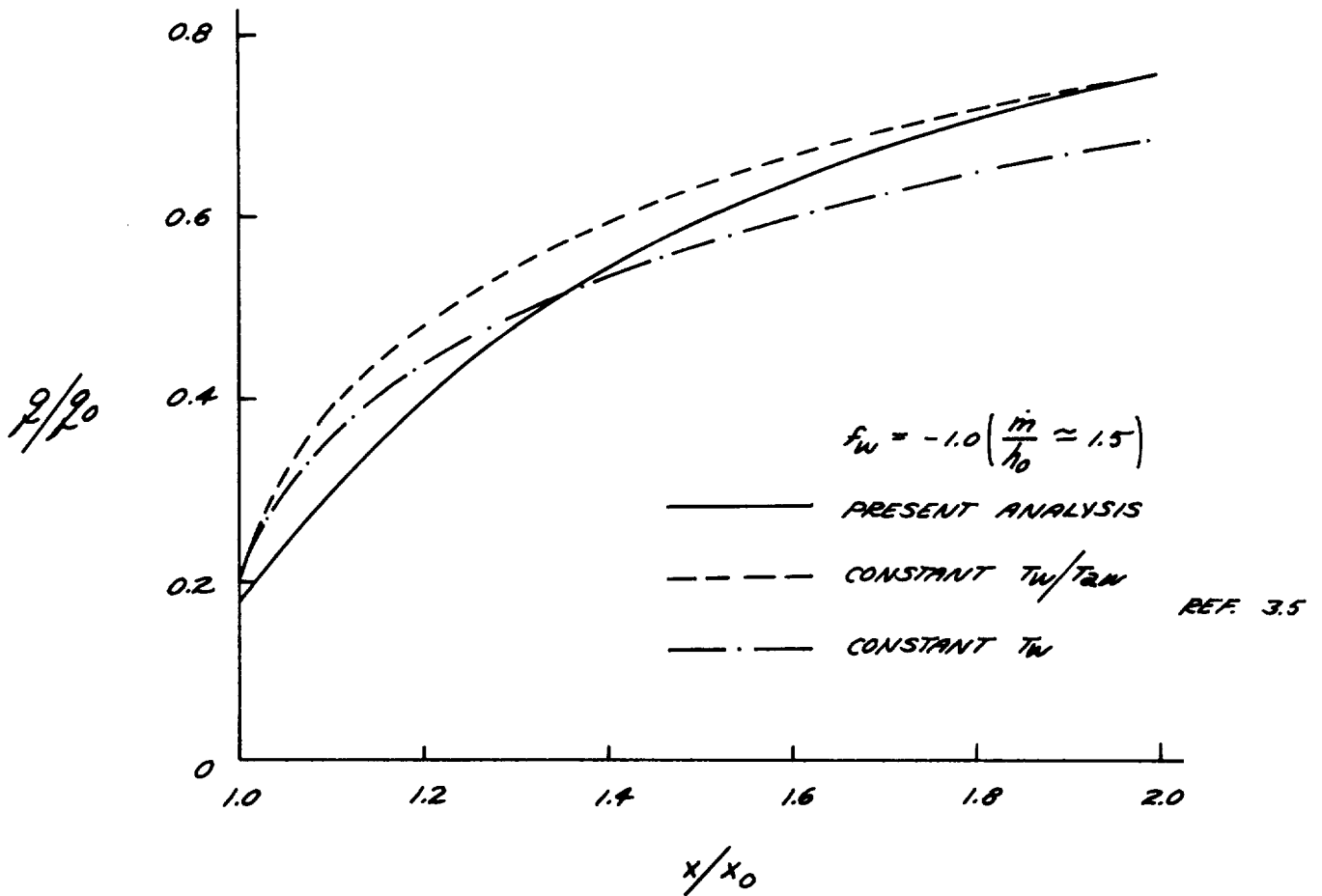
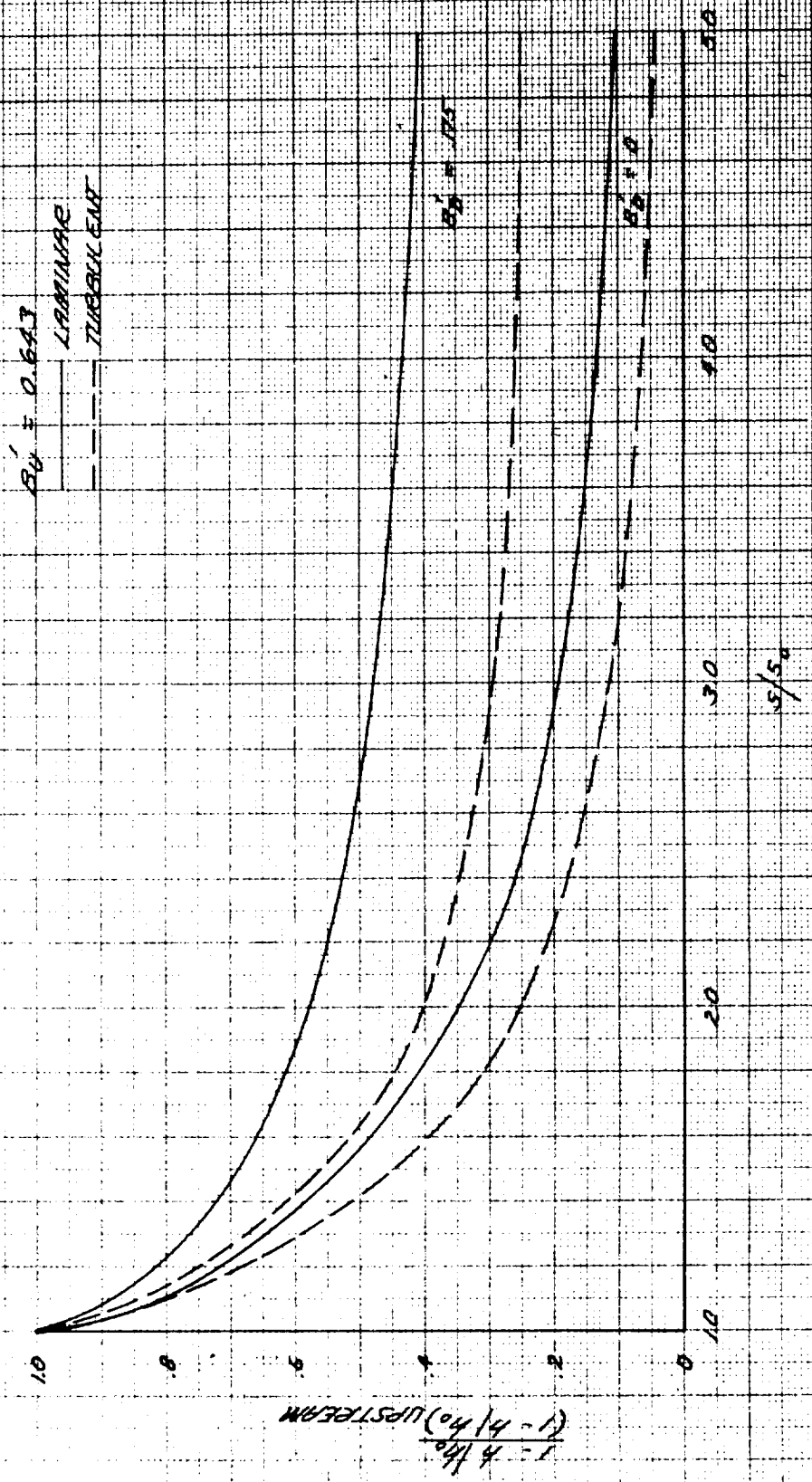
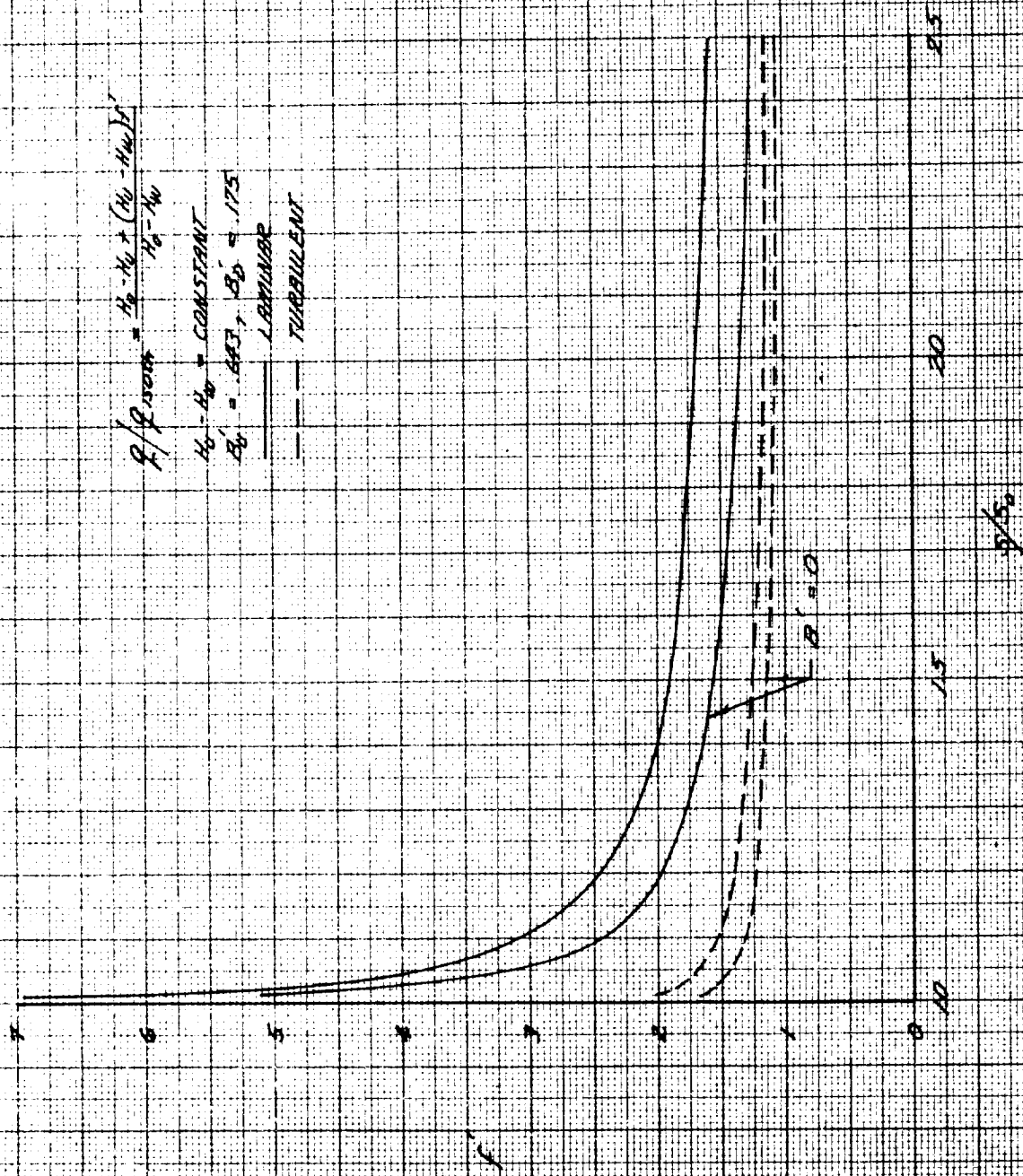


FIGURE 3-5  
 INFLUENCE OF UPSTREAM INJECTION ON THE DOWNSTREAM HEAT TRANSFER

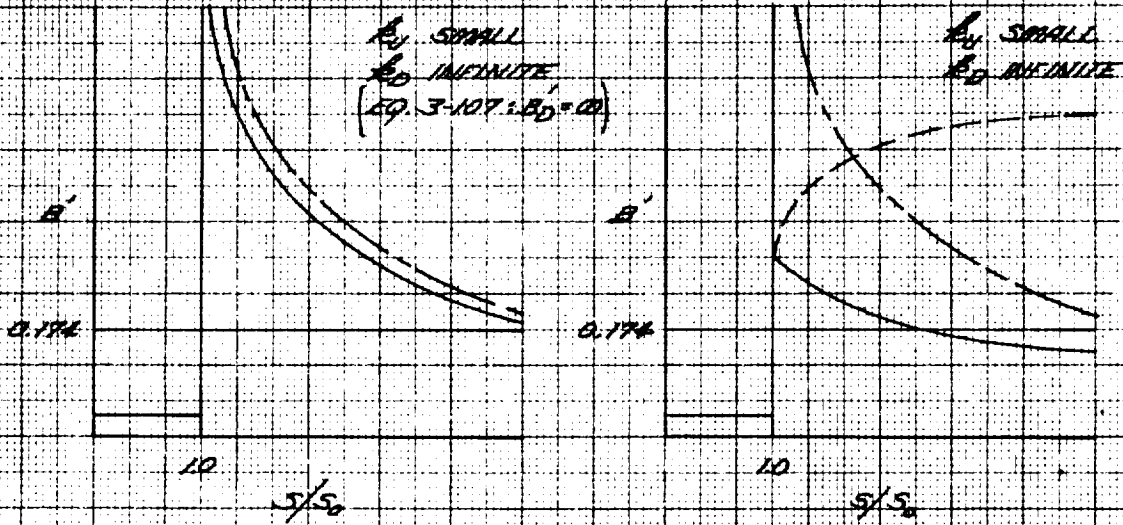


**FIGURE 3-6**  
**INFLUENCE OF UPSTREAM INJECTION ON NON-ISOTHERMAL EFFECT**



9/5

**FIGURE 3-7**  
**QUALITATIVE COMPARISON OF ACTUAL & APPROXIMATE COMBUSTION RATES**



—— ACTUAL  
 - - - - EQ. 3.100 (DIFFUSION LIMITED)  
 - - - - EQ. 3.107 (REACTION RATE CONTROLLED)

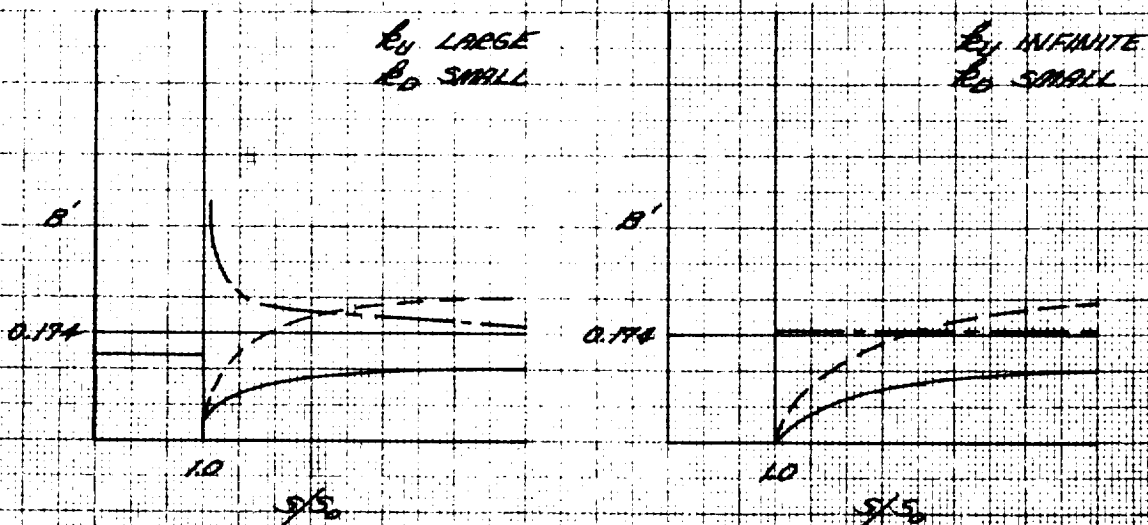
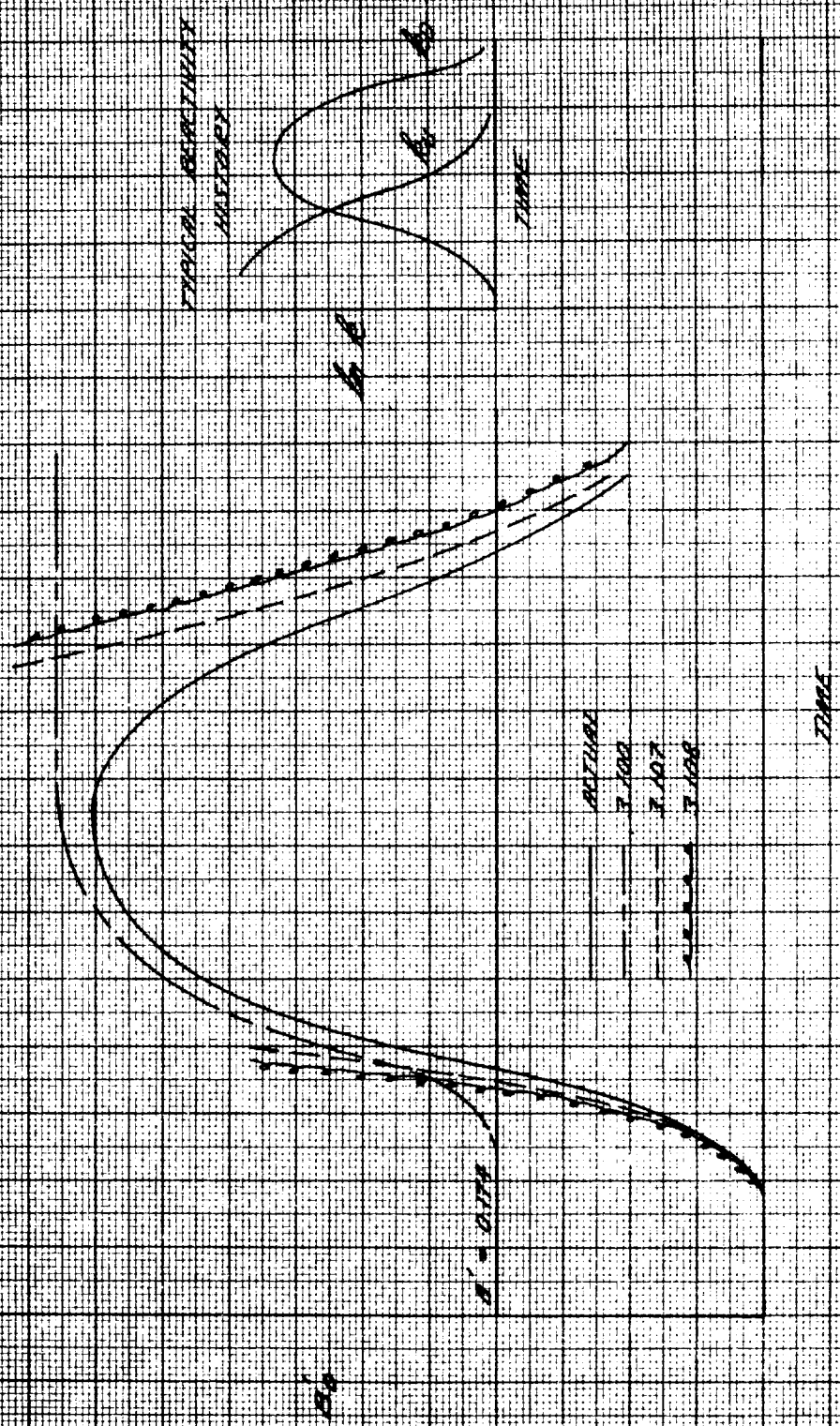


FIGURE 3-8  
 INFLUENCE OF REACTION RATE DISCONTINUITY ON SUBCARRIER  
 COMBUSTION

1973 = CONSTANT



Prepared	NAME <i>cjl</i>	DATE	LOCKHEED MISSILES & SPACE COMPANY A GROUP DIVISION OF LOCKHEED AIRCRAFT CORPORATION	Page	TLMP	PERM
Checked			TITLE	Model		
Approved				Report No.		

**FIGURE 3--9**  
**CALORIMETER CHARACTERISTICS**

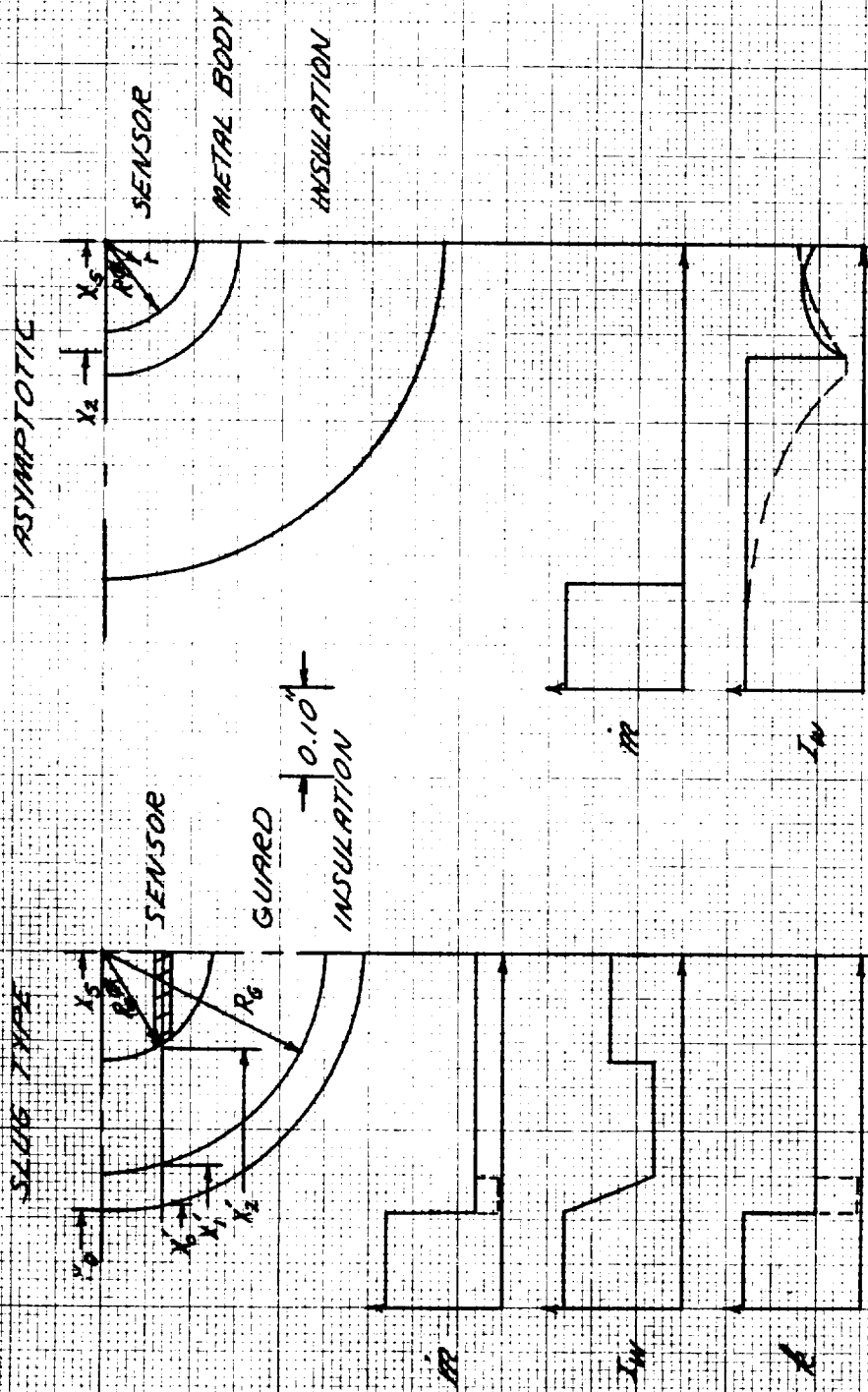
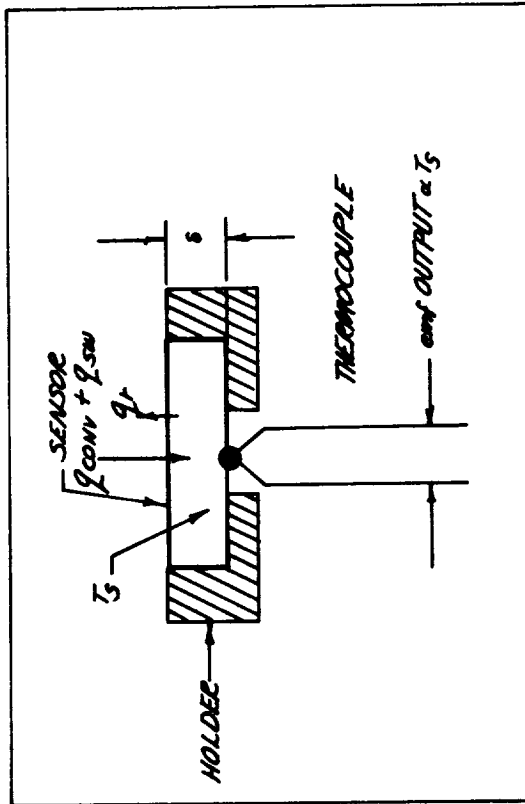


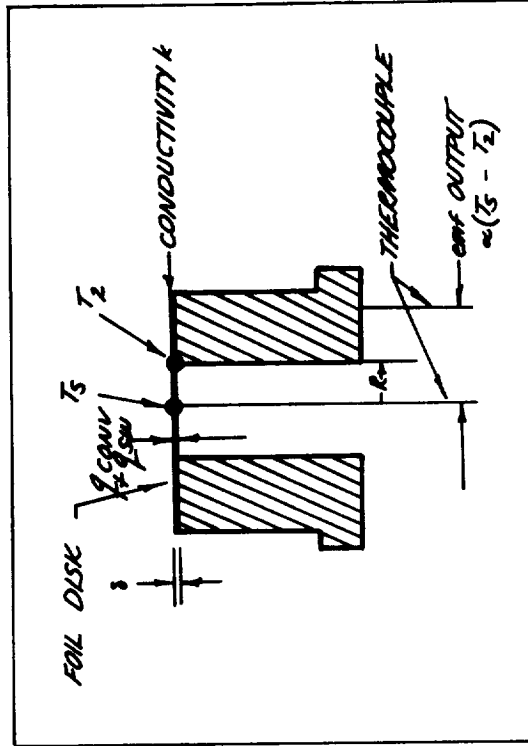
**FIGURE 3-10**  
**IDEAL AEROTHEMAL HEAT RATE SENSORS**

CAPACITANCE TYPE CALORIMETER



$$q_{net} = \rho c_p \delta \frac{dT_s}{dt} + q_r$$

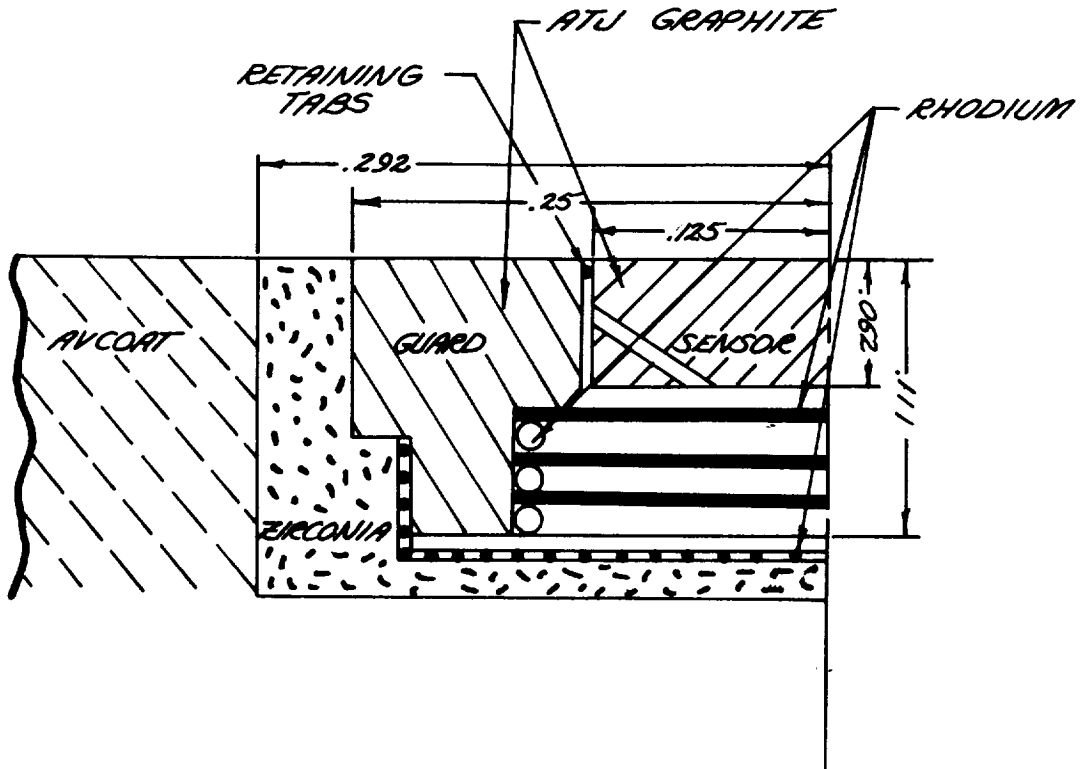
ASYMPTOTIC TYPE CALORIMETER



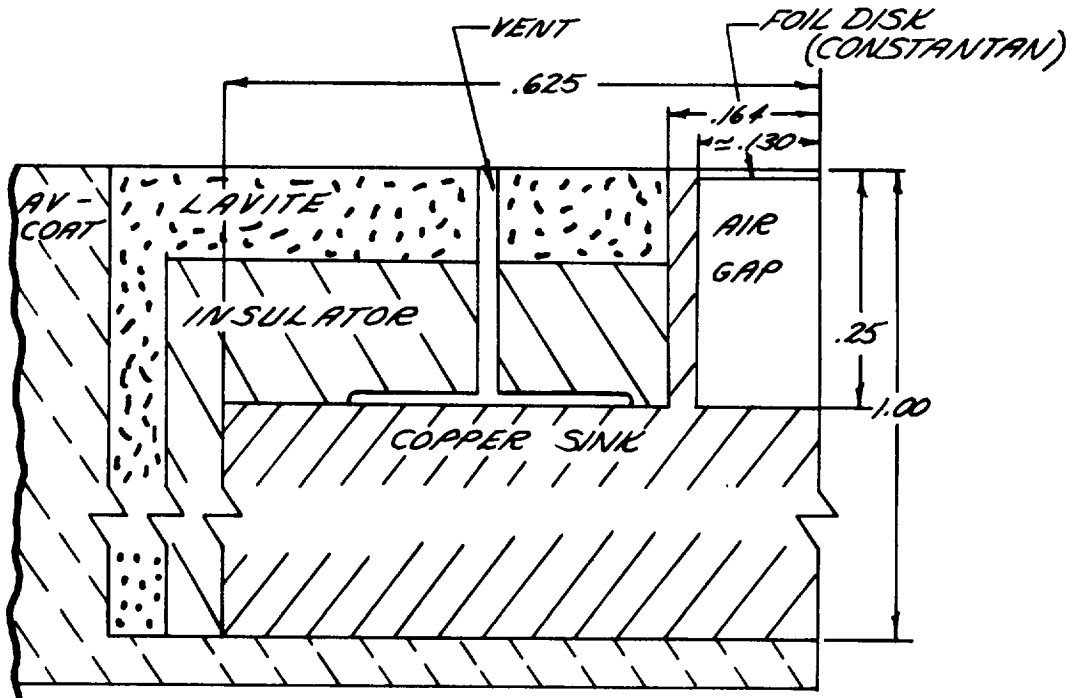
$$q_{net} = \frac{4h\delta}{\pi^2} (T_s - T_2)$$



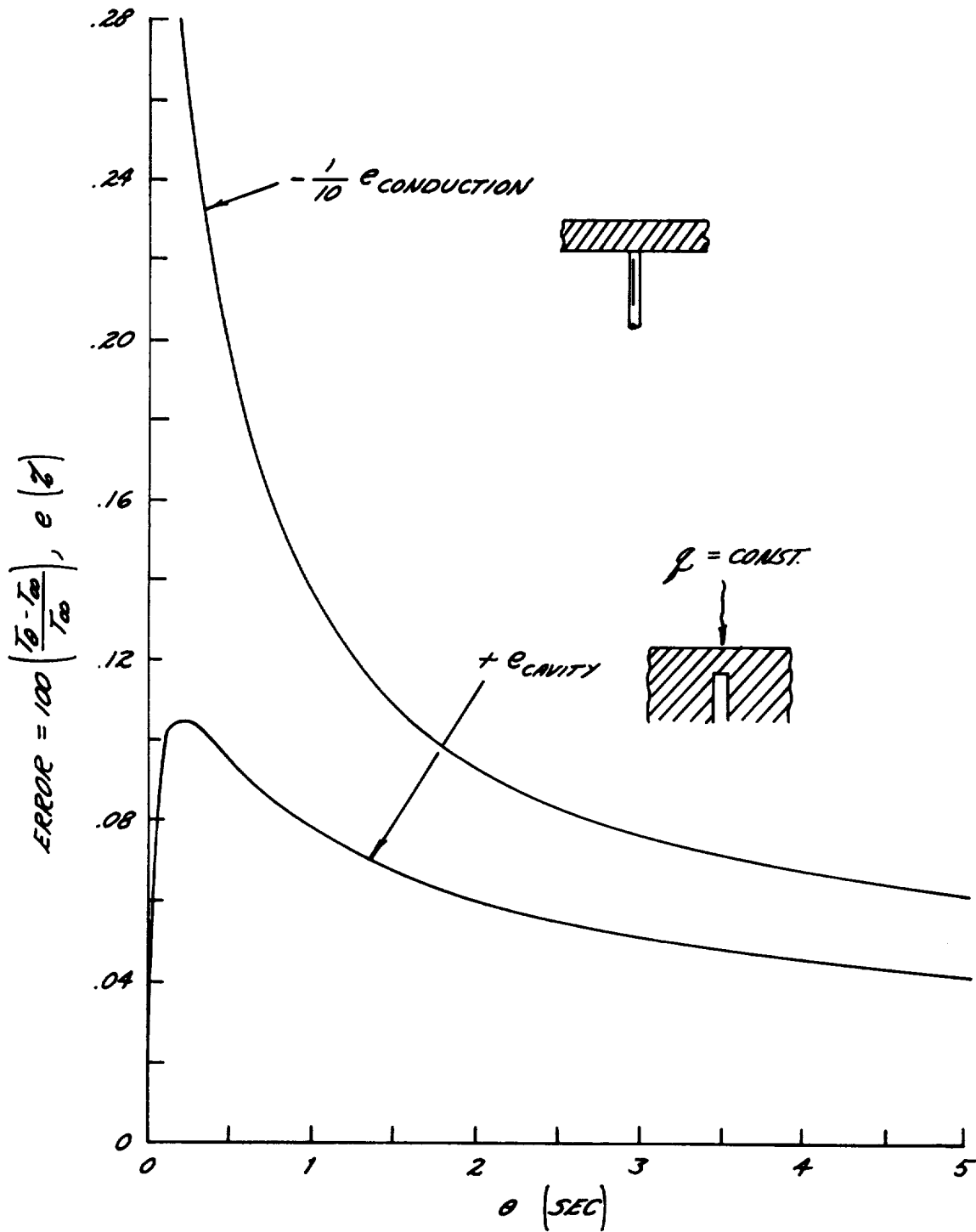
**FIGURE 3-11**  
**SLUG CALORIMETER**



**ASYMPTOTIC CALORIMETER**



**FIGURE 3-12**  
**TEMPERATURE MEASUREMENT DISTURBANCES**



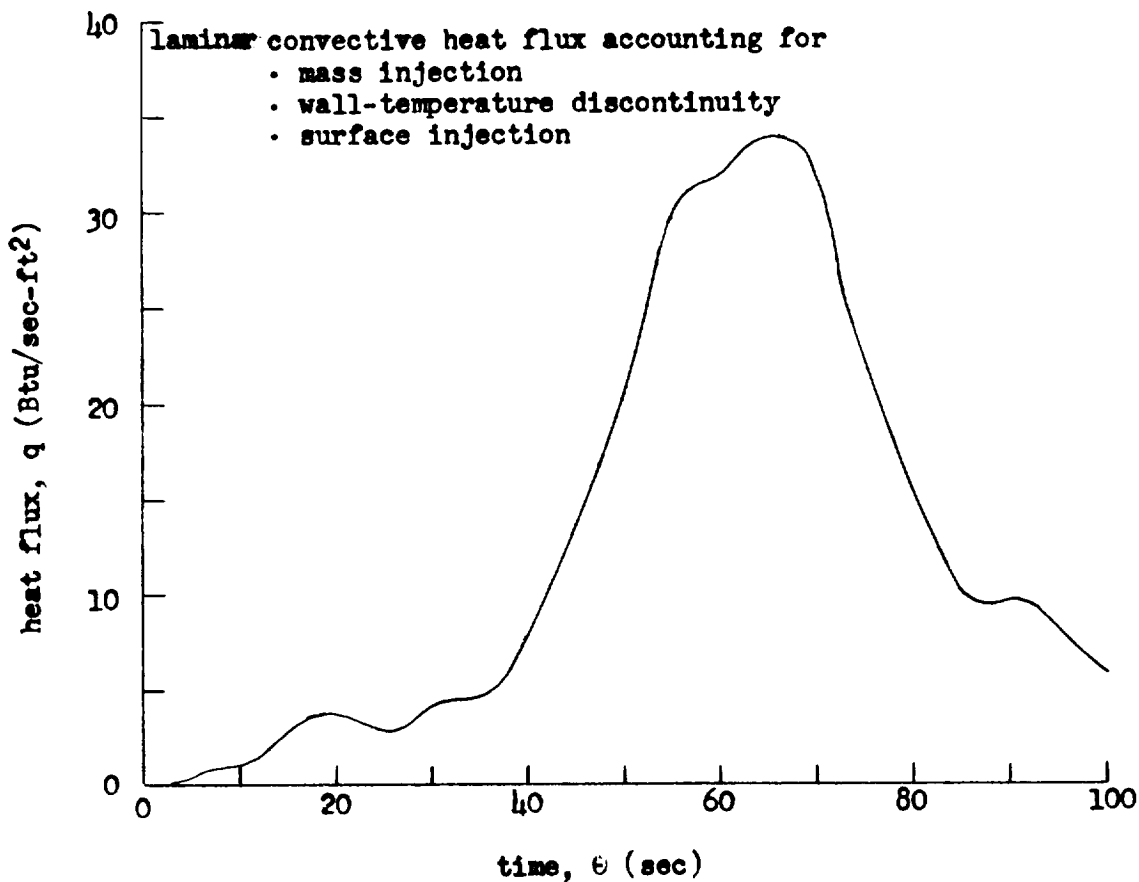
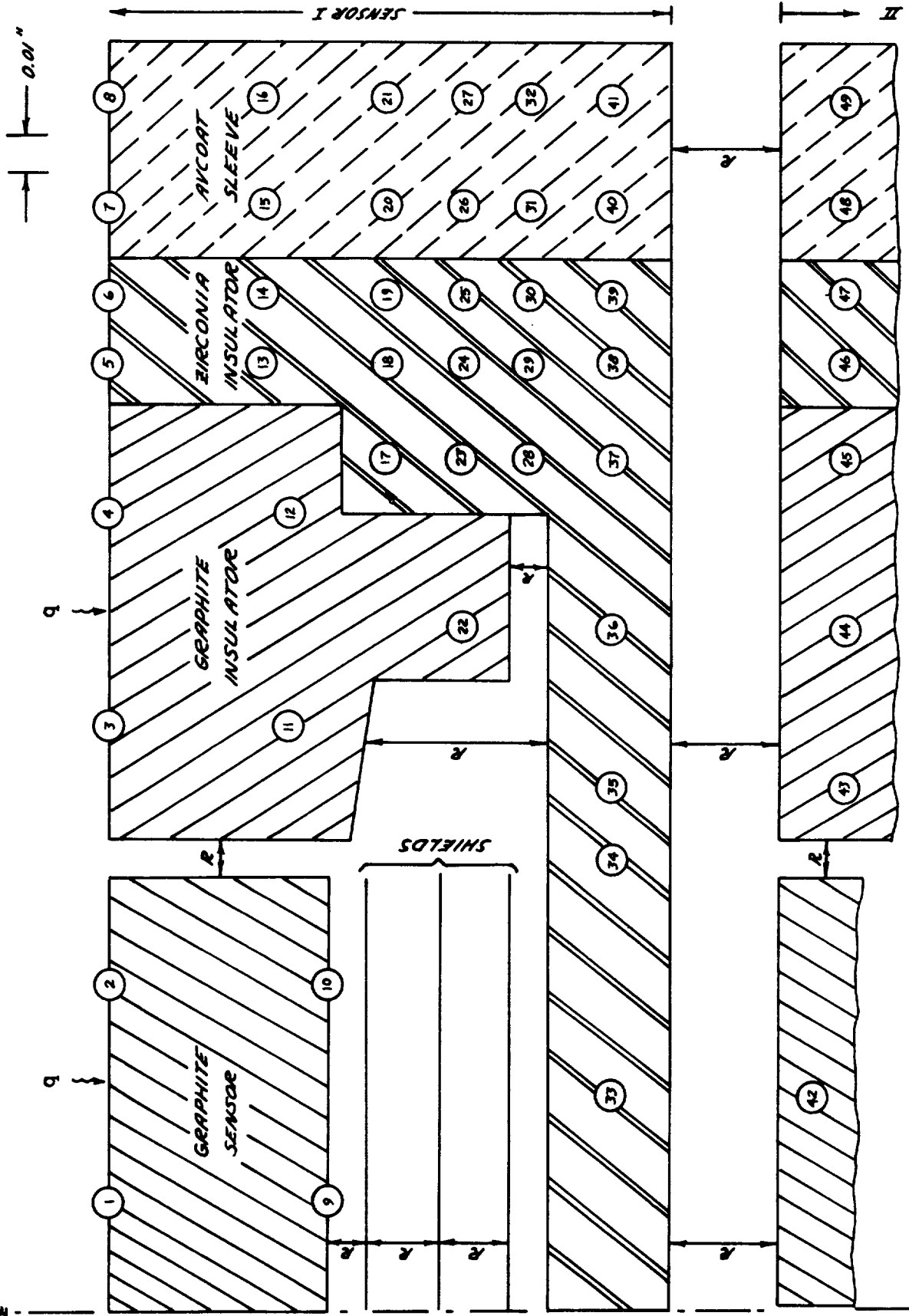


Fig. 3-13 Corrected heat-flux history for calorimeter study input.

Fig. 3-14 Calorimeter geometry and principal temperature calculation points.



R = radiation boundary

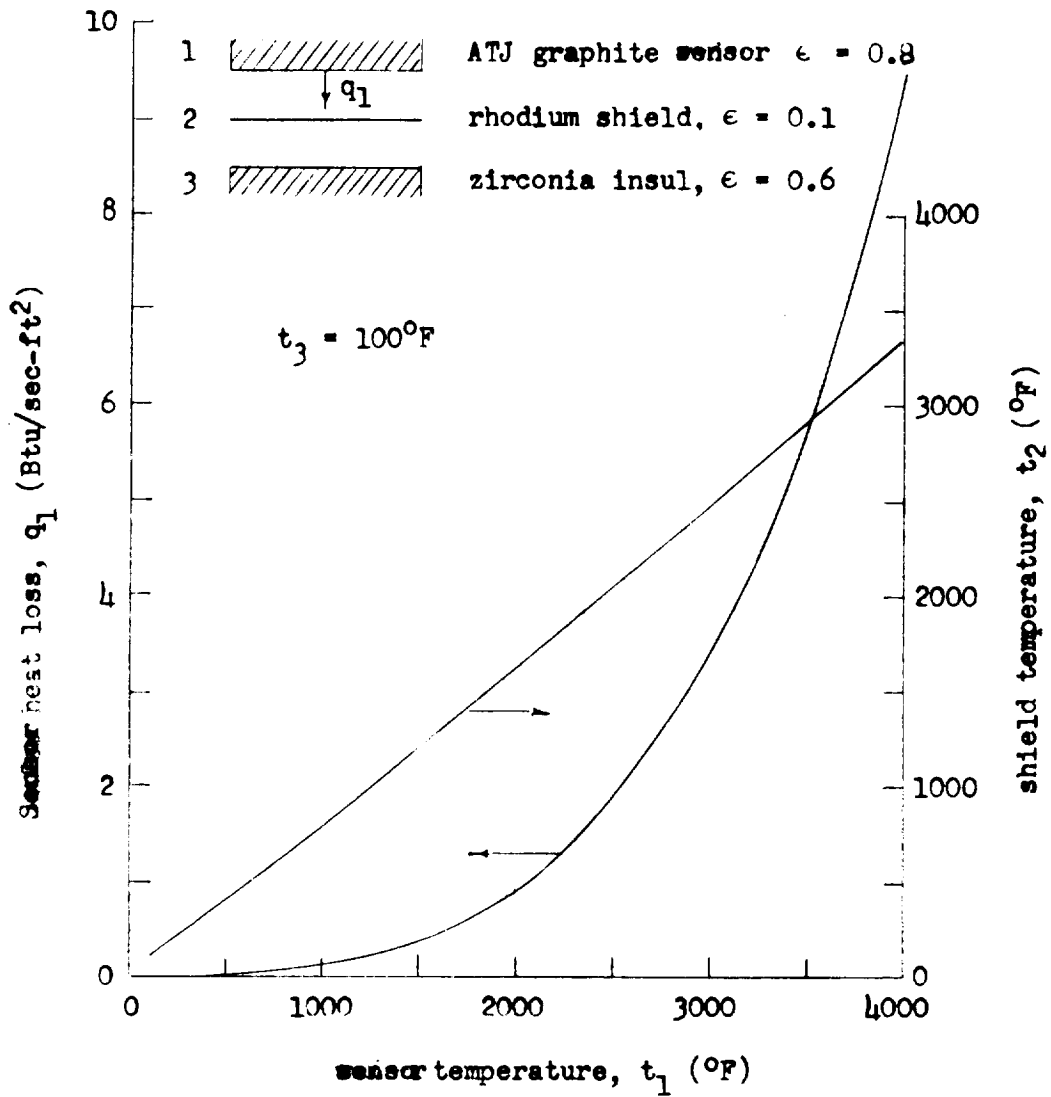
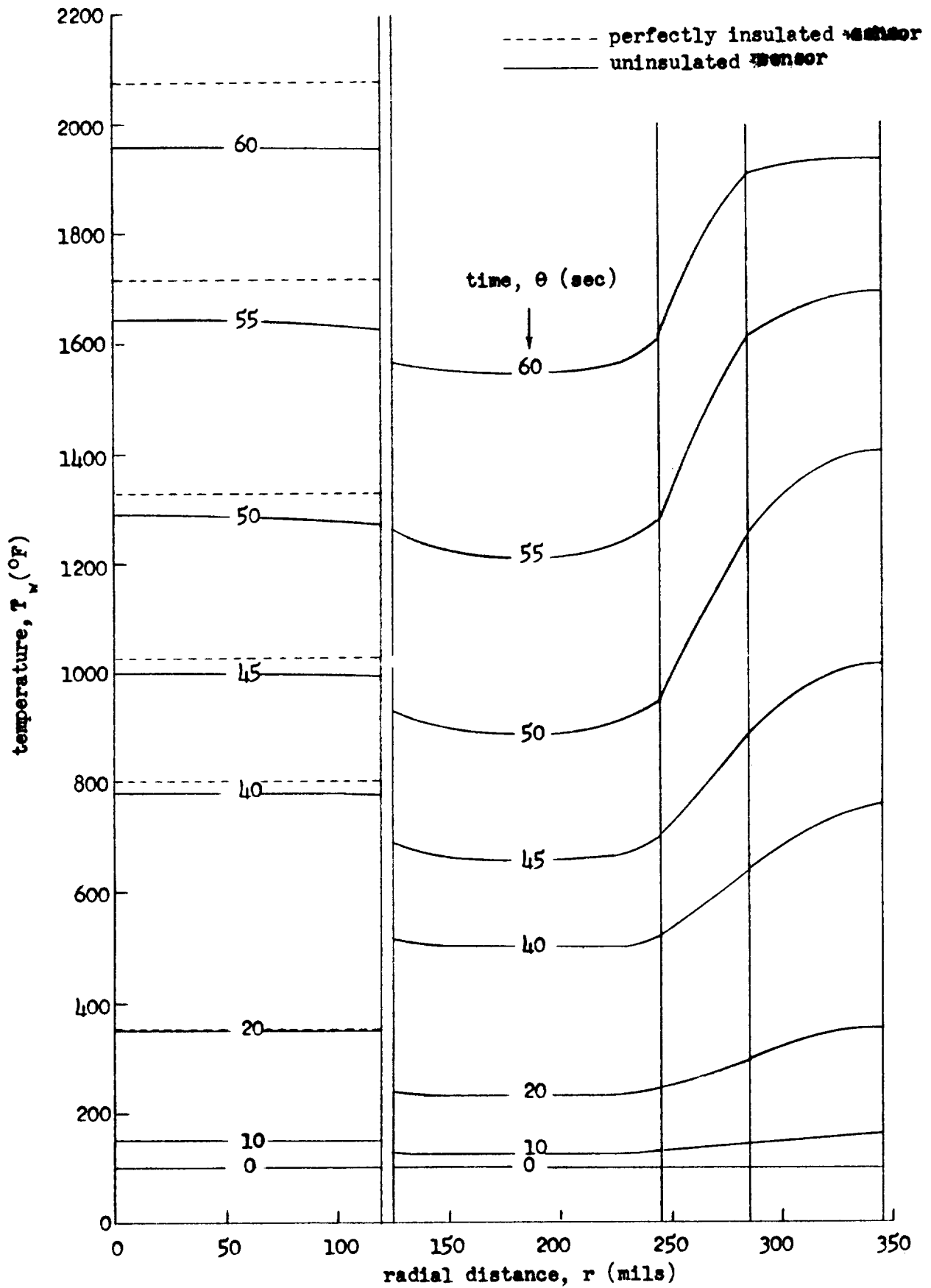


Fig. 3-15 Steady-state effectiveness of rhodium shield.

Fig. 3-16 Instantaneous calorimeter surface temperature distributions.



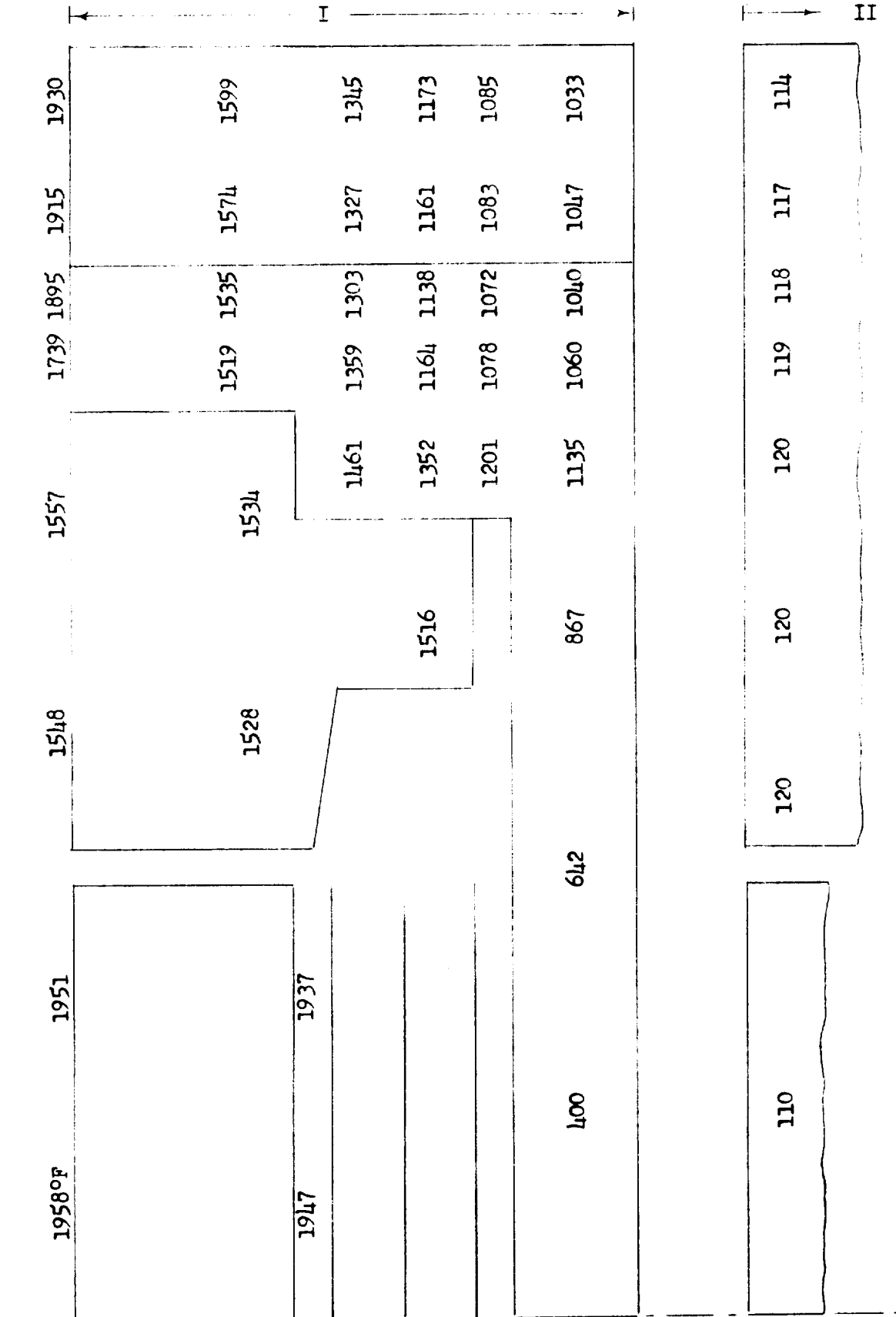


Fig. 3-17 Instantaneous temperature distribution at  $\theta = 60$  sec.

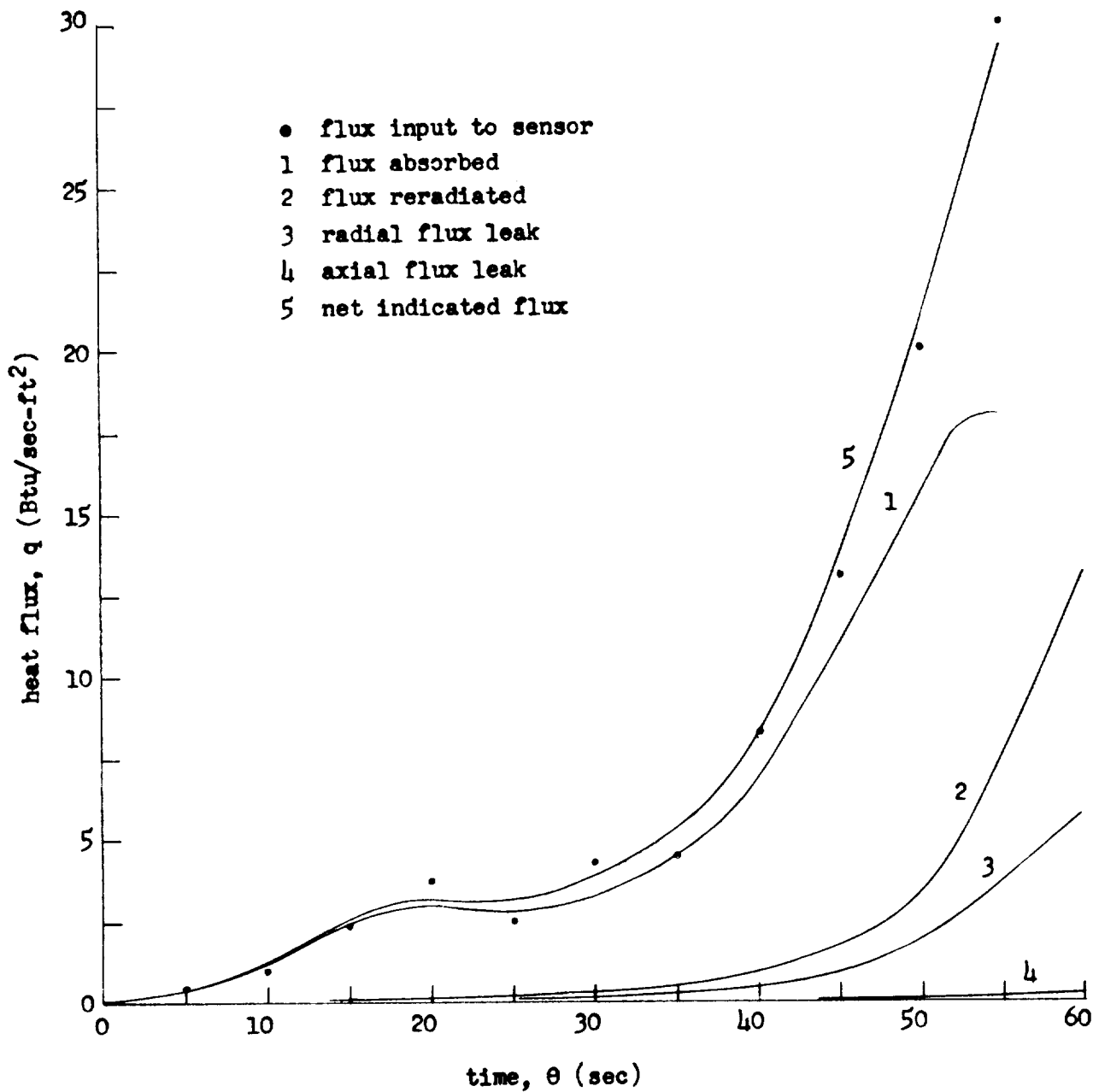
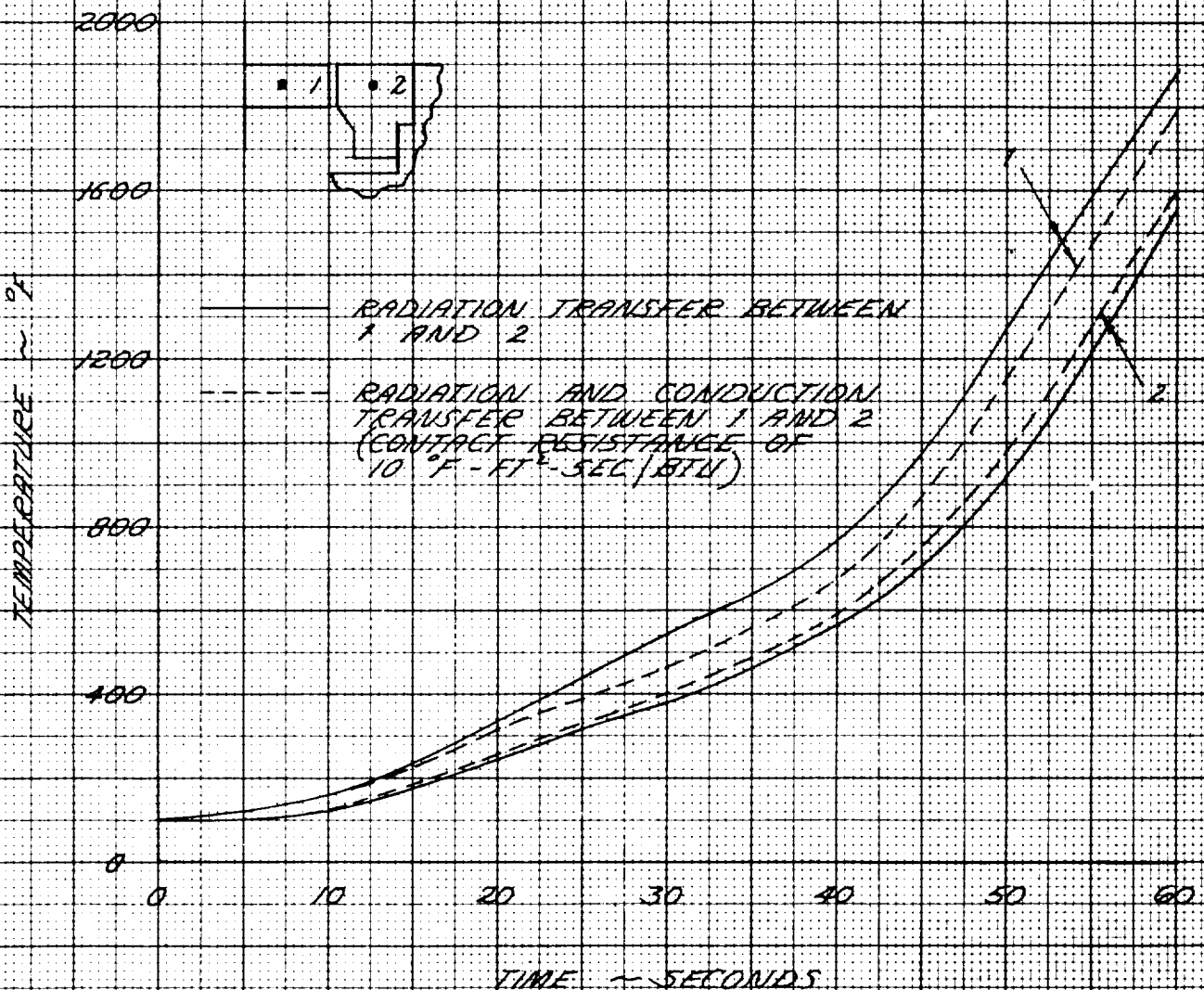


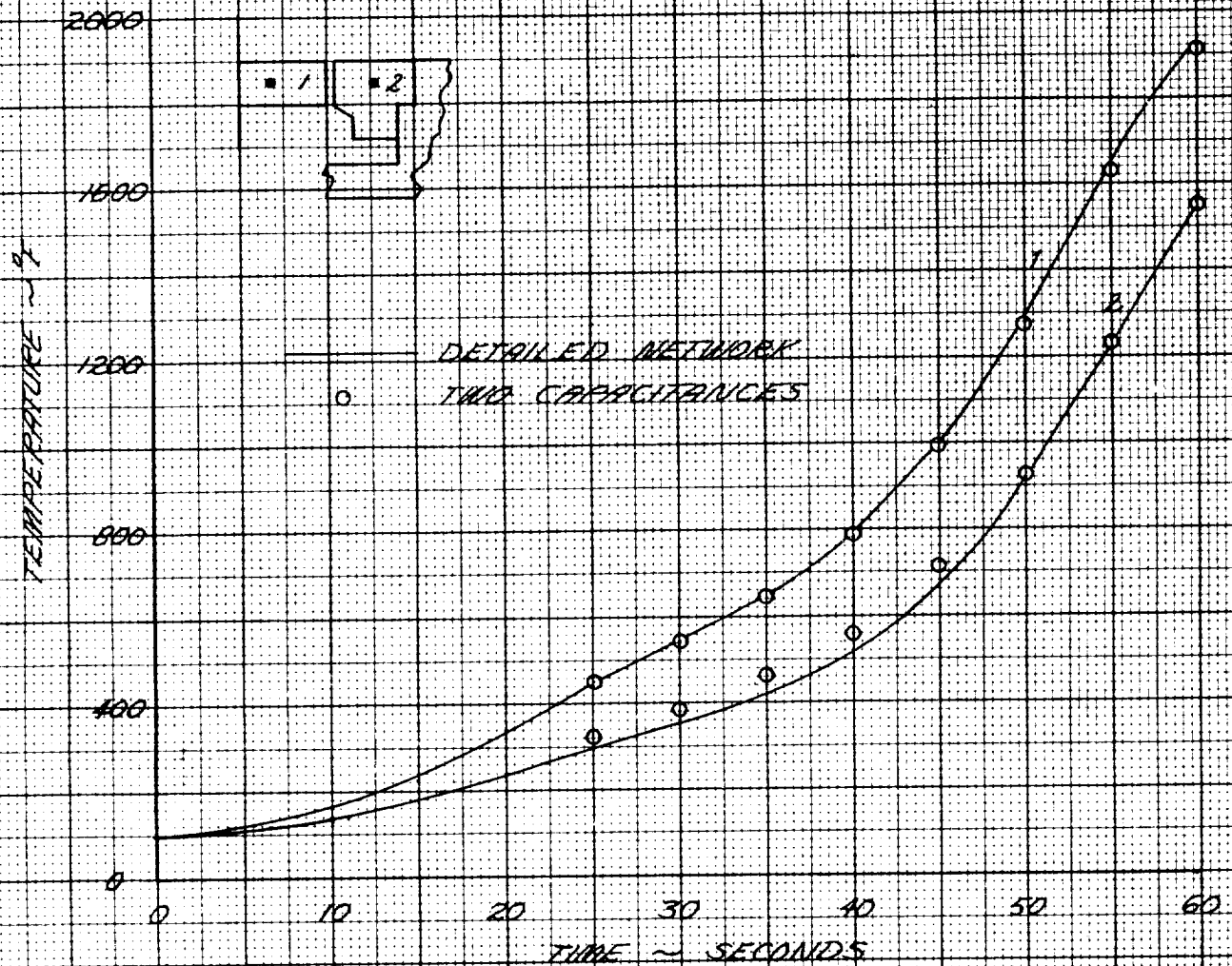
Fig. 3-18 Sensor data reduction.



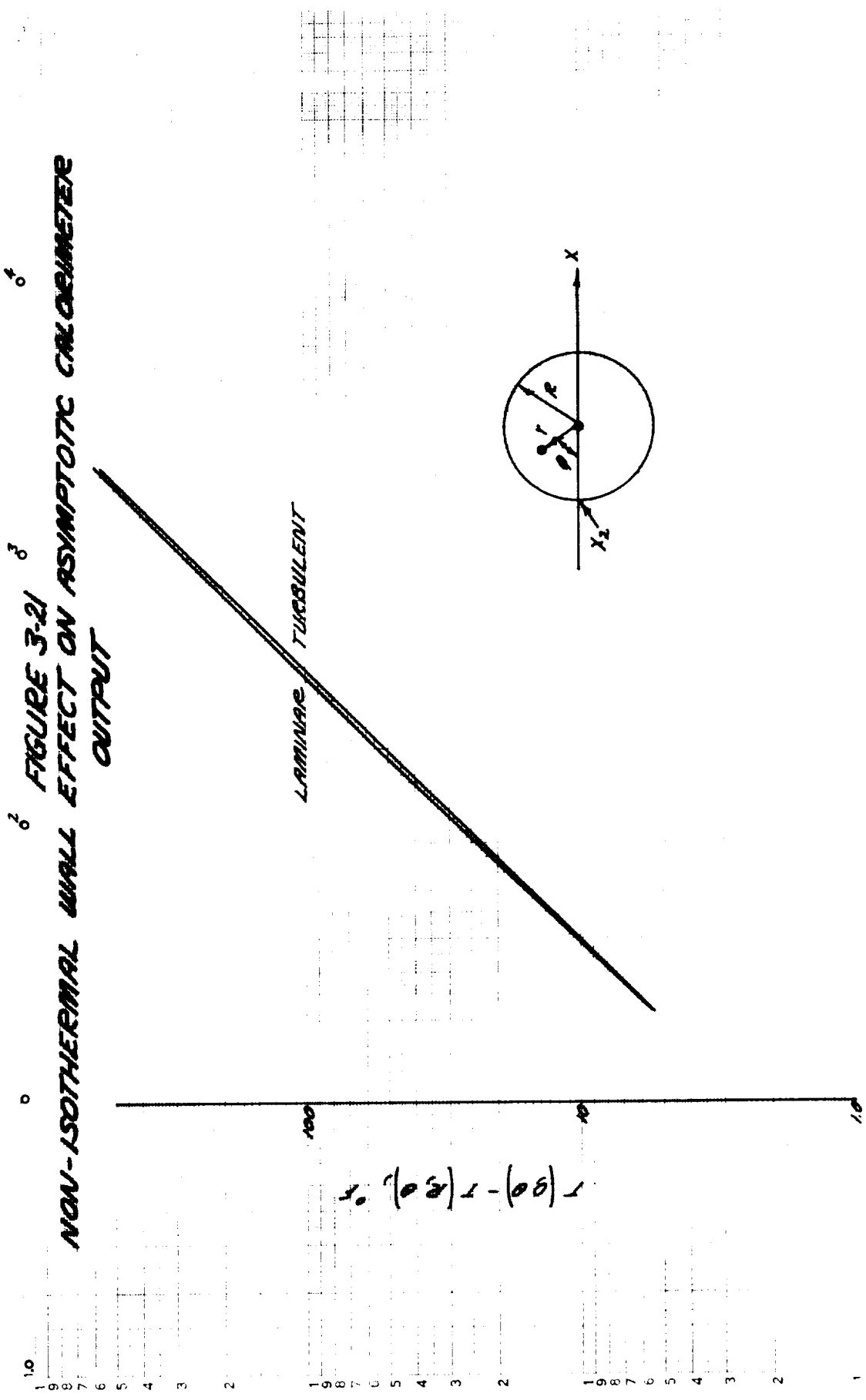
**FIGURE 3-19**  
**INFLUENCE OF SENSOR TABS ON**  
**TEMPERATURE RESPONSE**



**FIGURE 3-20**  
**COMPARISON OF APPROXIMATE AND**  
**DETAILED TEMPERATURE SOLUTIONS**



**NON-ISOTHERMAL WALL EFFECT ON ASYMPTOTIC CALORIMETER OUTPUT**



$$R^2 \frac{h}{K_S} \left( \frac{H_1 - H_2}{x_2 + R - d} \right)^{\beta} = \frac{BR^2}{K_S} \theta F$$

**FIGURE 3-22**  
**NON-ISOTHERMAL WALL EFFECT ON THE HEATING**  
**RATE TO AN ASYMPTOTIC CALORIMETER**  
 $\theta = 0^\circ, 180^\circ$

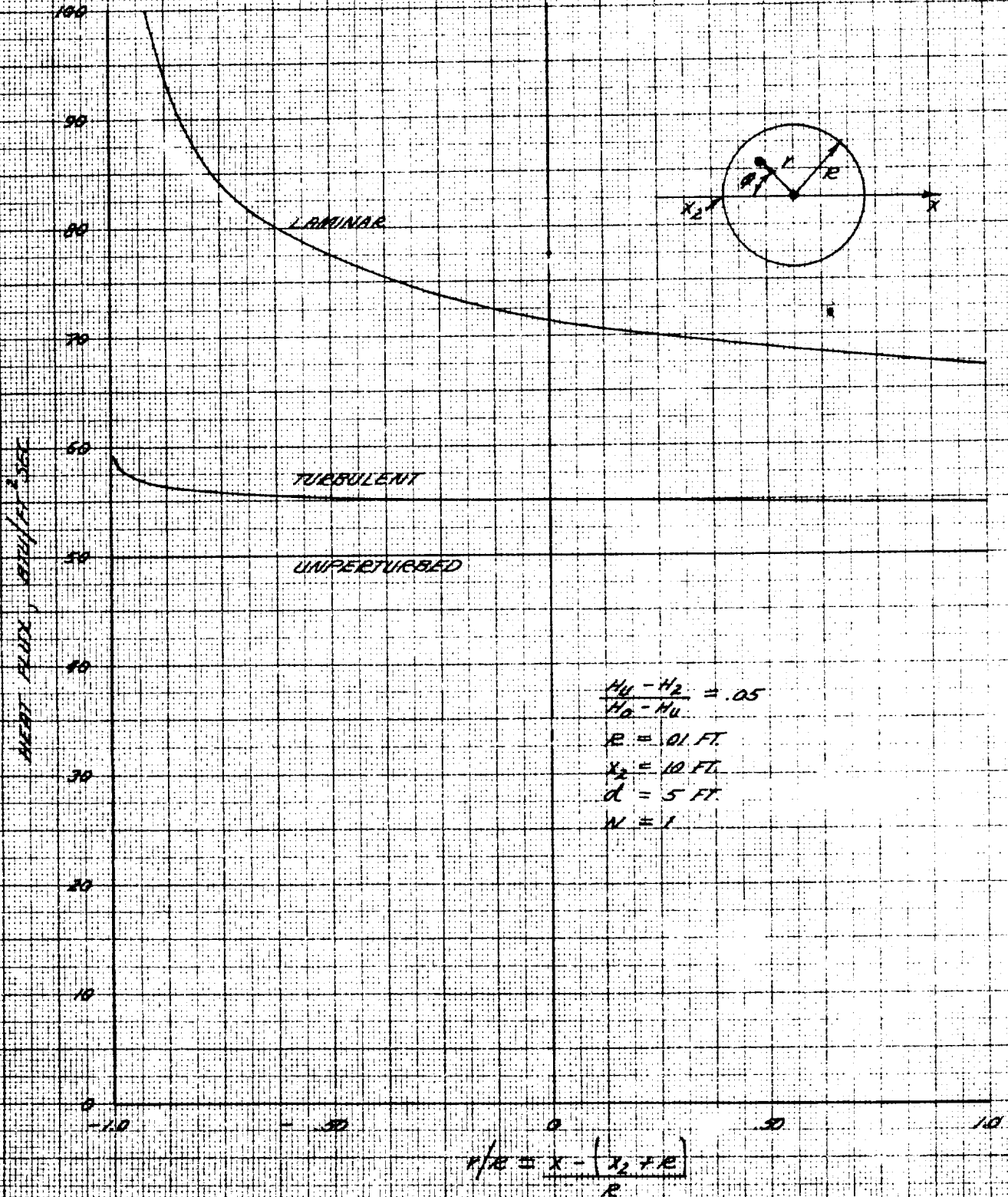


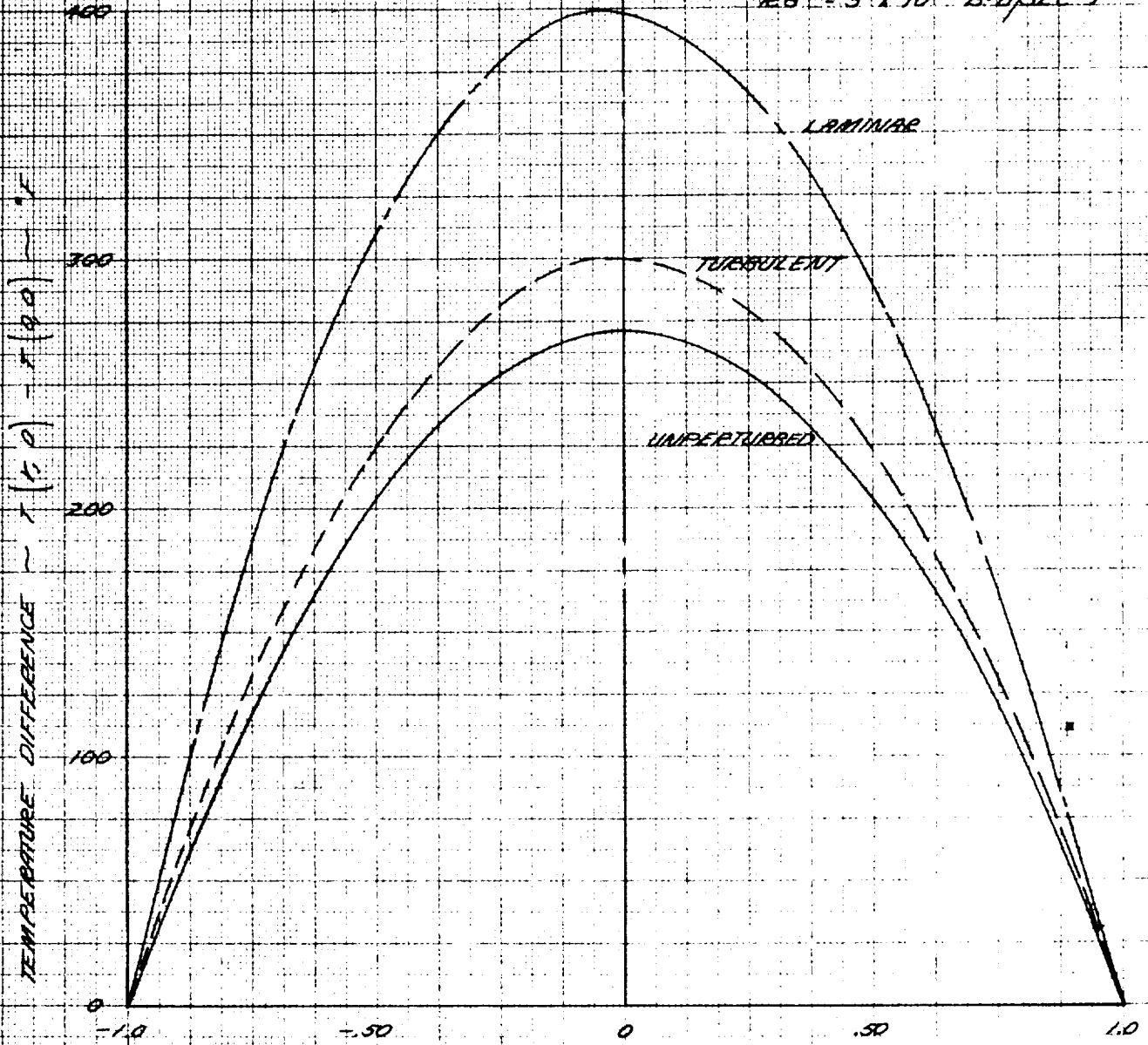
**FIGURE 3-23**

**NON-ISOTHERMAL WALL EFFECT ON THE TEMPERATURE OF AN ASYMPTOTIC CALORIMETER**

$\theta = 0^\circ, 180^\circ$

NOTE: ENVIRONMENT GIVEN IN FIG. 3-22

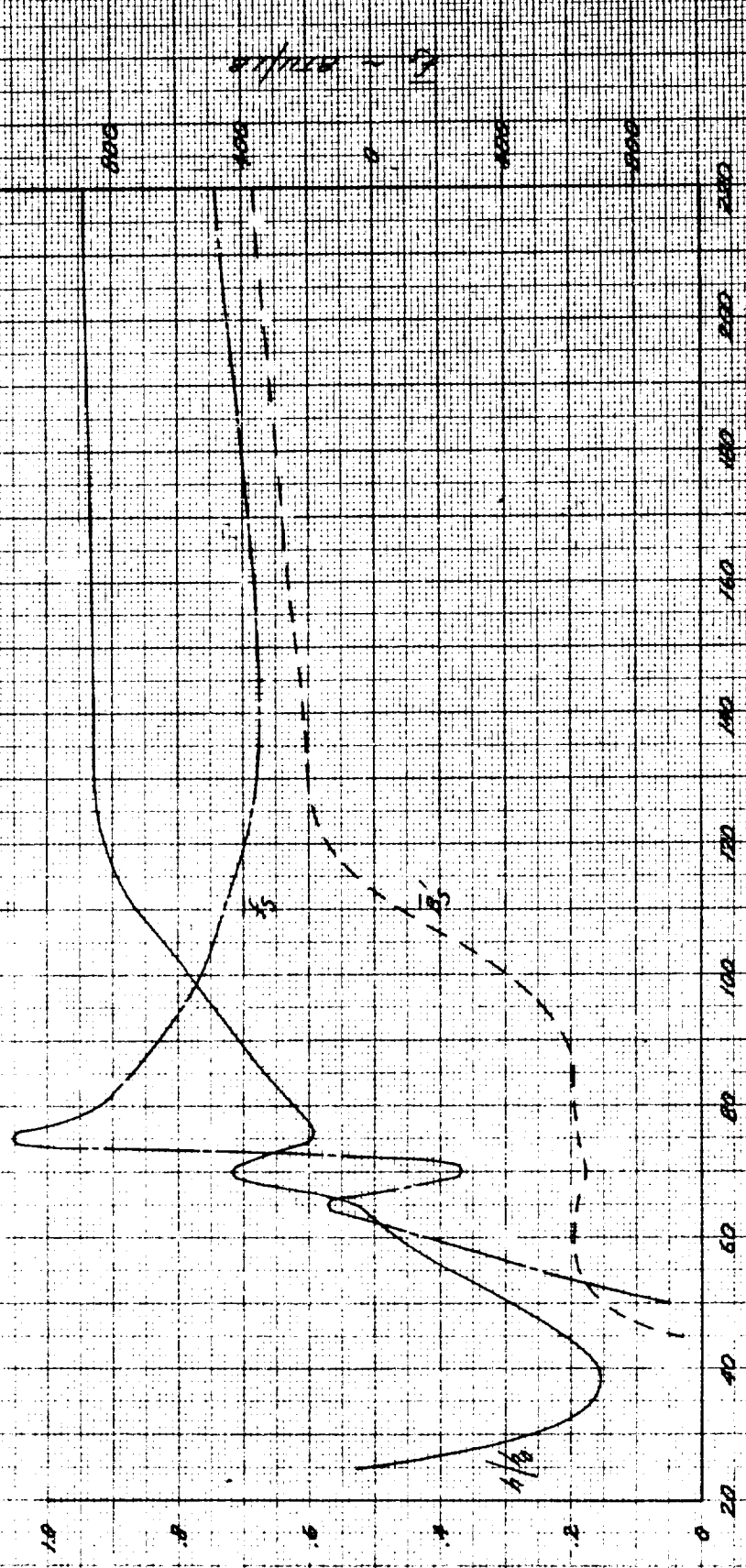
$k_0 = 5 \times 10^6 \text{ BTU/SEC}^\circ\text{F}$



$$x/r = \frac{x - (x_2 + R)}{R}$$

**FIGURE J-24**  
**HEAT SHIELD - SENSOR INTERACTIONS**

$\lambda/\rho_{max} = 0.88$   
 TRANSDUCER EFFECT:  $(\lambda/\rho)_{s}$   
 SURFACE COMBUSTION EFFECT:  $B_s$   
 NON-ISOTHERMAL EFFECT:  $B_n$



TIME FROM 40000 FT - SECONDS

**FIGURE 3-25**  
**CALORIMETER TEMPERATURE RESPONSE**

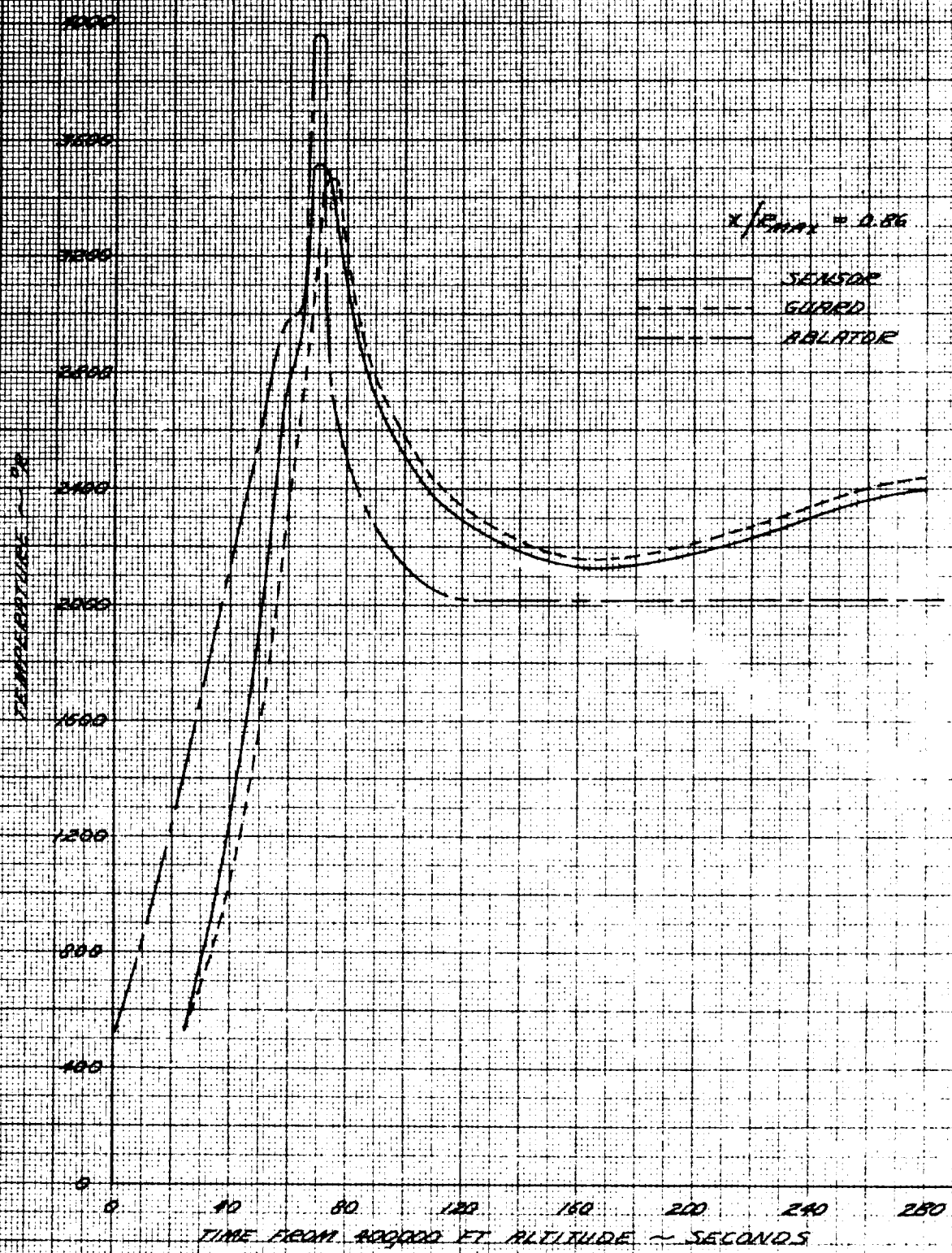
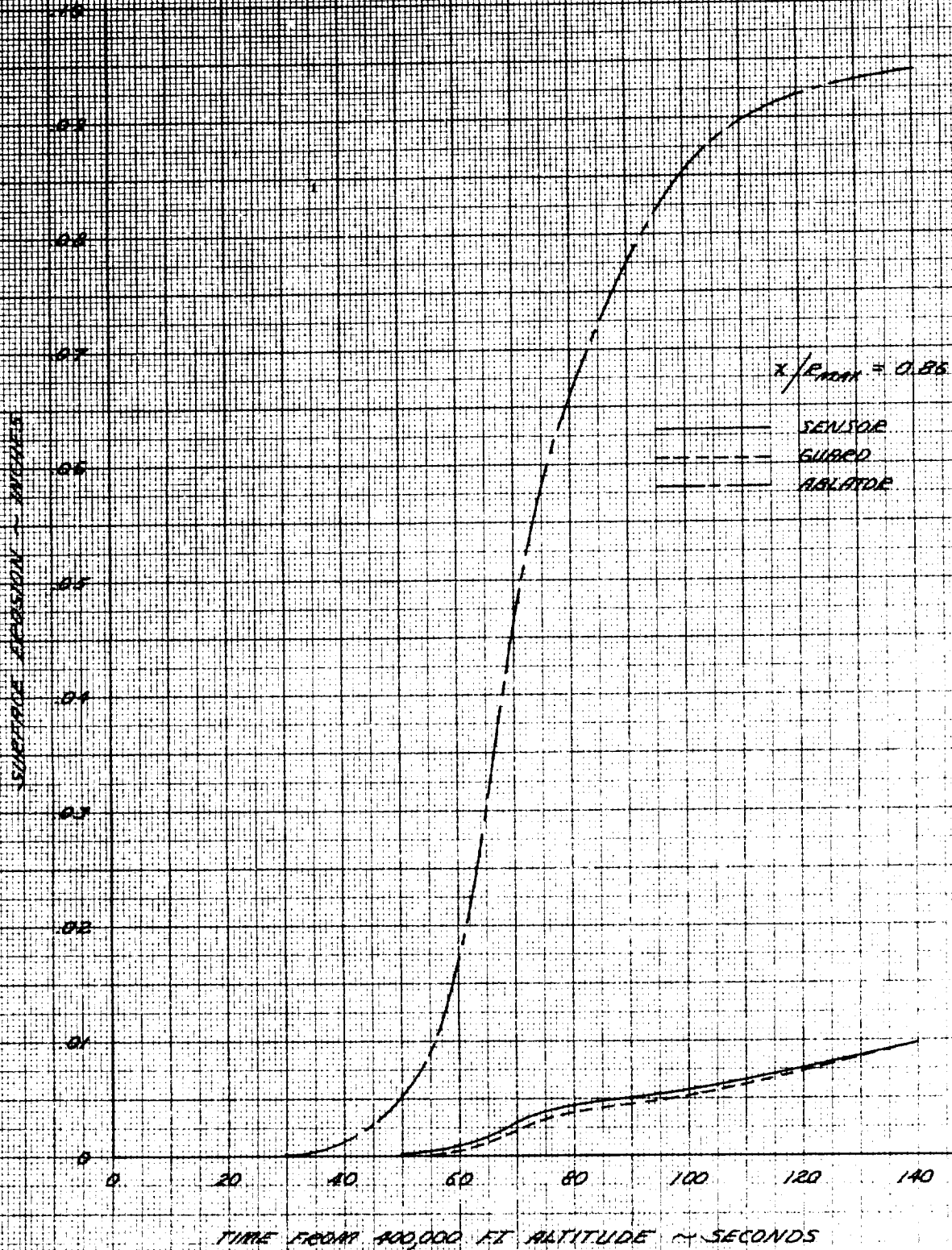
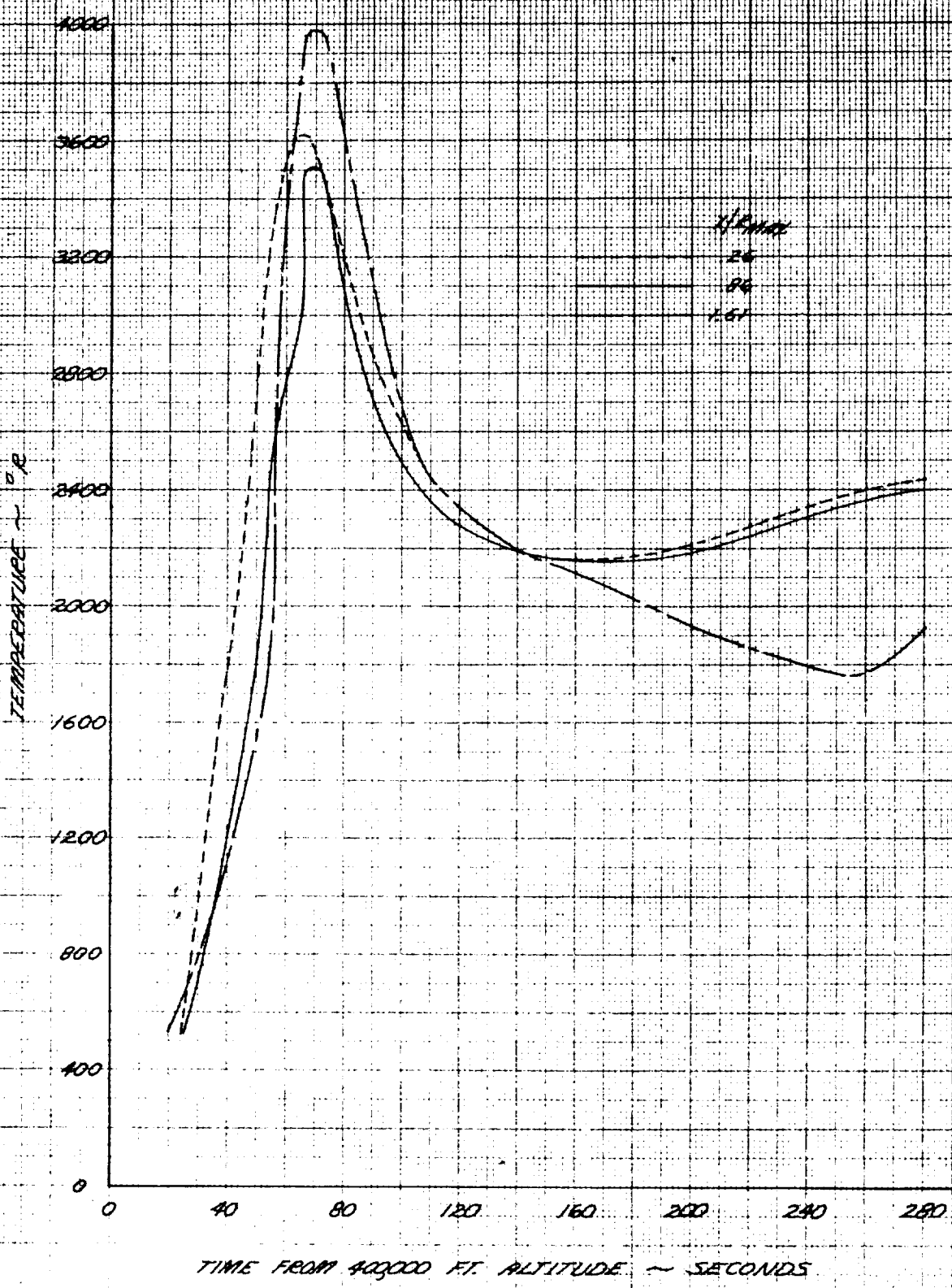


FIGURE 3-26  
SURFACE EROSION





**FIGURE 3-27**  
**SENSOR TEMPERATURE RESPONSE**



**FIGURE 3-18**  
**ASYMPTOTIC CALORIMETER RESPONSE**

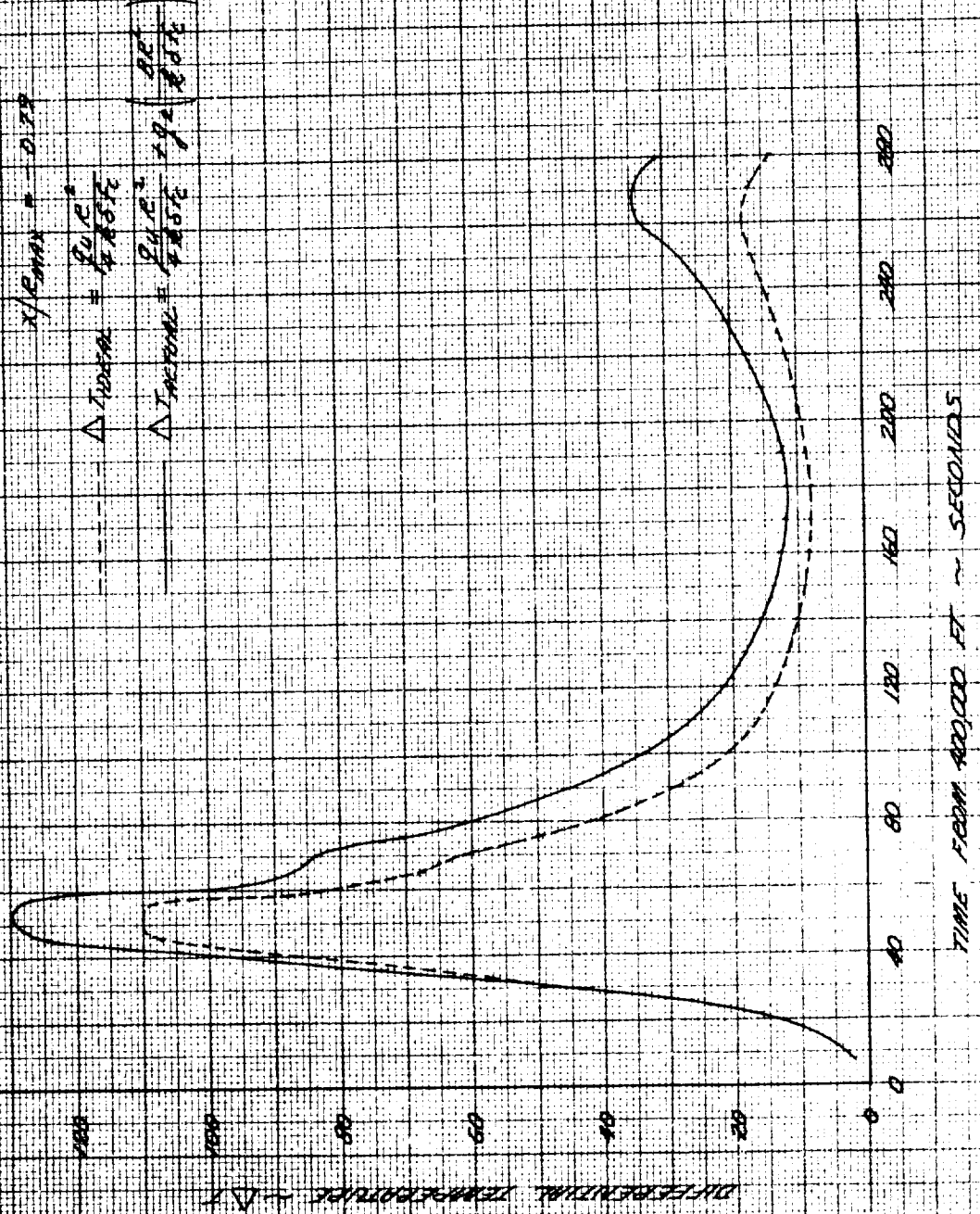
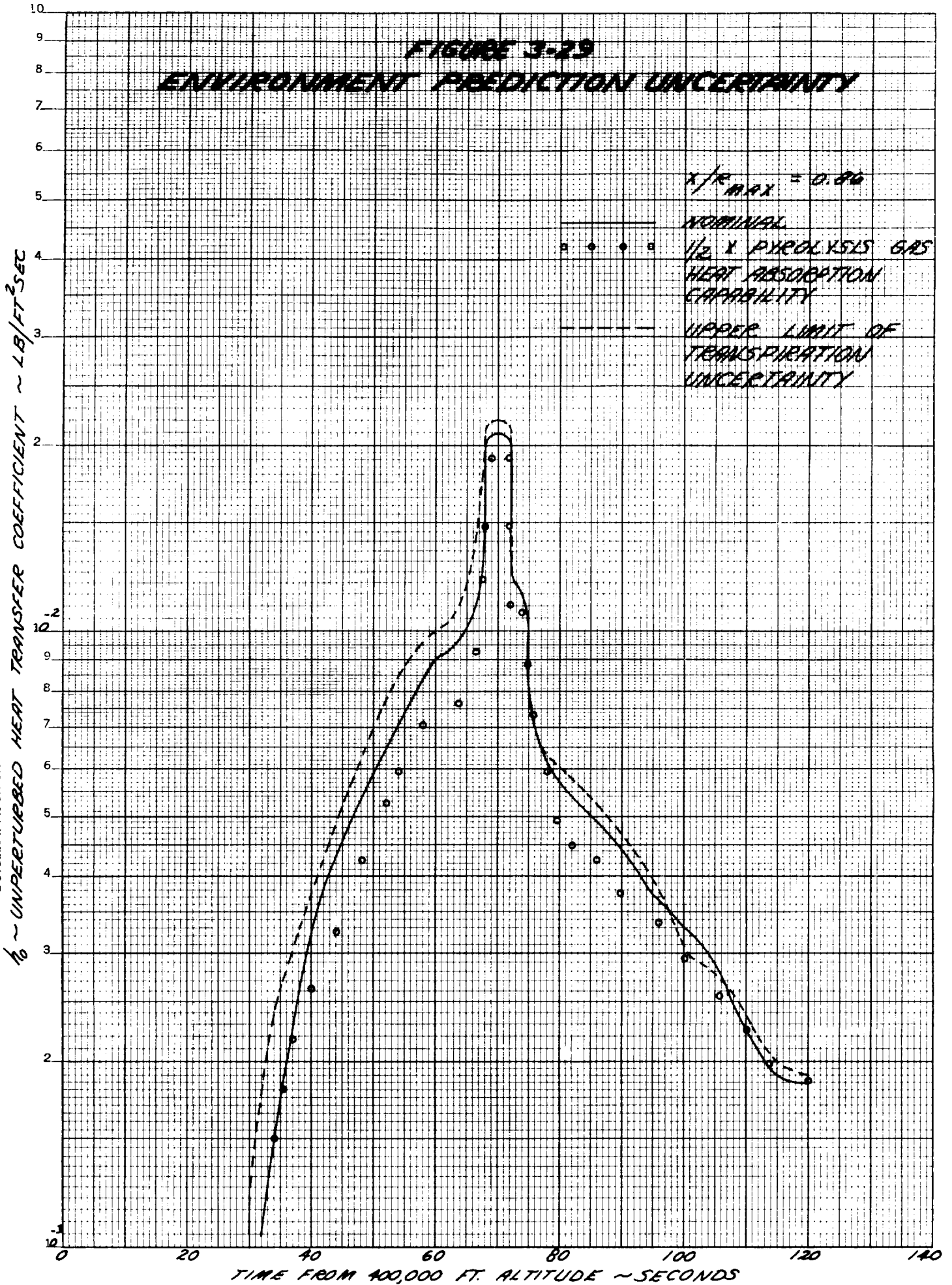


**FIGURE 3-29**  
**ENVIRONMENT PREDICTION UNCERTAINTY**



K-E SEMI-LOGARITHMIC 359-63  
 KEUFFEL & ESSER CO. MADE IN U.S.A.  
 2 CYCLES X 140 DIVISIONS

FIGURE 3-30  
 SENSOR CONVECTIVE HEATING UNCERTAINTY

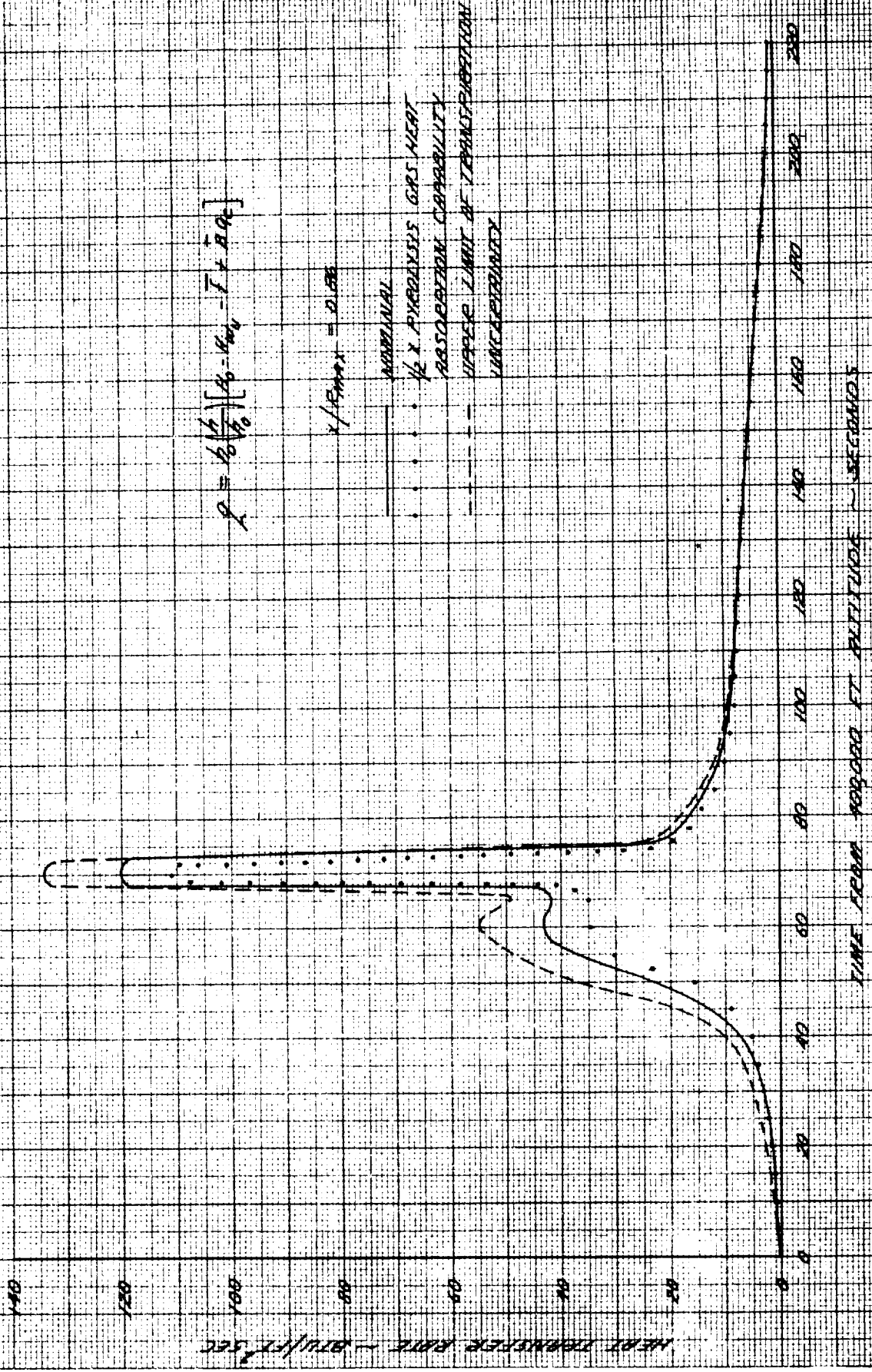


**FIGURE 3-31**  
**SENSOR TEMPERATURE UNCERTAINTY**

